Exploring electronic delocalization in porphyrin oligomers

Michael Jirásek

St Peter’s College

University of Oxford

A thesis submitted for the degree of

Doctor of Philosophy

Michaelmas 2019

Acknowledgement

Firstly, I would like to thank Prof. Harry L. Anderson for accommodating me in his group and for his constant support and time that he has dedicated to me over the years of my DPhil study.

I would like to thank all former and current Part II, DPhil and postdoctoral researchers who I have worked with during the last three years for creating a great atmosphere – Alistair, Andreas, Andrew, Anjul, Anne, Bart, Boom, Cécile, Connor, Dan, Denis, Henrik, Hiromu, Hua-Wei, Ibrahim, Isaac, Isabel, James, Jeff, Jibin, Joe, Jonathan, Julia, Kate, Kenny, Keith, Kristina, Lara, Lorel, Martin, Michel, Nun, Pernille, Przemek, Renee, Sabine, Sebastian, Sili, Steffen, Stuart, Takayuki, Tom, Virginia, Wenjun, Will, and Yaoyao.

Specifically, I would like to thank Dr. Martin Peeks who advised me many times on computational issues. Special thanks belong to Dr. Michel Rickhaus for his great academic mentoring and the time we spent together during many NMR oxidation experiments. I would like to thank Henrik Gotfredsen, Keith Andrews, James Thomas and Lorel Scriven for proof-reading this thesis for me and providing useful comments on it. Also, I would like to thank my summer student Hiromu Kubo, who dedicated an intense two months of work with me.

I would like to acknowledge the Arc support team for their prompt troubleshooting of all problems regarding the computational work I carried out on the arcus server. Namely Mrs. Tina Friedrich, Mrs. Yassamine Mather and Dr. Steven Young.

I would like to thank the whole ULTRA team in the Central Laser Facility for their dedication and general help with the ultrafast spectroscopy experiments. Namely Dr. Gregory M. Greetham, Dr. Igor V. Sazanovich, Dr. Paul M. Donaldson, Dr. Michael Towrie and Dr. Anthony W. Parker

I am very grateful to Oxford University for providing me a Scatcherd European Scholarship, generously supporting me during my DPhil study.

I thank Prof. Tim W. Claridge and Dr. Nader Amin from whom I received a lot of help during my NMR experimental campaign.

Finally, I would like to thank to my wife Veronika for the constant support during my studies and to our two sons who made our time in Oxford extraordinary.

Abstract

The general theme of this thesis is a study of electronic communication within porphyrin oligomers.

Chapter 1 reviews briefly the porphyrins: their chemical structure, advantages of their use in supramolecular chemistry and some of their basic photo-physical properties.

Chapter 2 discusses a study of the origin of an unusual intensity of certain IR bands in two porphyrin oligomer cations. The study uses a polarised time-resolved IR (TR-IR) to understand relative orientation of the intensified vibrations, corroborated with DFT calculations. Coupling between individual IR modes and with the electronic band is documented by 2D-IR spectroscopy and further understanding of the system dynamics upon excitation is understood thanks to the detail kinetic analysis.

Chapter 3 focuses on aromaticity. The basis of aromaticity as a concept is reviewed and examples of theoretical and experimental investigations of aromaticity of some π-conjugated species is presented. The experimental part discusses the preparation of large globally (anti)aromatic species *via* oxidation of the otherwise globally non-aromatic nanorings and its evaluation with NMR. All these studies are supported with DFT calculations corroborating the correct interpretation.

Chapter 4 discuses the design and synthesis of a large Möbius-strip-shaped porphyrin nanoring. Firstly, a brief overview of the concept of Möbius aromaticity is reviewed, followed by examples of various designs and reported syntheses of Möbius molecules.

This is followed by the design and synthesis and study of two novel nanorings, one which is suspected of adopting Möbius confirmation.

Supplement to Statement of Authorship

Chapter 2 discusses the ultrafast spectroscopy study performed in the Rutherford Appleton Laboratory, in the Central Laser Facility (CLF). The experiments were carried out by the author together, in very close collaboration, with another DPhil student William Kendrick, with equal contribution to the work. William Kendrick also carried out the kinetic analysis of the 2D-IR (LIFETime – based) spectra evolution given in this chapter.

The experimental setup in the CLF was built on demand by CLF scientists: Dr. Gregory M. Greetham (TR-IR, polarization experiments), Dr. Igor V. Sazanovich (TR-IR, polarization experiments), Dr. Paul M. Donaldson (2D-IR) and Dr. Michael Towrie (2D-IR). The work in the CLF was supervised by Dr. Anthony W. Parker. The project was designed by Prof. Harry L. Anderson, Dr. Antony W. Parker and Dr. Martin D. Peeks. DFT calculations presented were initiated (frequency calculation of ***l*-P2**$^{+\bullet}$) by Dr. Martin D. Peeks and further developed by the author.

In **Chapter 3**, all NMR experiments were carried out by the author, some of them in collaboration with Dr. Michel Rickhaus. The correct setup of the NMR experiments was consulted with Prof. Tim W. Claridge and Dr. Nader Amin.

Synthesis of ***c*-P6[e$_6$]·T6***, ***c*-P6[be$_5$]·T6*** and ***c*-P8[e$_8$]·(T4*)$_2$**, was carried out by Dr. Michel Rickhaus and Dr. Lara Tejerina. Compounds ***c*-P5[b$_5$]·T5** and ***c*-P7[b$_7$]·T7** were synthesized by Dr. Lara Tejerina. Synthesis of ***c*-P6[b$_5$e]·T6** was carried out by Dr. Hua-Wei Jiang and Dr. Renee Haver. Novel templates **T6e**, **T6ef** and **T6f** were designed by the author in collaboration with Dr. Michel Rickhaus and were synthesized by Dr. Michel Rickhaus and Dr. Henrik Gotfredsen.

In **Chapter 4**, part of the synthesis was repeated by a talented summer student Hiromu Kubo under the authors supervision.

Content

List of Abbreviations

AFM	Atomic force microscopy
Ar	Aryl
b	Broad
CV	Cyclic voltammetry
COSY	Correlation spectroscopy
CPDIPS	Cyanopropyl(di*iso*propyl)silyl
CPP	Cyclo-*para*-phenylene
d	Doublet
Da	Dalton (units)
DABCO	1,4-diazabicyclo[2.2.2]octane
dba	Dibenzylideneacetone
DDQ	2,3-Dichloro-5,6-dicyano-*para*-benzoquinone
DFT	Density functional theory
DOSY	Diffusion ordered spectroscopy
EM	Effective molarity
EXSY	Exchange spectroscopy
FT-IR	Fourier-transform infrared spectroscopy
GPC	Gel permeation chromatography
HF	Hartree-Fock
HMBC	Heteronuclear multiple-bond correlation spectroscopy
HOESY	Heteronuclear Overhauser enhancement spectroscopy
HOMO	Highest occupied molecular orbital
HSQC	Heteronuclear single-quantum correlation spectroscopy
LUMO	Lowest unoccupied molecular orbital
LR	Long range
m	Multiplet
MALDI	Matrix-assisted laser desorption ionisation
MM	Molecular mechanics
MW	Molecular weight
NBS	*N*-Bromosuccinimide
NIR	Near-infra-red
NMR	Nuclear magnetic resonance
NOE	Nuclear Overhauser effect
NOESY	Nuclear Overhauser effect spectroscopy
OD	Optical density
Ph	Phenyl
Py	Pyridine
s	Singlet
SEC	Size exclusion chromatography
t	Triplet
TBAF	Tetrabutylammonium fluoride
TBAP	Tetrabutylammonium hexafluorophosphate
TD	Time-dependent
TFA	Trifluoroacetic acid
THF	Tetrahydrofuran
THS	Trihexylsilyl
ToF	Time of flight
TIPS	tri*iso*propylsilyl
TLC	Thin layer chromatography
TOCSY	Total correlation spectroscopy
TR-IR	Time-resolved infrared spectroscopy
UV	Ultraviolet
vis	Visible
r.t.	Room temperature
QY	Quantum yield

1

Introduction

1.1. Porphyrins

Porphyrins are omnipresent in nature, as well as in many synthetic laboratories, where they are studied for their interesting (photo)physical properties and supramolecular behaviour.[1] Chemically, the basic porphyrin (**1.1**) is a cyclic molecule consisting of four methine-bridged pyrroles. Numerous structural motifs and porphyrin modifications have been described, both natural and synthetic (**Figure 1**).[1,2] Porphyrin-like compounds can be decorated with functional groups at various positions,[3–6] be partly saturated (e.g. chlorins, (iso)bacteriochlorines),[7–9] or exhibit various structural isomerism (e.g. hemiporphycene, porphycene).[10–21] Part(s) of the molecule can be replaced with heteroatoms (e.g. phthalocyanines).[22–28] Moreover, the whole cycle can be expanded (e.g. [26]hexaphyrin, [36]octaphyrin),[29–36] or contracted (subphthalocyanines).[37–39] Every modification introduces new properties and represents a handle for tuning the properties for a specific purpose.

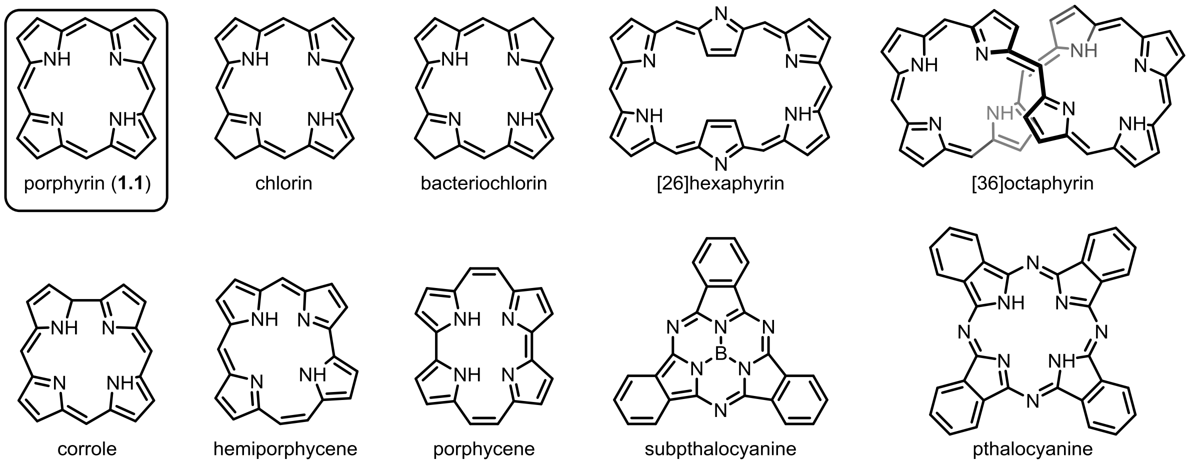

Figure 1: Structure of the basic porphyrin (**1.1**) and selected isomers and analogues.

An important feature of the porphyrins is their capability of binding a metal cation in the cavity by coordinating the metal to the pyrrolic nitrogens, acting as a tetradentate ligand (**Figure 2**).

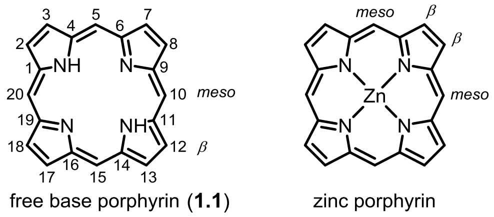

Figure 2: Structure of the free-base porphyrin **1.1** (left) and a zinc porphyrin complex (right) together with the standard numbering and labelling nomenclature established in the literature.

---

[1] Search on 26th of August 2019 using porphyrin bare scaffold with the widest similarity criteria (keeping the core connectivity) yielded 53,666 individual porphyrin based compounds described in 38,953 documents.

In literature, over 65 different metals have been described as being inserted into the porphyrins, also often capable of adopting more than one oxidation state.[2,40–43] Depending on the size of the metal, its fit in the cavity, and its degree of interaction and electronic mixing with the porphyrin electrons, the metal can significantly affect the photophysical and supramolecular behaviour of the porphyrin, opening up another dimension to the modification of porphyrin.

Synthetically, insertion of metals is usually carried out by simply reacting the free-base porphyrin with an appropriate metal salt in a polar organic solvent.[2] The metal brings an additional function to the structure and modulates both the chemical and photophysical properties of the porphyrin.

One function introduced by metal insertion can be the capability of coordination to an additional ligand(s) in a very defined geometry and/or modulation of the metal's properties by the presence of any ligand.

The coordination capability of the various metals significantly differ. For example, in the case of an insertion of a Pd^{2+} cation, the palladium lacks any affinity toward additional ligands.[44] The opposite behaviour is observed, for example, in magnesium porphyrins. The Mg^{2+} cation in the porphyrin is capable of coordination to two axial ligands and such six-coordinated Mg^{2+} complexes have been documented.[45]

In the case of the zinc porphyrins, generally a strong affinity toward one axial ligand is observed. Interestingly, such complex with one axial ligand possesses only negligible affinity toward a second ligand. Zinc-porphyrins with 6-coordinated zincs have only been described in the solid states,[46,47] or in the well preorganised systems forcing the ligands to hover over the 'right' place.[48]

The binding strength of the ligand is quantifiable with an equilibrium constant of the binding K_f. For pyridine binding in the non-polar solvents, the binding constant is $K_\mathrm{f} \sim 10^4\ \mathrm{M}^{-1}$ for the first binding. This value is interpretable such, that if one equivalent of the pyridine is present, at a classical chemical concentration (~units of mM), the majority of the porphyrin is associated with the pyridine. Contrary to that, the equilibrium binding constant of the second binding is $K_\mathrm{f} = \sim 0.1–1\ \mathrm{M}^{-1}$, which means that even in neat pyridine, the majority of the porphyrins might not be associated with a second axial ligand.[49–51]

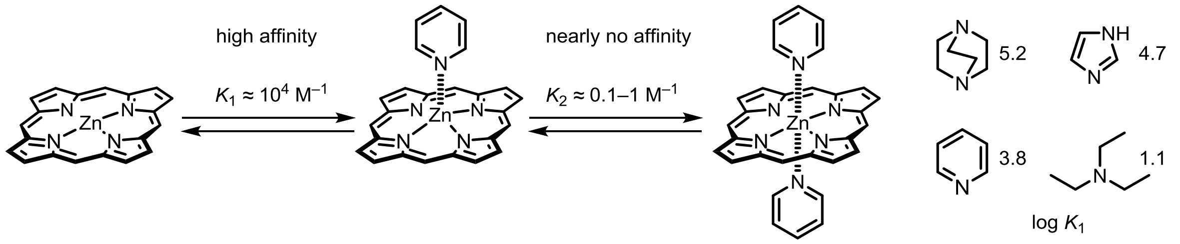

Figure 3: (left) Zinc porphyrins exhibit strong affinity toward one axial ligand, but not for the second one. (right) Association constants (in benzene or toluene) of the first binding process of porphyrin with nitrogen-based ligands.[49–51]

The binding strength of the ligand toward the porphyrin correlates with the ligand basicity, although additional effects may play a more important role.

Such single point strong binding in a preferred axial coordination is a unique feature, that makes the zinc porphyrins perfect building blocks for designing supramolecular assemblies.[52–54]

1.2. Use of porphyrins in supramolecular chemistry

Various strategies have been developed to construct large, cyclic, π-conjugated architectures. The simplest one is to let pre-bent building blocks react together and hope cyclic products will be formed. This approach can yield macrocycles of various sizes, which can be advantageous if, for example, a series of the macrocycles is to be studied. The drawback is that the only way to change the product distribution is to change the substrate rather than the reaction conditions.

A very prototypical example of this synthetic strategy is the statistical synthesis of large cycloparaphenylenes (**CPPs**) by reacting pre-bent building blocks, decorated with iodo- and boronic ester functionalities, using Suzuki coupling conditions (**Figure 4**).[55]

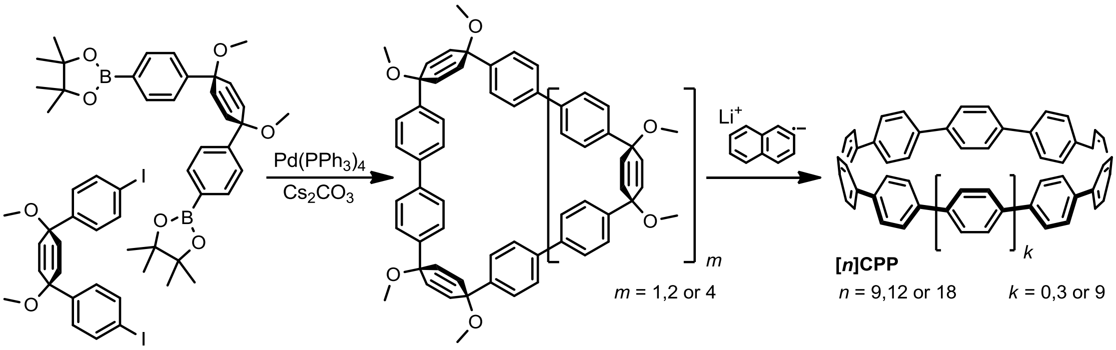

Figure 4: Synthesis of strained cyclo-para-phenylenes carried out by subjecting pre-bent phenylene precursors to statistical Suzuki coupling conditions followed by re-aromatisation.[55]

If a different distribution of macrocycles is required, either the monomer building block has to be modified or a whole linear oligomer precursor has to be built.[56–59] Alternatively, the coupling has to be facilitated *via* a conceptually different method.[60–62]

Equally famous π-conjugated systems to the **CPPs** are the oligothiophenes, which are interesting synthetic targets for their optical and electrochemical properties.[63–68] Several approaches toward giant cyclic oligothiophenes have for example been presented by Bäuerle,[69,70] Oda,[71] Iyoda,[72,73] Mayor[74] and many others. The syntheses have mainly relied on the random, substrate-based cyclisations using various homocoupling conditions (**Figure 5**).

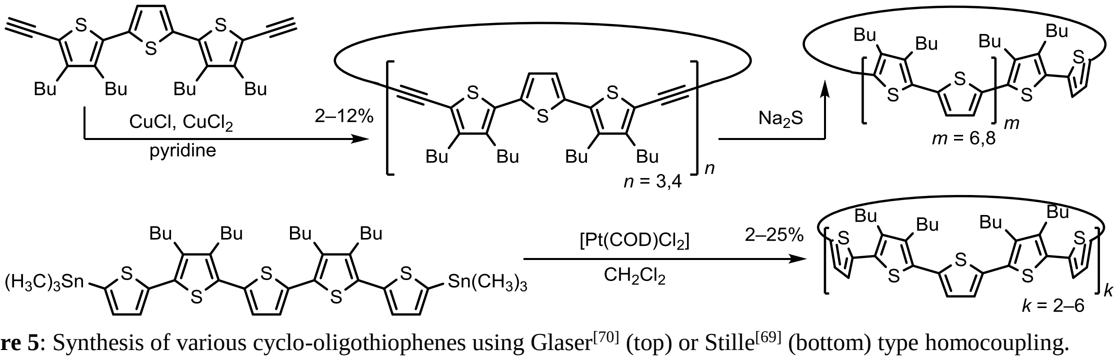

Figure 5: Synthesis of various cyclo-oligothiophenes using Glaser[70] (top) or Stille[69] (bottom) type homocoupling.

Similarly, the condensation of pyrrole-containing building blocks with aldehyde functionalities also allowed for the construction of the large porphyrinoid, hexadecaphyrin (**Figure 6**).[75]

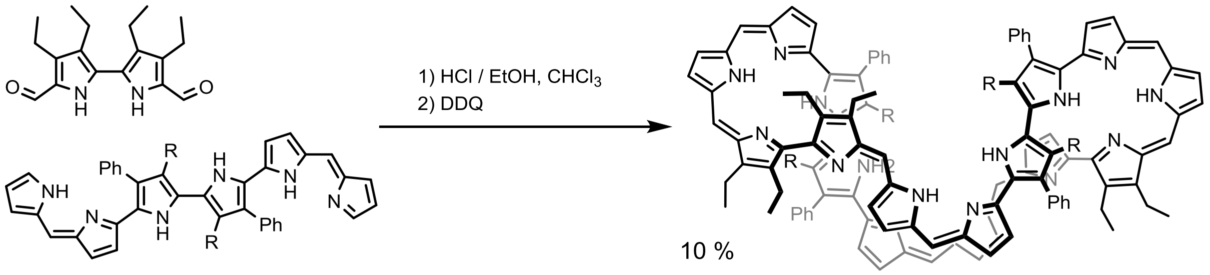

Figure 6: Synthesis of the large hexadecaphyrin. R = –CO_2Et.[75]

Another interesting giant system was presented by Osuka.[76] The authors constructed large, porphyrin containing systems *via* oxidative homo-coupling, forming meso—meso linked porphyrin macrocycles. The cyclisation is geometrically predefined by the 1,3-phenylene linker, dictating a hexagonal shape, however, causing a π-electron deconjugation of the whole macrocycle (**Figure 7**).

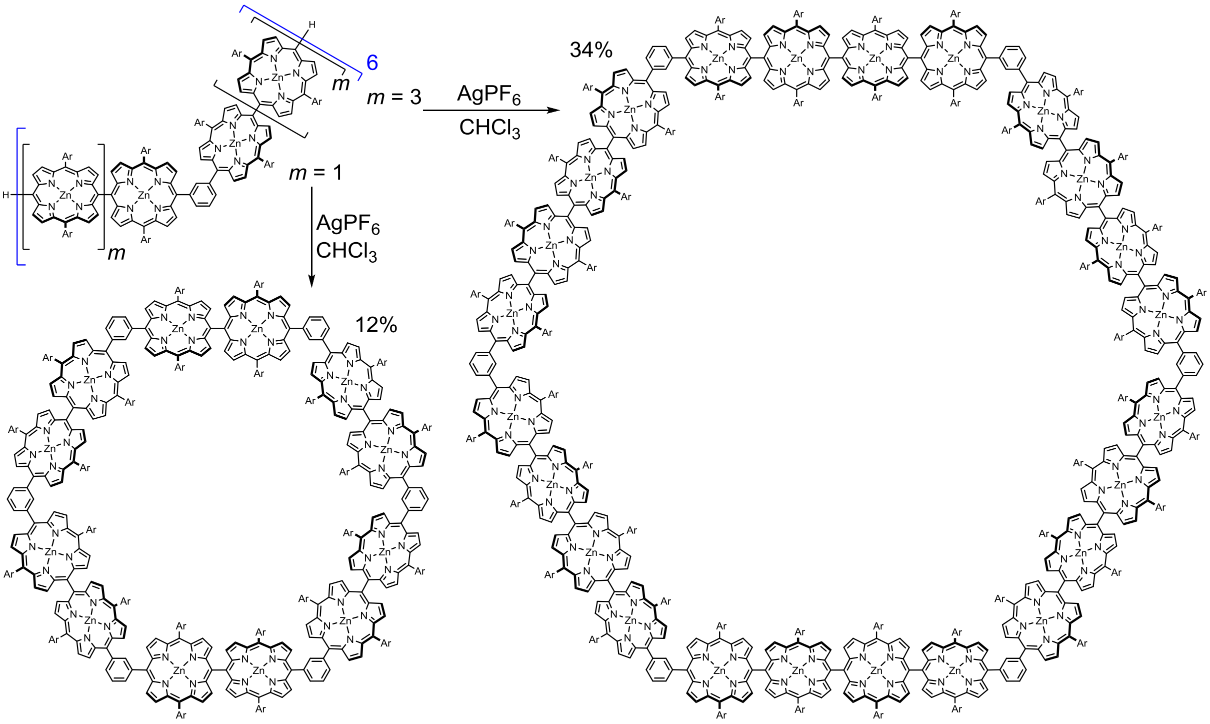

Figure 7: Synthesis of large porphyrin containing macrocycles. Ar = *para*-dodecyloxyphenyl.[76]

A good example of a cyclisation dictated by the substrate is Yamashita's synthesis of a π-conjugated square porphyrin dodecamer (**Figure 8**). The authors used Hay coupling to join the pre-bent unit with terminal ethynyl groups in a 90° angle, biasing the squared-shaped product.[77]

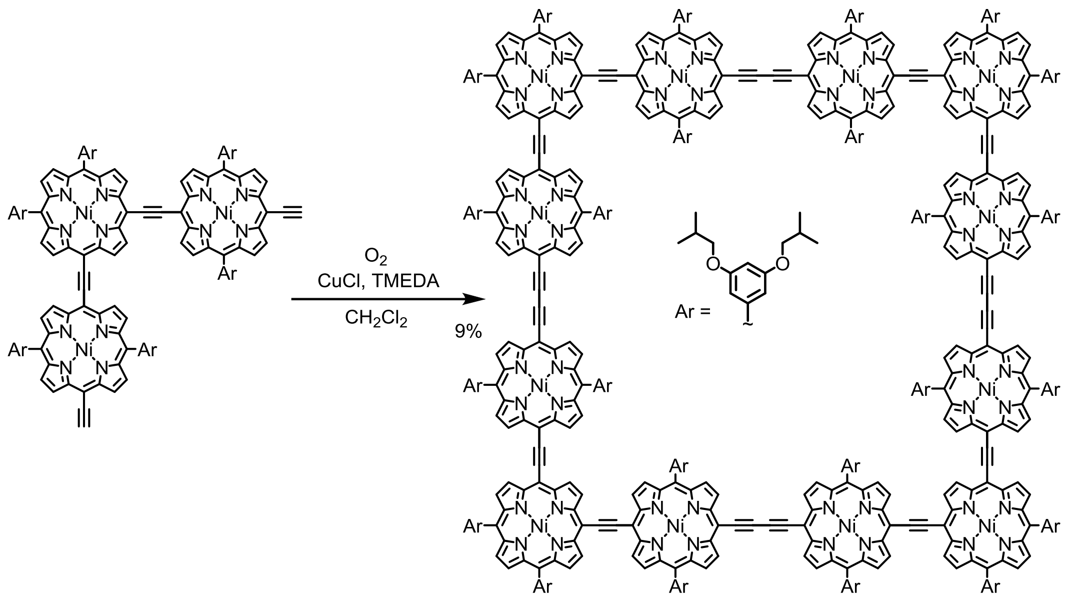

Figure 8: Synthesis of the square-shape porphyrin dodecamer.[77]

An alternative method to define the number of units in the cyclic oligomer is by concurrently scaffolding the monomers to a central core. This approach was for example used by Höger et al., who synthesised a large π-conjugated macrocycle with ‘spokes’ positioning the precursors in the pre-defined circular shape (**Figure 9**).[78]

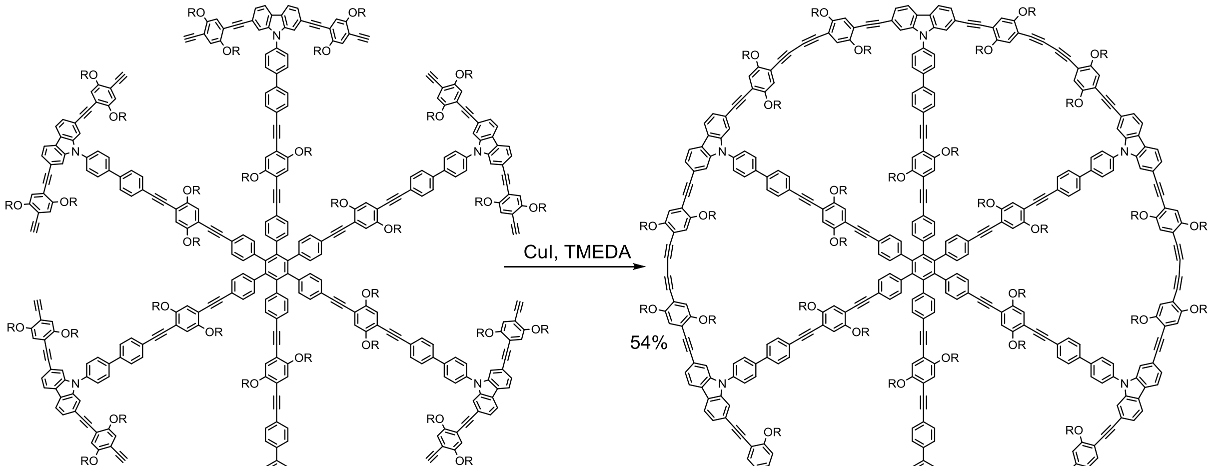

Figure 9: Synthesis of a large, π-conjugated, ‘spokes’ stabilised macrocycle. $R = -C_8H_{17}$.[78]

In this last example, the central part remained an integral part of the molecule. The further step in the synthetic strategy would be the eventual removal of the central scaffold. This approach is referred to as a template-directed synthesis (the template dictates the shape of the product, but does not become an inherent part of the constructed architecture).[79,80] The stabilising scaffold, or template, does not have to be forming a covalent bond with the building blocks. As pioneered by Anderson and Sanders, for example, reaction of the bis((3-ethynyl)phenyl)porphyrin under Hay coupling conditions yielded preferentially either the dimer or the trimer, based on the chosen template present in the reaction. The templates possess pyridine functionalities coordinating to the zinc porphyrins, and thus stabilising the desired cyclic oligomer (**Figure 10**). [81,82]

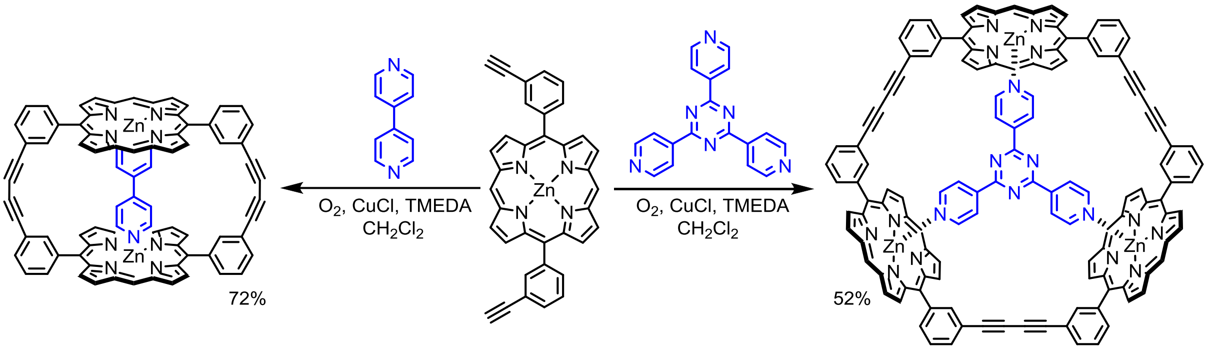

Figure 10: Template-directed synthesis of a porphyrin dimer and trimer. Solubilising alkyl groups on *beta* positions omitted for clarity.[81,82]

This concept was demonstrated also in 3D by Konishi et al., who used gold nanoparticles with an approximate spherical symmetry, and which were decorated with many pyridyl groups. The template coordinated six alkene-functionalised porphyrin monomers and these alkene parts were reacted under olefin metathesis conditions, to yield a 3D hexa-porphyrin cage (**Figure 11**).[83]

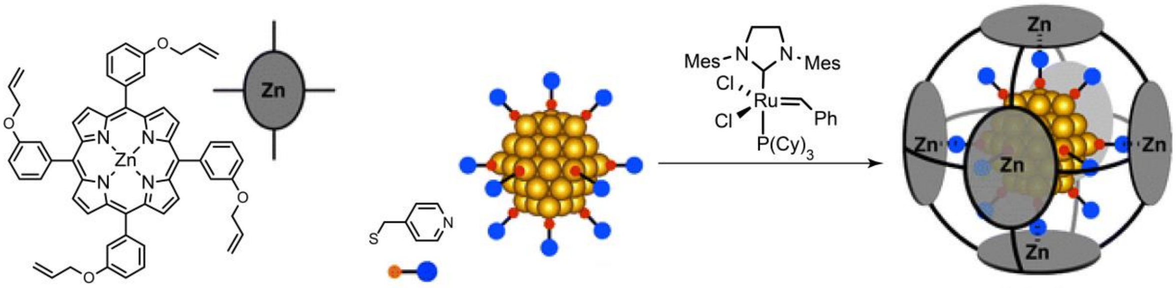

Figure 11: Synthesis of the porphyrin containing cage using a 3D template consisting of a gold nanoparticle decorated with pyridyl functions. Image redrawn with permission from *Chem. Comm.* **2003**, (11), 1282–1283. Copyright 2003 Royal Society of Chemistry.

Over a decade, multiple successful syntheses of a cyclic π-conjugated butadiyne-linked porphyrin oligomers have been developed and presented by Anderson et al. The syntheses related on various templates possessing various valences and appropriately engineered sizes in order to have a good fit to the desired macrocycle. The use of the template was found to be absolutely vital for the cyclisations. In the absence of template, no spontaneous cyclisation was observed. The formation of the butadiyne links was facilitated by coupling of the ethynyl functions *via* homo-coupling reactions under Hay or Sonogashira-type homocoupling conditions. The most efficient conditions have proved to be the use of catalytic amounts of Pd^{2+} and Cu^{1+} salts together with an amine base and 1,4-benzoquinone as an oxidant (**Figure 12**).

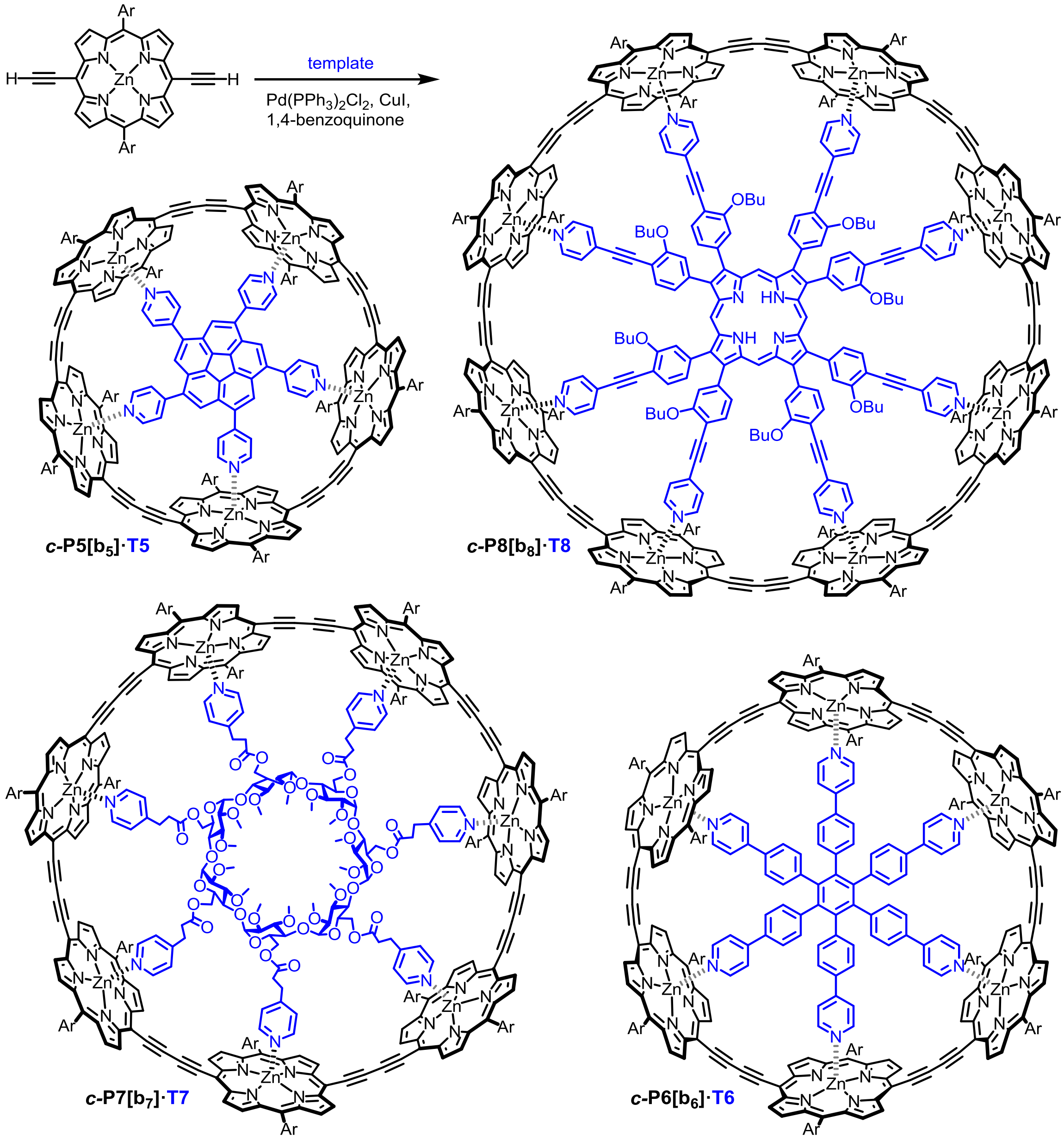

Figure 12: General scheme of the synthesis of 5–8 porphyrin nanorings using various templates. Ar = 3,5-bis(tert-butyl)phenyl, 3,5-bis(*n*-octyloxy)phenyl or 3,5-bis(trihexylsilyl)phenyl.[84–87]

The size of the required template scales with the diameter of the targeted nanoring. Therefore, for very large nanorings, even the template molecules might become a synthetic challenge. Thus, an alternative strategy requiring only 'small' templates have been designed. If the number of the porphyrin units *N* in the reacting porphyrin building block ***l*-P*N*** is not a divisor of the number *X* of the pyridyl sites in the template **T*X***, then the macrocycle of the template-designed size cannot be formed (no ***c*-P*X***). Instead, a macrocycle, of the size of the lowest common multiple of *N* and *X* is formed. This approach was referred to as a Vernier templating. For example, when linear porphyrin tetramer ***l*-P4** is reacted at the conditions of Sonogashira-type homocoupling in presence of hexavalent template **T6**, the number of porphyrin units in the macrocycle is expected to be a common multiple of 4 and 6. In this case, a cyclic dodecamer ***c*-P12** is formed as a major product (**Figure 13**).[88,89]

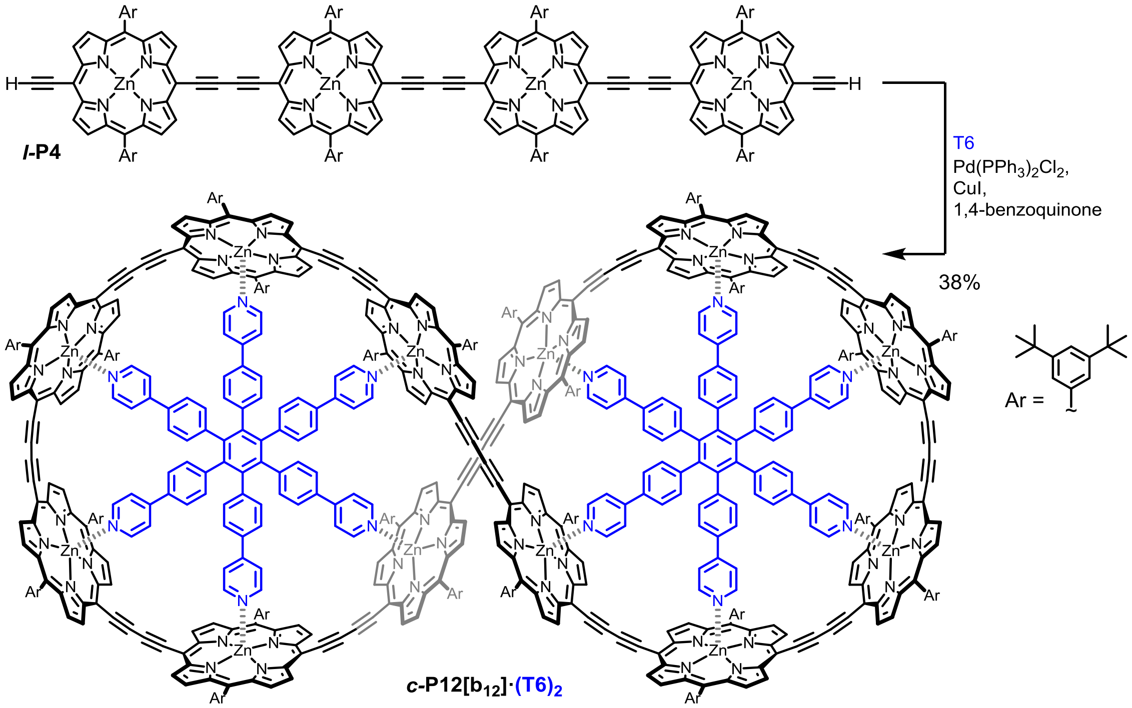

Figure 13: Vernier template synthesis of the 12-porphyrin macrocycle.[88,89]

An analogous strategy was used for the synthesis of even larger structures. For example, the reaction between linear porphyrin hexamer ***l*-P6** and octavalent template **T8**, yielded the giant 24-porphyrin macrocycle ***c*-P24**.[90]

A general behaviour observed with large porphyrin architectures, both linear and cyclic, is a tendency to aggregate. Even when relatively large 3,5-bis(*n*-octyloxy)phenyl groups are placed in every free *meso* porphyrin position, the aggregation of the relatively small tetramer ***l*-P4** have been documented. In the absence of any ligand capable of coordinating to the zinc-porphyrin coordination, the aggregate consisting of three molecules ((***l*-P4**)$_3$) was described and characterised (**Figure 14**).[91] The process could be nicely followed by NMR where a very complicated ^{1}H NMR spectrum is observed in pure $CDCl_3$, illustrating the aggregation-caused low molecular symmetry. Addition of very small amount of pyridine leads to a complete disaggregation, resulting in a simpler spectrum expected for a linear tetramer (**Figure 15**).

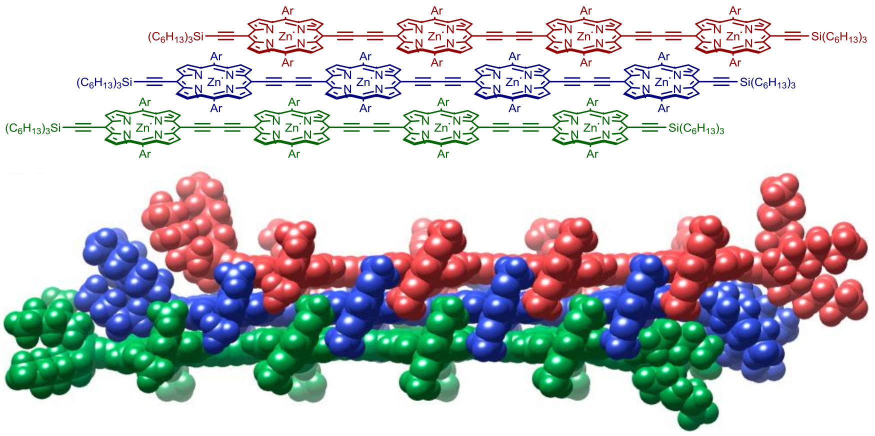

Figure 14: Three aggregated ***l*-P4** molecules (top, Ar = 3,5-bis(octyloxy)phenyl) and the molecular model (bottom). Model reprinted with permission from *J. Am. Chem. Soc.*, **2013**, (135), *34*, 12798–12807. Copyright 2013 American Chemical Society.

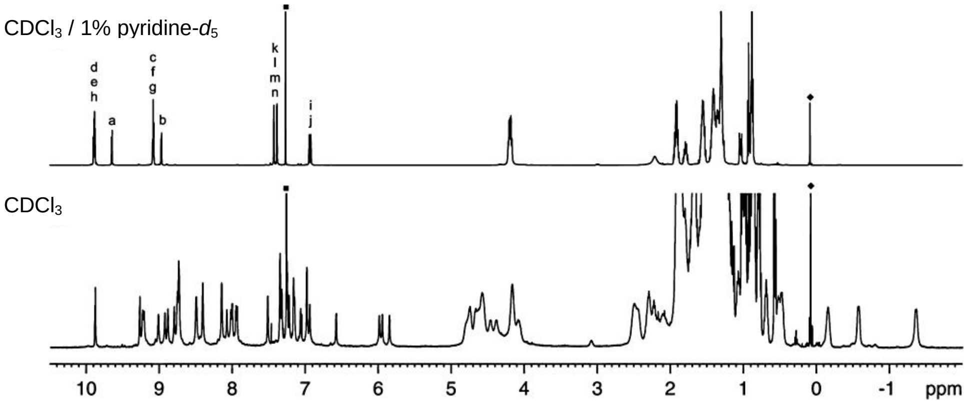

Figure 15: ^{1}H NMR (500 MHz) of ***l*-P4** in CDCl3/1% pyridine-d5 (top) and CDCl3 (bottom). Reprinted with permission from *J. Am. Chem. Soc.*, **2013**, (135), *34*, 12798–12807. Copyright 2013 American Chemical Society.

If a porphyrin oligomer is mixed with a bidentate ligand (instead of monodentate one), alternative stacked porphyrin architectures can be constructed. These arrays are often referred to as ladder complexes (**Figure 16**).[92–96]

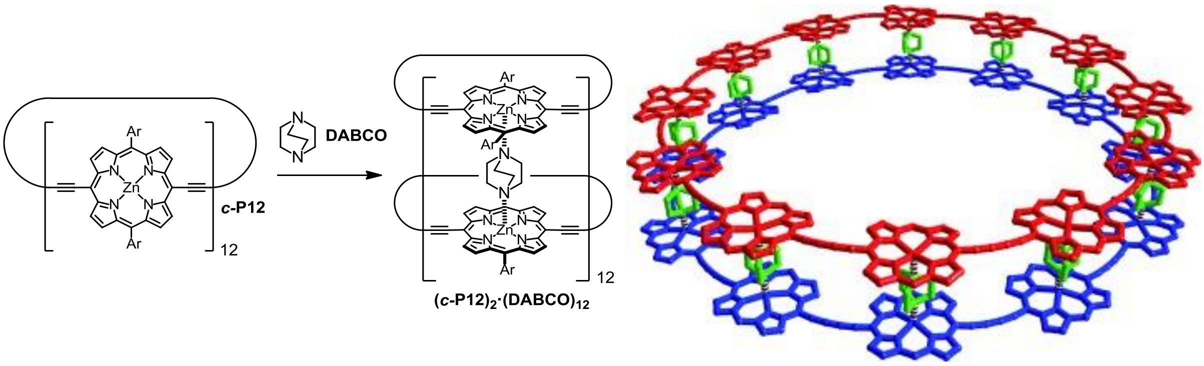

Figure 16: Edited and reprinted with permission from *Angew. Chem. Int. Ed.*, 50, 5572–5575. Ar = 3,5-bis(tert-butyl)phenyl.[92]

Formation of such ladder complexes represents a general strategy for rigidifying porphyrin oligomers without the need for constructing a specific, size- and valency-matching template.

1.3. Photochemical properties of porphyrins

The name porphyrin originates from the Greek “πορφύρα” (porphyra) meaning purple,[97,98] after the colour of a bare symmetric porphyrin core. Nevertheless, a whole palate of colours can be reached when the porphyrins are variously substituted, various metals are inserted and/or additional ligands to the metal are coordinated. Nature has developed this chromophore and its versatility is documented by the number of its uses in different biological architectures.[98,99]

Generally, absorption bands in spectra of porphyrins are assigned as a Soret band (the one of a higher energy) and a so-called Q band. The Soret band corresponds to the excitation transition $S_0 \rightarrow S_2$, the Q band to $S_0 \rightarrow S_1$. The origin of the bands can be rationalised when analysing molecular orbitals (MOs) of the bare porphyrin core, described using Gouterman’s orbitals (**Figure 17**).[100,101]

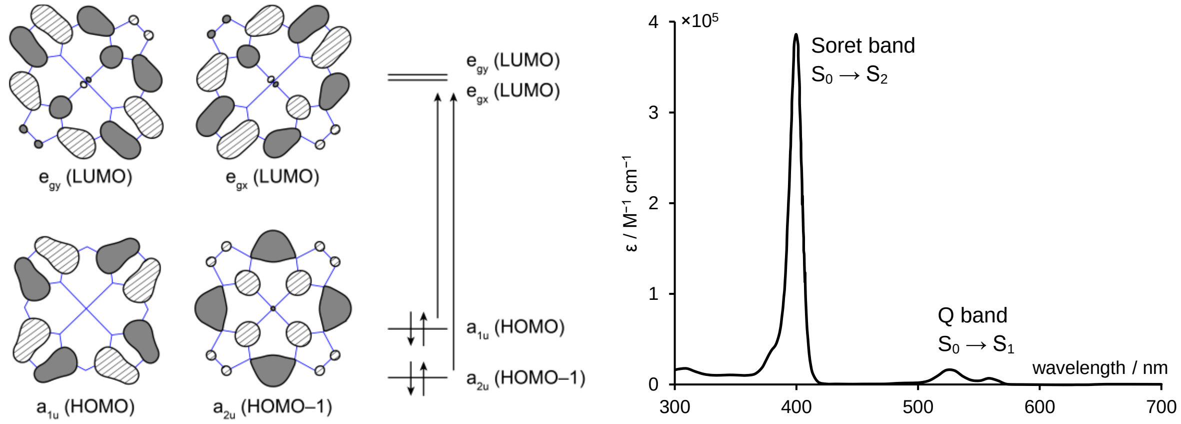

Figure 17: Calculated MO of zinc porphyrin (B3LYP/6-31G(d)) in agreement with assignment in literature.[102] UV-vis absorption spectrum of a zinc porphyrin.[103,104]

As a result of the configuration interaction, the $a_{1u} \rightarrow e_{g(x,y)}$ and $a_{2u} \rightarrow e_{g(x,y)}$ transitions are mixed and a constructive interaction leads to an intense, higher energy Soret band, while the intensity of the lower energy Q band is attenuated.

Two orientations of the light-absorption-related transition dipole moments can be expected, with orientation along the *x* axis and orthogonally along the *y* axis. In non-symmetrically *meso* substituted porphyrins, the components cease to be degenerate. Furthermore, a vicinity of another chromophore can yield to a further splitting of the energies. In the simple model of a porphyrin dimer, where the length of the dimer is oriented along the *x* axis, it can be shown how the exciton coupling interaction splits the possible excitation modes into an allowed mode, with the dipoles oriented in the same direction, and forbidden modes with opposite dipoles orientation. From an electrostatic point of view, the allowed mixing of dipoles *x* components lowers the energy of the transition, which is observed as a red shift.

Contrary, an allowed transition of the orthogonal *y* component, leads to an increase of the energy, observed as a blue shift (**Figure 18**).[105]

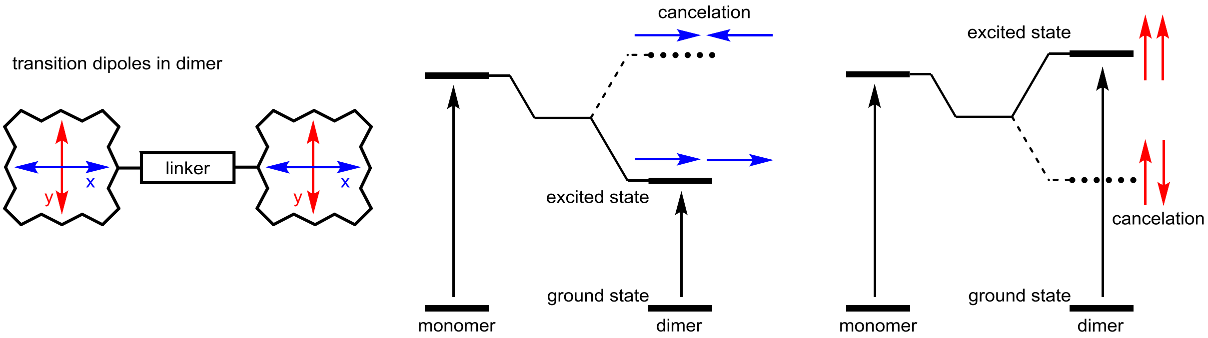

Figure 18: Kasha's model for the exciton model in the porphyrin dimer.[105]

Generally, according to Kasha's model, the exciton coupling effect on the energy splitting can be described for the orientation of the dipoles depicted in **Figure 19** following the equation **Eq. 1**.

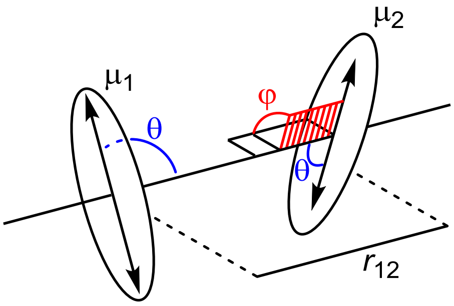

Figure 19: Relative orientation of the transition dipoles of the two units in the porphyrin dimer.

$$\Delta E = \frac{2|\mu_1 \mu_2|}{r_{12}^3}(\cos\varphi + 3\cos^2\Theta) \tag{1}$$

This means that the highest energy split is expected when the dipoles are co-planar (φ = 0°) and the transition dipoles assembled are parallel along the line (θ = 0°). Of course, the exciton model ignores the π-conjugation between porphyrins, when connected with conductive linkers, however still it can comment on certain spectral features, observed in the butadiyne-linked porphyrin oligomer family. In the UV-vis spectra of a series of linearly butadiyne-linked porphyrin oligomers, a progressive red shift of the Q_x band is apparent. Interestingly, as the change of the absorption occurs mainly in the visible region, the oligomers are distinguishable by the naked eye (**Figure 20**).

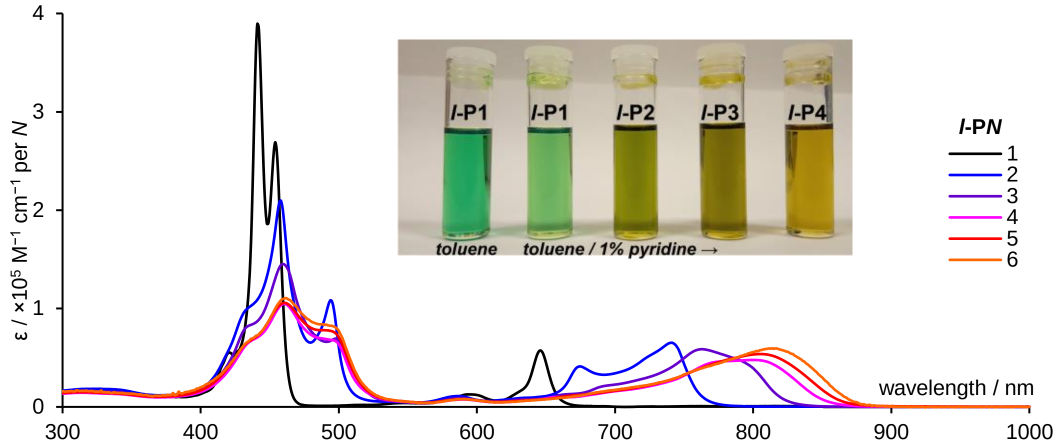

Figure 20: UV-vis-NIR absorption spectra of butadiyne linked oligomers ***l*-P*N***, where N = 1–6 denotes number of porphyrin units. (insert) A photo of vials with solutions of protected-bis(ethynyl)caped butadiyne-linked oligomers in toluene (first from the left) and toluene / 1% pyridine (the rest).

Supramolecular porphyrin architectures are also be found in nature and form an instrumental part of the light-harvesting complexes. Notoriously known and studied is the system found in purple bacteria, the complex LH2 (**Figure 21**).[106–108]

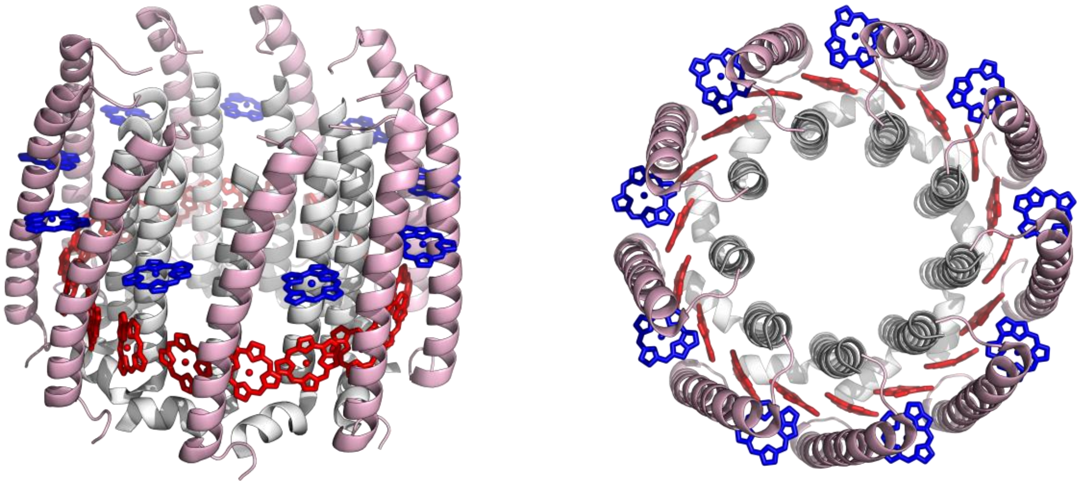

Figure 21: Schematic representation of the light-harvesting complex LH2 scaffolding the porphyrin chromophores into the two arrays.

The LH2 possess two tight arrays of the bacteriochlorophyll chromophores in order to facilitate very fast energy transport upon light absorption, to prevent a loss of the absorbed energy. One array typically consist of 8–9 flat porphyrins (**Figure 21**, blue), and another series of more tightly stacked chromophores perpendicular to the former consisting of typically 18 bacteriochlorophyll chromophores (**Figure 21**, red). Such tight chromophore-contact facilitates the energy migration through the system even without direct π-conjugation between the chromophores.

Analogous processes have been studied in synthetic porphyrin nanorings. These processes can be followed by the measurement of the polarisation of fluorescence. Upon irradiation of the porphyrins with linearly polarised light, the intensity of either the parallel ($I_{\parallel}$)

or perpendicularly ($I_\perp$) polarised emission can be used to estimate the overall anisotropy r, calculated according to **Eq. 2**.[109]

$$r = \frac{I_\parallel - I_\perp}{I_\parallel + 2 \cdot I_\perp} \tag{2}$$

In an isotropic solution, (i.e. with randomly distributed orientations of the molecules), for static molecules (at the time scale of the fluorescence measurement) the expected anisotropy should be:

$$r = 0.4 \cdot \frac{3\cos^2\theta - 1}{2} \tag{3}$$

Where θ is an angle between absorption and emission dipoles. In a straight, linear oligomer, the emission is parallel to the absorption ($\theta = 0°$) when irradiating the Q band and the emission should not lose the spatial orientation. Therefore, a high anisotropy of the fluorescence is expected, with a maximum of $r = 0.4$. However, if the exciton is rapidly delocalised within the 2D plane of a curved oligomer or nanoring, the emission anisotropy is expected to drop to $r = 0.1$ (**Figure 22**).

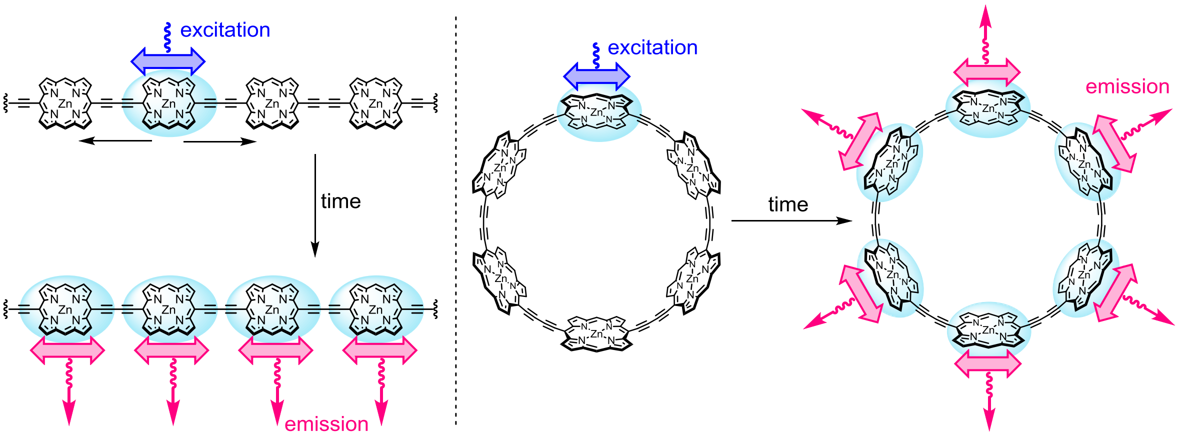

Figure 22: Conceptual description of the exciton delocalisation and the partial loss of the polarisation in the nanorings.

Such depolarisation was observed to occur extremely rapidly (within 0.2 ps) in the nanorings, exhibiting the values of $r \sim 0.1$.[110] This fast drop of anisotropy was found in the nanorings of all sizes up to the 42 porphyrin nanoring, illustrating the extreme mobility of the exciton within the butadiyne-linked porphyrin scaffold. Beside the nanorings, the loss of the polarisation was also observed in linear oligomers, when wrapped around the template to adopt a cyclic shape (**Figure 23**).[111]

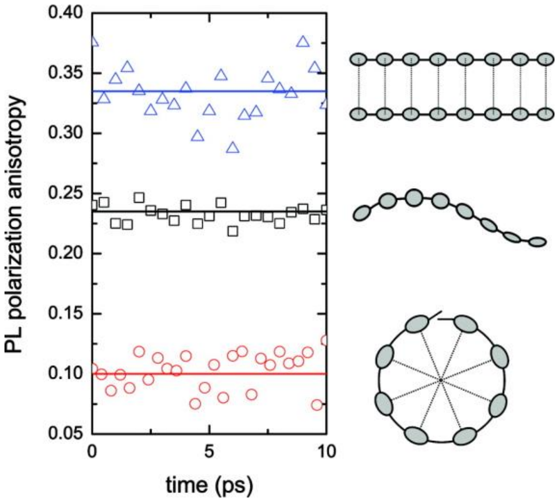

Figure 23: Comparison of the anisotropy of the fluorescence upon excitation of the porphyrin octamer ladder (***l*-P8**)$_2$·(DABCO)$_8$ (blue triangles), free linear oligomer ***l*-P8** (black squares) and oligomer 'cyclised' around the template ***l*-P8·T8** (red circles). Reprinted with permission from *J. Am. Chem. Soc.* **2008**, *130*, 10171–10178. Copyright 2014 American Chemical Society.[111]

This general introduction is followed by three experimental chapters, each containing a specific introduction and discussing the synthesis and properties of various porphyrin oligomers. In **Chapter 2** the investigation of the origin of intensified IR bands in the monocations of porphyrin oligomers is described. In **Chapter 3**, (anti)aromaticity and its limits in porphyrin nanorings cations is studied. **Chapter 4** describes the design and synthesis of a Möbius-strip-shaped nanoring.

1.4. References

[1] R. Willstätter, *J. Am. Chem. Soc.* **1915**, *37*, 323–345.

[2] K. Kadish, K. M. Smith, R. Guilard, *The Porphyrin Handbook (Volume 3),* Academic Press, **2000**.

[3] C. J. Medforth, M. O. Senge, K. M. Smith, L. D. Sparks, J. A. Shelnutt, *J. Am. Chem. Soc.* **1992**, *114*, 9859–9869.

[4] C.-H. Lee, J. S. Lindsey, *Tetrahedron* **1994**, *50*, 11427–11440.

[5] J. S. Lindsey, *The Synthesis of Meso-Substituted Porphyrins*, Springer Netherlands, Dordrecht, **1994**.

[6] M. Senge, in *Porphyrin Handbook*, **2000**, pp. 239–347.

[7] H. W. Whitlock, R. Hanauer, M. Y. Oester, B. K. Bower, *J. Am. Chem. Soc.* **1969**, *91*, 7485–7489.

[8] L. Limantara, P. Koehler, B. Wilhelm, R. J. Porra, H. Scheer, *Photochem. Photobiol.* **2006**, *82*, 770–780.

[9] S. Aronoff, *Chem. Rev.* **1950**, *47*, 175–195.

[10] E. Vogel, P. Scholz, R. Demuth, C. Erben, M. Bröring, H. Schmickler, J. Lex, G. Hohlneicher, D. Bremm, Y.-D. Wu, *Angew. Chem. Int. Ed.* **1999**, *38*, 2919–2923.

[11] E. Vogel, M. Bröring, J. Fink, D. Rosen, H. Schmickler, J. Lex, K. W. K. Chan, Y.-D. Wu, D. A. Plattner, M. Nendel, K. N. Houk, *Angew. Chem. Int. Ed.* **1995**, *34*, 2511–2514.

[12] S. Neya, K. Imai, H. Hori, H. Ishikawa, K. Ishimori, D. Okuno, S. Nagatomo, T. Hoshino, M. Hata, N. Funasaki, *Inorg. Chem.* **2003**, *42*, 1456–1461.

[13] R. Paolesse, S. Nardis, M. Stefanelli, F. R. Fronczek, M. G. H. Vicente, *Angew. Chem. Int. Ed.* **2005**, *44*, 3047–3050.

[14] E. Vogel, M. Bröring, S. J. Weghorn, P. Scholz, R. Deponte, J. Lex, H. Schmickler, K. Schaffner, S. E. Braslavsky, M. Müller, S. Pörting, J. L. Sessler, C. J. Fowler, *Angew. Chem. Int. Ed.* **1997**, *36*, 1651–1654.

[15] J. Waluk, in *Handbook of Porphyrin Science*, World Scientific Publishing Company, **2010**, pp. 359–435.

[16] S. Peukert, M. Kijak, J. Ostapko, J. Sepioł, C. Le Bris, A. Zehnacker-Rentien, M. Gil, J. Waluk, *J. Chem. Phys.* **2018**, *149*, 134307.

[17] Y. Fang, F. Mandoj, S. Nardis, G. Pomarico, M. Stefanelli, D. O. Cicero, S. Lentini, A.

Vecchi, Y. Cui, L. Zeng, K. M. Kadish, R. Paolesse, *Inorg. Chem.* **2014**, *53*, 7404–7415.

[18] J. P. Gisselbrecht, M. Gross, E. Vogel, P. Scholz, M. Bröring, J. L. Sessler, *J. Electroanal. Chem.* **2001**, *507*, 244–249.

[19] J. Ostapko, K. Nawara, M. Kijak, J. Buczyńska, B. Leśniewska, M. Pietrzak, G. Orzanowska, J. Waluk, *Chem. Eur. J.* **2016**, *22*, 17311–17320.

[20] S. Neya, C. K. Chang, D. Okuno, T. Hoshino, M. Hata, N. Funasaki, *Inorg. Chem.* **2005**, *44*, 1193–1195.

[21] C. J. Fowler, J. L. Sessler, V. M. Lynch, J. Waluk, A. Gebauer, J. Lex, A. Heger, F. Zuniga-y-Rivero, E. Vogel, *Chem. Eur. J.* **2002**, *8*, 3485–3496.

[22] A. B. P. Lever, *The Phthalocyanines,* Academic Press, **1965**.

[23] D. D. Eley, *Nature* **1948**, *162*, 819.

[24] P. Gregory, *J. Porphyr. Phthalocyanines* **2000**, *04*, 432–437.

[25] D. R. Tackley, G. Dent, W. Ewen Smith, *Phys. Chem. Chem. Phys.* **2001**, *3*, 1419–1426.

[26] H. J. Wagner, R. O. Loutfy, C.-K. Hsiao, *J. Mater. Sci.* **1982**, *17*, 2781–2791.

[27] N. Kobayashi, *Curr. Opin. Solid State Mater. Sci.* **1999**, *4*, 345–353.

[28] T. Inabe, H. Tajima, *Chem. Rev.* **2004**, *104*, 5503–5534.

[29] S. K. Pushpan, A. Srinivasan, V. G. Anand, S. Venkatraman, T. K. Chandrashekar, B. S. Joshi, R. Roy, H. Furuta, *J. Am. Chem. Soc.* **2001**, *123*, 5138–5139.

[30] A. Krivokapic, A. R. Cowley, H. L. Anderson, *J. Org. Chem.* **2003**, *68*, 1089–1096.

[31] J. L. Sessler, D. Seidel, *Angew. Chem. Int. Ed.* **2003**, *42*, 5134–5175.

[32] Y. Pareek, M. Ravikanth, T. K. Chandrashekar, *Acc. Chem. Res.* **2012**, *45*, 1801–1816.

[33] L. K. Blusch, Y. Hemberger, K. Pröpper, B. Dittrich, F. Witterauf, M. John, G. Bringmann, C. Brückner, F. Meyer, *Chem. Eur. J.* **2013**, *19*, 5868–5880.

[34] J. L. Sessler, A. K. Burrell, *Expanded Porphyrins - Macrocycles*, Springer Berlin Heidelberg, **1992**.

[35] R. Misra, T. K. Chandrashekar, *Acc. Chem. Res.* **2008**, *41*, 265–279.

[36] F. D'Souza, *Angew. Chem. Int. Ed.* **2015**, *54*, 4713–4714.

[37] J. Guilleme, D. González-Rodríguez, T. Torres, *Angew. Chem. Int. Ed.* **2011**, *50*, 3506–3509.

[38] D. González-Rodríguez, T. Torres, D. M. Guldi, J. Rivera, M. Á. Herranz, L. Echegoyen, *J. Am. Chem. Soc.* **2004**, *126*, 6301–6313.

[39] C. G. Claessens, D. González-Rodríguez, T. Torres, *Chem. Rev.* **2002**, *102*, 835–854.

[40] S. Cotton, *Lanthanide and Actinide Chemistry (Inorganic Chemistry: A Textbook Series)*, Wiley-WCH, **2006**.

[41] Y. Zhang, J. Shi, Y. Zheng, M. Yu, G. Liu, *Synth. React. Inorganic, Met. Nano-Metal Chem.* **2009**, *39*, 605–608.

[42] L. Cuesta, J. L. Sessler, *Chem. Soc. Rev.* **2009**, *38*, 2716–2729.

[43] C.-P. Wong, R. F. Venteicher, W. D. Horrocks, *J. Am. Chem. Soc.* **1974**, *96*, 7149–7150.

[44] J. W. Buchler, C. Dreher, F. M. Künzel, in (Eds.: J.W. Buchler, C. Dreher, F.M. Künzel, S. Licoccia, R. Paolesse, J. Šima), Springer Berlin Heidelberg, Berlin, Heidelberg, **1995**, pp. 1–69.

[45] J. R. Miller, G. D. Dorough, *J. Am. Chem. Soc.* **1952**, *74*, 3977–3981.

[46] W. R. Scheidt, C. W. Eigenbrot, M. Ogiso, K. Hatano, *Bull. Chem. Soc. Jpn.* **1987**, *60*, 3529–3533.

[47] S. G. DiMagno, V. S. Y. Lin, M. J. Therien, *J. Am. Chem. Soc.* **1993**, *115*, 2513–2515.

[48] L. Favereau, A. Cnossen, J. B. Kelber, J. Q. Gong, R. M. Oetterli, J. Cremers, L. M. Herz, H. L. Anderson, *J. Am. Chem. Soc.* **2015**, *137*, 14256–14259.

[49] M. Sakuragi, K. Ichimura, H. Sakuragi, *Bull. Chem. Soc. Jpn.* **1992**, *65*, 1944–1949.

[50] H. Imai, S. Nakagawa, E. Kyuno, *J. Am. Chem. Soc.* **1992**, *114*, 6719–6723.

[51] P. Bhyrappa, V. Krishnan, M. Nethaji, *J. Chem. Soc., Dalt. Trans.* **1993**, 1901–1906.

[52] A. Satake, Y. Kobuke, *Tetrahedron* **2005**, *61*, 13–41.

[53] S. Durot, J. Taesch, V. Heitz, *Chem. Rev.* **2014**, *114*, 8542–8578.

[54] I. Beletskaya, V. S. Tyurin, A. Y. Tsivadze, R. Guilard, C. Stern, *Chem. Rev.* **2009**, *109*, 1659–1713.

[55] R. Jasti, J. Bhattacharjee, J. B. Neaton, C. R. Bertozzi, *J. Am. Chem. Soc.* **2008**, *130*, 17646–17647.

[56] T. J. Sisto, M. R. Golder, E. S. Hirst, R. Jasti, *J. Am. Chem. Soc.* **2011**, *133*, 15800–15802.

[57] J. Xia, R. Jasti, *Angew. Chem. Int. Ed.* **2012**, *51*, 2474–2476.

[58] H. Omachi, S. Matsuura, Y. Segawa, K. Itami, *Angew. Chem. Int. Ed.* **2010**, *49*, 10202–10205.

[59] E. R. Darzi, T. J. Sisto, R. Jasti, *J. Org. Chem.* **2012**, *77*, 6624–6628.

[60] N. Hayase, Y. Miyauchi, Y. Aida, H. Sugiyama, H. Uekusa, Y. Shibata, K. Tanaka, *Org. Lett.* **2017**, *19*, 2993–2996.

[61] A. Yahav-Levi, I. Goldberg, A. Vigalok, *J. Am. Chem. Soc.* **2006**, *128,* 8710–8711.

[62] T. Iwamoto, Y. Watanabe, Y. Sakamoto, T. Suzuki, S. Yamago, *J. Am. Chem. Soc.* **2011**, *133*, 8354–8361.

[63] A. Mishra, C.-Q. Ma, P. Bäuerle, *Chem. Rev.* **2009**, *109*, 1141–1276.

[64] T. Otsubo, Y. Aso, K. Takimiya, *J. Mater. Chem.* **2002**, *12*, 2565–2575.

[65] P. Bäuerle, *Adv. Mater.* **1992**, *4*, 102–107.

[66] D. Fichou, *J. Mater. Chem.* **2000**, *10*, 571–588.

[67] P. F. Xia, X. J. Feng, J. Lu, S.-W. Tsang, R. Movileanu, Y. Tao, M. S. Wong, *Adv. Mater.* **2008**, *20*, 4810–4815.

[68] P. F. Xia, X. J. Feng, J. Lu, R. Movileanu, Y. Tao, J.-M. Baribeau, M. S. Wong, *J. Phys. Chem. C* **2008**, *112*, 16714–16720.

[69] F. Zhang, G. Götz, H. D. F. Winkler, C. A. Schalley, P. Bäuerle, *Angew. Chem. Int. Ed.* **2009**, *48*, 6632–6635.

[70] J. Krömer, I. Rios-Carreras, G. Fuhrmann, C. Musch, M. Wunderlin, T. Debaerdemaeker, E. Mena-Osteritz, P. Bäuerle, *Angew. Chem. Int. Ed.* **2000**, *39*, 3481–3486.

[71] T. Kawase, H. R. Darabi, R. Uchimiya, M. Oda, *Chem. Lett.* **1995**, *24*, 499–500.

[72] K. Nakao, M. Nishimura, T. Tamachi, Y. Kuwatani, H. Miyasaka, T. Nishinaga, M. Iyoda, *J. Am. Chem. Soc.* **2006**, *128*, 16740–16747.

[73] H. Shimizu, K. H. Park, H. Otani, S. Aoyagi, T. Nishinaga, Y. Aso, D. Kim, M. Iyoda, *Chem. Eur. J.* **2018**, *24*, 3793–3801.

[74] M. Mayor, C. Didschies, *Angew. Chem. Int. Ed.* **2003**, *42*, 3176–3179.

[75] G. Anguera, W.-Y. Cha, M. D. Moore, J. Lee, S. Guo, V. M. Lynch, D. Kim, J. L. Sessler, *J. Am. Chem. Soc.* **2018**, *140*, 4028–4034.

[76] T. Hori, N. Aratani, A. Takagi, T. Matsumoto, T. Kawai, M.-C. Yoon, Z. S. Yoon, S. Cho, D. Kim, A. Osuka, *Chem. Eur. J.* **2006**, *12*, 1319–1327.

[77] A. Kato, K. Sugiura, H. Miyasaka, H. Tanaka, T. Kawai, M. Sugimoto, M. Yamashita, *Chem. Lett.* **2004**, *33*, 578–579.

[78] A. V. Aggarwal, A. Thiessen, A. Idelson, D. Kalle, D. Würsch, T. Stangl, F. Steiner, S.-S. Jester, J. Vogelsang, S. Höger, J. M. Lupton, *Nat. Chem.* **2013**, *5*, 964–970.

[79] D. H. Busch, *J. Incl. Phenom. Mol. Recognit. Chem.* **1992**, *12*, 389–395.

[80] S. Anderson, H. L. Anderson, J. K. M. Sanders, *Acc. Chem. Res.* **1993**, *26*, 469–475.

[81] H. L. Anderson, J. K. M. Sanders, *Angew. Chem. Int. Ed.* **1990**, *29*, 1400–1403.

[82] H. L. Anderson, J. K. M. Sanders, *J. Chem. Soc., Chem. Commun.* **1989**, 1714–1715.

[83] T. Inomata, K. Konishi, *Chem. Commun.* **2003**, 1282–1283.

[84] P. Liu, Y. Hisamune, M. D. Peeks, B. Odell, J. Q. Gong, L. M. Herz, H. L. Anderson, *Angew. Chem. Int. Ed.* **2016**, *55*, 8358–8362.

[85] M. Hoffmann, J. Kärnbratt, M.-H. Chang, L. M. Herz, B. Albinsson, H. L. Anderson, *Angew. Chem. Int. Ed.* **2008**, *47*, 4993–4996.

[86] P. Liu, P. Neuhaus, D. V. Kondratuk, T. S. Balaban, H. L. Anderson, *Angew. Chem. Int. Ed.* **2014**, *53*, 7770–7773.

[87] M. Hoffmann, C. J. Wilson, B. Odell, H. L. Anderson, *Angew. Chem. Int. Ed.* **2007**, *46*, 3122–3125.

[88] M. C. O'Sullivan, J. K. Sprafke, D V Kondratuk, C. Rinfray, T. D. W. Claridge, A. Saywell, M. O. Blunt, J. N. O'Shea, P. H. Beton, M. Malfois, H. L. Anderson, *Nature* **2011**, *469*, 72–75.

[89] D. V Kondratuk, J. K. Sprafke, M. C. O'Sullivan, L. M. A. Perdigao, A. Saywell, M. Malfois, J. N. O'Shea, P. H. Beton, A. L. Thompson, H. L. Anderson, *Chem. Eur. J.* **2014**, *20*, 12826–12834.

[90] D. V Kondratuk, L. M. A. Perdigao, M. C. O'Sullivan, S. Svatek, G. Smith, J. N. O'Shea, P. H. Beton, H. L. Anderson, *Angew. Chem. Int. Ed.* **2012**, *51*, 6696–6699.

[91] M. Hutin, J. K. Sprafke, B. Odell, H. L. Anderson, T. D. W. Claridge, *J. Am. Chem. Soc.* **2013**, *135*, 12798–12807.

[92] J. K. Sprafke, B. Odell, T. D. W. Claridge, H. L. Anderson, *Angew. Chem. Int. Ed.* **2011**, *50*, 5572–5575.

[93] H. L. Anderson, *Inorg. Chem.* **1994**, *33*, 972–981.

[94] M. Drobizhev, Y. Stepanenko, A. Rebane, C. J. Wilson, T. E. O. Screen, H. L. Anderson, *J. Am. Chem. Soc.* **2006**, *128*, 12432–12433.

[95] P. N. Taylor, H. L. Anderson, *J. Am. Chem. Soc.* **1999**, *121*, 11538–11545.

[96] T. E. O. Screen, J. R. G. Thorne, R. G. Denning, D. G. Bucknall, H. L. Anderson, *J. Am. Chem. Soc.* **2002**, *124*, 9712–9713.

[97] A. Kyriakides, *Modern Greek - English Dictionary*, Anesti Constantinides, Athens, **1909**.

[98] L. R. Milgrom, *The Colours of Life: An Introduction to the Chemistry of Porphyrins and Related Compounds*, Oxford University Press, **1997**.

[99] D. Wohrle, *Adv. Mater.* **1997**, *9*, 1191–1192.

[100] M. Gouterman, *J. Mol. Spectrosc.* **1961**, *6*, 138–163.

[101] M. Gouterman, G. H. Wagnière, L. C. Snyder, *J. Mol. Spectrosc.* **1963**, *11*, 108–127.

[102] H. L. Anderson, *Chem. Commun.* **1999**, 2323–2330.

[103] X. Liu, E. K. L. Yeow, S. Velate, R. P. Steer, *Phys. Chem. Chem. Phys.* **2006**, *8*, 1298.

[104] D. K. Dogutan, M. Ptaszek, J. S. Lindsey, *J. Org. Chem.* **2007**, *72*, 5008–5011.

[105] M. A. Kasha, M., Rawls, H. R. & El-Bayoumi, *Pure Appl. Chem.* **1965**, *11*, 371–392.

[106] R. G. Saer, R. E. Blankenship, *Biochem. J.* **2017**, *474*, 2107–2131.

[107] G. McDermott, S. M. Prince, A. A. Freer, A. M. Hawthornthwaite-Lawless, M. Z. Papiz, R. J. Cogdell, N. W. Isaacs, *Nature* **1995**, *374*, 517–521.

[108] R. Jimenez, S. N. Dikshit, S. E. Bradforth, G. R. Fleming, *J. Phys. Chem.* **1996**, *100*, 6825–6834.

[109] J. R. Lakowicz, *Principles of Fluorescence Spectroscopy*, Second Edition. New York : Kluwer Academic/Plenum, **1999**.

[110] C.-K. Yong, P. Parkinson, D. V Kondratuk, W.-H. Chen, A. Stannard, A. Summerfield, J. K. Sprafke, M. C. O’Sullivan, P. H. Beton, H. L. Anderson, L. M. Herz, *Chem. Sci.* **2015**, *6*, 181–189.

[111] M.-H. Chang, M. Hoffmann, H. L. Anderson, L. M. Herz, *J. Am. Chem. Soc.* **2008**, *130*, 10171–10178.

2

The origin of intensified IR absorption in porphyrin oligomer monocations

2.1. Abstract

In this chapter is described study of the origin of the unusual intensity of certain IR bands in two porphyrin oligomer cations using ultrafast spectroscopy. Simple time-resolved IR (TR-IR) was first used to understand general features and changes associated with the IR spectra upon pump-probe excitation. Polarized TR-IR was then used to examine the relative orientations of individual vibrational modes, in order to understand which modes are intensified and why. The polarized TR-IR study was also corroborated with DFT simulations, providing hints for the mechanism of the IR band intensification. Lastly, 2D-IR techniques were used to demonstrate strong coupling between each intensified IR band. Rigorous kinetic analysis of the 2D-IR unveiled the processes occurring upon IR excitation.

All ultrafast spectroscopy experiments were performed in the Rutherford Appleton Laboratory, in Central Laser Facility (CLF) using setups built by the CLF scientists. **The experiments were carried out by the author in a very close collaboration with another DPhil student William Kendrick, with equal contribution to the work** (see Supplement to statement of authorship). The study in the CLF was supervised by Dr. Antony W. Parker.

Presented work in this chapter was submitted for publication:
W. J. Kendrick†, M. Jirasek†, M. D. Peeks, G. M. Greetham, I. V. Sazanovich, P. M. Donaldson, M. Towrie, A. W. Parker* and H. L. Anderson*
Mechanisms of IR Amplification in Radical Cation Polarons
submitted

† These authors contributed equally

2.2. Introduction

The Born-Oppenheimer approximation describes molecular dynamics by separating motions of electrons and nuclei on the basis of their significant mass difference.[1] Such a simplification is practical for performing quantum chemical calculations and is justified by experimental observations for many molecular systems. In terms of excitation of molecules to higher-energy states, chemists often divide these processes into either electronic or vibrational excitation leading to related electronic or vibrational excited state. Electronic excitation is described as populating higher-energy orbitals with an electron from lower-energy occupied orbital. Vibrational excitation is imagined as nuclei performing higher-energy oscillatory motion. An implication of the Born-Oppenheimer approximation is that any change in a position of nuclei is immediately responded by electrons. On the contrary, any electron redistribution is not immediately reflected by nuclei, but it takes time to reorganize the molecule.[2]

The approximation works if the two processes are in different energy ranges. Vibrational excitations are typically in the energy range of 500–3000 cm^{-1} (equivalent to ~6–36 kJ/mol or 3300–20,000 nm) and are consequently probed spectroscopically by light of these energies. Typical electronic excitation energies are of the order of ~10000 cm^{-1} and higher (equivalent to 120 kJ/mol or 1000 nm) and are probed with light of this energy range. Furthermore, experimentally observed absorptions related with electronic excitations are typically 100–1000× more intense than vibrational, due to the higher transition dipole moment associated with the transition (**Figure 1**).

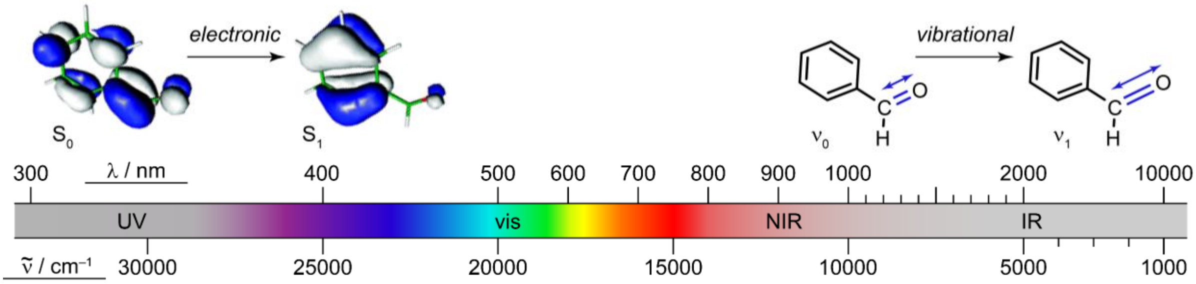

Figure 1. (top) Illustration of typical electronic (left) and vibrational (right) excitation on molecule of benzaldehyde. (bottom) Scale of the energy in wavenumber and wavelength units. Molecular orbitals adapted from *Phys. Chem. Chem. Phys.* **2009**, *11*, 11479–11486.[3]

However, when the energy of an electronic transition is lowered to an order of magnitude typical for vibrational excitations, the Born-Oppenheimer approximation breaks down. Such lowering of the electronic excitation energy was documented in the series of butadiyne-linked porphyrin oligomers in monocation oxidation states.[4]

Neutral oligomers **_l_-P_N_**, where N indicates number of porphyrin units, possess a lowest energy electronic excitation transition (Q band) in the vis-NIR region, corresponding to the HOMO → LUMO electronic excitation. Oxidation of the molecules leads to formal subtraction of one electron from the HOMO, creating two new low-energy transition modes: the low-energy HOMO−1 → HOMO transition, conventionally assigned as a polaron band P_1;[5–7] and the transition HOMO → LUMO, conventionally called the P_2 band, with energy closer to the original Q band of the neutral species (**Figure 2**).[6,8,9]

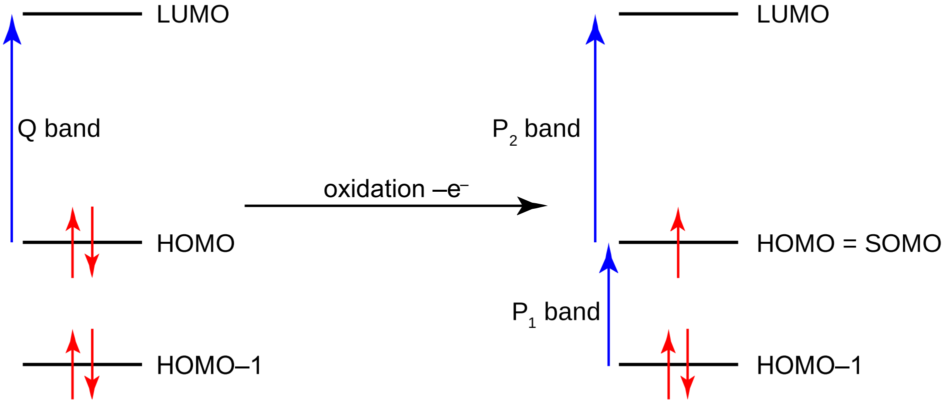

Figure 2. Simple model describing origin of two bands P_1 and P_2 with lower energies relative to Q band absorption.

Importantly, the P_1 band can become very low in energy, as documented on the series of vis-NIR-IR spectra of the neutral and monocations of **_l_-P_N_** for $N = 1–5$, where the P_1 bands shift to the IR region (**Figure 4**).

It is notable that the P_1 bands do not progressively red-shift with the increasing size of the porphyrin oligomers, but rather remain the same for $N \geq 3$. The charge delocalization in the porphyrin oligomers was studied computationally and experimentally using EPR. Major conclusion of the study is that the charge can be understood as a polaron localized over 2–3 porphyrin units of the porphyrin oligomer (**Figure 3**).[9]

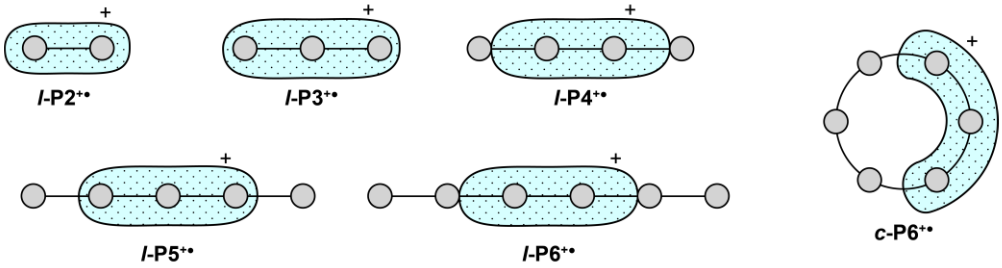

Figure 3. Scheme of expected charge distribution in porphyrin oligomers monocations. Polaron is localized on 2–3 porphyrin units.

This has the consequence, that with the larger oligomers, the spectral features related to the polarons do not change with increasing size, and new, Q-band-like structure appears, corresponding to the neutral parts of the oligomer.

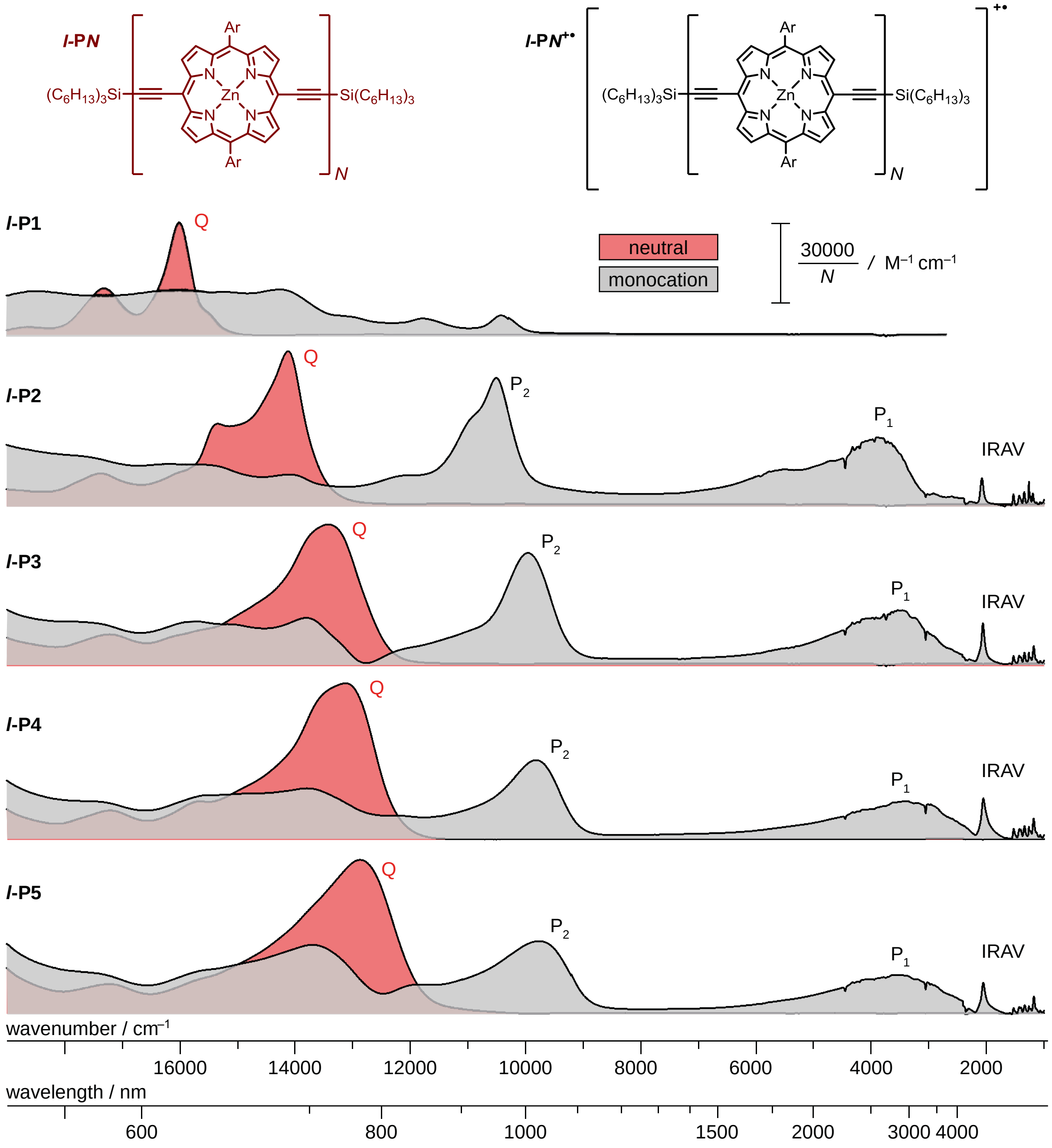

Figure 4. Vis-NIR-IR spectra of the neutral (red) and monocations (grey) of series of linear oligomers.

Beside new electronic modes, there are changes in the IR region of the spectrum. IR vibrations are relatively weak compared to the electron transition (Q band) in neutral porphyrin oligomers. However, upon oxidation, significant amplification of some IR signals to a similar magnitude to the electronic transitions is observed (**Figure 5**). Such features are often called 'infrared activated vibrations' (IRAVs).[10–16] This name origins from the hypothesis that the intense mode were originally IR silent, Raman-active modes, that are 'activated' for the IR absorption.[17,18]

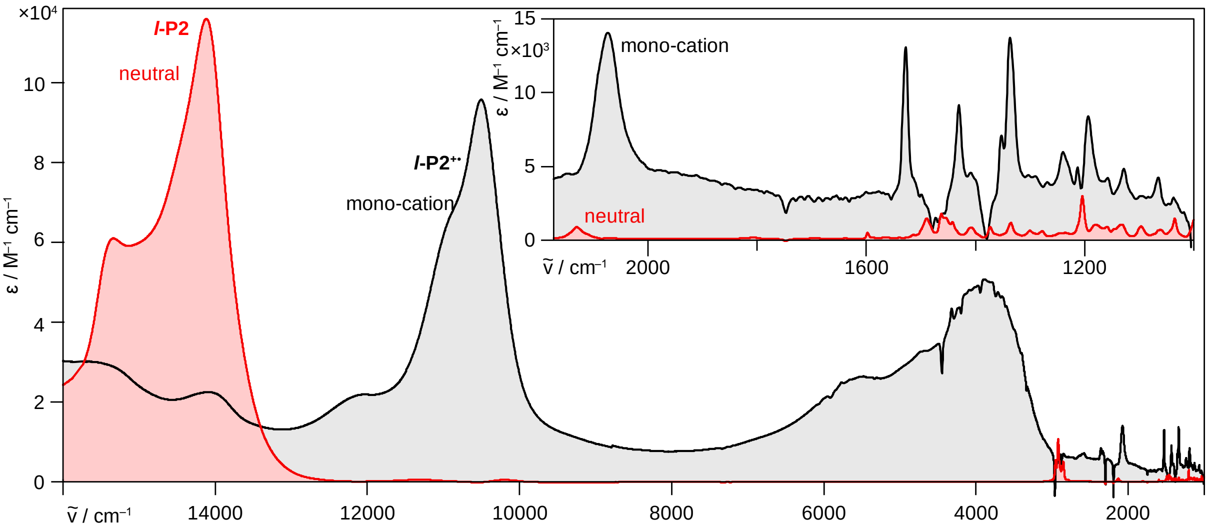

Figure 5. NIR-IR spectra of the neutral (red) and monocations (grey) of porphyrin dimer (***l*-P2** / ***l*-P2**$^{+\bullet}$). IR signals in region 1000–2200 cm^{-1} become significantly intensified upon oxidation.

Similarly intensified IR bands are observed in π-conjugated polymer cations or anions, such as polythiophenes or polyfluorenes, respectively (**Figure 6a**).[13,16,19–26] Besides conjugated polymers, IR mode intensifications were observed in a mixed-valence coordination complexes (**Figure 6b**).[27]

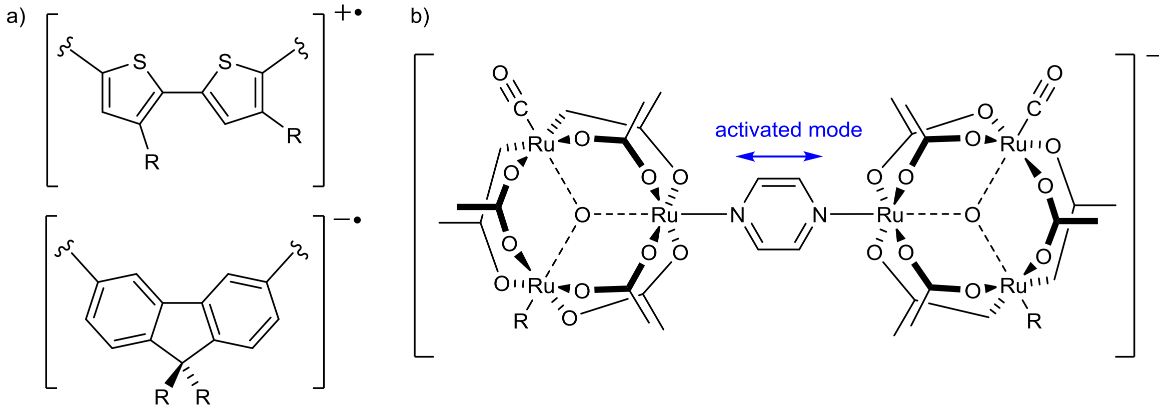

Figure 6. Typical molecules exhibiting the IRAVs. a) Polymers susceptible to doping by oxidation or reduction can exhibit enhanced IR modes due to the presence of a mobile polaron.[5,28] b) Robin-Day Class II organometallic complexes can exhibit IRAVs at oxidation states at which either ‘side’ bears different charge. Symmetric, originally only Raman active, modes can become activated for IR.[27]

The actual mechanism of the IR mode intensification could be visualized using two models. Firstly, the vibrational motion could be ‘mechanically’ inducing redistribution of the mobile polaron, resulting in a large transition dipole moment. A larger transition dipole moment increases the oscillator strength related to the transition and amplifies the absorption. Alternatively, vibronic mixing between low-lying electronic and vibrational transitions can occur, leading to intensification of the vibrational mode *via* the so-called energy borrowing mechanism.[27–30] Either of these mechanisms could explain the observation of intensified IR modes in the butadiyne-linked porphyrin oligomers monocations (**Figure 7**).

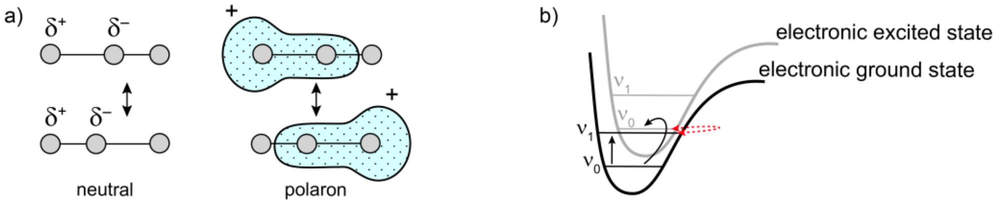

Figure 7. Two possible origins of IR modes intensifications in monocations: a) mobile polaron redistributes along the molecule as a response to the vibrational mode, leading to significant dipole moment change. b) Vicinity of the energetic levels of the vibrational and electronic leads to strong vibronic mixing and intensity borrowing.

Both concepts were considered to be the origin of IRAVs, for example in polyfluorenes anions. Miller et al. presented model where upon distortion of the IRAV mode 945 cm^{-1}, mobile polaron changes position leading to the significant dipole moment change (**Figure 8**).[28]

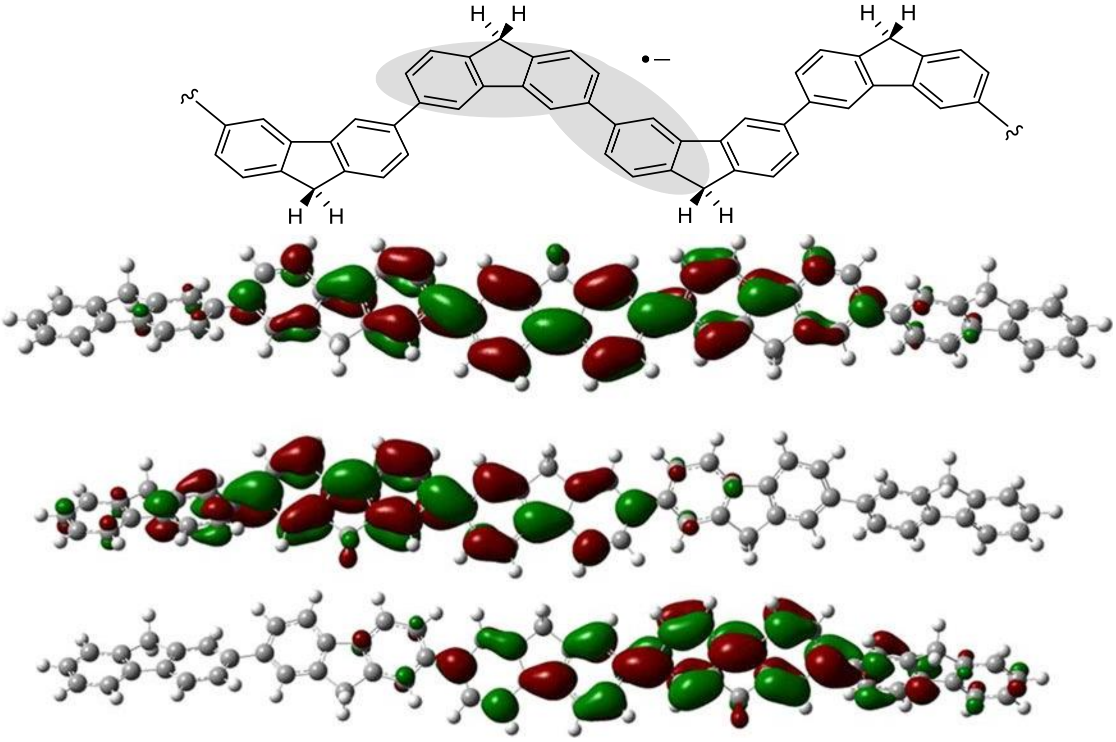

Figure 8. Polyfluorene anion molecule (top) modeled in the calculations (ωPBE/3-21G) as linear pentamer. The polaron, mapped as a SOMO, is in the optimal geometry localized over 3 units (middle). Upon distortion along the IRAV mode 945 cm^{-1} in either direction of the vibration, the mobile polaron moves along the chain in the response to the distortion (bottom two panels). Molecular orbitals calculation adapted with permission from *Nat. Comm.*, 2013, (4), 2818. Copyright © 2013, Springer Nature.

Although there were several attempts presented to unveil the origin of the IRAVs using ultrafast spectroscopies,[10,31–36] most of the studies used polymers and blends of non-uniform composition. Monocations of porphyrin oligomers are suitable systems to study structure-property relationship since the species are well-defined, possess well-characterized polarons and exhibit IRAVs. We therefore selected two molecules to study to elucidate the mechanism of the IRAVs using cutting-edge ultrafast spectroscopies: time-resolved infrared spectroscopy (TR-IR) and two-dimensional infrared spectroscopy (2D-IR).

2.3. Experimental setup

2.3.1. Generation of the monocations and sample preparation

To study origin of the IRAVs in porphyrin oligomer monocations, two model species were chosen. Linear dimer ***l*-P2**$^{+\bullet}$ as a model for a molecular polaron, and a cyclic hexamer ***c*-P6·T6**$^{+\bullet}$ (**Figure 9**).

Neutral porphyrin oligomers ***l*-P2** and ***c*-P6·T6** were synthesized according to previously published procedures.[37–39] The porphyrins were functionalised on free *meso* positions with 3,5-*bis*(trihexylsilyl)phenyl groups to improve the solubility and enable us to work in absence of pyridine (otherwise necessary to prevent porphyrins aggregation). It was found that the presence of pyridine leads to partial degradation of the porphyrins monocations and is thus incompatible with the experiment.[40,41]

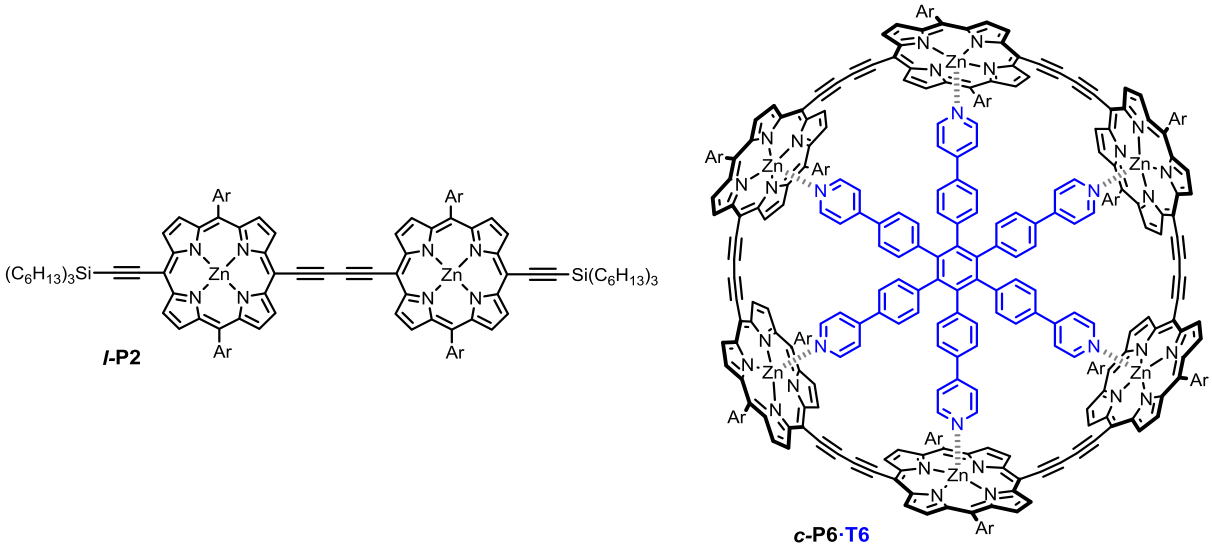

Figure 9. Chemical structure of studied molecules ***l*-P2** and ***c*-P6·T6**. Ar = 3,5-*bis*(trihexylsilyl)phenyl.

As mentioned previously, porphyrin oligomers monocations are expected to possess very broad electronic band P_1 in IR region and certain number of intensified IR vibrational modes.

***l*-P2**$^{+\bullet}$ exhibits a broad P_1 absorption band of electronic origin in the region 3000–6000 cm^{-1} and relatively sharp IR bands. One distinctive sharp IRAV mode is found around 2050 cm^{-1}, corresponding to the −C≡C− stretching vibration. A series of multiple sharp IRAVs is observed the fingerprint region (1000–1600 cm^{-1}). The −C≡C− vibrational stretch absorption in ***l*-P2**$^{+\bullet}$ is isolated in energy between the formally electronic P_1 band and the IRAVs in the IR fingerprint region, providing a unique handle to explore the behavior of the polaron and IRAVs (**Figure 10**, bottom).

_c_-P6·T6$^{+\bullet}$ exhibit a Fano-type anti-resonance around 2050 cm^{-1}, due to the overlap of the −C≡C− stretching vibration mode with the electronic type P_1 polaron band, which can be found in region 1600–4000 cm^{-1}. This spectral overlap causes a cancellation of oscillator strengths creating apparent ‘dip’ in the continuum of the electronic band P_1. As the P_1 band ‘ends’ at ~1600 cm^{-1}, all the fingerprint region is not affected by it and multiple IRAVs in the window 1000–1600 cm^{-1} are observed (**Figure 10**, top).[7,9,42]

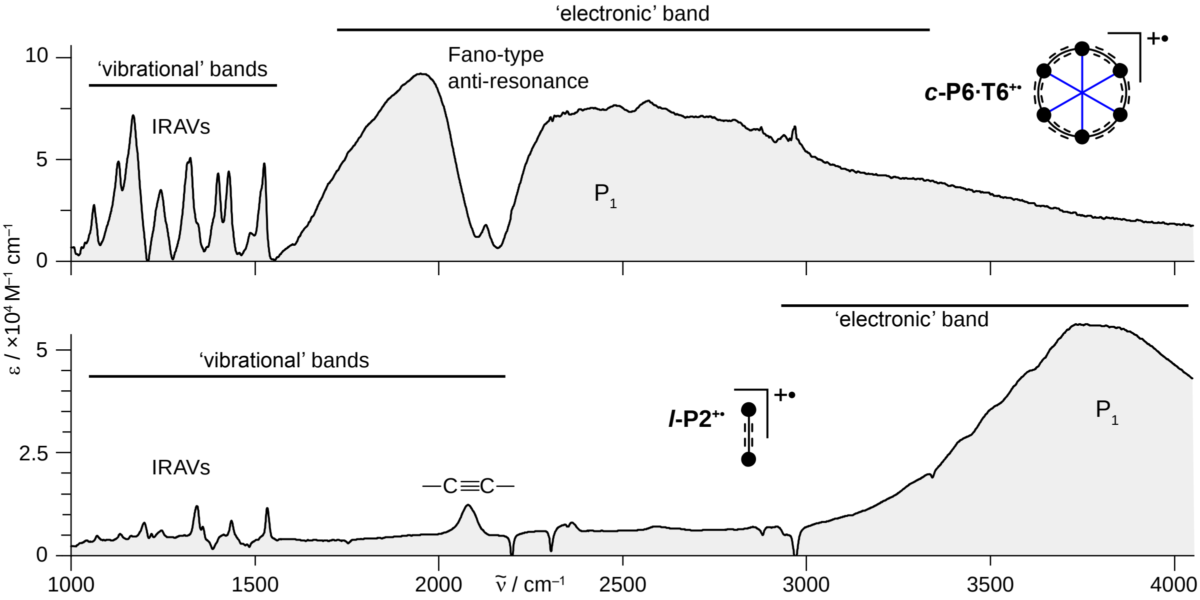

Figure 10. FTIR spectra of monocations **_l_-P2**$^{+\bullet}$ (bottom) and **_c_-P6·T6**$^{+\bullet}$ (top).

To generate monocations and assess them by IR spectroscopy, a spectro-electrochemical setup was used.

An alternative approach of generating monocations by addition of 0.5–1 equivalent of a chemical oxidant to a porphyrin solution and tightly sealing the mixture in the IR Harrick cell under inert atmosphere was also tested. This approach, however, showed a poor monocation concentration stability as the species were found to relatively rapidly turn back to neutral state.

Experiments were therefore performed in an optically transparent thin-layer electrochemical cell (OTTLE, *vide infra*) fitted with CaF_2 windows enabling transmission of the IR light in desired regions.[43] The optical path length was ~0.2 mm. CD_2Cl_2 was chosen as a solvent as the IR absorption bands of CH_2Cl_2 coincides with the bands of interest. 0.1 M tetra-*n*-butylammonium hexafluorophosphate (Bu_4NPF_6) was used as a supporting electrolyte.

Square wave voltammograms of **_l_-P2** and **_c_-P6·T6** show a 1+ → 2+ transition close to the 0 → 1+ transition peak. To avoid contamination of the monocation signal with potentially IR-active 2+ states, electrochemical potentials were adjusted for each sample and measurement. The desired composition was a mixture of neutral, which is relatively silent in the IR, and optically active monocation states. The composition of the OTTLE electrochemical cell was monitored using vis-NIR-IR spectroscopy, where the ratio of the neutral porphyrin Q band and the monocation P_2 band was used to determine the ratio and absolute sample concentration. ***l*-P2**$^{+\bullet}$ and ***c*-P6·T6**$^{+\bullet}$ concentrations were adjusted to maintain ~1:1 ratio of neutral : monocation species by adjusting the applied voltage with reference to the known oxidation potentials of the porphyrin radical cations (**Figure 11**).[9]

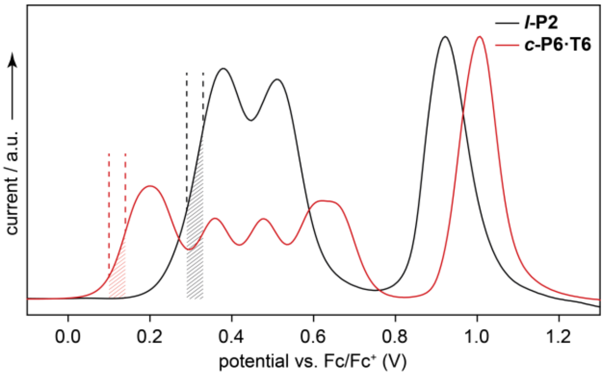

Figure 11. Square wave voltammogram (CH_2Cl_2/0.1 M Bu_4NPF_6) of porphyrin oligomers ***l*-P2** (black) and ***c*-P6·T6** (red) referenced to Fc/Fc^+. Shaded areas represent potential range within which were potentials held during experiments to maintain the desired ~1:1 ratio of neutral : monocation species.

The spectroscopy was carried out after masking the cell window with electrical tape and aluminium foil such that the only transparent path went through the mesh of the working electrode. Such masking is necessary, as the oxidation process proceeds mainly in the vicinity of working electrode and the rest of the window remains un-oxidised. The whole cell could be than placed into the conventional FTIR and UV-vis spectrometer (**Figure 12**).

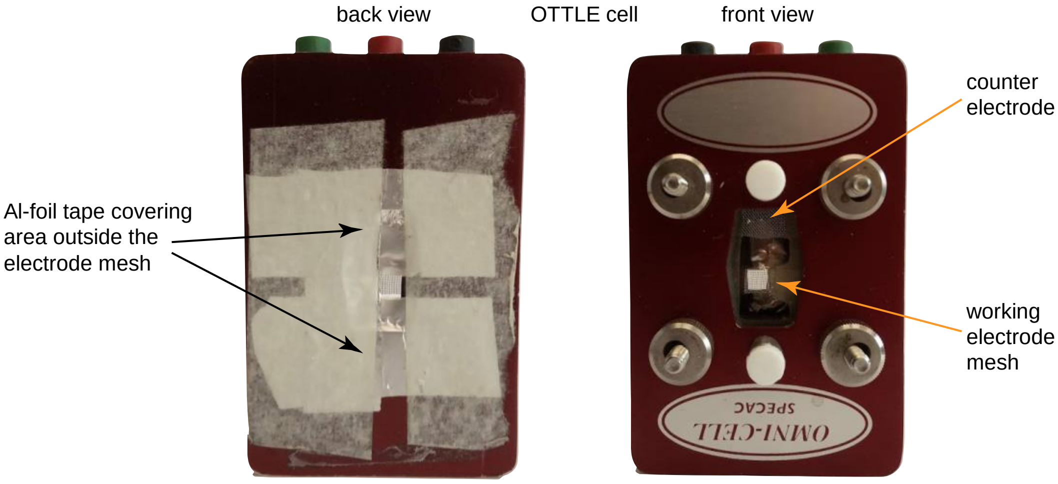

Figure 12. OTTLE cell masked with aluminium foil and a tape to cover all areas outside the mesh of the working electrode.

The cell was filled with neutral solutions of ***l*-P2** and ***c*-P6·T6** with concentrations of ~2 mg/mL in CD_2Cl_2, which is equivalent to ~0.5 and 0.2 mM, respectively. This corresponded to maximum optical density of 0.4–0.8 in the Q band.

Monocations were prepared by performing a CV routine, stopping it at the steepest gradient of the first oxidation peak. The potential at this position was then held during the experiment. This processed could be performed with the cell in the spectrometer, enabling an almost immediate readout of the cell composition and rapid change of the composition to desired ratio.

FTIR spectra of ***l*-P2**$^{+\bullet}$ and ***c*-P6·T6**$^{+\bullet}$ were collected by first recording a background measurement of the OTTLE cell in neutral state and then generating the monocation without physical manipulation with OTTLE cell.

The 1:1 neutral : monocation ratio yielded to 0.4–0.8 OD in the P_2 band, which is equivalent to optical densities of 0.2–0.5 in the IR absorptions regions. At such conditions, the concentration of the monocations was ~0.1–0.2 mM.

2.3.2. Ultrafast spectroscopies

The ultrafast spectroscopy measurements were performed in STFC Rutherford Appleton Laboratory in the Central Laser Facility. These experiments used a pump-probe setup, enabling first the excitation of the molecule and shortly after probing the excited state. For the time-resolved infra-red (TR-IR), a simple two pulse setup, with one pump and one probe, was used (**Figure 13**). For the 2D-IR measurements, more complicated 3 and 4 pulses routines were used.

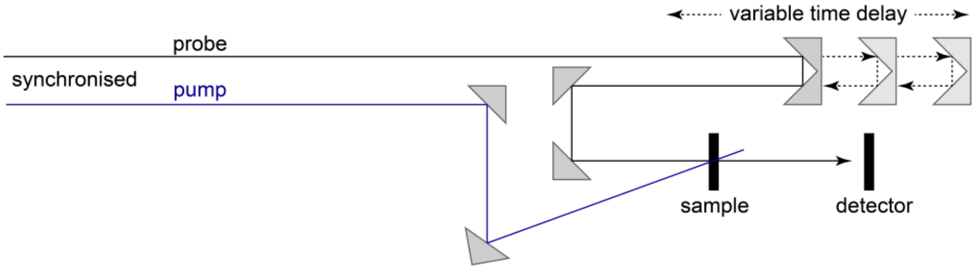

Figure 13. Simplified scheme of pump-probe experimental setup. Change of the path length of either pump or probe can be used to finely tune the probe time delay.

Upon generation of the ***l*-P2**$^{+\bullet}$ and ***c*-P6·T6**$^{+\bullet}$ cations, the OTTLE cell was placed to the setup such that the pump and probe beams coincided within the single hole of the mesh of the working electrode in the OTTLE cell (**Figure 14**).

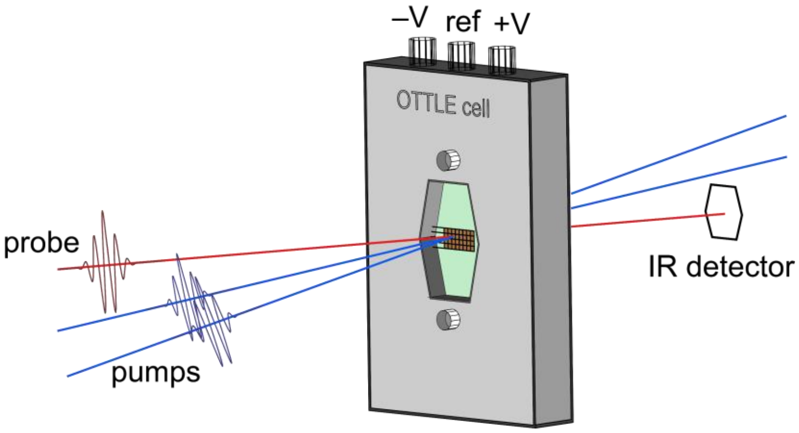

Figure 14. Laser beams for pump-probe ultrafast experiments were adjusted such, that they coincide in OTTLE cell within one hole of the working electrode.

In general, upon oxidation, the samples were found to be stable for up to ~45 min (while keeping a constant applied potential). This was confirmed for the ultrafast measurements by recording vis-NIR spectra before and after the experiment. If the concentration of the monocation species changed significantly (by more than ~30%), and particularly if the drift was caused by over-oxidation, leading to risk of generation of the IR-active 2+ state, the OTTLE cell was neutralized, refilled with a fresh solution and the experiment redone (**Figure 15**).

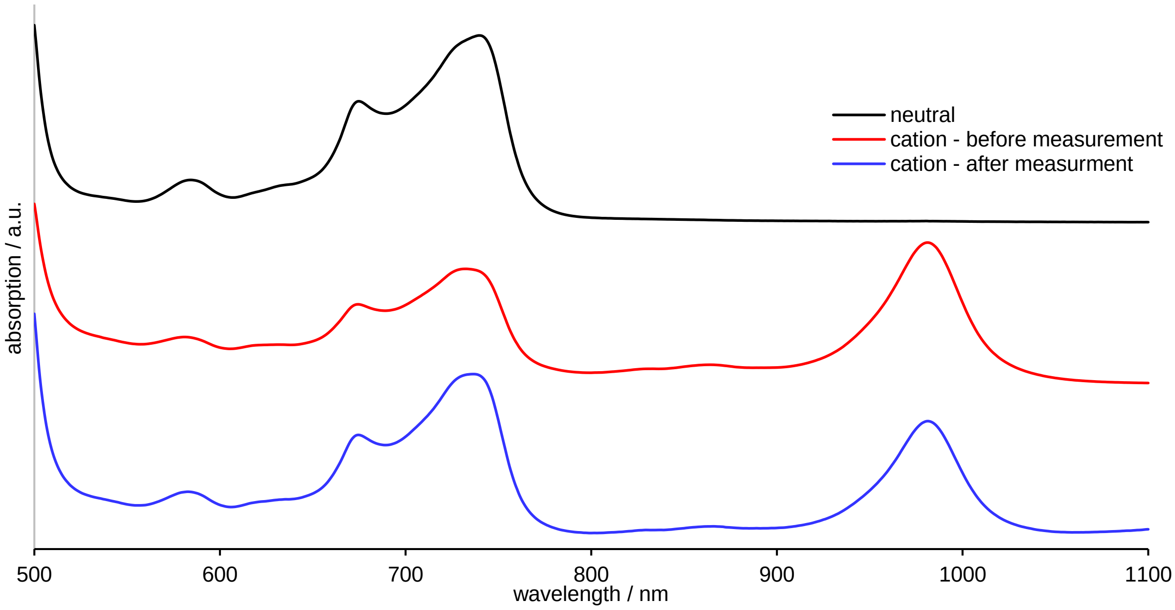

Figure 15. Representative series of vis-NIR absorption spectra of ***l*-P2** taken before oxidation (neutral) (black), after oxidation (indicating ~1:1 mixture of neutral : monocation) (red) and after ~30 min experiment (blue). It is evident, that concentration has changed during the experiment disbalancing the mixture toward neutral species. However, such change was considered as acceptable.

The negative effects of concentration changes during the experiment, potentially obscuring kinetic profiles, were minimized by randomization of the probe delays. This should ensure that any linear change of the concentration with time should be visible in the kinetic profiles as noise, rather than obscuring the lifetime of signal decays/grows.

2.4. Time-resolved IR measurements (TR-IR)

2.4.1. General setup for TR-IR

Time-resolved IR (TR-IR) spectra were collected using spectrometers at the STFC Rutherford Appleton Laboratory, using setups ULTRA A and ULTRA B, a titanium sapphire amplifier system with broadband, shorter pulse capability (10 kHz, > 50 fs, > 300 cm^{-1}), with capability to tune ultrafast pump and probe pulses frequencies, as described in detail elsewhere.[44]

The good time resolution of the system is essentially coupled with low resolution in the pump wavenumber distribution (bandwidth ~300 cm^{-1}). Due to this limitation, TR-IR experiments did not allow very selective irradiation of selected signals. For these reasons and due to rather broad features of the spectra, two positions for the pumps were chosen – the triple bond stretch (or associated Fano-type antiresonance) at ~2050 cm^{-1}, the features rather isolated from other IRAVs (**Figure 16**, **pump A**) and the polaron band P_1. In case of pumping P_1, several different positions were chosen and tested for the kinetic analysis and for the polarization experiments (*vide infra*), all within 2500–3200 cm^{-1} region. For the kinetic analysis, pumps were centered at ~3000 cm^{-1} (**Figure 16**, **pump B**).

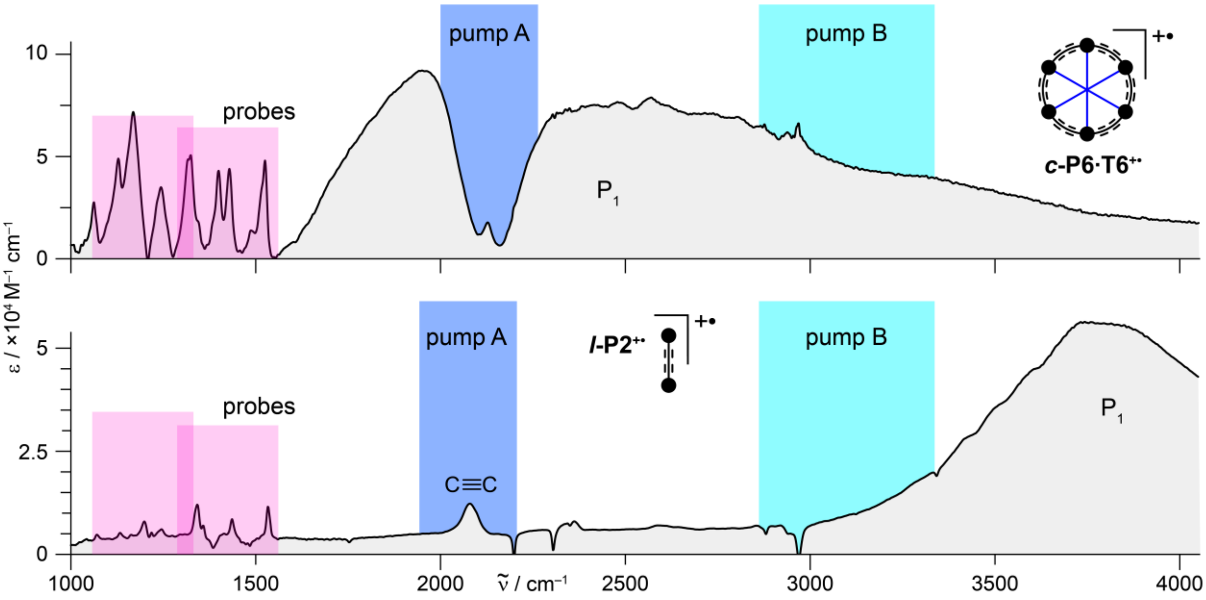

Figure 16. FTIR spectra of ***c*-P6·T6**$^{+\bullet}$ (top) and ***l*-P2**$^{+\bullet}$ (bottom) with highlighted area which were pumped for the kinetic analysis of the TRIR spectra.

When the system is 'pumped', it is transformed to some excited state. If the process was conventional vibrational excitation ($\nu_0 \rightarrow \nu_1$), due to vibrational anharmonicity, a new absorption (corresponding to the $\nu_1 \rightarrow \nu_2$ process) is expected to be observed with a lower energy. Furthermore, such excitation leads to reduction in the original absorption ($\nu_0 \rightarrow \nu_1$) since a portion of the ground state molecules are temporarily excited and therefore the concentration of the molecules in ground state is reduced. If the original and the new, transient spectra are subtracted, two peaks are expected. Positive, red-shifted excited-state absorption (ESA) and negative ground state bleach (GSB) on the position of the original absorption band (**Figure 17**).

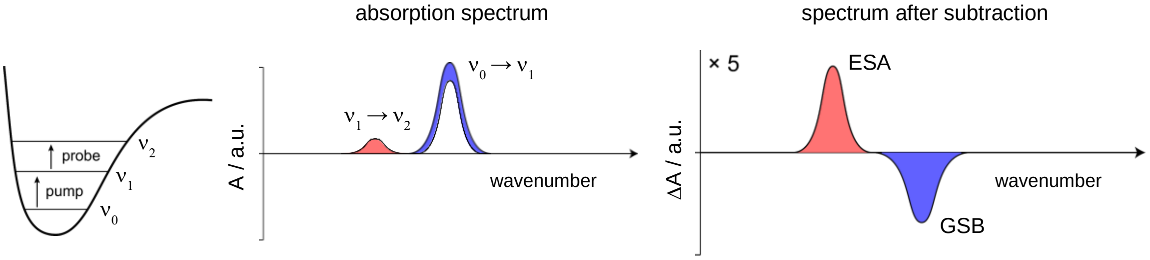

Figure 17. Schematic representation of the pump-probe spectroscopy and origin of the ESA and GSB pair as a resulting of subtraction of original and excited state spectra.

The model described above relates to the situation when the probe light is probing directly the pumped region. However, when a region different from the pumped is probed, GSB appearance together with the red-shifted ESA is expected only if the vibrational modes are coupled.[45] Such coupling can be of any origin. It can result from a through-space electrostatic interaction of the transition dipoles as well as through-bond coupling where the modes spatially overlap. Similar interpretation would be drawn from observing off-diagonal peaks in the 2D-IR spectra (*vide infra*).[46–48] Observation of such ESA or GSB thus documents exitance of a coupling (of any kind) between the pumped and probed vibrational mode.

By varying the probe time delay, different spectra can be expected. If the pump and probe pulses have no time delay and consequently overlap, interference between the pulses can significantly obscure the picture. Later probe delays then follow the evolution of transient spectra. All TR-IR spectra can be then stitched to the 2D contour plot (**Figure 18**).

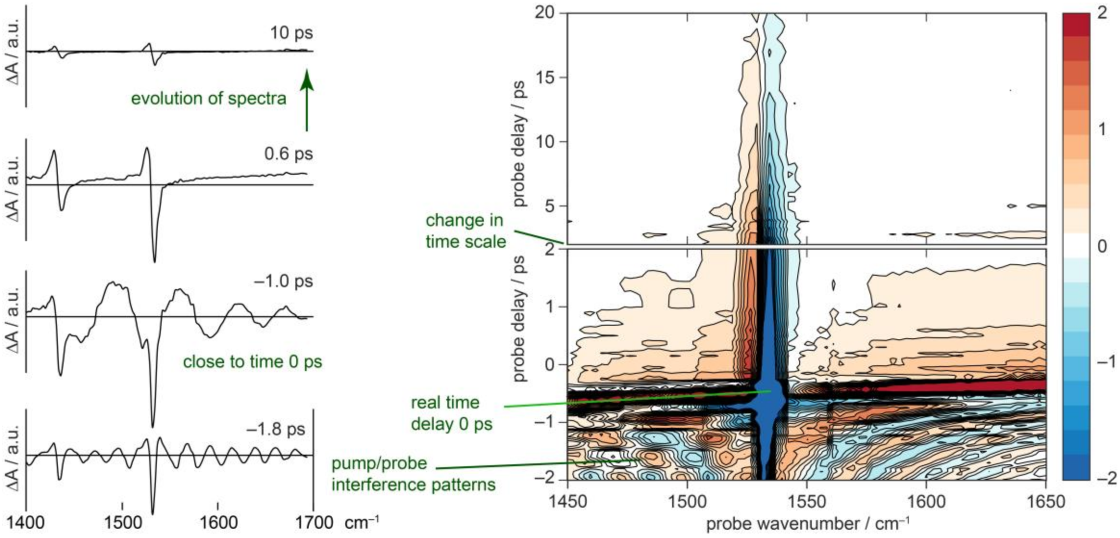

Figure 18. (left) Selected TR-IR spectra at various pump-probe delays. (right) Prototypical 2D contour plot of TR-IR spectra at various pump-probe delays.

The time evolution of the signal intensity after the time $t = 0$ can be followed for each wavenumber by fitting it to a mono- (**Eq. 1**) or bi-exponential (**Eq. 2**) decay/grow function:

$$y = A \cdot e^{-\frac{t}{\tau}+} \tag{1}$$

$$y = A_1 \cdot e^{-\frac{t}{\tau_1}} + A_2 \cdot e^{-\frac{t}{\tau_2}} \tag{2}$$

If the fit of the whole time-scale (including negative times) is desired, the instrument response function (IRF) needs to be implemented as well (*vide infra*). For the TR-IR, if the IRF was used, the fitting was carried out using SurfaceXplorer.[49] For such analysis, the spectra were chirp-corrected and noisy areas were cropped away.

This general section is now followed by a section discussing TR-IR experimental results.

2.4.2. TR-IR of *l*-P2$^{+\bullet}$

The IR fingerprint region 1100–1700 cm^{-1} was probed with two windows covering 1100–1450 cm^{-1} and 1380–1700 cm^{-1} (**Figure 16**, probes). When pumping at the polaron band P_1, centered to ~3000 cm^{-1} (pump B, **Figure 16**, bottom), in the probe window 1100–1450 cm^{-1}, instantly, two ground state bleaches (GSB) and one excited state absorption (ESA) signals are observed. Since the region that was probed is different to that pumped, the observation of ESA/GSB implies the strong coupling between the fingerprint modes and the triple bond stretch mode. The observation of a GSB but not a ESA/GSB pair suggests that the ESA is overwhelmed by a more intense GSB. At early probe delay times (0–0.3 ps), only strong, dominant GSB is observed. At delays of ~0.3 ps, intensity of the GSB is reduced significantly and a more classical ESA/GSA pair appear (**Figure 19**).

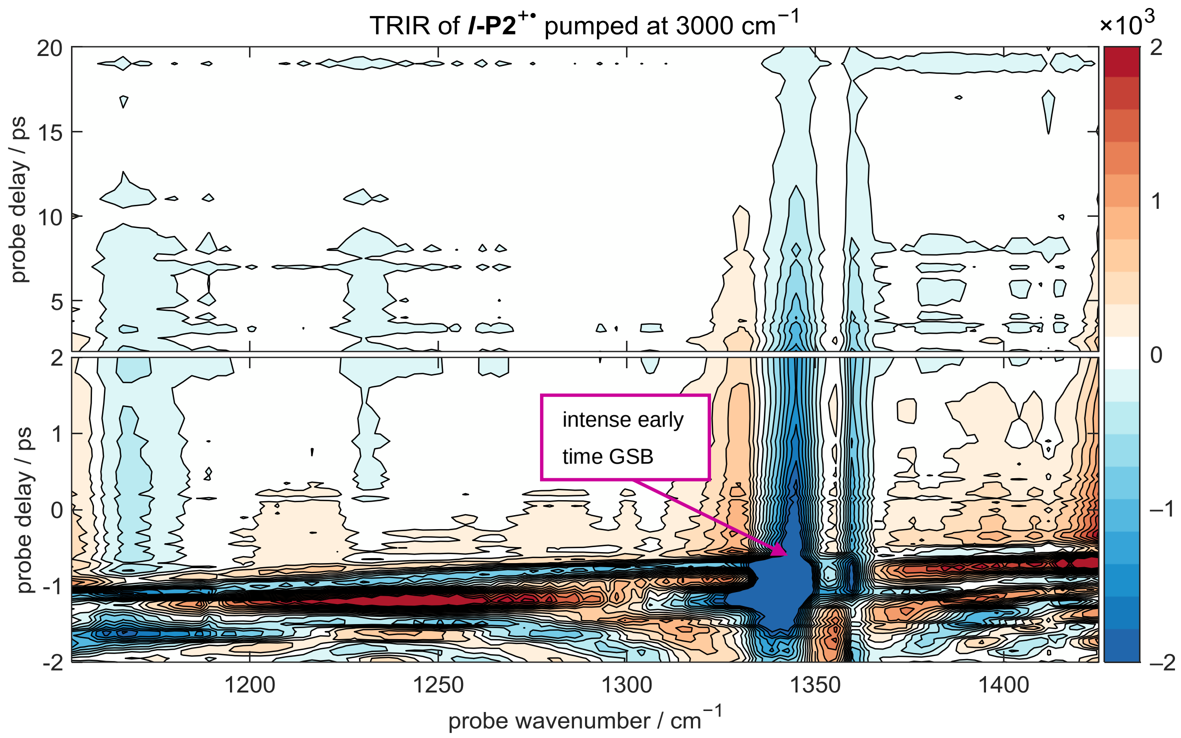

Figure 19. Contour plot of TR-IR spectra of ***l*-P2**$^{+\bullet}$ pumped at ~3000 cm^{-1} and probed at 1100–1400 cm^{-1}.

The individual regions can be analysed, and kinetic profiles of individual wavenumbers fitted to mono- or biexponential decays/recoveries (**Figure 20**). These analyses suggest more complex kinetics of the GSB, well fitted with the bi-exponential recovery. The fitted faster component of the bi-exponential recovery is, however, often faster than the instrument response function, making its correct interpretation difficult. Also, at early times the whole TR-IR data suffer from the pump-probe interference.

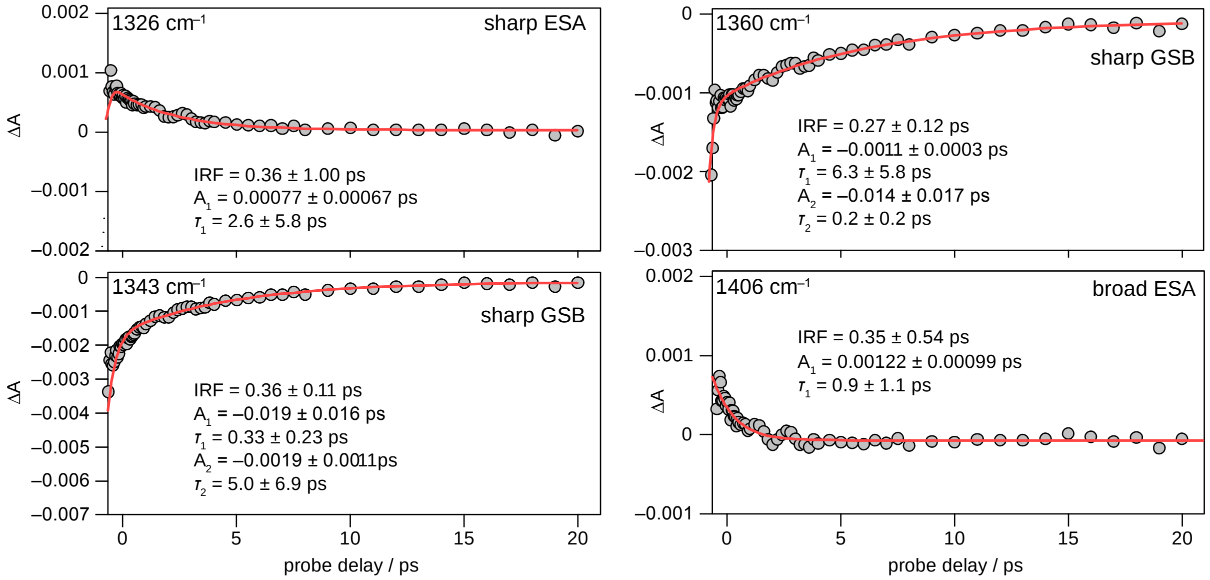

Figure 20. Kinetic profiles of selected probed wavenumbers and their fit with either monoexponential or biexponential function convoluted with instrument response function, as implemented in the SurfaceXplorer.

In the probe region 1380–1700 cm^{-1} at early times, very intense GSB and broad positive transient features are observed. These vanish within 2 ps, followed with two, standard (~1:1 intensity), ESA/GSB pairs, corresponding to the two IRAVs in the 1400–1600 cm^{-1} region (**Figure 21**). It is apparent that in both probe windows, at later times, all sharp ESA decay and GSB recover with a similar rate.

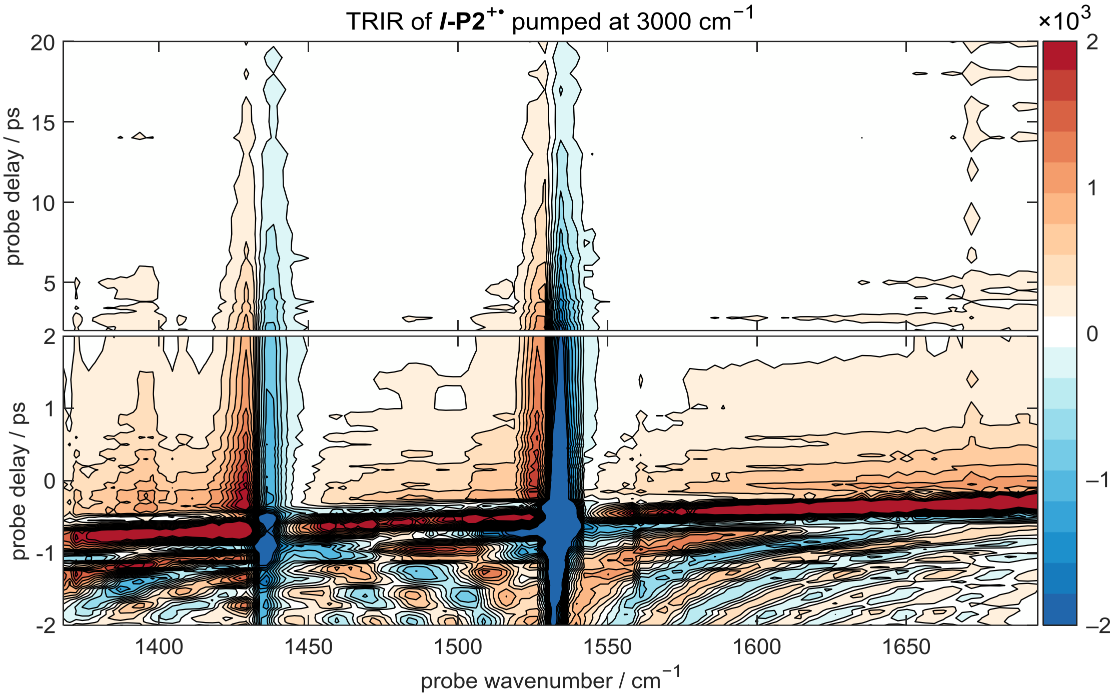

Figure 21. Contour plot of TR-IR spectra of ***l*-P2**$^{+\bullet}$ pumped at ~3000 cm^{-1} and probed in the fingerprint region.

When the system was pumped at the −C≡C− stretch mode at ~2050 cm^{-1} (pump A, **Figure 16**, bottom), very similar features were observed: In the 1100–1450 cm^{-1} window, two GSB and one ESA signals were observed, as with the ~3000 cm^{-1} pump. Furthermore, broad positive transient features were observed at earlier times. Additionally, the fast decaying GSB (although not that dominant) was observed. The second window provided two sets of GSB/ESA pairs, analogously to the 3000 cm^{-1} pumped system. The two probed windows were stitched together allowing a more comprehensive look at the kinetic profiles of the transient signals in region 1250–1600 cm^{-1} (**Figure 22**).

To help to recognize observed effects in the 2D plot, several slices at various time delays are plotted in **Figure 23**. Evidently, at least two (but more likely three) processes occur upon excitation, as documented by the bi-exponential character of the GSB and various fitted constants. The very fast component is observed only for the GSB, suggesting that the very early excited state does not have (or only very broad) associated ESA (*vide infra*, **Section 2.7**).

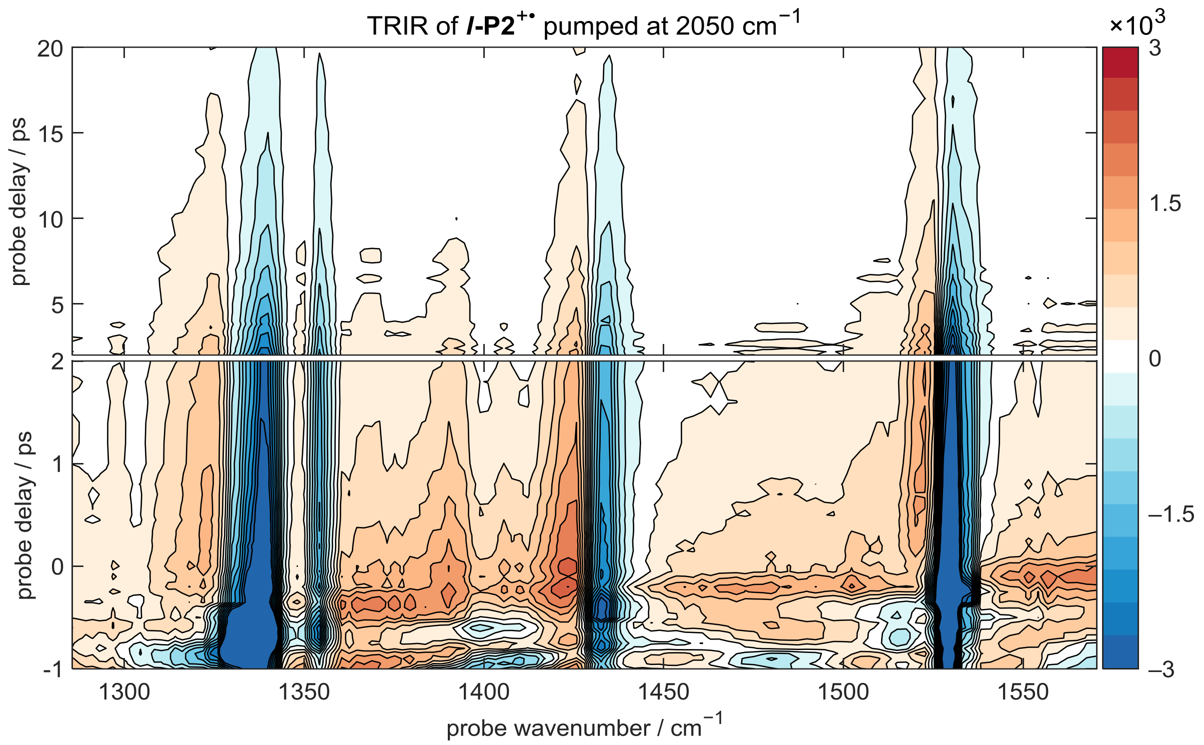

Figure 22. Contour plot of TRIR spectra of ***l*-P2**$^{+\bullet}$ pumped at ~2050 cm^{-1} and probed at 1280–1575 cm^{-1}

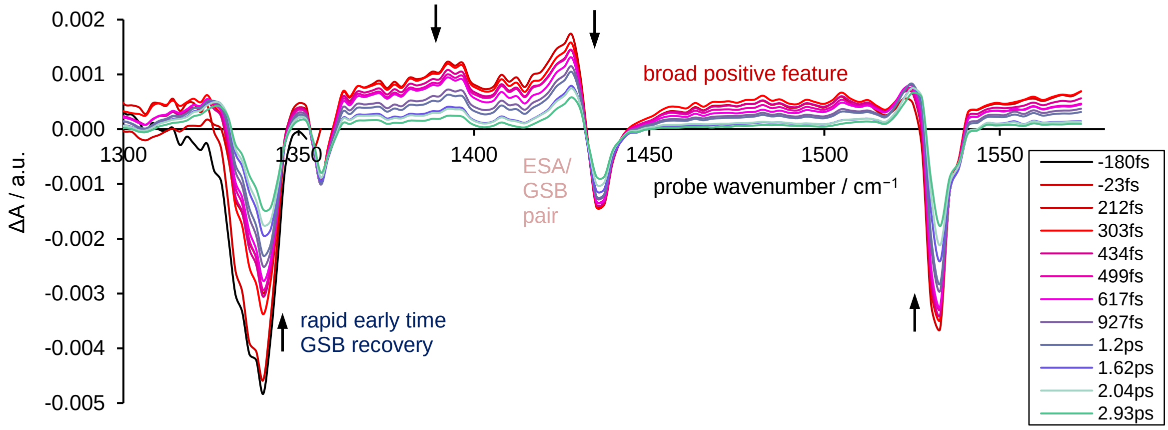

Figure 23. TRIR spectra at selected probe delays of ***l*-P2**$^{+\bullet}$ pumped at ~2050 cm^{-1} and probed at 1280–1575 cm^{-1}.

Although the fitted lifetimes of the slow components vary for individual peaks, their typical values are within of 3–9 ps and the overall shape of the 2D plots implies that all later-time sharp ESA/GSB pairs decay/recover at the same rate. Furthermore, the very broad ESA, apparent as a positive offset, decays at a medium lifetime of ~1–2 ps, not matching either of the GSB components, implying the existence of a total of three processes following the initial excitation (more details in **Section 2.7**). Generally, when analyzing individual peaks for the ESA decays, a mono-exponential functions provide a good fit. Whereas for the GSB recoveries, use of a bi-exponential function is essential for the good fit. Individual fitted parameters are summarized in **Table 1**.

~3000 cm^{-1} pump / probe	IRF / ps	τ_1 / ps	A_1	τ_2 / ps	A_2
ESA 1328 cm^{-1}	0.36 ± 1.0	2.6 ± 5.8	0.000077 ± 0.00067	—	—
GSB 1343 cm^{-1}	0.36 ± 0.11	5.0 ± 6.9	0.0019 ± 0.0011	0.33 ± 0.23	0.019 ± 0.016
GSB 1360 cm^{-1}	0.27 ± 0.12	6.3 ± 5.8	0.0011 ± 0.00003	0.2 ± 0.2	0.014 ± 0.017
ESA 1406 cm^{-1}	0.35 ± 0.54	0.9 ± 1.1	0.0012 ± 0.00099	—	—
ESA 1395 cm^{-1}	0.35 ± 0.46	1.0 ± 1.1	0.0019 ± 0.0014	—	—
ESA 1429 cm^{-1}	0.13 ± 0.19	2.3 ± 1.5	0.0024 ± 0.0008	—	—
GSB 1438 cm^{-1}	0.46 ±0.17	8.8 ± 9.1	0.0013 ± 0.0004	0.35 ± 0.39	0.01 ± 0.01
ESA 1524 cm^{-1}	0.13 ±0.35	3.5 ± 4.4	0.0016 ± 0.0007	—	—
GSB 1537 cm^{-1}	0.48 ± 0.14	6.5 ± 2.8	0.0019 ± 0.0005	0.2 ± 0.3	0.04 ± 0.25

Table 1. Fitted instrument response functions (IRF), and the lifetime (or lifetimes when bi-exponential function are used) for the analysed fingerprint region of ***l*-P2**$^{+\bullet}$, when pumped at ~3000 cm^{-1}.

Interestingly, the shape of the TR-IR spectra at later times (> +0.5 ps) is nearly identical, regardless the pumped position. Pumping at both the 'vibrational' −C≡C− stretch mode at 2050 cm^{-1} and the 'electronic' polaron P_1 at ~3000 cm^{-1} leads to the same late-time TR-IR spectra consisting of several ESA/GSB pairs (**Figure 24**). This suggests the strong coupling between the vibrational-origin −C≡C− mode and the electronic band P_1.

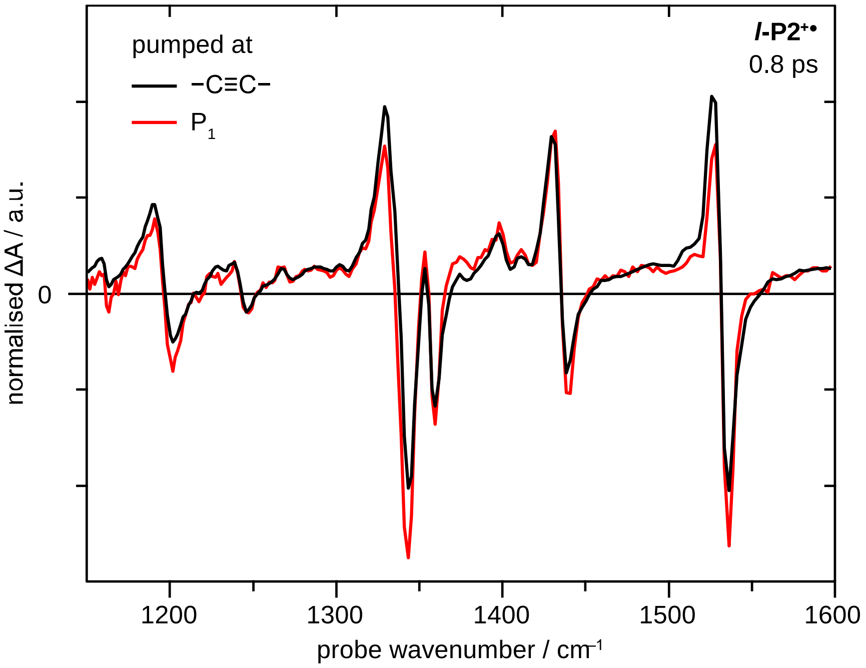

Figure 24. Normalised TRIR spectra at 0.8 ps probe time delay of ***l*-P2**$^{+\bullet}$ when pumped at 'vibrational' mode at 2050 cm^{-1} (black) or at 'electronic mode P_1 at 3000 cm^{-1} (red).

2.4.3. TR-IR of *c*-P6·T6$^{+\bullet}$

The fingerprint region of ***c*-P6·T6**$^{+\bullet}$ was probed in two windows which were later stitched together. First, the nanoring was pumped to P_1 band with the pulse centered at ~3000 cm^{-1} (**Figure 25**). The analogous experiment was performed also for the pump centred at the Fano-antiresonance at 2050 cm^{-1} providing similar TR-IR spectra (**Figure 26**). However, it needs to be pointed out, that the pump centered on the anti-resonance is not selective and significant overlap with the P_1 occurs.

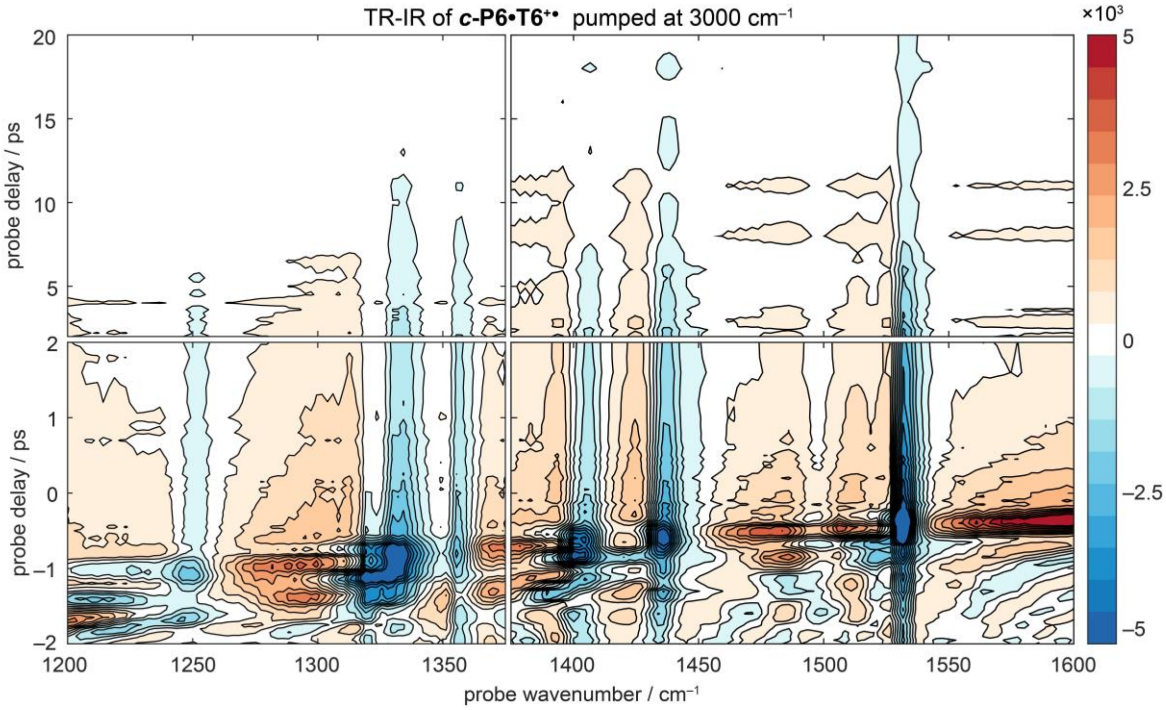

Figure 25. Contour plot of stitched TR-IR spectra of ***c*-P6·T6**$^{+\bullet}$ pumped at ~3000 cm^{-1} and probed in 1200–1600 cm^{-1}, experimentally covered by two windows stitched together.

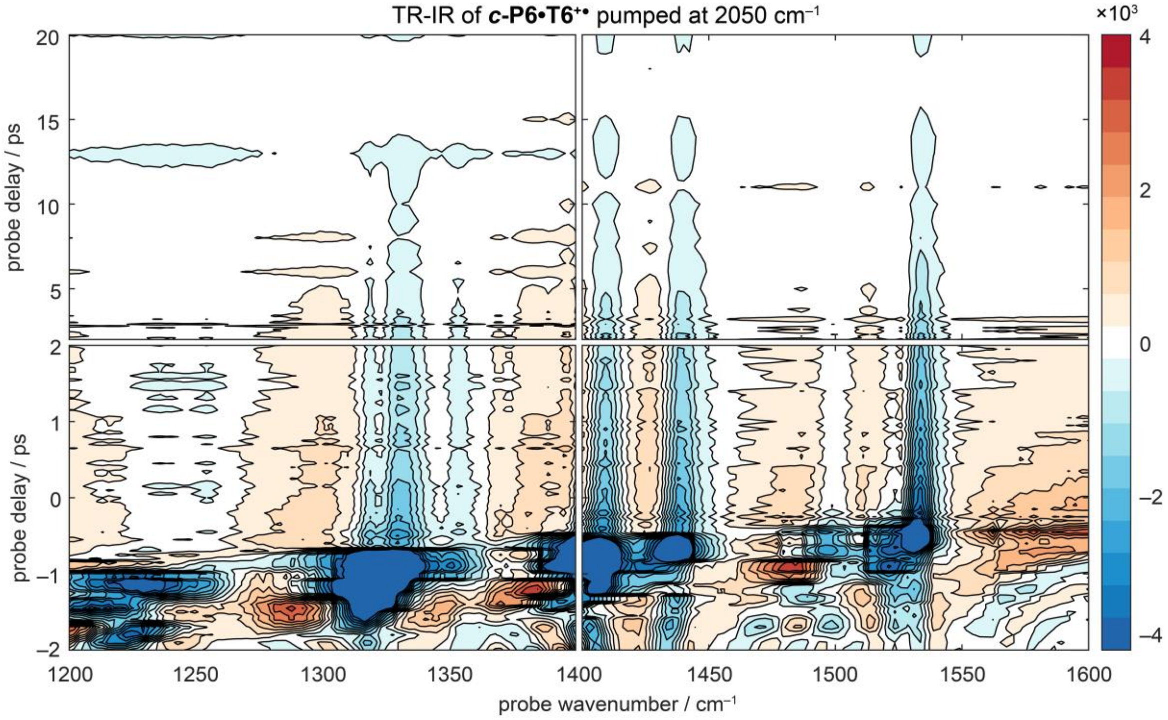

Figure 26. Contour plot of stitched TR-IR spectra of ***c*-P6·T6**$^{+\bullet}$ pumped at ~2050 cm^{-1} and probed in 1200–1600 cm^{-1}, experimentally covered by two windows stitched together.

Both TR-IR spectra showed very dominant GSB at early probe delay times. At later times, ESA/GSB pairs of similar intensity were observed. The GSB recovery can be fitted with the bi-exponential function with fast and slow components found in range τ = 0.1–0.3 ps and τ = 2–3 ps, respectively. Both TR-IR spectra can be compared at later times (> +0.5 ps) showing very similar features, regardless the pump position. This observation is analogous to the ***l*-P2**$^{+•}$ and implies the existence of only one, longer-living excited state (**Figure 27**).

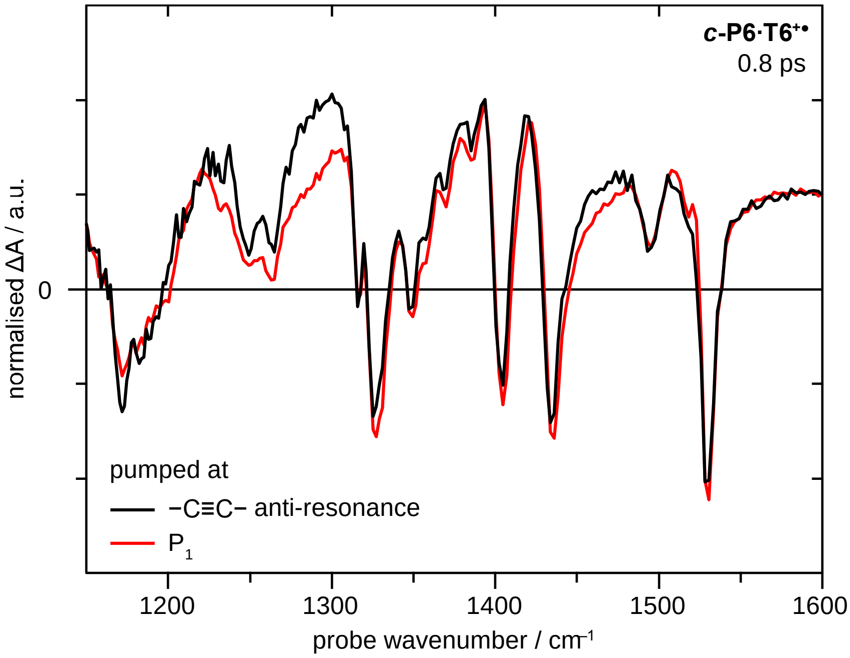

Figure 27. Normalised TRIR spectra at 0.8 ps probe time delay of ***c*-P6·T6**$^{+•}$ when pumped at the Fano-type antiresonance at 2050 cm^{-1} (black) or at ‘electronic mode P$_1$ at 3000 cm^{-1} (red).

2.4.4. TR-IR summary

TR-IR spectra in the fingerprint region for both ***l*-P2**$^{+•}$ and ***c*-P6·T6**$^{+•}$ show similar features, regardless of the pump position, particularly for the later (> 1 ps) probe delay times. These, later time TR-IR spectra consisted of the ESA/GSB pairs decaying uniformly with the lifetimes 3–9 ps and 2–3 ps for ***l*-P2**$^{+•}$ and ***c*-P6·T6**$^{+•}$, respectively.

Early time recovery of the typical GSB exhibits more complex character with a very fast component and had to be described with the bi-exponential function. The fast component lifetimes were typically in the range 0.2–0.4 ps, mixed within the instrument response, showing a rapid process happening after the excitation.

Furthermore, a broad featureless ESA was observed across the whole probe window with the decay lifetime ~1 ps.

This supports a hypothesis of the existence of two excited states with observable ESA. One excited state possesses features often attributed to the ‘electronic’ excited state (broad ESA) and one consist of rather sharp ESA/GSB pairs, typical for ‘vibrational’ excited states.

A further detailed and rigorous kinetic analysis will be developed in **Section 2.7**, using LIFEtime’s 2D-IR, which setup significantly reduced the pump-probe interference with the phase-cycling mechanism.

2.5. TR-IR anisotropy analysis

To understand the origin of the IRAVs, it is useful to assign the vibrational modes that are amplified and discover their relative orientations with respect to the pumped −C≡C− stretch or P_1 polaron transition dipole moment, which both are parallel with the butadiyne linker.

To access the relative orientations of the vibrational modes experimentally, polarization experiments can be used. When a certain mode is pumped with one polarization, it is expected that the ESA/GSB transient intensity will have dependence on the relative orientation of the pumped and probed dipole moments. Dipoles of the individual vibrational modes can have relative orientation with an angle θ, as depicted in **Figure 28**:

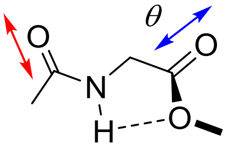

Figure 28. Relative orientation of the dipole of the C=O stretch modes in the molecule.

The difference in intensity of ESA and GSB if pump and probe are either parallel ($\Delta A_{\|}$) or perpendicular ($\Delta A_{\perp}$) can be defined by the anisotropy r as:

$$r = \frac{\Delta A_{\|} - \Delta A_{\perp}}{\Delta A_{\|} + 2 \cdot \Delta A_{\perp}} \tag{3}$$

As demonstrated for example by Rubstov et al.[47] and Meech et al.[50,51] who studied conventional vibrations and their couplings, or Bakulin et al.[31] who studied IRAVs in doped conjugated polymers using polarization ultrafast spectroscopy, the relative vibrational dipole moments orientation θ is directly related to the anisotropy as:

$$\langle \cos^2 \theta \rangle = \frac{5r - 1}{3} \tag{4}$$

This relation implies that in an isotropic solution, the anisotropy is expected to be in the range $-0.2 < r < 0.4$. In the static molecule, without molecular motions and exciton delocalization, if the relative orientation of both pumped and probed dipole is parallel (i.e. $\theta = 0°$), then the anisotropy should be $r = 0.4$. If the orientation of the dipole is perpendicular (i.e. $\theta = 90°$), the expected value is $r = -0.2$. If it is somewhere between these two extremes, r should be found in the range <−0.2, 0.4> according to **Eq. 4**.

If the original orientation of the dipoles was parallel, but due to, for example, exciton delocalization, the orientation of the probed dipole is redistributed within the 2D plane, a value of $r = 0.1$ would be expected instead. If, for example due to tumbling motion of the whole molecule, the probed transition dipole would be completely disoriented in the 3D space, $r = 0$ would be expected.

A series of TR-IR spectra of ***l*-P2**$^{+\bullet}$ and ***c*-P6·T6**$^{+\bullet}$ with parallel, magic angle and perpendicular orientation of the pump and probe was recorded. Pumped regions were 2100 cm^{-1}, 2500 cm^{-1} or 3250 cm^{-1}. Excited states were probed in the fingerprint region. A change of the relative orientation was achieved by an automatic $\lambda/2$ plate, that rotated the orientation of the pump. Time delays were randomized to minimize the effect of fluctuations in the sample concentration and always the parallel, magic angle and perpendicular pump-probe orientations were recorded at each time delay, within ~10 s, to minimize any effect of a potentially changing cation concentration. If the nature of the experiment required acquisition of more data (e.g. to increase signal-to-noise ratio), more cycles were performed while keeping low averaging time for each cycle.

The correct setup of the polarization experiment was checked using a known sample described in literature, $W(CO)_6$. Pumping and probing CO stretch mode at ~2100 cm^{-1} provided high anisotropy at early times ($r \sim 0.3$) with rapid decay, in agreement with published spectra (**Figure 29**).[52] The anisotropy decay in $W(CO)_6$ can occur both *via* intramolecular energy redistribution and by the rapid rotation of the molecule, disorienting the originally pumped mode.[52]

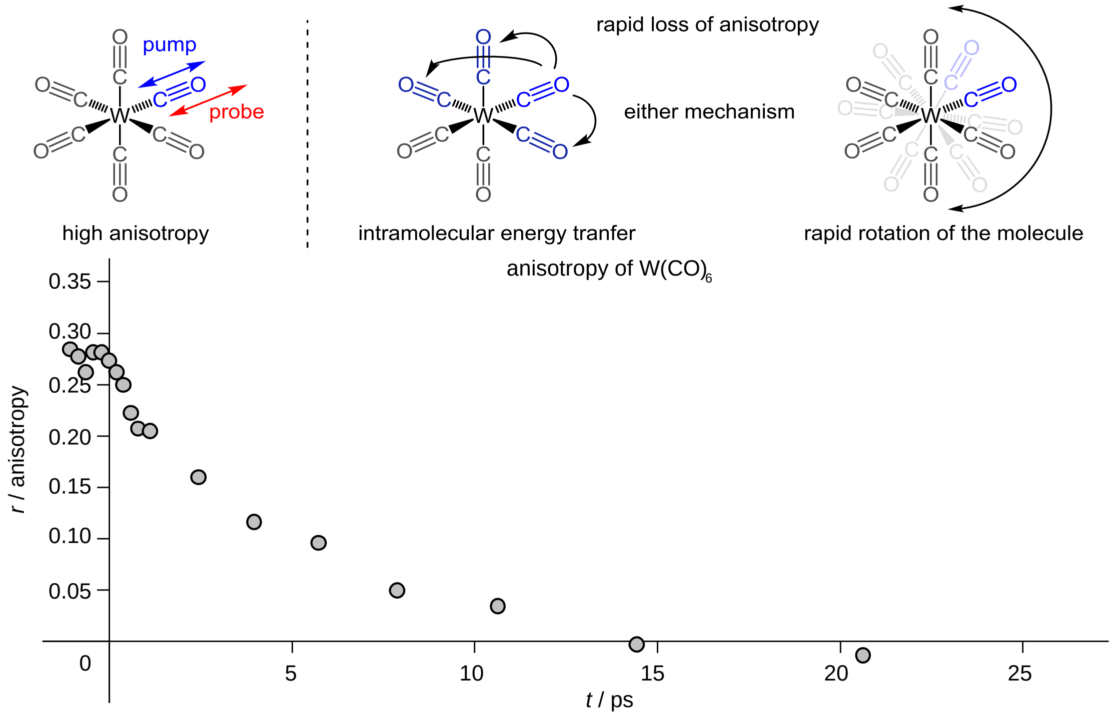

Figure 29. (top) $W(CO)_6$ is expected to possess high anisotropy of the pumped/probed 2100 cm^{-1} CO stretch. The loss of the anisotropy can occur both *via* intramolecular energy redistribution and by molecular rotation, disorienting the pumped CO ligand. (bottom) Plot of experimentally measured anisotropy of $W(CO)_6$ in hexane, pumped and probed at the CO vibrational stretch mode. Results are comparable with the published data.[52]

Furthermore, as a crosscheck, the relation between parallel and perpendicular to the magic angle values was used. It is known that the polarization data must obey **Eq. 5**.

$$\Delta A_{mag} = \frac{\Delta A_{\parallel} + 2 \cdot \Delta A_{\perp}}{3} \tag{5}$$

Comparison of experimental magic angle data and the predicted (as weighted average of the parallel and perpendicular data according to **Eq. 5**) showed good match for all polarization data. Illustrative example of GSB recovery for various pump-probe orientations is plotted in **Figure 30**.

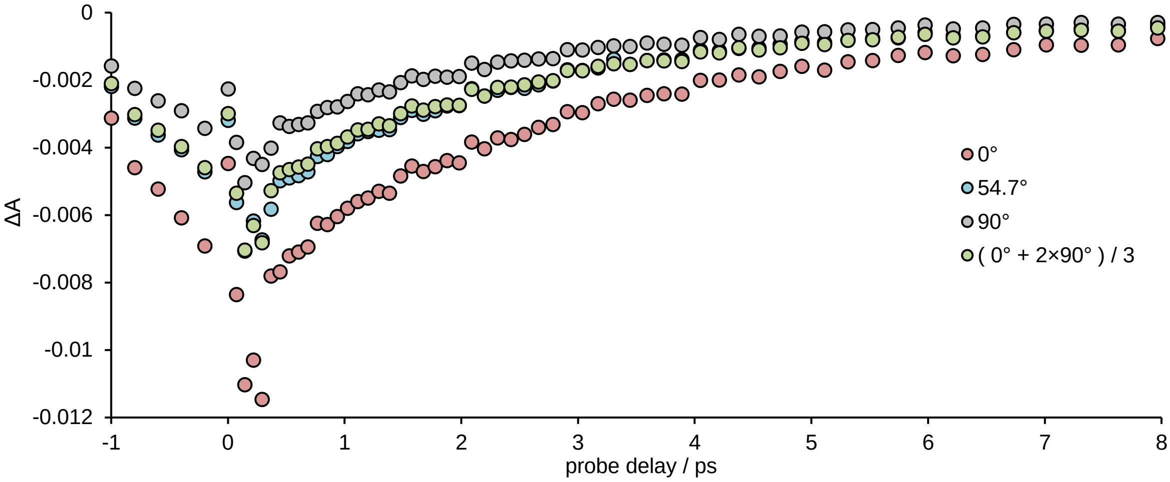

Figure 30. GSB intensity of ***l*-P2**$^{+\bullet}$ dependence on pump-probe orientation for pump at 2050 cm^{-1} and probe at 1533 cm^{-1}. Weighed sum of parallel and perpendicular orientations according to **Eq. 5** yields values similar to the experimentally observed magic angle orientation data.

To calculate and assess the TR-IR anisotropy, relatively good signal-to-noise ratio is necessary. Since, the anisotropy is calculated by the division of two small numbers, it is tremendously affected by noise, leading to high oscillations in anisotropy plots, which makes visual assessment difficult. Therefore, only selected regions with the signal-to-noise ratio above an arbitrarily chosen threshold and with the ΔA intensity further from the baseline ($\Delta A = 0$) were used for the anisotropy analysis (**Figure 31** and **Figure 32**).

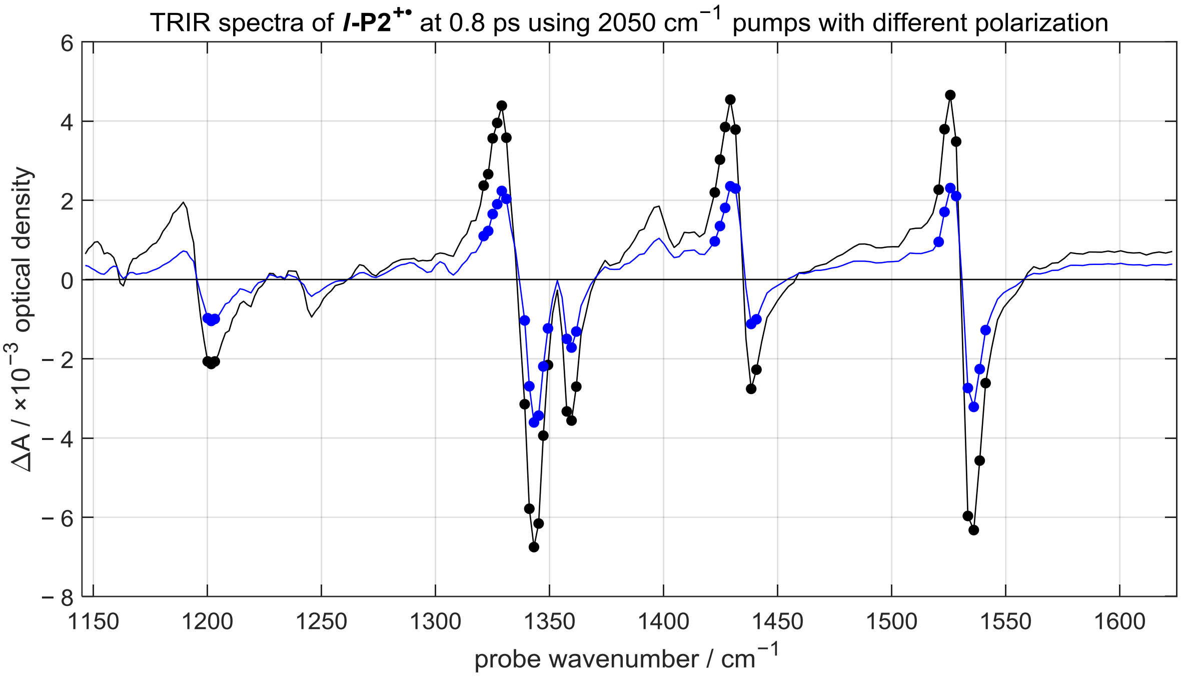

Figure 31. TRIR spectra of ***l*-P2**$^{+•}$ pumped at 2050 cm^{-1} with parallel (black) and perpendicular (blue) orientation to the probe delayed by 0.8 ps. The positions indicated by filled circles were used for the anisotropy analysis.

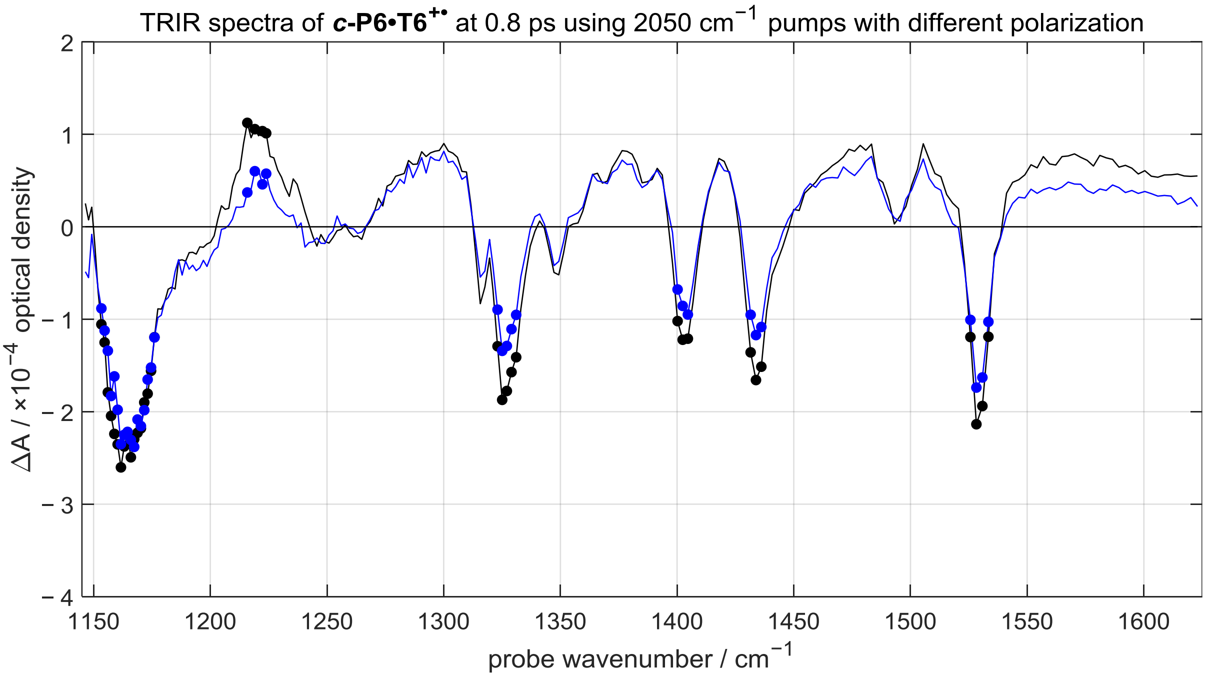

Figure 32. TRIR spectra of ***c*-P6·T6**$^{+•}$ pumped at 2050 cm^{-1} with parallel (black) and perpendicular (blue) orientation to the probe delayed by 0.8 ps. The positions indicated by filled circles were used for the anisotropy analysis.

From **Figure 31** is immediately apparent, that when using parallel orientation of the pump and probe, more than 2× higher intensity of the ESA and GSB is observed than in case of perpendicular orientation for ***l*-P2**$^{+•}$.

It was found that all ESA and GSB behave very similarly, suggesting similar orientation of the IRAVs. Furthermore, the anisotropy does not change over the time, since the molecules are very heavy (4.0 kDa and 11 kDa for **_l_-P2** and **_c_-P6·T6**, respectively) and do not physically reorient within the life of the excited state (**Figure 33**, **Figure 34**).

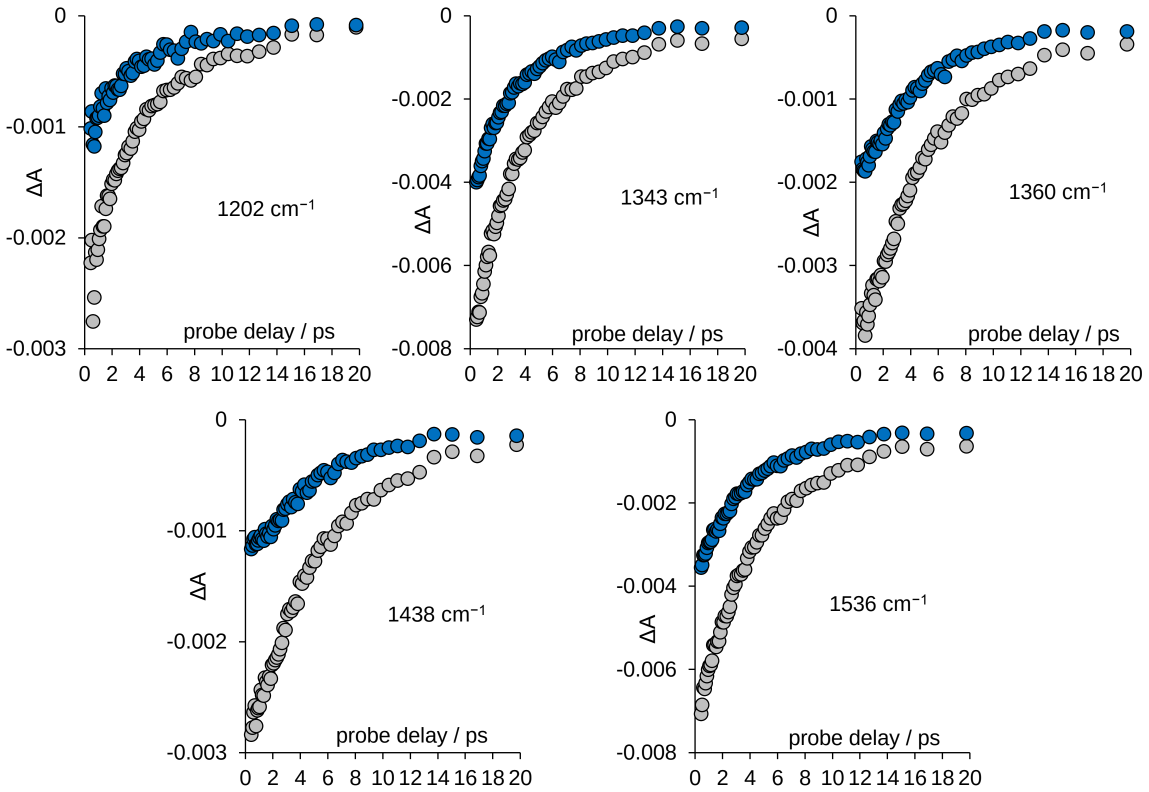

Figure 33. Kinetic profiles of the ΔA of GSB when using parallel (grey) or perpendicular (blue) pump-probe orientation for various wavenumber positions of the spectrum of **_l_-P2**$^{+\bullet}$ pumped at 2050 cm^{-1}. All 5 different IRAVs GSB show high anisotropy and its stability over time.

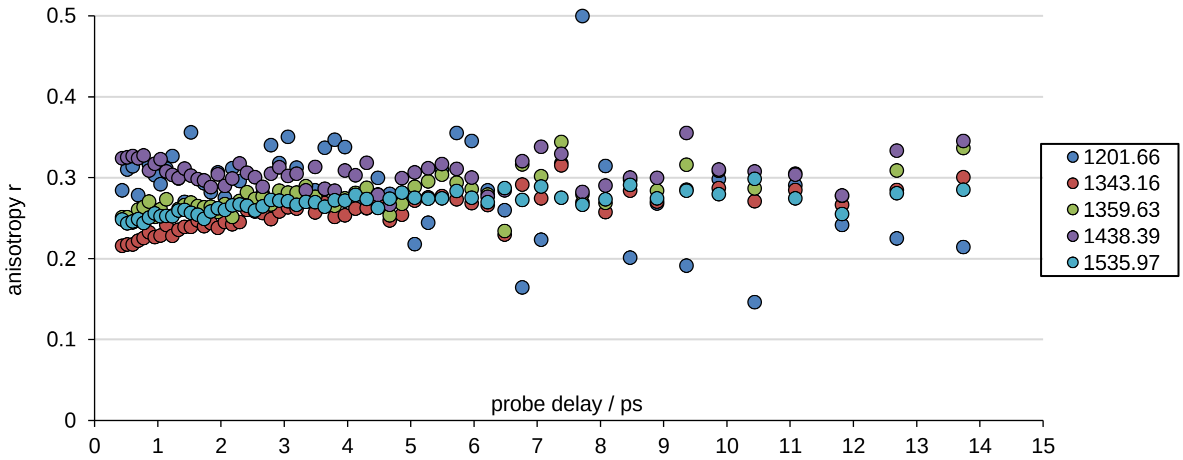

Figure 34. Plot of anisotropy of TR-IR using data from **Figure 33** according to **Eq. 3**. All 5 different IRAVs GSB show high anisotropy and its stability over time.

Since the anisotropy data are in general disrupted with the noise, analysis of single pixel/wavenumber could lead to misinterpretation in term of observed trends. To estimate anisotropy for each IRAV mode, average value of the whole ESA/GSB region (consisting of 6–10 pixels) for each IRAV averaged over the time delays 0.5–12 ps was calculated.

These results show high anisotropy for the ***l*-P2**$^{+\bullet}$ in the range 0.25–0.35 for all IRAVs, with an average value, representing whole set r = 0.31 (**Figure 35**).

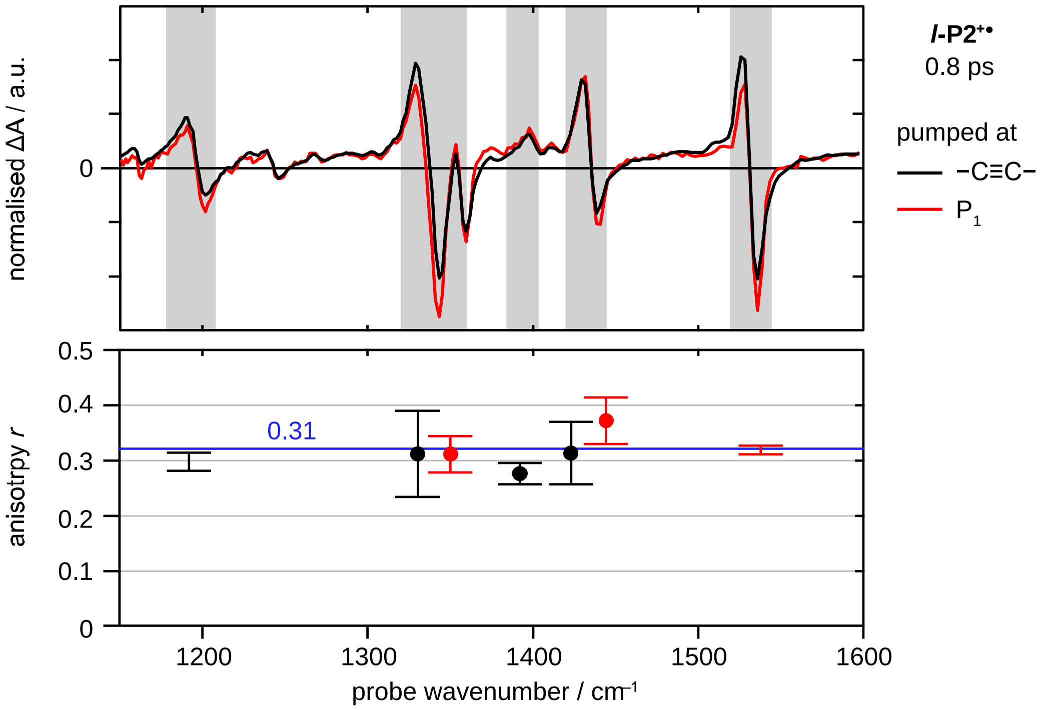

Figure 35. Plot of anisotropy of selected IRAV modes as an average for the ESA/GSB signals averaged over pump-probe delay times 0.5–12 ps. Error bar shows ±1SD.

Such a high value of anisotropy is close to the theoretical maximum 0.4, which could be interpreted such, that the amplified vector component of the intensified mode seen as an IRAV is parallel with the length of the ***l*-P2**$^{+\bullet}$ molecule (**Figure 36**).

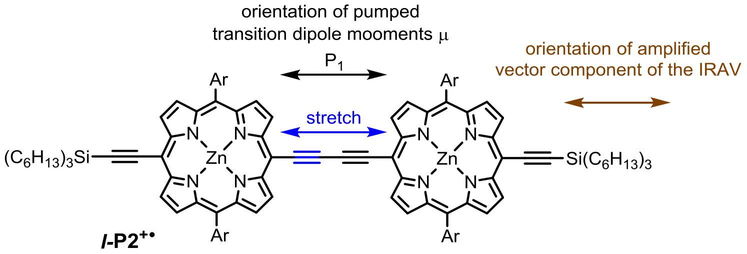

Figure 36. Scheme of orientation of the probed IRAVs transition dipoles in respect to the pumped mode orientation.

When the data of the ring ***c*-P6·T6**$^{+\bullet}$ (**Figure 32**) were analyzed, significantly lower anisotropy was observed. If each GSB/ESA region corresponding to each IRAV were analyzed individually, as for the ***l*-P2**$^{+\bullet}$, no significant difference among the peaks and only subtle dependence on the pump energy was observed. The average value of anisotropy of all IRAVs, representing whole set is r = 0.08 (**Figure 37**).

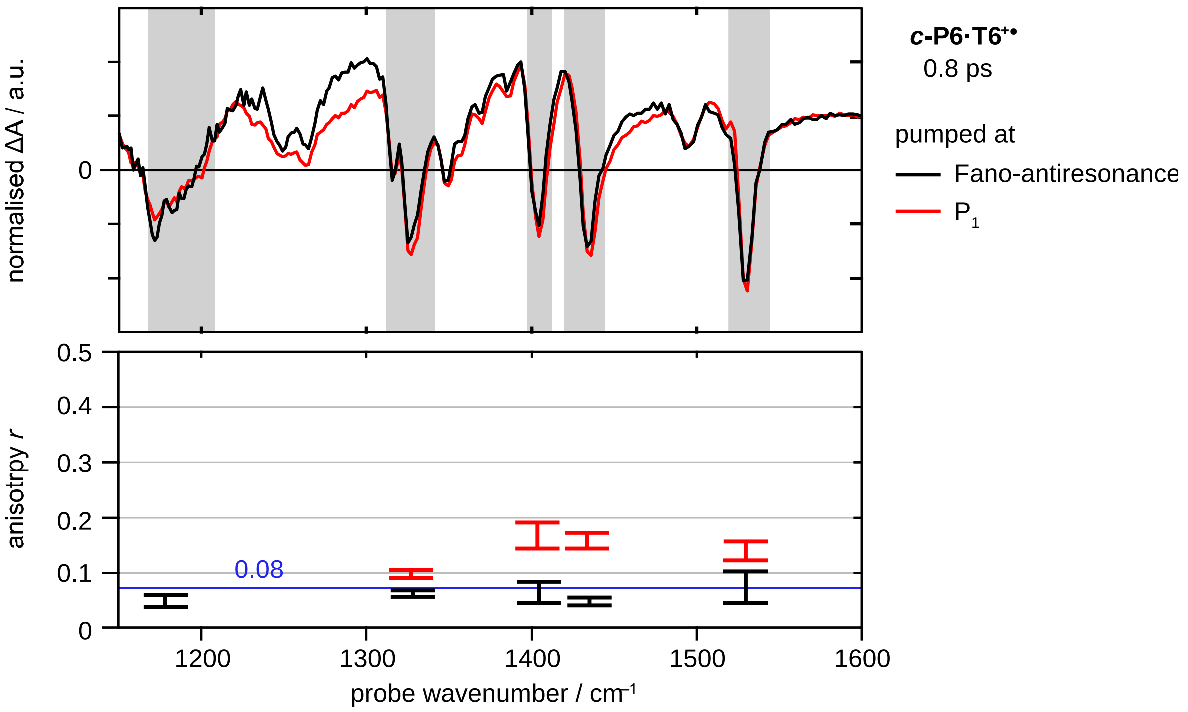

Figure 37. Plot of anisotropy of selected IRAV modes as an average for the ESA/GSB signals averaged over pump-probe delay times 0.5–8 ps. Error bar shows ±1SD.

It is reasonable to assume that mechanism of the IRAVs intensification is the same in ***c*-P6·T6**$^{+•}$ as in the case of ***l*-P2**$^{+•}$. The significantly lower anisotropy should be then explained by the loss of orientation in 2D, which would lead to the drop of anisotropy from 0.4 to 0.1.

This would imply, that in the vibronic excited state, the polaron is mobile along the length of the molecular backbone, consistent with observations of polaron mobility in polymer chains.[28] Such 2D delocalization would have to happen within 0.5 ps at 298 K (**Figure 38**). Analysis of the earlier probe time delays is unreliable as some pump-probe pulses interference occurs, significantly obscuring anisotropy values.

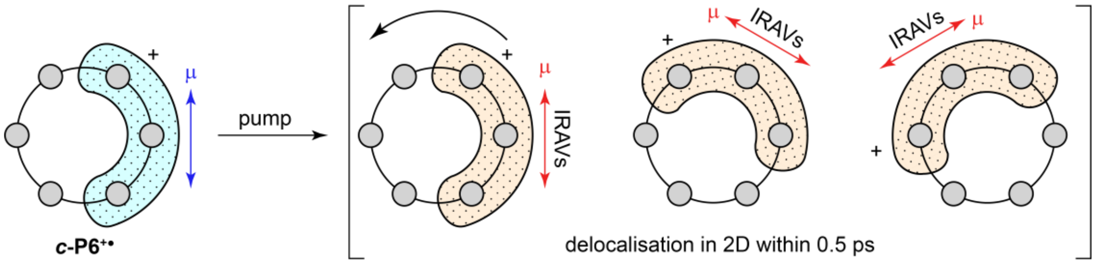

Figure 38. The polaron is localized on 2–3 porphyrin units. Upon excitation, it rapidly delocalises along the ring circumference within 0.5 ps.

Interestingly, in contrast to fast hopping in vibronic excited state (documented in this TR-IR study), in a frozen solvent at 80 K, at the ground state the polaron migration is slow on the EPR time scale (~100 ns).[9]

2.6. Calculations

Quantum chemical calculations were carried out in order to elucidate the assignment of the IRAVs and support the experimental findings from the polarisation TR-IR.

Since the nanoring ***c*-P6·T6**$^{+\bullet}$ exhibits a Fano-antiresonance and such behaviour cannot be well covered by DFT, the focus of calculations was put on ***l*-P2**$^{+\bullet}$. A model geometry for the ***l*-P2** molecule was created by replacing the solubilizing aryl and THS protecting groups with −H. Geometry was optimized as either neutral molecule with singlet multiplicity or as a monocation in doublet multiplicity using long-range corrected functional LC-ωPBE[53–55] (with ω = 0.2) and 6-31G* basis set using the Gaussian09 software,[56] as the prediction of this method was found to most correlate with the experimental data of monocations.[4]

Frequency calculations confirmed that the found geometry is a true minimum and all predicted vibrations were real. Calculated IR spectra in neutral and monocation states predicted significant intensification of certain signals by factor ~20–100. Among others, one intensified vibrational mode was the −C≡C− stretching mode, in line with the experiment. Although, the experimentally documented enhancement is lower (amplification by factor ~10–20), qualitative agreement of experimental and calculated spectra can be seen in comparison in **Figure 39**.

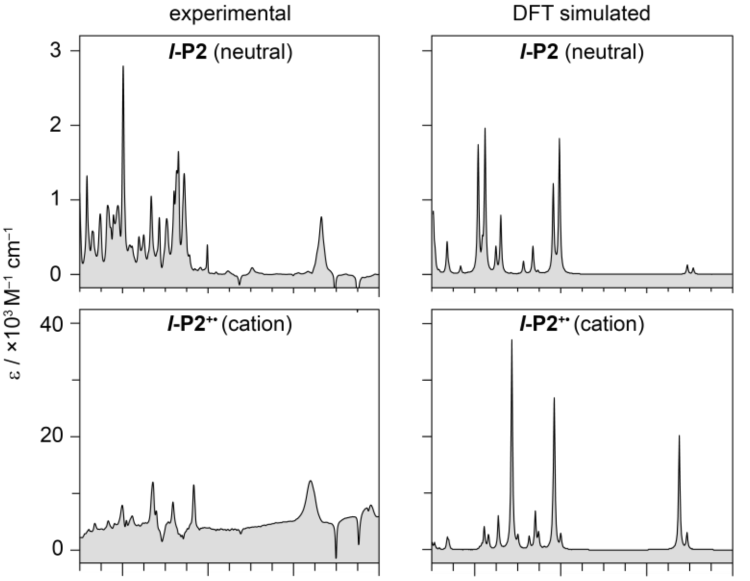

Figure 39. Experimental (left) and simulated (right) IR absorption spectra of the neutral ***l*-P2** (top) and the monocation ***l*-P2**$^{+\bullet}$ (bottom).

Analysis of the orientation of the transition dipole corresponding to each calculated vibrational mode showed that the most intensified absorptions exhibit 100% directionality along the length of the ***l*-P2**$^{+\bullet}$ molecule. This is in agreement with experimentally found high IRAVs anisotropy.

The effect of the vibrational displacement on the highest occupied, half-filled molecular orbital SOMO nicely documents the origin and the orientation of the high transition dipole moment (and thus high oscillator strength) in monocations, as a result of the polaron mobility. Upon molecular geometry distortion along the intensified vibrational mode, the SOMO localises on one of the porphyrin units, leading to significant change of the dipole moment, which changes magnitude and orientation along the length of the molecule. The simplest mode for understanding its directionality is the ~2050 cm^{-1} −C≡C− stretching mode (**Figure 40**).

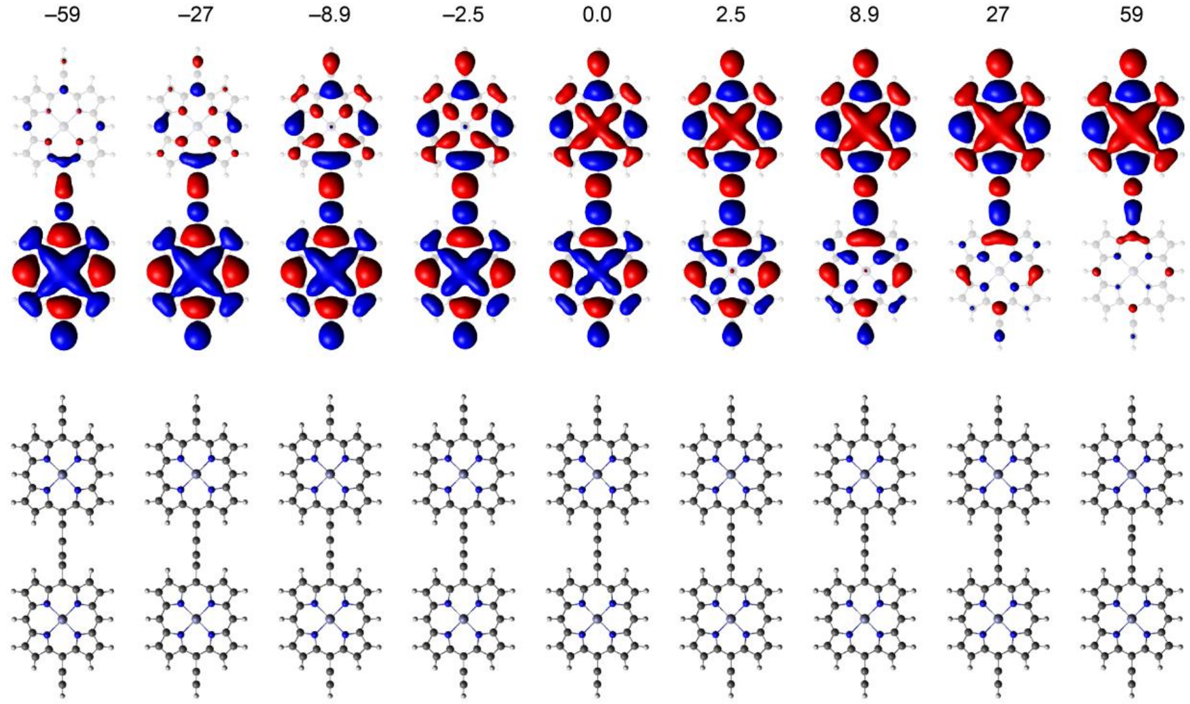

Figure 40. Highest occupied half-filled molecular orbital SOMO of the ***l*-P2**$^{+\bullet}$ at undistorted, minimal geometry (middle) and on distorted geometries along the −C≡C− stretch vibrational mode. Numbers indicate how much the structure is distorted as a multiple of the classical vibrational turning point (energy of the distorted structure is higher by *factor* × 2050 cm^{-1}).

For all assessed predicted IRAV modes, vibrational distortions lead to the same change in SOMO. The most intensified IRAV modes, at 1373 cm^{-1} and 1570 cm^{-1}, correspond to the more complex, porphyrin breathing modes. Although, it may not be easy to intuitively recognise the directionality of the transition dipole related with these modes, it is still along the length of the molecule.

In the case of 1570 cm^{-1} mode, during the porphyrin anti-symmetric ‘breathing’ motions, certain C_β—C_β bonds are contracted and this result in an anti-bonding interaction ‘repelling’ the electron density to the other porphyrin, and *vice versa*. The 1373 cm^{-1} mode is a complex half-ring stretching. Such motions are in the ***l*-P2**$^{+\bullet}$ cooperative, occurring in an anti-symmetric way on the two porphyrin cores (**Figure 41**).

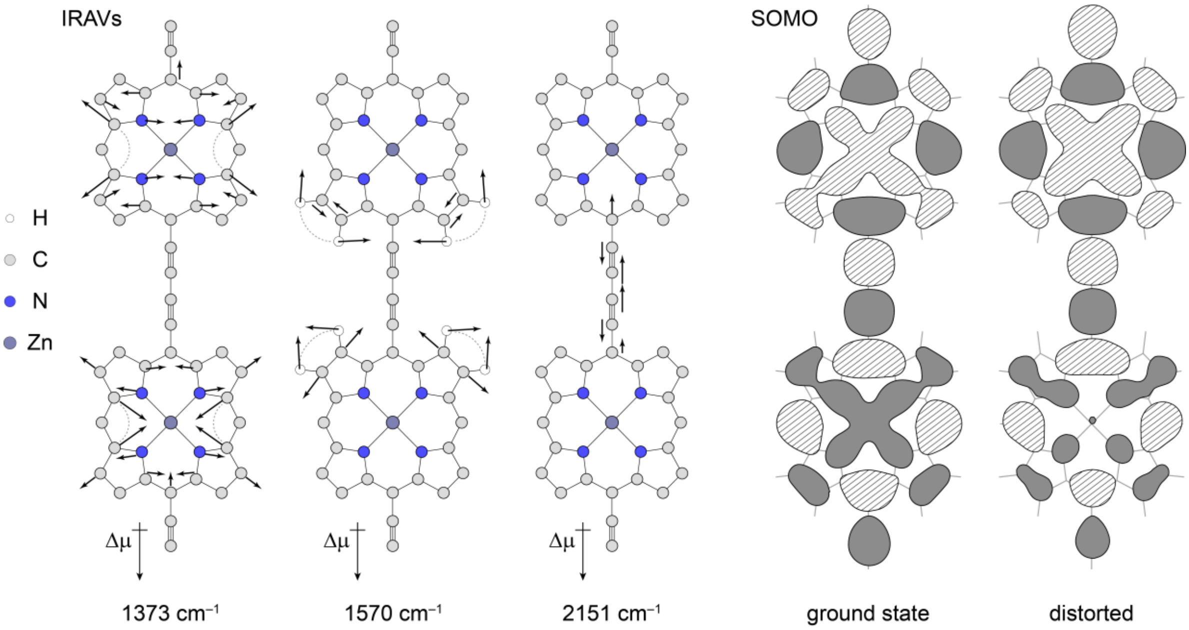

Figure 41. (left) Three most intensified vibrational modes of ***l*-P2**$^{+\bullet}$ with displacement vectors and dipole moment change related with the vibrations. Calculated SOMO of vibrationally relaxed and distorted 1570 cm^{-1} mode (distortion by factor of ~10 of the classical turning point) of ***l*-P2**$^{+\bullet}$, showing SOMO density redistribution away from contracted ring.

This mechanism moves the electron density from one porphyrin unit to the other as a response to the vibrational distortion. This is in agreement with free polaron redistribution model presented by Zamadar et al,[28] and in line with our observation of a high polaron mobility in ***c*-P6·T6**$^{+\bullet}$, where the polaron is expected to travel around the circumference rapidly.

Another support for this interpretation can be taken from the paper presented by Spiro et al., who assigned, using isotopic labeling with deuterium, fingerprint IR modes in a porphyrin monocations and commented on the moderate intensification of some of the bands. The authors proposed that some of the ring contraction and expansion leads to a charge redistribution in order to avoid anti-bonding interactions in some contracting parts of porphyrin ring. Such charge redistribution is than accompanied with the overall transition dipole oriented along the *meso*—*meso* positions (**Figure 42**).[29,57]

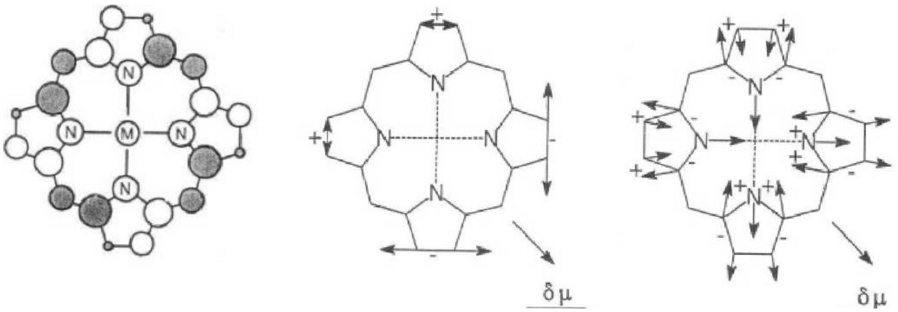

Figure 42. (left) HOMO orbital of a zinc porphyrin radical cation.[57,58] Assignment of slightly intensified IR modes absorbing at 1538 cm^{-1} (middle) and ~1309 cm^{-1} (right) identified in a copper tetraphenyl porphyrin radical cation. Arrows indicate expansion (+) or contraction (−) associated with the mode, the total transition dipole is indicated by the arrow in bottom right corner. Reprinted with permission from *Jour. Am. Chem. Soc.*, **1993**, (115), 12029–12034. Copyright (1993) American Chemical Society.

2.7. 2D-IR

While the TR-IR, using ULTRA A/B systems, have the advantage of probing very broad windows of the IR spectrum in very short acquisition times (~few seconds per time delay), it lacks resolution on the pump axis. Due to the natural broadness of the pump, only very isolated IR signals, such as the −C≡C− stretch mode, can be selectively irradiated.

The 2D-IR technique can be used to elucidate structural dynamics and vibrational coupling (of any origin and mechanism) between all signals within the pump and probe windows.[45,59–61] It provides very good resolution of both pump and probe axes, as well as the time resolution (< 1 ps). Such experiment thus creates a snapshot of the coupling between vibrational modes at a given pump-probe delay time.[44] Analogously to TR-IR, acquisition of these snapshots at various probe delay times enables the analysis and study of chemical dynamics and evolution of the vibration coupling in molecules upon selective vibration excitation.

Although the 2D-IR experiment comprises much more information than the TR-IR spectra, when using ULTRA A/B systems the 2D-IR snapshot required substantial longer acquisition experimental time (typically 30 min).[61] Due to these longer acquisition times and samples instability, only very few snapshots of selected time delays were acquired for the 2D-IR spectra of the fingerprint region, where ULTRA's broadband is very advantageous, covering many IRAVs at once.

For the kinetic analysis of the 2D-IR data, LIFEtime instrument, with significantly faster throughput was used. LIFEtime is a laser system with narrow bandwidth (< 200 $\mathrm{cm^{-1}}$), using two probe beams, enabling acquisition of two separate probed windows. This is advantageous for the stitching of the individual windows *via* concurrent acquiring of on-diagonal and different off-diagonal regions, *vide infra*.[62] Furthermore, LIFEtime system has significant advantage for the kinetic analysis over the simple TR-IR setup. The pump pulses are modulated in an acousto-optic pulse-shaper, attenuating significantly, the pump-probe interreference.[61]

2.7.1. Fingerprint region

Using ULTRA A/B systems, several 2D-IR spectra of the pump-probe window 1250–1550 cm^{-1} at selected time delays were recorded. The earliest assessable pump-probe time delay was 0.5 ps.

In ***l*-P2**$^{+\bullet}$, at 0.5 ps probe delay, a set of on-diagonal and off-diagonal peaks appeared between each and every fingerprint IRAV, showing very strong coupling. Off-diagonal signals consisted of strong GSB and less intense ESA. At later acquisition time (1.5 ps), the ESA/GSB signal ratio was more equalized, however no other significant change in the spectrum was observed (**Figure 43**). The on-diagonal signals were rather dominated with the GSB and only weak ESA was observed. The on-diagonal peak at ~1480 cm^{-1} appearing at both time-delays results from the residual neutral species (*vide infra*).

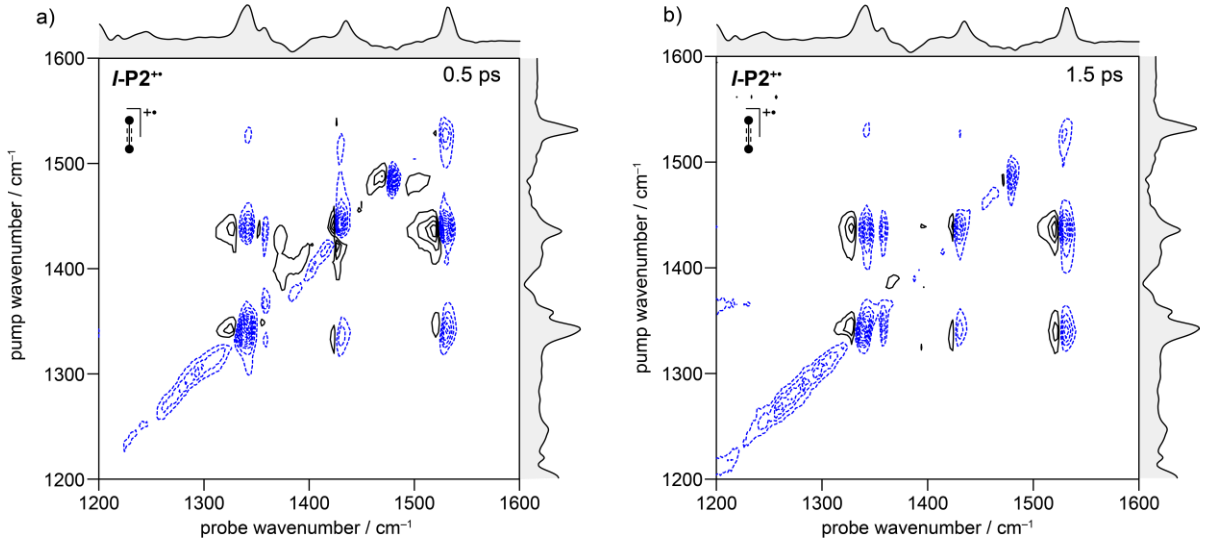

Figure 43. 2D IR spectrum of the ***l*-P2**$^{+\bullet}$ in the fingerprint region showing immediate appearance of the off-diagonal peaks within 0.5 ps (left) and prevailing during later time (right). Dashed blue and black plain contours correspond to negative and positive values, respectively.

In the case of ***c*-P6·T6**$^{+\bullet}$, a set of on- and off-diagonal peaks between all IRAV modes within the 1250–1550 cm^{-1} window was observed at early time, analogous to the ***l*-P2**$^{+\bullet}$. However, at early time 0.5 ps, some spectral features were obscured with positive artefacts and nearly all on- and off-diagonal signals were dominated with, or consisted solely of, negative GSB. At the later time, at 1.5 ps delay, part of the strong GSB quickly disappeared, giving the expected ESA/GSB pairs, however still with dominant GSB (**Figure 44**).

In general the peaks were more intense for ***c*-P6·T6**$^{+\bullet}$ than for ***l*-P2**$^{+\bullet}$. This is expected as the 2D-IR signals intensity is quadratically dependent on the molar absorption coefficient.[61]

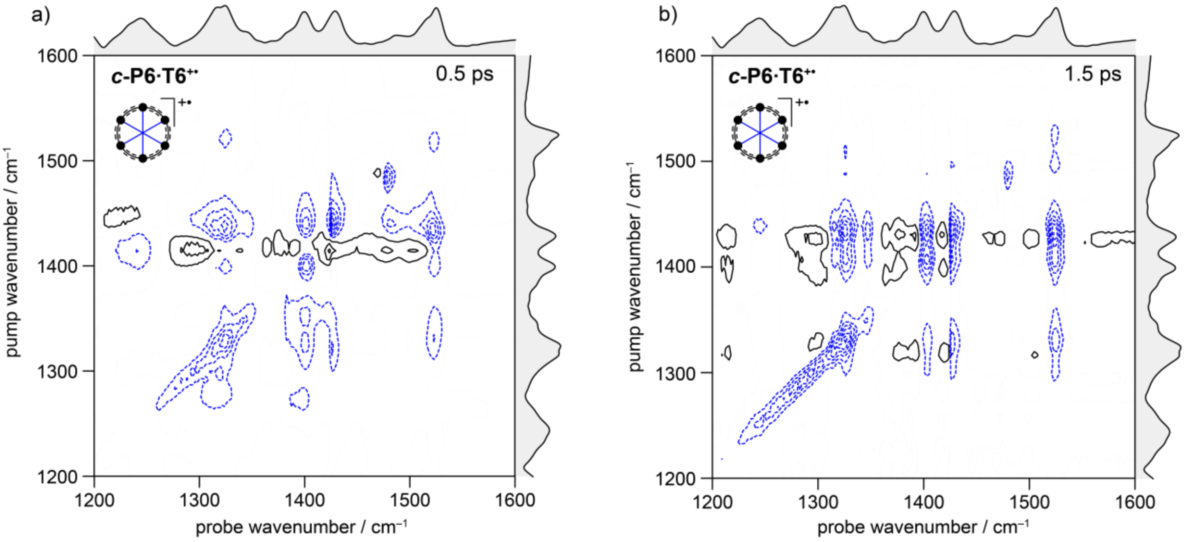

Figure 44. 2D IR spectrum of the ***c*-P6·T6**$^{+\bullet}$ in the fingerprint region showing immediate appearance of the off-diagonal peaks within 0.5 ps consisted mainly by GSB (left). At later time delay of 1.5 ps, intensity of the dominant GSB drops significantly and the ESA/GSB pair appears in the spectrum. (right). Dashed blue and black plain contours correspond to negative and positive values, respectively.

Observation of strong GSB and absence of nearly any ESA at early time delays must be related with the significantly smaller oscillator strength of the associated IR modes in the early excited state. Since the ground state possesses unusually strong IR absorption activated by the polaron, a direct implication is that the excitation leads to switching off of these effects.

Furthermore, as control experiments, a series of the 2D-IR spectra were acquired for the neutral molecules. Concentration was significantly increased to reach equivalent optical density comparable with the monocations. Neutral 2D-IR spectra are in general silent and only a few on- and off-diagonal signals are observed (**Figure 45**).

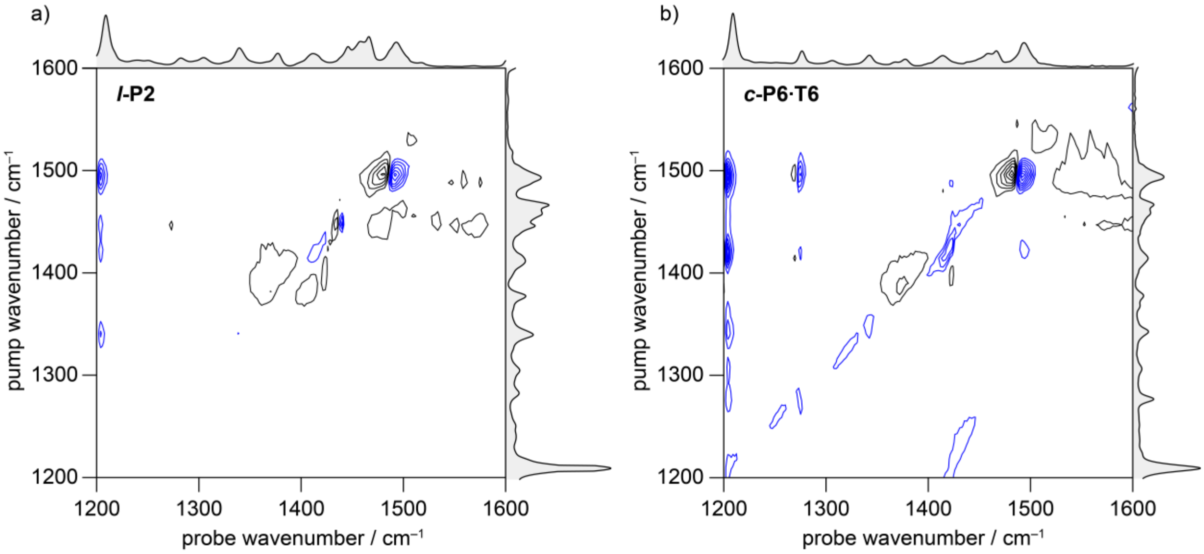

Figure 45. Absence of off-diagonal and on-diagonal signals on the neutral ***l*-P2** (left) and ***c*-P6·T6** (right) in 2D IR spectrum at early (0.4 ps) time delay. Concentration of the sample was ~40 higher as in the monocations to maintain comparable optical density of ~0.2. Dashed blue and black plain contours correspond to negative and positive values, respectively.

2.7.2. Pumping the −C≡C− stretch region.

2D-IR with the pump axis covering the −C≡C− stretch mode region was carried out using the LIFEtime instrument. The narrowband pump, with full width at half maximum (FWHM) of ~80 cm^{-1} was centered at ~2100 cm^{-1}, in resonance with the −C≡C− stretch IRAV of ***l*-P2**$^{+\bullet}$ and the Fano-type anti-resonance of ***c*-P6·T6**$^{+\bullet}$.

As mentioned above, the LIFEtime instrument allows quick acquisition of 2D-IR spectra at the expense of narrower pump and probe windows. Advantageously, the setup allowed concurrent acquisition of the on-diagonal and selected off-diagonal regions, enabling normalization of the off-diagonal regions to the on-diagonal in order to stich multiple windows from independent 2D-IR experiments.[62]

Five windows, covering in total the region 1300–2150 cm^{-1}, were probed, conducted as a five separate experiments. The resulting 2D-IR spectra showed the expected features: immediate formation of the ESA/GSB for all IRAVs (**Figure 46**).

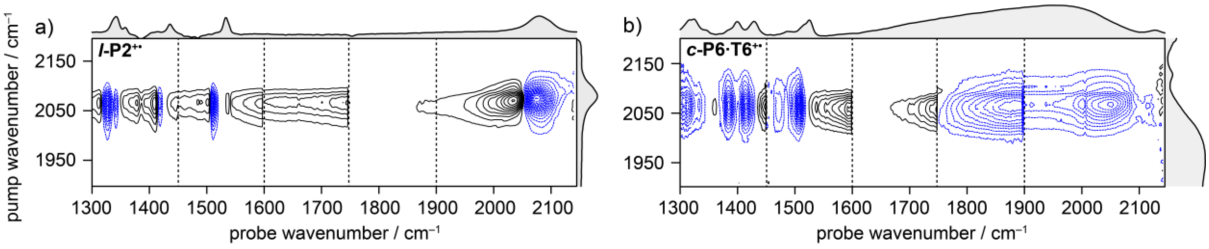

Figure 46. 2D-IR spectra of the ***l*-P2**$^{+\bullet}$ (left) and ***c*-P6·T6**$^{+\bullet}$ (right) when pumping ~2100 cm^{-1} and probing 1300–2100 cm^{-1} region in 5 separate windows as 5 separate experiments. Pump-probe time delay is 0.5 ps. Windows were stitched upon normalization to the intensity of the on-diagonal GSB. Dashed blue and black plain contours correspond to negative and positive values, respectively.

This setup is in principle very similar to the TR-IR when pumping the −C≡C− as an isolated feature in case of ***l*-P2**$^{+\bullet}$. The time evolution of the signals exhibited a relatively complex behavior.

Firstly, the on-diagonal GSB for both species and the off-diagonal GSB of ***c*-P6·T6**$^{+\bullet}$ exhibited bi-exponential recovery with an extremely fast component of lifetime ~0.2 ps and a slower of lifetimes 2–6 ps.

Secondly, a broad positive feature appears across whole spectrum shortly after the pump and decays with a lifetime of ~0.8 ps for both species.

Lastly, sharp off-diagonal ESA signals of IRAVs exhibit a slow component with the lifetimes ~2–6 ps.

Since the fastest component of the GSB recovery is very short (τ ~0.2 ps) it is mixed to a great extend within the instrument response (as a consequence of the time-duration of the pulses). The instrument response causes ‘blurring‘ of the early time data and simple exponential functions cannot be used for the fit. These two processes can be distinguished by fitting the data with a function convoluting the instrument response function (IRF) with the exponential decay/grows functions, as described by Mouton et al.[63] Such a function is a sum of N products of exponential functions with the Gaussian distribution with the FHWM σ (**Eq. 6**).

$$\Delta A(t,\sigma) = \sum_{j=1}^{N} A_j \cdot \mathrm{e}^{-\frac{t}{\tau_j}} \cdot \mathrm{e}^{-\frac{t^2}{2\sigma^2}} \tag{6}$$

Where A_j are preexponential factors for each component and τ_j are the associated lifetimes. σ is the full width at half maximum describing the instrument response around the time 0. For practical purposes, **Eq. 6** is converted into an analytical expression using error function (*erf*), yielding a function suitable for the fitting (**Eq. 7**).[63]

$$\Delta A(t,\sigma) = \sum_{j=1}^{N} A_j \cdot \mathrm{e}^{\left(\frac{\sigma^2}{2\cdot\tau_j{}^2}-\frac{t}{\tau_j}\right)} \cdot \left(1 - erf\left(\frac{\frac{\sigma^2}{\tau_j} - t}{\sqrt{2}\sigma}\right)\right) \tag{6}$$

To describe such complex behavior, individual kinetics, corresponding to the important points in the 2D-IR spectrum (on- and off-diagonal GSB, sharp and broad ESA features) were analyzed and fitted with the smallest number of rate constants necessary for the good fit. Eventually, the simplest fitting model involved three components. These components describe qualitatively similar lifetime parameters (fast (~0.2 ps), medium (~0.8 ps) and slow (~4 ps) and were shared for all fits within one species.

The fits were performed using *symfit* package[64] using home-made Python script written by Dr. Martin Peeks and William Kendrick and carried out by William Kendrick.

All three lifetimes parameters at once (as a tri-exponential function) were not used for all positions, if the simpler model of bi- and mono-exponential function was sufficient. Lifetime constants and the kinetic complexity associated with each region is summarized in **Table 2**:

	***l*-P2**$^{+\bullet}$		***c*-P6·T6**$^{+\bullet}$	
peak type	number of components	shared lifetimes	number of components	shared lifetimes
on-diagonal GSB	3	τ_1, τ_2, τ_3	2	τ_1, τ_3
off-diagonal GSB	2	τ_1, τ_2	2	τ_1, τ_3
ESA sharp peaks	2	τ_1, τ_2	2	τ_1, τ_2
ESA broad feature	1	τ_2	2	τ_1, τ_2

Table 2. Number of exponential components necessary for the good fit of the data of the selected regions from 2D-IR.

Four analyzed regions and typical kinetic data and their fitting are plotted for illustration on ***c*-P6·T6**$^{+\bullet}$ in **Figure 47**.

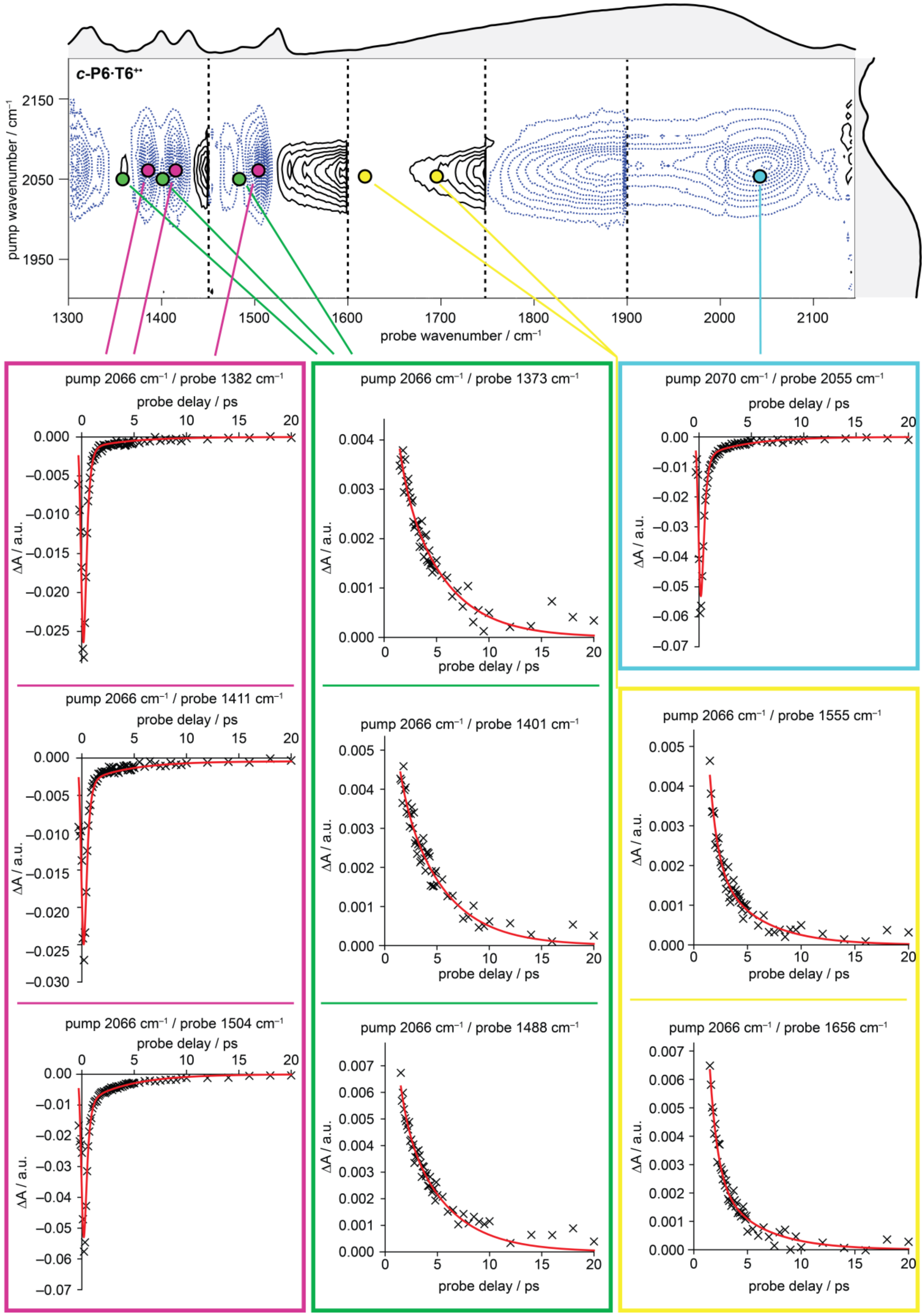

Figure 47. Plot illustrating kinetic traces of selected pump-probe datapoint form the 2D-IR spectrum. Important regions are: on-diagonal GSB (blue), off-diagonal GSB (magenta), sharp ESA (green) and broad ESA in between the distinctive peaks (yellow).

The FHWM was fitted for all data yielding $\sigma = 183 \pm 7$ and $\sigma = 191 \pm 7$ fs for ***l*-P2**$^{+\bullet}$ and ***c*-P6·T6**$^{+\bullet}$, respectively. This is in a good agreement with the expected instrument response (0.25–0.3 ps). Closeness of the values obtained from independent sets of data from different molecules is reassuring that the fitting algorithm correctly fitted parameter σ to the ‘right’ spectral features.

Results of the fit, using the smallest possible number of the components (*cf.* **Table 2**) in four analyzed regions (*cf.* **Figure 47**) while sharing the appropriated parameters, can be summarized as three processes:

Very fast process

The fastest process was observed as a fast component of the on-diagonal GSB signal in ***l*-P2**$^{+\bullet}$ and both on- and off-diagonal signals of GSB of ***c*-P6·T6**$^{+\bullet}$. The fitted lifetime associated with the component is $\tau = 0.15 \pm 0.02$ ps and $\tau = 0.29 \pm 0.01$ ps for ***l*-P2**$^{+\bullet}$ and ***c*-P6·T6**$^{+\bullet}$, respectively. This component is not observed for any ESA, assuming the initial excited state is relative IR silent or possess extremely broad undetectable ESA.

Medium fast process

One excited state is appearing concurrently with the decay of the fastest component and possess very broad (at least 1300–2000 cm^{-1}) featureless ESA. Such broad band characteristics implies that the state has nature of the ‘electronic’ rather than ‘vibrational’ excited state. Intensity of the ESA decay with the fitted lifetime $\tau = 0.92 \pm 0.01$ ps, $\tau = 0.74 \pm 0.07$ ps for ***l*-P2**$^{+\bullet}$ and ***c*-P6·T6**$^{+\bullet}$, respectively.

Slowest process

This component is associated with a classical ‘vibrational’ ESA/GSB pairs of similar intensity and associated decay/recovery to the ground state. The fitted lifetime associated with the component is $\tau = 5.7 \pm 0.1$ ps and $\tau = 4.1 \pm 0.3$ ps for ***l*-P2**$^{+\bullet}$ and ***c*-P6·T6**$^{+\bullet}$, respectively.

Observed kinetic profiles can be summarized in a model with three excited states (**Figure 48**). Note, that no transformation from ‘vibrational’ to ‘electronic’ excited state (or other way around) is observed.

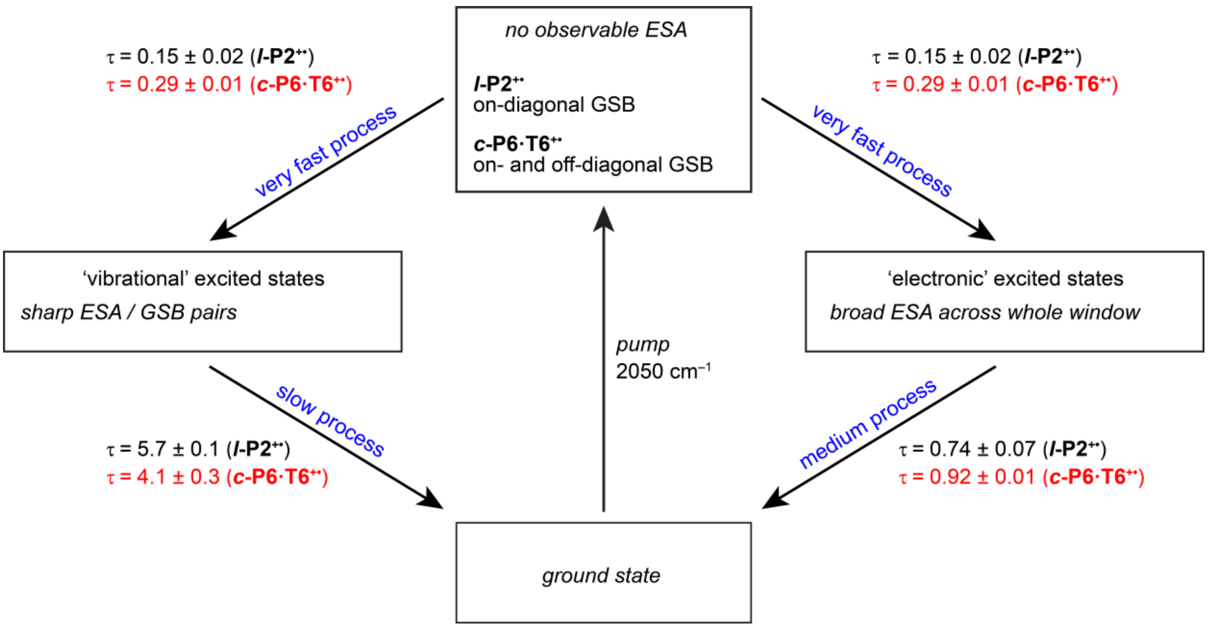

Figure 48. Scheme of the processes observed from the kinetic analysis upon excitation with the pump. Shortly after initial excitation, two different excited states are populated, decaying later independently.

The scheme in **Figure 48** of the ongoing processes upon excitation is deliberately avoiding any comment on the energy of the individual species, as it is unclear what type of 'electronic' and 'vibrational' modes are populated and what are their relative energies.

2.8. Summary and conclusions

Both 2D-IR and TR-IR spectroscopies were used to elucidate the mechanism of the huge intensification of certain IR modes in porphyrins oligomers monocations ***l*-P2**$^{+\bullet}$ and ***c*-P6·T6**$^{+\bullet}$.

2D-IR spectra showed sets of off-diagonal peaks, both ESA and GSB, appearing at very early pump-probe delay times (0.5 ps) between each and every IRAV mode within the assessed fingerprint window (1300–1600 cm^{-1}). This observation documents the existence of very strong vibrational coupling between all IRAV modes.

Detailed kinetic analysis of the 2D-IR spectra evolution with various pump-probe delays, when pumping 2050 cm^{-1} and probing 1300–2100 cm^{-1} region, showed very complex behaviour. Fitting of the data evolution in time at various pump-probe positions with multi-exponential functions led to understanding that the use of three different lifetimes is sufficient in order to describe well all processes observed upon initial excitation.

The fastest process is associated to the immediate relaxation of the initial excited state (lacking any ESA) into two different excited states. One excited state possesses a broad ESA feature typical for an 'electronic' excited state. The other state possesses sharp ESA/GSB pairs, typical for 'vibrational' excited states. Although the whole chapter is focused on the study of strong mixing between electronic and vibrational modes and the apparent break down of the Born-Oppenheimer approximation is being pointed out, it is still practical to comment on the observed features of the excited states, even though the states are mixed in origin.

The 'electronic' excited state relaxes to the ground state mono-exponentially with the lifetimes $\tau = 0.92 \pm 0.01$ ps, $\tau = 0.74 \pm 0.07$ ps for ***l*-P2**$^{+\bullet}$ and ***c*-P6·T6**$^{+\bullet}$, respectively.

The vibrational excited state relaxes to the ground state with lifetimes $\tau = 5.7 \pm 0.1$ ps and $\tau = 4.1 \pm 0.3$ ps for ***l*-P2**$^{+\bullet}$ and ***c*-P6·T6**$^{+\bullet}$, respectively.

Based on the TR-IR observations, both excited states are generated, regardless if the pump position is centered on the 2050 cm^{-1} vibrational-origin absorption or on electronic polaron band P_1 (2500–3250 cm^{-1}). This serves as another piece of evidence for the strong vibronic coupling.

Polarization TR-IR showed, that in the case of ***l*-P2**$^{+\bullet}$, the orientation of the transition dipole of the IRAV modes (or at least their amplified components) is same for all modes and is in line with the butadiyne backbone (the length of the ***l*-P2** molecule). In the case of ***c*-P6·T6**$^{+\bullet}$, polaron in the excited state is rapidly delocalized along the nanoring circumference within 0.5 ps. This interpretation is based on observed values of anisotropy of all IRAVs signals, which are stable in time. The average values of anisotropy for all peaks are $r = 0.31$ and $r = 0.08$ for

***l*-P2**$^{+\bullet}$ and ***c*-P6·T6**$^{+\bullet}$, respectively. These values are close to the theoretical maxima for situation when pumped and probed transition possess transition dipoles orientated in parallel and in the latter case then delocalized in the 2D plane, r = 0.4 and r = 0.1, respectively. Very analogous interpretation was concluded in study of an electronic excited states of neutral molecules, operating in very different energy regimes, by measuring polarisation of the neutral molecules fluorescence.[38]

The experimental findings of the polarization experiments were corroborated with the DFT simulations predicting amplification of certain IR modes when assessing neutral and monocation model of ***l*-P2**. Calculated dipole derivative for the IRAVs showed orientation along the butadiyne backbone. Fingerprint IRAV modes, identified by the DFT, were predicted to exhibit anti-symmetric porphyrin breathing motions. Such contraction–expansion motions are coupled with significant polaron redistribution from one porphyrin to other, explaining the high oscillator strength associated with the vibration.

2.9. References

[1] M. Born, R. Oppenheimer, *Ann. Phys.* **1927**, *389*, 457–484.

[2] P. W. Atkins, J. De Paula, *Atkins' Physical Chemistry*, **2014**.

[3] I. Alata, R. Omidyan, C. Dedonder-Lardeux, M. Broquier, C. Jouvet, *Phys. Chem. Chem. Phys.* **2009**, *11*, 11479–11486.

[4] M. D. Peeks, C. E. Tait, P. Neuhaus, G. M. Fischer, M. Hoffmann, R. Haver, A. Cnossen, J. R. Harmer, C. R. Timmel, H. L. Anderson, *J. Am. Chem. Soc.* **2017**, *139*, 10461–10471.

[5] N. Takeda, J. R. Miller, *J. Phys. Chem. B* **2012**, *116*, 14715–14723.

[6] D. P. Arnold, R. D. Hartnell, G. A. Heath, L. Newby, R. D. Webster, *Chem. Commun.* **2002**, *2*, 754–755.

[7] R. Österbacka, X. M. Jiang, C. P. An, B. Horovitz, Z. V. Vardeny, *Phys. Rev. Lett.* **2002**, *88*, 4.

[8] J. Rawson, P. J. Angiolillo, M. J. Therien, *Proc. Natl. Acad. Sci.* **2015**, *112*, 13779–13783.

[9] M. D. Peeks, C. E. Tait, P. Neuhaus, G. M. Fischer, M. Hoffmann, R. Haver, A. Cnossen, J. R. Harmer, C. R. Timmel, H. L. Anderson, *J. Am. Chem. Soc.* **2017**, *139*, 10461–10471.

[10] C.-X. Sheng, T. Basel, B. Pandit, Z. V Vardeny, *Org. Electron.* **2012**, *13*, 1031–1037.

[11] D. Moses, A. Dogariu, A. J. Heeger, *Chem. Phys. Lett.* **2000**, *316*, 356–360.

[12] E. K. Miller, K. Lee, J. Cornil, Q. Pei, F. Wudl, A. J. Heeger, J. L. Brédas, *Synth. Met.* **1997**, *84*, 631–632.

[13] O. Khatib, J. D. Yuen, J. Wilson, R. Kumar, M. Di Ventra, A. J. Heeger, D. N. Basov, *Phys. Rev. B* **2012**, *86*, 195109.

[14] O. Khatib, B. Lee, J. Yuen, Z. Q. Li, M. Di Ventra, A. J. Heeger, V. Podzorov, D. N. Basov, *J. Appl. Phys.* **2010**, *107*, 123702.

[15] J.-M. Zhuo, L.-H. Zhao, P.-J. Chia, W.-S. Sim, R. H. Friend, P. K. H. Ho, *Phys. Rev. Lett.* **2008**, *100*, 186601.

[16] H. Neugebauer, *J. Electroanal. Chem.* **2004**, *563*, 153–159.

[17] S. Kahmann, M. A. Loi, C. J. Brabec, *J. Mater. Chem. C* **2018**, *6*, 6008–6013.

[18] S. Hotta, W. Shimotsuma, M. Taketani, *Synth. Met.* **1984**, *10*, 85–94.

[19] S. Hotta, M. Soga, N. Sonoda, *J. Phys. Chem.* **1989**, *93*, 4994–4998.

[20] A. Cravino, H. Neugebauer, S. Luzzati, M. Catellani, A. Petr, L. Dunsch, N. S. Sariciftci, *J. Phys. Chem. B* **2002**, *106*, 3583–3591.

[21] A. J. Maliakal, *ACS Appl. Mater. Interfaces* **2013**, *5*, 8300–8307.

[22] Y. H. Kim, A. J. Heeger, *Phys. Rev. B* **1989**, *40*, 8393–8398.

[23] J. Holt, S. Singh, T. Drori, Y. Zhang, Z. V Vardeny, *Phys. Rev. B* **2009**, *79*, 195210.

[24] Y. Furukawa, in *Handb. Vib. Spectrosc.* (Ed.: N.J. Everall), John Wiley & Sons, Ltd, Chichester, UK, **2007**.

[25] K. F. Voss, C. M. Foster, L. Smilowitz, D. Mihailović, S. Askari, G. Srdanov, Z. Ni, S. Shi, A. J. Heeger, F. Wudl, *Phys. Rev. B* **1991**, *43*, 5109–5118.

[26] Y. H. Kim, D. Spiegel, S. Hotta, A. J. Heeger, *Phys. Rev. B* **1988**, *38*, 5490–5495.

[27] C. H. Londergan, J. C. Salsman, S. Ronco, C. P. Kubiak, *Inorg. Chem.* **2003**, *42*, 926–928.

[28] M. Zamadar, S. Asaoka, D. C. Grills, J. R. Miller, *Nat. Commun.* **2013**, *4*, 2818.

[29] E. T. Shimomura, M. A. Phillippi, H. M. Goff, W. F. Scholz, C. A. Reed, *J. Am. Chem. Soc.* **1981**, *103*, 6778–6780.

[30] J. Yin, Z. Wang, D. Fazzi, Z. Shen, C. Soci, *J. Phys. Chem. C* **2016**, *120*, 1994–2001.

[31] A. A. Bakulin, D. Y. Parashchuk, P. van Loosdrecht, M. S. Pshenichnikov, *Quantum Electron.* **2009**, *39*, 643–648.

[32] A. A. Bakulin, D. S. Martyanov, D. Y. Paraschuk, M. S. Pshenichnikov, P. H. M. van Loosdrecht, *J. Phys. Chem. B* **2008**, *112*, 13730–13737.

[33] P. B. Miranda, D. Moses, A. J. Heeger, *Phys. Rev. B* **2004**, *70*, 85212.

[34] U. Mizrahi, E. Ehrenfreund, D. Gershoni, Z. Vardeny, *Polymer* **2003**, *44*, 691–694.

[35] Z. V. Vardeny, in *Relax. Polym.*, World Scientific, **1993**, pp. 166–214.

[36] K. Stallhofer, M. Nuber, R. Kienberger, V. Körstgens, P. Müller-Buschbaum, H. Iglev, *J. Phys. Chem. C* **2019**, *123*, 28100–28105.

[37] P. N. Taylor, J. Huuskonen, G. Rumbles, R. T. Aplin, E. Williams, H. L. Anderson, *Chem. Commun.* **1998**, 909–910.

[38] J. K. Sprafke, D. V. Kondratuk, M. Wykes, A. L. Thompson, M. Hoffmann, R. Drevinskas, W. H. Chen, C. K. Yong, J. Kärnbratt, J. E. Bullock, M. Malfois, M. R. Wasielewski, B. Albinsson, L. M. Herz, D. Zigmantas, D. Beljonne, H. L. Anderson, *J. Am. Chem. Soc.* **2011**, *133*, 17262–17273.

[39] C. E. Tait, P. Neuhaus, H. L. Anderson, C. R. Timmel, *J. Am. Chem. Soc.* **2015**, *137*, 6670–6679.

[40] F. C. Grozema, C. Houarner-Rassin, P. Prins, L. D. A. Siebbeles, H. L. Anderson, *J.*

Am. Chem. Soc. **2007**, *129*, 13370–13371.

[41] C. E. Tait, P. Neuhaus, M. D. Peeks, H. L. Anderson, C. R. Timmel, *Phys. Chem. Chem. Phys.* **2016**, *18*, 5275–5280.

[42] C. Minot, C. Flytzanis, *Chem. Phys. Lett.* **1979**, *68*, 501–506.

[43] M. Krejčik, M. Daněk, F. Hartl, *J. Electroanal. Chem. Interfacial Electrochem.* **1991**, *317*, 179–187.

[44] P. M. Donaldson, G. M. Greetham, D. J. Shaw, A. W. Parker, M. Towrie, *J. Phys. Chem. A* **2018**, *122*, 780–787.

[45] N. T. Hunt, *Chem. Soc. Rev.* **2009**, *38*, 1837.

[46] I. V. Rubtsov, R. M. Hochstrasser, *J. Phys. Chem. B* **2002**, *106*, 9165–9171.

[47] I. V Rubtsov, J. Wang, R. M. Hochstrasser, *J. Phys. Chem. A* **2003**, *107*, 3384–3396.

[48] G. Duxbury, *Concepts and Methods of 2D Infrared Spectroscopy, by Peter Hamm and Martin Zanni*, Cambridge University Press, Cambridge, **2011**.

[49] *SurfaceXplorer 4.3.0, 2002-2014, Ultrafast Syst. LLC* **2014**.

[50] A. L. Stelling, K. L. Ronayne, J. Nappa, P. J. Tonge, S. R. Meech, *J. Am. Chem. Soc.* **2007**, *129*, 15556–15564.

[51] M. Kondo, J. J. J. Nappa, K. L. Ronayne, A. L. Stelling, P. J. Tonge, S. R. Meech, *J. Phys. Chem. B* **2006**, *110*, 20107–20110.

[52] M. Banno, K. Iwata, H. O. Hamaguchi, *J. Chem. Phys.* **2007**, *126*, 204501.

[53] O. A. Vydrov, G. E. Scuseria, *J. Chem. Phys.* **2006**, *125*, 234109.

[54] O. A. Vydrov, J. Heyd, A. V. Krukau, G. E. Scuseria, *J. Chem. Phys.* **2006**, *125*, 74106.

[55] O. A. Vydrov, G. E. Scuseria, J. P. Perdew, *J. Chem. Phys.* **2007**, *126*, 154109.

[56] M. J. Frisch, G. W. Trucks, H. B. Schlegel, G. E. Scuseria, M. A. Robb, J. R. Cheeseman, G. Scalmani, V. Barone, B. Mennucci, G. A. Petersson, H. Nakatsuji, M. Caricato, X. Li, H. P. Hratchian, A. F. Izmaylov, J. Bloino, G. Zheng, J. L. Sonnenberg, M. Hada, M. Ehara, K. Toyota, R. Fukuda, J. Hasegawa, M. Ishida, T. Nakajima, Y. Honda, O. Kitao, H. Nakai, T. Vreven, J. A. Montgomery, J. E. Peralta, F. Ogliaro, M. Bearpark, J. J. Heyd, E. Brothers, K. N. Kudin, V. N. Staroverov, R. Kobayashi, J. Normand, K. Raghavachari, A. Rendell, J. C. Burant, S. S. Iyengar, J. Tomasi, M. Cossi, N. Rega, J. M. Millam, M. Klene, J. E. Knox, J. B. Cross, V. Bakken, C. Adamo, J. Jaramillo, R. Gomperts, R. E. Stratmann, O. Yazyev, A. J. Austin, R. Cammi, C. Pomelli, J. W. Ochterski, R. L. Martin, K. Morokuma, V. G. Zakrzewski, G. A. Voth, P. Salvador, J. J. Dannenberg, S. Dapprich, A. D. Daniels,

Farkas, J. B. Foresman, J. V Ortiz, J. Cioslowski, D. J. Fox, **2016**.

[57] S. Hu, T. G. Spiro, *J. Am. Chem. Soc.* **1993**, *115*, 12029–12034.

[58] X. Y. Li, R. S. Czernuszewicz, J. R. Kincaid, P. Stein, T. G. Spiro, *J. Phys. Chem.* **1990**, *94*, 47–61.

[59] N. T. Hunt, *Dalt. Trans.* **2014**, *43*, 17578–17589.

[60] A. L. Le Sueur, R. E. Horness, M. C. Thielges, *Analyst* **2015**, *140*, 4336–4349.

[61] P. Hamm, M. Zanni, *Concepts and Methods of 2D Infrared Spectroscopy*, Cambridge University Press, Cambridge, **2011**.

[62] P. M. Donaldson, G. M. Greetham, D. J. Shaw, A. W. Parker, M. Towrie, *J. Phys. Chem. A* **2018**, *122*, 780–787.

[63] N. Mouton, M. Sliwa, G. Buntinx, C. Ruckebusch, *J. Chemom.* **2010**, *24*, 424–433.

[64] M. Roelfs, P. C. Kroon, *Zenodo* **2019**, *June 21*, DOI 10.5281/zenodo.1133336.

3

Global aromaticity of porphyrin nanorings

3.1. Abstract

This chapter discusses the preparation and study of the largest aromatic and anti-aromatic species reported at the time. The introduction reviews the basis of the [4*n*+2] Hückel rule together with the definitions and implications of (anti)aromaticity. Both theoretical and experimental tools for its assessment are presented. Selected examples from literature of large aromatic species are discussed to show the current size limits of (anti)aromaticity. This is followed by an experimental and theoretical assessment of the aromaticity in the porphyrin nanorings cations.

First a basic symmetric six-porphyrin nanoring is re-examined and both theoretical and experimental results scrutinised. This study is extended to variously linked 6-porphyrin nanorings. Later, larger systems are studied, with increasing size up to a 12-porphyrin nanoring. The octacation and hexacation of this 12-porphyrin nanoring represent the largest (anti)aromatic species with 160 and 162 π electrons, respectively. Switching off the induced ring current in the 12-porphyrin nanoring is demonstrated by changing its shape from a circular to a figure-of-eight conformation.

Part of this study was published in:

- M. Rickhaus[†], M. Jirasek[†], L. Tejerina, H. Gotfredsen, M. D. Peeks, R. Haver, H.-W. Jiang, T. D. W. Claridge and H. L. Anderson, Global Aromaticity at the Nanoscale. *ChemRxiv preprint* **2019**, DOI: 10.26434/chemrxiv.8953565. Accepted for publication in *Nat. Chem.*

- R. Haver, L. Tejerina, H.-W. Jiang, M. Rickhaus, M. Jirasek, I. Grübner, H. J. Eggimann, L. M. Herz and H. L. Anderson, 'Tuning the Circumference of Six-Porphyrin Nanorings', *J. Am. Chem. Soc.*, **2019**, *141*, 7965–7971.

- M. Rickhaus, A. Vargas Jentzsch, L. Tejerina, I. Grübner, M. Jirasek, T. D. Claridge and H. L. Anderson, 'Single-Acetylene Linked Porphyrin Nanorings', *J. Am. Chem. Soc.*, **2017**, *139*, 16502–16505

[†] These authors contributed equally

3.2. Introduction

3.2.1. What is aromaticity?

Aromaticity is a key concept in organic chemistry, and one of the most discussed themes in the chemical literature.[1] Originally, the term was used to describe compounds with a similar odour as 'benzene' and was first used by Hofmann in 1855.[1] Today we use it to comment on higher stability, magnetic behaviour or reactivity of certain compounds.

Classical aromatic compounds are cyclic planar molecules possessing [4n+2] conjugated π electrons. Many geometry- and energy-related criteria were studied and proposed for numerating the degree of aromaticity, such as: reduced bond length alternation,[2,3] energetic stabilisation[4] or the benzene-type reactivity toward electrophiles.[5] Although all these effects were observed, too many exceptions were documented when only certain criteria are met, while other not at all. This makes the rigorous definition of aromaticity a very controversial task. The author's personal preference for the most general definition of the aromatic system is the fact, that the molecule sustains a diatropic ring current in an external magnetic field. The diatropic ring current is such a current, imaginable as the circulation of π electrons, that induces another magnetic field opposing the external magnetic field inside the cycle. This effectively shield/weakens the field inside and de-shield/strengthen the field outside of the cycle.

The general rule determining that (co)planar structures with [4n+2] π electrons will be aromatic originates from the work of Erich Hückel.[6–8] He developed the quantum chemical method, now called Hückel Molecular Orbital theory (HMO).[9,10]

3.2.1.1. Origin of [4*n*+2] rule – Hückel molecular orbital theory

The famous Hückel Rule predicts that cycles with [4n+2] π electrons are aromatic, in the original description meant as stabilised. Hückel Molecular Orbital theory (HMO) uses the concept of the Linear Combination of Atomic Orbitals (LCMO) developed by Sir John Lennard-Jones.[11] LCMO postulates that the wavefunction ψ can be described as a linear combination of individual atomic orbitals. Mixing of n atomic orbitals results in n new molecular orbitals as their linear combination (**Eq. 1**)

$$\Psi_j = C_{j1}\phi_1 + C_{j2}\phi_2 + \cdots + C_{ji}\phi_i + \cdots + C_{jn}\phi_n \qquad \Psi_j = \sum_{1}^{n} C_{ij}\phi_i \tag{1}$$

---

[1] Based on literature search on 2nd of October 2019, 27780 documents contained word 'aromaticity' in a title or in the abstract.

Hückel further approximated, that in unsaturated molecules, the wavefunction of the molecule can be separated into the σ and π parts, and only the π component, as the product of the individual molecular orbitals, would be examined from the 'connectivity point of view' (**Eq. 2**).

$$\Psi = \Phi_\sigma \Phi_\pi \qquad\qquad \Phi_\pi = \prod_k \psi_k \tag{2}$$

To estimate the energy of the system *E*, the Hamiltonian $\widehat{\mathcal{H}}$ operator has to be applied to the wavefunction (**Eq. 3**).[12,13]

$$\widehat{\mathcal{H}}\Psi = E\Psi \tag{3}$$

Even if we do not know, how the Hamiltonian $\widehat{\mathcal{H}}$ looks, we can comment on the energy calculation. From the variation principle, it is known, that the time averaged energy $\langle E \rangle$, obtained from the wavefunction Ψ described in any way (in terms of LCAO described by any C_{ij} coefficients combination, cf. **Eq. 1**), will always be higher (or equal) to the lowest systems energy (**Eq. 4**).

$$\langle E \rangle = \frac{\int \Psi \widehat{\mathcal{H}} \Psi d\tau}{\int \Psi^2 d\tau} > E_0 \tag{4}$$

Eq. 4 describes in other words, that by changing the C_{ij} coefficients, one approaches the real value E_0 from top when minimizing the $\langle E \rangle$. This minimization can be done by varying the individual coefficients C_{ij}, weighing the contribution of individual atomic orbitals. And since E_0 represents the minimum, the problem to be solved can be described as **Eq. 5**:

$$\frac{\partial \langle E \rangle}{\partial C_{ij}} = 0 \tag{5}$$

To analyse it, we can explicitly write **Eq. 4** as:

$$\langle E \rangle = \frac{\int (C_{i1}\phi_1 + C_{i2}\phi_2 + \cdots + C_{in}\phi_n) \widehat{\mathcal{H}} (C_{i1}\phi_1 + C_{i2}\phi_2 + \cdots + C_{in}\phi_n) d\tau}{\int (C_{i1}\phi_1 + C_{i2}\phi_2 + \cdots + C_{in}\phi_n)^2 d\tau} \tag{6}$$

The sub-integrals can be 'hidden' with **Eq. 7**:

$$H_{ij} = \int \phi_i \widehat{\mathcal{H}} \phi_j d\tau \qquad\qquad S_{ij} = \int \phi_i \phi_j d\tau \tag{7}$$

The H_{ij} and S_{ij} have their physical meanings and are often called the overlap and exchange integrals, respectively.[10] The equation is then reorganised and the application of **Eq. 5** for all *i* (from 1 to *n*) yield a series of equations that can be rewritten in a condense form using the matrix and vector notation (**Eq. 8**):

$$\begin{bmatrix} (H_{11}-\langle E\rangle\cdot S_{11}) & (H_{12}-\langle E\rangle\cdot S_{12}) & \cdots & (H_{1n}-\langle E\rangle\cdot S_{1n}) \\ (H_{21}-\langle E\rangle\cdot S_{21}) & (H_{22}-\langle E\rangle\cdot S_{12}) & \cdots & (H_{2n}-\langle E\rangle\cdot S_{2n}) \\ \vdots & \vdots & \ddots & \vdots \\ (H_{n1}-\langle E\rangle\cdot S_{n1}) & (H_{n2}-\langle E\rangle\cdot S_{n2}) & \cdots & (H_{nn}-\langle E\rangle\cdot S_{nn}) \end{bmatrix} \begin{bmatrix} C_1 \\ C_2 \\ \vdots \\ C_n \end{bmatrix} = 0 \qquad (8)$$

A nontrivial solution (trivial is that all $C_{ij} = 0$) of the systems of linear equations organised in this matrix notation must have the secular determinant equal to zero (**Eq. 9**):

$$\begin{vmatrix} (H_{11}-\langle E\rangle\cdot S_{11}) & (H_{12}-\langle E\rangle\cdot S_{12}) & \cdots & (H_{1n}-\langle E\rangle\cdot S_{1n}) \\ (H_{21}-\langle E\rangle\cdot S_{21}) & (H_{22}-\langle E\rangle\cdot S_{12}) & \cdots & (H_{2n}-\langle E\rangle\cdot S_{2n}) \\ \vdots & \vdots & \ddots & \vdots \\ (H_{n1}-\langle E\rangle\cdot S_{n1}) & (H_{n2}-\langle E\rangle\cdot S_{n2}) & \cdots & (H_{nn}-\langle E\rangle\cdot S_{nn}) \end{vmatrix} = 0 \qquad (9)$$

Equations can be further simplified when considering the postulated **Eq. 10**, which is the consequence of normalisation.

$$for\ i = j \quad S_{ij} = \int \phi_i \phi_j d\tau = 1 \qquad (10)$$

And furthermore, an approximation (**Eq. 11**) can be made:

$$for\ i \neq j \quad S_{ij} = \int \phi_i \phi_j d\tau = 0 \qquad (11)$$

Leading to a simple determinant (**Eq. 12**):

$$\begin{vmatrix} (H_{11}-\langle E\rangle) & (H_{12}) & \cdots & (H_{1n}) \\ (H_{21}) & (H_{22}-\langle E\rangle) & \cdots & (H_{2n}) \\ \vdots & \vdots & \ddots & \vdots \\ (H_{n1}) & (H_{n2}) & \cdots & (H_{nn}-\langle E\rangle) \end{vmatrix} = 0 \qquad (12)$$

The physical meaning of the H_{ij} terms is the exchange interaction energy. For the $i = j$, we can define $H_{ij} = \alpha$, which numerically represents the energetic contribution of the electron to its core (**Eq. 13**).

$$\begin{vmatrix} \alpha-\langle E\rangle & H_{12} & \cdots & H_{1n} \\ H_{21} & \alpha-\langle E\rangle & \cdots & H_{2n} \\ \vdots & \vdots & \ddots & \vdots \\ H_{n1} & H_{n2} & \cdots & \alpha-\langle E\rangle \end{vmatrix} = 0 \qquad (13)$$

The off-diagonal H_{ij} terms can be split into two groups. For the neighbouring atomic orbitals ($i = j \pm 1$), it is defined $H_{ij} = \beta$, representing the exchange interaction between two neighbouring atomic orbitals. The last approximation will be to define all other terms ($i > j + 1$ or $i < j-1$) to be $H_{ij} = 0$, assuming no exchange interaction longer than one bond. This is again indeed a very crude approximation. Further 'visual' simplification is division of the determinant by β and substitution with **Eq. 14**:

$$x = \frac{\alpha - \langle E \rangle}{\beta} \tag{14}$$

Depending on the molecule's connectivity, the secular determinant will have a simple structure as summarised in **Figure 1**. This type of matrix and its determinant is well known in mathematics as a *circulant*, which is solvable even for the general case.[14,15] This allows one to calculate the solution for each topology and connectivity even without knowing the size of the system (n atoms).

molecule	*linear*	*cyclic*	*half-twisted cyclic*
AOs	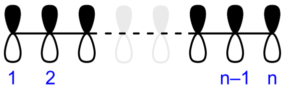	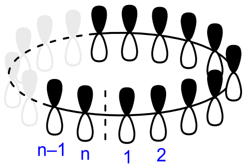	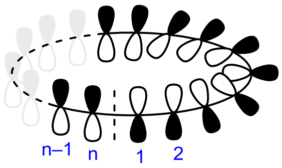
determinant	$\begin{vmatrix} x & 1 & 0 & \cdots & 0 \\ 1 & x & 1 & \cdots & 0 \\ 0 & 1 & x & \cdots & 0 \\ \vdots & \vdots & \vdots & \ddots & \vdots \\ 0 & 0 & \cdots & 1 & x \end{vmatrix} = 0$	$\begin{vmatrix} x & 1 & 0 & \cdots & 1 \\ 1 & x & 1 & \cdots & 0 \\ 0 & 1 & x & \cdots & 0 \\ \vdots & \vdots & \vdots & \ddots & \vdots \\ 1 & 0 & \cdots & 1 & x \end{vmatrix} = 0$	$\begin{vmatrix} x' & 1 & 0 & \cdots & -1 \\ 1 & x' & 1 & \cdots & 0 \\ 0 & 1 & x' & \cdots & 0 \\ \vdots & \vdots & \vdots & \ddots & \vdots \\ -1 & 0 & \cdots & 1 & x' \end{vmatrix} = 0$
solution	$x_j = -2\cos\left(\frac{\pi j}{n+1}\right)$	$x_j = -2\cos\left(\frac{2\pi j}{n}\right)$	$x'_j = -2\cos\left(\frac{(2j+1)\pi}{n}\right)$
	$j = 0, 1, \cdots, (n-1)$	$j = 0, \pm 1, \cdots, \pm\left(\frac{n}{2} - 1\right), \frac{n}{2}$	$j = \pm 0, \pm 1, \cdots, \pm\left(\frac{n}{2} - 1\right)$

Figure 1: Comprehensive summary of the HMO description of linear, cyclic and half-twisted Möbius molecules, their HMO secular determinants and their solutions for x_j.

All solutions for linear and cyclic molecules are harmonic functions. If we replace the substitution from **Eq. 14** back with explicit E, α and β we get functions predicting the energy of all n number of molecular orbitals (**Figure 2**):

	linear	*cyclic*	*half-twisted cyclic*
E_j	$E_j = \alpha + 2\beta\cos\left(\frac{\pi j}{n+1}\right)$	$E_j = \alpha + 2\beta\cos\left(\frac{2\pi j}{n}\right)$	$E_j = \alpha + 2\beta'\cos\left(\frac{(2j+1)\pi}{n}\right)$
	$j = 0, 1, \cdots, (n-1)$	$j = 0, \pm 1, \cdots, \pm\left(\frac{n}{2} - 1\right), \frac{n}{2}$	$j = \pm 0, \pm 1, \cdots, \pm\left(\frac{n}{2} - 1\right)$

Figure 2: Summary of the HMO predicted MO energies of linear, cyclic and half-twisted Möbius molecules.

In the case of linearly conjugated molecules, each molecular orbital has a different energy from the lowest, $\alpha - 2{\cdot}\beta$ (β is negative), to the highest $\alpha + 2{\cdot}\beta$, in energy. In the case of cyclic molecules, all molecular orbital levels are doubly degenerated except the lowest and the highest MO, with energies $\alpha - 2{\cdot}\beta$ and $\alpha + 2{\cdot}\beta$, respectively. A special case, discovered and worked out by Heilbronner,[16] is observed when the set of π atomic orbitals accommodate single, 180° twist (Möbius topology), and then all MOs are grouped into degenerate pairs.

This, general feature of HMO theory for the prediction of molecular orbital energy-level spacing, is depicted for two examples of systems with 6 and 8 atomic orbitals (**Figure 3**). Such energy diagram is often drawn on circles, serving as a mnemonic (Frost cycle) relating energy and even spacing of energy levels on a circle, as a consequence of the harmonic function solution.

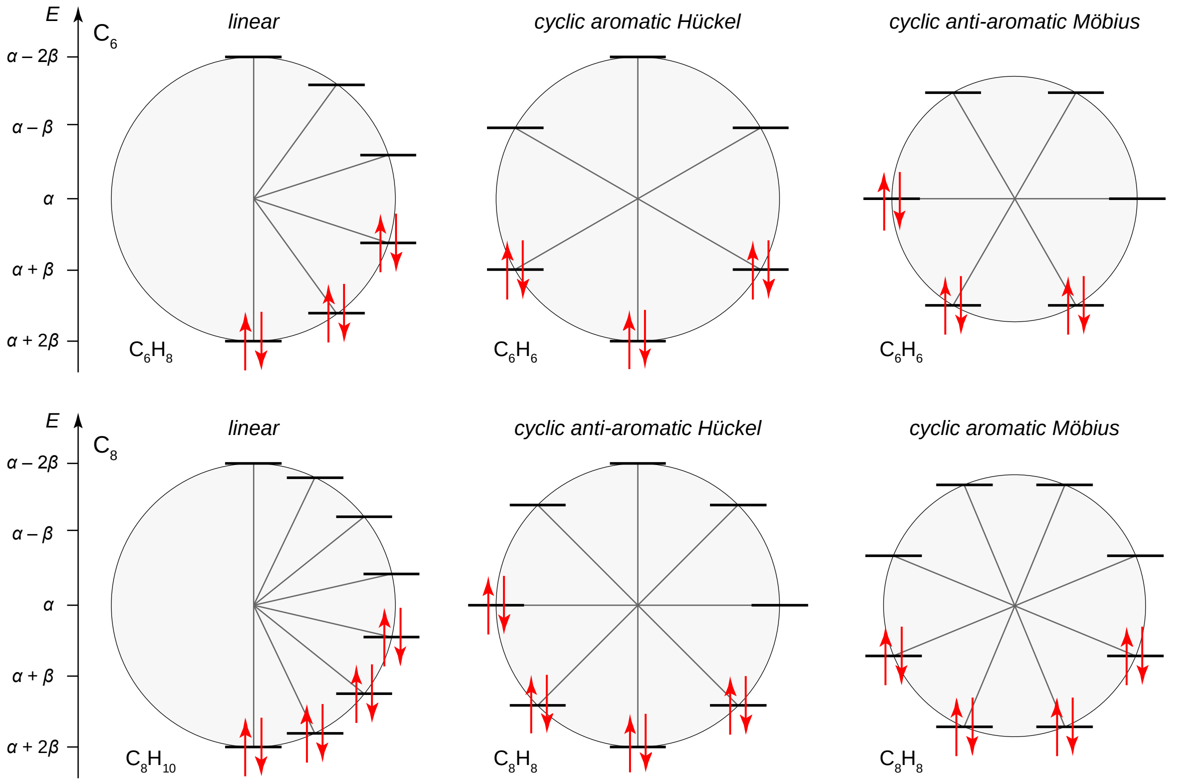

Figure 3: Frost cycles representing energy levels of MOs of linear, cyclic and Möbius cyclic π-conjugated molecules containing 6 (top) or 8 (bottom) conjugated AOs. Occupancy of the MOs with electrons inherently assumes singlet multiplicity and Jahn-Teller-distortion induced lowering of energy of one of the formerly degenerated HOMO orbitals in anti-aromatic states.

The mnemonics, together with MO occupation leads to various energy relations between linear and cyclic molecules for states with [4*n*+2] and [4*n*] π electrons. The total energy of linear systems calculated as a sum of all molecular energies multiplied by their electronic occupation (0 or 2) will rise monotonically.

On the other hand, the total energy of the cyclic system will rise in an alternating pattern. As for [4*n*+2] states, two degenerate HOMO orbitals will be fully occupied, whereas for [4*n*] states one of the HOMO orbitals will be occupied and one will be empty (**Figure 4**). Such states are often referred to as aromatic [4*n*+2] and anti-aromatic [4*n*], the latter term proposed by Breslow.[17] The Möbius aromaticity problem will be discussed in more details in **Chapter 4**.

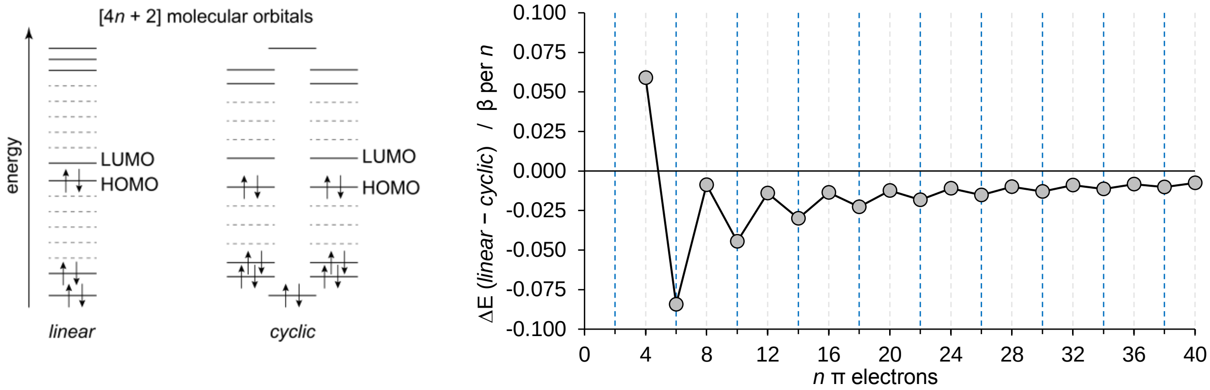

Figure 4: Energy levels of [4*n*+2] π electron system (left) and energy difference between cyclic and linear molecule (right).

These results of HMO theory describe only the energetic levels of individual MOs. Further solution of **Eq. 3** yields C_{ij} coefficients for every MO. Qualitatively, solution of a cyclic, Hückel molecule with *n* AOs leads to the known pattern: Lowest MO has all C_{ij} coefficient of the same sign, therefore with no nodal planes (vertical plane in respect to the molecule). With increasing energy, every pair of the degenerate MO has +1 nodal plane up to the highest energy MO with *n*/2 nodal planes. Probably, the most iconic example of this solution is the MO diagram for benzene and hexatriene (**Figure 5**).

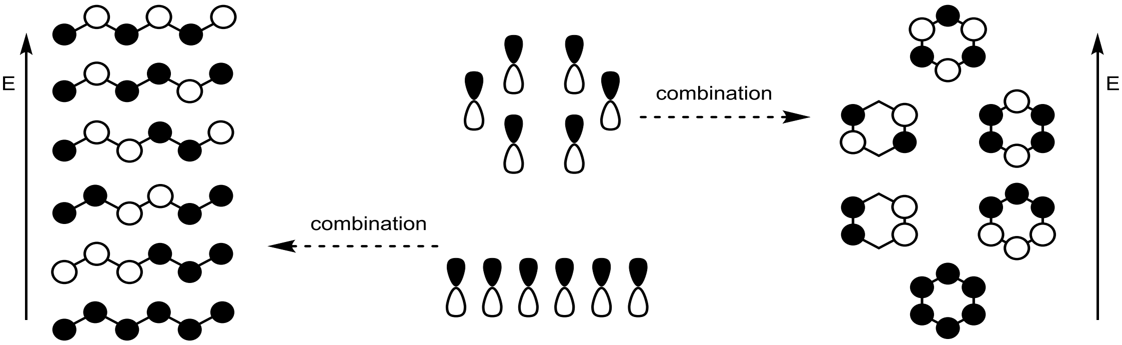

Figure 5: Qualitative description of molecular orbitals of hexatriene (left) and benzene (right) as a result of the linear combination of atomic orbitals.

This pattern is general for any [*n*]annulene and has an implication to the predicted shape of frontier molecular orbitals. In an aromatic system with [4*n*+2] electrons, HOMO possesses ((*n*−2)/4) nodes whereas the LUMO possesses one nodal plane more, ((*n*+2)/4) nodes. In an anti-aromatic system with [4*n*] electrons, both HOMO and LUMO are expected to possess same number of nodal planes, (*n*/4).

3.2.1.2. Energetic and geometric criteria of aromaticity

The most intuitive criterion of aromaticity is apparent from the discussion of MO energy levels (*cf*. **Figure 4**). Aromatic systems, with [4*n*+2] π electrons should be relatively stabilised, while anti-aromatic states with [4*n*] π electrons should be destabilised. Over many decades, scientists have theoretically and experimentally assessed aromaticity and its contribution to the total energy of the system. In a classical experimental approach, this can be done, for example by considering, hydrogenation of double bonds. If the energy gain from saturation is lower than would be expected from simple additivity, this would suggest aromatic stabilisation, while the higher energetic gain is an indication of anti-aromaticity (**Figure 6**).

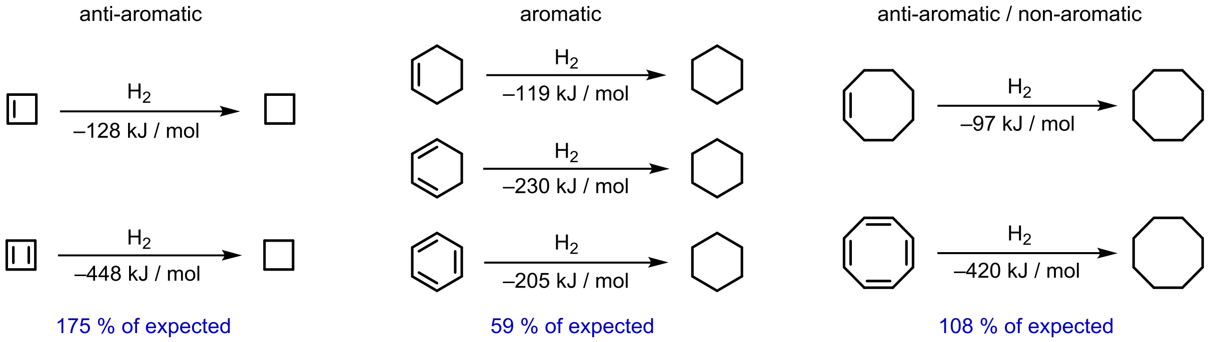

Figure 6: Hydrogenation energy as a tool to assess aromatic stabilisation. Based on thermochemical data from literature.[18–22] Graphics layout adapted from literature.[23]

A special tool to assess aromatic stabilisation, used particularly in theoretical calculations, is the study of *isodesmic reactions*.[24–26] In these, often only hypothetical reactions, the number of atoms and their bond types are not changed. This typically involves 'transfer' of the double bond(s) from an aromatic system (in order to disrupt the π electron communication) to a saturated skeleton (**Figure 7**).

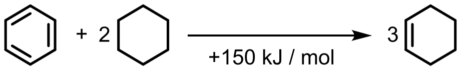

Figure 7: Isodesmic reaction causing benzene deconjugation.

Isodesmic reactions have a big advantage for calculations, as additive errors in the energy estimation (present due to various approximations and model imperfections) can be subtracted and thus more accurate results are obtained. Similarly, to isodesmic reactions, the energy change can be assessed for isomerisation reactions involving deconjugation (**Figure 8**).

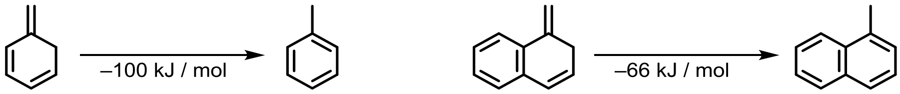

Figure 8: Rearrangements yielding systems aromatisation. Based on experimental thermochemical data from literature.[27]

Further, a very popular criterion for assessing aromaticity in molecules is their reactivity, particularly with electrophiles. Unlike non-aromatic olefins which react *via* electrophilic addition on the system, aromatic compounds are expected to undergo aromatic electrophilic substitution (**Figure 9**). This criterion has a rather limited use and many exceptions exist, particularly found in systems larger than 6 π electrons.

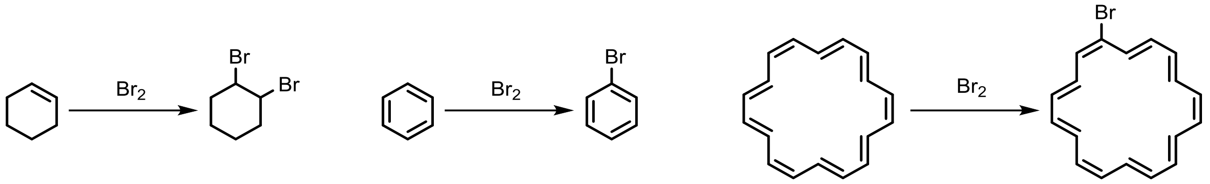

Figure 9: Reactivity of Br2 toward non-aromatic cyclohexene and aromatic benzene and [18]annulene.[28]

A further criterion, enumerating the degree of aromaticity is the change in bond length. One important model – the Harmonic Oscillator Model of Aromaticity (HOMA) provides a quantitative measure for aromaticity, by comparing the individual bond lengths in the system with respect to a reference aromatic molecule, such as benzene.[29,30] The sum is divided by the number of atoms involved and normalised (**Eq. 15**).[30,31]

$$\mathrm{HOMA} = 1 - \frac{\alpha}{n}\sum_{i=1}^{n}\left(R_{opt} - R_i\right)^2 \tag{15}$$

For this simplest form of HOMA, the empirically found value of optimal C—C aromatic bond length is R_{opt} = 1.388 Å (values for benzene are found in a range R_{benzene} = 1.378–1.394 Å) and normalisation factor α = 257.7 Å^{-1}.[31] Such parameters scale the HOMA values to be ~1 for aromatic (like benzene) and ~0 for non-aromatic rings. This approach can also be used to assess aromaticity of individual rings in larger molecules, e.g. in the polycyclic aromatic hydrocarbons (**Figure 10**).

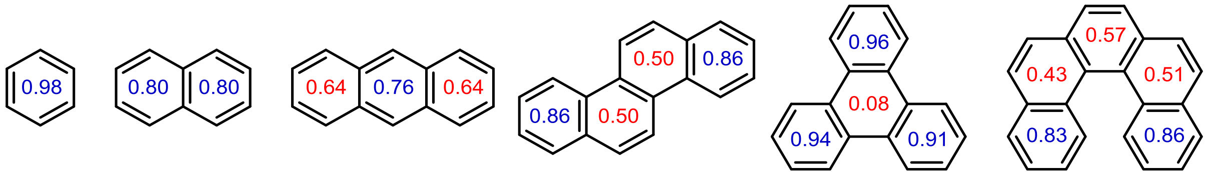

Figure 10: Experimental[3,32–34] HOMA values of individual rings of selected polycyclic hydrocarbons. Values of HOMA > 0.75 are in blue indicating more aromatic rings, values < 0.75 are in red, emphasizing less and non-aromatic rings.

3.2.1.3. Induced ring current in aromatic molecules

The last criterion of aromaticity discussed here is the observation of induced currents in an external magnetic field. It is expected, that when an aromatic molecule is placed in an external magnetic field, a ring current will be induced. This current will induce another magnetic field opposing the external field inside the cycle at the molecule. Such behaviour was proposed, surprisingly even before the invention and advent of NMR spectroscopy[35,36] and such current is commonly called *diatropic*, as its macroscopic manifestation is so that the bulk aromatic material becomes diamagnetic.

On the contrary, when an anti-aromatic system is placed in an external magnetic field, a current in the opposite direction, a *paratropic* ring current, is observed. This manifest itself into a paramagnetic property of the bulk of the anti-aromatic molecules.

Beside its macroscopic properties, the induced ring current significantly changes the local magnetic field strength inside and outside the aromatic ring. This is very well known in NMR spectroscopy as shielding/de-shielding effects.

Since the applied external magnetic field (at commonly reachable strengths) has negligible effect on the total energy of the molecule, perturbation theory can be used for its theoretical description. For weak magnetic fields, which are used in typical NMR experiments, 1st order perturbation is sufficient to describe the induced current **J**. If the system is extremely magnetically susceptible or some very strong magnetic fields are applied, the magnetic field may need to be explicitly described in the Hamiltonian. Practically, this was for example developed in time-dependent current DFT method (TD-CDFT).[37–40]

To describe the effect of the magnetic field, a magnetic vector potential $A(r)$ is implemented in the kinetic energy term of the Hamiltonian (**Eq. 16**).

$$T = \frac{1}{2}\left(-i\nabla - A(r)\right)^2 \tag{16}$$

Where $A(\mathrm{r})$ is related to the magnetic field intensity as **Eq. 17**:

$$A(\boldsymbol{r}) = \frac{1}{2}\boldsymbol{B} \times \left(\boldsymbol{r} - \boldsymbol{R_{orig}}\right) \tag{17}$$

Where $\boldsymbol{R_{orig}}$ is an arbitrarily chosen gauge origin and $\boldsymbol{B}$ magnetic field. Since the total induced ring currents and induced magnetic field are physical properties, it is required that such results are independent on the choice of gauge origin. However, a smart choice of gauge origin can help to interpret the contribution of certain MOs to the ring current. One choice is the Continuous Transformation of the Origin of the Current Density (CTOCD) continuously transforming gauge origin ($\boldsymbol{r} = \boldsymbol{R_{orig}}$, for each $\boldsymbol{r}$), also called the *ipsocentric* method, developed and popularised by Steiner and Fowler.[41] Another method uses a fixed gauge origin, for example in the centre of the molecule (*monocentric* method). Comparison of the two methods, and the advantage of the *ipsocentric* approach, can be illustrated on the ring current calculations of benzene and analysis of each MO contribution.

Benzene is an aromatic molecule and thus a diatropic ring current is expected. Interaction of the system with a magnetic field proceeds through transitions from the occupied molecular orbitals to virtual states (empty molecular orbitals), induced by the perturbation with an external magnetic field. Benzene possesses three π-symmetric occupied molecular orbitals, two HOMO and one HOMO−1. In the monocentric method, all MOs exhibit some degree of induced diatropic ring current (**Figure 11, bottom**). In the case of ipsocentric method, the HOMO−1 orbital shows no contribution to the ring current and only the HOMOs are responsible for the induced ring current (**Figure 11, top**). The total sum, and thus the physically observed ring current is same in both cases.

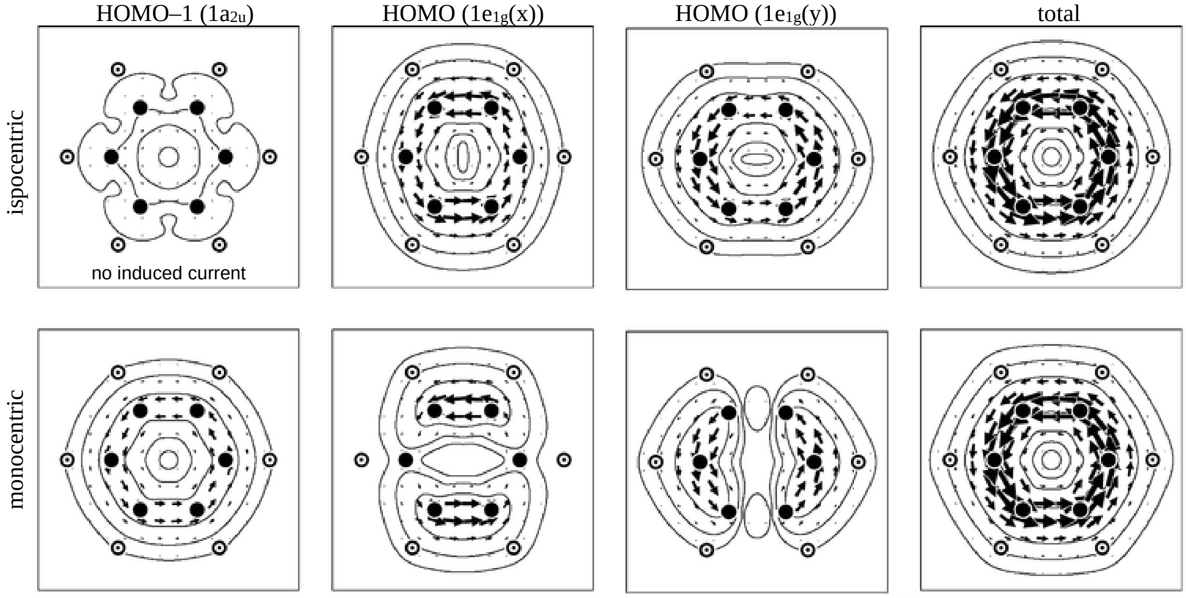

Figure 11: Induced ring current and contribution of individual MO in benzene using ipsocentric (top) and monocentric (bottom) method. ⊙ H atoms, ● C atoms positions. Magnetic field is perpendicular to the plane, oriented toward it. Figure is adapted with permission from *Phys. Chem. Chem. Phys.* **2004**, (6), 261–272. Copyright 2004 The Royal Chemical Society.[41]

The ipsocentric method provides, according to Steiner and Fowler, the most realistic interpretation and the simplest picture of the MO contributions to the observed induced ring current. Useful, symmetry-related rules for the MO contribution can be mathematically deduced from the ipsocentric approach.[42–44]

The *occupied → virtual* MO transition is accompanied by a MO symmetry change. If the relevant symmetry transformation (relative to the applied magnetic field) corresponds to the translational (within the plane) operator, then the ring current is diatropic. Such transformations will be allowed only if the angular momentum number changes by ±1 (**Figure 12, left**). If the *occupied → virtual* transformation is rotationally symmetric along the magnetic field axis, the paratropic ring current is induced (**Figure 12, right**). This transition is allowed when the angular momentum number during MO interaction does not change.

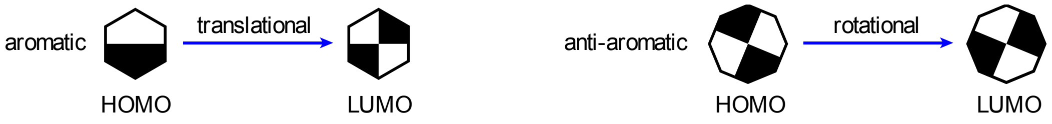

Figure 12: Simplified molecular orbital symmetries and their symmetrical relations.[43]

In aromatic species, the sole component of the ring current is the diatropic ring current induced by a four-electron interaction between the HOMO and the LUMO (**Figure 13, left**).

Since there is no occupied/virtual pair of MOs with rotational symmetry, no paratropic component is expected. In the case of anti-aromatic species, the two electron HOMO → LUMO interaction, possessing a very small energy gap, with rotational symmetry and no change in angular momentum, is responsible for the dominant paratropic ring current. Any potential diatropic ring current caused by interactions between the HOMO−1 and the LUMO are insignificant, as the energy gap is far larger and thus contribute less than the HOMO → LUMO transition (**Figure 13, right**).

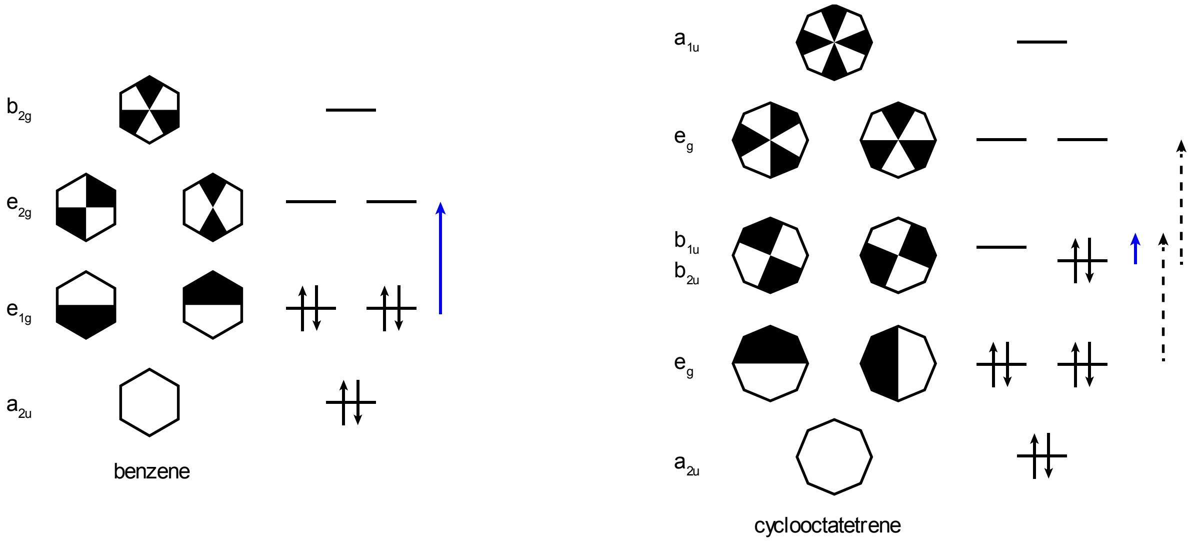

Figure 13: Origin of the diatropic (left) and paratropic (right) ring current in aromatic benzene and the hypothetical anti-aromatic, planar cyclooctatetraene, respectively. Graphical MO symmetry representation style adapted from literature.[43]

Such analysis explains the relation between the Hückel Rule, predicting energy levels and MO symmetries of [*n*]annulenes, and the induced ring currents.

Although, the ipsocentric method promoted by Fowler has mentioned advantages, its practical execution is more or less restricted to an expert community as the method and visualisation of the results are not implemented in any of the well accessible commercial tools for theoretical calculations for organic chemists (such as Gaussian or Turbomole). On the other hand, a very popular and widely used tool among organic chemists for calculation of induced currents, is the calculation of Anisotropy Induced Current Density (AICD), developed by Herges.[45] The AICD method is based on calculation of the 1st order perturbation with a magnetic field and the calculation of the perturbed wavefunction. Further, in the biggest simplification, the AICD method calculates induced currents, related to the delocalised electrons, while cancelling out local (from inner shells) induced diamagnetic currents. Such local currents have higher intensity, usually by several orders, and their presence in the plot would completely swamp the current map and obscure the picture.[46] Visualisations of such anisotropy induced currents can serve to map delocalised electrons in the structure and is thus not restricted to aromaticity problems. AICD was used, for example, to analyse through space conjugation and hyperconjugation effects in non-aromatic molecules (**Figure 14, right**).

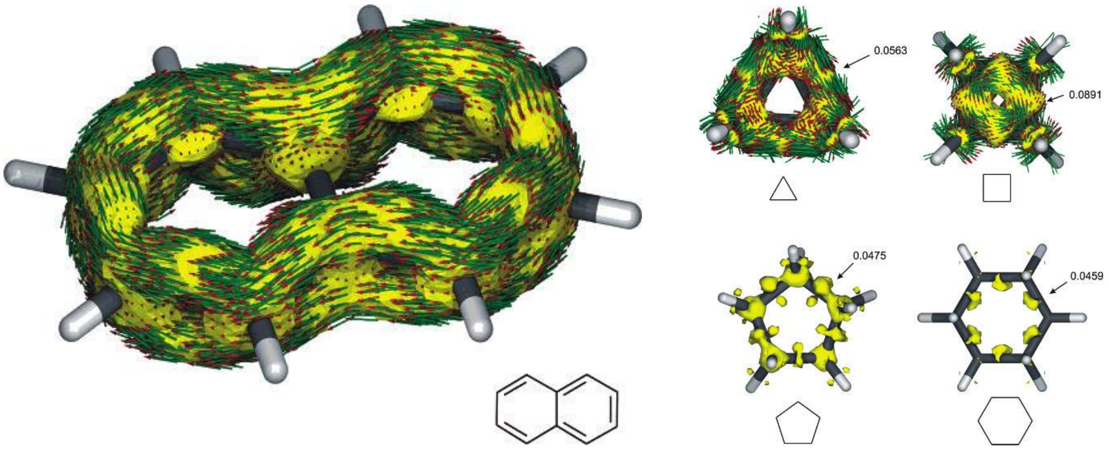

Figure 14: (left) AICD plot predicting diatropic ring current in aromatic naphthalene. (right) AICD calculated visualisation of hyperconjugation in small saturated cyclic hydrocarbons. Figures adapted with permission from *Chem. Rev.* **2005**, (105), *10*, 3758–3772. Copyright 2005 American Chemical Society.[45]

Another important theoretical tool for accessing aromaticity is calculation of the induced magnetic field as an indirect probe of the present ring current. This can be carried out by calculating the Nucleus Independent Chemical Shift (NICS) in centres and planes of the assessed molecules. This method was introduced and popularised by Schleyer et al.[47]

The concept of NICS is to evaluate the NMR chemical shift using a purely theoretical spectator atom as a non-chemical probe. This probe is often implemented in a chemical software as a ghost atom. Such ghost atoms are thus placed in the area of interest, most commonly in the centre of the examined (anti)aromatic ring (**Figure 15**). The NMR chemical shift, measured in ppm, provides information of the induced magnetic field intensity and relative orientation with respect to the external magnetic field. Beside the single ghost atom calculations, scans along the dimension(s) of interest have been studied.

A complication with the NICS calculation is the possible uncertainty of the induced magnetic field origin. Local, σ-bonds originating diatropic currents, present in any molecule, can affect and obscure the NICS value, if measured in the vicinity of σ-bonds. When the σ and π components are assessed separately, it is observed that the local σ-bond diatropic ring currents diminishes quickly above the plane, whereas ring currents originating from π-electrons have significantly longer-range effect (**Figure 15**).

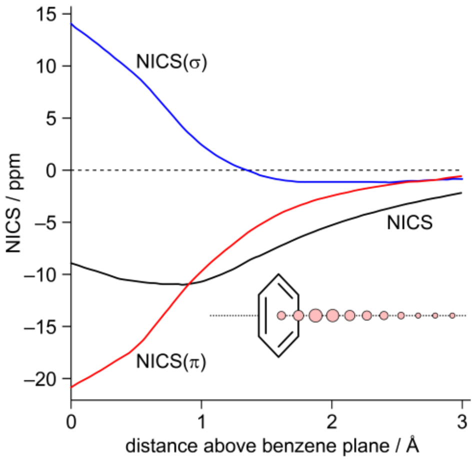

Figure 15: NICS calculated on the D_{6h} symmetry axis going through the centre of an aromatic benzene molecule. σ (blue) and π (red) components of the total NICS sum (black) is plotted as a function of height above the benzene plane. At the distance of ~1 Å above the benzenes aromatic plane, the σ component nearly diminishes to zero, leaving the π component as the dominant part of the total NICS. Data redrawn from literature.[48]

Beside mentioned scans perpendicular to the studied rings (**Figure 15**), 1D scans along the polyaromatic hydrocarbons are popular as a tool for individual ring (anti)aromaticity assessment. Such scans were popularized by Stanger with his script Aroma.[48]

To obtain a more comprehensive picture of aromaticity, and to ensure that the single value in the centre is not misinterpreted due to some local effects, the 2D NICS scans were used.[49] Particularly for the small rings, it is advised that NICS values should be calculated at height of 1 Å above the plane of the σ bonds to filter out local effects. The calculation is then often referred to as NICS(1), indicating the 1 Å height, whereas values in the plane of the molecule are abbreviated as NICS(0) (**Figure 16**).

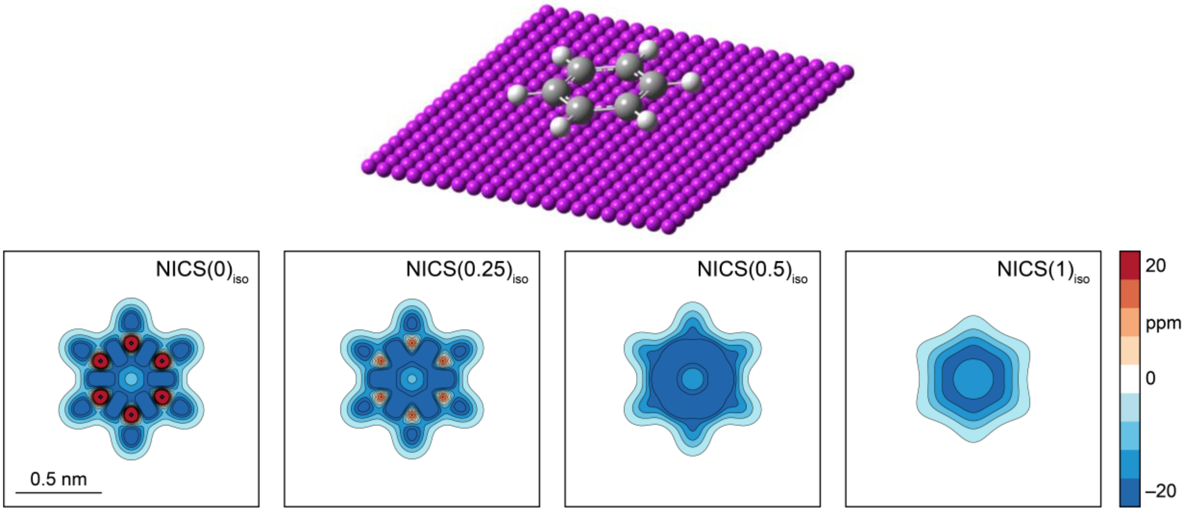

Figure 16: NICS calculation (B3LYP/6-31G*) on the benzene molecule as a 2D scan in plane of the molecule (NICS(0)) or slightly above the plane, indicating quick disappearance of the local effects.

Furthermore, even a 3D scans have been used to visualise induced magnetic field, (**Figure 17**).

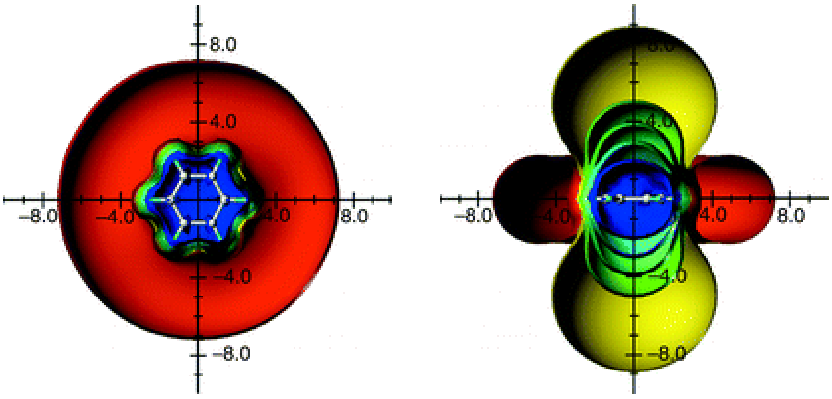

Figure 17: Calculated 3D scan of chemical shift in benzene, plotted as isosurfaces of NICS values: 0.1 ppm (red), −0.1 ppm (yellow), −0.5 ppm (green), −1 ppm (green-blue), −2 ppm (cyan), −5 ppm (blue). Figure adapted from *J. Chem. Soc., Perkin Trans. 2*. **2001**, 1893–1898. Reproduced by permission of The Royal Chemical Society.[50]

The calculated NICS values plotted in **Figure 16** and **Figure 17** represent the so-called *isotropic* values, the average of all three possible orthogonal orientations of external magnetic field and the sum of its effects. This type of value is often denoted with subscript *iso*. However, the complete NICS calculation result is the magnetic shielding tensor, in which all components are stored as 3×3 matrix (three dimensions of applied and induced magnetic field orientations). The component of both external and induced magnetic field perpendicular to the assessed ring is often called *ZZ*, assuming ring plane orientation being in the x-y plane and the z axis being perpendicular to the plane of the ring. Such NICS_{ZZ} values provide a 'cleaner' measure of the global aromaticity, and further avoid contributions from local effects unrelated to the global ring current. Comparison of AICD, $\text{NICS(1)}_{\text{iso}}$ and NICS(1)_{ZZ} calculated on an aromatic free-base porphyrin is shown in **Figure 18**.

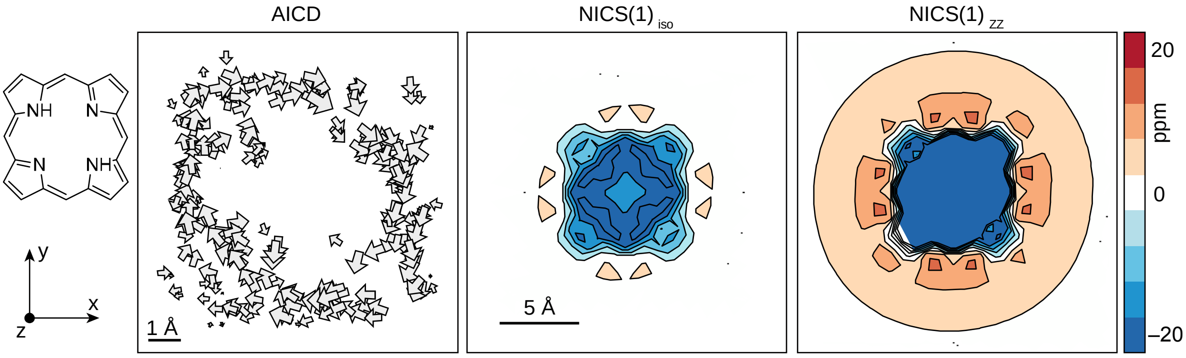

Figure 18: From left to right: Porphyrin structure and orientation. Diatropic ring current of the porphyrin calculated (B3LYP/6-31G*) with AICD assuming orientation of external magnetic field along the z axis, replotted with authors own script (surface of the arrows is proportional to the current magnitude). $\text{NICS(1)}_{\text{iso}}$ and NICS(1)_{ZZ} of the porphyrin showing significant shielding inside the rings, expected for aromatic compounds.

3.2.2. Size limit of aromaticity and local vs global aromaticity

The fact that a planar, unsaturated macrocycle possess a conjugated path comprising [4*n*+2] π electrons does not guarantee that the system is aromatic. There is a general tendency to localise π electrons, the tendency increasing with the increasing size of the system. In other words, the aromatic energetic stabilisation tends to decrease with increasing size. For example, this was theoretically examined on series of [*n*]annulenes, documenting a rapid aromaticity stabilisation energy drop for $n > \sim 30$ (**Figure 19**).

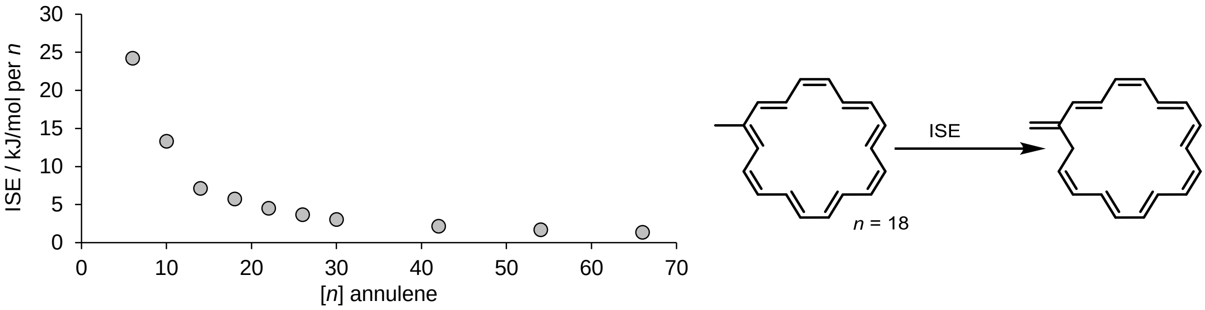

Figure 19: Energy of aromatic stabilisation, theoretically assessed by double-bond isomerisation reactions causing a break of the global conjugation path. Energy per carbon CH unit drops significantly for [*n*]annulenes with *n* above ~20–30.[51]

This lack of significant aromatic stabilisation allows thermally induced conformational changes to disrupt the conjugation and such large molecules start to behave as non-aromatic. Experimentally, [18]annulene is observed as an aromatic compound in NMR, with an inner to outer proton exchange energy barrier of $\Delta G^{\ddagger} = 69.8$ kJ/mol, measured by NMR signal coalescence and exchange spectroscopy (EXSY).[52,53] This barrier is lower for larger [22]annulene $\Delta G^{\ddagger} = 53.5$ kJ/mol, and low temperatures (−90°C) were required to record a NMR spectrum within the slow exchange regime.[54] In other words, aromatic stabilisation is not high enough to maintain the flat, aromatic shape at room temperature. This led to the belief that the general limit of aromaticity is approached near the size of ~22 π electrons.[55]

Although, the aromatic stabilisation energy diminishes rapidly with the size of the system, if the structure is kept in the planar shape, strong induced ring currents are still predicted. Both NICS and ring current calculations show intense diatropic ring currents for [4*n*+2] annulenes up to [66]annulene (**Figure 20**).[51,56]

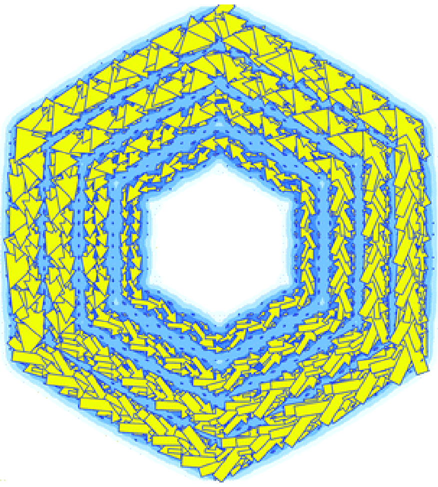

Figure 20: Induced diatropic ring current in [66], [54], [42] and [30]annulene, concentric stacked plot of all structures. Figure adapted from *Phys. Chem. Chem. Phys.* **2004**, 277–284. Reproduced by permission of The Royal Chemical Society.[56]

If the large π-conjugated macrocycle consists of smaller, potentially aromatic subunits, then the preferred electronic arrangement is to form a set of small, local aromatic rings, rather than one large globally aromatic ring. One iconic molecule serving to document such behaviour is Kekulene. Kekulene attracted a lot of attention, because it represents the unit cell of a 2D graphene-type porous material and it is a theoretically important molecule, as its structure provokes a clash between two theories of the bond (de)localisation. The Kekulene synthesis, accomplished by Staab and Diederich answered this question and provided the rule of thumb that local Clar sextets best represent the preferred electronic arrangement (**Figure 21**).[57,58] Such findings were also supported recently with a high-resolution AFM study.[59]

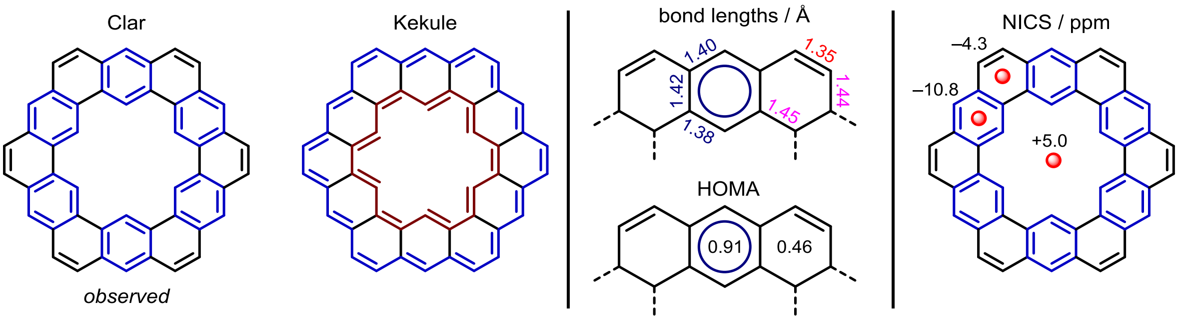

Figure 21: (left) Kekulene structure. The Clar sextet aromaticity localisation is the correct description of electronic arrangements, rather than two, concentric [30] and [18] aromatic 'annulenes'. (middle) This finding was supported by XRD analysis, experimental NMR as well as theoretical NICS (right) calculation.

The absence of supra-aromaticity was documented by ^{1}H NMR: The chemical shifts of both inner and outer protons correspond to the aromatic region (8–11 ppm). If Kekulene had been globally aromatic, shielding and deshielding of the inner and outer protons, respectively, would have been expected. A study of the bond length, obtained by XRD, suggest the same aromaticity localisation on one type of benzene core over the other, enumerable as HOMA for both aromatic and non/less-aromatic rings 0.906 and 0.462, respectively.[60] The NICS calculation supports the absence of global aromaticity as the calculated positive value of 5.0 ppm in the centre of the molecule suggest only the local aromaticity. The centres of the aromatic and non/less-aromatic ring shows NICS values of −10.8 and −4.3 ppm, respectively.[61] These findings were followed with many theoretical studies, arguing that a weak, rather than none, global aromatic character might be present.[61–66] However, experimental studies of Kekulene analogues provide further clear evidence of the preferred local aromaticity arrangement, represented by Clar's sextets (**Figure 22**).[67,68]

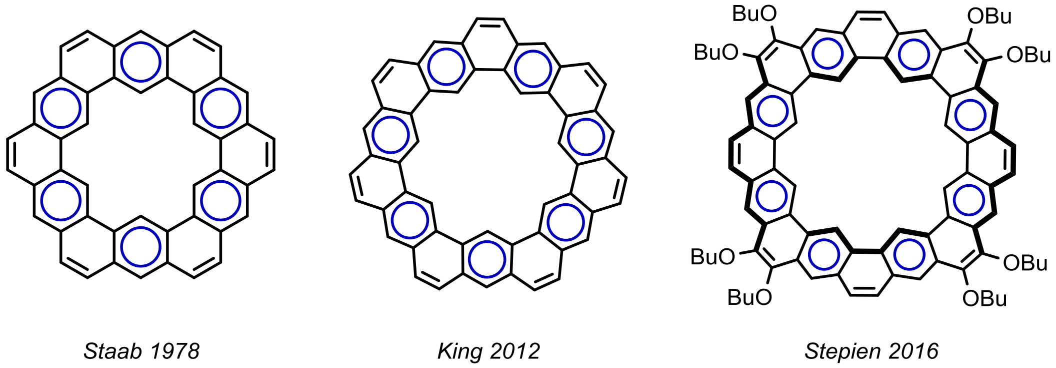

Figure 22: Kekulene and larger analogues were successfully synthesized, and their NMR-based study confirms the aromaticity localisation.[57,58,67,68]

Similar features were observed in cycloparaphenylenes (CPPs), where the formally conjugated path does not lead to globally aromatic nor anti-aromatic states, but rather to the localisation of individually aromatic benzene cores.[69] However, both theoretical and experimental studies have shown that such local aromaticity can be disrupted, for example by oxidation. Driven by the disruption of local aromaticity and charge delocalization within the whole structure, a global diatropic ring current is observed in the dications of CPPs, unveiling their global aromatic character.[69–71] Such states obeys the Hückel rule when the number of subtracted electrons during the oxidation is considering in the total π-electron count (N×4 − charge) (**Figure 23**).

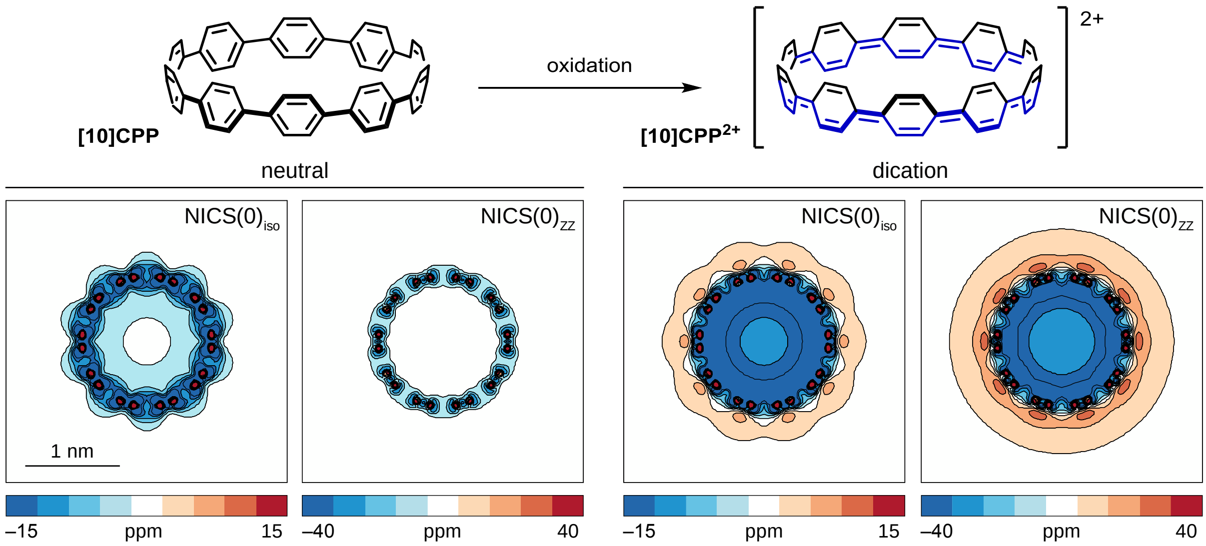

Figure 23: (top) Neutral and dication of 10-benzene-containing cycloparaphenylene **[10]CPP**. (bottom) Calculated NICS showing local aromaticity of individual benzenes (left), and the global ring current, triggered by oxidation (right). Recalculated and replotted by the author from data available in literature.[69]

Note, that although 20 double bonds are drawn to be in conjugation in **[10]CPP**, two electrons need to be subtracted in the count, as it is the dication being formed. This formalism led to a count of 38 π electrons, which is [$4n+2$]. Analogous experiments were shown as well for reduction where reduced CPP showed a ring current in agreement with the Hückel rule.[69]

Oxidation or reduction can be also used to alter the aromatic character of previously (anti)aromatic species. A representative example is the aromatic [18]annulene, for which reduction with two equivalents of elemental potassium leads to the anti-aromatic dianion with 20 π electrons. Such anti-aromatic character was confirmed by the reversal of the chemical shifts in NMR, when the originally shielded inner protons were significantly deshielded and *vice versa* (**Figure 24**).[72]

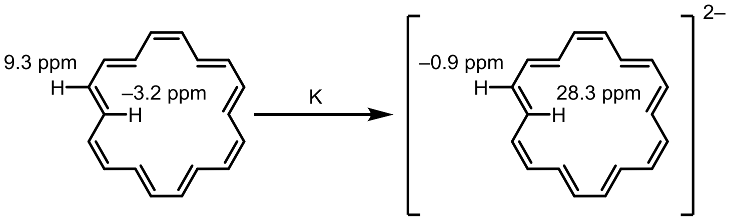

Figure 24: Reduction of the aromatic [18]annulene with two equivalents of potassium to the anti-aromatic dianion, as confirmed by ^{1}H NMR.[72]

In light of these difficulties and strategies, experimental chemists trying to synthesise large aromatic species often use expanded porphyrins, for which rich (electro)chemistry allows them to construct large π-conjugated architectures.[73–75] Large systems studied in literature are for example [36]- and [38]octaphyrin, decorated with perfluorophenyl groups (**Figure 25**).[76]

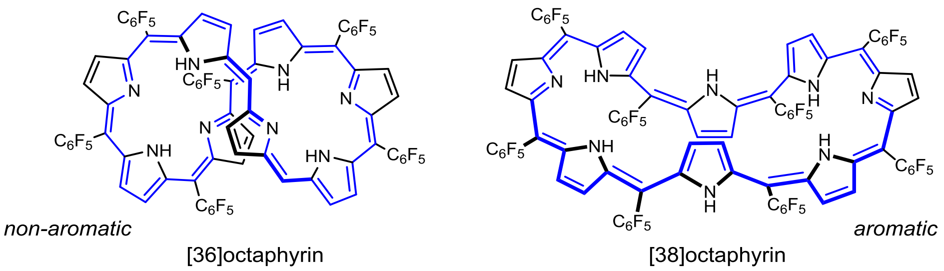

Figure 25: Structures of non-aromatic and aromatic [36]- and [38]octaphyrin, respectively.

Although containing the same number of carbon and nitrogen atoms, chemical reduction and oxidation lead to different π-conjugation paths. The [36]octaphyrin adopts a figure-of-eight shape and does not exhibit any sign of anti-aromaticity, but rather is described as non-aromatic based on XRD and ^{1}H NMR analysis. Whereas, the [38]octaphyrin is expected to adopt a more planar structure and a weak, but notable, diatropic ring current was observed.[76] Such structures also exhibit rather high flexibility and probably various topologies, including Möbius, might be populated.

A very large aromatic system, presented by Osuka et al., is the perfluorophenyl-decorated dodecaphyrin (**Figure 26**).[77] Depending on the oxidation states of the individual pyrroles, it can contain [52], [50] and [48] π electrons in the conjugation path. Note that in this case, it is the chemical oxidation of the pyrroles altering the π-conjugated pathway, rather than the subtraction of electrons from the same path as in **Figure 23** (i.e. oxidation of the pyrrole units is accompanied by deprotonation to maintain a neutral charge state).

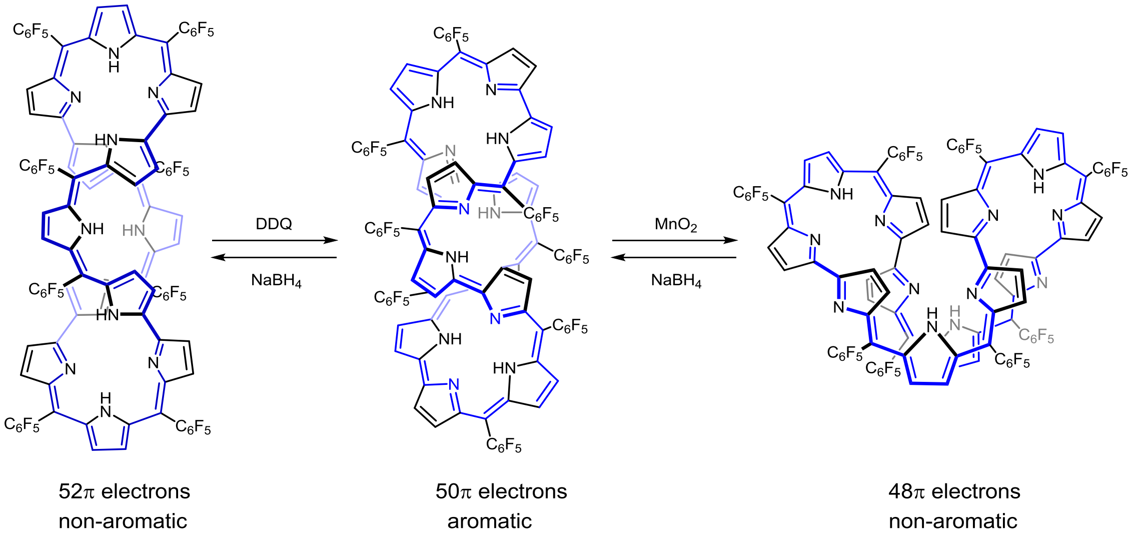

Figure 26: Dodecaphyrin and its rich chemistry, enabling by chemical oxidation to transform the system to possess [52], [50] or [48] conjugated π electrons.[77]

Study of these large systems showed similar features as with smaller octaphyrins. States with [4*n*] π electrons in the conjugation path behaved as non-aromatic. A state with [4*n*+2] π electrons, [50]dodecaphyrin, exhibited in the presence of acid and at low temperature diatropic current indicating global aromaticity. This, tetra-protonated [50]dodecaphyrin showed, at low temperature, 20 deshielded resonances corresponding to the outer nuclei with chemical shifts in the range 20.54 – 12.19 ppm. Furthermore, 14 shielded resonances, corresponding to the nuclei inside the macrocycle were found in the −2.94 – −7.73 ppm region. Global aromaticity was further supported with calculated NICS, approximately in the centre of the macrocycle, yielding a value −12.7 ppm.

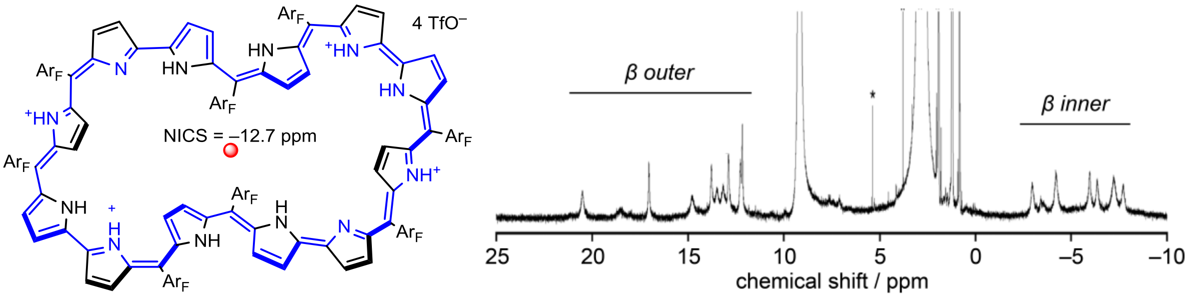

Figure 27: Tetraprotonated [50]dodecaphyrin chemical structure (left) and corresponding ^{1}H NMR (CD_3CN, −44°C) spectrum documenting presence of a diatropic ring current in the molecule. The red dot represents an approximate centre of the macrocycle together with the calculated NICS at the point. Ar_F = perfluorophenyl.

Another, very large aromatic system is the [54]dodecaphyrin (**Figure 28**).[78] Such a quadruply-twisted structure was suspected by authors to exhibit the global aromaticity, corroborated by the calculated NICS and predicted ^{1}H NMR shifts. ^{1}H resonances assignment showed indeed a deshielding of the inner and a shielding of the outer nuclei to regions of 8.59 – 6.79 ppm and 4.22 ppm, respectively.

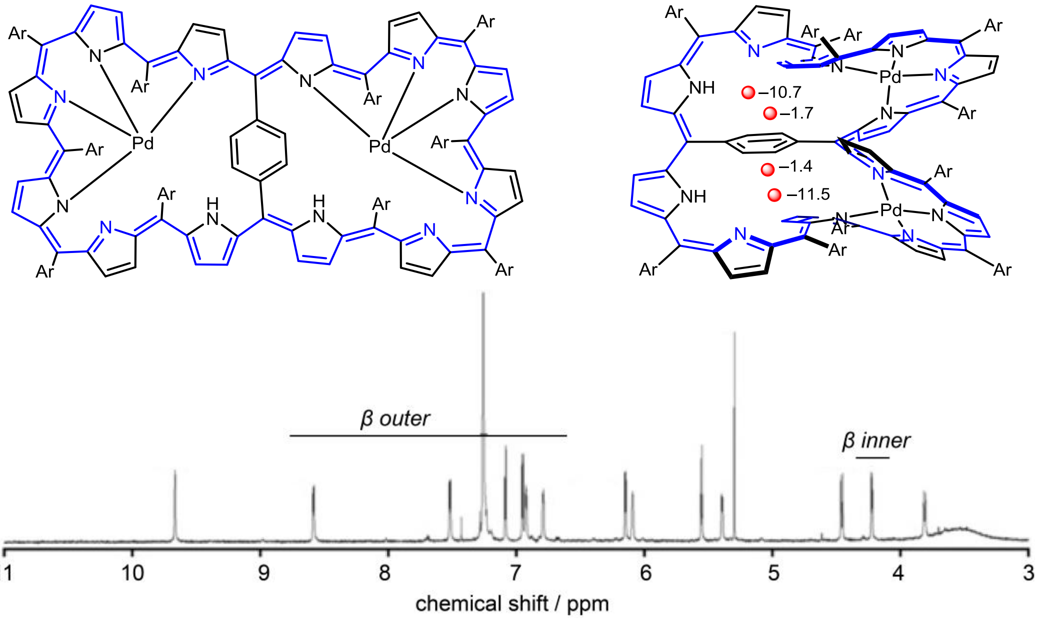

Figure 28: Scheme of a quadruply-twisted [54]dodecaphyrin (top) and a corresponding ^{1}H NMR ($CDCl_3$, 25°C) spectrum documenting presence of a weak diatropic ring current in the molecule. The red dots represent points close to centre of the macrocycle, values correspond to the calculated NICS at the points. Ar = perfluorophenyl.[78]

Probably the largest globally aromatic system outside work from our group was presented recently by Osuka et al. They presented the synthesis of the large, tetradecaphyrin, which, when as a free base, behaves as globally non-aromatic with NMR resonances grouped to the expected regions of 7.32 – 5.43 ppm for *beta* resonances.[79] The tetradecaphyrin was structurally stabilized by insertion of two zinc cations. The resulting complex exhibited a very weak global aromaticity, as the *beta* resonances were grouped to inner and outer into a slightly shielded region 9.39 – 7.72 ppm and slightly deshielded 6.42 – 6.11 ppm, respectively (**Figure 29**).[80]

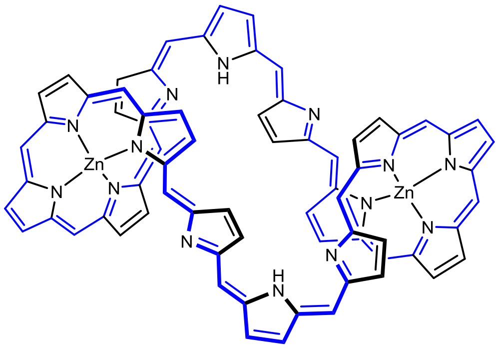

Figure 29: Weakly globally aromatic [62]tetradecaphyrin.[80]

3.2.3. *c*-P6[b$_6$] porphyrin nanoring aromaticity

Porphyrin nanorings are π-conjugated macrocycles, exhibiting some electronic communication along the circumference. However, the NMR spectra of various neutral nanorings show no sign of global (anti)aromatic ring currents.[81–90] The π electrons are localised within the individual, aromatic porphyrin units.

A former DPhil student in our group, Dr. Martin D. Peeks, studied the ***c*-P6[b$_6$]·T6** nanoring and successfully demonstrated that oxidation of the nanoring establishes a global ring current, according to the Hückel Rule (**Figure 30**).

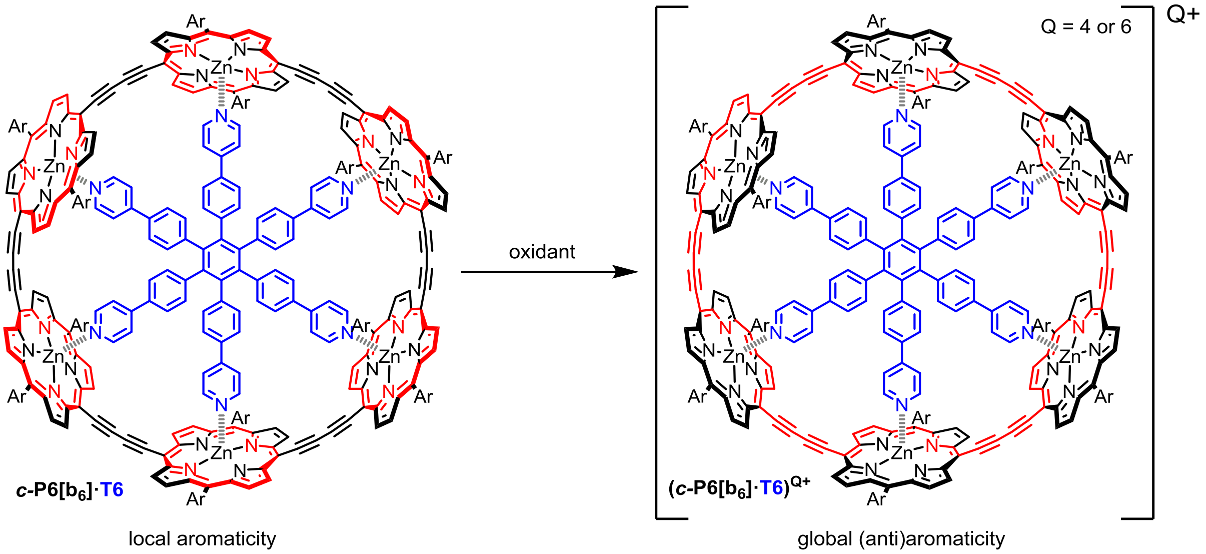

Figure 30: Oxidation of the porphyrin nanoring ***c*-P6[b$_6$]·T6** leads to disruption of local aromatic ring currents and global (anti)aromaticity is observed. Ar = 3,5-bis(trihexylsilyl)phenyl.

Based on the electrochemical data, Dr. Peeks was able to choose the right oxidant with a potential exactly matching the oxidation potential of the desired oxidation state of the nanoring (4+, 6+ and 12+) (**Figure 31**). He successfully observed and documented the anti-aromatic 4+ state, the aromatic 6+ state and locally anti-aromatic 12+ state. Aromaticity was assigned based on ^{1}H NMR spectroscopy (**Figure 32**).

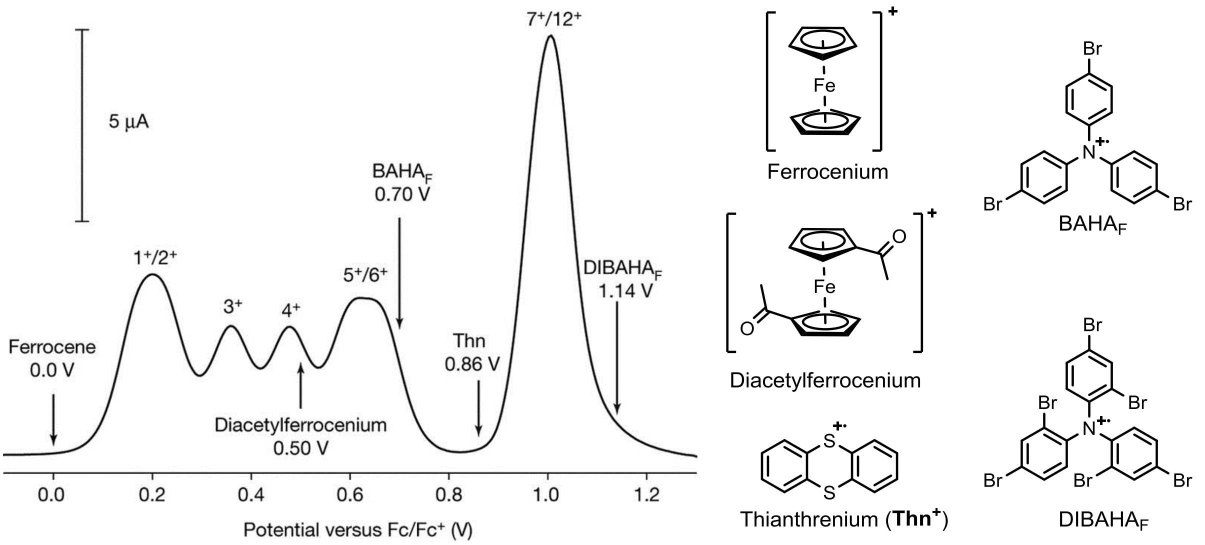

Figure 31: Square wave voltammetry of ***c*-P6[b$_6$]·T6** with highlighted potentials of several one-electron oxidants. Figure adapted with permission from *Nature* **2017**, (541), 200–203. Copyright 2016, Springer Nature.

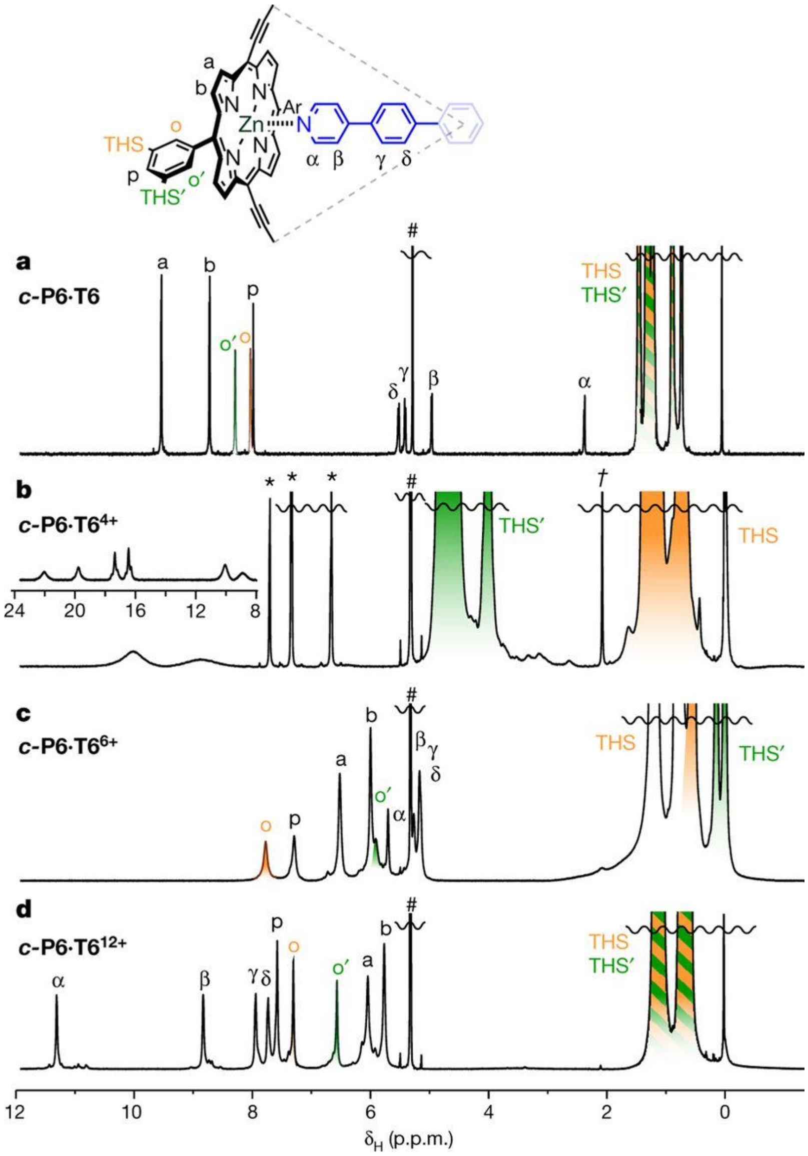

Figure 32: ^{1}H NMR spectra of neutral, 4+, 6+ and 12+ oxidation state of ***c*-P6[b$_6$]·T6**. Figure adapted with permission from *Nature* **2017**, (541), 200–203. Copyright 2016, Springer Nature.

The tetracation formally possesses 80 π conjugated electrons and thus was the largest anti-aromatic species documented at the time. The inner resonances, particularly the template signals were significantly deshielded to up to +22 ppm, documenting the global paratropic ring current.

The hexacation possesses 78 π electrons and a weaker but clear global diatropic ring current was observed. Further oxidation led to a dodecacation, which exhibited ring current localisation. At such 12+ oxidation state, all six porphyrin unit behaved as a locally anti-aromatic units, like porphyrin dications with 16 π electrons.

These, and other oxidation states were reached using an alternative method by the author and therefore, a more thorough analysis will be discussed later in **Section 3.3.1**.

The local aromaticity of the neutral nanoring and global aromaticity of tetra- and hexacations were corroborated also by NICS and AICD calculations (**Figure 33**).

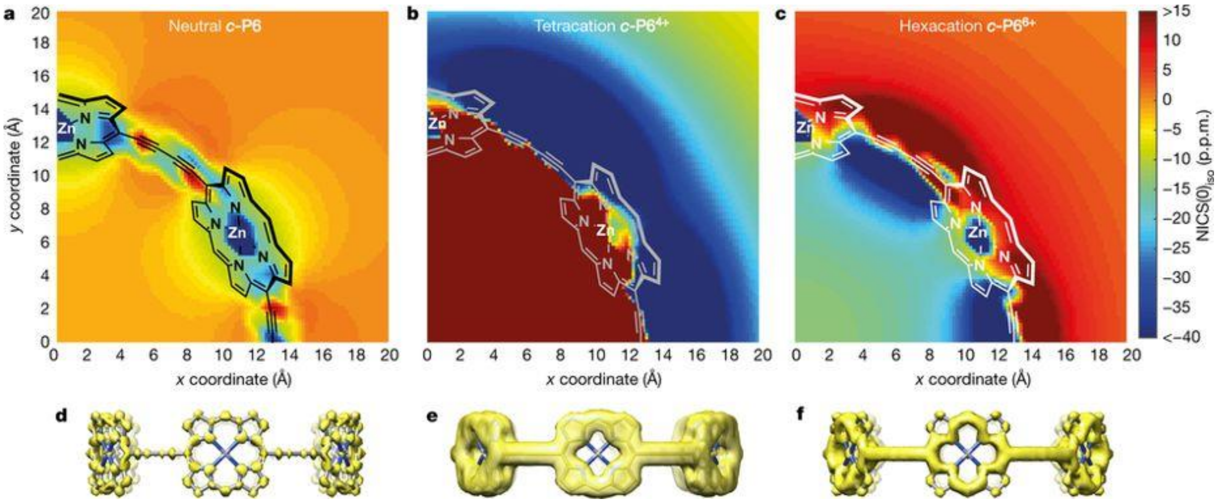

Figure 33: (top) $NICS(0)_{iso}$ (B3LYP/6-31G*) of neutral, 4+ and 6+ oxidation state of ***c*-P6[b$_6$]·T6**, calculated on one ring quadrant in absence of template T6. (bottom) AICD calculation documenting expected strong global ring current for 4+ and 6+ oxidation state. Figure adapted with permission from *Nature* **2017**, (541), 200–203. Copyright 2016, Springer Nature.

Analogous experiments were also recently conducted by reduction of the nanoring.[91] This successful sets of experiments, together with the knowledge of existing of 4+ and 6+ oxidation states, representing at the time the largest anti-aromatic and aromatic species, respectively, were the starting point for the research carried out by the author.

3.3. Aromaticity of 6-porphyrin nanorings

3.3.1. Case study – *c*-P6[b$_6$] nanoring aromaticity

The symmetric, 6-porphyrin nanoring with butadiyne linkers can be expressed by the formula ***c*-P6[b$_6$]**, where ***c*-** stands for *cyclic*, **P*N*** stands for *N* number of porphyrin units and subscript with **b** determines how many butadiyne linkers are in the structure. The presence of the template **T6** is then abbreviated as ***c*-P6[b$_6$]·T6** (**Figure 34**).

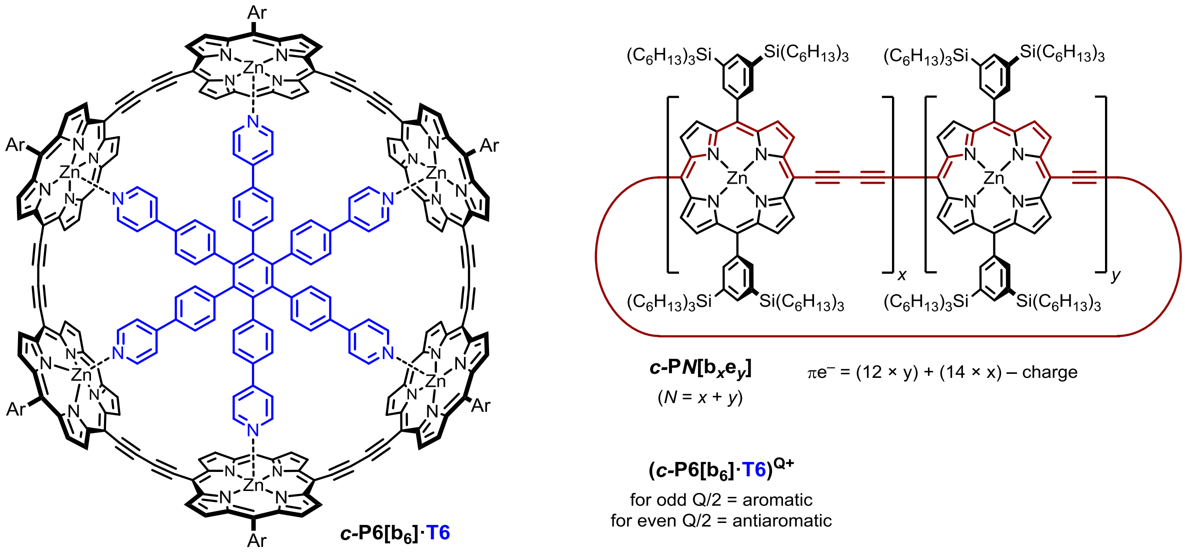

Figure 34: (left) Structure of ***c*-P6[b$_6$]·T6**. (right) General structure of the nanorings and the π electron count formalism. c) Application of the π counting formalism to ***c*-P6[b$_6$]·T6** cations.

The organic chemical formalism of counting π electrons in nanorings yields the general sum (regardless on the chosen path) consisting of the number of porphyrins involved (10 πe^- per porphyrin) and the ethyne or butadiyne linker (2 πe^- or 4 πe^- per linker, respectively). Furthermore, if the structure is oxidized to $Q+$ state, Q needs to be subtracted from the count.

For the ***c*-P6[b$_6$]·T6** cations, the count predicts 2+ to be aromatic, 4+ anti-aromatic and 6+ aromatic. Note that at the time of the seminal study, the 2+ state was not observed and it was thought to be lacking coherently delocalised charge around the ring and was believed to exist in a charge-separated bi-polaron state (possibly with triplet multiplicity).

3.3.1.1. Theoretical models

3.3.1.1.1. Model for nanoring structure

Model structural geometries for ***c*-P6[b$_6$]·T6** and its cations were obtained by DFT optimisation of ***c*-P6[b$_6$]** both with and without the presence of the **T6** template. The solubilising aryl groups were replaced with hydrogen atoms. Geometries were optimised for every oxidation state, assuming singlet configurations, using Gaussian16/A.03.[92] Due to the highly demanding nature of the calculations when the template was present (due to the large number of electrons and degrees of freedom), for the structures optimised with templates it was not possible to rigorously confirm local minima *via* frequency calculations, which were otherwise routinely conducted. The frequency calculations for the structures with templates could only be carried out for the most symmetric structures (which showed no imaginary frequencies). Still it is very likely that all the optimised structures represent minima, as the geometries do not deviate significantly from the template-free rings and due to the fact that the initial geometries were minima from B3LYP optimised structures without the template.[2] Structures optimised in the absence of the template were evaluated by frequency calculations as the local minima. The presence of the template has the advantage of being a more realistic model when comparing the NICS values with the NMR experiment (in which, in this case, the template was used).

A significant difference in geometries were observed for optimisation at the anti-aromatic states with and without template – as in the absence of the template, Jahn-Teller-type distortions were noted. This distortion can attenuate the ring current and is highly dependent on the DFT method used (See below **Chapter 3.5.2.1**, page 149). The presence of a template in the structure does not allow this significant distortion of the nanoring which maintain a nearly unchanged circular shape. However, the general empirical finding is that the results of the NICS calculations are qualitatively insensitive to the exact geometry.

3.3.1.1.2. NICS calculation on the nanorings

Although the geometry differs slightly from different methods (and the presence/absence of the template), it was found that the dominant effect on the predicted NICS, was the used functional and its (in)correct description of charge delocalisation within the nanoring.

The NICS/susceptibility calculations were conducted using the GIAO methods, as implemented in Gaussian16/A.03. The 2-dimensional scan of the induced magnetic field was conducted by placing ghost atoms in the x-y plane (plane defined by the least-square fit to the Zn atoms positions) as described in the literature[93] (**Figure 35**), generated by author's own MATLAB script.

---

[2] It seems to be non-economical to carry out the frequency calculations for so many states since the typical calculation for C_1 symmetric nanoring was far from completion after 8 days of calculations on a 16-core processor node.

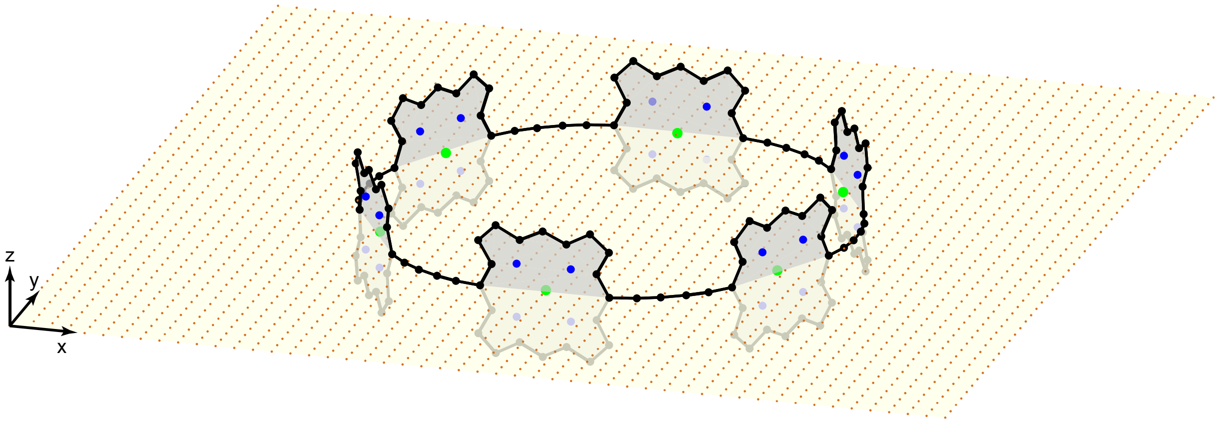

Figure 35: Structure of ***c*-P6[b$_6$]** ring (optimised with **T6** present, subsequently removed for NICS) and the model grid of ghost atoms (50×50 Å^2, spaced 1 Å) scanning the x-y plane (i.e. NICS(0)). Atom colour scheme: C – black, N – blue, Zn – green, Bq (ghost) – beige. H atoms are not shown for clarity. The x-y-z mark does not represent the axis origin (0,0,0), which is in the centre of the molecule.

Orientation of all structures in the thesis follows common rules. In the case of all-same-linkers nanorings (***c*-P*N*[b/e$_N$]**), an ellipse passing through the Zn atom positions was fitted, and its longer axis defines the x axis. For symmetric ***c*-P6** rings, the x-axis was chosen to go through the centres of the linkers. For structures with defects, such as contraction or expansion of one linker by one -C≡C- unit, the centre of the defect was oriented toward the positive values of the x axis.

Empirically, the limit for a single NICS calculation on the available supercomputer *arcus-b* consisted of up to ~25000 ghost atoms. Above this number, the calculations tend to fail due to insufficient available memory space (for calculation was typically allocated 55 GB). Due to this constrain, certain calculations were run in parallel, calculating very finely spaced ghost atom strips, which were combined later. Nevertheless, this approach seemed to be unnecessarily wasteful and it was found that for typical grid sizes, 50×50–100×100 Å^2, the ghost atoms spacings of 0.4–1 Å provide maps detailed enough and manageable in a single calculation, without the need of parallelisation.

Several DFT methods for both optimisation and NICS were tested. Initially, the B3LYP functional with 6-31G(d) basis set was used. This method yields chemically realistic geometries, with mostly qualitatively correct NICS predictions. Nonetheless, particularly for paratropic ring currents, the NICS values were significantly exaggerated (**Figure 36**).

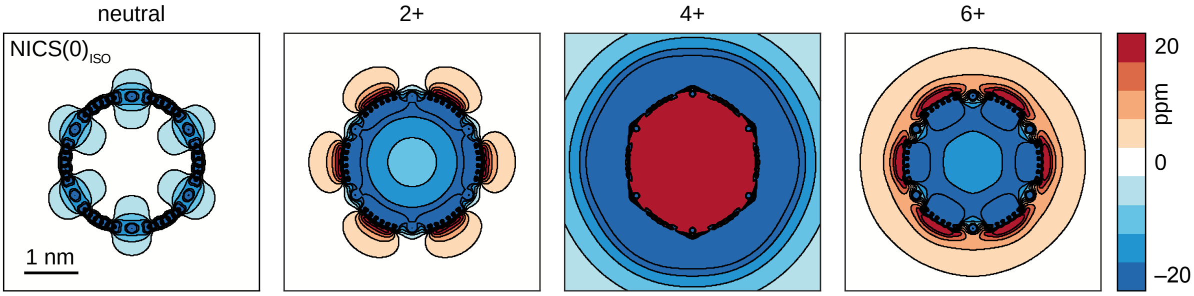

Figure 36: NICS(0)$_{iso}$ calculation of ***c*-P6[b$_6$]** at oxidation states 0, 2+, 4+ and 6+. Structure was optimised without template for each oxidation state and NICS were calculated on the grid 50×50 Å with 0.1 Å spacing using B3LYP/6-31G* method.

Among various other functionals tested, the LC-ωhPBE (ω = 0.1) functional with 6-31G* basis set was found as a best compromise with the experimental observations. This, more charge-localising functional, yielded more realistic values with a slight tendency to 'over-localise' the charge for some antiaromatic states (*vide infra*).

The presence and the coordination of the template pyridyl groups in the structure causes geometrical distortion of the Zn environment, and pulls out the Zn atoms from the plane of the porphyrin by ~0.1 Å.[94] It is desirable to remove the template prior to the NICS calculation in order to not obscure the NICS by local effects from the template's phenyl units. Therefore, it was tested, whether the simple removal of template prior to NICS (and thus leaving the Zn atoms in a non-relaxed geometry) affects the result. It was found that this distortion of the Zn atoms in the absence of template has virtually no effect on the predicted aromaticity and NICS of the nanorings (**Figure 37**).

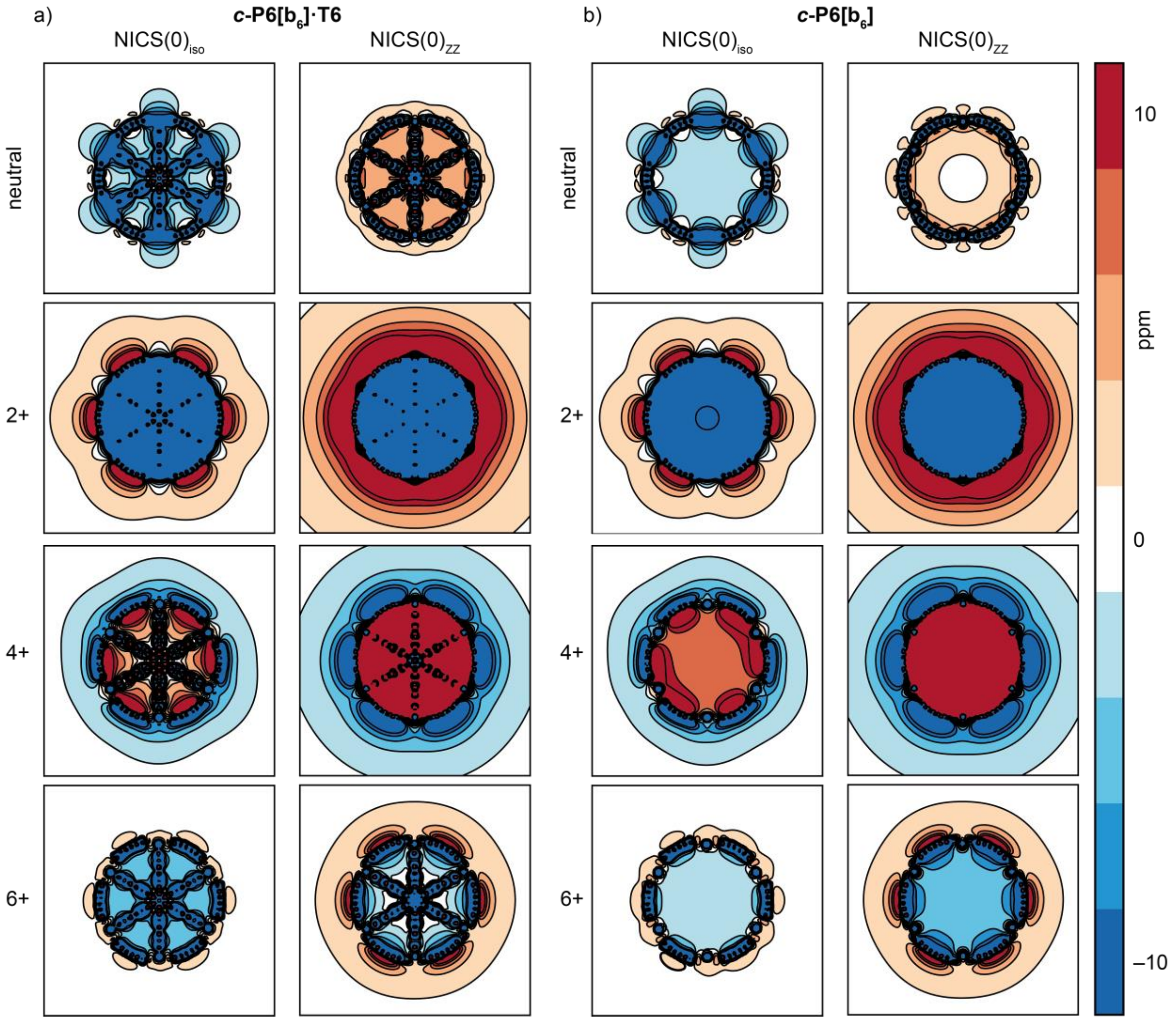

Figure 37: NICS(0)iso and NICS(0)ZZ scans of ***c*-P6[b6]·T6** and ***c*-P6[b6]** at various oxidation states. Structures were optimised with template present using the LC-ωhPBE (ω = 0.1) / 6-31G* method and the template was either left or removed prior NICS (same method, grid 50×50 Å, spacing 0.4 Å).

Beside conventional NICS(0) scans in the plane of the nanorings (defined by Zn atom positions), to assess any special distribution of the induced magnetic field, vertical scans were also conducted. These show a cone of zero induced magnetic field lying at the expected[95–97] magic angle (**Figure 38**), as it would be in a regular electric current in a coil. The region of nearly no induced ring current spatially overlaps with the outer THS groups, suggesting that nearly no effect of ring current should be observed for these groups.

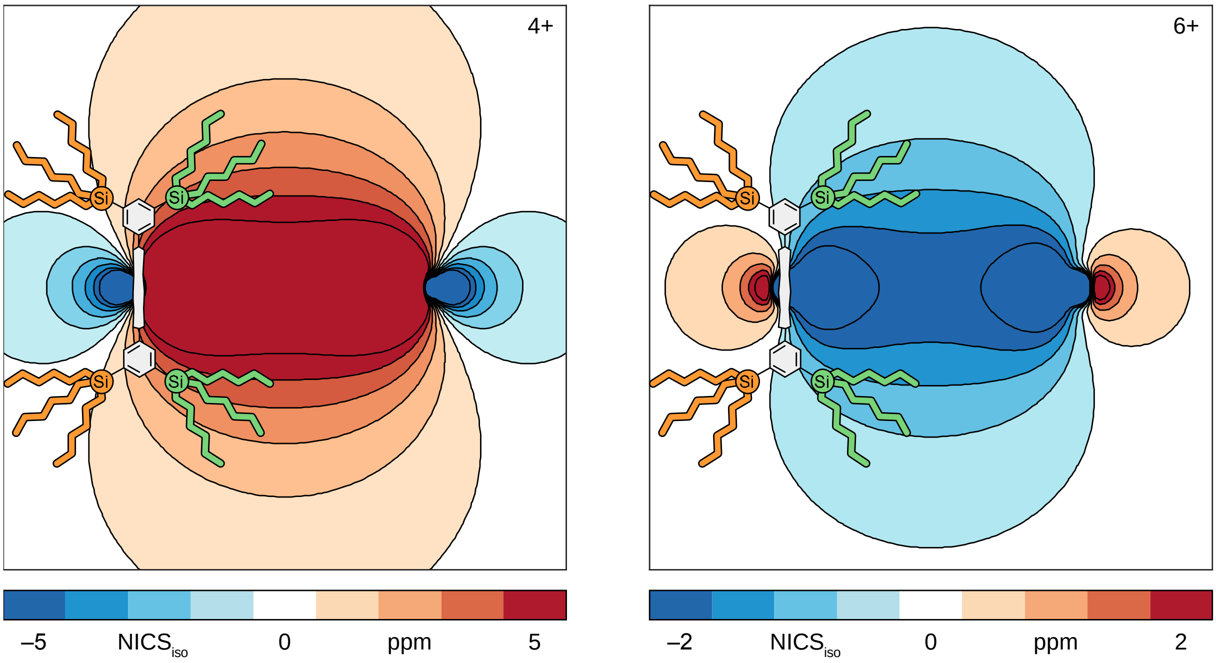

Figure 38: NICS(vertical)$_{iso}$ of the ***c*-P6[b$_6$]** at 4+ and 6+ oxidation states. The vertical scan plane goes through centres of the butadiyne linkers (plane defined as: y = 0). Grid 50×50 Å, spacing 0.4 Å. Approximately in scale with the structure of solubilising groups were placed on top of the scans to illustrate the strong effect on inner and nearly no effect on outer THS groups.

To access more rigorously the expected effect of the global ring current on the inner and outer THS groups, a more advanced model was built. Four 3,5-bis(trihexylsilyl)phenyl groups were put on the ***c*-P6[b$_6$]** structure assuming common bond lengths. To imitate the high flexibility of the hexyl groups and nearly free rotation along all bonds, a model cone of ghost atoms was created by rotation of the static THS groups along the C_{Ar}—Si bond. The positions of hydrogen atoms were then used for NICS calculations on the original ***c*-P6[b$_6$]** geometry (**Figure 39**).

NICS(THS)$_{iso}$ for both two inner and two outer THS groups are binned into histograms on **Figure 40** and **Figure 41** for the 4+ and 6+ state, respectively.

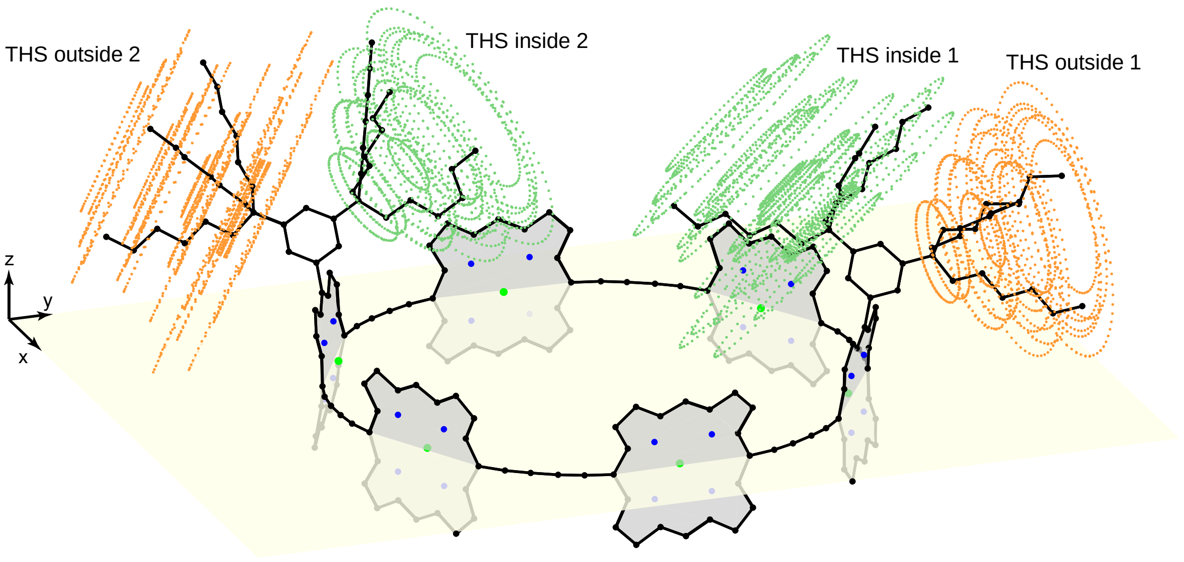

Figure 39: Structure of ***c*-P6[b$_6$]** with ghost atoms representing the effective spaced occupied by THS groups. Skeletons of the 3,5-bis(trihexylsilyl) phenyl groups (in black) illustrates its origin, however were not present for the NICS.

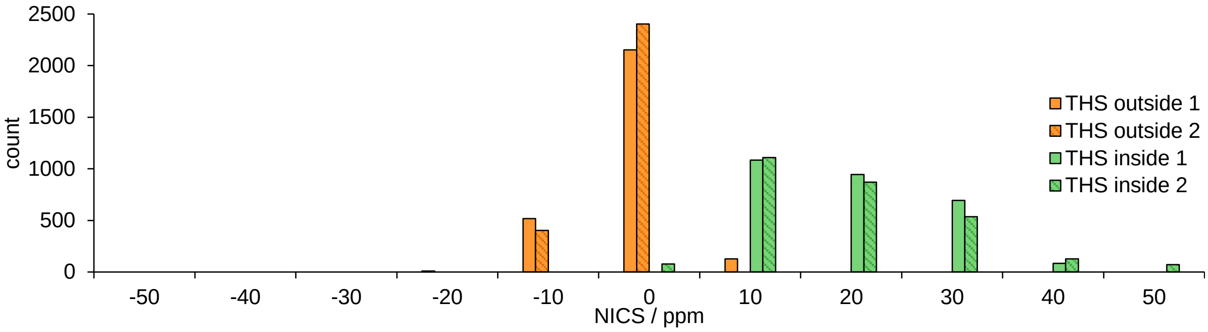

Figure 40: NICS$_{\text{iso}}$ values of regions occupied by inner (green) or outer (orange) THS groups at ***c*-P6[b$_6$]**$^{4+}$. Two different bis(THS)silyl groups were used, distinguished by hatching. Values are binned using 10 ppm wide intervals.

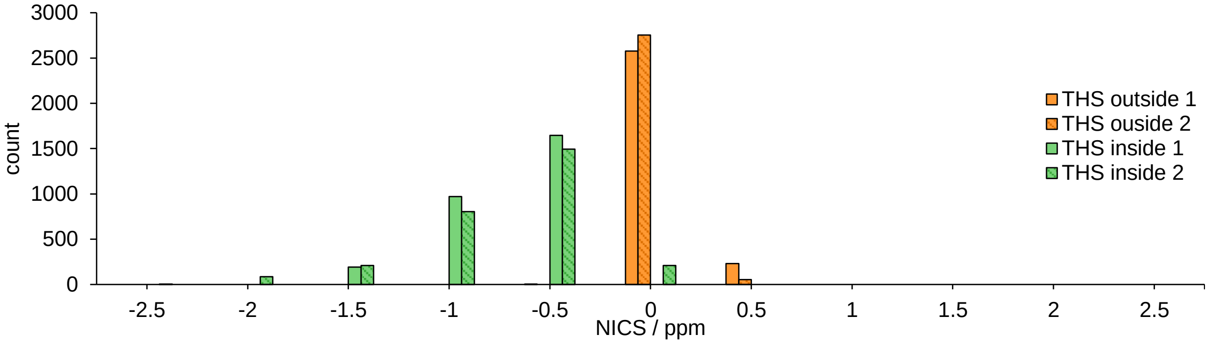

Figure 41: NICS$_{\text{iso}}$ values of regions occupied by inner (green) or outer (orange) THS groups at ***c*-P6[b$_6$]**$^{6+}$. Two different bis(THS)silyl groups were used, distinguished by hatching. Values are binned using 0.5 ppm wide intervals.

From **Figure 40** and **Figure 41** it is evident, that the NMR chemical shift of the outer THS shall be only marginally affected. Average values for the 4+ state are: $\delta_{\text{THS(in)}} = 19.5$ ppm and $\delta_{\text{THS(out)}} = -1.7$ ppm. For 6+ state, the average values are: $\delta_{\text{THS(in)}} = -0.71$ ppm and $\delta_{\text{THS(out)}} = 0.06$ ppm. For both aromatic and anti-aromatic states, NICS(THS)$_{\text{iso}}$ predicts the inner THS to be affected 12× more than outer ones.

3.3.1.2. Experimental study

3.3.1.2.1. Nanorings electrochemistry – general features

The first observation, from studying the electrochemical behaviour by cyclic and square wave voltammetry was the general similarity of the oxidation states available within similar envelopes for different nanorings. From the square wave voltammetry (SW) of porphyrin nanorings ***c*-P6[b$_6$]·T6**, ***c*-P8[b$_8$]·(T4)$_2$**, ***c*-P12[b$_{12}$]·(T6)$_2$** (containing 6, 8 and 12 porphyrins in the structure, respectively) one can extrapolate, that the general electrochemical profile of the ***c*-P*N*** nanoring possess *N* oxidation states, from 1+ to *N*+, all within a window of 0.15–0.65 V (vs Fc/Fc$^+$ couple) (**Figure 42**). States 1+ and 2+ seem to be very close and for larger rings nearly merged. Similarly, states *N*+ and (*N*−1)+ have oxidation potentials closer than other states.

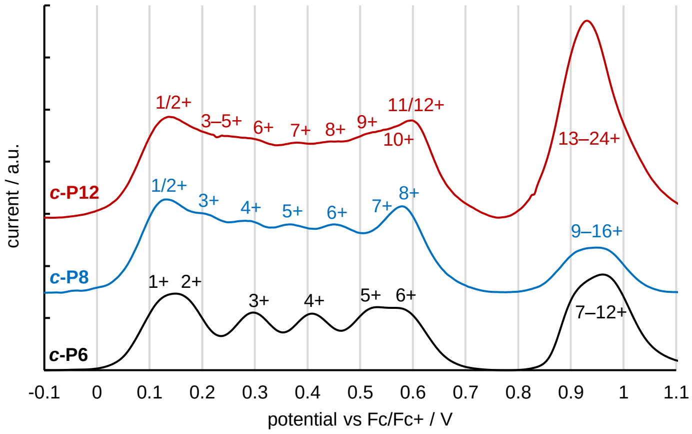

Figure 42: SW of the ***c*-P12[b$_{12}$]·(T6)$_2$**, ***c*-P8[b$_8$]·(T4)$_2$**, ***c*-P6[b$_6$]·T6** showing similar electrochemical behaviour.

In order to study various oxidation states of various nanorings, controllable addition of a strong oxidant is a more versatile method, than tailoring the oxidant's potential to each state.

The oxidant should be relatively stable for handling and ideally have high enough potential to reach all interesting oxidation states (1+ – *N*+). The reduction potential of the oxidant should be, however, lower than the oxidation potential for the higher *N*+ oxidation states (> *N*+), which are expected to be less stable and less interesting, as they exhibit only **local** anti-aromaticity (2*N*+ states).

Initially author tested **BAHA**, which is a commonly used oxidant (often referred to as magic blue)[98,99], but it was rejected for its too low oxidation potential (~0.70 V). During initial tests it was found that to reach the clean **{*c*-P6·T6}$^{6+}$** state (not mixed with lower oxidation states), significant excess of the **BAHA** had to be added to move the equilibrium toward the 6+ state. Based on a literature search, a chlorinated version was designed, as it was expected to have higher potential, but still be within the *N*+/2*N*+ gap. The chlorinated derivative tris(4-

chlorophenyl)ammonium hexafluoro-antimonate (**CAHA**) was synthesised, however, it showed a nearly identical potential to **BAHA**. Eventually, thianthrenium hexafluoroantimonate (**Thn**$^+$)[99–101] was synthesised and tested, showing good handing stability and an ideal potential in between the *N*+ and 2*N*+ states.

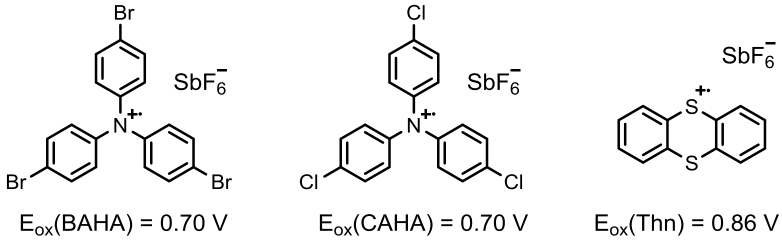

Figure 43: Tested oxidants, **BAHA**, **CAHA** and thianthrenium **Thn**$^+$.

A minor drawback of the **Thn**$^+$ is its poor solubility in CD_2Cl_2. Practically, this problem was solved by vigorous stirring of the suspension, yielding a homogenous mixture. It was possible to transfer this suspension by syringe and to treat it as if it was a solution. Homogeneity of this fine suspension was tested by systematic additions of small increments to a porphyrin monomer and dimer in a UV-vis cuvette, yielding linear increase of absorption due to the formation of the monocation. (**Figure 44**)

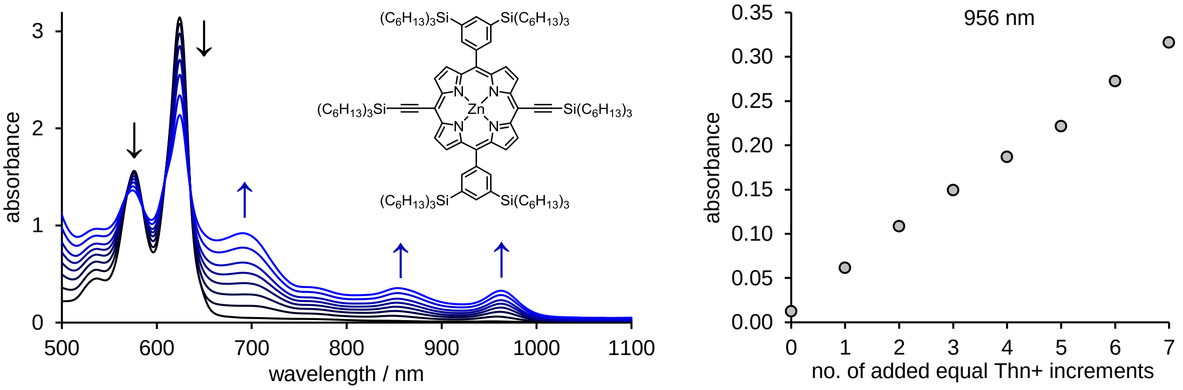

Figure 44: (left) UV-vis-NIR spectra of neutral zinc porphyrin monomer in CH_2Cl_2 (black) and a mixture of neutral and monocation porphyrin after **Thn**$^+$ additions (blue, various lightness). (right) Absorption at 956 nm for each **Thn**$^+$ addition documenting a linear increase of the monocation concentration.

The UV-vis-NIR assay was further developed as a precise control over the oxidant concentration/activity. The concentration of the **Thn**$^+$ should be, in principle, precisely controllable by weighing the oxidant and solvent. However, it was observed that the oxidant does not possess 100% activity. The concentration of the effective oxidant was found in the range of 80–90%. This can be due to lower chemical purity of the **Thn**$^+$ and its contamination with inert inorganic salts. **Thn**$^+$ was prepared by reacting neutral thianthrene with SbF_5 and isolated as a precipitate by an addition of diethyl ether. Due to low solubility, it was not possible to re-dissolve the **Thn**$^+$ in order to filter off any insoluble impurities, and thus only soluble impurities could be removed by washing. Another possible source of lower effective **Thn**$^+$ concentration can be the partial reduction of **Thn**$^+$, which might occur during handling and solution preparation, by reaction with moisture (both from air and solvent).

The concentration of **Thn**$^+$ was therefore accurately estimated by oxidation of porphyrin monomer (with known concentration) with several additions of the **Thn**$^+$ suspension. The resulting UV-vis-NIR absorption spectra were fitted with known[102] spectra of neutral and monocation species to deconvolute the composition and thus determine the amount of **Thn**$^+$ added.

3.3.1.2.2. NMR experiments – general features

The solvent chosen for the oxidation experiments was CD_2Cl_2, as it possess a sufficient electrochemical stability window[103] and allows the use of low temperatures (m.p. = −97°C)[104] essential for the oxidations. Generally, the nanorings with THS groups are very soluble, in non- and less- polar solvents such as hexanes, toluene or CD_2Cl_2. It was, however, observed, that upon cooling of a solution of ***c*-P6[b$_6$]·T6** in CD_2Cl_2, the nanoring precipitates at approx. −40°C. This is most likely caused by the high temperature dependence of solvent polarity for CH_2Cl_2 (and most likely for CD_2Cl_2 as well), correlated by electric permittivity (**Figure 45**).[105]

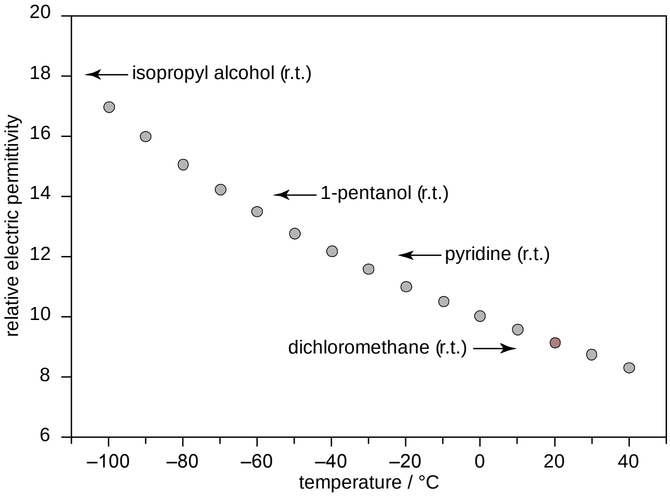

Figure 45: Temperature dependence relative electric permittivity of CH_2Cl_2. Increasing values of permittivity (with decreasing temperature) are commented with r.t. based permittivity of polar solvents. Based on data published in literature.[105]

Nevertheless, it was found that upon oxidation, the solubility is improved, and from ~*N*/3+ states, the nanoring cations are fully soluble at low temperatures (*vide infra*). This fact needs to be taken into account when seeking early oxidation states, where a balance between compound stability and temperature-dependent solubility needs to be achieved. Use of alternative solubilising groups such as bis(octyloxy)phenyl or bis(tert-butyl)phenyl overcomes the issue of low solubility of neutral states. However, it was found that the oxidised species are than far less stable in comparison to when THS solubilising groups are used.

It was found that oxidised nanorings are not very oxygen sensitive and therefore samples were not degassed prior to oxidation (in order to reduce the risk of NMR tube breakage). It was found that samples are moderately sensitive to the presence of moisture (spectra of early oxidation states were found significantly broader when small amount of water was present) and therefore the CD_2Cl_2 was dried and stored over 3 Å molecular sieves. Oxidised species were found to be very temperature sensitive as they would decompose readily above ~−10°C. Oxidised species can be stored for several days at −78°C in a sealed NMR tube, however, not longer than ~5 days.

Addition of **Thn**$^+$ suspension was conducted using a special glass manifold (see **Figure 146**, page 194) enabling cooling of the NMR tube by a dry ice/acetone bath and at the same time protecting the tube neck with a high positive pressure of dry argon. Rubber seals were deliberately avoided as it was observed that small rubber debris from needle punctures can quench the oxidised species.

Upon **Thn**$^+$ additions, two signals in the ^{1}H NMR spectra, corresponding to neutral **Thn**, emerge. The integrals of the **Thn** signals can be an additional check of the amount of oxidant added. During titration, when the *N*+ oxidation states are approached, small amounts of **Thn**$^+$ start to be present in solution and its dynamic exchange with neutral **Thn** leads to broadening of the **Thn** signals. This behaviour is very convenient, as it reports the end of the titration and the fact that the *N*+ state has been reached (**Figure 46**). Interestingly, when toluene-d_8 is used, chemical exchange between **Thn** and **Thn**$^+$ is slow on the NMR time scale (500 MHz NMR instrument) and the signals of neutral **Thn** do not disappear upon reaching the end of the titration.

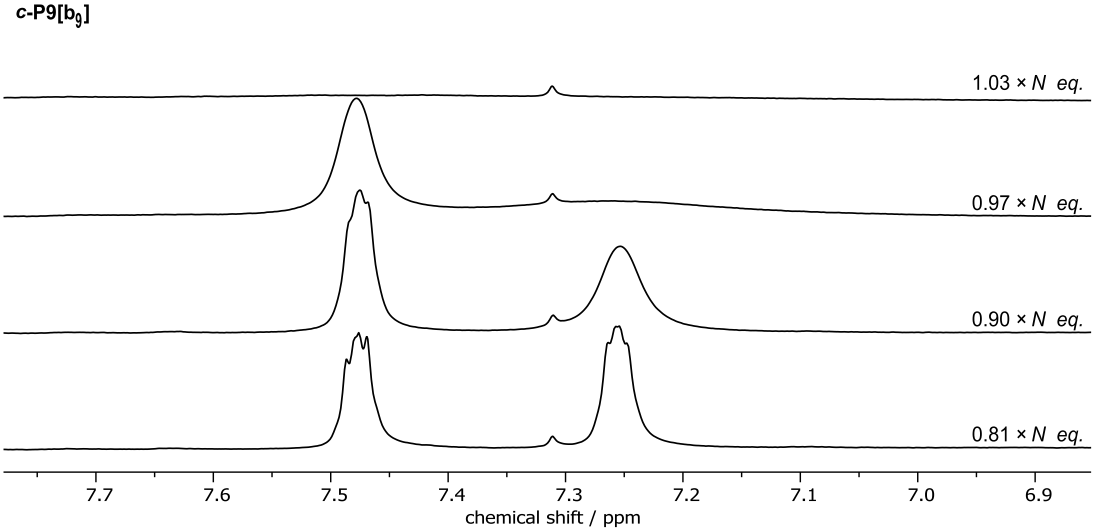

Figure 46: ^{1}H NMR spectra taken from oxidation of ***c*-P9[b$_9$]** illustrating the general behaviour when the *N*+ state is approached (*N* = 9 in this case). Neutral **Thn** signals gradually disappear when ~*N* equivalents of the **Thn**$^+$ is added as a result of **Thn**$^+$ presence (there is nothing to reduce it to **Thn** anymore) and dynamic exchange with **Thn** takes place.

3.3.1.2.3. Detailed NMR characterisation and analysis of porphyrin nanoring cations

General consideration for NMR assignments

In order to evaluate the presence and direction of the global ring current, it is essential to identify the resonances pointing inside the ring and, if possible, those pointing outside the nanoring. From analysis of the spatial arrangement, ^{1}H nuclei can be grouped and ordered by how much they are expected to be affected by the ring current (in descending order):

pointing inside and strongly affected

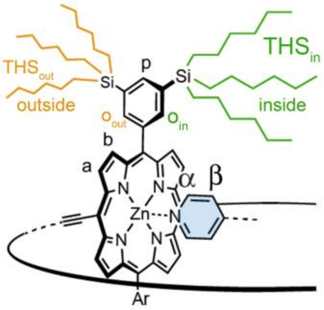

- the template resonances, particularly the **α** and **β** resonances on the pyridine facing the porphyrins. The γ and δ resonances are expected to be affected less, almost equally. The **α** resonance is expected to be offset by approx. +2 ppm relative to other template signals as a result of pyridine nitrogen induction effect (regardless the ring current). This is noticeable for weak ring currents.
- inner ortho resonance $\mathbf{o}_{\mathbf{in}}$ from the solubilising group
- inner trihexylsilyl solubilising groups ($\mathbf{THS}_{\mathbf{in}}$)

pointing outside and affected

- outer ortho resonance $\mathbf{o}_{\mathbf{out}}$

unaffected

- outer trihexylsilyl solubilising groups ($\mathbf{THS}_{\mathbf{out}}$). Although pointing outside, they lie in the cone of no induced magnetic field (**Figure 38**).
- *beta porphyrin* resonances **a**/**b**, as they are located at the circumference
- *para*-solubilising-aryl resonances **p**, as they are located at the circumference

The local ring current is ‘switched’ off in oxidised states, and therefore the *unaffected* resonances may be found at different positions then those in the neutral nanorings (e.g. **a** and **b** are strongly de-shielded by the local aromatic ring current in the neutral state).

2D-NMR spectra analysis

Certain carbon nuclei possess unique ^{13}C-NMR chemical shifts and can thus serve as a handle for analysing the spectra. This is due to the larger spectral window of ^{13}C-NMR relative to ^{1}H-NMR (0 – 200 ppm vs 30 – −10 ppm, respectively). Although the induced field affects the chemical shifts of ^{1}H and ^{13}C resonances equally, the greater spectral width makes the ^{13}C-NMR relatively less affected than the ^{1}H-NMR spectra. Direct observation of ^{13}C-NMR is limited, due to limited amount of the nanorings and their high molecular mass (10–30 kDa). Nevertheless, the ^{13}C nuclei can be detected indirectly through their ^{1}H-^{13}C HSQC correlations. A limitation of this, and of other heteronuclear correlations is the width of the ^{1}H resonances. ^{1}H signals of the nanoring cations happened to be relatively broad, probably due to ring current effects (where a small change in the space will lead to big chemical shift difference) and possibly also the presence of open shell species allowing fast nuclear spin relaxation. The approximate limit peak-width of the ^{1}H resonance, enabling recording ^{1}H-^{13}C HSQC, is ~150 Hz, as this is the approximate value of the ^{1}H–^{13}C J_1 coupling.

For these reasons, the dominant signals used for identification were less affected and very intense signals **THS$_{in}$** and **THS$_{out}$**. The phase sensitive ^{1}H-^{13}C HSQC routine enables one to distinguish –CH_2– and –CH_3 units and therefore provides a tool for identifying the resonances Si-R-**CH_3** and Si-**CH_2**-R, being well separated (within the ^{13}C-NMR region: 10–15 ppm) from other THS signals (**Figure 47**).

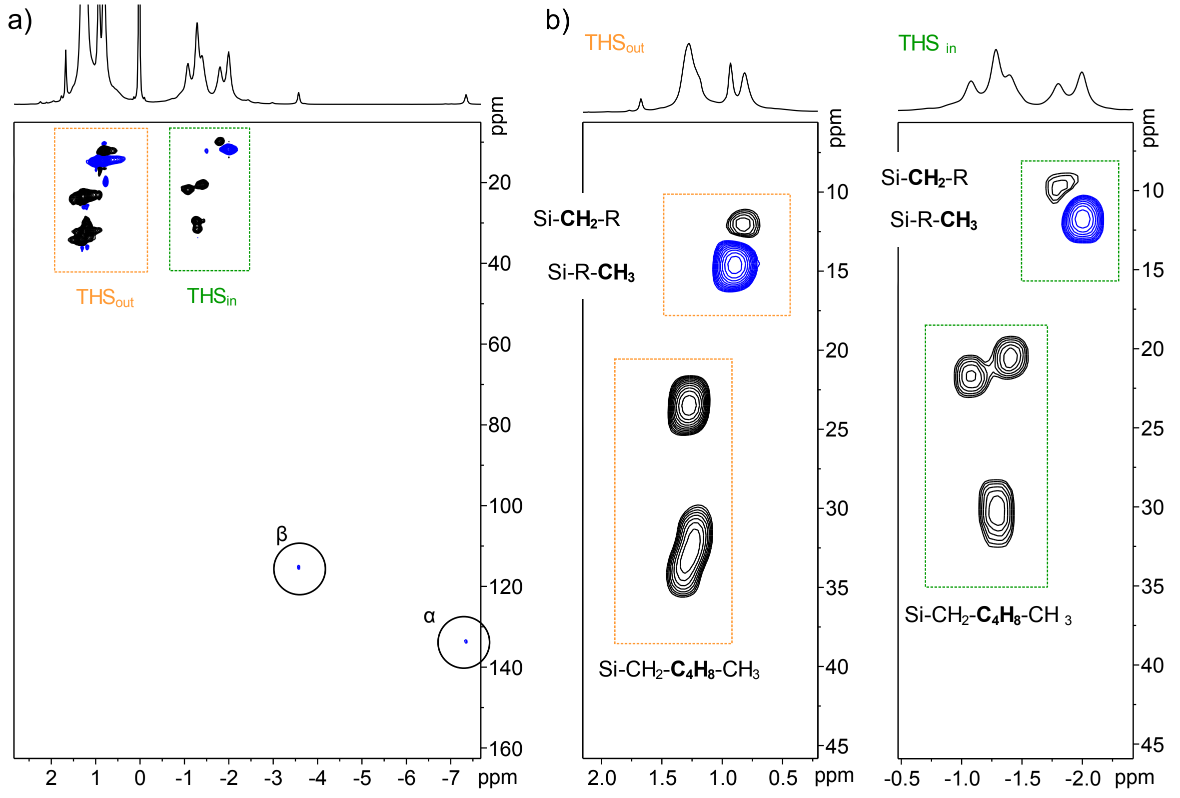

Figure 47: ^{1}H-^{13}C HSQC (500 MHz, 223 K, CD_2Cl_2) of **(*c*-P6[e$_6$]·T6*)**$^{2+}$ used to identify THS$_{in}$, THS$_{out}$, α and β resonances.

Other unique ^{13}C NMR resonances were those of **α** and **β**, expected at ~150 and 120 ppm, respectively. ^{13}C NMR resonances of **o$_{in}$**, **o$_{out}$** and **p** are expected at ~140 ppm. In **Figure 47** are shown ^{1}H-^{13}C cross-peaks from **α** and **β** resonances, however, these are clearly shifted by approximately −10 ppm from their expected position. This is due to the ring current effect, which is affecting both H and C resonances nearly equally (as they are at nearly the same position relative to the nanoring). These effects need to be considered and both ^{1}H and ^{13}C positions needs to be assessed in term of the expected conventional chemical shifts. In this example, it is clear that the ^{1}H NMR resonance at ~−7 ppm was from an aromatic proton signal with an original position at ~7 ppm; and thus both ^{1}H and ^{13}C nuclei are expected to be shifted by approximately −14 ppm. This is true for all resonances and it was found that the chemical shifts of nuclei are strongly correlated (**Figure 48**). This can serve as another handle for analysis and assignment.

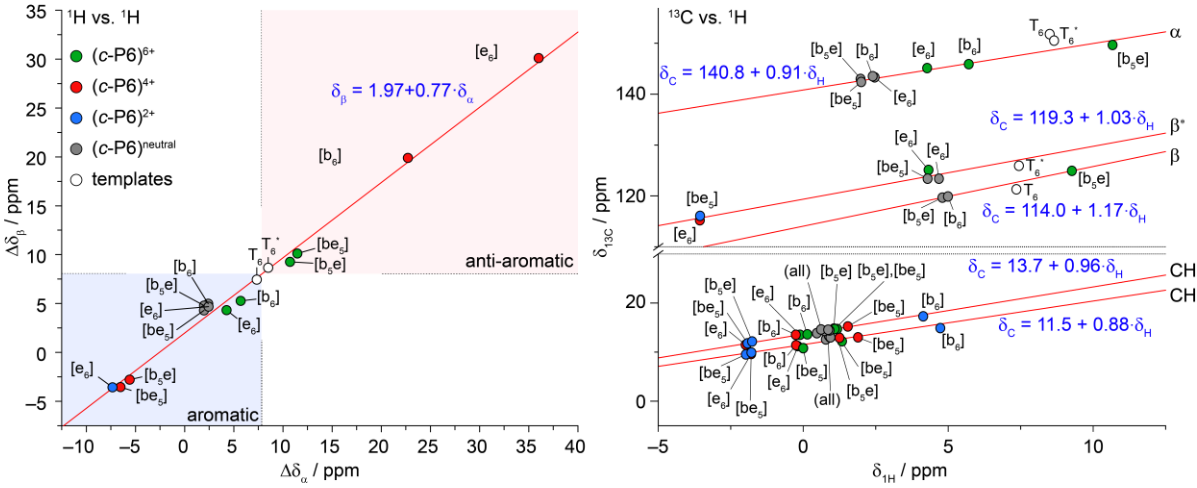

Figure 48: (left) Plot of relative chemical shifts (subtracted from the unbound) of template resonances **α** versus relative chemical shifts of **β** at various oxidation states of 6-porphyrin nanorings (with various linkers [b_xe_y]). (right) Plot of ^{1}H and ^{13}C absolute chemical shifts of selected resonances showing their strong correlation.

After identification of the two THS regions and the template resonances, ^{1}H-^{1}H-NOESY, which is less sensitive to peak-width, can provide further insight. In **Figure 49** a representative ^{1}H-^{1}H-NOESY spectrum is shown with several areas highlighted. These highlighted areas show regions of interest that can be used to assign the spectrum, outlined in detail in **Figure 50**.

In **Figure 50**, *region A* shows a clear correlation between **α** and **β**, as expected for neighbouring protons on the pyridine ring. Typically, the **α** proton is more strongly affected by a change in the environment and shows a more pronounced shift change than **β**. *Region B* shows selective NOE between **THS$_{in}$** and the template resonances and the absence of one to **THS$_{out}$**.

Subtraction of the THS shift inside and outside of the ring gives $\Delta\delta_{THS} = \delta_{THSin} - \delta_{THSout}$ and the $\Delta\delta_{THS}$ can serve as a measure of the ring current strength, that can be correlated with the chemical shifts of other resonances (**Figure 48**, right).

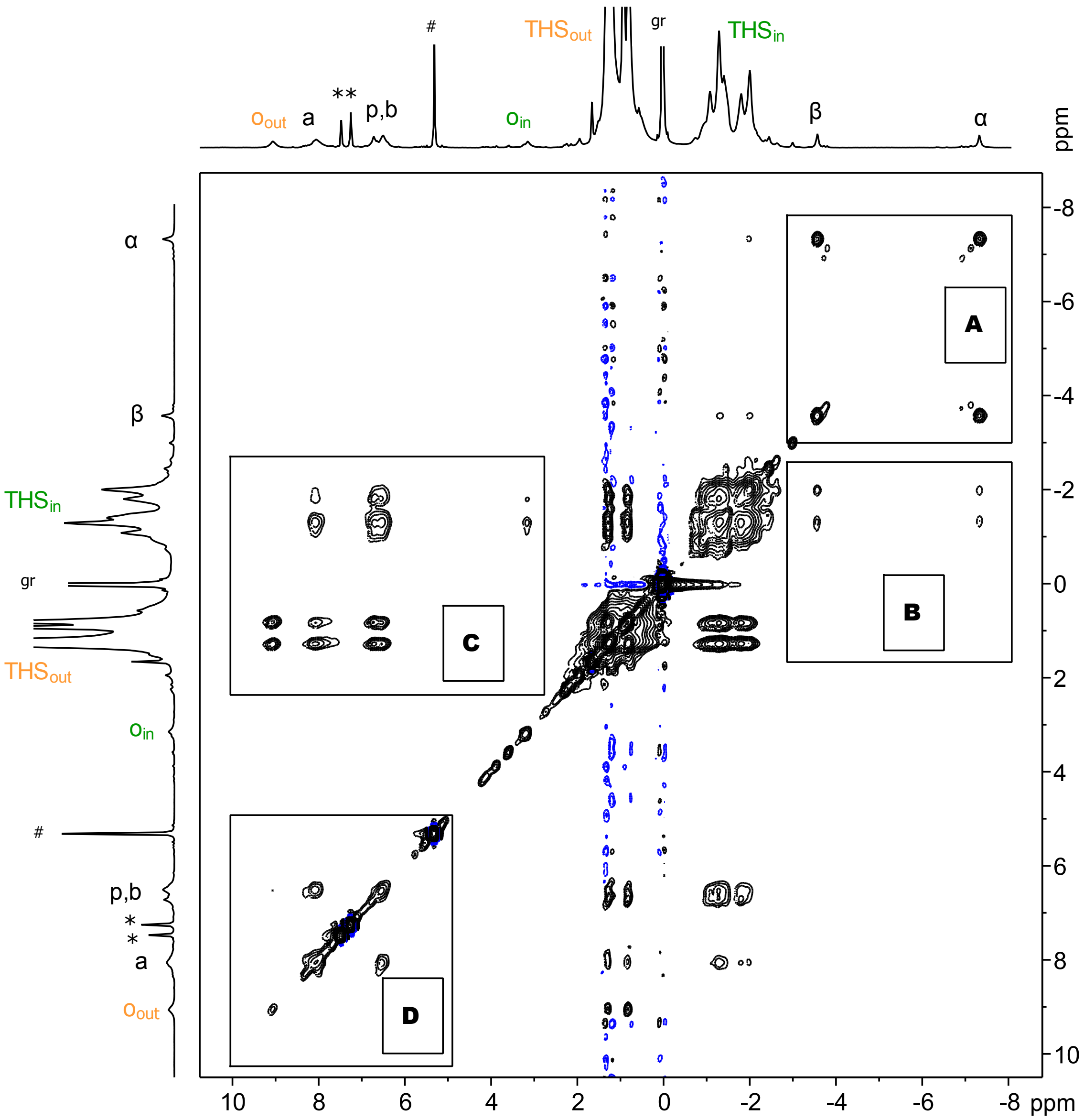

Figure 49: ^{1}H-^{1}H NOESY (500 MHz, 223K, CD_2Cl_2, mixing time = 0.8 s) spectrum of (*c*-**P6[e6]·T6***)$^{2+}$ generated by titration with **Thn+**. Inserts highlight the most relevant regions. *: neutral thianthrene; #: residual solvent peak; gr: silicon grease.

Furthermore, it can be identified that the *ortho* protons (**o$_{in}$**, **o$_{out}$**, *region C*) are in NOE contact with the respective THS environments. The remaining signals **a**, **b**, and **p** are located at the periphery and thus show equal interactions with **THS$_{in}$** and **THS$_{out}$**. *Region D* was used to identify the neighbouring porphyrin's *beta* signals **a** and **b**, which are in strong NOE contact. In addition, **b** usually shows a weak NOE to the *ortho*-aryl protons **o$_{in}$** and **o$_{out}$**, while **a** does not. The remaining *para*-aryl proton **p** is located far away from the ring-plane and can usually be assigned by exclusion, as it shows weak (if any) NOEs to all other resonances (except **THS$_{in}$** and **THS$_{out}$**). In some cases, not all resonances could be unambiguously assigned, even after substantially extending the number of scans. Such ambiguous signals are then not labelled in the spectra, even though they can often be identified by comparison with unambiguously assigned spectra of closely related species.

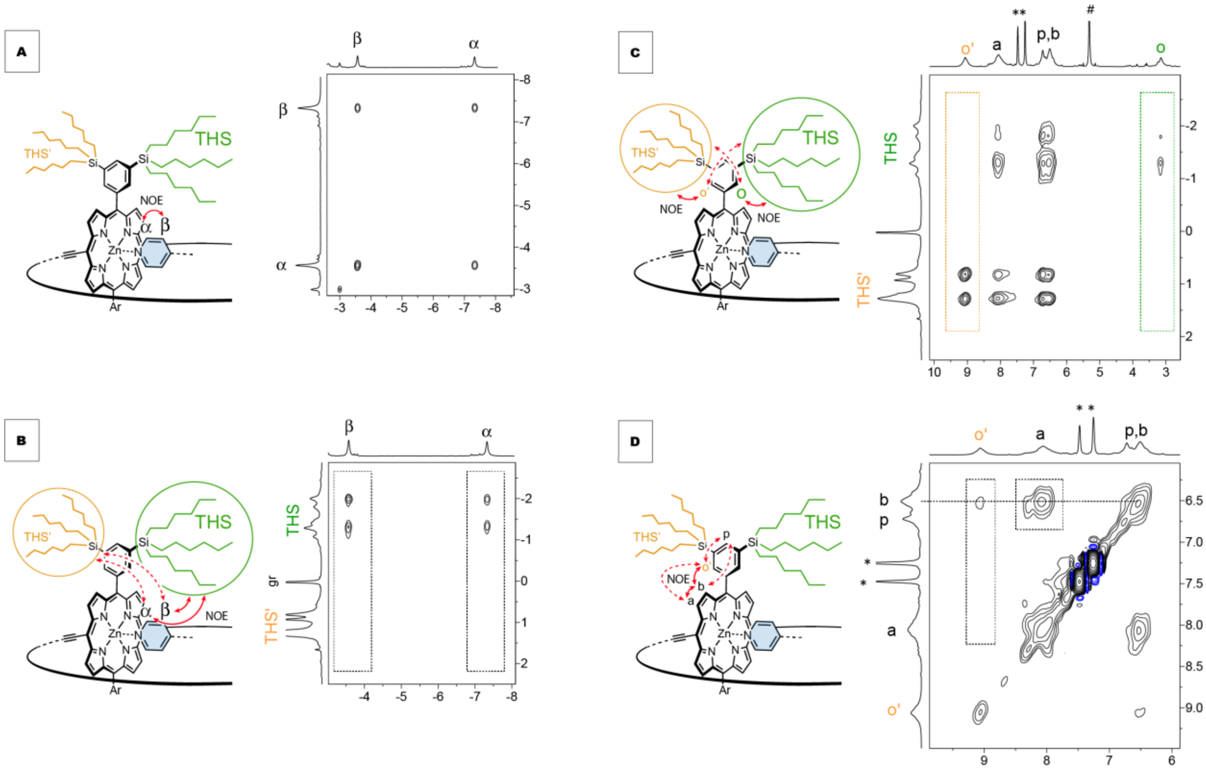

Figure 50: Parts of the ^{1}H-^{1}H NOESY spectrum for (***c*-P6[e$_6$]·T6***)$^{2+}$ (same as **Figure 49**) and schematic representation of analysed cross-peaks. A) NOE between template resonances **α** and **β**; B) NOEs between template (**α**, **β**) and interior THS; C) NOEs between THS and *ortho* aryl resonances (**o$_{in}$**, **o$_{out}$**); D) NOEs between porphyrin beta resonances (**a**, **b**), and aryl resonances (**o$_{out}$**, **p**). Red lines indicate NOE, dotted red lines absence thereof.

^{1}H-^{1}H TOCSY and COSY NMR spectra were recorded for most of the states and helped to cross-validate the assignment.

^{19}F nucleus as a unique NMR probe

For several key molecules, special templates containing —CF$_3$ groups were designed and synthesised. Such templates provide a unique handle for ring current analysis and for assignment. Any observed ^{19}F resonance can be unambiguously assigned to the —CF$_3$ group as there is always only one symmetrically equivalent —CF$_3$ group in the structure. Observation of more than one ^{19}F signal indicates the presence of several species and the resonance position, relative to that of unbound template, unambiguously reports on the species' aromaticity.

Furthermore, the ^{19}F resonance can be used for ^{1}H assignment of neighbouring ^{1}H nuclei *via* selective ^{19}F→^{1}H NOE magnetisation transfer (HOESY) (*vide infra*). Analysis involving ^{19}F NMR will be discussed for each compound individually.

3.3.1.3. NMR oxidation of *c*-P6[b$_6$]·T6

The ^{1}H NMR spectrum of neutral ***c*-P6[b$_6$]·T6** shows no global ring current, but strong local aromatic character. This significantly affects the chemical shifts of the templates' pyridine legs, however it does not lead to any significant differentiation between the inside and outside of the ring, as no splitting is observed in the THS region (**Figure 51a**). When two equivalents of **Thn$^+$** are added, at −20°C, the previously unobserved 2+ state is revealed as being globally aromatic. The globally aromatic character is evidenced by the THS$_{in}$ resonances, shielded by ~2 ppm.

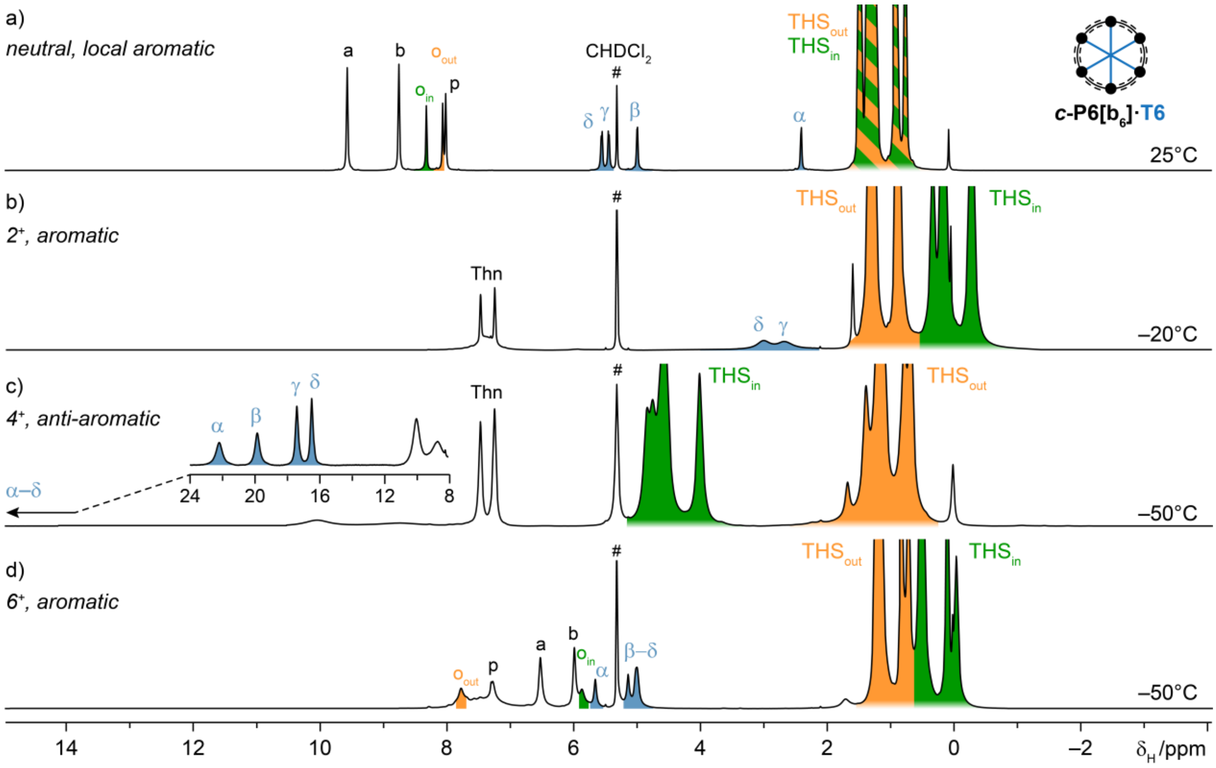

Figure 51: ^{1}H NMR (500 MHz, CD_2Cl_2) spectra of ***c*-P6[b$_6$]·T6** at neutral, 2+, 4+ and 6+ oxidation states.

Addition of four equivalents and six equivalents of **Thn$^+$** yielded the 4+ and 6+ oxidation states, described previously as being anti-aromatic and aromatic, respectively. Beside significant **THS$_{in}$** shifts, most of the resonances can be assigned and corroborate the interpretation of the aromaticity character.

Beside THS-decorated nanorings, initially, other solubilising groups were tested as well. The nanoring with 3,5-bis(*n*-octyloxy)phenyl solubilizing groups (**C8 *c*-P6[b$_6$]·T6**) was oxidized to 2+, 4+ and 6+ state. These states possess the same global (anti)aromaticity as the THS-based nanoring (**Figure 52**). The octyloxy sidechains provide some unique ^{1}H NMR resonances (e.g. –OCH_2–) and help to interpret aromaticity in the same way as the THS groups.

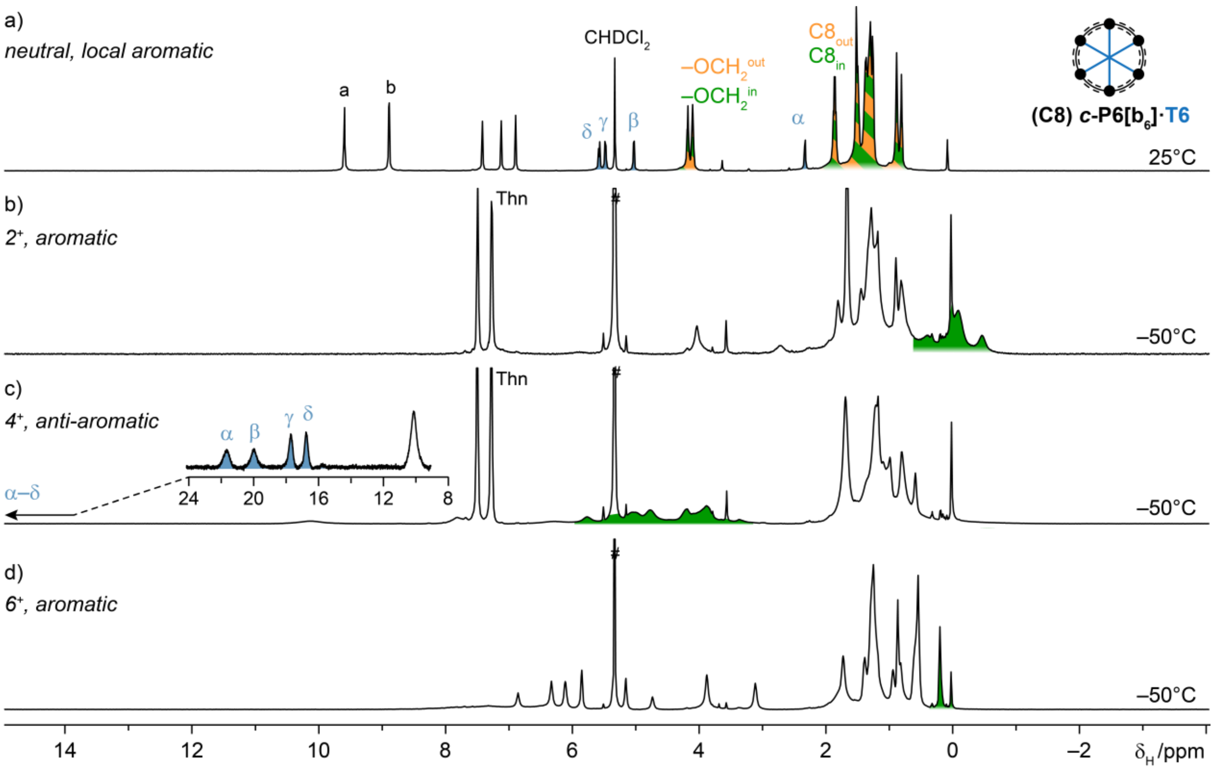

Figure 52: ^{1}H NMR (500 MHz, CD_2Cl_2) spectra of ***c*-P6[b$_6$]·T6**, with 3,5-bis(octyloxy)phenyl instead of THS groups, at neutral, 2+, 4+ and 6+ oxidation states. Octyloxy- resonances (filled in green) are found to be at similar positions as THS.

3.3.1.4. Fluorinated templates

For a better understanding of the 2+ state and unambiguous assignment of the **T6** resonances in 4+ states, a special template **T6f** was designed. The synthesis was carried out by Dr. Henrik Gotfredsen (**Figure 53**).

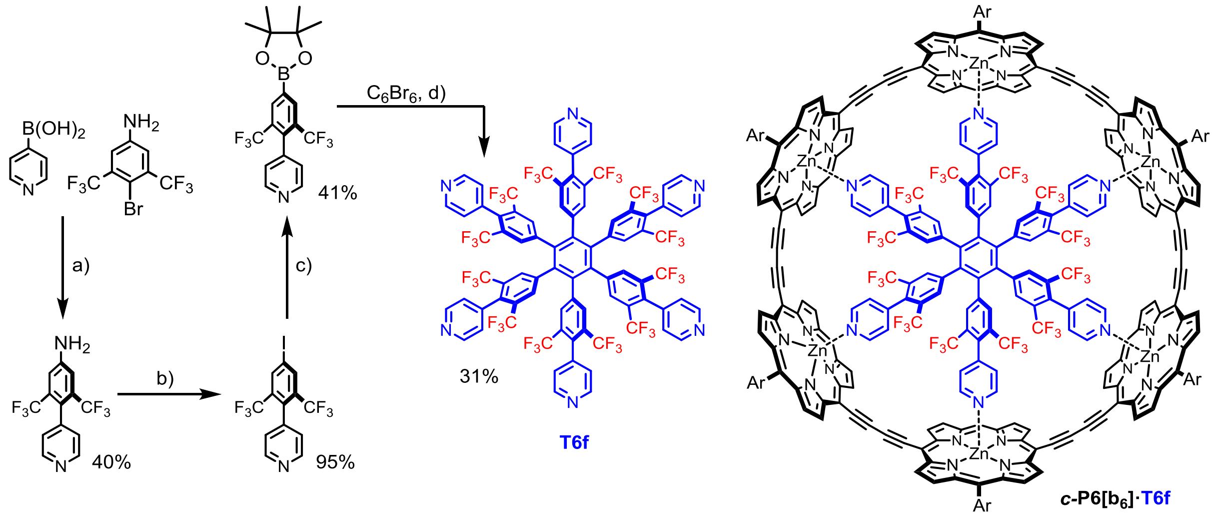

Figure 53: (left) Scheme of **T6f** synthesis, (right) ***c*-P6[b$_6$]·T6f** complex. a) $Pd(PPh_3)_4$, K_2CO_3; b) $NOBF_4$, KI; c) B_2pin_2, $Pd(dppf)Cl_2$, KOAc; d) $Pd(PPh_3)_4$, K_2CO_3.

A total twelve –CF_3 groups are present in the **T6f** molecule, replacing all of the γ protons in **T6**. Originally, a monosubstituted version (with six –CF_3 groups) was synthesized which exhibited rotamer isomerism with slow chemical exchange on the NMR time scale, and thus would have been a very impractical probe for NMR analysis. Hexafluorobenzene (C_6F_6) was used as an internal standard for ^{19}F resonances (−164.8 ppm) for its stability toward oxidation, spectral simplicity and relative remoteness to the $–CF_3$ resonance in the templates.

The chemical shift (^{19}F) of unbound template in CD_2Cl_2 was −60.3 ppm. Upon template complexation to form ***c*-P6[b₆]·T6f**, the ^{19}F resonance shifts by $\Delta\delta_F = -1.4$ ppm, reflecting the shielding effect of locally aromatic porphyrins. Upon ***c*-P6[b₆]·T6f** oxidation to the 2+ state, the $-CF_3$ resonance moves relatively to the unbound by $\Delta\delta_F = -4.44$ ppm, indicating global aromaticity. At 4+ state, resonance is shielded by $\Delta\delta_F = 8.8$ ppm. At the aromatic 6+ state, $\Delta\delta_F = -2.6$ ppm was observed (**Figure 54**, inserts). Interestingly, a small residual ^{19}F peak, with a stable chemical shift (~59.3 ppm) was observed, indicating that some part (~10%) of the molecule is either decomposed or corrupted and does not exhibit a ring current. A portion of this residual signal was substantially larger if the sample had experienced more warming-up cycles to ~ −20°C.

The ^1H NMR spectra of ***c*-P6[b₆]·T6** are analogous to those of ***c*-P6[b₆]·T6**, with missing γ resonances (**Figure 54**). Furthermore, a putative open-shell state, corresponding to 5+, was discovered thanks to the $–CF_3$ probe. The 5+ state has very broad ^1H NMR features, but a distinctive ^{19}F peak. The whole titration plot provides probably the clearest overview, with ^1H and ^{19}F NMR spectra for every increment of oxidant added (**Figure 55**).

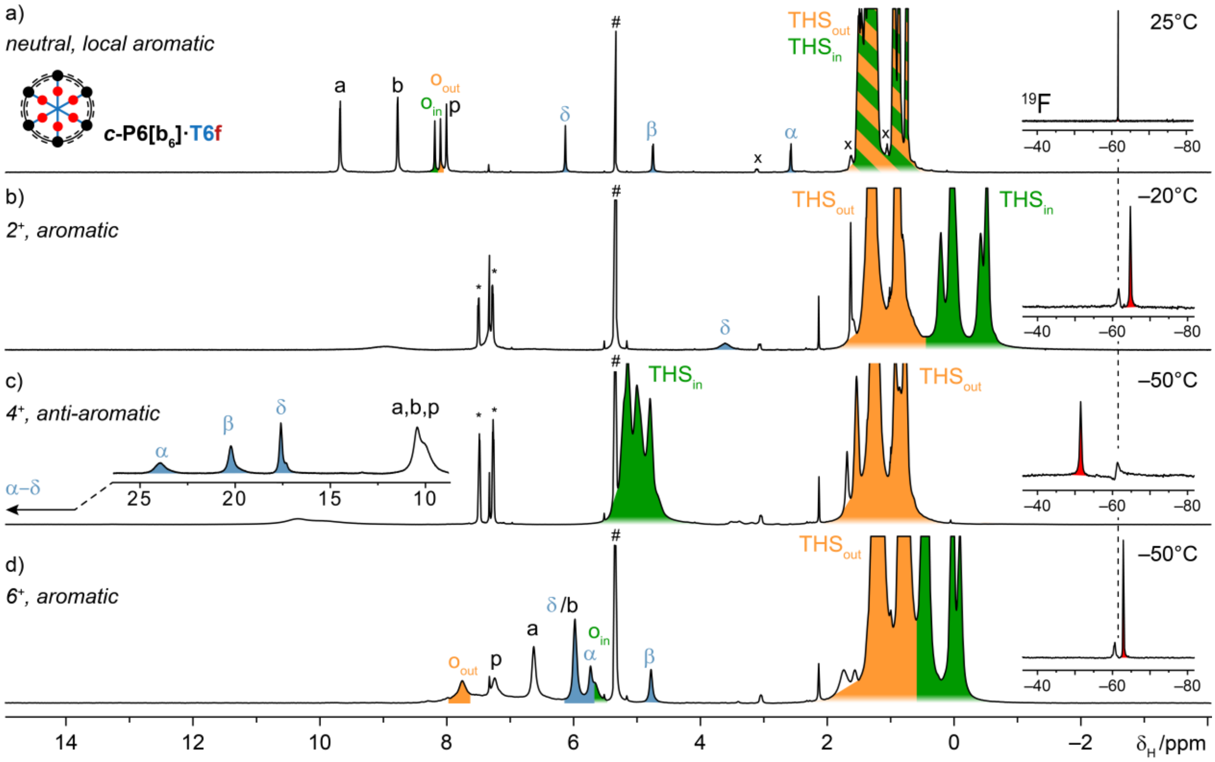

Figure 54: ^1H NMR (500 MHz, CD_2Cl_2) and inserts from ^{19}F NMR (471 MHz) spectra of ***c*-P6[b₆]·T6f** at neutral, 2+, 4+ and 6+ oxidation states..

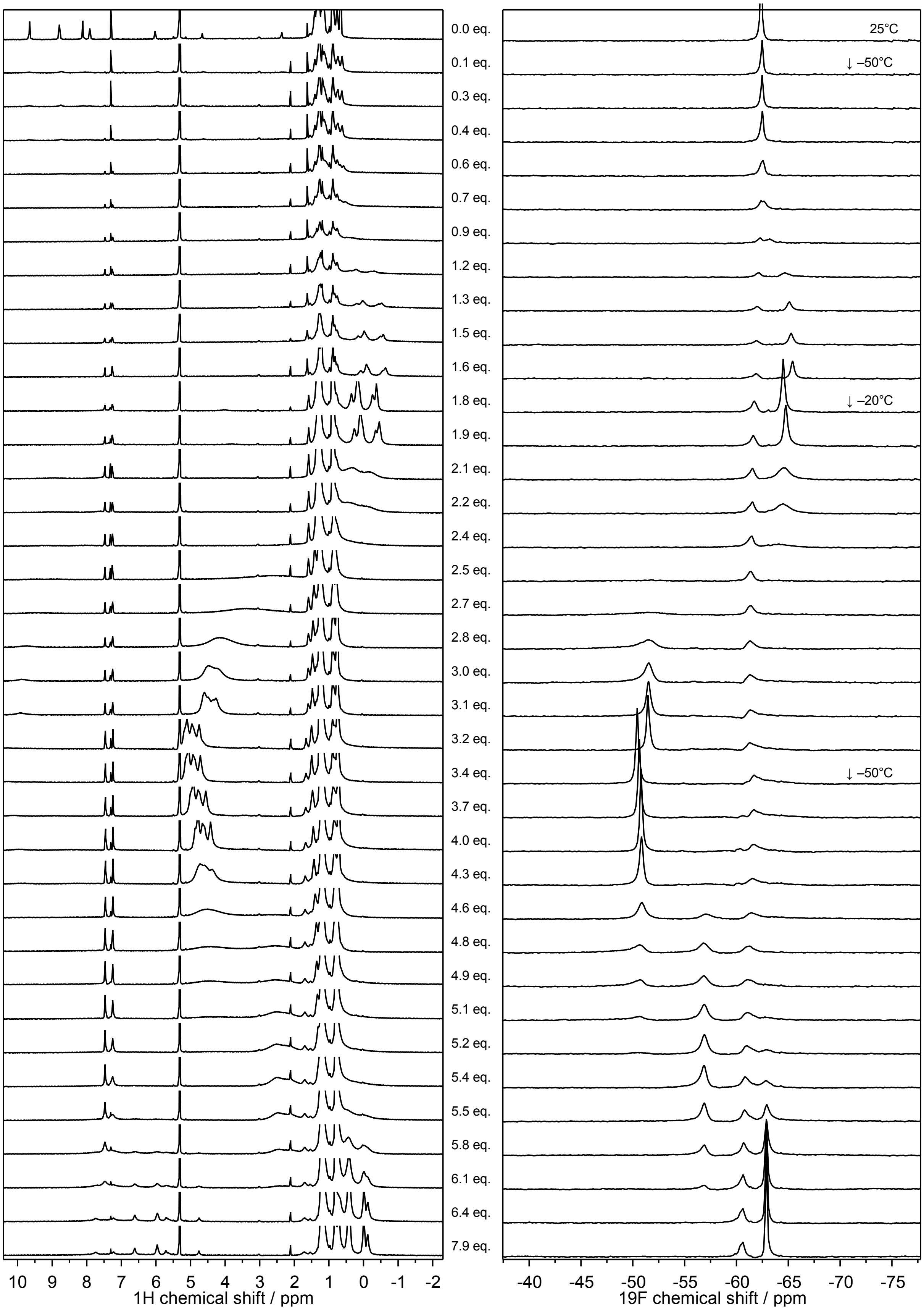

Figure 55: ^{1}H and ^{19}F NMR (CD_2Cl_2, 500/471 MHz) spectra of ***c*-P6[b$_6$]·T6f** for every oxidant increment added. Titration stack plot shows subsequent evolution of 2+, 4+, 5+ and 6+ states.

Heteronuclear NOE (HOESY) provide information about which ^{1}H nuclei are in the vicinity of the –CF$_3$ group by different magnetisation transfer (^{19}F→^{1}H). Neutral ***c*-P6[b$_6$]·T6f** can serve as a reference state. The strongest magnetisation transfer is to **δ**, then **β**, ***α*** and the weakest to **THS$_{in}$** (**Figure 56**).

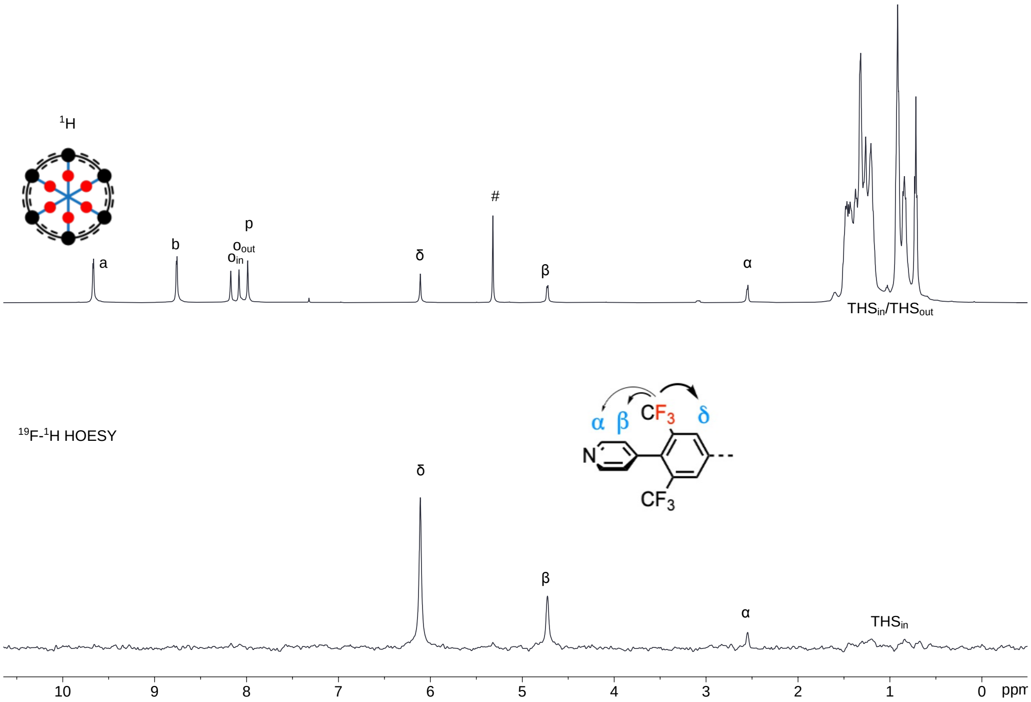

Figure 56: (top) ^{1}H NMR (500 MHz, CD$_2$Cl$_2$) of ***c*-P6[b$_6$]·T6f**. (bottom) Selective 1D ^{1}H-^{19}F HOESY, showing magnetisation transfer from the –CF$_3$ group to nearest δ, β, α and THS$_{in}$ resonances.

Such 1D ^{1}H-^{19}F HOESY was also performed for the 2+, 4+ and 6+ states, confirming and aiding correct assignment of the resonances.

The –CF$_3$ probe unveiled the existence of species with relatively sharp ^{1}H and ^{19}F NMR spectra, coinciding with the addition of the 5 equivalents of oxidant. The temperature dependence of the chemical shifts of the unusual 5+ state was studied together with the anti-aromatic 4+ and aromatic 6+, all showing a linear Curie dependence (**Figure 57**).

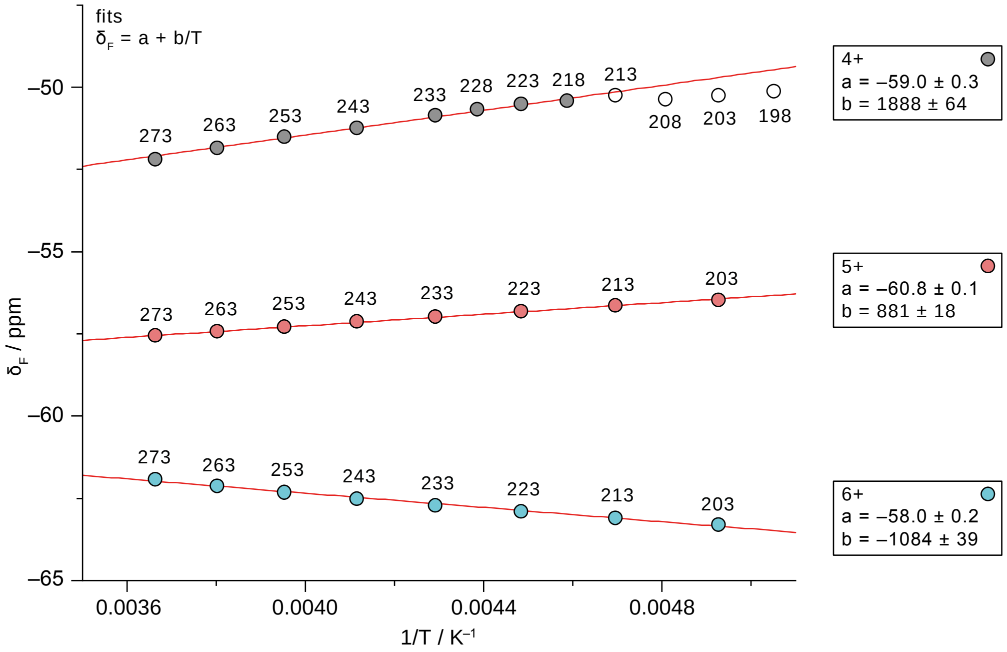

Figure 57: Scatter plot of observed ^{19}F chemical shifts of oxidised ***c*-P6[b₆]·T6f** (4+, 5+, 6+) vs. 1/*T* for temperatures of 203–273 K. The red line represents the linear fit through all filled points of the corresponding oxidation state, colours represent oxidation states.

3.3.2. *c*-P6[b$_5$e] – reversing the ring currents

Oxidation of a nanoring by two electrons reverses the aromaticity, in agreement with the Hückel Rule and with the idea of π electron delocalisation paths. A complementary way of altering the ring current in a 6-porphyrin nanoring is to make a subtle structural change in its linker. For example, replacement one butadiyne linker for ethyne (***c*-P6[b$_6$]** → ***c*-P6[b$_5$e]**, **Figure 58**) should alter the π electron count of the neutral species from 84 to 82.

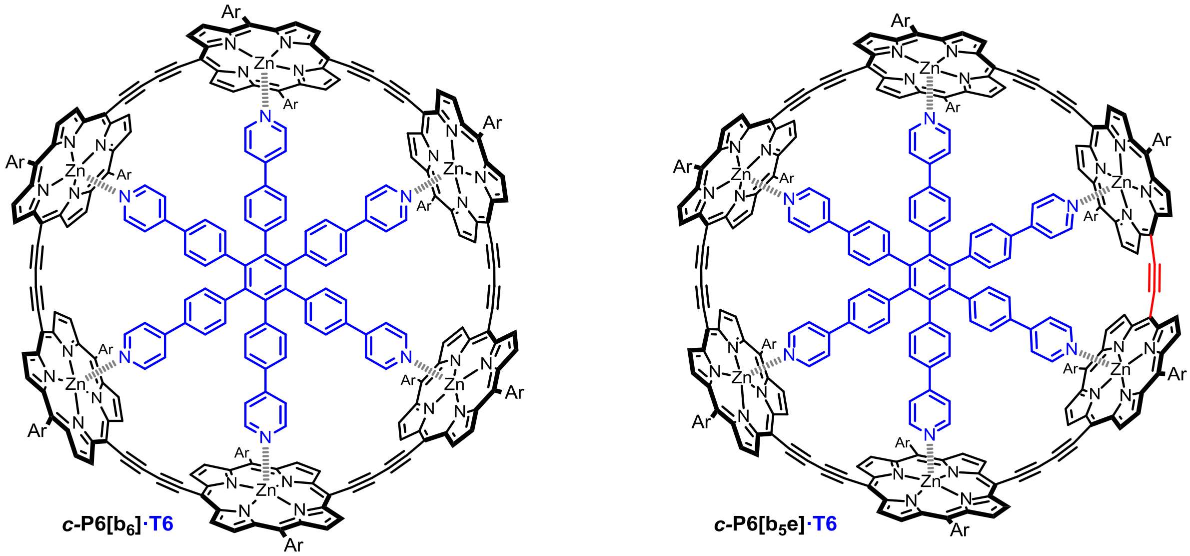

c-P6[b$_6$]·T6

c-P6[b$_5$e]·T6

Figure 58: Structures of ***c*-P6[b$_6$]·T6** and ***c*-P6[b$_5$e]·T6**. Ar = 3,5-bis(trihexylsilyl)phenyl.

3.3.2.1. Synthesis and study of neutral *c*-P6[b$_5$e]·T6

The DFT based model suggests that the template **T6** should fit very well in the nanoring, maintaining the ideal Zn—N distance at ~2.1 Å (**Figure 59**).

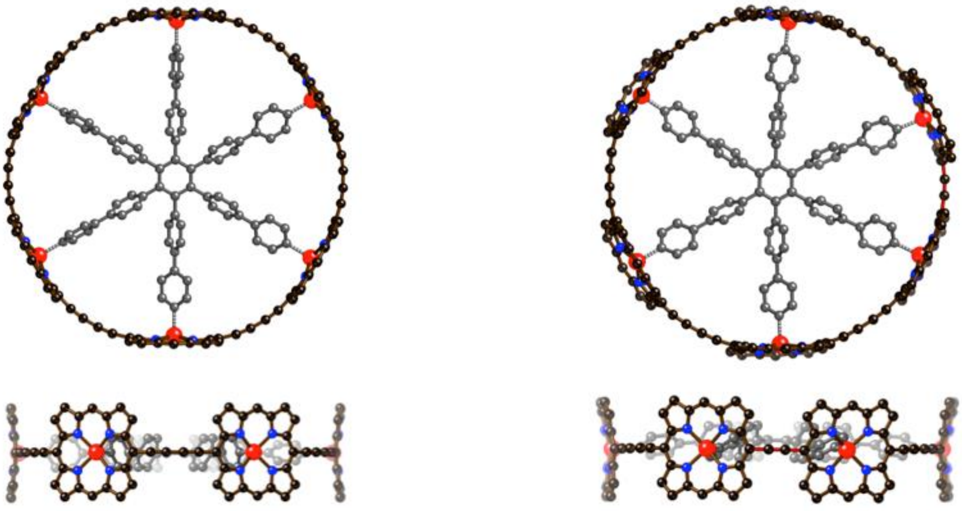

Figure 59: Structures of ***c*-P6[b$_6$]·T6** (left) and ***c*-P6[b$_5$e]·T6** (right) as local minima (confirmed by frequency calculation) optimized by B3LYP/6-31G* DFT method. Solubilising aryl groups were truncated to –H.[106]

Unlike symmetric ***c*-P6[b$_6$]·T6**, the truncated ring ***c*-P6[b$_5$e]·T6** required sequential synthesis in order to control the insertion of the ethyne 'defect'. The synthesis was carried out by Dr. Hua-Wei Jiang and Dr. Renee Haver.[106] Dr. Renee Haver also performed the characterisation and peak assignment of the neutral ***c*-P6[b$_5$e]·T6**.

3.3.2.2. NMR spectra – general features

The defect changes the structural symmetry from D_{6h}, which would be the highest possible for ***c*-P6[b$_6$]·T6**,[3] to C_{2v}. One, therefore, should expect 6 environments of **a** and **b** *beta* porphyrin protons and 3 environments for templates (**α**–**δ**), and solubilising groups (**THS**, **o$_{in}$**, **o$_{out}$** and **p**) (**Figure 60**).

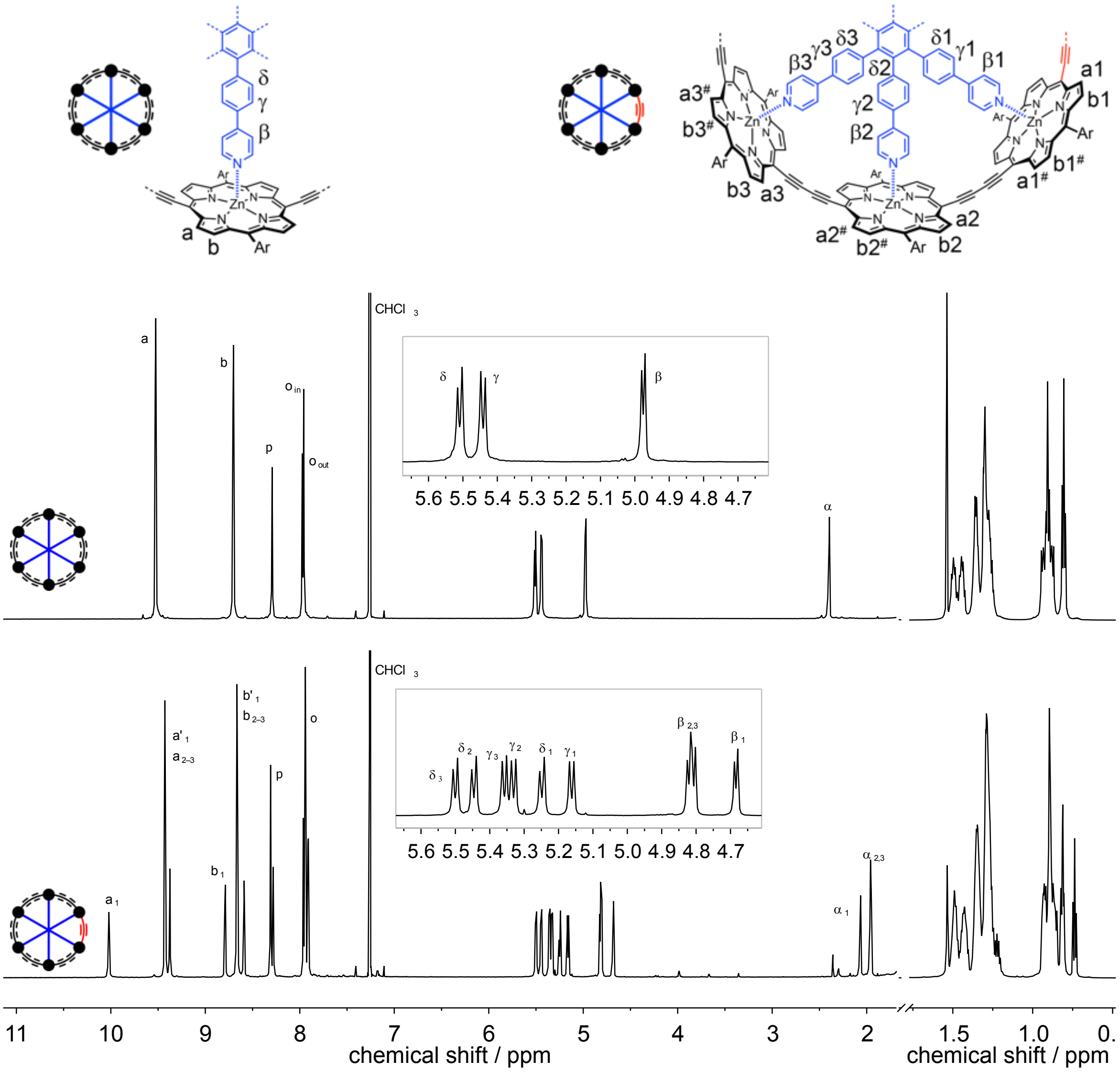

Figure 60: (top) Assignment legend, (middle) ^{1}H NMR spectra (500 MHz, CDCl$_3$, 298 K) of ***c*-P6[b$_6$]·T6** and (bottom) ***c*-P6[b$_5$e]·T6**. Resonances a$_1$ and b$_1$ stand out in the porphyrin region.

---

[3] Although the optimised minima might have lower symmetry (C_6, C_3, … C_1), effective time-averaged NMR picture suggests D_{6h} symmetry.

Although many inequivalent signals overlap, the signals **a_1** and **b_1**, corresponding to resonances next to the ethyne linker, stand out. This can be explained by the higher influence of the de-shielding cone from neighbouring porphyrin, as the nuclei are relatively closer to the next porphyrin, compared with ones next to a butadiyne linker. This observation can be generalised in ^{1}H NMR; **a** resonances (in $CDCl_3$) next to ethyne and butadiyne linkers are to be found at ~10 and ~9.5 ppm, respectively. This was corroborated by other ethyne-linked nanorings (c.f. ***c*-P6[e$_6$]·T6*** and ***c*-P6[be$_5$]·T6***, **Chapter 3.3.3** below).

As expected from the model, UV-vis based experiments, performed by Dr. Jiang, estimated that the ***c*-P6[b$_5$e]** has approximately the same affinity toward **T6** as ***c*-P6[b$_6$]**. However, the uncertainty of these UV-vis titrations did not allow direct comparison between ***c*-P6[b$_5$e]** and ***c*-P6[b$_6$]**. For this reason, the author designed and carried out a competition NMR experiment.

Solutions of equal quantities of ***c*-P6[b$_6$]** and ***c*-P6[b$_5$e]·T6** (1:1 mole ratio; approximately 1 mg of each; 0.1 µmol) in $CDCl_3$ (0.5 mL) were mixed in an NMR tube (**Figure 62, top**). The exchange of the template **T6** proceeds very slowly without the presence of a competing ligand to catalyse the de-coordination of **T6**, and therefore, *N*-methylimidazole (40 µL, 500 µmol) was added serving as a stronger competing ligand. After 1 hour, equilibrium was achieved, the solution was evaporated, and *N*-methylimidazole was removed under vacuum. The solid residue was dissolved in $CDCl_3$ (0.5 mL). ^{1}H NMR integration showed that the mole ratio of ***c*-P6[b$_6$]·T6** and ***c*-P6[b$_5$e]·T6** was 1.25, indicating a marginally higher affinity of ***c*-P6[b$_6$]** towards **T6** (**Figure 62, bottom**). This experiment was also conducted in the reversed order, starting with an equimolar mixture of ***c*-P6[b$_5$e]** and ***c*-P6[b$_6$]·T6**, yielding a similar result (mole ratio = 1.21, **Figure 63**). This confirms that the mixture is at equilibrium under the experimental conditions and confirms that ***c*-P6[b$_6$]** has a slightly higher affinity toward **T6** than ***c*-P6[b$_5$e]** (**Figure 61**).

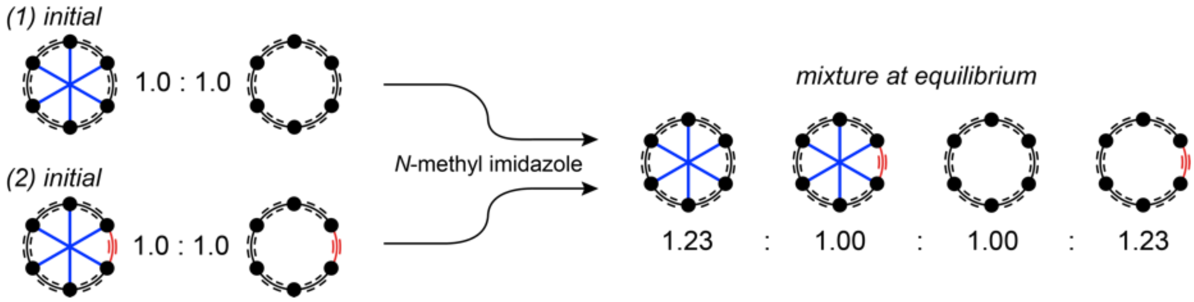

Figure 61: Competitive binding experiment investigating the relative affinity of ***c*-P6[b$_6$]** and ***c*-P6[b$_5$e]** towards **T6**.

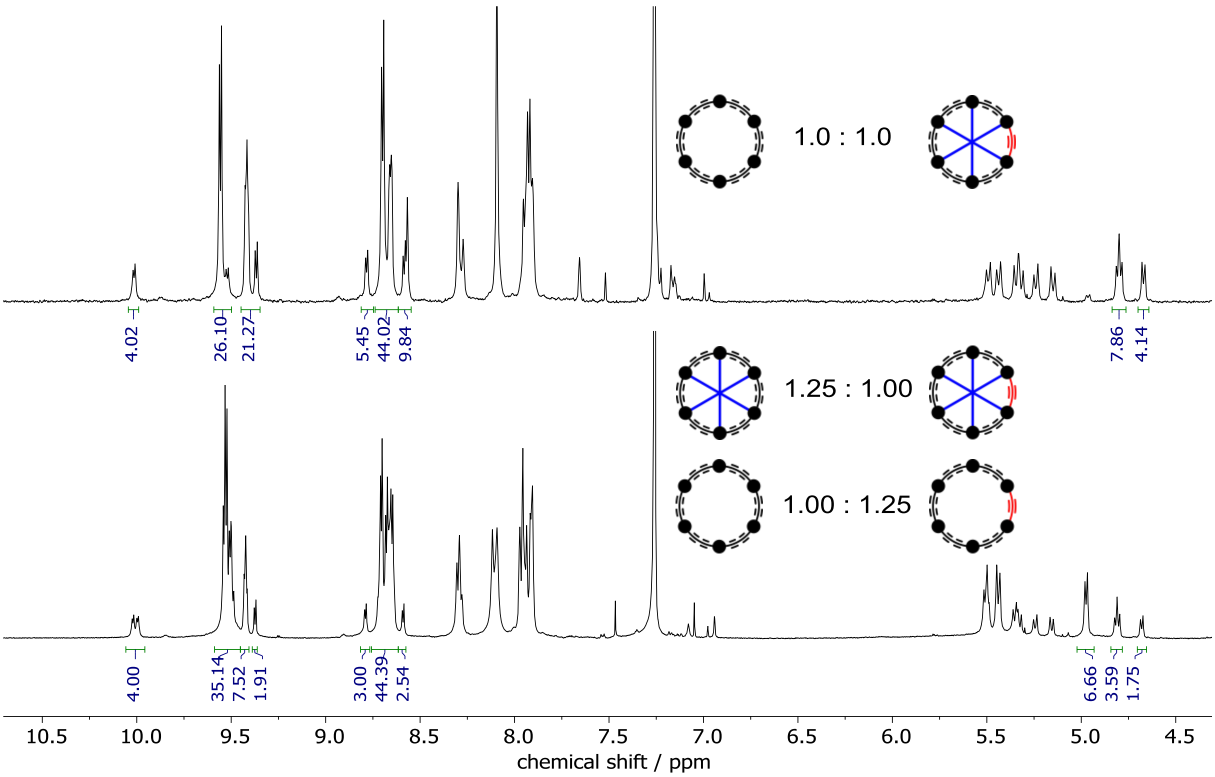

Figure 62: ^{1}H NMR spectra (500 MHz, CDCl$_3$, 298 K) of an initially equimolar mixture ***c*-P6[b$_6$]** and ***c*-P6[b$_5$e]·T6** (top) and after template redistribution catalysed by *N*-methylimidazole (bottom).

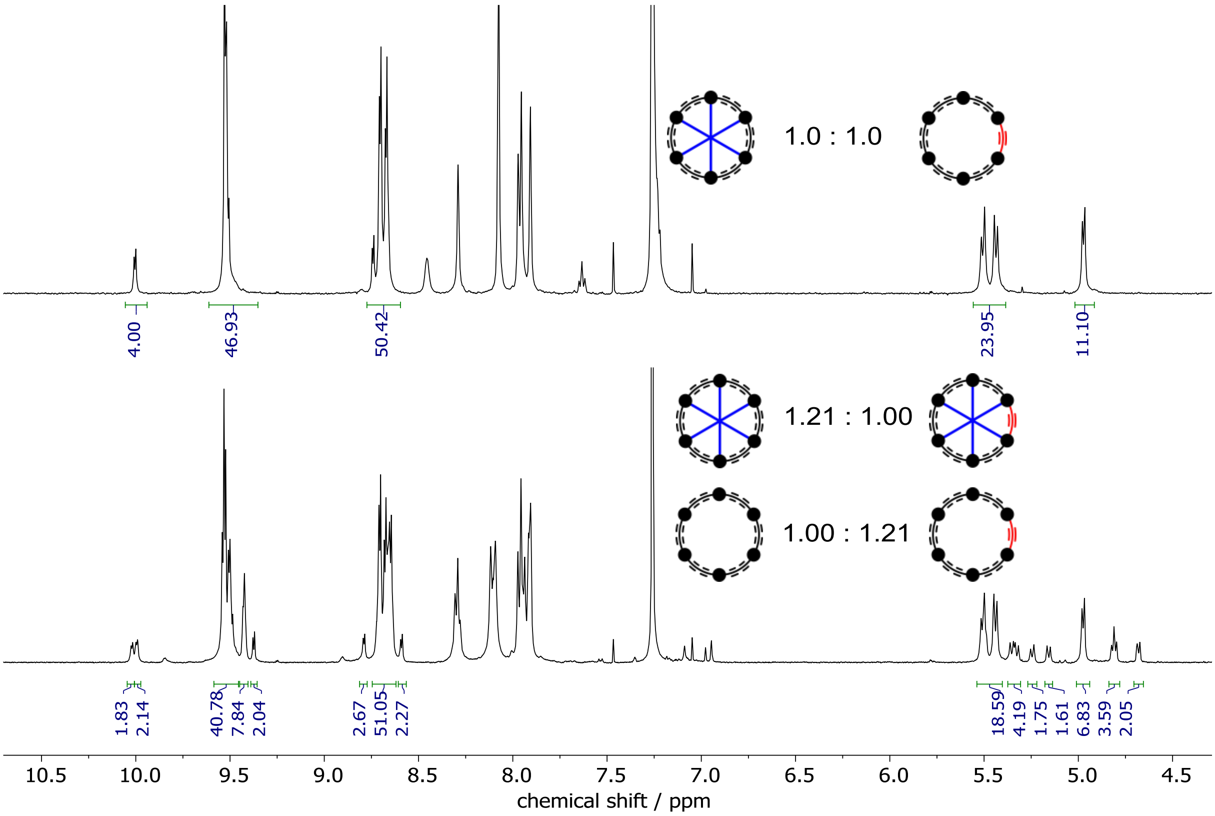

Figure 63: ^{1}H NMR spectra (500 MHz, CDCl$_3$, 298 K) of initially equimolar mixture ***c*-P6[b$_6$]·T6** and ***c*-P6[b$_5$e]** (top) and after template redistribution catalysed by *N*-methylimidazole (bottom).

3.3.2.3. NICS of *c*-P6[b$_5$e]·T6

The ***c*-P6[b$_5$e]·T6**, according to the Hückel Rule, is expected to have anti-aromatic 2+ and 6+ states and an aromatic 4+ oxidation state, reversed in comparison to the ***c*-P6[b$_6$]·T6**. The neutral state is expected to be locally aromatic in the same way as ***c*-P6[b$_6$]·T6**. NICS(0)$_{iso}$ calculations illustrate this alternating pattern (**Figure 64**)

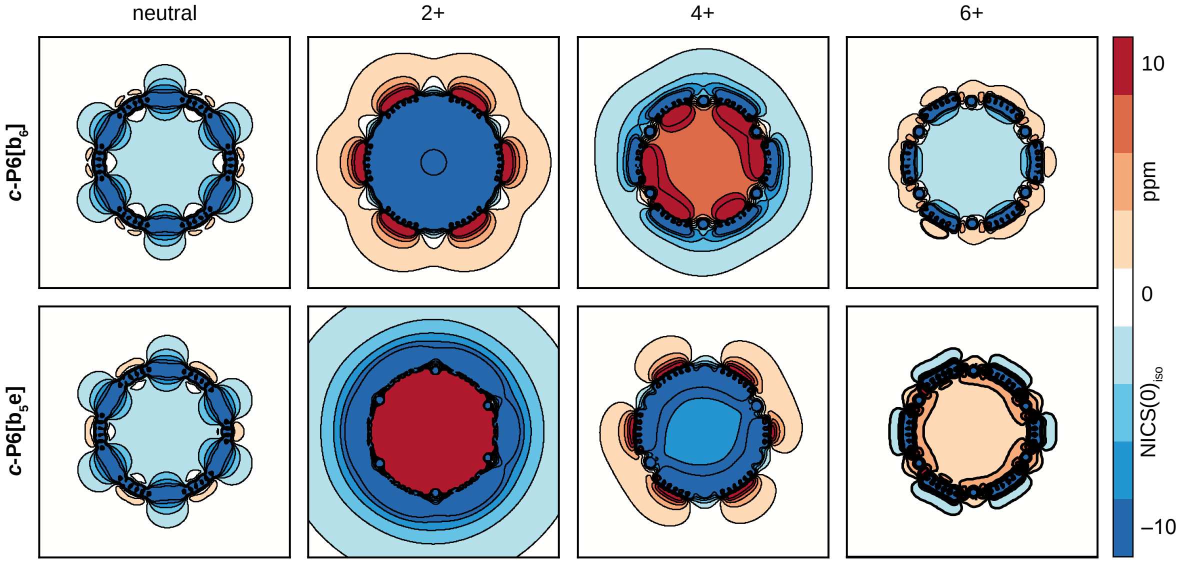

Figure 64: NICS(0)$_{iso}$ (LC-ωhPBE/6-31G*, ω = 0.1) of ***c*-P6[b$_6$]·T6** and ***c*-P6[b$_5$e]·T6** at oxidation states 0, 2+, 4+ and 6+. Templates **T6** were removed prior to NICS calculations.

DFT calculations, particularly of the +2+ state, were challenging, since many functionals describe these systems incorrectly and thus the resulting NICS were in contradiction with the Hückel Rule (**Figure 65**). Probably, a correct description of charge (de)localisation needs to be delicately balanced to allow an interplay between two extremes: localised bi-polaron and delocalised anti-aromatic state. It was found, that rather more localising functionals like LC-ωhPBE (with values ω ≥ 0.1) or ωB97X provide the predictions in agreement with Hückel Rule.

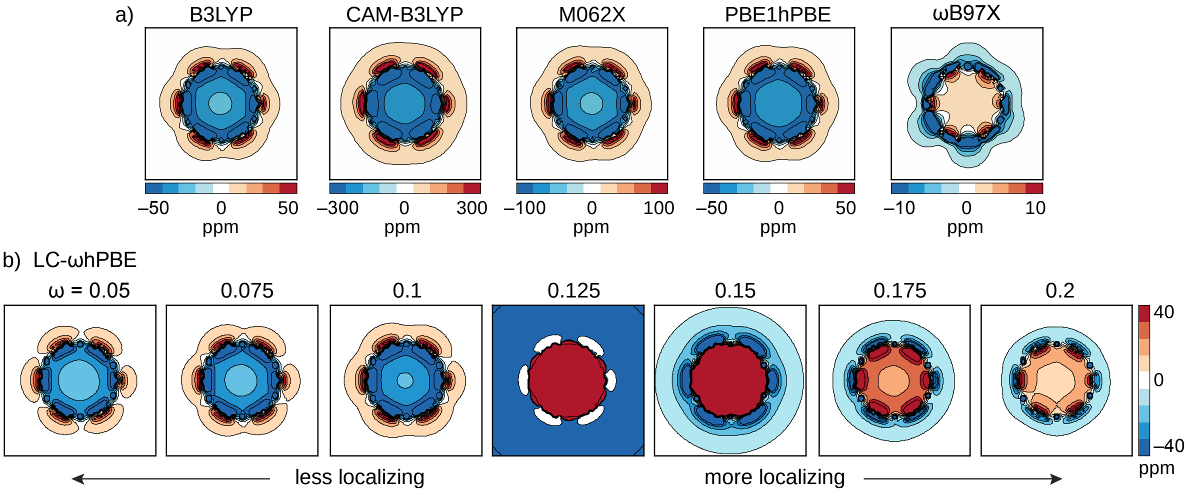

Figure 65: Problematic NICS(0)$_{iso}$ of **(*c*-P6[b$_5$e])$^{2+}$**; a) various functionals / 6-31G*; b) LC-ωhPBE/6-31G* with various ω values. Geometry was optimised using B3LYP/6-31G* methods and was kept constant for the NICS screening.

3.3.2.4. NMR Oxidation of *c*-P6[b$_5$e]·T6

Experimentally, the ***c*-P6[b$_5$e]·T6** was assessed in the same way as ***c*-P6[b$_6$]·T6**. NMR oxidisation yielded a broad anti-aromatic 2+ state and very well resolved aromatic 4+ and anti-aromatic 6+ states (**Figure 66**).

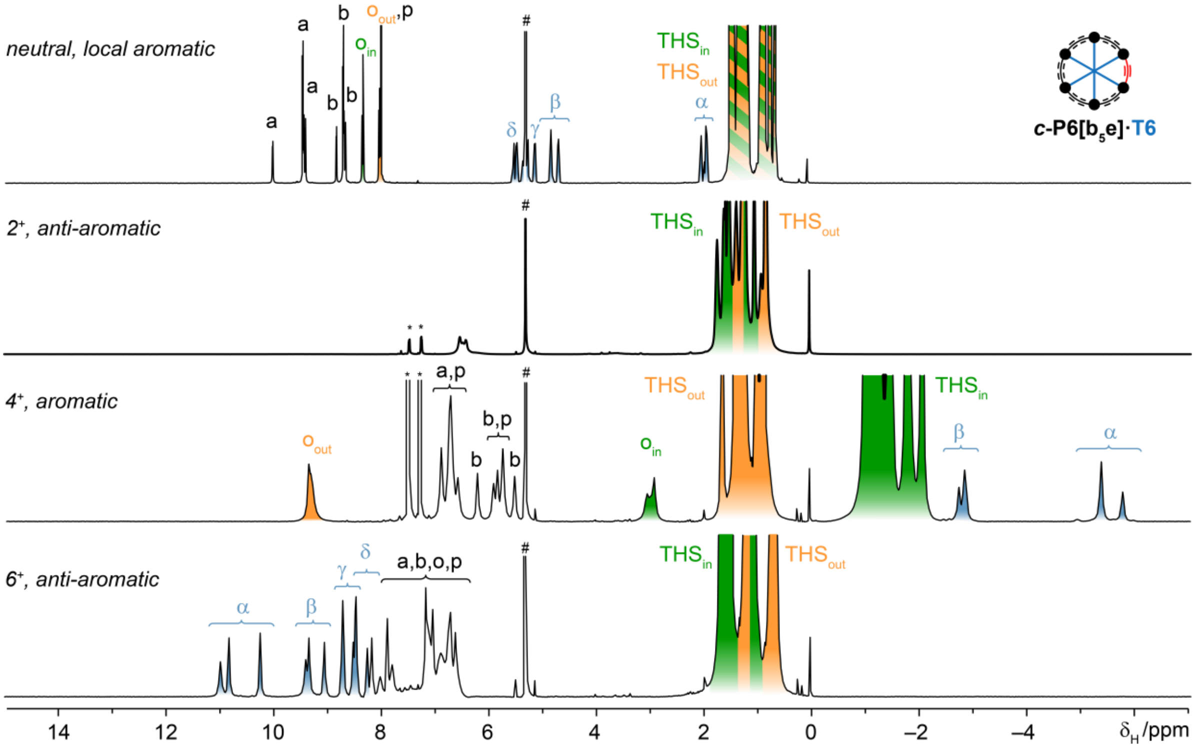

Figure 66: ^{1}H NMR spectra of ***c*-P6[b$_5$e]** at 0, 2+, 4+ and 6+ oxidation states with highlighted THS (inner in green, outer in orange) and template (blue) signals.

To prove beyond reasonable doubt that the ring current was reversed and that the oxidation states were correctly assigned, a mixture of ***c*-P6[b$_6$]·T6** and ***c*-P6[b$_5$e]·T6** was prepared (approx. 1:1 ratio) and the NMR oxidation titration was performed, proving the coexistence of the same oxidation states (**Figure 67**).

This can serve as an additional comment on the potential (anti)aromatic energetic (de)stabilisation. The fact, that both species co-exists at 4+ oxidation state with either aromatic or anti-aromatic character suggests nearly no effect of the aromaticity on the energy at these sizes of systems. If the aromatic states were significantly more stable than the anti-aromatic one, potential preference for formation of an aromatic {***c*-P6[b$_6$]·T6**}$^{6+}$ and an aromatic {***c*-P6[b$_5$e]·T6**}$^{4+}$ would be a plausible mechanism how to avoid anti-aromaticity when 5 equivalents of the oxidant was added. Alternatively, when approximately 3 equivalent of the oxidant was added, the system could split the charge as an aromatic {***c*-P6[b$_6$]·T6**}$^{2+}$ and an aromatic {***c*-P6[b$_5$e]·T6**}$^{4+}$. This is however not observed and both aromatic and anti-aromatic species emerge concurrently.

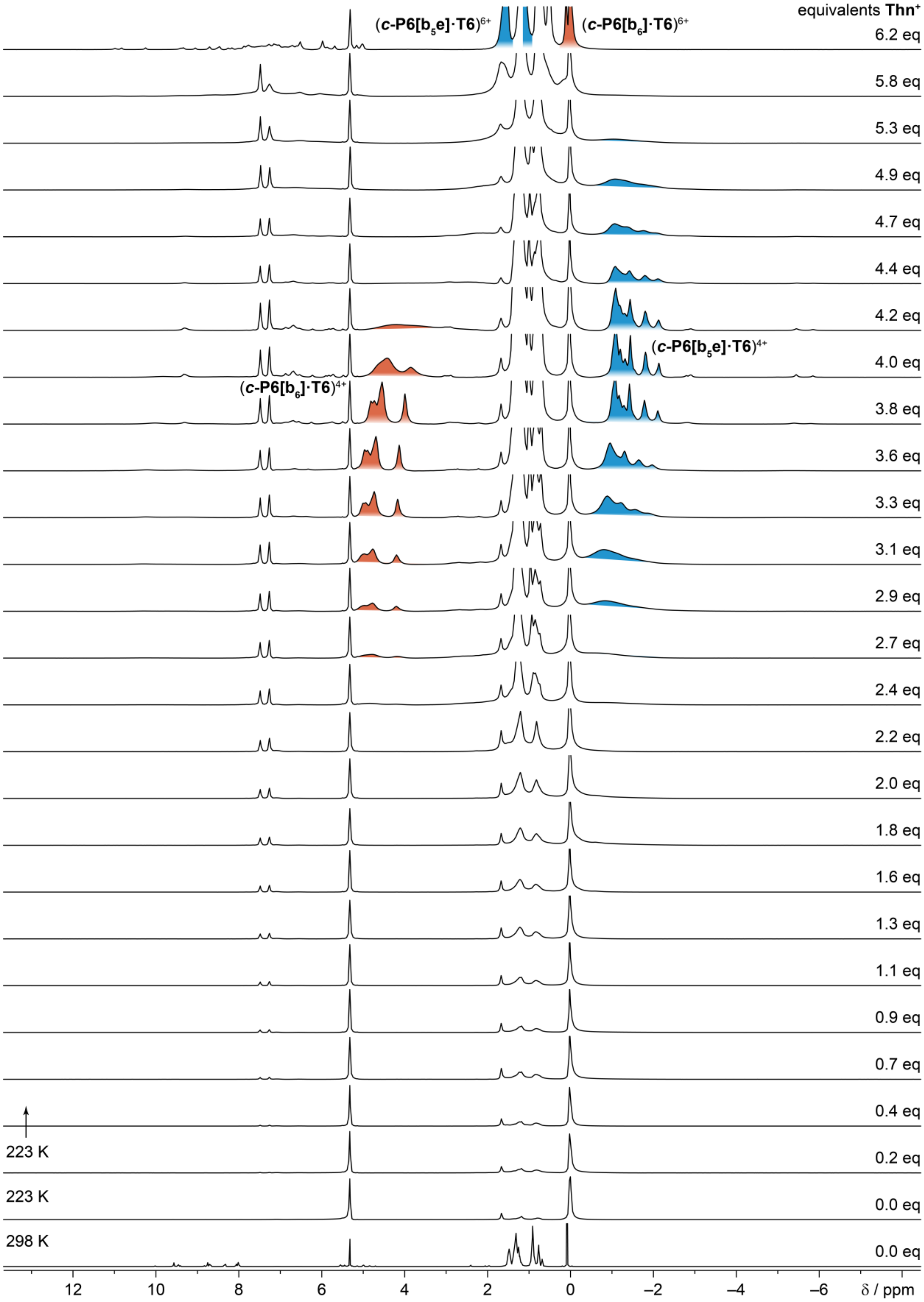

Figure 67: ^{1}H NMR oxidation titration of a mixed sample of ***c*-P6[b$_6$]·T6** and ***c*-P6[b$_5$e]·T6** (500 MHz, 223 K, CD_2Cl_2). THS$_{in}$ resonances are highlighted in color. The concomitant evolution of an aromatic (***c*-P6[b$_5$e]·T6**) and anti–aromatic (***c*-P6[b$_6$]·T6**) current for 4+ and in reverse for 6+ demonstrates the possibility to chemically direct the current without compromising the integrity of the system.

3.3.3. Ethyne-linked 6-porphyrin nanorings *c*-P6[e$_6$] and *c*-P6[be$_5$]

Another class of 6-porphyrin nanoring studied were the ethyne-linked nanorings ***c*-P6[e$_6$]·T6*** and ***c*-P6[be$_5$]·T6*** expanded by one ethyne unit (**Figure 68**).

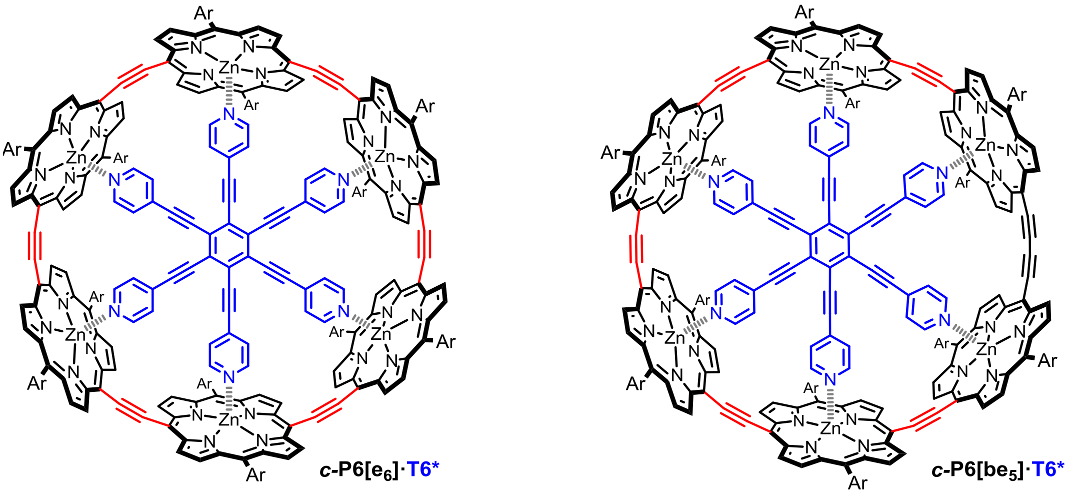

Figure 68: Ethyne-linked nanorings ***c*-P6[e$_6$]·T6*** and ***c*-P6[be$_5$]·T6*** expanded by one ethyne unit.

3.3.3.1. Synthesis and characteristics

The calculated minimum-energy geometries (DFT, B3LYP/6-31G(d)) of the complexes show a relatively bad fit of the **T6*** to make the ***c*-P6[e$_6$]** nanoring, yielding a dome-shaped structure of the **T6***. On the contrary, in a slightly larger ***c*-P6[be$_5$]** nanoring, **T6*** fits ideally (**Figure 69**). This was supported experimentally by UV-vis-NIR complex denaturation titrations. The association constant of **T6*** toward ***c*-P6[e$_6$]** and ***c*-P6[be$_5$]** were found to be 10^{28} M^{-1} and 10^{39} M^{-1}, respectively.

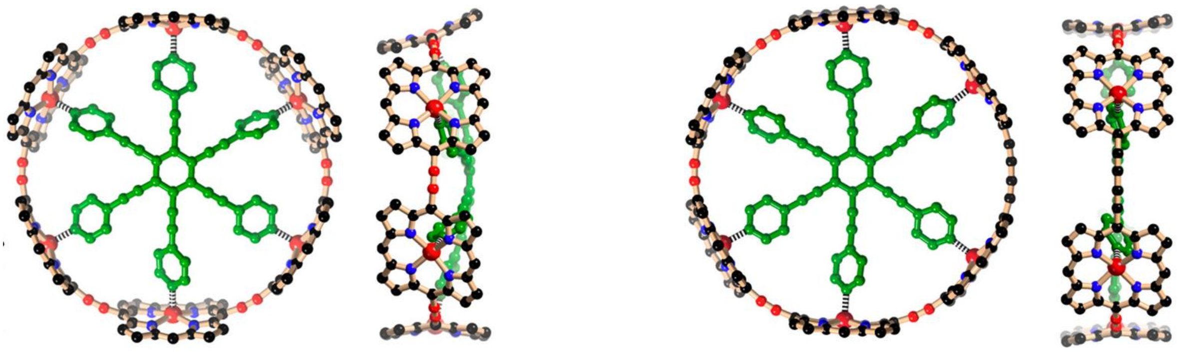

Figure 69: Optimized geometries of ***c*-P6[e$_6$]·T6*** left), and ***c*-P6[be$_5$]·T6*** right).

3.3.3.1.1. Synthesis

Synthesis of symmetric, butadiyne-linked nanorings proceeds *via* Sonogashira-type homo-coupling reaction between two, ethyne-functionalised porphyrins. Nanorings with ethyne linkers are substantially more challenging targets, since the build-up of the oligomer must be carried out *via* Sonogashira cross-coupling. This requires two different coupling partners and any homo-coupling, readily happening in presence of copper salt and traces of oxygen, jeopardise the synthesis of longer oligomers from simple monomers. The synthesis requires a stepwise build-up of hexamer with one halogen- and one ethyne-decorated ends and subsequent cyclisation with template. This challenging synthesis was proposed and carried out by Dr. Michel Rickhaus and Dr. Lara Tejerina (**Figure 70**). The truncated hexadentate ligand **T6*** was designed to fit into the smaller nanoring.

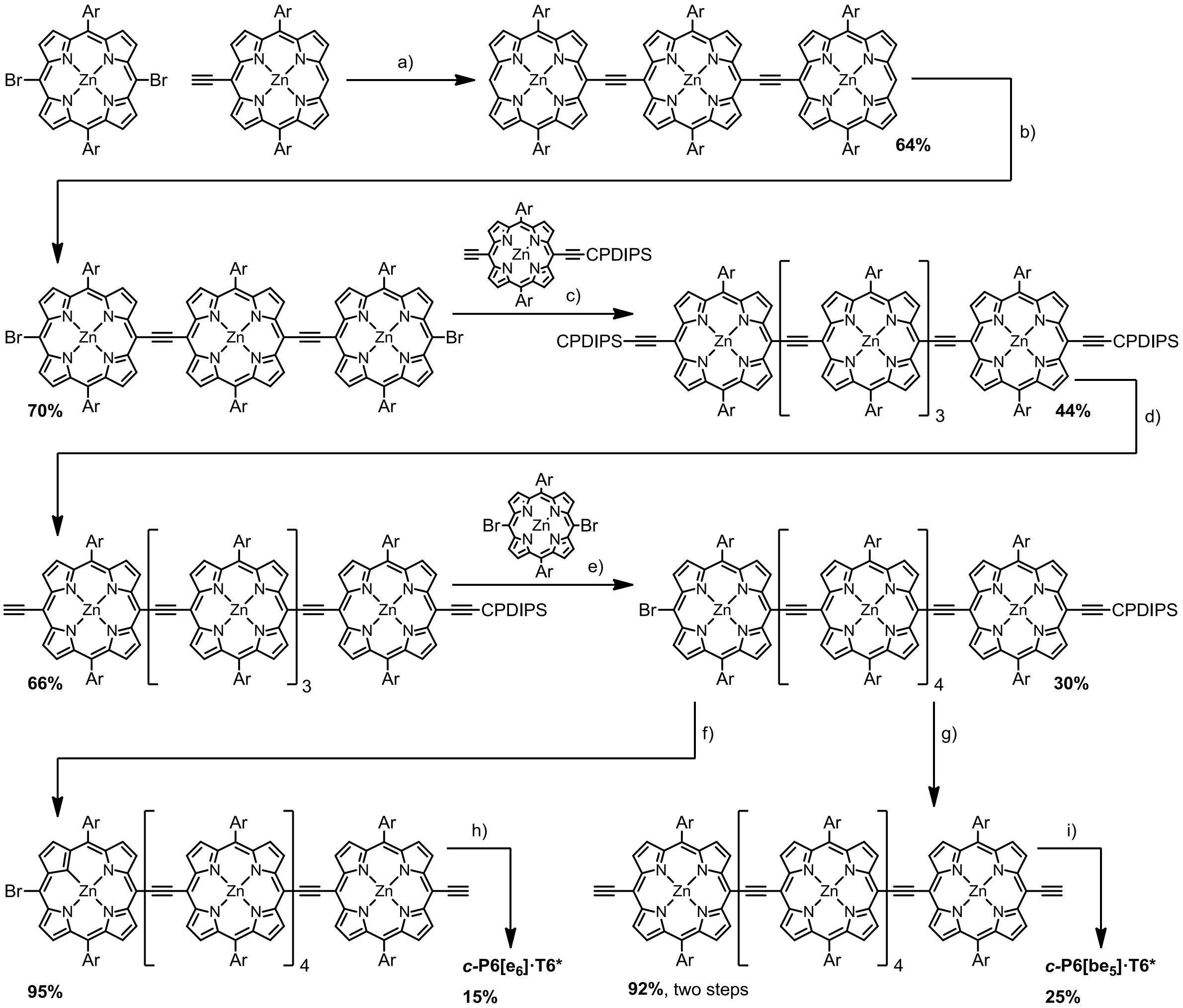

Figure 70: Synthesis of ethyne-linked nanoring ***c*-P6[e$_6$]·T6*** and by one ethyne unit expanded ***c*-P6[be$_5$]·T6***. a) Pd_2dba_3, PPh_3, CuI. b) NBS. c) Pd_2dba_3, PPh_3, CuI. d) TBAF e) $Pd(PPh_3)_4$, CuI. f) TBAF. g) CPDIPS-acetylene, $Pd(PPh_3)_2Cl_2$, CuI; then TBAF. h) **T6***, $Pd(PPh_3)_4$, CuI. i) **T6***, $Pd(PPh_3)_2Cl_2$, CuI, 1,4-benzoquinone.

3.3.3.1.2. NMR characterisation of neutral compounds

^{1}H NMR spectra show similar, inverted features as in case of ***c*-P6[b$_6$]**/***c*-P6[b$_5$e]** pair. ^{1}H NMR of ***c*-P6[e$_6$]** is simple, indicating a D_{6h} symmetric structure on the NMR time scale with resonance **a** at approx. 10 ppm indicating ethyne linked porphyrins. Spectra of ***c*-P6[be$_5$]** possess three sets of template resonances and 6 *beta* porphyrin resonances **a** with one resonance (**a1**) standing out at 9.5 ppm, corresponding to the one next to the butadiyne linker (**Figure 71**). Similar effects are observed for **b** resonances.

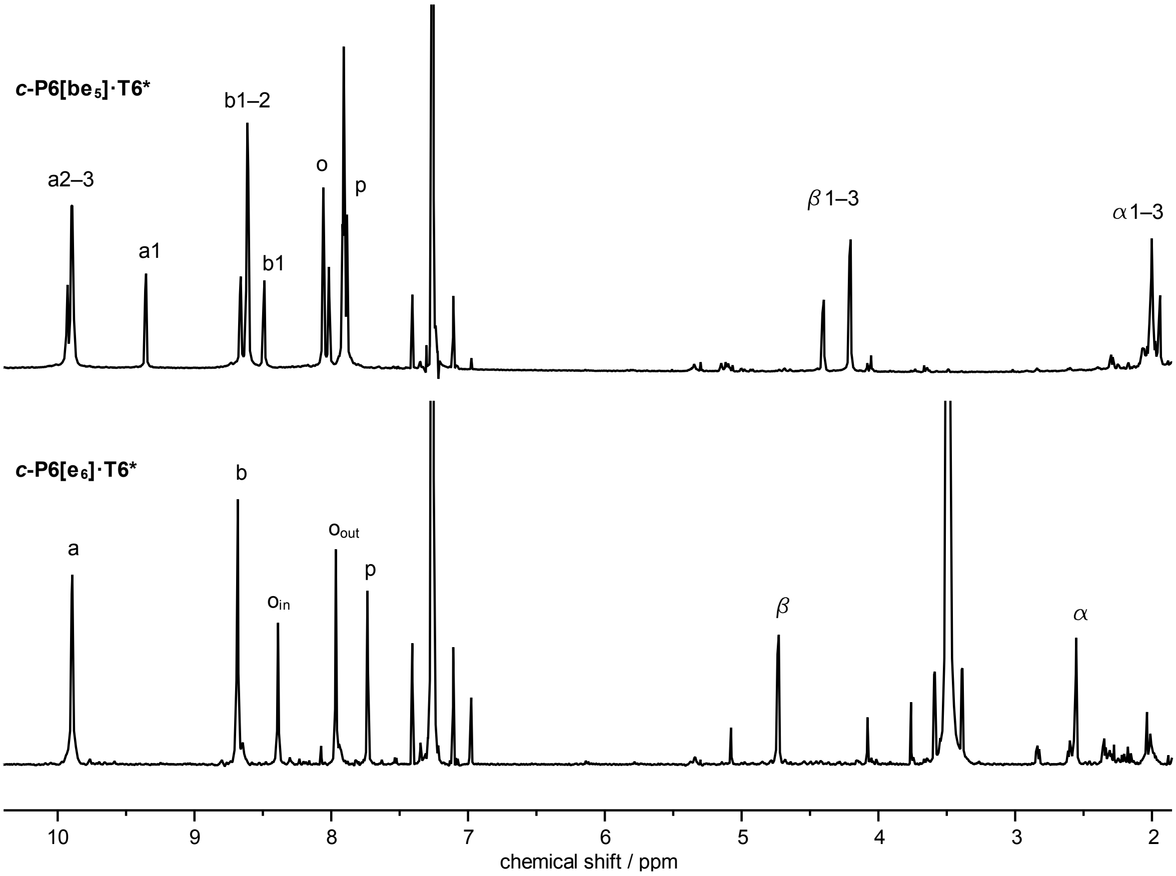

Figure 71: ^{1}H NMR (700 MHz, $CDCl_3$, 25°C) spectra of ***c*-P6[e$_6$]·T6*** and by one ethyne unit expanded ***c*-P6[be$_5$]·T6***.

3.3.3.1.3. Electrochemistry

CV and SW measurements of ***c*-P6[e$_6$]·T6*** show states 1+ to 6+ to be spaced within a wider range than in the case of ***c*-P6[b$_6$]·T6** (**Figure 72**). This finding suggests, that electronic communication within the ethyne linked system is much stronger than in the butadiyne-linked one. In this case, due to low potential of the first oxidation (0 → 1+), referencing to the Fc/Fc+ couple had to be done indirectly, using decamethylferrocene as standard.

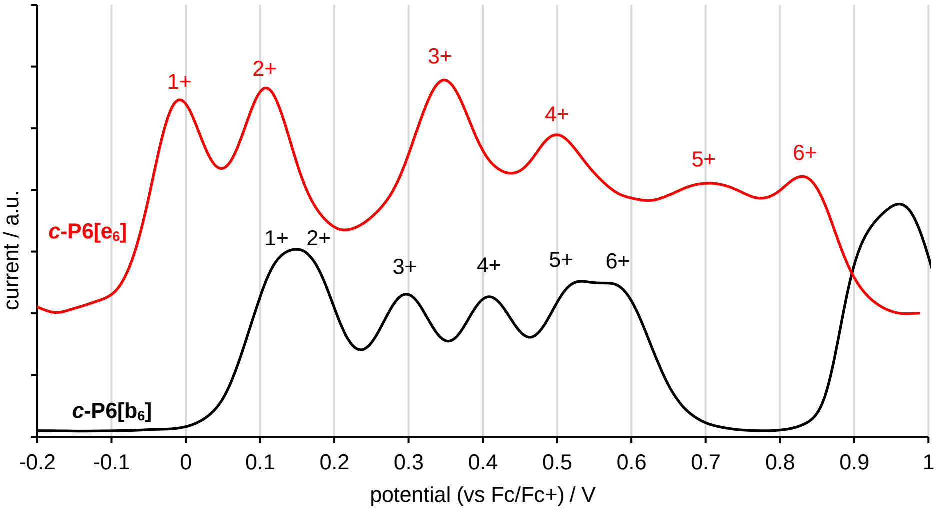

Figure 72: Square-wave voltammogram of ***c*-P6[b$_6$]·T6** (black) and ***c*-P6[e$_6$]·T6*** (red) showing a significantly wider electrochemical envelope within which are spaced reduction potential of 1+ to 6+ states.

3.3.3.1.4. NICS calculation

NICS calculations predict the behaviours expected from Hückel's Rule, the alternation of ring current between states and systems (**Figure 73**). The relation between the symmetric nanoring **_c_-P6[e$_6$]·T6*** and with the butadiyne defect expanded **_c_-P6[be$_5$]·T6*** is analogous to the **_c_-P6[b$_6$]·T6/_c_-P6[b$_5$e]·T6** pair. NICS predicts the strongest ring current for 2+ and 4+ states, regardless of the (anti)aromaticity, and notably, a weaker current for the 6+ state. This is analogous to previous observations, that the *N*+ oxidation states tend to exhibit weaker ring currents.

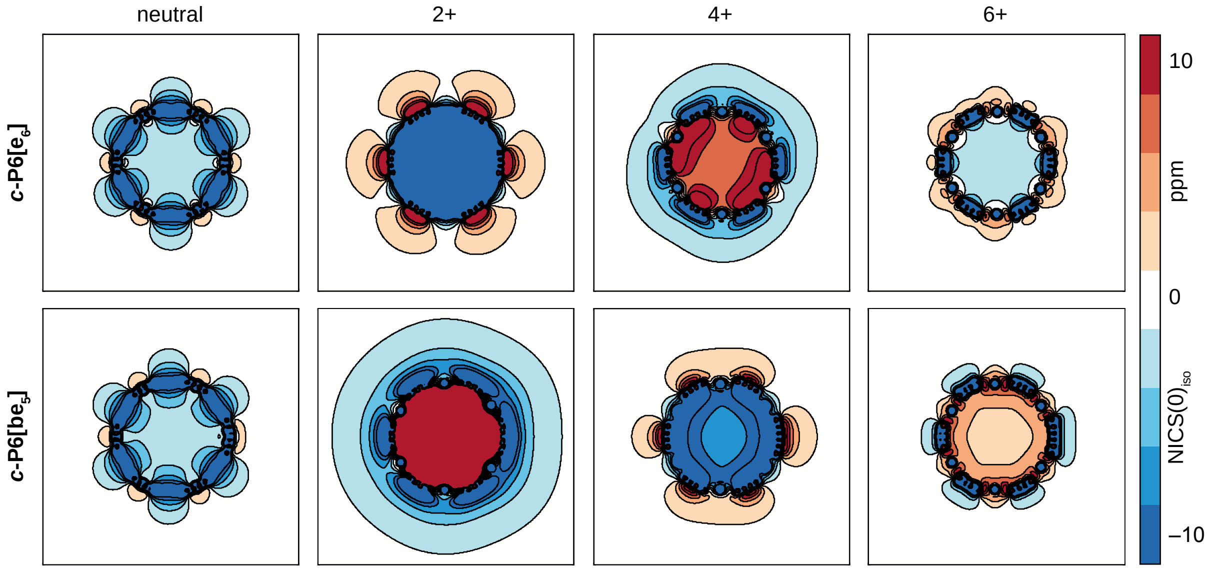

Figure 73: NICS(0)$_{iso}$ (LC-ωhPBE/6-31G*, ω = 0.1) of **_c_-P6[e$_6$]·T6*** and **_c_-P6[be$_5$]·T6*** at oxidation states 0, 2+, 4+, 6+. Templates **T6*** were removed prior NICS calculations.

3.3.3.1.5. NMR oxidations

NMR oxidation was conducted in the same way as with the previous systems. In the case of **_c_-P6[e$_6$]·T6*** (**Figure 74**), surprisingly, a very clear aromatic 2+ state, with sharp NMR signals was observed. This can be explained by the stronger electronic communication in the ethyne-linked nanorings. In the 2+ state of the **_c_-P6[be$_5$]·T6*** (**Figure 75**), only broad features suggesting the global anti-aromaticity were observed. The 4+ states showed the strongest ring currents in both species, affecting most the **α** resonances, which were shifted to +36 and −7 ppm, in an anti-aromatic (**_c_-P6[e$_6$]·T6***)$^{4+}$ and an aromatic (**_c_-P6[be$_5$]·T6***)$^{4+}$, respectively. The 6+ state showed weaker, but clearly identifiable (anti)aromaticity, obeying the Hückel Rule.

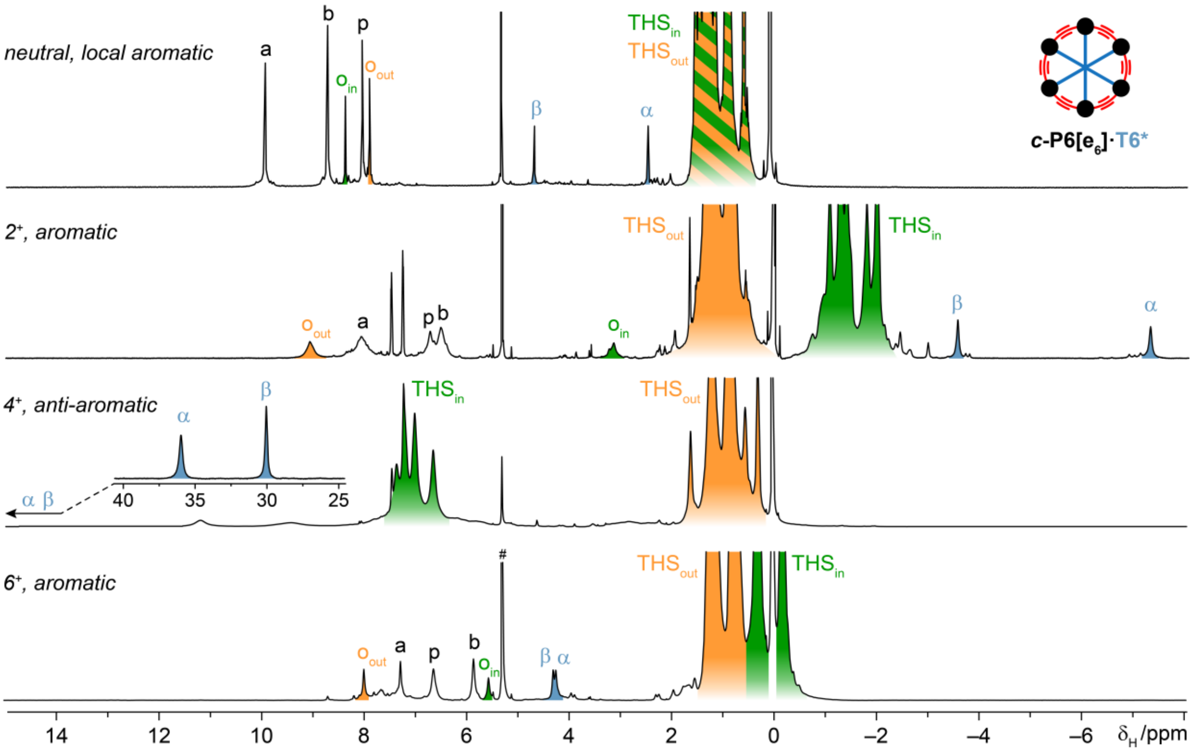

Figure 74: ^{1}H NMR (500 MHz, CD_2Cl_2) of 0, 2+, 4+ and 6+ state of ***c*-P6[e₆]·T6***.

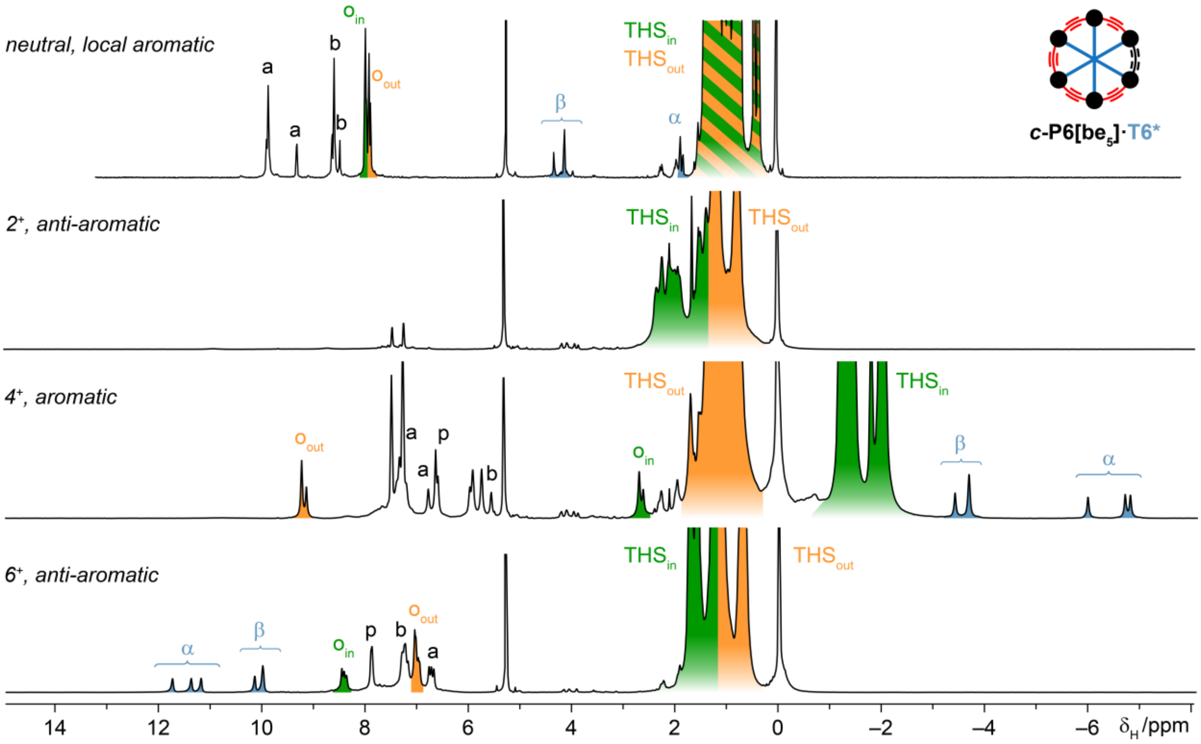

Figure 75: ^{1}H NMR (500 MHz, CD_2Cl_2) of 0, 2+, 4+ and 6+ state of ***c*-P6[be₅]·T6***.

3.3.4. Summary of 6-porphyrin nanorings aromaticity

The oxidation of four 6-porphyrin nanorings to oxidation states 2+, 4+ and 6+ has provided six globally aromatic and six globally anti-aromatic species. This series has assessed the alternation of ring current by oxidation and by tuning the π electron count by varying the type and number of linkers. This self-complemental check creates a solid foundation for the analysis and interpretation of the changes in chemical shifts of oxidised nanorings and allow for the conclusion that the observed effects solely originate from the global (anti)aromaticity (**Table 1**).

	Hückel π electron count				*Experimental $\Delta\delta_{THS}$ values*			
	c*-P6[e$_6$]·T6	***c*-P6[be$_5$]·T6***	***c*-P6[b$_5$e]·T6**	***c*-P6[b$_6$]·T6**	***c*-P6[e$_6$]·T6***	***c*-P6[be$_5$]·T6***	***c*-P6[b$_5$e]·T6**	***c*-P6[b$_6$]·T6**
neutral	72	74	82	84	−2.22	−2.52	−1.63	−1.44
2+	70	72	80	82	−12.6	14.1	25.3	−10.9
4+	68	70	78	80	7.38	−7.60	−6.70	6.35
6+	66	68	76	78	−2.09	2.80	1.63	−1.84

Table 1: π-electron count and observed differences Δδ, between inner and outer THS groups. Globally aromatic and anti-aromatic states are highlighted in blue and red, respectively.

The observed effects were further supported by DFT NICS calculations, both in the absence (**Figure 76**) and presence (**Figure 77**) of templates within the structures.

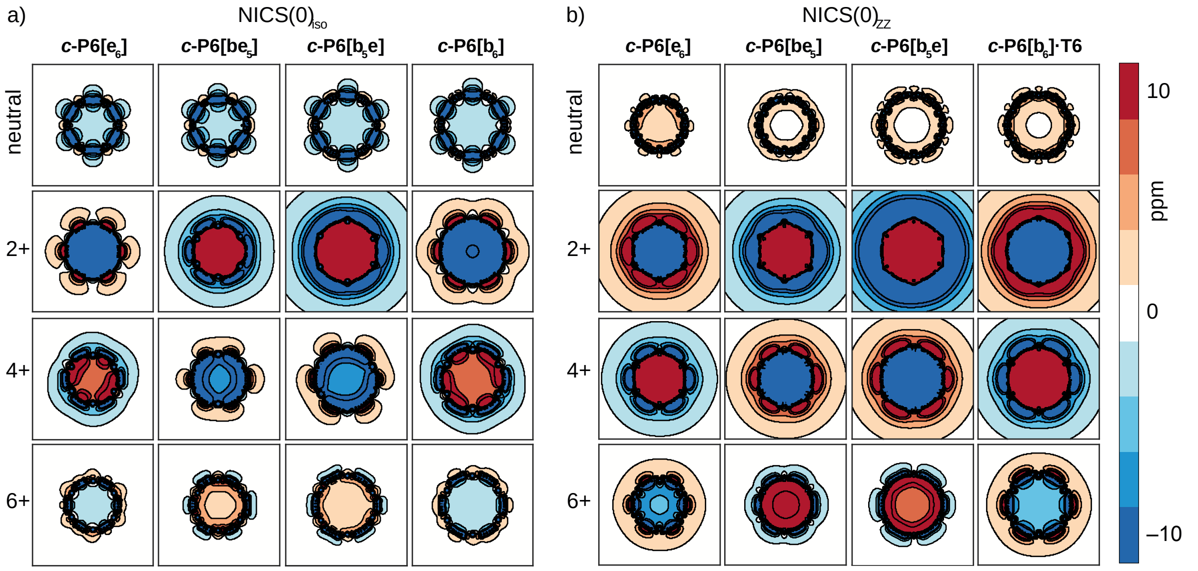

Figure 76: a) NICS(0)$_{\mathrm{iso}}$ and b) NICS(0)$_{\mathrm{ZZ}}$ plots of ***c*-P6[e$_6$]**, ***c*-P6[be$_5$]**, ***c*-P6[b$_5$e]** and ***c*-P6[b$_6$]** at oxidation states 0, 2+, 4+ and 6+. Geometries were optimised using LC-ωhPBE/6-31G* with ω = 0.1 at every oxidation state with the appropriate template. NICS were calculated in the absence of template on a planar grid bisecting the Zn atoms (50 Å × 50 Å, spacing 0.4 Å). The colour axis is truncated above (red) and below (blue) 10 ppm and −10 ppm, respectively. Contours are drawn every 2.5 ppm, from –10 to 10 ppm.

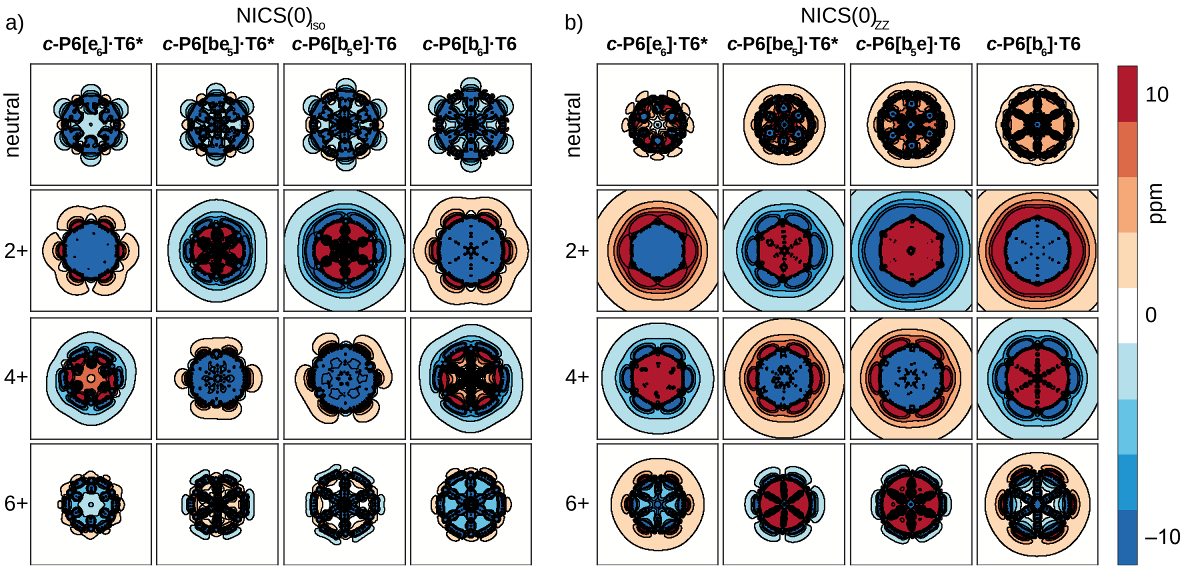

Figure 77: a) NICS(0)$_{iso}$ and b) NICS(0)$_{ZZ}$ plots of ***c*-P6[e$_6$]**, ***c*-P6[be$_5$]**, ***c*-P6[b$_5$e]** and ***c*-P6[b$_6$]** at oxidation states 0, 2+, 4+ and 6+. Geometries were optimised using LC-ωhPBE/6-31G* with ω = 0.1 at every oxidation state with the appropriate template. NICS were calculated in the absence of template on a planar grid bisecting the Zn atoms (50 Å × 50 Å, spacing 0.4 Å). The colour axis is truncated above (red) and below (blue) 10 ppm and −10 ppm, respectively. Contours are drawn every 2.5 ppm, from –10 to 10 ppm.

More details from experimental NMR data are summarised in **Tables 2–6**.

c*-P6[e$_6$]·T6	**0+** / 298K		**2+** / 223 K		**4+** / 253 K		**6+** / 233 K	
	^{1}H	**^{13}C**	**^{1}H**	**^{13}C**	**^{1}H**	**^{13}C**	**^{1}H**	**^{13}C**
α	2.46	143.3	−7.33	133.6	36.0	—	4.27	145.1
β	4.68	123.4	−3.57	115.2	30.1	—	4.32	125.1
a	9.93	130.3	8.06	129.9	—	—	7.31	127.0
b	8.71	133.5	6.51	—	—	—	5.88	134.2
p	8.03	140.0	6.72	—	—	—	6.66	142.3
o$_{in}$	8.36	139.7	3.15	—	—	—	5.59	—
o$_{out}$	7.89	140.6	9.07	—	—	—	8.02	—
THS$_{in}$-CH$_2$	0.96, 0.90	13.1, 13.0	−1.80	9.9	—	—	−0.16	10.9
THS$_{out}$-CH$_2$	0.96, 0.90	13.1, 13.0	0.82	12.2	0.79, 0.60	12.6, 12.6	0.81	12.1
THS$_{in}$-CH$_3$	0.60, 0.88	14.2, 14.4	−1.99	11.5	7.42–6.71	—	−0.11	13.5
THS$_{out}$-CH$_3$	0.60, 0.88	14.2, 14.4	0.93, 0.81	14.5, 14.5	0.83, 0.65	15.0, 15.0	0.90, 0.83	14.0, 14.3

Table 2: NMR data obtained for observed oxidation states of ***c*-P6[e$_6$]·T6***.

c*-P6[be$_5$]·T6	**0+** / 298 K		**2+** / 223 K		**4+** / 223 K		**6+** / 223 K	
	^{1}H	**^{13}C**	**^{1}H**	**^{13}C**	**^{1}H**	**^{13}C**	**^{1}H**	**^{13}C**
α	2.01, 1.94	143.1, 142.9	—	—	−6.00, −6.72, −6.82	134.7, 134.2, 134.6	11.8, 11.4, 11.2	—
β	4.39, 4.18	123.5, 123.3	—	—	−3.42, −3.70	116.1, 116.0	10.2, 10.0	—
a	9.95–9.92, 9.37	129.9, 130.3	—	—	7.33–7.21, 6.78, 6.59	—	6.81–6.72	—
b	8.66, 8.61, 8.49	133.0, 133.2, 133.3	—	—	5.97–5.56	132.6	7.32–7.22	—
p	7.96	140.3	—	—	6.63	140.0	7.93–7.92	—
o$_{in}$	8.06, 8.01	139.2, 139.6	—	—	2.70, 2.60	135.5, 135.6	8.50–8.41	—
o$_{out}$	7.94	140.3	—	—	9.23–9.14	137.6	7.09–6.99	—
THS$_{in}$-CH$_2$	0.78	12.6	—	—	−1.98	9.5	1.34	12.2
THS$_{out}$-CH$_2$	0.88	12.6	0.84	12.1	0.86	12.2	0.71	12.0
THS$_{in}$-CH$_3$	0.51, 0.43	13.9, 13.8	1.54, 1.51	15.2, 14.6	−1.80, −2.05	11.9, 11.7	1.17	14.7
THS$_{out}$-CH$_3$	0.89	14.1	0.80	14.4	0.97, 0.81	14.7, 14.5	0.74	14.3

Table 3: NMR data obtained for observed oxidation states of ***c*-P6[be$_5$]·T6***.

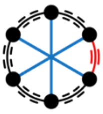

c-**P6[b$_5$e]·T6**	**0+** / 298 K		**2+** / 253 K		**4+** / 223 K		**6+** / 223 K	
	^{1}H	^{13}C	^{1}H	^{13}C	^{1}H	^{13}C	^{1}H	^{13}C
α	2.06, 2.00–1.95	142.4, 142.4	—	—	−5.79, −5.39	—	11.0, 10.8, 10.2	149.5, 150.0, 149.5
β	4.86–4.83, 4.71	119.6, 119.7	—	—	−2.74, −2.85	—	9.40, 9.34, 9.06	124.8, 124.8, 125.1
γ	5.35, 5.15	124.4, 124.0	—	—	—	—	8.71–8.51	127.2
δ	5.54, 5.49, 5.27	131.1, 131.1, 131.1	—	—	—	—	8.47–8.25	127.0
a	10.0, 9.46–9.41	130.9, 131.1	—	—	7.48, 6.89–6.57	—	8.17–6.62	—
b	8.84, 8.71–8.66	133.8, 133.8	—	—	6.21, 5.91–5.53	—	8.17–6.62	—
p	8.00	139.7	—	—	6.70, 5.73	—	8.17–6.62	—
o$_{in}$	8.36, 8.33	140.0	—	—	3.06–2.92	—	8.17–6.62	—
o$_{out}$	8.05–8.03	141.6	—	—	9.34–9.30	—	8.17–6.62	—
THS$_{in}$-CH$_2$	0.92	12.9	1.25	12.9	−1.79	9.61	1.19	12.2
THS$_{out}$-CH$_2$	0.92	12.9	0.86	12.6	0.88	12.3	0.72	11.8
THS$_{in}$-CH$_3$	0.90, 0.77, 0.69	14.5, 14.5, 14.5	1.06	14.8	−1.42, −2.11	12.5, 11.8	1.13	14.7
THS$_{out}$-CH$_3$	0.90, 0.77, 0.69	14.5, 14.5, 14.5	0.85	14.5	1.00	14.8	0.79	14.3

Table 4: NMR data obtained for observed oxidation states of ***c*-P6[b$_5$e]·T6**.

c-**P6[b$_6$]·T6**	**0+** / 298 K		**2+** / 253 K		**4+** / 223 K		**6+** / 223 K	
	^{1}H	^{13}C	^{1}H	^{13}C	^{1}H	^{13}C	^{1}H	^{13}C
α	2.41	143.4	—	—	22.7	—	5.71	145.9
β	4.99	119.9	—	—	19.9	—	5.27	—
γ	5.45	124.3	2.69	—	—	—	5.17	—
δ	5.56	131.2	3.00	—	—	—	5.17	—
a	9.56	130.6	—	—	—	—	6.52	128.2
b	8.75	133.3	—	—	—	—	5.99	133.4
p	8.02	139.9	—	—	—	—	7.92	—
o$_{in}$	8.32	140.8	—	—	—	—	5.91	—
o$_{out}$	8.06	141.6	—	—	—	—	7.92	—
THS$_{in}$-CH$_2$	0.92	13.0	−0.25	11.4	4.73	14.9	0.00	10.8
THS$_{out}$-CH$_2$	0.92	13.0	0.88	12.4	0.80	11.7	0.73	11.6
THS$_{in}$-CH$_3$	0.91	14.4	−0.26	13.5	4.14	17.3	0.14	13.6
THS$_{out}$-CH$_3$	0.77	14.4	0.92	14.6	0.69	13.9	0.84	14.2

Table 5: NMR data obtained for observed oxidation states of ***c*-P6[b$_6$]·T6**.

c-**P6[b$_6$]·T6f**	**0+** / 298 K			**2+** / 253 K			**4+** / 223 K			**6+** / 223 K		
	^{1}H	^{13}C	^{19}F	^{1}H	^{13}C	^{19}F	^{1}H	^{13}C	^{19}F	^{1}H	^{13}C	^{19}F
α	2.55	142.4	—	—	—	—	24.0	—	—	5.82	—	—
β	4.74	123.4	—	1.63	—	—	20.2	—	—	4.76	—	—
δ	6.12	130.9	—	3.66	—	—	17.6	—	—	5.96	—	—
a	9.68	130.3	—	—	—	—	—	—	—	6.61	—	—
b	8.76	133.2	—	—	—	—	—	—	—	5.96	—	—
p	8.00	139.5	—	—	—	—	—	—	—	7.23	—	—
o$_{in}$	8.17	140.1	—	—	—	—	—	—	—	5.64	—	—
o$_{out}$	8.09	141.2	—	—	—	—	—	—	—	7.74	—	—
THS$_{in}$-CH$_2$	0.92	12.6	—	−0.34	11.1	—	4.91	15.6	—	−0.12	11.1	—
THS$_{out}$-CH$_2$	0.84	12.6	—	0.86	12.3	—	0.91	11.7	—	0.72	11.9	—
THS$_{in}$-CH$_3$	0.91	14.4	—	−0.45	13.0	—	4.74	18.1	—	0.00	13.6	—
THS$_{out}$-CH$_3$	0.72	14.0	—	0.90	14.4	—	0.75	14.3	—	0.83	14.4	—
—CF$_3$^{a}	—	—	−61.7	—	—	−64.7, −61.7	—	—	−51.5, −61.7	—	—	−62.9, −60.7

Table 6: NMR data obtained for observed oxidation states of ***c*-P6[b$_6$]·T6f**. ^{19}F referenced to hexafluorobenzene (−164.8 ppm).

3.4. Aromaticity of 7- and 8-porphyrin nanorings

The natural expansion of this aromaticity study is toward larger porphyrin nanorings. Butadiyne-linked, 7- and 8- nanorings form a logical pair, as the aromaticity, according to Hückel's rule and applied formalism, is a opposite for the same oxidation states. Another nanoring included in the study was the 8-porphyrin nanoring, with all-ethyne linkers (***c*-P8[e$_8$]**) which should have the same global (anti)aromaticity character as the butadiyne-linked nanoring ***c*-P8[b$_8$]** (**Figure 78**).

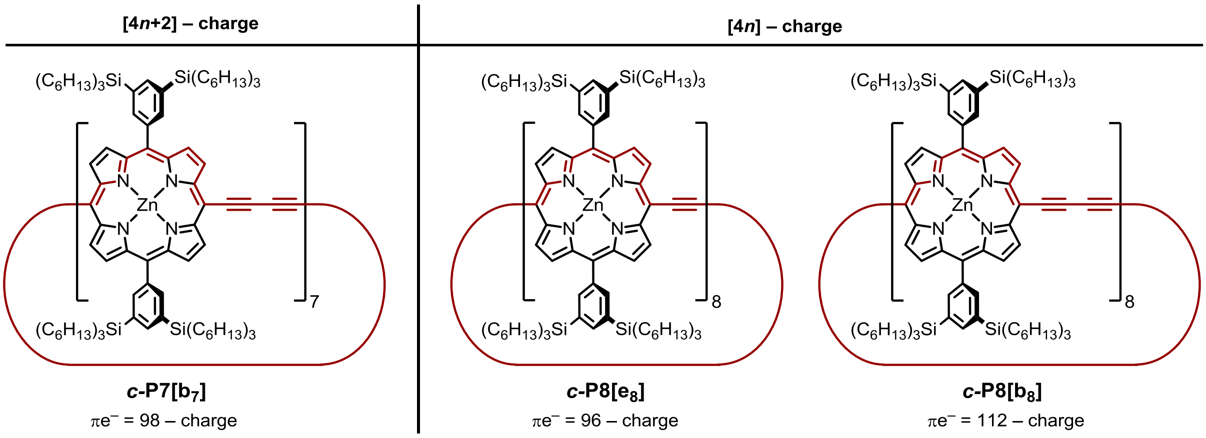

Figure 78: Hückel aromaticity count formalism for ***c*-P7[b$_7$]**, ***c*-P8[e$_8$]**, and ***c*-P8[b$_8$]** cations.

The synthesis of ***c*-P7[b$_7$]** and ***c*-P8[b$_8$]** rings, although with different solubilising groups, has already been reported by our group.[87] The challenging synthesis of ***c*-P8[e$_8$]** has been described elsewhere.[107] The synthesis of ***c*-P7[b$_7$]** and ***c*-P8[e$_8$]** nanorings for this study was performed by Dr. Lara Tejerina and Dr. Michel Rickhaus; while ***c*-P8[b$_8$]** was synthesised by the author.

In this chapter, only template-stabilised complexes will be discussed. Template-free experiments on nanorings ***c*-P7[b$_7$]** and ***c*-P8[b$_8$]** are included in another logical series in **Section 3.5**.

3.4.1. *c*-P7[b$_7$]·T7

3.4.1.1. Model

Synthesis of the 7-porphyrin nanorings followed the recipe reported in literature.[87] The reported heptadentate template **T7** is based on modified β-cyclodextrin (*β*-CD), allowing the otherwise rare 7-fold symmetry (**Figure 79**).

T7

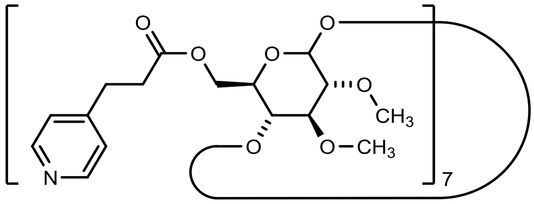

Figure 79: The chemical structure of template **T7**.

The cyclodextrin-based template **T7** is not symmetric with respect to the plane defined by the Zn atoms of the nanoring and the pyridine legs are covalently joined to the cyclodextrin scaffold on the narrower rim. Therefore, the cone of the β-CD points toward one side and this imprints the cone shape to the whole porphyrin scaffold. One can, therefore, expect two environments for both inner and outer THS groups (**Figure 80**).

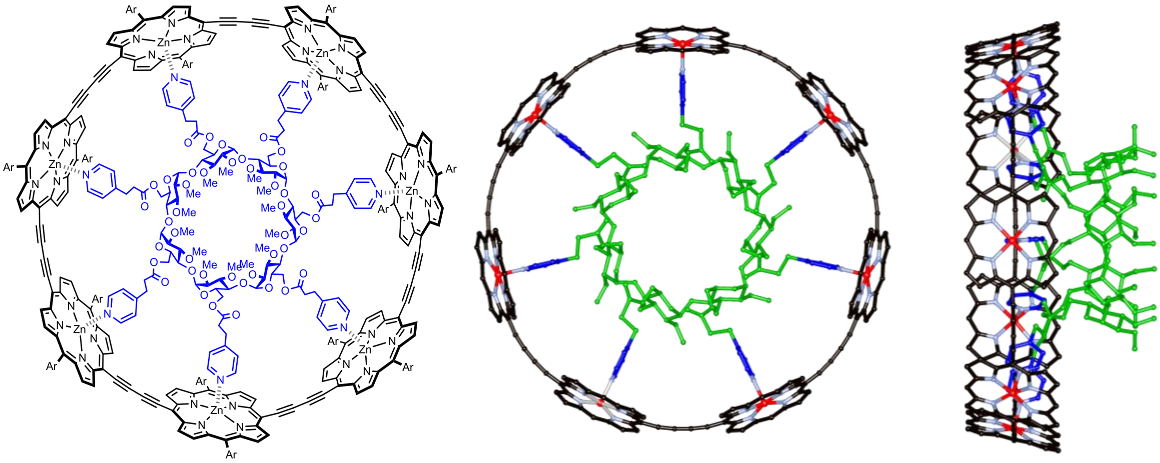

Figure 80: (left) Structure of ***c*-P7[b$_7$]·T7**. Ar = 3,5-bis(trihexylsilyl)phenyl. (middle and right) Molecular mechanics (Hyperchem) based model of the ***c*-P7[b$_7$]·T7** complex.[87]

3.4.1.2. NICS

Due to the complex nature of the **T7**, the computational study was simplified to only template-free nanorings. DFT optimised structures for 4+ and 6+ oxidation states maintained the circular shape and thus were proved to be sufficiently good models for the complex. NICS calculations at these states predicted the aromatic 4+ and the anti-aromatic 6+ state, in agreement with Hückel's rule formalism (**Figure 81**).

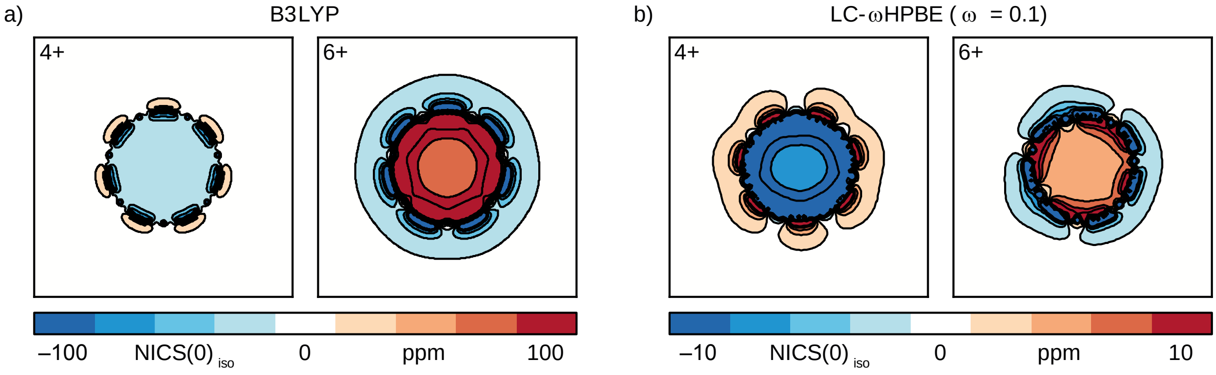

Figure 81: NICS(0)$_{iso}$ of ***c*****-P7[b$_7$]** using a) B3LYP and b) LC-ωhPBE (ω = 0.1) /6-31G* method on geometries optimised with the same methods of 4+ and 6+ states. Different functionals provide qualitatively the same aromaticity prediction, in line with the Hückel Rule.

3.4.1.3. Electrochemistry

The electrochemistry and accessible oxidation states of ***c*****-P7[b$_7$]·T7** was assessed by cyclic and SW voltammetry (**Figure 82**). As expected, several oxidation states within the range of 0.3–1 V (vs. Fc/Fc$^+$) are observed. The 1+ and 2+ states are collapsed as expected; 3+ and 4+ states are well isolated. Interestingly, the 5+, 6+ and 7+ states are very close together, nearly merging into one peak. This could be the result of an anti-aromatic nature of the 6+ state and its ‘vicinity’ to the *N*+ oxidation state.

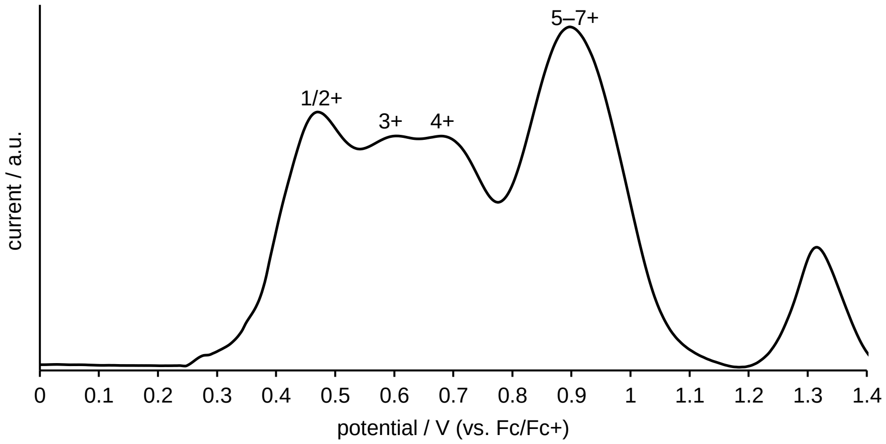

Figure 82: Square-wave voltammogram of ***c*****-P7[b$_7$]·T7** (CH_2Cl_2, −45°C, 0.1 M TBAP as a supporting electrolyte).

3.4.1.4. NMR oxidation

The NMR oxidation titration was performed in the same way as previously described. When approximately 2 equivalents of oxidant were added, weak NMR signals started to intensify, probably as a result of increased solubility of the cations, however, no significant shift of the THS resonances accompanied with this 2+ state was observed. When four equivalents of oxidant were added, the first globally aromatic state was observed with **THS$_{in}$** resonances in the range 0 – −4 ppm, clearly consisting of two THS subunits as a result of the structural dissymmetry (**Figure 83** and **Figure 84**). Further resonances at approximately

−6 ppm were observed, presumably assignable to **T7** (probably **α**/**β** pyridyl signals). These signals were, however, very broad and could not be rigorously assigned by any 2D NMR technique. Upon the addition of a total of six equivalents of oxidant, a globally anti-aromatic state was observed with deshielded $\mathbf{THS_{in}}$ resonances at 1.5 – 4.5 ppm. With further additions of oxidant, soon after, the apparent loss of the **Thn** signals was observed indicating the dynamic exchange between **Thn** and $\mathbf{Thn^{+}}$, further indicating that the *N*+ state had been reached. This 7+ state had no distinctive resonances besides sharp THS signals, at chemical shits similar to non-aromatic states. The reason for such NMR signal broadening is probably one of paramagnetic nature of such an open-shell state promoting fast nuclear relaxation. THS signals were observable probably due to their high intensity, relative remoteness and limited electronic communication with any unpaired spin being localised somewhere on the porphyrin scaffold. Clearly, no global ring current is observed for this 7+ state.

The observed 4+ and 6+ states confirm the Hückel Rule and their aromaticity is reversed compared to ***c*-P6[b$_6$]·T6**. In **Figure 83**, a full titration is shown to illustrate the absence of any observable 2+ state and to show clear aromatic 4+ and anti-aromatic 6+ states.

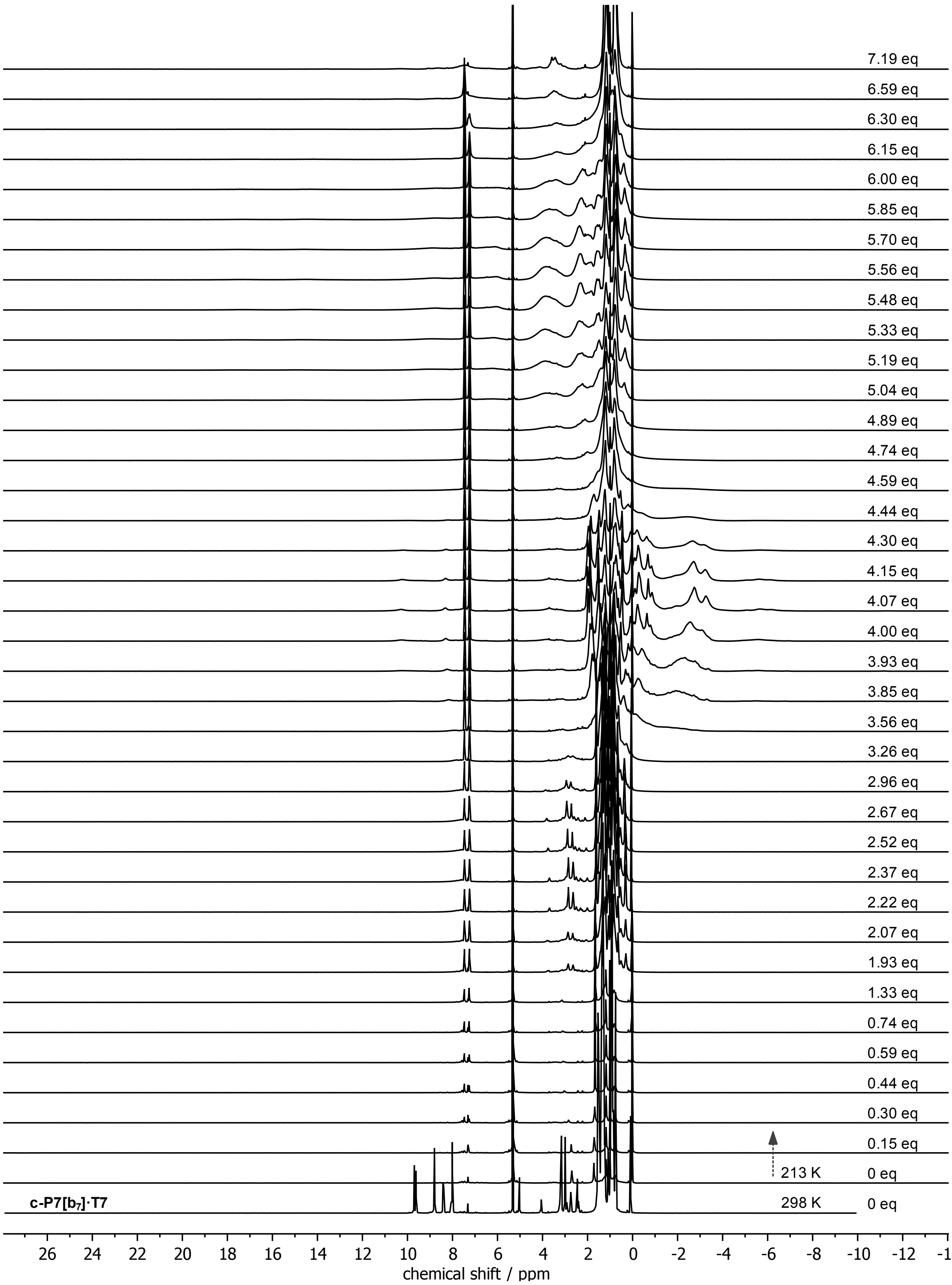

Figure 83: ^{1}H NMR spectra (500 MHz, CD_2Cl_2, 25°C and −60°C) from the oxidation titration of ***c*-P7[b$_7$]·T7**.

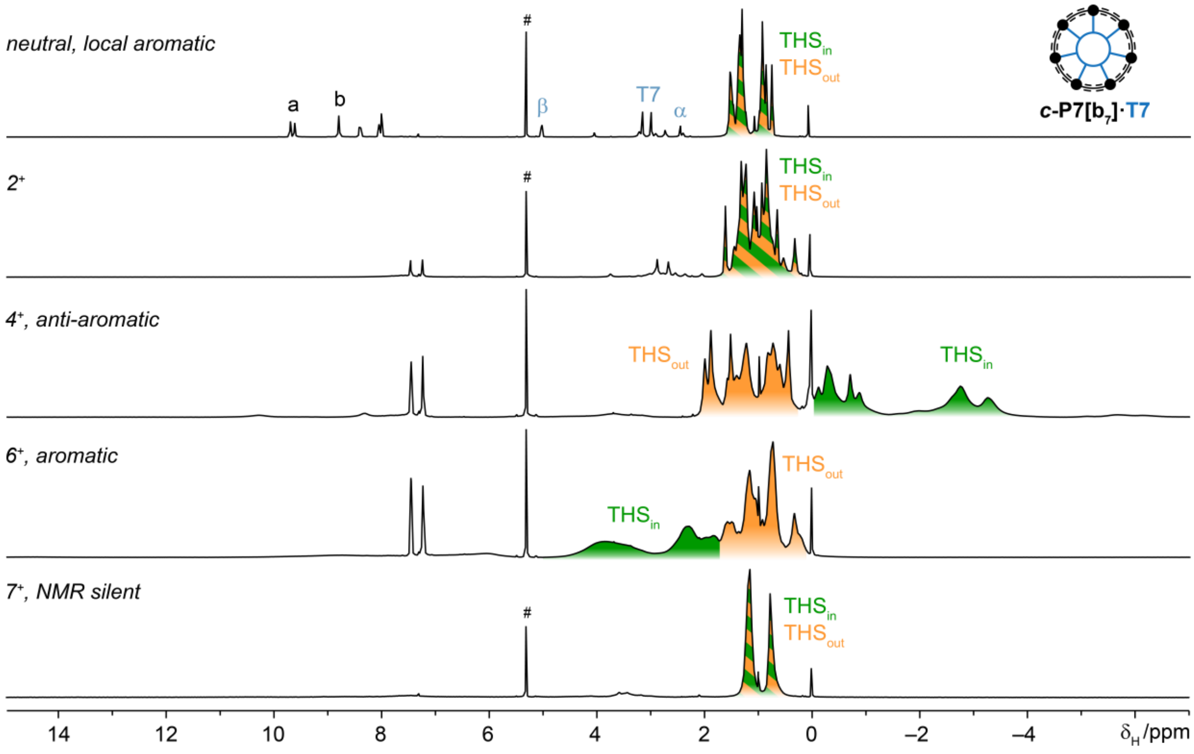

Figure 84: ^{1}H NMR spectra of neutral, 2+, 4+, 6+ and 7+ oxidation states of ***c*-P7[b$_7$]·T7**.

3.4.2. *c*-P8[b$_8$]·(T4)$_2$

A further expansion of the study was toward the 8-porphyrin nanorings. In order to structurally stabilise the ***c*-P8[b$_8$]**, two tetradentate templates, **T4**, were used. The reported[81] octadentate template **T8**, possess an electrochemical active porphyrin core, which can be oxidised to the 1+ state. This would interfere with NMR experiment and therefore the **T8** template was not used (**Figure 85**).

Importantly, ***c*-P8[b$_8$]·(T4)$_2$** is a stable complex, as the tetradentate **T4** is bound sufficiently strongly not to dissociate. Such dissociation would interfere with the NMR oxidations *via* possible nucleophilic pyridine attack toward any oxidised porphyrin).[84]

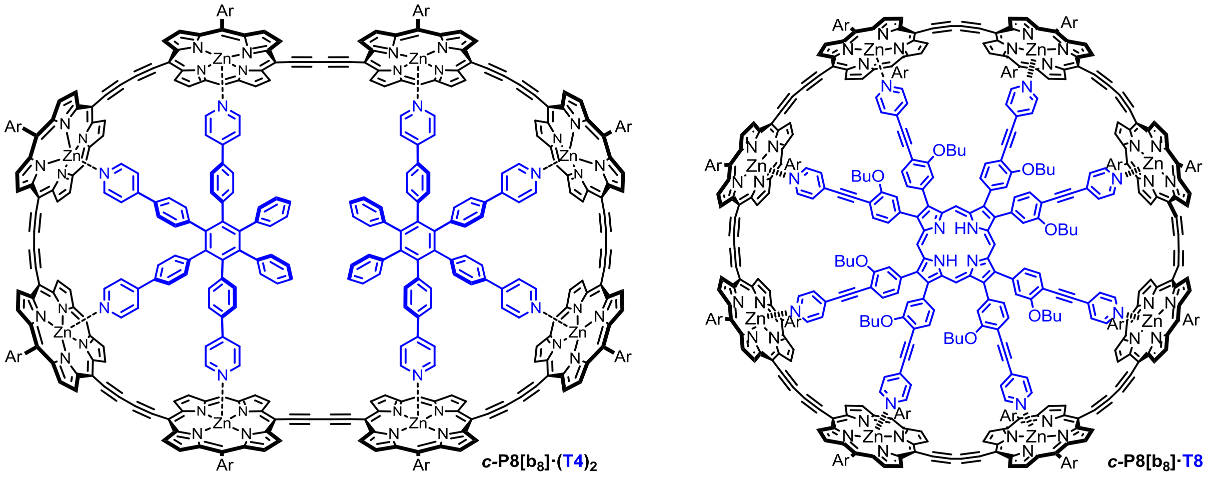

Figure 85: Structures of ***c*-P8[b$_8$]·(T4)$_2$** and ***c*-P8[b$_8$]·T8**.

3.4.2.1. Model

The structure of ***c*-P8[b$_8$]·(T4)$_2$** with the aryl solubilising groups replaced by −H, was optimised using DFT methods (same as for the NICS) for each observable oxidation states. The structures adopt a flat, elliptic shape which barely deviates between the different oxidation states. Such structural rigidity is probably the result of a good template fit (**Figure 86**).

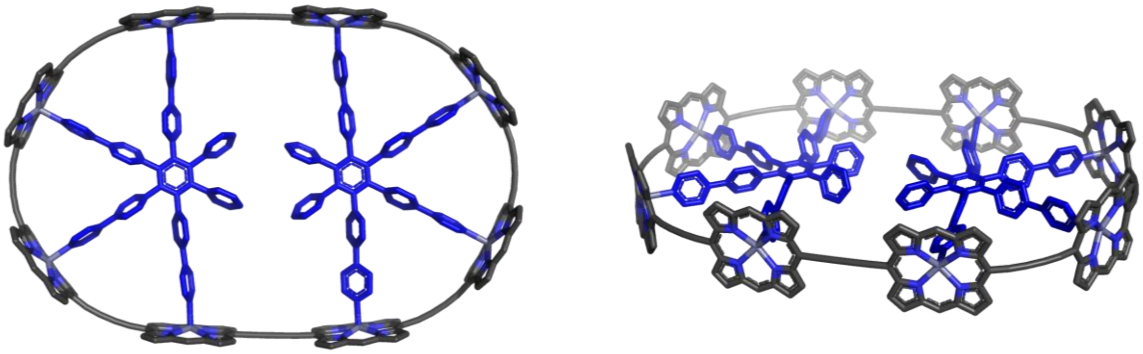

Figure 86: The model of ***c*-P8[b$_8$]·(T4)$_2$**, geometry was optimised using the B3LYP/6-31G* method.

3.4.2.2. NICS

NICS calculations corroborates the predictions of Hückel theory for the anti-aromatic 4+ and 8+, and aromatic 6+ state. The B3LYP functional-based NICS exaggerates the ring current of the anti-aromatic 4+ state and predicts a weak paratropic ring current for the 8+ state. The more localising LC-ωhPBE functional predicts a much weaker paratropic ring current for the 4+ state and exaggerates the diatropic ring current for the 6+ state. Interestingly, both methods predict significantly weaker ring current for the 8+ state, and in the case of the LC-ωhPBE functional, this is nearly negligible (**Figure 87**).

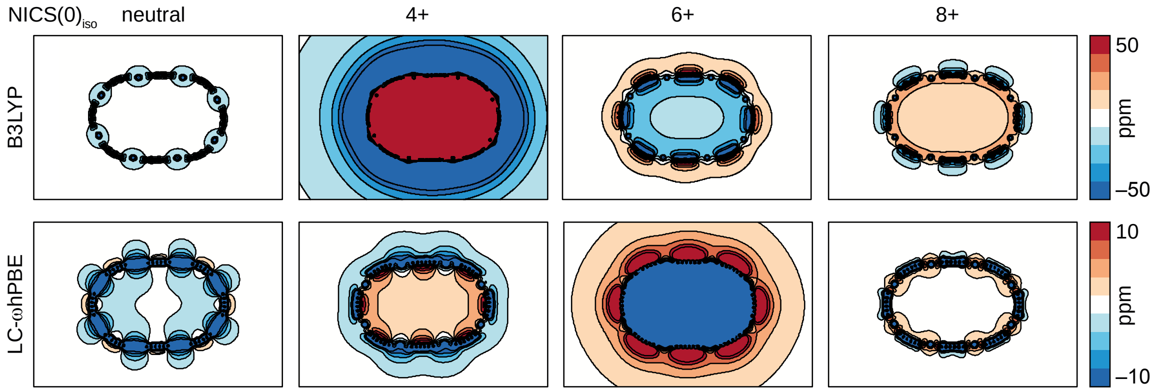

Figure 87: NICS(0)$_{iso}$ of neutral, 4+, 6+ and 8+ of optimised ***c*-P8[b$_8$]·(T4)$_2$**, using B3LYP (top) or LC-ωhPBE (bottom). Templates were removed prior to NICS, the grid size is 50×75 Å^2 with 0.4 Å spacing.

3.4.2.3. NMR oxidation

Oxidations were performed similarly as to discussed previously. The first observed oxidation state was the 4+. The 4+ oxidation state emerges after addition of approximately 2 equivalents of **Thn**$^+$ and the ^{1}H NMR signal intensity of the state continue to grow until a total 4 equivalents of added **Thn**$^+$ have been reached. This can be explained by a higher solubility (at −50°C) of the observed 4+ state, in comparison to any present lower oxidation states or neutral species that may be insoluble or, if soluble, be NMR silent. This hypothesis is supported by the observation that at approximately two equivalents of oxidant, a significant amount of the sample material was clearly not in solution. Use of higher temperatures (e.g. −30°C) was not tested in order to avoid (even partial) decomposition of the nanoring. The 4+ oxidation state was characterised in terms of inner and outer parts by NOESY, however, the inner aromatic signals (**o$_{in}$**, **T4**) were indistinguishable. No ^{1}H-^{13}C NMR correlations were observed for resonances other than **THS**, due to the broad nature of the ^{1}H signals. The anti-aromaticity of the 4+ state is most obviously documented by deshielded **THS$_{in}$** resonances, at 1 – 2.5 ppm. The observed 6+ state is clearly globally aromatic, with **THS$_{in}$** resonances shielded to 0 – −2 ppm and template signals shielded further to −3 – −4 ppm. The 8+ state shows very weak (cf. NICS predicted anti-aromaticity of *N*+ state, **Figure 87**), however, noticeable character of global anti-aromaticity documented by the split of the **THS$_{in/out}$** resonances. Due to the broad nature of the THS signals, the signals of **THS$_{in}$** and **THS$_{out}$** significantly overlap, however, ^{1}H-^{13}C HSQC allows the assignment of these resonances thanks to higher spectral resolution (**Figure 88**).

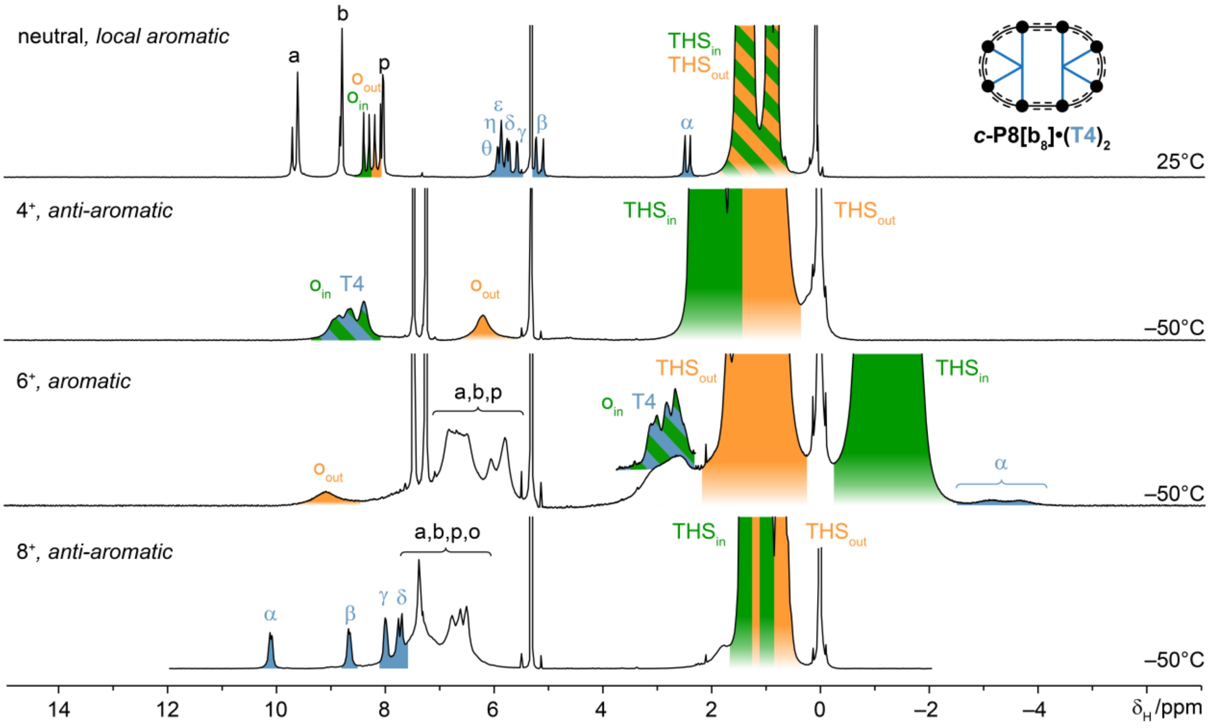

Figure 88: ^{1}H NMR spectra of the neutral, 4+, 6+ and 8+ oxidation states of ***c*-P8[b$_8$]·(T4)$_2$**. Insert in 6+ state shows peaks at ~3 ppm from a slightly different stage of the titration as their sharpest state appeared at a slightly different amount of oxidant added.

3.4.3. *c*-P8[e$_8$]·(T4)$_2$

Another studied member of the 8-porphyrin nanoring family, was the all-ethyne-linked ***c*-P8[e$_8$]·(T4*)$_2$** (**Figure 89**).[107] This nanoring-template complex is analogous to the all-butadiyne-linked complex ***c*-P8[b$_8$]·(T4)$_2$** described above.

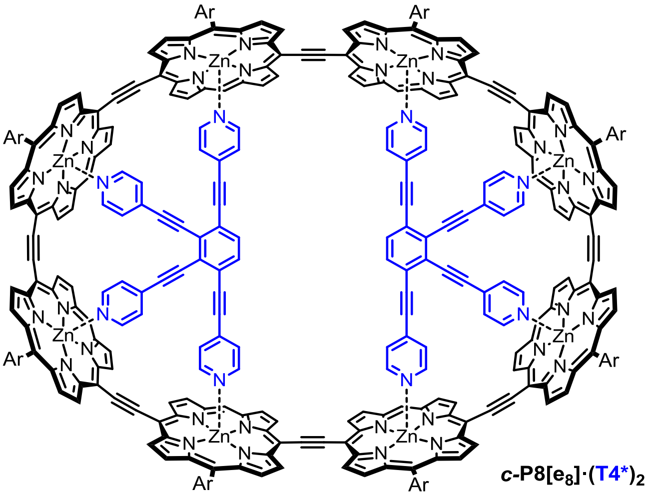

Figure 89: Structure of ***c*-P8[e$_8$]·(T4*)$_2$**.

The synthesis of ***c*-P8[b$_8$]·(T4)$_2$** was conducted by Dr. Michel Rickhaus and Dr. Lara Tejerina by the stepwise build-up of a linear oligomer followed by its cyclisation in the presence of **T4*** template (**Figure 90**).[107]

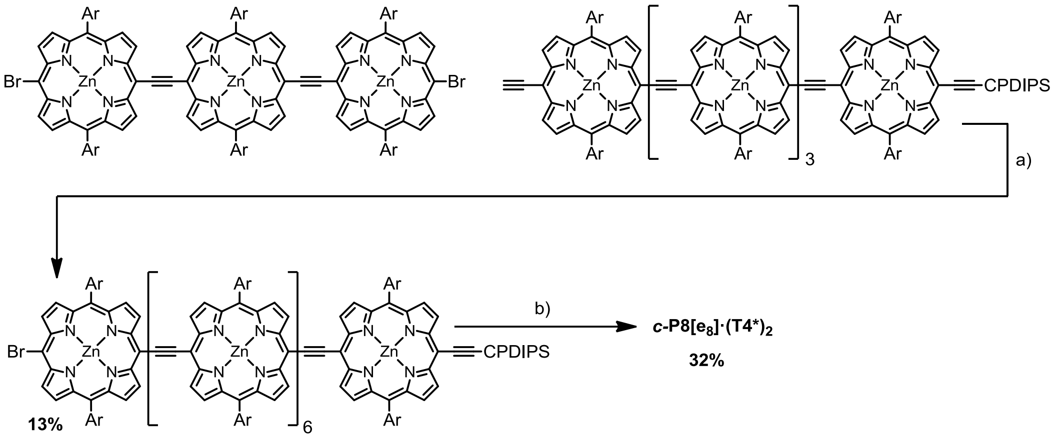

Figure 90: Synthesis of ***c*-P8[e$_8$]·(T4*)$_2$**. a) Pd_2dba_3, PPh_3, CuI. b) TBAF, then **T4***, Pd_2dba_3, PPh_3, CuI.

3.4.3.1. Model

The structure of ***c*-P8[e$_8$]·(T4*)$_2$**, with aryl solubilising groups replaced by −H, was optimised using DFT methods (same as for the NICS) for each of the observable oxidation states. The structure adopts a flat, elliptic shape. Due to the closer vicinity of neighbouring porphyrins, the porphyrin array adopts a slight zig-zag shape (**Figure 91**). These, local, dihedral twists co-planarises more and more, with the increasing oxidation state.

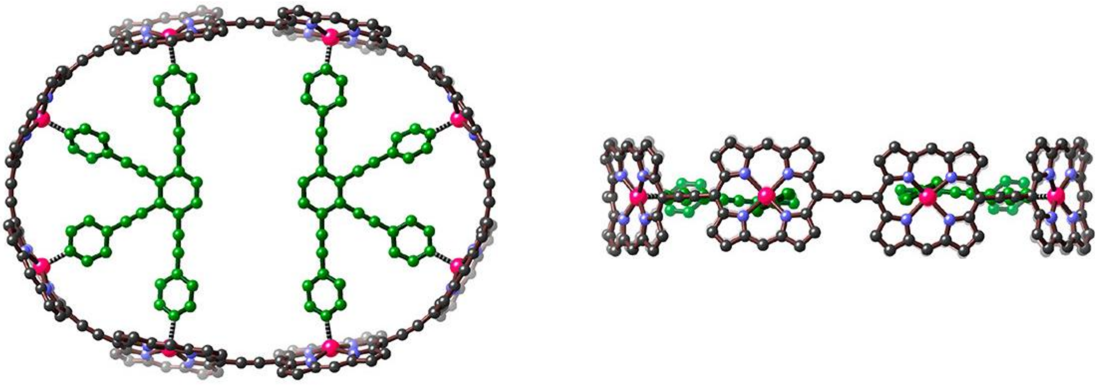

Figure 91: Model of ***c*-P8[e$_8$]·(T4*)$_2$**, geometry was optimised using the B3LYP/6-31G* method.

3.4.3.2. NICS

The NICS calculations corroborated the prediction from the Hückel Rule of an anti-aromatic 4+ and 8+, and an aromatic 2+ and 6+ states. Both B3LYP and LC-ωhPBE functionals provide comparable NICS, predicting strong ring currents for the 2+, 4+ and 6+ states, and significantly weaker currents for the 8+ state (**Figure 92**). Similarly, to NICS calculated for other nanorings, the B3LYP functional-based results exaggerate the strength of the ring current in an anti-aromatic states, and the LC-ωhPBE functional-based results exaggerate the ring current in an aromatic states.

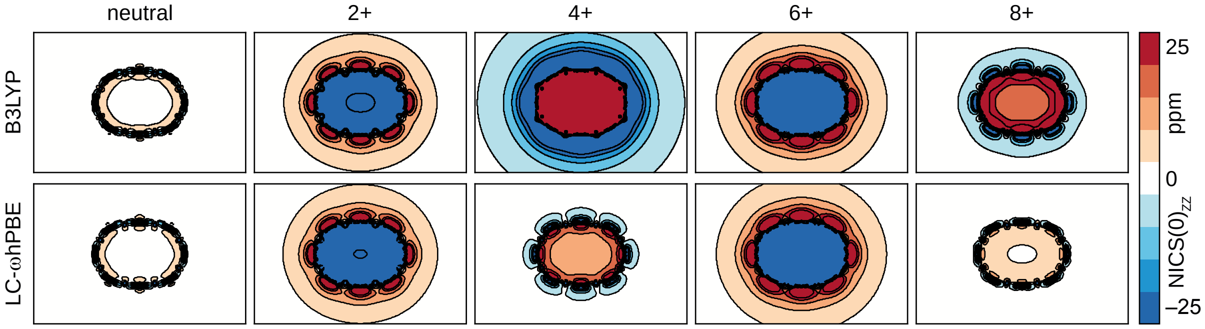

Figure 92: NICS(0)$_{iso}$ (B3LYP or LC-ωhPBE (ω = 0.1)/6-31G*) of neutral, 2+, 4+, 6+ and 8+ calculated on ***c*-P8[e$_8$]·(T4*)$_2$** geometry, optimised for each oxidation state using B3LYP (top) or LC-ωhPBE (ω = 0.1) (bottom). Templates were removed prior to NICS, the grid size is 50×75 Å^2 with 0.4 Å spacing.

3.4.3.3. Electrochemistry

Square wave voltammetry of ***c*-P8[e$_8$]·(T4*)$_2$** and its comparison with ***c*-P8[b$_8$]·(T4)$_2$** confirms the trend observed for the ***c*-P6[e$_6$]·T6*/*c*-P6[b$_6$]·T6** pair (cf. **Figure 72**) of a significantly higher degree of electronic communication in the ethyne-linked nanorings. The electrochemical envelope within which the 1+ – 8+ states of ***c*-P8[e$_8$]·(T4*)$_2$** are distributed is noticeable broader (0–0.9 V vs. Fc/Fc$^+$) (**Figure 93**).

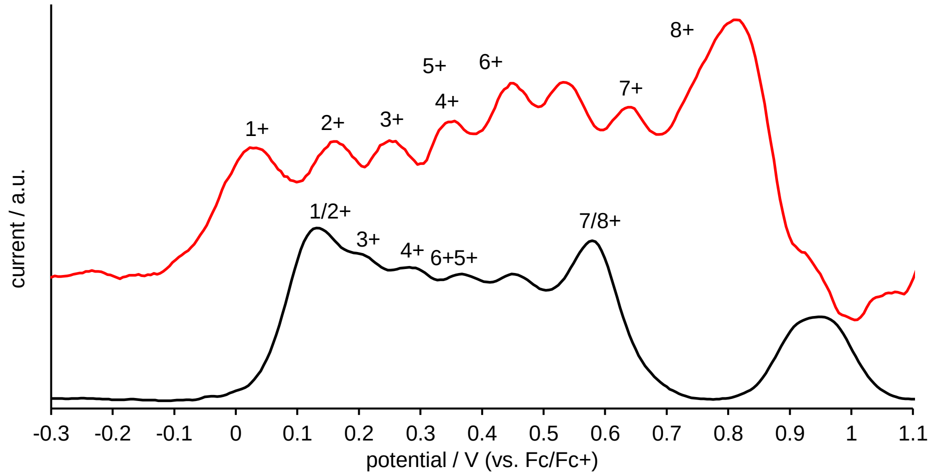

Figure 93: Comparison of SW of the ***c*-P8[e$_8$]·(T4*)$_2$** (red) and ***c*-P8[b$_8$]·(T4)$_2$** (black) (CH_2Cl_2, −45°C, 0.1 M TBAP as a supporting electrolyte).

3.4.3.4. NMR oxidation

The oxidative titration of ***c*-P8[e$_8$]·(T4*)$_2$** showed rather complex behaviour as is apparent from the full titration overview (**Figure 94**).

Firstly, the unexpected 2+ state was observed, as a globally aromatic state documented by the shielding of the **THS$_{in}$** resonances to the region of 0.5 – −1.5 ppm. However, the signal broadness did not allow observation of any other resonances. In addition, further, clear ^{1}H NMR spectra corresponding to 3+, 4+, 5+, 6+ and 8+ states were observed. The 4+ and 8+ states are anti-aromatic, while 2+ and 6+ states are aromatic, as expected from the Hückel Rule.

The states corresponding to 3+ and 5+ exhibit a paratropic ring current. It is not clear what dominant ring current should be expected for these open-shell species (cf. **Figure 13** and reference [108]). However, the fact that the open shell states possess rather sharp NMR spectra is surprising. This is probably the result of very strong electron communication within the porphyrin scaffold, leading to broadening of only the porphyrin resonances, and not the **THS$_{in/out}$**.

The 4+ state possess very deshielded **THS$_{in}$** resonances at ~6 ppm, indicative of a very strong paratropic ring current. The 3+ and 5+ states, exhibit a weaker paratropic ring current, deshielding the **THS$_{in}$** to suspiciously ca. half that of the 4+ state resonance (~3–4 ppm). For all: 3+, 4+ and 5+ states, very deshielded (15–25 ppm) template resonances are observed as well. The unexpected series of the 3+, 4+, 5+ and 6+ states show some overlap, indicating that the species can coexist in slow-exchange regime. Neither extended time delays between **Thn$^+$** additions, nor warm-up cycles (−50°C → −20°C (5 min) → −50°C) changed the ratios between the 3+/4+ and 4+/5+ states, indicating the species and in a thermodynamic equilibrium. All the observed species seem to be assignable to the specific of number of **Thn**$^+$ equivalents added as was confirmed by multiple repeated titrations.

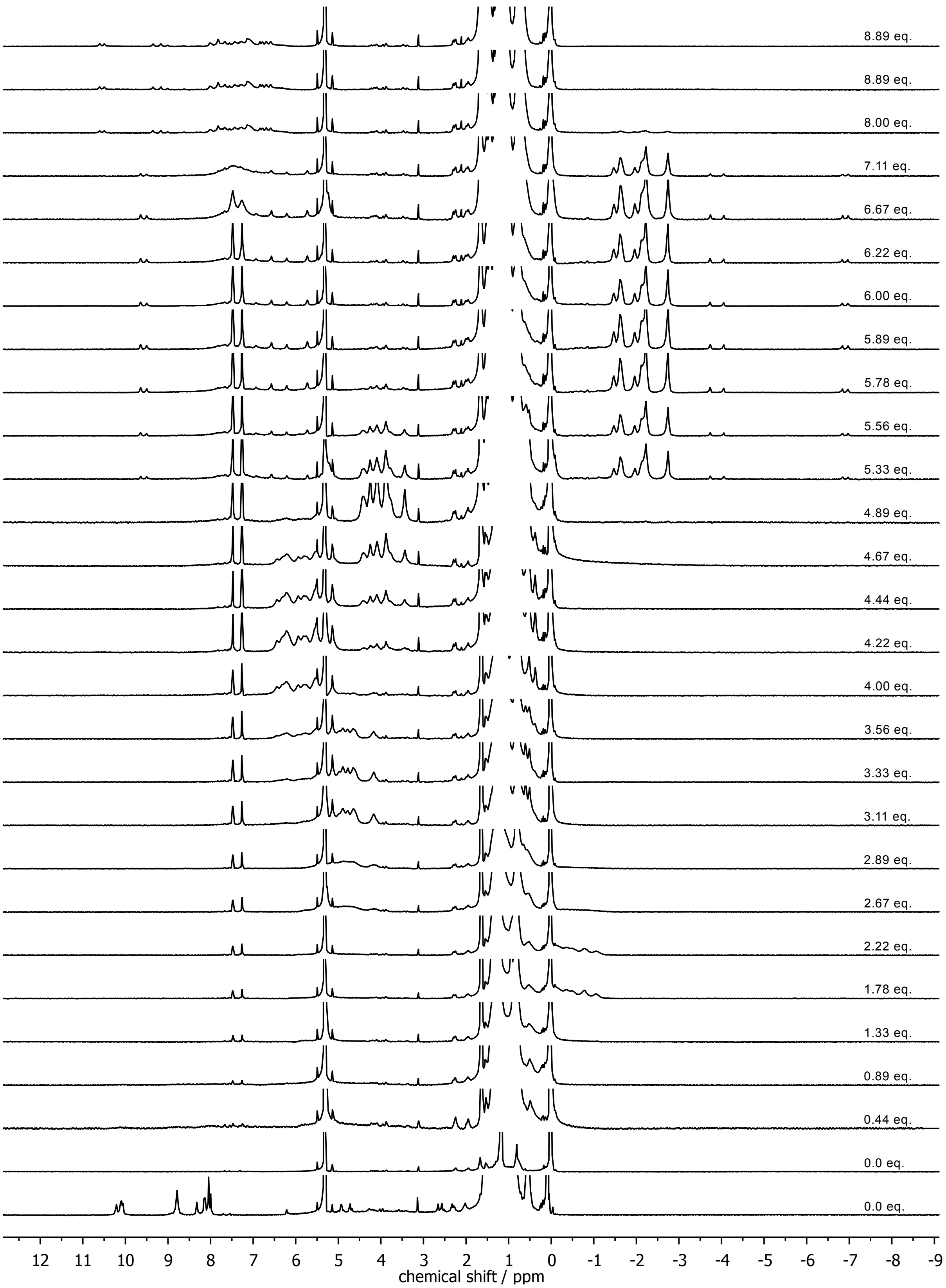

Figure 94: ^{1}H NMR (500 MHz, CD_2Cl_2, 25°C (neutral) and −50°C) spectra of oxidation titration of ***c*-P8[e$_8$]·(T4*)$_2$**.

An alternative explanation for the observed 3+, 4+ and 5+ states would be that in each case, only the 4+ state is observed but as a stable aggregate with another oxidised ring, affecting the observed resonances of the 4+ state (i.e. 3+···4+ and 5+···4+ association complex). Such speculation, however, does not explain why this is only observed in the 4+ state but not in the 6+ oxidation state as no 7+ state is observed.

The 6+ state shows clear evidence of global aromaticity with the **THS$_{in}$** resonances shielded to the range −1 – −3 ppm and with well resolved and assignable α and β resonances deshielded to approximately −7 ppm and −4 ppm, respectively.

The anti-aromatic 8+ state exhibits the weakest global ring current, still with clearly separated **THS$_{in}$/THS$_{out}$** signals and moderately deshielded inner template resonances by ~1 ppm from the chemical shifts of the free template.

The ^{1}H NMR spectra of all the characterised close-shell states are summarised in **Figure 95**, documenting the basic peak assignment (as always based on 2D NMR analysis).

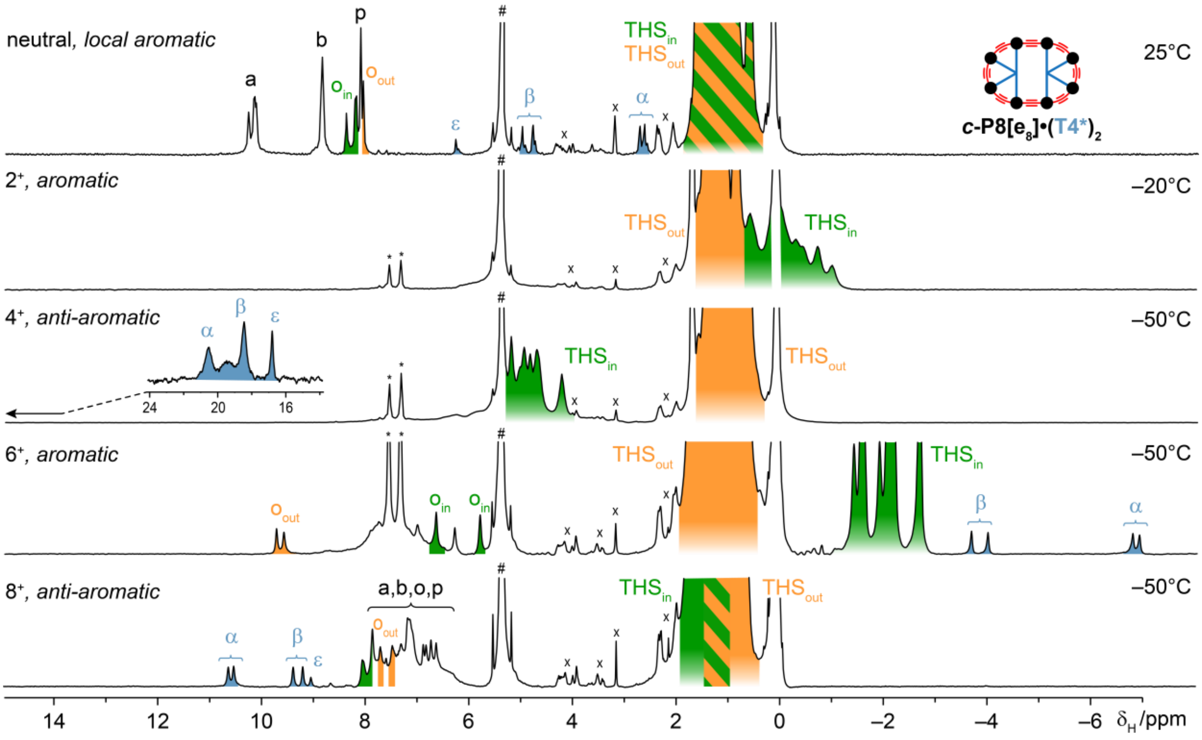

Figure 95: ^{1}H NMR (500 MHz, CD_2Cl_2) spectra of neutral, 2+, 4+, 6+ and 8+ oxidation states of ***c*-P8[e$_8$]·(T4*)$_2$**. The × indicates unidentified impurities, # indicates $CDHCl_2$ signals.

3.4.4. Summary

The 7- and 8- porphyrin nanorings confirm the trends of observing clear ^{1}H-NMR for even-number oxidation states of charges above ~ +*N*/3. All such states obey the Hückel Rule.

The ***c*-P8[e$_8$]·(T4)$_2$** complex exhibits surprisingly sharp ^{1}H-NMR spectra for the open-shell species 3+ and 5+, exhibiting a paratropic ring current. On the contrary, ***c*-P7[b$_7$]·T7** at the 7+ state, which should be the chemically cleanest *N*+ state (without any chemical exchanges etc.), was NMR silent and only some residual THS signals were observed.

Analysed and processed results are summarised in **Tables 7–9** below:

	Hückel π electron count			*Experimental $\Delta\delta_{THS}$ values*		
	***c*-P7[b$_7$]·T7**	***c*-P8[e$_8$]·(T4*)$_2$**	***c*-P8[b$_8$]·(T4)$_2$**	***c*-P7[b$_7$]·T7**	***c*-P8[e$_8$]·(T4*)$_2$**	***c*-P8[b$_8$]·(T4)$_2$**
neutral	98	96	112	—	−0.24	0.00
2+	96	94	110	—	−1.36	—
4+	94	92	108	−2.66	3.46	0.91
6+	92	90	106	2.13	−3.44	−2.33
8+	—	88	104	—	0.23	0.28

Table 7: π-electron count and observed differences Δδ, between inner and outer THS groups, based on –C*H*$_3$ resonances. Globally aromatic and anti-aromatic states are highlighted in blue and red, respectively.

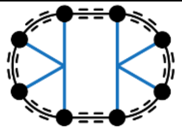

***c*-P8[b$_8$]·(T4)$_2$**	**0+** / 298 K		**2+**		**4+** / 223 K		**6+** / 223 K		**8+** / 223 K	
	^{1}H	**^{13}C**	**^{1}H**	**^{13}C**	**^{1}H**	**^{13}C**	**^{1}H**	**^{13}C**	**^{1}H**	**^{13}C**
T4$^{a)}$	—	—	—	—	8.96–8.38	—	3.11–2.48	—	7.38–6.51	
α	2.50, 2.40	143.3, 143.3	—	—	—	—	−3.13, −3.65	—	10.1	149.9
β	5.23, 5.10	120.0, 120.0	—	—	—	—	—	—	8.67, 8.64	125.1
γ	5.72, 5.58	124.4, 124.4	—	—	—	—	—	—	8.01, 7.97	—
δ	5.86, 5.77	131.7, 131.5	—	—	—	—	—	—	7.77–7.69	—
ε–θ	6.03–5.86	—	—	—	—	—	—	—	—	—
a	9.71, 9.62–9.59	130.7	—	—	—	—	6.85–5.79	—	7.38–6.51	—
b	8.83, 8.79	133.4	—	—	—	—	6.85–5.79	—	7.38–6.51	—
p	8.09, 8.03	140.0, 140.0	—	—	—	—	6.85–5.79	—	7.38–6.51	—
o$_{in}$	8.39, 8.30	140.8, 141,0	—	—	8.96–8.38	—	3.11–2.48	—	7.38–6.51	—
o$_{out}$	8.19, 8.09	141.5, 141.5	—	—	6.21	—	9.10	—	7.38–6.51	—
THS$_{in}$-CH$_2$	0.94	13.0	—	—	1.98	12.8	−1.51	9.5	0.96	10.9
THS$_{out}$-CH$_2$	0.94	13.0	—	—	0.87	12.2	0.88	11.8	0.69	10.5
THS$_{in}$-CH$_3$	0.91, 0.81	14.6, 14.5	—	—	1.79, 1.63	15.4, 15.4	−1.12, −1.66	12.3, 11.8	1.00, 0.92	13.6, 13.3
THS$_{out}$-CH$_3$	0.91, 0.81	14.6, 14.5	—	—	0.80	14.5	1.07, 0.81	14.4, 14.2	0.76, 0.60	13.3, 13.3

Table 8: NMR data obtained for the observed oxidation states of ***c*-P8[b$_8$]·(T4)$_2$**. a) Peaks assignable to template *via* NOESY however, inseparable to individual template resonances.

***c*-P8[e$_8$]·(T4*)$_2$**		**0+** / 298 K		**2+** / 233 K		**4+** / 233 K		**6+** / 233 K		**8+** / 233 K	
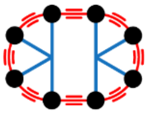		**^{1}H**	**^{13}C**			**^{1}H**	**^{13}C**	**^{1}H**	**^{13}C**	**^{1}H**	**^{13}C**
	α	2.66, 2.57	143.9, 144.0	—	—	11.8	—	−6.84, −6.97	—	10.6, 10.5	—
	β	4.93, 4.72	124.2, 124.1	—	—	19.4–16.7	—	−3.73, −4.05	—	9.35, 9.16	—
	ε	6.21	130.7	—	—	19.4–16.7	—	—	—	9.01	—
	a	10.2–10. 1	130.3	—	—	—	—	7.82–6.21	—	7.81–6.59	—
	b	8.79	133.3	—	—	—	—	7.82–6.21	—	7.81–6.59	—
	p	8.05	139.9	—	—	—	—	7.82–6.21	—	7.81–6.59	—
	o$_{in}$	8.33–8.13	139.5	—	—	—	—	6.57/5.72	—	8.01, 7.82	—
	o$_{out}$	8.04–8.00	140.8	—	—	—	—	9.64/9.50	—	7.67, 7.44	—
	THS$_{in}$-CH$_2$	0.88	13.3	—	—	—	—	—	—	—	—
	THS$_{out}$-CH$_2$	0.88	13.3	—	—	0.78	12.4	0.72	12.1	0.71	11.3
	THS$_{in}$-CH$_3$	0.65, 0.58	14.6, 14.6	0.52– −1.06	—	4.15	17.9	−2.24, −2.77	11.3, 11.1	1.02	14.6
	THS$_{out}$-CH$_3$	0.88, 0.83	14.8, 14.7	1.39–0.79	—	0.80, 0.59	14.6. 14.1	1.10, 0.94, 0.76	15.0, 14.9, 14.5	0.79	15.4

Table 9: NMR data obtained for the observed oxidation states of ***c*-P8[e$_8$]·(T4*)$_2$**.

3.5. Aromaticity of template-free, butadiyne-linked 5- to 9-nanorings

Sections **3.3** and **3.4** dealt with the global aromaticity characteristics of various cations of 6- to 8- porphyrin nanorings, linked both *via* ethyne or butadiyne linkers (or a combination of the two). Those studies covered a range of globally (anti)aromatic species with 66–108 π electrons. All nanorings were stabilised structurally using appropriately designed templates, which also served as NMR probes to help unambiguously NMR-characterise inner, and thus also outer nanoring environment. A logical question is then, when critically assessing these data, whether the template has any influence on the chemical shifts of the nanorings and thus on the correct interpretation of the NMR data in terms of global aromaticity.

In this section, the study of 5-, 6-, 7-, 8- and 9- butadiyne-linked porphyrin nanoring cations is presented, covering the range of 70–126 π electrons for the neutral states and thus this series creates another, logical and self-complemental group assessing the aromaticity limits.

3.5.1. Introduction

It is reasonable to assume that all template-free nanorings will maintain approximately circular shapes, although subjected to various distortions. Such distortions can be of thermal (e.g. vibrational) origin, but they can also be related with an anti-aromaticity character (e.g. Jahn-Teller distortion). Any significant distortion from a circular shape could possibly attenuate the electronic communication between the units and thus can lead to decreased ring current. Another degree of freedom in porphyrin nanorings without templates is the rotational motion of individual porphyrins along the linker axis. This can position neighbouring porphyrins in an orthogonal arrangement, deconjugating the whole nanoring. Although the "co-planar" conformation of porphyrins represents the most probable energetic minimum for any nanoring, it was found that the exchange between inner and outer environment in the neutral ***c*-P6[b$_6$]**, proceeds *via* such rotation with a very small energetic barrier of ~40 kJ/mol.[91] This leads to the speculation of whether it is even practically possible to prepare and characterise oxidised nanorings without templates when their dynamic nature can lead to total NMR-signal broadening.

On the other hand, a positive feature of the template-free nanorings is their structural simplicity and thus spectral similarity within the series. Also, nanorings, for which it is very difficult to design and impractical to synthesise a suitable template (e.g. 9- porphyrin nanoring), can be included into the study.

3.5.2. Models and NICS

3.5.2.1. Benchmarking on *c*-P6[b$_6$]

The geometries were optimised using the LC-ωhPBE functional with different values of ω, which were screened for ***c*-P6[b$_6$]** to test how localising the nature of the functional affects the optimal geometry. The optimised geometries of an anti-aromatic tetracation (***c*-P6[b$_6$]**)$^{4+}$ exhibit relatively severe distortions (**Figure 96, left**). Such distortion can be quantified by fitting an ellipse to the Zn atom positions and using its two main axes a and b to calculate the eccentricity e (**Eq. 18**).

$$e = \sqrt{1 - \frac{a^2}{b^2}} \tag{18}$$

As expected, the more localising functional (with higher values of ω) yielded a more elliptical geometry. For ω values 0.05, 0.1, 0.2 and 0.4 the eccentricities e were: 0.36, 0.43, 0.54 and 0.64.

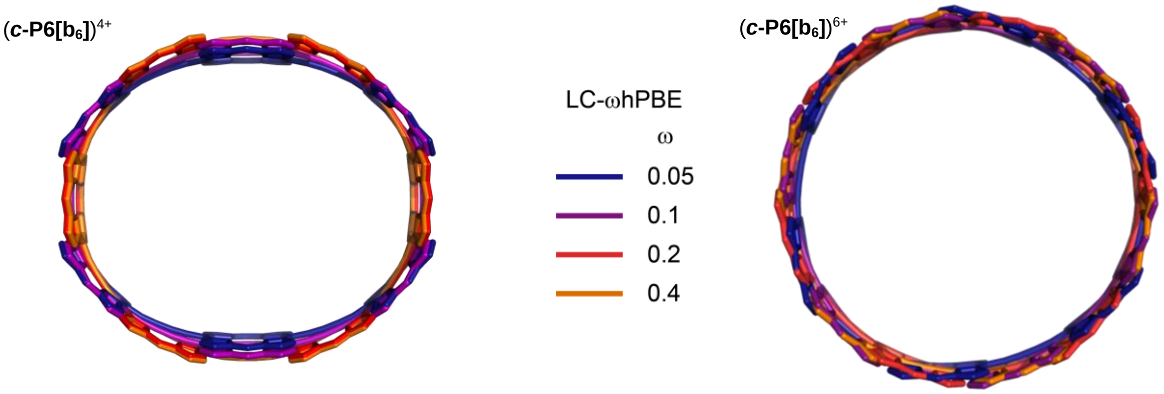

Figure 96: The structures of the tetracation (***c*-P6[b$_6$]**)$^{4+}$ (left) and hexacation (***c*-P6[b$_6$]**)$^{6+}$ (right) optimised using LC-ωhPBE/6-31G* with various ω values. Colour code: ω = 0.05, blue; ω = 0.1, magenta; ω = 0.2, red; ω = 0.4, orange.

For the aromatic hexacation (***c*-P6[b$_6$]**)$^{6+}$, all energy-minimised structures adopted a nearly circular shape (**Figure 96, right**). The fitted eccentricities for ω values 0.05, 0.1, 0.2 and 0.4 were 0.02, 0.06, 0.01 and 0.02, respectively.

The charge localisation was examined by summing the Mulliken charges for all atoms per each bis(ethynyl)porphyrin unit. The data obtained for the anti-aromatic tetracation show significant charge localisation on certain porphyrins while leaving others less charged (**Table 10**).

units numbering (no.)	no. ω	charge per bis(ethynyl)porphyrin ***c*-P6[b$_6$]**$^{4+}$						
		1	2	3	4	5	6	sum
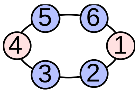	0.05	0.74	0.63	0.63	0.74	0.63	0.63	4.00
	0.1	0.78	0.61	0.61	0.78	0.61	0.61	4.00
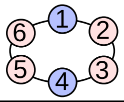	0.2	0.42	0.79	0.79	0.42	0.79	0.79	4.00
	0.4	0.30	0.85	0.85	0.30	0.85	0.85	4.00

Table 10: Charge distribution in different bis(ethynyl)porphyrin units in tetracation ***c*-P6[b$_6$]$^{4+}$**, LC-ωhPBE/6-31G* method.

The same analysis was performed for the aromatic hexacation state and showed no charge disproportionation at all (**Table 11**).

no. ω	charge per bis(ethynyl)porphyrin ***c*-P6[b$_6$]**$^{6+}$						
	1	2	3	4	5	6	sum
0.05	1.00	1.00	1.00	1.00	1.00	1.00	6.00
0.1	1.00	1.00	1.00	1.00	1.00	1.00	6.00
0.2	1.00	1.00	1.00	1.00	1.00	1.00	6.00
0.4	1.00	1.00	1.00	1.00	1.00	1.00	6.00

Table 11: Charge distribution in different bis(ethynyl)porphyrin units in hexacation ***c*-P6[b$_6$]$^{6+}$**, LC-ωhPBE/6-31G* method.

The calculated NICS show the expected trends: a very strong ring current is observed for small ω values, while for higher values, significant localising effects are observed and global ring currents are completely attenuated (**Figure 97**).

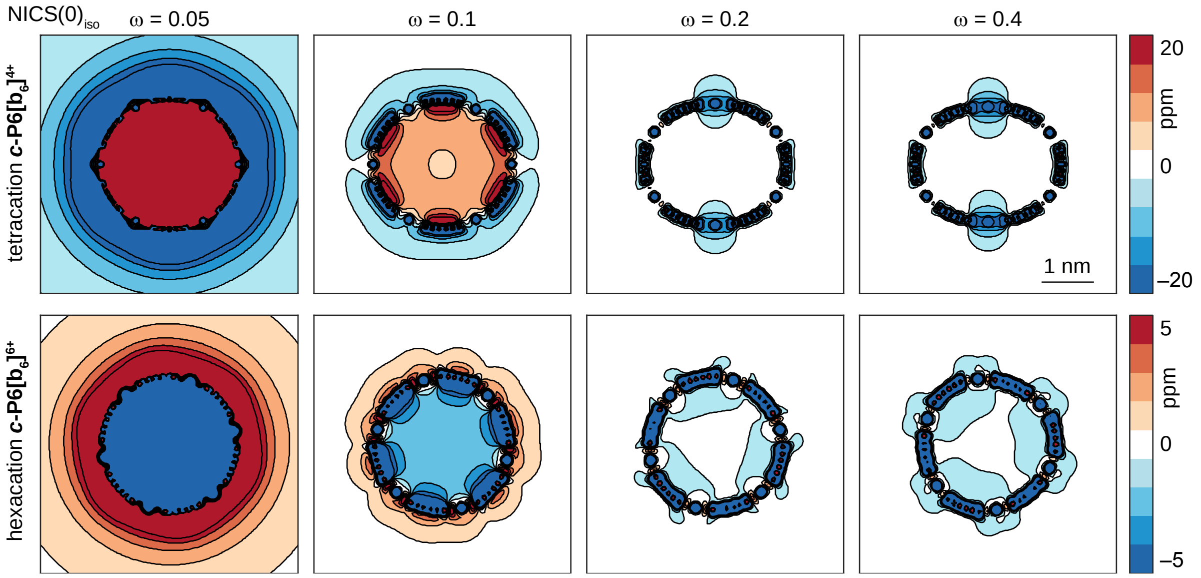

Figure 97: NICS(0)$_{iso}$ (LC-ωhPBE/6-31G*, various ω) of (***c*-P6[b$_6$]**)$^{4+}$ and (***c*-P6[b$_6$]**)$^{6+}$ calculated on the grid of ghost atoms with size 50×50 Å and spacing 0.4 Å. Structures were optimised in absence of template using same methods.

Such localisation can be seen on the tetracations for the used values ω = 0.2 and 0.4, where significant charge localisation leads to charge splitting with highly charged four porphyrin units and two, nearly neutral, locally aromatic units.

As observed for many other systems studied previously, the LC-ωhPBE (ω = 0.1) functional was chosen as the functional most accurately predicting the behaviour, in agreement with experimental observations and the Hückel Rule.

3.5.2.2. *c*-P5[b$_5$], *c*-P6[b$_6$], *c*-P7[b$_7$], *c*-P8[b$_8$] and *c*-P9[b$_9$]

The Hückel Rule formalism applied to the general nanoring ***c*-P*N*[b$_N$]** predicts an alternation of aromaticity for the same oxidation state. For example, for the 4+ state, aromaticity and anti-aromaticity is expected for odd and even *N*, respectively. For the 6+ state, the reversed pattern is expected (**Figure 98**).

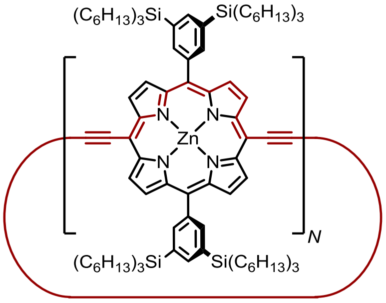

***c*-P*N*[b$_N$]$^{Q+}$**

$\pi e^- = (14 \times N) - \text{charge}$

tetracation	*hexacation*
for odd *N* – aromatic for even *N* – anti-aromatic	for odd *N* – anti-aromatic for even *N* – aromatic

Figure 98: The general structure of ***c*-P*N*[b$_N$]** and the π electron count formalism and expected (anti)aromaticity of the tetra- and hexacation.

The geometries of the tetracations (***c*-P5[b$_5$]**)$^{4+}$, (***c*-P6[b$_6$]**)$^{4+}$, (***c*-P7[b$_7$]**)$^{4+}$, (***c*-P8[b$_8$]**)$^{4+}$ and hexacations (***c*-P6[b$_6$]**)$^{6+}$, (***c*-P7[b$_7$]**)$^{6+}$, (***c*-P8[b$_8$]**)$^{6+}$, (***c*-P9[b$_9$]**)$^{6+}$ were optimised using the LC-ωhPBE/6-31G* (ω = 0.1) method, yielding relatively circular geometries. The calculated NICS for the tetracations (**Figure 99**) and hexacations (**Figure 100**) were fully in agreement with the Hückel Rule and showed the expected alternation of aromaticity.

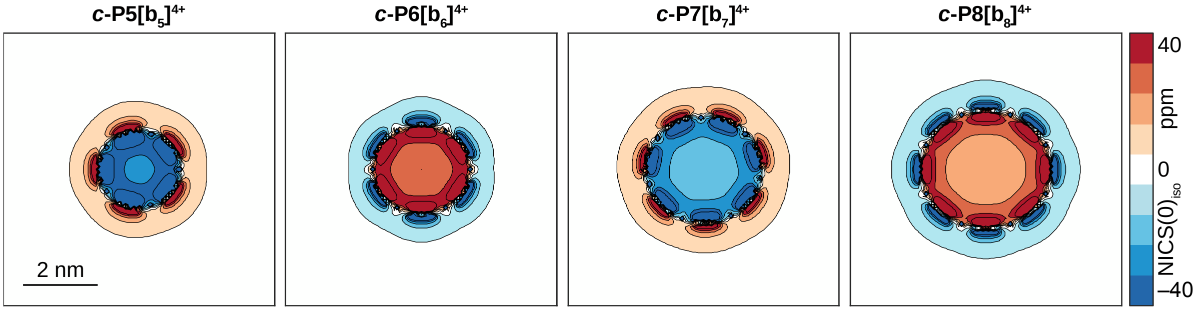

Figure 99: NICS(0)$_{iso}$ (LC-ωhPBE/6-31G*, ω = 0.1) of tetracations (***c*-P5[b$_5$]**)$^{4+}$, (***c*-P6[b$_6$]**)$^{4+}$, (***c*-P7[b$_7$]**)$^{4+}$ and (***c*-P8[b$_8$]**)$^{4+}$ calculated on a grid of ghost atoms with size 75×75 Å and spacing 0.75 Å. Structures were optimised in absence of template using the same method.

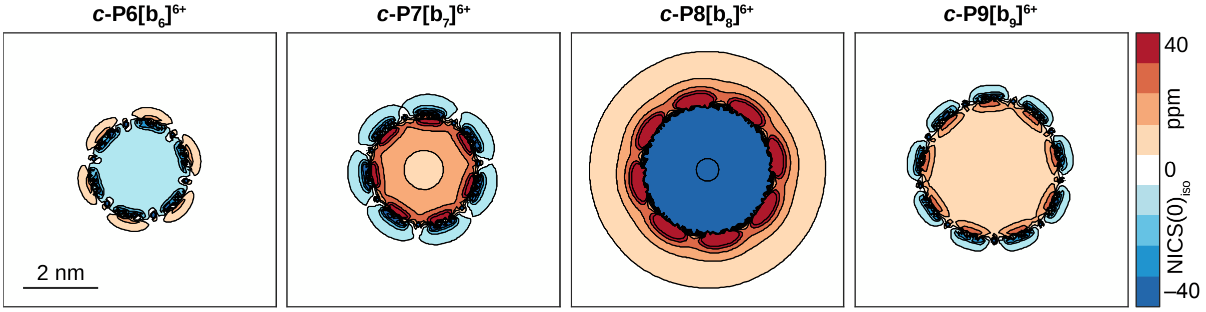

Figure 100: NICS(0)$_{iso}$ (LC-ωhPBE/6-31G*, ω = 0.1) of hexacations (***c*-P6[b$_6$]**)$^{6+}$, (***c*-P7[b$_7$]**)$^{6+}$, (***c*-P8[b$_8$]**)$^{6+}$ and (***c*-P9[b$_9$]**)$^{6+}$ calculated on a grid of ghost atoms with size 75×75 Å and spacing 0.75 Å. Structures were optimized in absence of template using the same method.

3.5.3. NMR titrations – overview

The NMR oxidations of the 5- to 9- butadiyne-linked porphyrin nanorings were performed as discussed previously. All the observed oxidation states obey the Hückel Rule. In the case of ***c*-P5[b$_5$]**, only the tetracation is observed in NMR, and neither the 2+ nor the 5+ (as an *N*+ state) oxidation state possess a sharp NMR spectrum. In the case of ***c*-P6[b$_6$]**, the 2+, 4+ and 6+ states have very sharp NMR spectra. For ***c*-P7[b$_7$]**, the aromatic tetracation and anti-aromatic hexacation were observed, as in the case of its templated complex. In the case of ***c*-P8[b$_8$]**, the 4+, 6+ and 8+ states were observed, however, only the 6+ provides sufficiently resolved NMR spectrum. The 4+ and 8+ states exhibit very broad signals, probably because of a faster porphyrin rotation dynamics and subsequent NMR signal coalescence. To condense the titrations of the 5- to 8-porphyrin nanorings, comprehensive 2D plots, as a surface of stacked spectra, were created. In the plots, the *x* axis is the ^{1}H NMR chemical shift, the *y* axis the number of **Thn$^+$** equivalents added and the *z* axis (surface) is the intensity of the NMR signal (**Figure 101**).

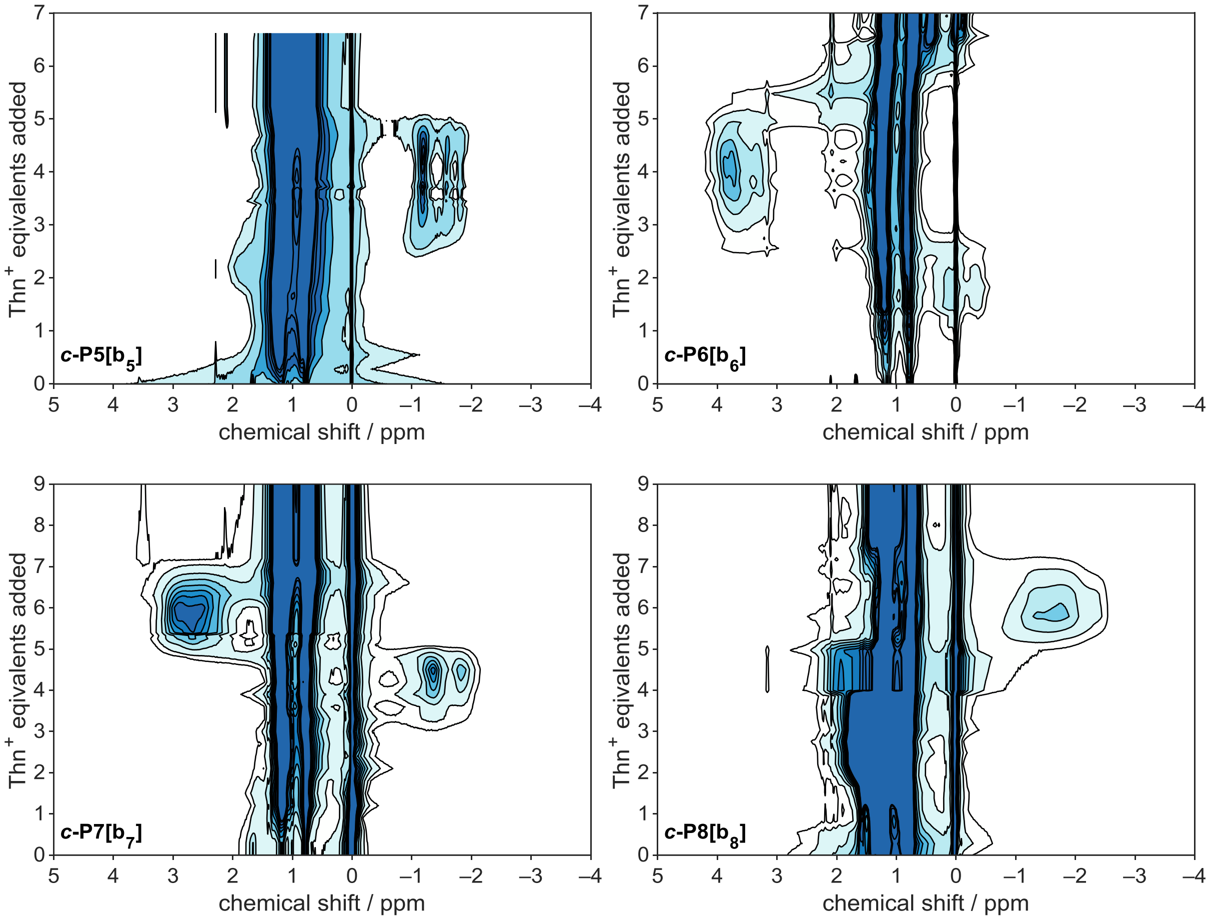

Figure 101: 2D plots of ^{1}H NMR traces from oxidation titrations of various rings. The contours are drawn using an arbitrarily chosen positive offset to clip off noise and at arbitrary chosen height the contour levels are clipped to one colour as some peaks (e.g. solvent peaks, sharp signals) have relatively very high intensity. Data are identical to the 1D ^{1}H NMR stacks (**Figure 102**–**Figure 105**).

The full NMR oxidative titration plots of ***c*-P5[b$_5$]** (**Figure 102**), ***c*-P6[b$_6$]** (**Figure 103**), ***c*-P7[b$_7$]** (**Figure 104**), ***c*-P8[b$_8$]** (**Figure 105**) and ***c*-P9[b$_9$]** (**Figure 106**) are presented, as the spectra stacks most clearly demonstrate an evolution of NMR-visible oxidation states and illustrate general trends and NMR dynamics.

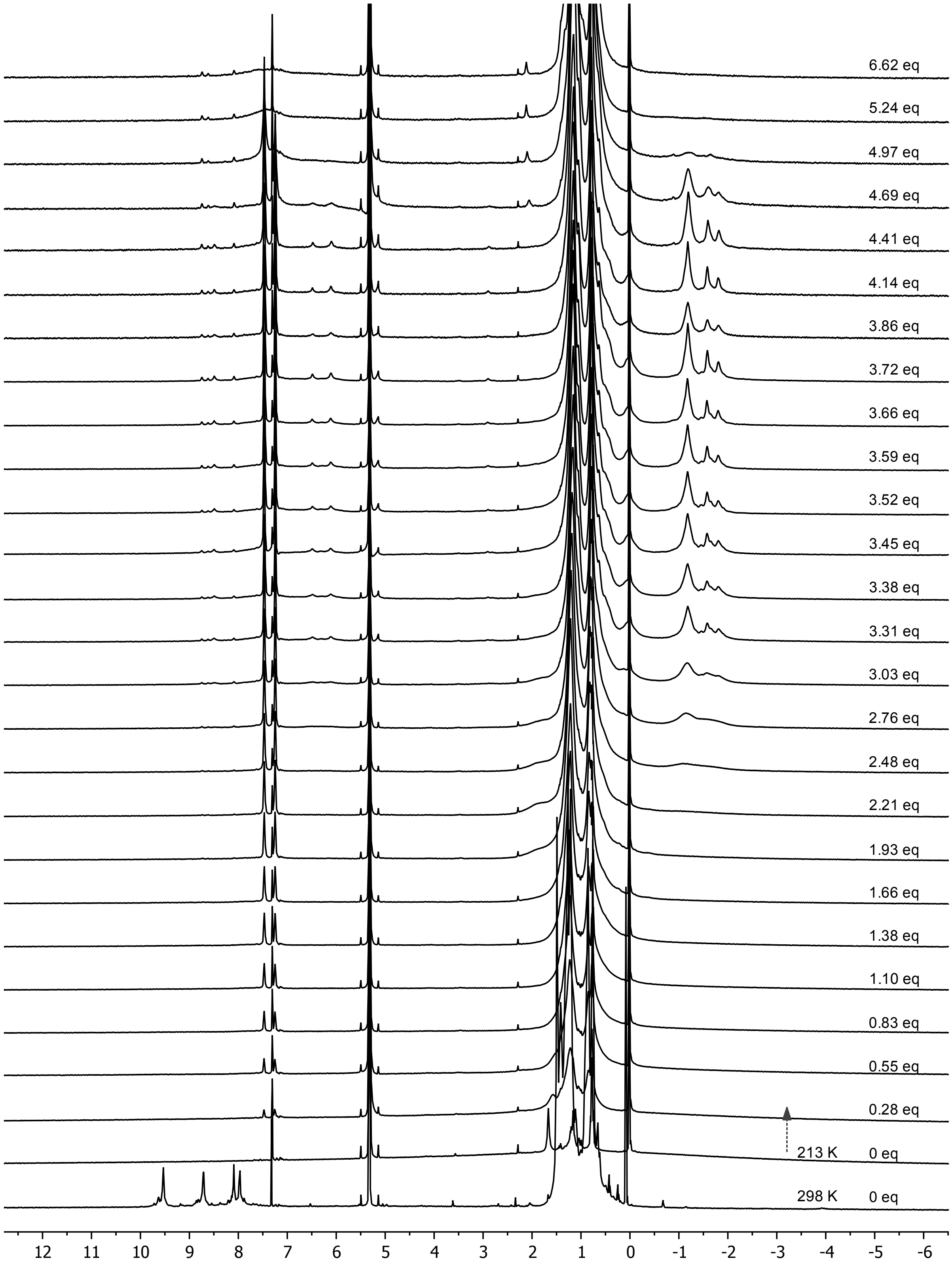

Figure 102: ^{1}H-NMR (500 MHz, CD_2Cl_2) oxidative (**Thn$^+$**) titration of ***c*-P5[b$_5$]**.

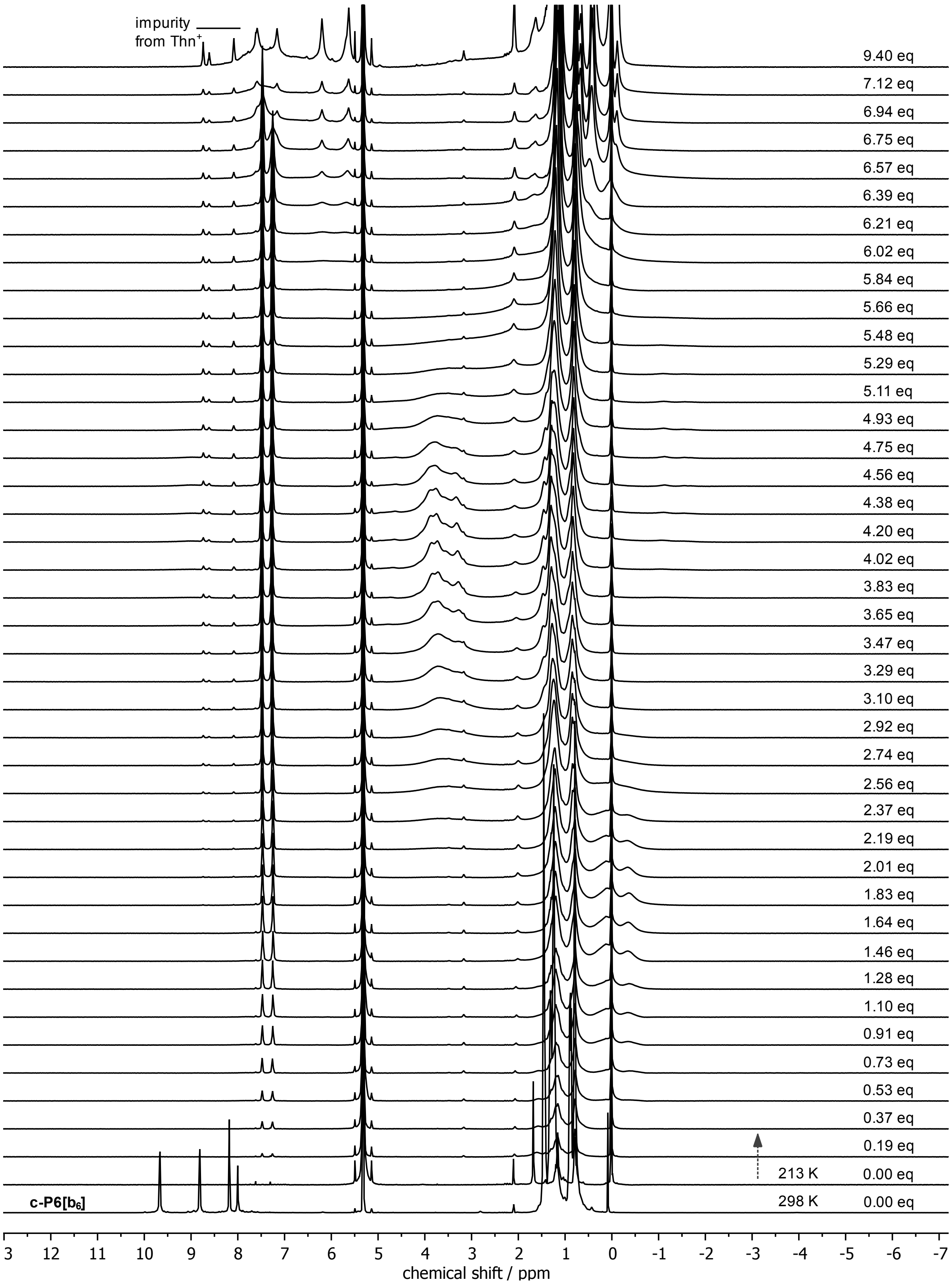

Figure 103: ^{1}H-NMR (500 MHz, CD_2Cl_2) oxidative (**Thn⁺**) titration of ***c*-P6[b₆]**.

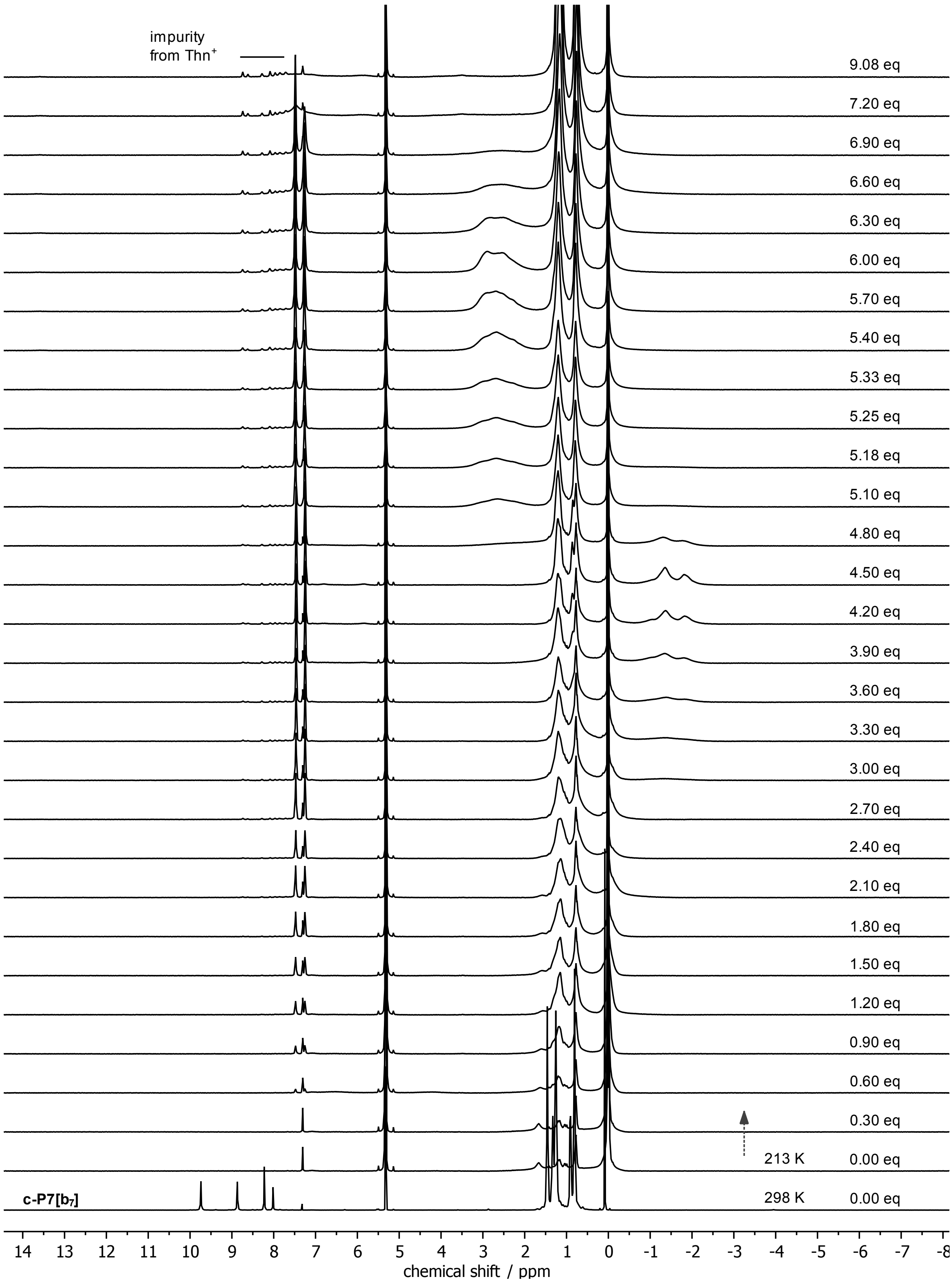

Figure 104: ^{1}H-NMR (500 MHz, CD_2Cl_2) oxidative (**Thn**$^+$) titration of ***c*-P7[b$_7$]**.

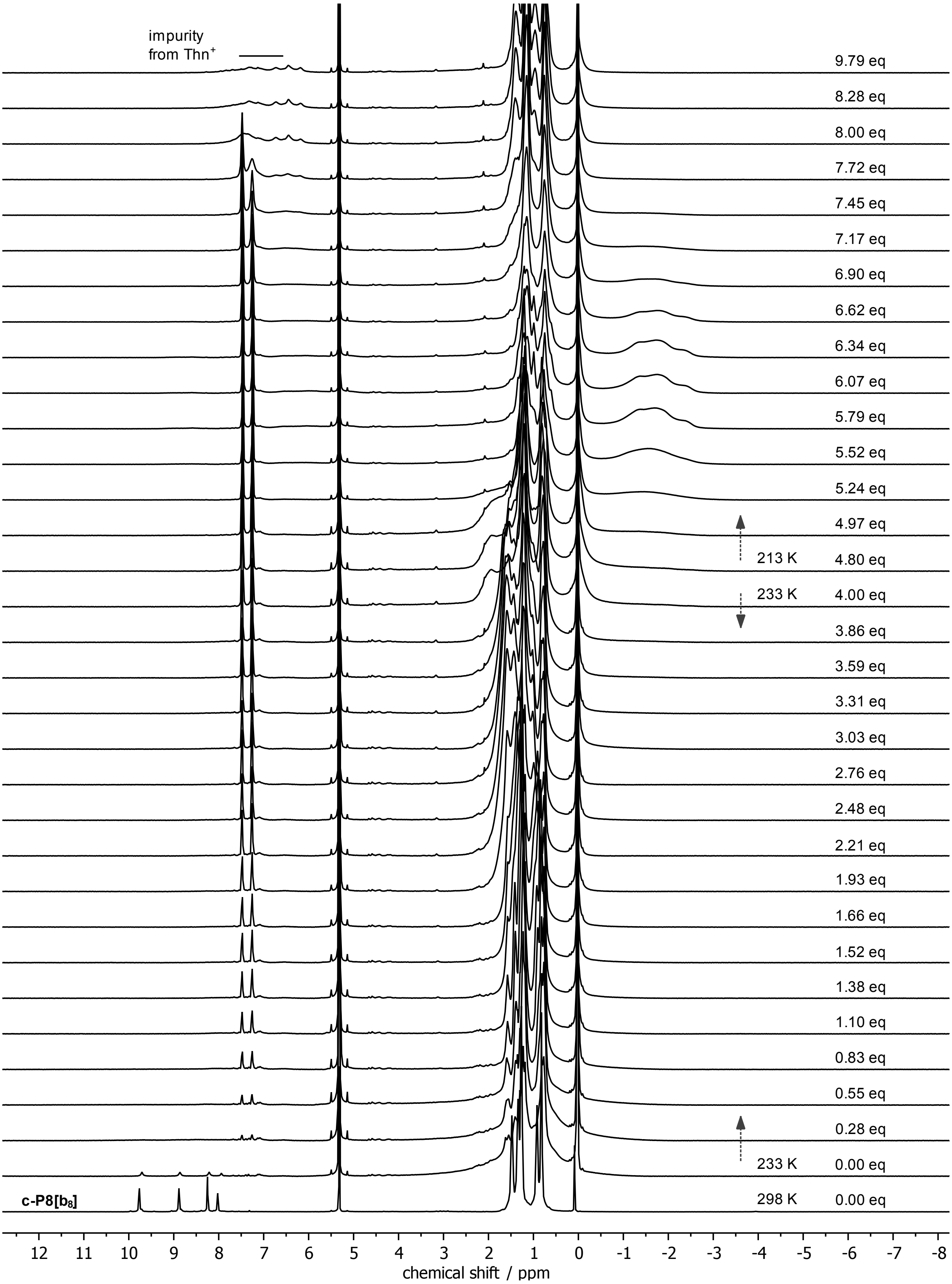

Figure 105: ^{1}H-NMR (500 MHz, CD_2Cl_2) oxidative (**Thn$^+$**) titration of ***c*-P8[b$_8$]**.

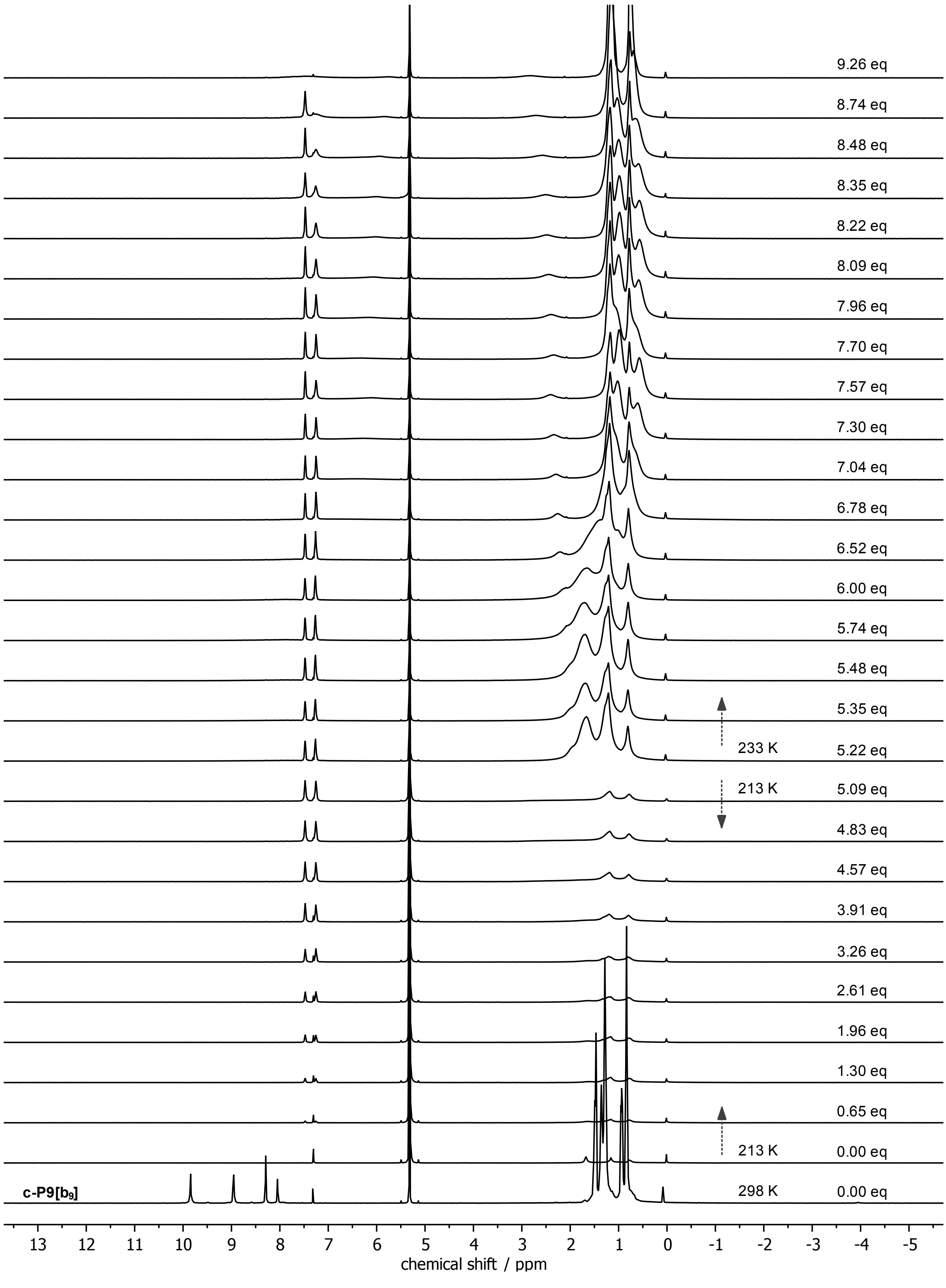

Figure 106: ^{1}H-NMR (500 MHz, CD_2Cl_2) oxidative (**Thn**$^+$) titration of ***c*-P9[b$_9$]**.

The practical size limit for NMR oxidative titrations of template-free nanorings is probably approached at the point of ***c*-P9[b₉]**. Significant line broadening is observed for the inner and outer THS signals in the 6+ and 8+ states at typical operation temperatures (−50°C). This is the result of the more rapid chemical exchange between the inner and outer environment (*via* porphyrin unit rotation) which rate at this point is similar to the NMR time scale (eventually leading to peak coalescence). Higher temperatures (−30°C) had to be used in order to fully bring the species' dynamics into the fast exchange mode. Such dynamics, where peaks represent a time-average of both **THS_{in}** and **THS_{out}** signals still do shift toward either side relative to the chemical shift of THS resonances in absence of the ring current, allowing the detection of global aromaticity.

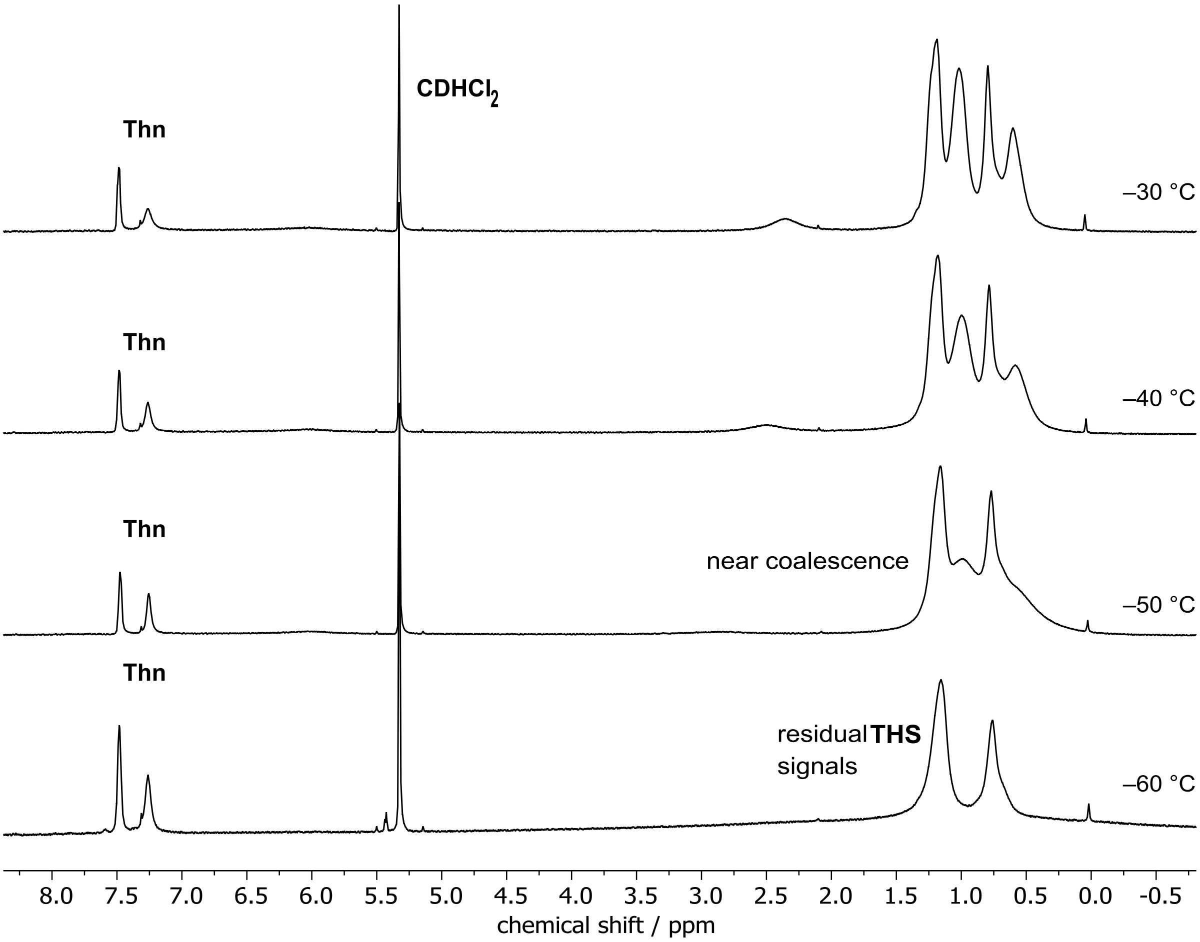

Figure 107: ^{1}H-NMR (500 MHz, CD_2Cl_2) of (***c*-P9[b₉]**)$^{8+}$ at various temperatures. The residual signals observed at low temperatures correspond probably to the odd-oxidation state or corrupted nanoring, not exhibiting any ring current and thus not subjected to the dynamics.

3.6. The largest aromatic compounds – 10- and 12-porphyrin nanorings

The next step in the study was to assess the 10- and 12-porphyrin nanorings.

3.6.1. Electrochemical limits

As mentioned in **Chapter 3.3.1.2.1**, the electrochemical envelope, within which the reduction potential of the states from 1+ to *N*+ are distributed, has a constant size, and for the butadiyne-linked nanorings, the envelope is approximately 0.6 V. The more porphyrins units the system contains, the closer the potential spacing will be between each state. When the potential difference is very small (~50 mV), it will not be possible to form 100% of the oxidation state as the partial disproportionation to neighbouring states will occur, even when a precise amount of strong oxidant (corresponding to the state) is added. To assess such behaviour, a simple equilibrium distribution of species at a given oxidation potential *E* can be calculated according to the Nernst equation (**Eq. 23**).

$$E = E^0 + \frac{RT}{nF} log(K) \tag{23}$$

Where *K* is the equilibrium constant weighing the distribution between the two states, *R* is the gas constant, *T* the temperature, *n* is the number of electrons involved in the reaction (in this case 1), *F* is the Faraday constant, E^0 is the electric potential of the process at standard conditions and *E* is the applied potential.

Assuming, that at potential *E*, the closest state *Q*+ can be mixed with both the (*Q*+1)+ and the (*Q*−1)+ states (but not with any state higher or lower than that) and with known potentials for every oxidation from SW voltammetry, the equilibria can be expressed as **Eq. 24**:

$$log\left(\frac{\chi_Q}{\chi_{(Q-1)}}\right) = \frac{nF(E-E_Q)}{RT} \quad \text{and} \quad log\left(\frac{\chi_{(Q+1)}}{\chi_Q}\right) = \frac{nF(E-E_{(Q+1)})}{RT} \tag{24}$$

Continuous change of potential and solving of the equations provides an idea of the expected amount of each component being present during the electrochemical oxidation. This should be analogous to the continuous addition of small increments of **Thn$^+$**.

Speciation analysis of ***c*-P6[b$_6$]·T6**, ***c*-P8[b$_8$]·(T4)$_2$**, ***c*-P10[b$_{10}$]·(T5)$_2$**, ***c*-P12[b$_{12}$]·(T6ef)$_2$**, ***c*-P6[e$_6$]·T6***, and ***c*-P8[e$_8$]·(T4*)$_2$** based on the corresponding square wave voltammograms was performed (**Figure 108**).

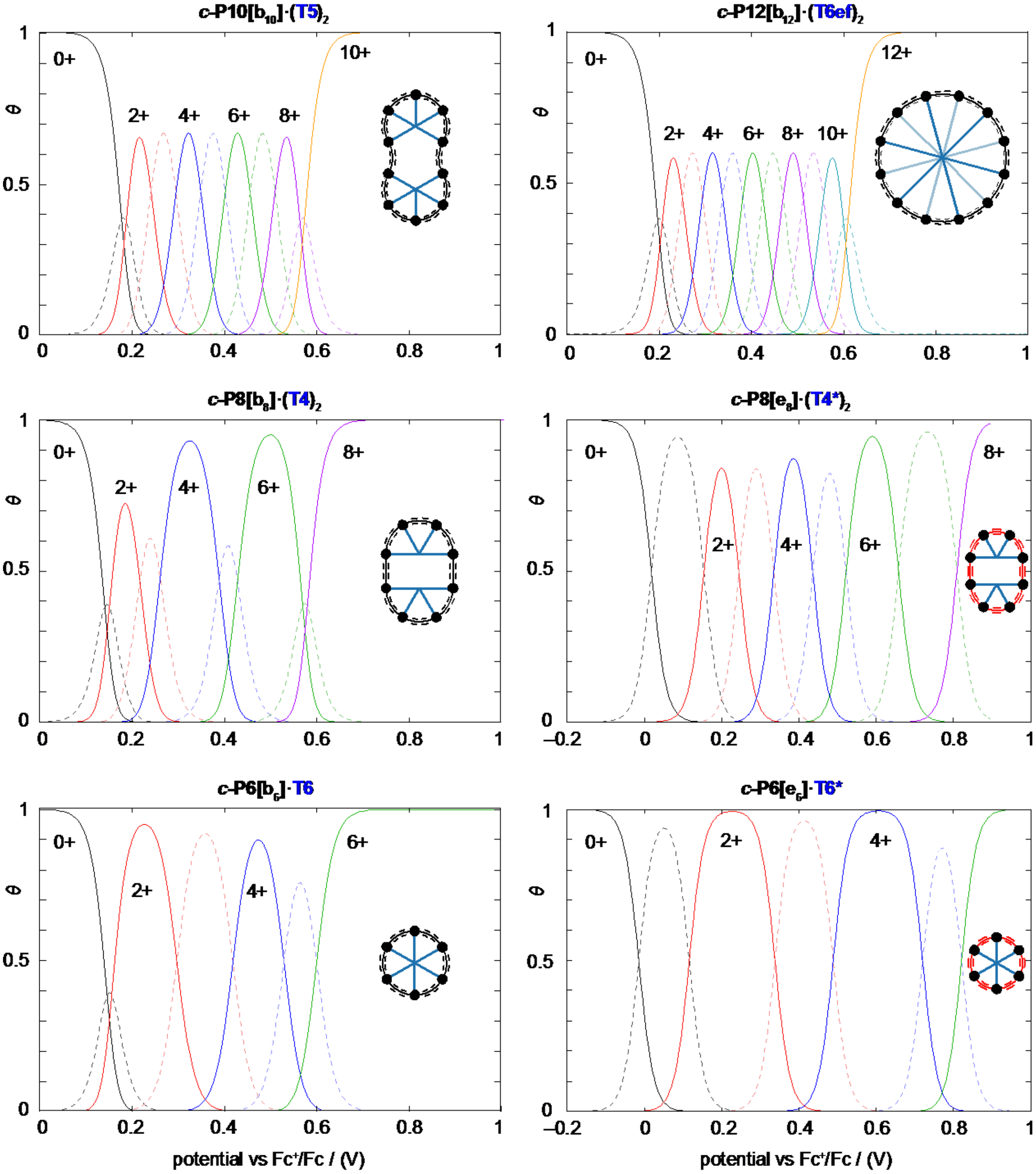

Figure 108: Expected mole fractions θ of each oxidation state during electrochemical oxidation of various nanorings, based on data obtained from SW voltammetry. For **c-P10[b$_{10}$]·(T5)$_2$** and **c-P12[b$_{12}$]·(T6ef)$_2$**, the resolution of the individual states within the envelope 1+ – N+ is poor and equal spacing of the states was assumed for the analysis. The molar fraction θ of any given state expect N+ is notably lower than 1 for the larger rings, pointing at expected coexistence of neighbouring states. Solid lines are even oxidation states (2+, 4+, …), dashed lines are odd states (1+, 3+, …).

From the speciation analysis it is apparent that oxidation states between 1+ and (N−1)+ in nanorings with 10 or more porphyrin units cannot be prepared cleanly. This could cause significant broadening of the NMR signals as a result of the potential dynamic chemical exchange between neighbouring states and the presence of large amount of open-shell species.

3.6.2. 10-Porphyrin nanoring *c*-P10[b$_{10}$]·(T5)$_2$

The large, 10- porphyrin nanoring ***c*-P10[b$_{10}$]** is expected to be conformationally very flexible (cf. **Chapter 3.5.2.2**) and therefore the structure needs to be stabilised with a template. No decavalent template has been synthesised. However, complexation of two pentavalent templates **T5** was reported to form a stable complex ***c*-P10[b$_{10}$]·(T5)$_2$** (**Figure 109**, left).[84] Although, the nanoring and complex was not reported in literature with THS solubilising groups, the system could be easily prepared in an analogous way to the reported procedure.[84] Based on the π electron count, the 2+, 6+ and 10+ oxidation states should be globally aromatic; and the 4+ and 8+ states globally anti-aromatic (**Figure 109**, right).

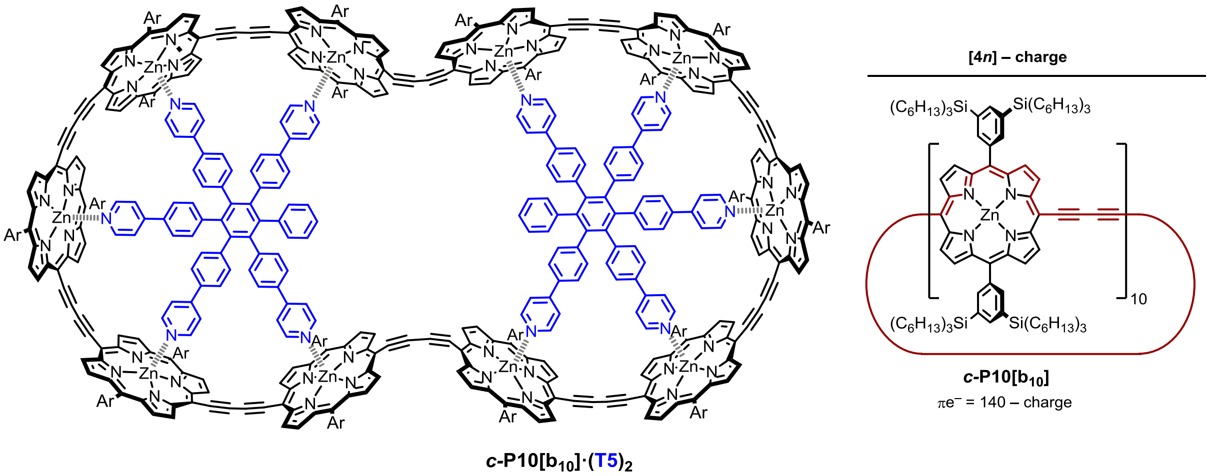

Figure 109: (left) Chemical structure of ***c*-P10[b$_{10}$]·(T5)$_2$**. Ar = 3,5-bis(trihexylsilyl)phenyl. (right) π electron count formalism for ***c*-P10[b$_{10}$]**.[84]

The DFT model confirms the relatively good template fit, inducing a small longitudinal twist (**Figure 112**).

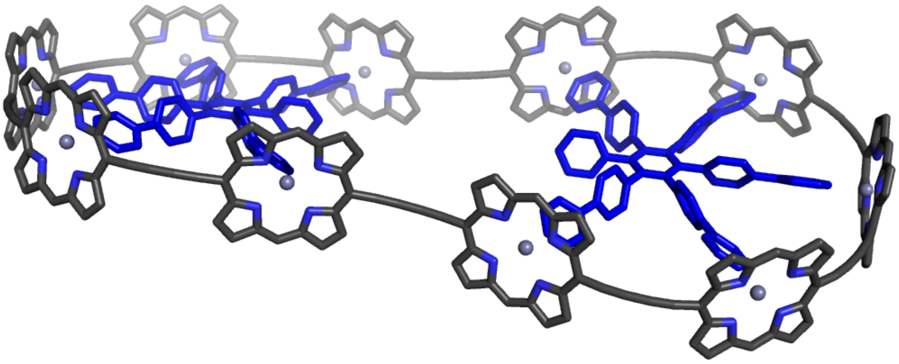

Figure 110: DFT (B3LYP/6-31G*) optimised geometry of the complex ***c*-P10[b$_{10}$]·(T5)$_2$**.

Although, the twist of the complex is marginal, for the NICS *x-y* scan, a surface alternative to the otherwise used plane, was designed. In order to best mimic the twist, a surface function $z = f(x,y,)$ defined as $z = a \cdot x \cdot y + b$ was used, and the parameters a and b were obtained by the fitting the function to pass through the butadiyne carbons and zinc atom positions (**Figure 111**). The function parameters were fitted for each optimised geometry of each oxidation state studied and serve also as a measure of the twist of thecomplex. It was observed, that with increasing charge, the superstructure becomes flatter, as the parameter a becomes smaller (**Table 12**).

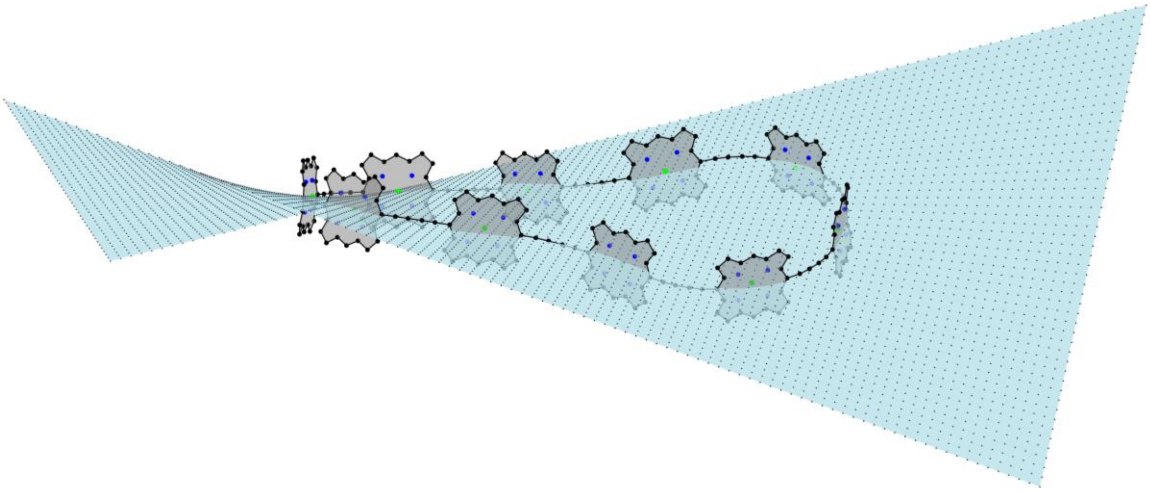

Figure 111: Grid of ghost atoms positioned on a surface $z = 0.001278 \cdot x \cdot y + 0.000003$ to examine the induced magnetic field of ***c*-P10[b₁₀]**, optimised using LC-ωhPBE (ω = 0.1)/ 6-31G* in the presence of templates.

$z = a \cdot x \cdot y + b$	neutral	2+	4+	6+	8+	10+
a	$1.278 \cdot 10^{-2}$	$7.905 \cdot 10^{-3}$	$-2.187 \cdot 10^{-3}$	$-2.72 \cdot 10^{-3}$	$-1.735 \cdot 10^{-3}$	$-4.699 \cdot 10^{-4}$
b	$3.031 \cdot 10^{-6}$	$5.688 \cdot 10^{-7}$	$1.9510 \cdot 10^{-7}$	$2.561 \cdot 10^{-7}$	$2.6620 \cdot 10^{-6}$	$2.585 \cdot 10^{-4}$

Table 12: Fit of parameters a and b of the surface $z = a \cdot x \cdot y + b$ to ***c*-P$_{10}$[b$_{10}$]·(T5)$_2$** geometries at various oxidation states optimised with LC-ωhPBE/6 31G* (ω = 0.1).

The calculated NICS, using both the B3LYP and LC-ωhPBE (ω = 0.1) functionals and the 6-31G* basis set, showed similar trends as observed in smaller systems. In the case of the B3LYP functional, globally aromatic 2+, 6+ and 10+ (with moderate aromatic ring current) and anti-aromatic 4+ and 8+ (with extremely strong paratropic ring current) were predicted. With the LC-ωhPBE functional, extremally exaggerated diatropic ring currents for the aromatic 2+ and 6+ states and very weak paratropic ring currents for anti-aromatic 4+ and 8+ states were predicted. Interestingly, effectively no global ring current was predicted for the 10+ oxidation state, which should be formally aromatic based on the Hückel Rule. This prediction suggests, that this size ($N = 10$) might be the limit for global ring currents for N+ states. The lack of charge delocalisation driving force (no ring current for $\overline{P_{ox}} = 1$, strong for $\overline{P_{ox}} = (0–1)$) for the global electron communication has evident effect. However, the absolute absence of ring current remains puzzling as no obvious close-shell arrangement, other than a global coherent communication along the circumference, can be imagined (as individual porphyrins cannot be closed shell locally at $\overline{P_{ox}} = 1+$) (**Figure 112**).

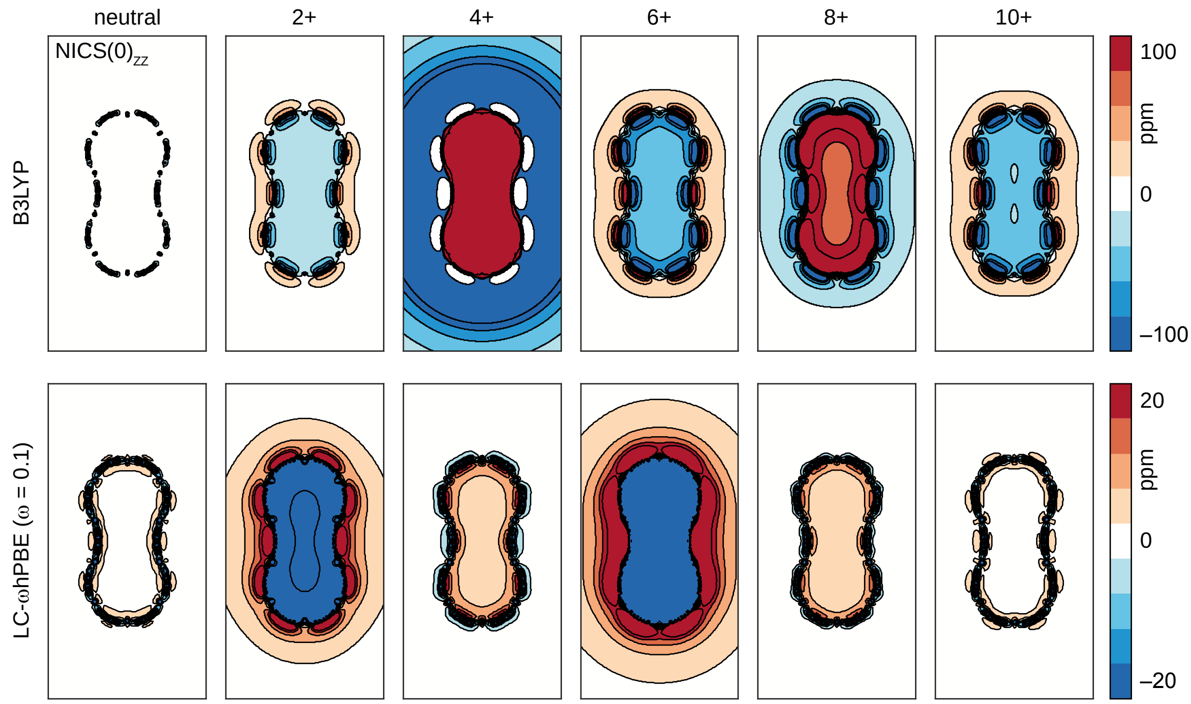

Figure 112: The ZZ component of NICS, calculated for the 0, 2+, 4+, 6+, 8+ and 10+ oxidation states of ***c*-P10[b$_{10}$]·(T5)$_2$** with B3LYP (top) and LC-ωhPBE (ω = 0.1) (bottom). Geometries were optimised using the same method and the templates were removed prior to the NICS. NICS were calculated on a grid of 100×50 Å size with ghost atom spacing 0.5 Å.

The NMR oxidation was carried out, leading to the successful observation of the 6+, 8+ and 10+ oxidation states.

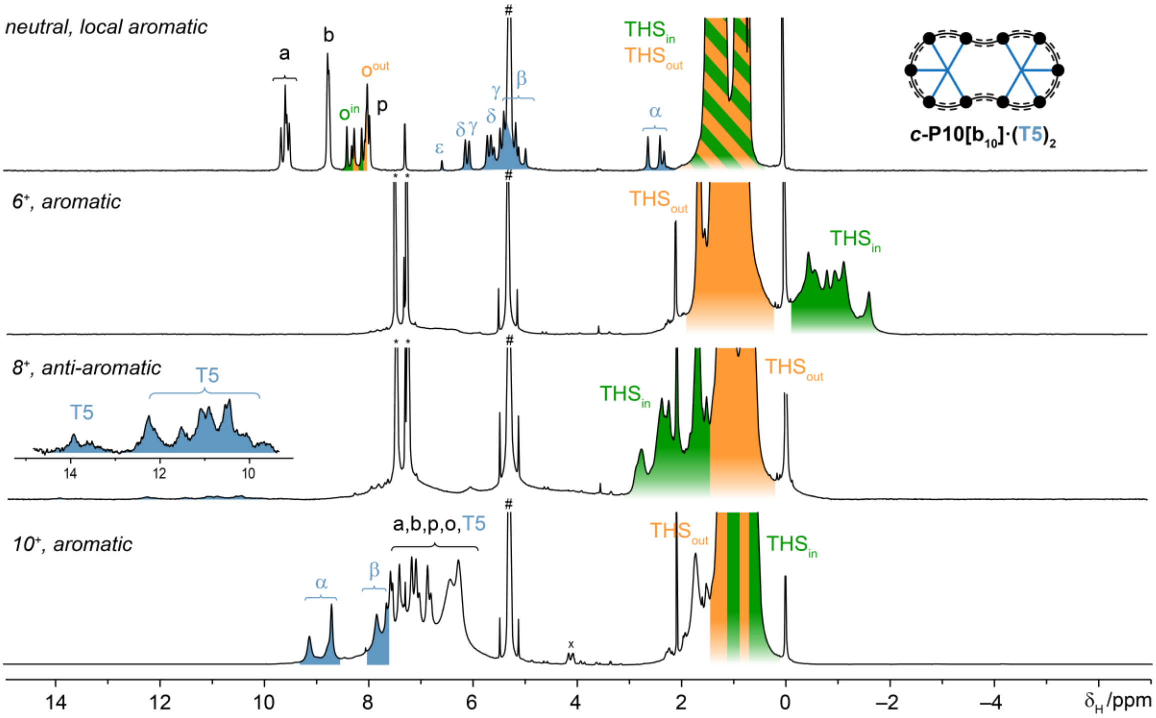

Figure 113: ^{1}H NMR (500 MHz, CD$_2$Cl$_2$, 25°C, −50°C) spectra of the neutral, 6+, 8+ and 10+ oxidation states of ***c*-P10[b$_{10}$]·(T5)$_2$**.

The early oxidation states 2+ and 4+ were not observed, probably due to their low solubility under the experimental conditions, or due to lack of coherent charge delocalisation in such large nanoring (one polaron is expected to be delocalised over 2–3 units, c.f. **Chapter 2**). The observed states are analysed in **Figure 113**.

The 6+ oxidation state showed significantly shielded **THS$_{\mathbf{in}}$** resonances at 0 to −2 ppm, indicating globally aromatic character. However, no other resonances were documented. The 8+ state exhibited a moderately deshielded **THS$_{\mathbf{in}}$** between 3 – 1 ppm, indicating global anti-aromaticity. This is further corroborated by deshielded **T5** resonances at 10 – 14 ppm. The broadness of the spectra, however, did not allow for much of the assignment.

Surprisingly the 10+ state does not exhibit any significant global ring current and at the same time no local effects are observed either. The template signal are observed at nearly the same chemical shifts as free template, suggesting switching-off of the local aromatic ring current, but not formation of a global one. In the 10+ state, multiple THS environments were recognised, however they are very closely spaced and since the structure has a low symmetry and at least three THS resonances are expected, its assignment is uncertain – either very weak globally aromatic character or non-aromaticity are possible interpretations. The recognized **T5** resonances did not show any significant deviation from unbound **T5**, suggesting non-aromaticity.

3.6.3. 12-Porphyrin nanoring *c*-P12[b$_{12}$]

3.6.3.1. Introduction

The largest aromatic system studied and presented in this thesis (and at the present time in the world) is the 12-butadiyne-linked porphyrin nanoring ***c*-P12[b$_{\mathbf{12}}$]**. The nanoring was studied in the presence of templates inducing either a circular geometry (**Chapter 3.6.3.2**) or a lemniscular shape (**Chapter 3.6.3.3**). The Hückel aromaticity formalism for ***c*-P12[b$_{\mathbf{12}}$]** is outlined in **Figure 114**.

***c*-P12[b$_{12}$]**

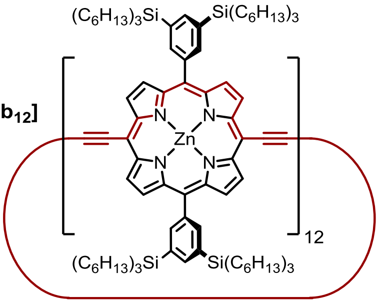

$\pi e^- = (14 \times N) - \text{charge}$

for $N = 12$ $\pi e^- = 168 - \text{charge}$
aromaticity character = $[4n] - \text{charge}$

2+, 6+, 10+	4+, 8+, 12+
aromatic	anti-aromatic

Figure 114: Structure of ***c*-P12[b$_{\mathbf{12}}$]** and the π electron count formalism and expected global (anti)aromaticity of its cations.

3.6.3.2. Circularly shaped c-P12

To maintain a circular shape of **_c_-P12[b$_{12}$]**, the previously described dodecadentate template **T12**, as well as the newly designed hexadentate templates **T6e** and its –CF$_3$ decorated analogue **T6ef** were used (**Figure 115**).

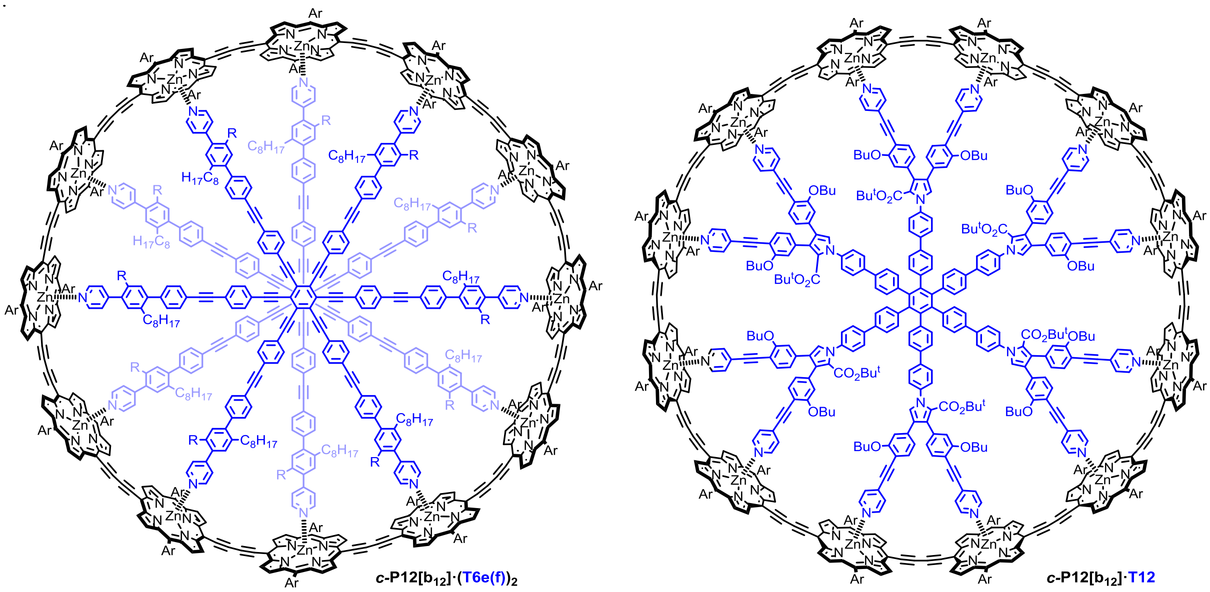

Figure 115: (left) Chemical structures of **_c_-P12[b$_{12}$]·(T6e)$_2$** (R = C_8H_{17}) and **_c_-P12[b$_{12}$]·(T6ef)$_2$** (R = CF_3). (right) Chemical structure of **_c_-P12[b$_{12}$]·T12**.

Due to the large number of atoms and degrees of freedom of the **_c_-P12[b$_{12}$]·T12** and **_c_-P12[b$_{12}$]·(T6e)$_2$** complexes, the DFT optimisation was not possible for the structures with templates. The nanoring complex geometry could be optimised using semiempirical methods (PM6) or by DFT in the absence of template. Use of the B3LYP and CAM-B3LYP/6-31G* methods for geometry optimisation of template-free nanoring yielded a very circularly shaped **_c_-P12[b$_{12}$]**. This geometry served as a model for NICS method screening, in which various functionals were tested. Surprisingly, many methods provided qualitatively opposite predictions, contrary to Hückel theory, particularly for Hückel anti-aromatic states (**Figure 116**).

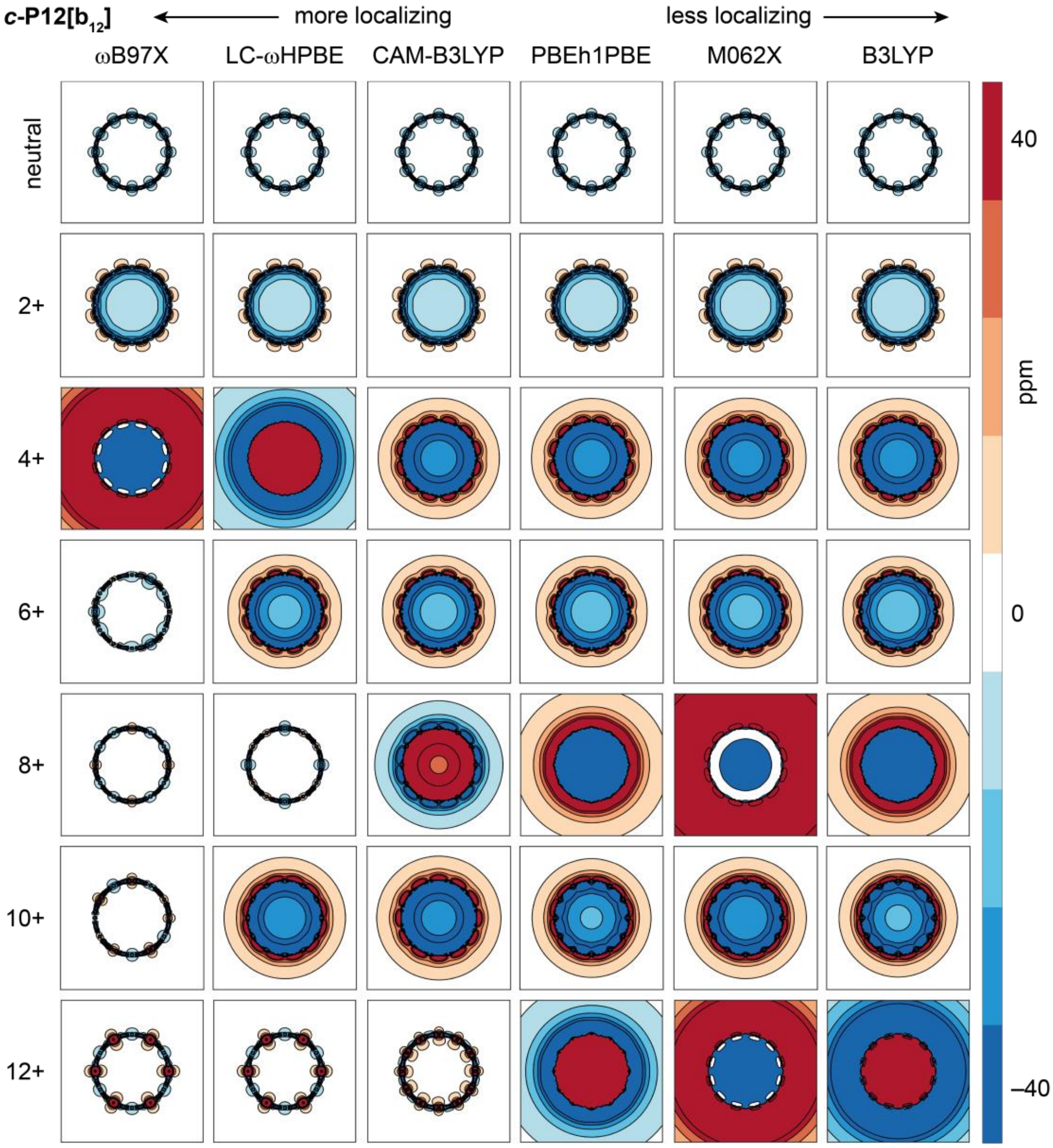

Figure 116: NICS(0)$_{iso}$ calculated with various methods assuming various oxidation states in ***c*-P12[b$_{12}$]**, obtained by optimisation using the CAM-B3LYP/6-31G* method.

The results of the functional screening can be organised according to the functional charge-localisation character. From **Figure 116**, a clear pattern appears that very localising functionals (ωB97X and LC-ωhPBE with default settings) tend to localize the charges onto the individual porphyrins, yielding either neutral or doubly charged porphyrin units exhibiting local aromaticity and anti-aromaticity, respectively. On the other hand, less localising functionals (e.g. B3LYP) predicts very strong ring currents and predicts the majority of oxidation states to exhibit diatropic currents, which is in contrast with the Hückel Rule.

Particularly interesting results are observed for the 12+ oxidation state. Depending on the method used, very different NICS patterns can be observed: Firstly, alternating charge localisation on the porphyrins in a 0 / 2+ / 0 / 2+… pattern together with local porphyrin aromaticity (neutral) and anti-aromaticity (2+), predicted by the ωB97X and

LC-ωhPBE/6-31G* methods (with default value of ω, (ω = 0.4 for LC-ωhPBE)). Secondly, a weak, globally antiaromatic state obtained with the CAM-B3LYP/6-31G* method or a very strong anti-aromatic character obtained with the PBEh1PBE and B3LYP/6-31G* method. Finally, a globally aromatic character, opposite to Hückel predictions, was predicted with the M062X/6-31G* method.

To study more closely these effects on the 12+ oxidation state, NICS using the LC-ωhPBE functional with various ω values were screened to empirically assess the effect of the functional's localisation character (**Figure 117**).

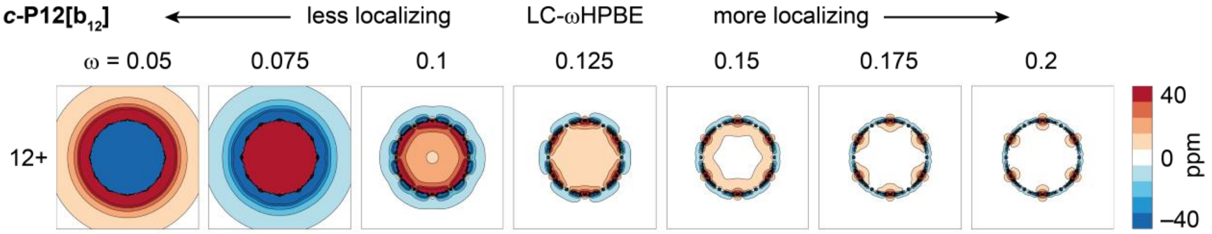

Figure 117: NICS(0)$_{iso}$ calculated with the LC-ωhPBE/6-31G* method testing various ω values at the 12+ oxidation state (***c*-P12[b$_{12}$]**)$^{12+}$. Geometry was obtained for neutral ***c*-P12[b$_{12}$]** structure optimisation using the CAM-B3LYP/6-31G* method.

Beside NICS, charge distribution at 12+ state predicted with various functional was assessed to document different tendencies in charge localisation (**Table 13**).

unit no. functional	1	2	3	4	5	6	7	8	9	10	11	12	sum
LC-ωhPBE ω = 0.1	1.10	0.90	1.10	0.90	1.10	0.90	1.10	0.90	1.10	0.90	1.10	0.90	12.0
LC-ωhPBE ω = 0.2	1.19	0.81	1.19	0.81	1.19	0.81	1.19	0.81	1.19	0.81	1.19	0.81	12.0
LC-ωhPBE default	1.28	0.72	1.28	0.72	1.28	0.72	1.28	0.72	1.28	0.72	1.28	0.72	12.0
B3LYP	1.00	1.00	1.00	1.00	1.00	1.00	1.00	1.00	1.00	1.00	1.00	1.00	12.0
PBEh1PBE	1.00	1.00	1.00	1.00	1.00	1.00	1.00	1.00	1.00	1.00	1.00	1.00	12.0
CAM-B3LYP	1.00	1.00	1.00	1.00	1.00	1.00	1.00	1.00	1.00	1.00	1.00	1.00	12.0

Table 13: Charge sum for each bis(ethynyl)porphyrin unit in (***c*-P12[b$_{12}$]**)12+ calculated with various functionals and the 6-31G* basis set.

3.6.3.2.1. *c*-P12[b$_{12}$]·T12

The prepared complex of ***c*-P12[b$_{12}$]** with **T12** was described and characterised in the literature[109] with different solubilising side chains and herein the THS decorated ***c*-P12[b$_{12}$]·T12** was prepared in analogous way.[90] The prepared complex possessed similar NMR and UV-vis-NIR characteristics and the chemical identity was confirmed with accurate mass spectrometry. The model geometry of the complex was optimised using molecular mechanics (MM) implemented in HyperChem (**Figure 118**). Although, visually the **T12** fits into the nanoring, significant bending of some template legs is required.

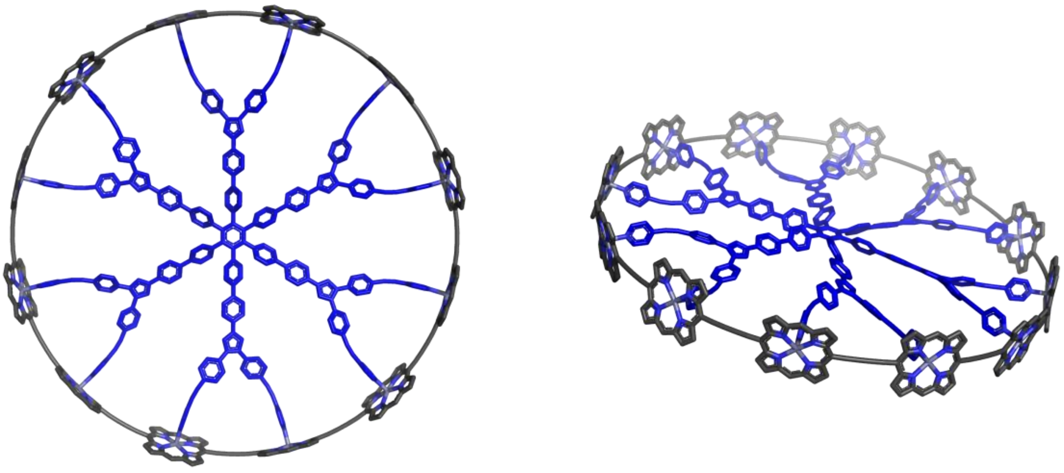

Figure 118: Model of ***c*-P12[b$_{12}$]·T12** optimised with HyperChem.

The ***c*-P12[b$_{12}$]·T12** complex was oxidised and the 8+, 10+ and 12+ oxidation states were observed and analysed (**Figure 119**).

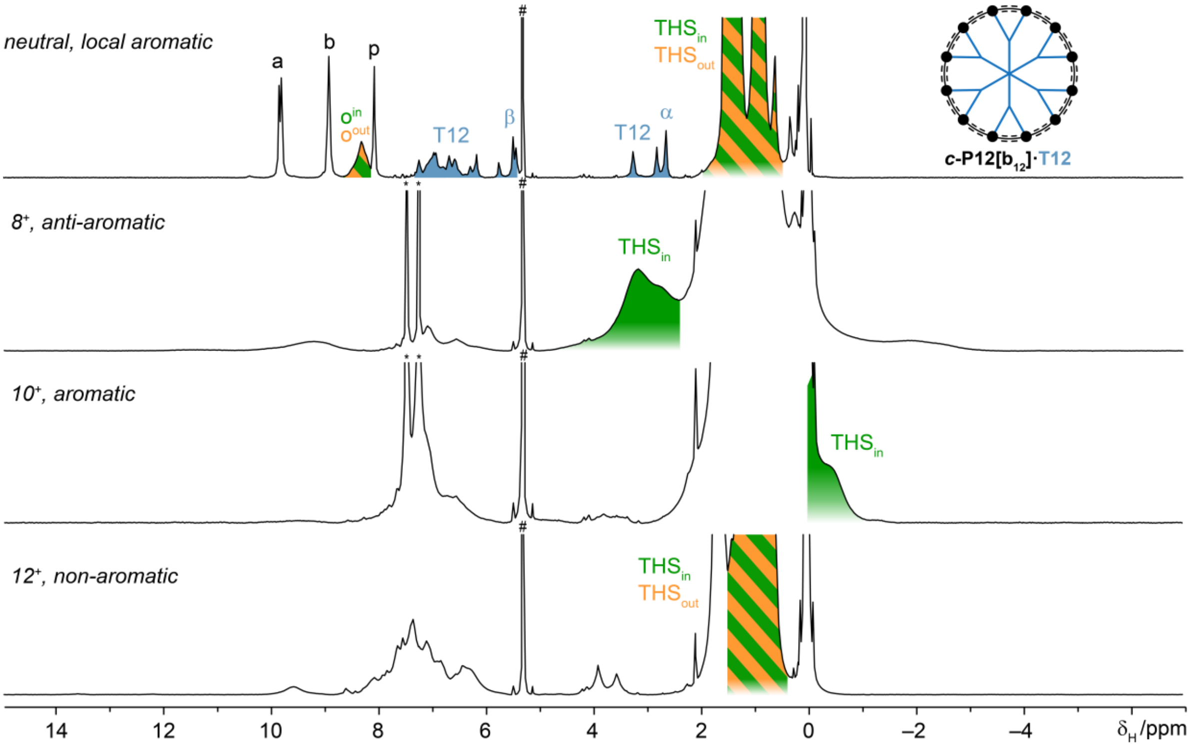

Figure 119: ^{1}H NMR spectra (500 MHz, CD_2Cl_2) of the neutral, 8+, 10+ and 12+ oxidation states of ***c*-P12[b$_{12}$]·T12**.

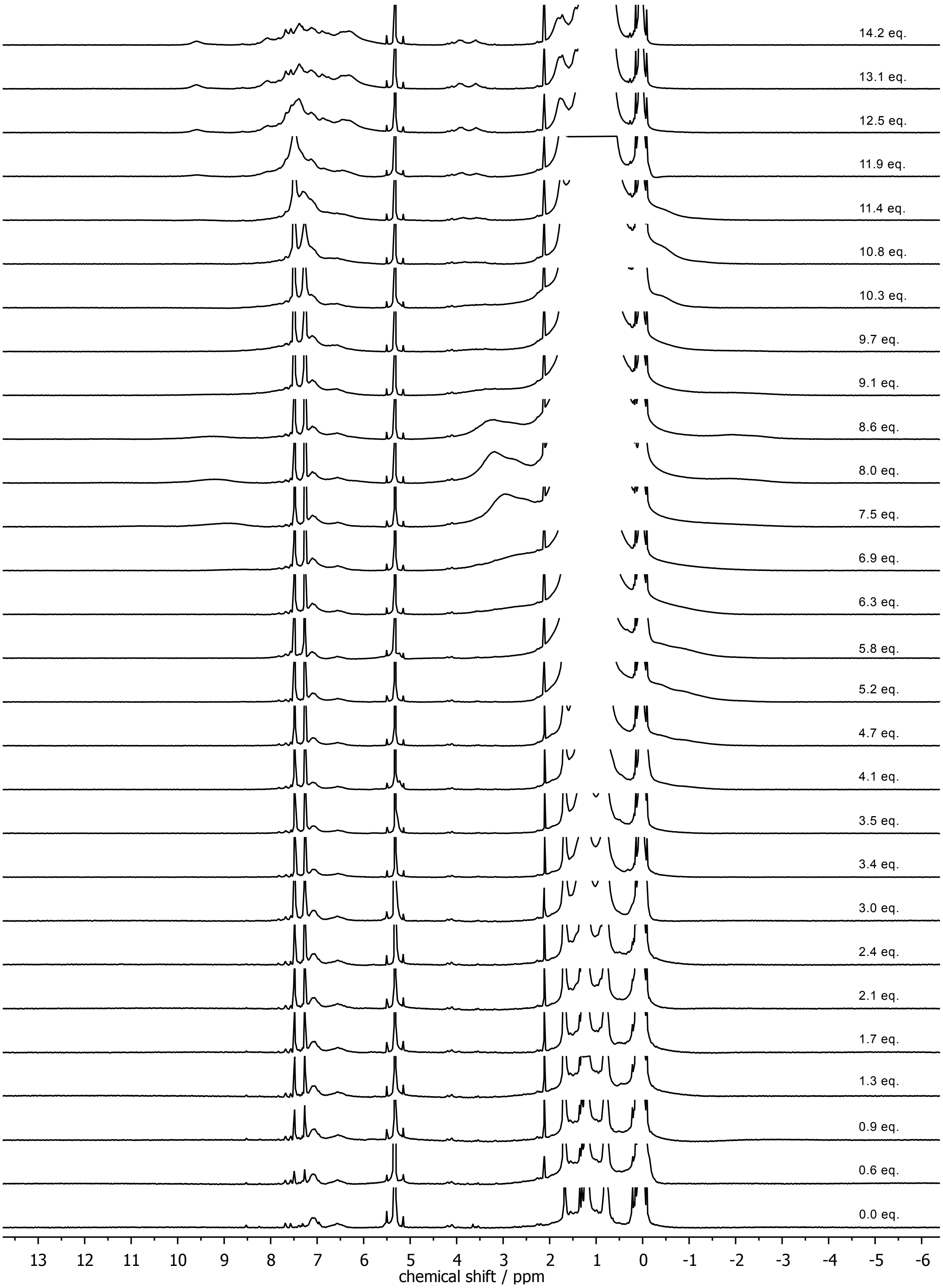

Figure 120: ^{1}H NMR (500 MHz, CD_2Cl_2) spectra of the oxidative titration of ***c*-P12[b$_{12}$]·T12**.

The observed NMR features were, however, very broad and the identity of the THS shoulders were assigned solely based on the similarity to previous systems as no good 2D NMR correlation could be recorded for such broad signals. To illustrate how signals appear at the right amount of oxidant, a full titration is presented in **Figure 120**.

3.6.3.2.2. *c*-P12[b$_{12}$]·(T6e)$_2$

A HyperChem based model of ***c*-P12[b$_{12}$]·T12** (**Figure 118**) suggests an imperfect template fit, as the size of **T12** seems to be too large. This imperfect fit, together with the very flexible nature of the **T12** legs could be a rational for the broadness of the NMR spectra of the ***c*-P12[b$_{12}$]·T12** cations. Therefore, new templates, with an improved fit were sought. A novel, hexadentate template **T6e**, fitting the circular ***c*-P12[b$_{12}$]** was designed (**Figure 121**).

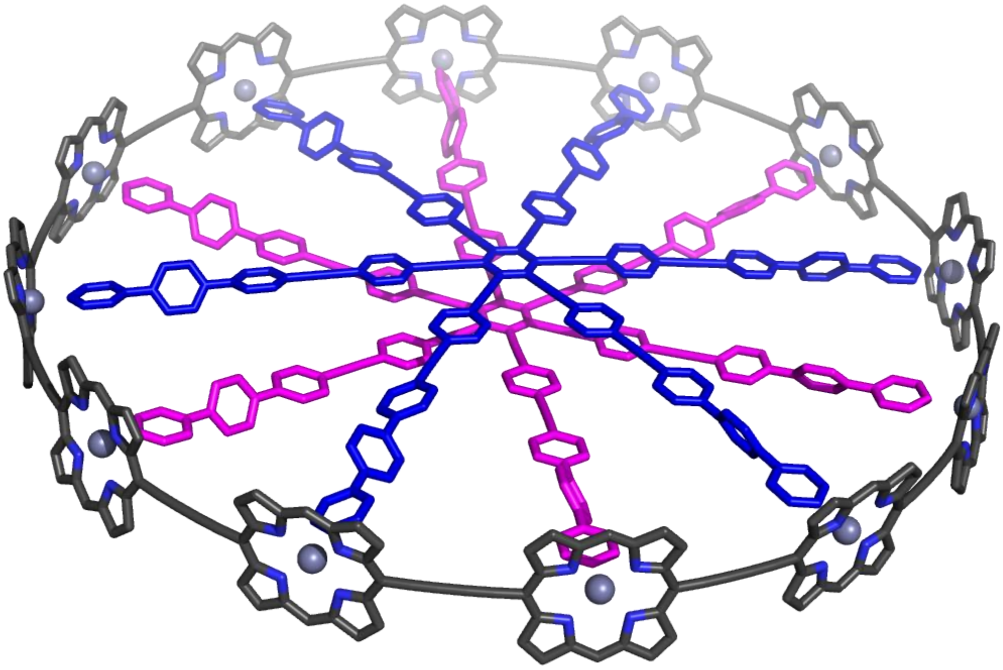

Figure 121: Model of the ***c*-P12[b$_{12}$]·(T6e)$_2$** optimised with the PM6 method. Two, identical **T6e** templates are highlighted in blue and magenta colour.

In order to satisfy all 12 zinc binding sites, two hexadentate templates need to be coordinated to ***c*-P12[b$_{12}$]**. In the design, it was taken into account that the core should be able to adopt a relatively flat shape, in order to stack well with another template. It was anticipated that the large radius of the nanoring (~2.5 nm) would enable two templates to stack with only a small degree of bending required. Assuming the stacked cores to be ~0.36 nm apart (typical π-π stack distance), the sum of the all bents angles of the templates rod would be ~8° and would be distributed over ~5 natural bending points (ethyne linker and phenyl–phenyl connections) (**Figure 122**).

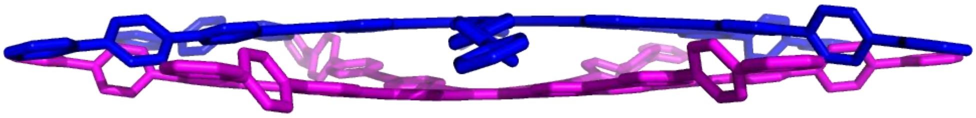

Figure 122: Side view on stacked templates **T6e**. illustrating required template bend.

The template and the synthetic strategy were designed by the author in collaboration with Dr. Michel Rickhaus. The synthesis itself was carried out by Dr. Michel Rickhaus and Dr. Henrik Gotfredsen (**Figure 123**).

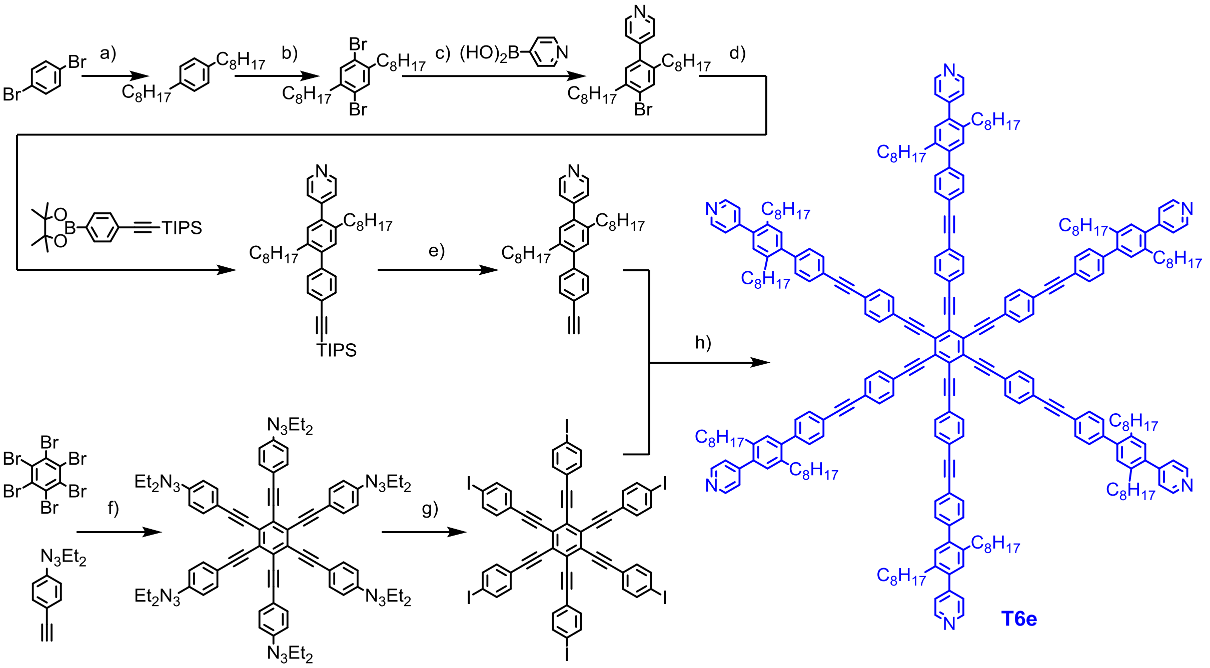

Figure 123: Scheme of **T6e** synthesis. a) *t*-BuLi, then $C_8H_{17}Br$; b) Br_2; c) $Pd(PPh_3)_4$, K_2CO_3, 46%; d) $Pd(PPh_3)_4$, K_2CO_3 60%; e) TBAF 95%; f) $Pd(PPh_3)_4$, CuI, 32%; g) CH_3I, 60%; h) $Pd(PPh_3)_4$, CuI, 74%.

Mixing of the ***c*-P12[b$_{12}$]** and **T6e** yielded to the desired 1:2 complex with a sharp ^{1}H NMR spectrum relative to ***c*-P12[b$_{12}$]·T12** (**Figure 125**). The assignment code for the ***c*-P12[b$_{12}$]·(T6e)$_2$** NMR spectrum is in **Figure 124**. The sharper NMR spectrum of ***c*-P12[b$_{12}$]·(T6e)$_2$** can be rationalised on the basis of a improved fit of the template and its rigid nature. In the case of **T6e**, any free rotation along any bond do not change the overall shape of the template, whereas rotation along certain bonds in **T12** would result in partial decoordination. Moreover, **T12** possess ester functionalities, most likely adopting various rotamer conformations further broadening the spectrum.

The NMR oxidation titration of ***c*-P12[b$_{12}$]·(T6e)$_2$** was successfully conducted, unveiling the previously not very resolved 6+ state (cf. **Figure 120**). Unfortunately, the observed 6+, 8+, 10+ and 12+ did not have significantly sharper features, and these findings only marginally reinforced the interpretation of the ***c*-P12[b$_{12}$]** cations (**Figure 126**).

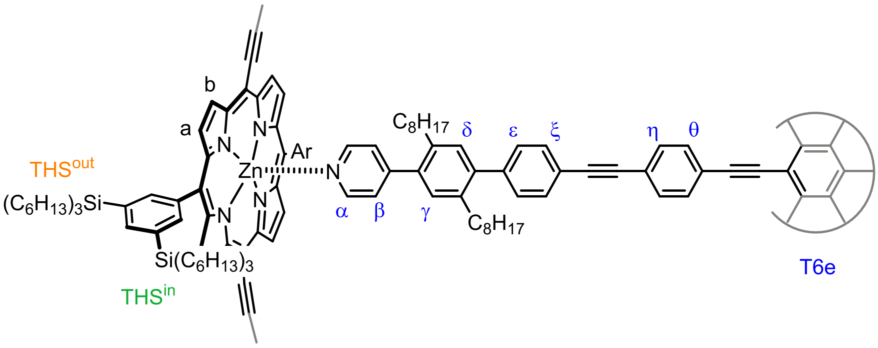

Figure 124: NMR labelling code for ***c*-P12[b$_{12}$]·(T6e)$_2$**.

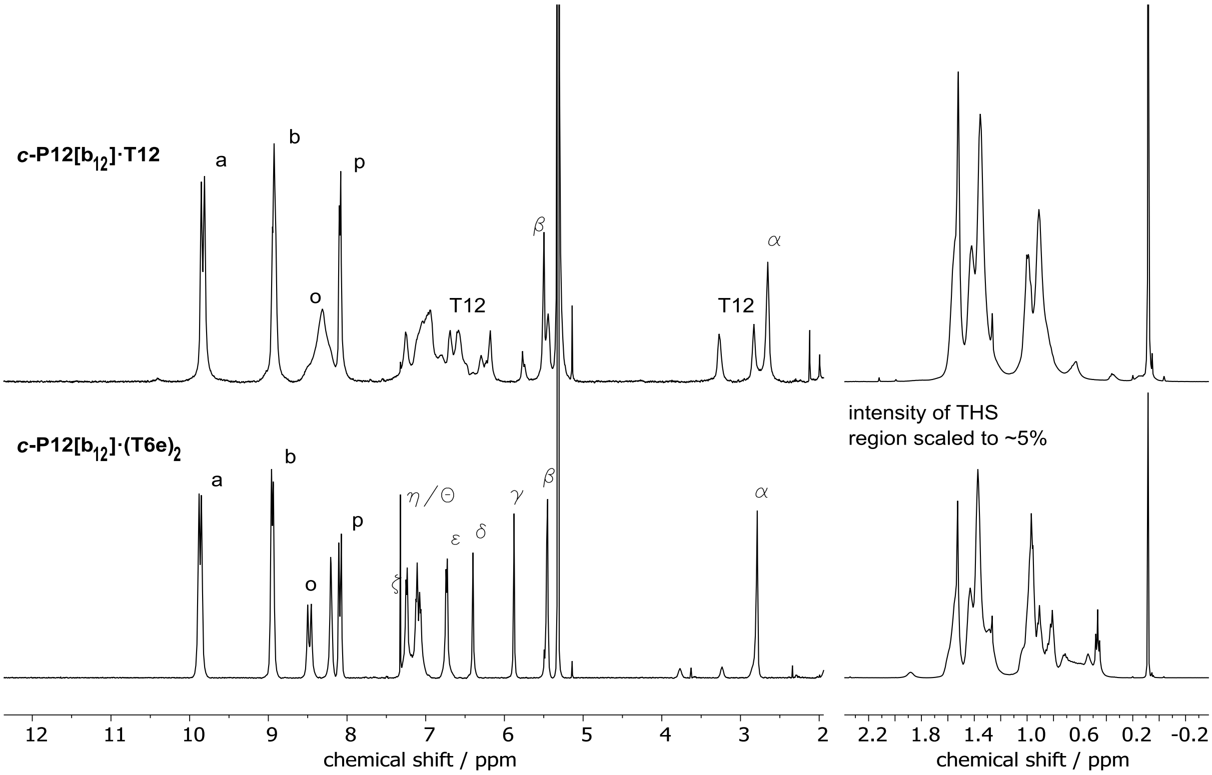

Figure 125: ^{1}H NMR (500 MHz, CD$_2$Cl$_2$) spectra of neutral ***c*-P12[b$_{12}$]·T12** (top) and ***c*-P12[b$_{12}$]·(T6e)$_2$** (bottom).

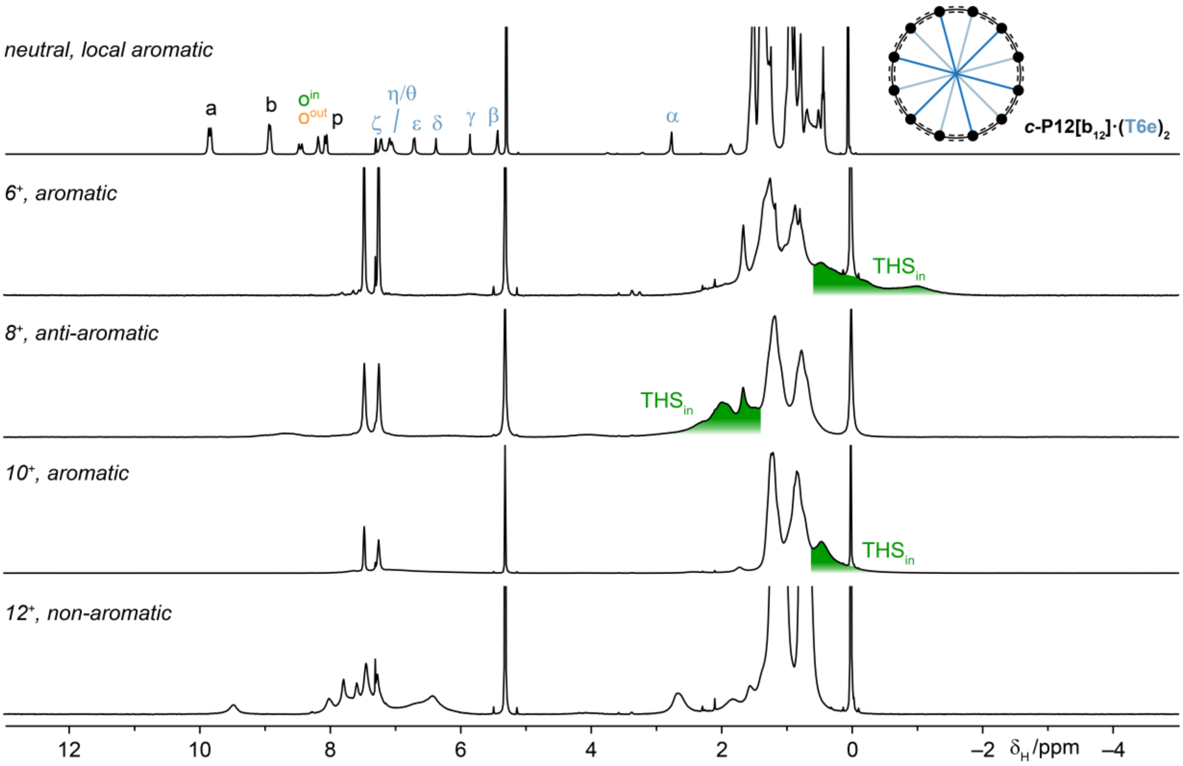

Figure 126: ^{1}H NMR spectra (500 MHz, CD_2Cl_2, 25°C (neutral) and −50°C (all other)) of the neutral, 6+, 8+, 10+ and 12+ oxidation states of ***c*-P12[b$_{12}$]·(T6e)$_2$**.

3.6.3.2.3. *c*-P12[b$_{12}$]·(T6ef)$_2$

As the template **T6e** provided only a limited improvement in the understanding of the aromaticity of ***c*-P12[b$_{12}$]** cations, the template was further developed and the previously (**Chapter 3.3.1.4**, page 113) successfully used $–CF_3$ ^{19}F NMR reporter group was engineered into the structure (**Figure 127**).

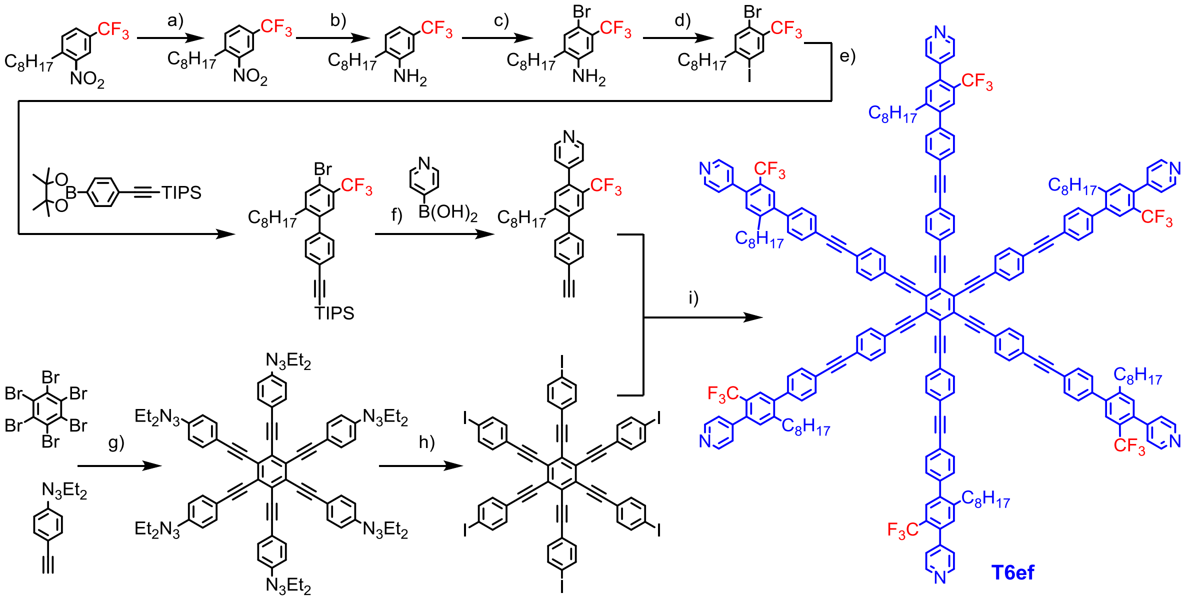

Figure 127: Scheme of **T6e** synthesis. a) $Pd(PPh_3)_4$, K_2CO_3, $C_8H_{17}B(OH)_2$, 63%; b) $SnCl_2$, 96%; c) NBS, 91%; d) $NaNO_2$/KI, *p*-TsOH, 95%; e) $Pd(PPh_3)_4$, K_2CO_3, 78%; f) $Pd(PPh_3)_4$, CuI, $PhB(OH)_2$, 98%, then TBAF 94%; g) $Pd(PPh_3)_4$, CuI, 59%; h) CH_3I, 79%; i) $Pd(PPh_3)_4$, CuI, 59%.

The presence of the –CF_3 groups cause **T6ef** to possess one, unique ^{19}F NMR signal at −59.4 ppm (vs. reference δ(C_6F_6) = −164.8 ppm). The complex ***c*-P12[b₁₂]·(T6ef)₂** was successfully formed analogously to ***c*-P12[b₁₂]·(T6e)₂** and this too possess also only one, slightly broadened, ^{19}F NMR signal, shielded by local aromatic porphyrins to approximately −59.6 ppm (**Figure 128**).

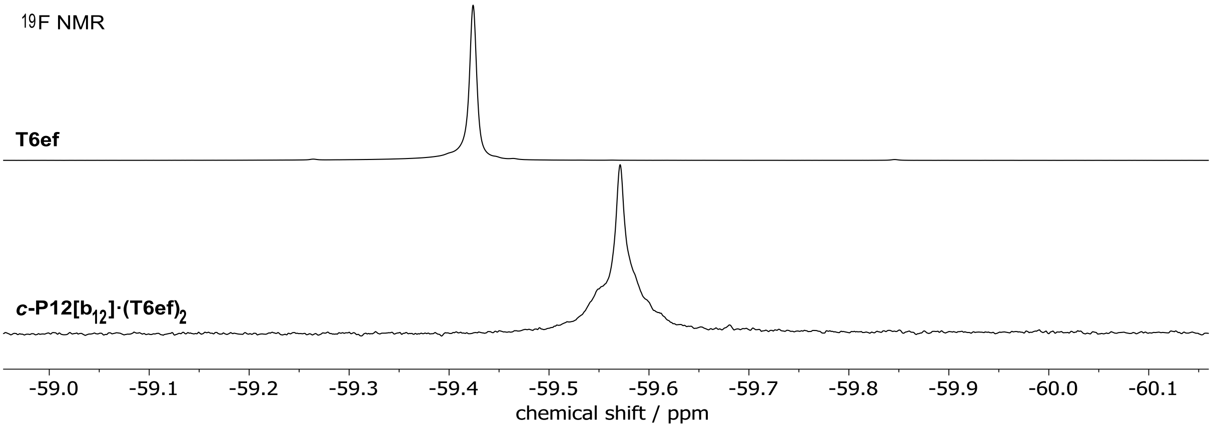

Figure 128: ^{19}F NMR (471 MHz, CD_2Cl_2, referenced to C_6F_6) spectra of·**T6ef** (top) and ***c*-P12[b₁₂]·(T6ef)₂** (bottom).

The –CF_3 group can be used as a handle for characterisation *via* 2D HOESY, observing magnetisation transfer from the –CF_3 group to neighbouring ^{1}H nuclei (**Figure 129**). The strongest magnetisation transfer is observed to the δ, then β and α template resonances.

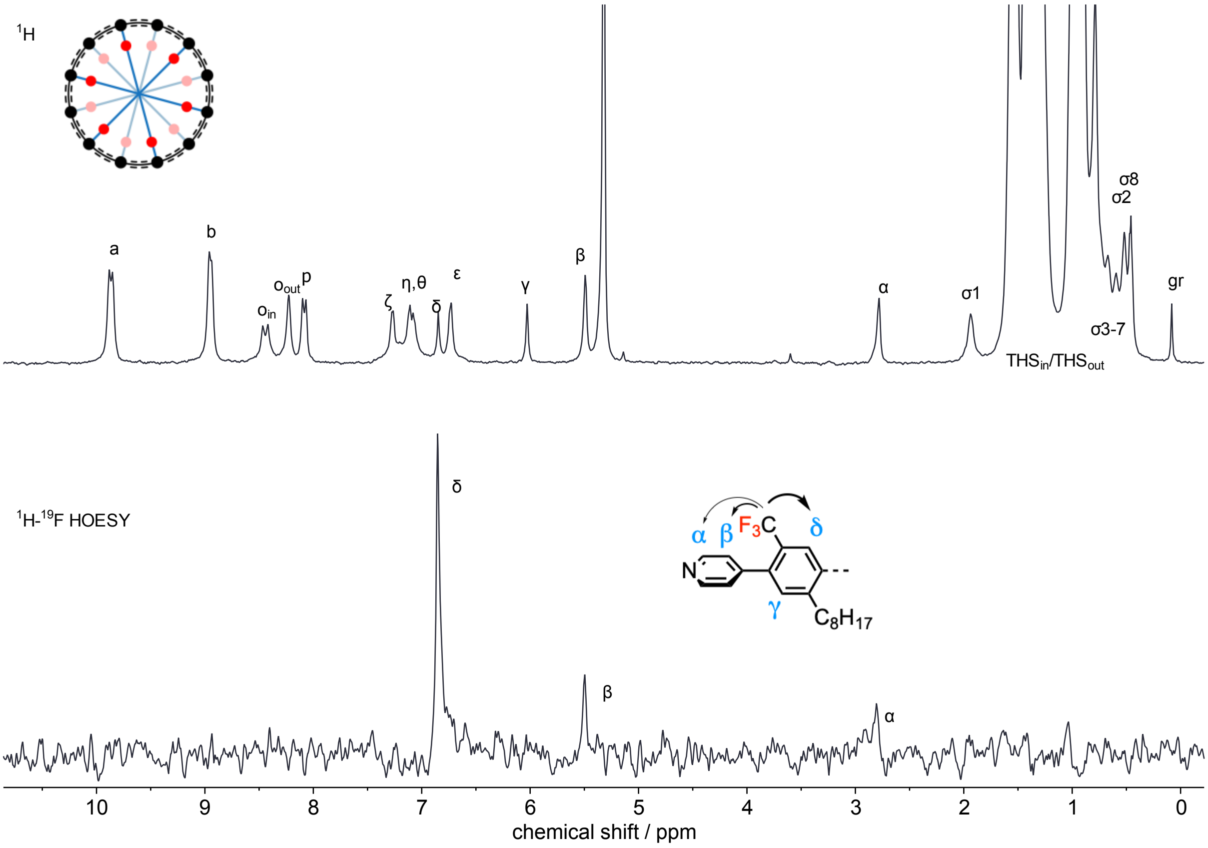

Figure 129: ^{19}F NMR (471 MHz, CD_2Cl_2, referenced to C_6F_6) spectra of·**T6ef** (top) and ***c*-P12[b₁₂]·(T6ef)₂** (bottom).

The oxidation titration was conducted in a way analogous to previous experiments and both ^{1}H and ^{19}F NMR channels were followed closely. The ^{1}H NMR spectra of each observed state were nearly identical with ***c*-P12[b$_{12}$]·(T6e)$_2$**, however, ^{19}F NMR spectroscopy provided a unique insight.

The general observation in ^{19}F NMR was that upon oxidation, some signal was observed at nearly unchanged chemical shift as free template **T6ef**, assignable to open-shell states without ring currents and/or possibly to the residual signal of decomposed or in some other way corrupted material. Further, shielded signals assignable to the aromatic 6+ and 10+ oxidation states as well as deshielded for the anti-aromatic 8+ states were evidence of the global (anti)aromaticity of such states. Interestingly, the 12+ oxidation state showed nearly no chemical shift difference, suggesting the absence of any global ring current (**Figure 130**).

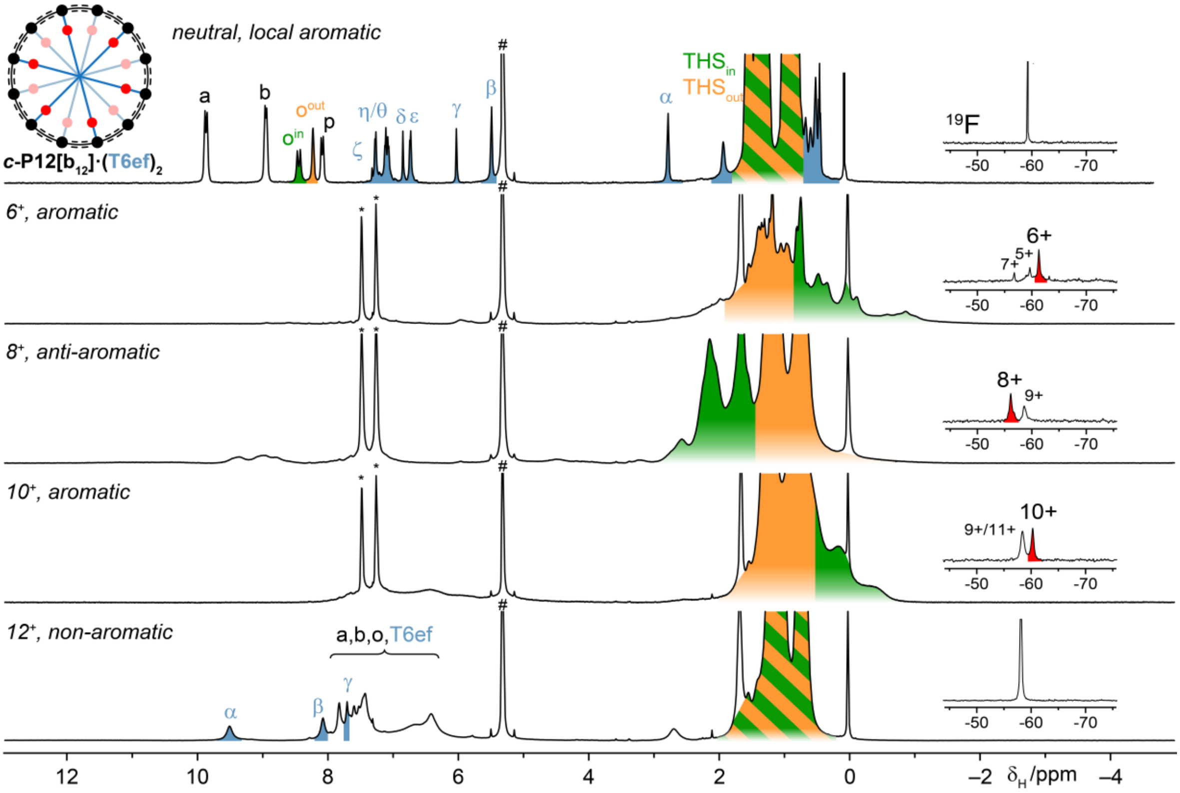

Figure 130: ^{1}H NMR spectra (500 MHz, CD_2Cl_2, 25°C (neutral) and −50°C (all other)) of the neutral, 6+, 8+, 10+ and 12+ oxidation states of ***c*-P12[b$_{12}$]·(T6e)$_2$**. ^{19}F NMR (471 MHz) inserts support the aromaticity interpretation.

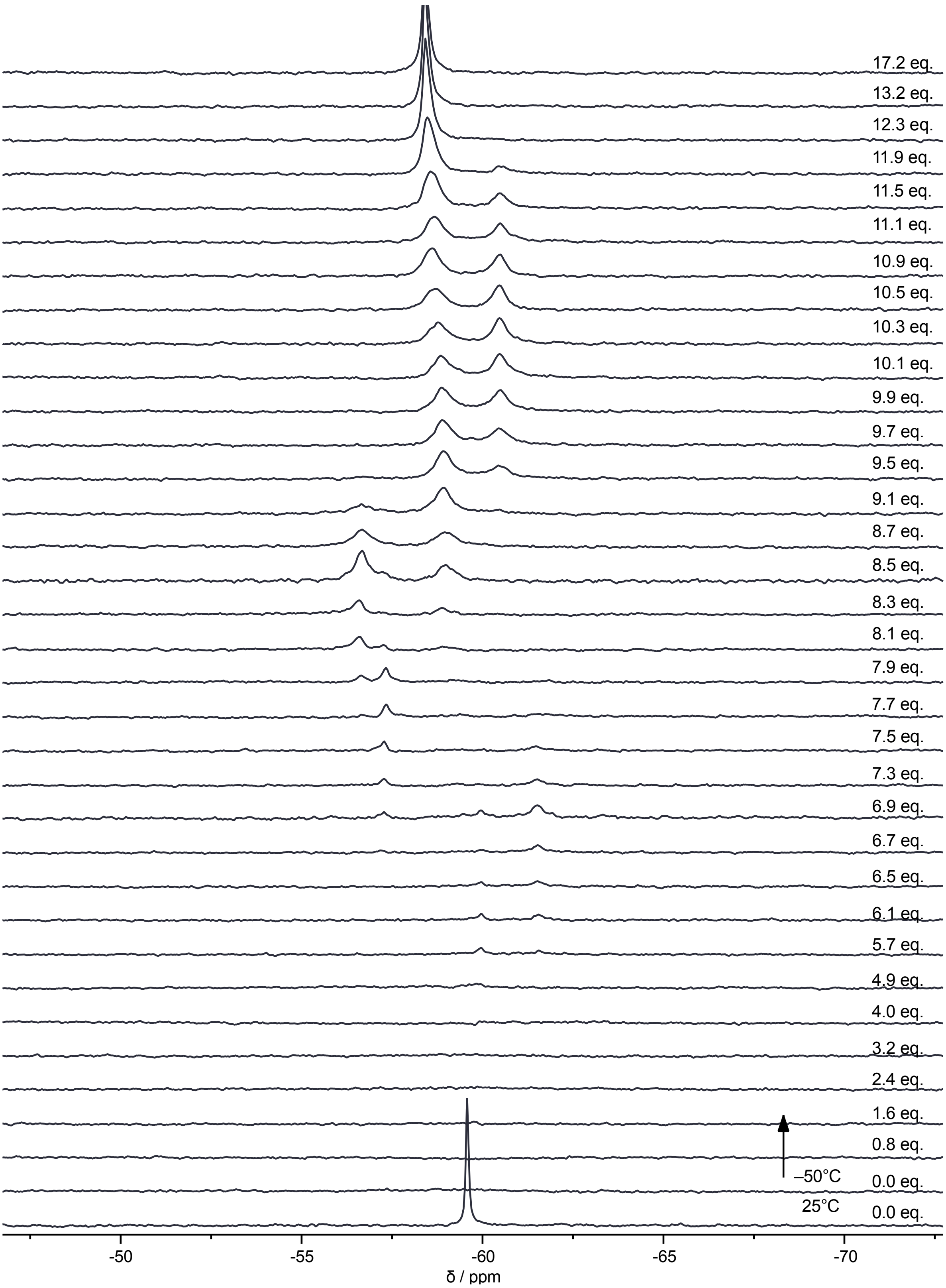

Figure 131: ^{19}F NMR (471 MHz, CD_2Cl_2, referenced to C_6F_6) spectra from the oxidative titration of ***c*-P12[b$_{12}$]·(T6e)$_2$**.

3.6.3.3. Figure-of-eight complex *c*-P12[b$_{12}$]·(T6f)$_2$

The study of the circularly shaped 12-porphyrin nanoring ***c*-P12[b$_{12}$]** documented the existence of the largest (anti)aromatic species, supported by the fluorine containing template. The ***c*-P12[b$_{12}$]** nanoring is known to be capable of binding two, small **T6** templates to form a figure-of-eight complex. This can be used to explore the relationship between 3D conformation and aromaticity. The magnitude of the ring current induced in a macroscopic ring of metal wire depends on the total magnetic flux passing through the ring. If the ring has a figure-of-eight shape, with two equal lobes such that the magnetic flux passing through each lobe induces an equal and opposite current, then there will be no net ring current (**Figure 132**).

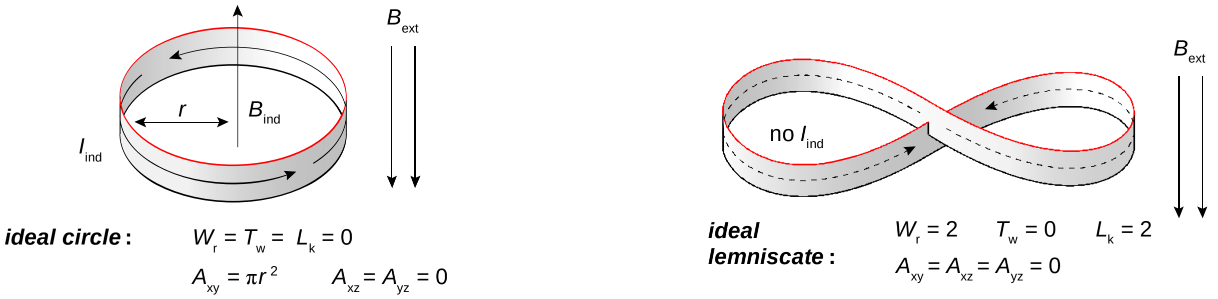

Figure 132: Comparison of the expected effects of an applied magnetic field to a globally aromatic species of at circular (left) or lemniscular (right) shape. The circular conformation is predicted to exhibit a ring currents and thus an induced magnetic moment upon the application of an external magnetic field. In the lemniscate, the two lobes induce opposite currents which cancel, and thus no ring current is expected

To test whether this principle applies on the molecular scale, the 1:2 complex ***c*-P12[b$_{12}$]·(T6f)$_2$** was prepared (**Figure 133**)

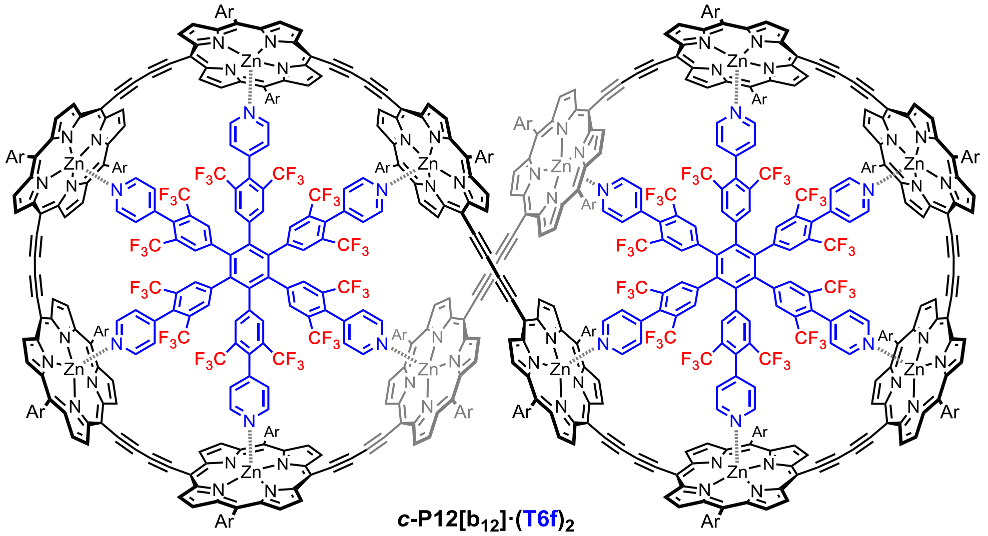

Figure 133: Chemical structure of lemniscular ***c*-P12[b$_{12}$]·(T6f)$_2$**.

It should be noted, that this system is doubly twisted, not Möbius and should, thus obey the Hückel Rule in the same way as circular ***c*-P12[b$_{12}$]·(T6ef)$_2$**. The suppression of ring currents in the figure-of-eight shaped annulenes has been predicted theoretically but it has not been observed experimentally in other figure-of-eight shaped aromatic systems, probably because in small molecules it is difficult to reach a sufficiently high figure-of-eight twist to achieve cancellation of the ring current. The topology of a closed ribbon can be described by the linking number *Lk*, the writhe *Wr* and the twist *Tw* (see **Chapter 4.1.**). Total cancellation of the ring current is expected for a geometry with $Wr = 2$, $Tw = 0$ and $Lk = 2$ with D_2 symmetry,[64] which is close to the geometry of ***c*-P12[b12]·(T6f)2** ($Wr = 1.8$, $Tw = 0.2$ and $Lk = 2$, from the crystal structure of ***c*-P12[b12]·(T6)2**.[85] As a model for ***c*-P12[b12]·(T6e)2**, the crystallographic geometry of the neutral complex ***c*-P12[b12]·(T6)2** and was used re-optimised with the PM6 method after replacement of the aryl solubilising groups with hydrogen atoms (**Figure 134**).

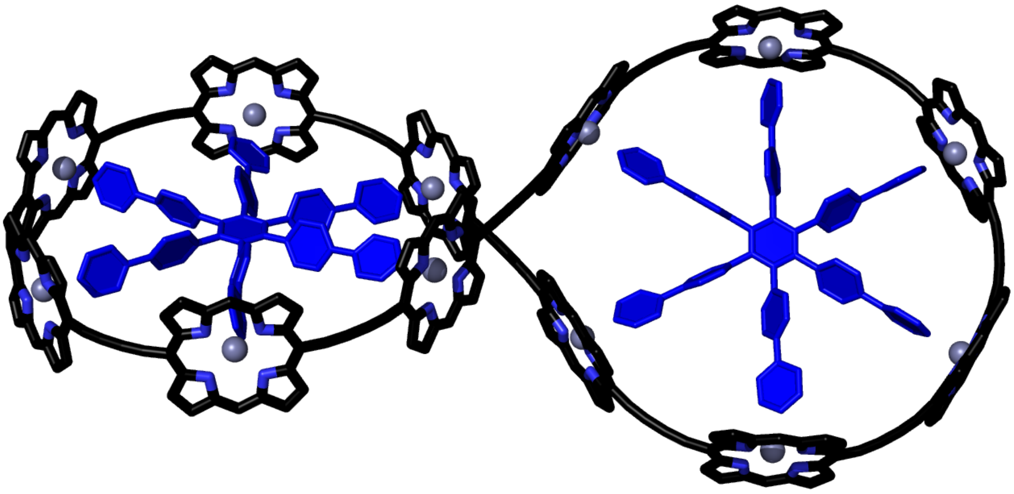

Figure 134: Model structure of ***c*-P12[b12]·(T6f)2**, based on reoptimised geometry taken from crystallographic coordinates.

The ***c*-P12[b12]·(T6ef)2** nanoring has a large cross sectional area ($A_{xy} = 22$ nm^2; $A_{xz} = A_{yz} = 0$) resulting in a substantial ring current, whereas the ***c*-P12[b12]·(T6f)2** lemniscate has a small net cross section ($A_{xy} = 0$, $A_{xz} = 2.3$ nm^2, $A_{yz} = 0.4$ nm^2). Such total area contained by the ***c*-P12[b12]·(T6)2** lemniscate as obtained from the three spatial projections. The area was calculated from the crystallographic coordinates as a sum of the areas of triangles constructed from three points: origin, position of atom and the next following atom. The atoms considered were the zinc centres, the *meso*-carbons attached to the butadiynes, and the butadiyne carbons. The sum is sensitive to the orientation of the area (clockwise assumed as positive, counter-clockwise as negative) (**Figure 135**).

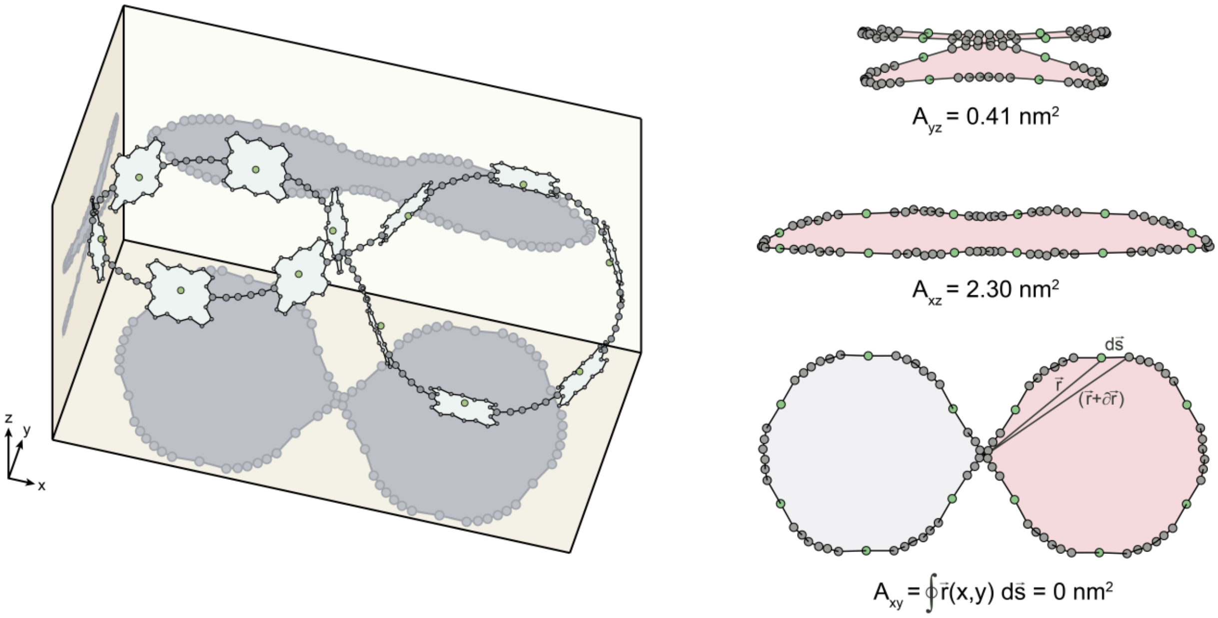

Figure 135: Calculation of the effective cross-section area of ***c*-P12[b$_{12}$]·(T6f)$_2$**.

The NICS scans on the ***c*-P12[b$_{12}$]·(T6f)$_2$** model were calculated on a surface constructed from three segments stitched along the longest (x) axis. Numerically, the three segments are described with: $z = -0.01283\cdot x - 0.131\cdot y - 0.1291$ for $x = (-50, -11.4)$; $z = 0.01632\cdot x\cdot y - 0.217$ for $x = (-11.4, 11.4)$ and $z = 0.05418\cdot x + 0.1324\cdot y - 0.9563$ for $x = (11.4, 50)$ (**Figure 136**).

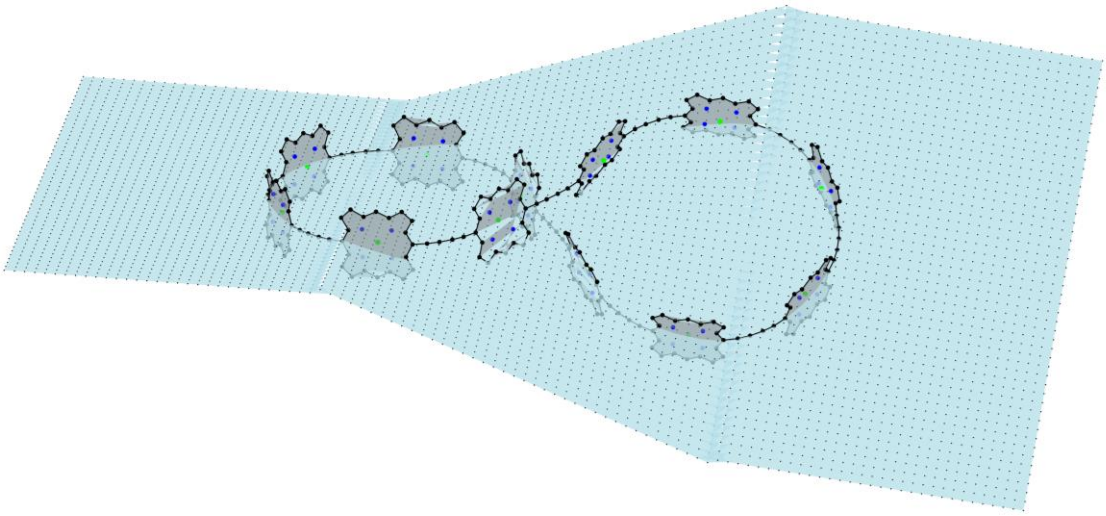

Figure 136: NICS grid for the ***c*-P12[b$_{12}$]·(T6)$_2$** model constructed from three segments.

The NICS calculated on the lemniscate could be directly compared with circularly-shaped ***c*-P12[b$_{12}$]**, obtained by geometry optimisation of complex ***c*-P12[b$_{12}$]·(T6ef)$_2$** using semiempirical PM6 method (**Figure 137**). In the case of the circular nanoring, a ring current is predicted, obeying Hückel’s rule (even though the geometry was optimised with a different method than NICS were calculated).

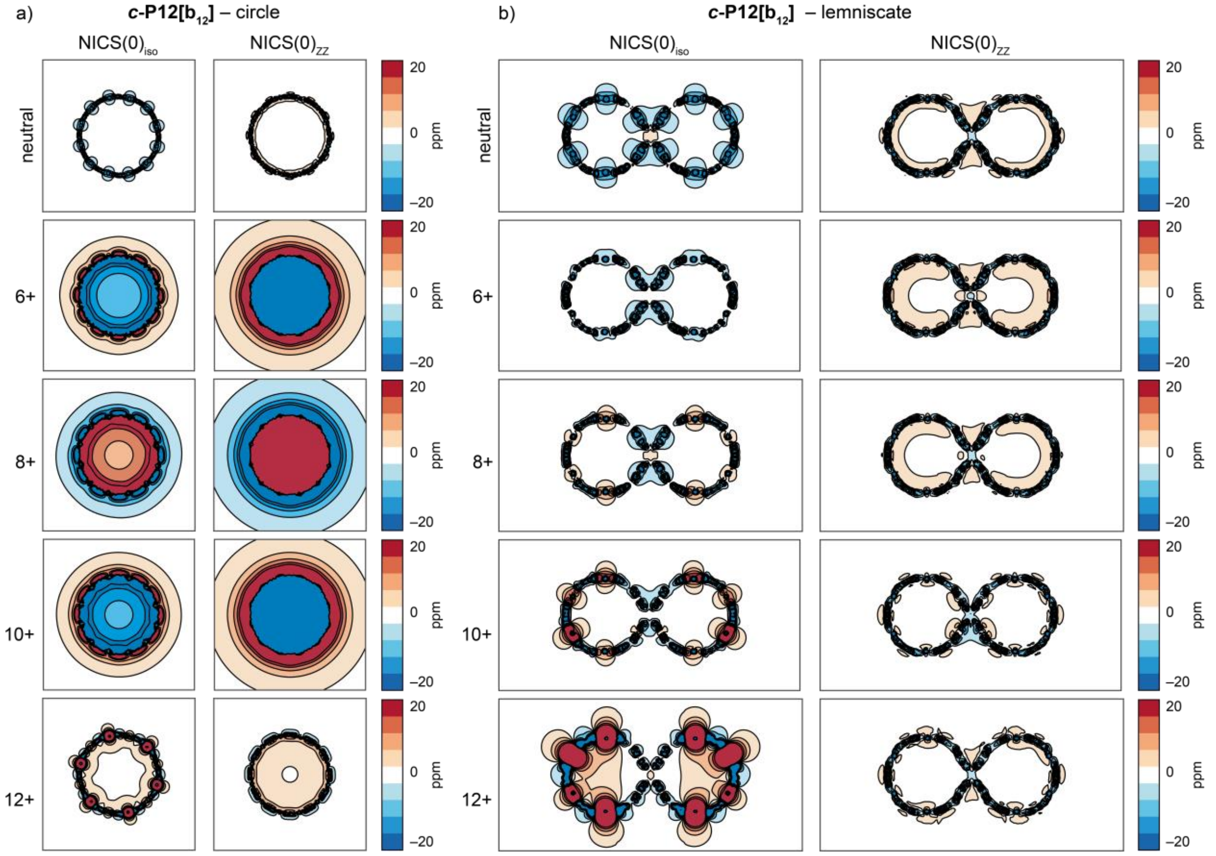

Figure 137: NICS (LC-ωhPBE (ω = 0.1)/6-31G*) calculated for circular ***c*-P12[b12]·(T6e)2** and lemniscular ***c*-P12[b12]·(T6)2**, using grid size of 100×100 Å (with spacing 1 Å) and 100×50 Å (with spacing 0.5 Å), respectively. Geometries were optimised using the semiempirical PM6 method. NICS document the predicted absence of any induced global ring current as a result of net cross section cancel.

NMR oxidation was performed under identical conditions to those used for the circular ***c*-P12[b12]·(T6ef)2**. The resulting ^{1}H, ^{13}C and ^{19}F NMR spectra show the absence of any detectable ring currents (Δδ <0.1 ppm) in the figure-of-eight nanoring, confirming that aromaticity can be switched on/off by the change of the 3D shape (**Figure 138**).

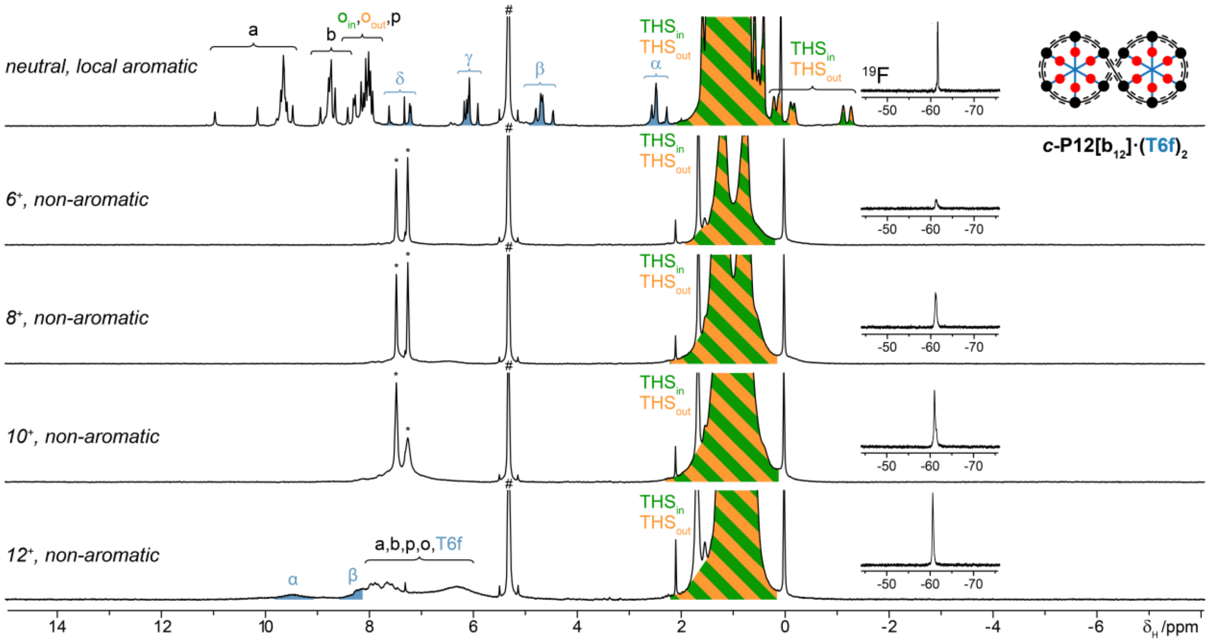

Figure 138: ^{1}H NMR (500 MHz, CD_2Cl_2, (neutral) 25°C and (rest) −50°C) of the neutral, 6+, 8, 10+ and 12+ oxidation states of lemniscular ***c*-P12[b$_{12}$]·(T6f)$_2$**.^{19}F NMR (471 MHz) inserts supports the 'observation' of the absence of the global ring current.

Since the absence of such rather subtle effect is a delicate result to present, the titration stack of the circular and lemniscular system at added integer equivalents of oxidant provides a good comparison (**Figure 139**). Note, that the presented titration stack is only a selection of titration points, in both cases over 80 additions were carried out and for each addition NMR spectra were recorded in order to ensure no observable state was missed.

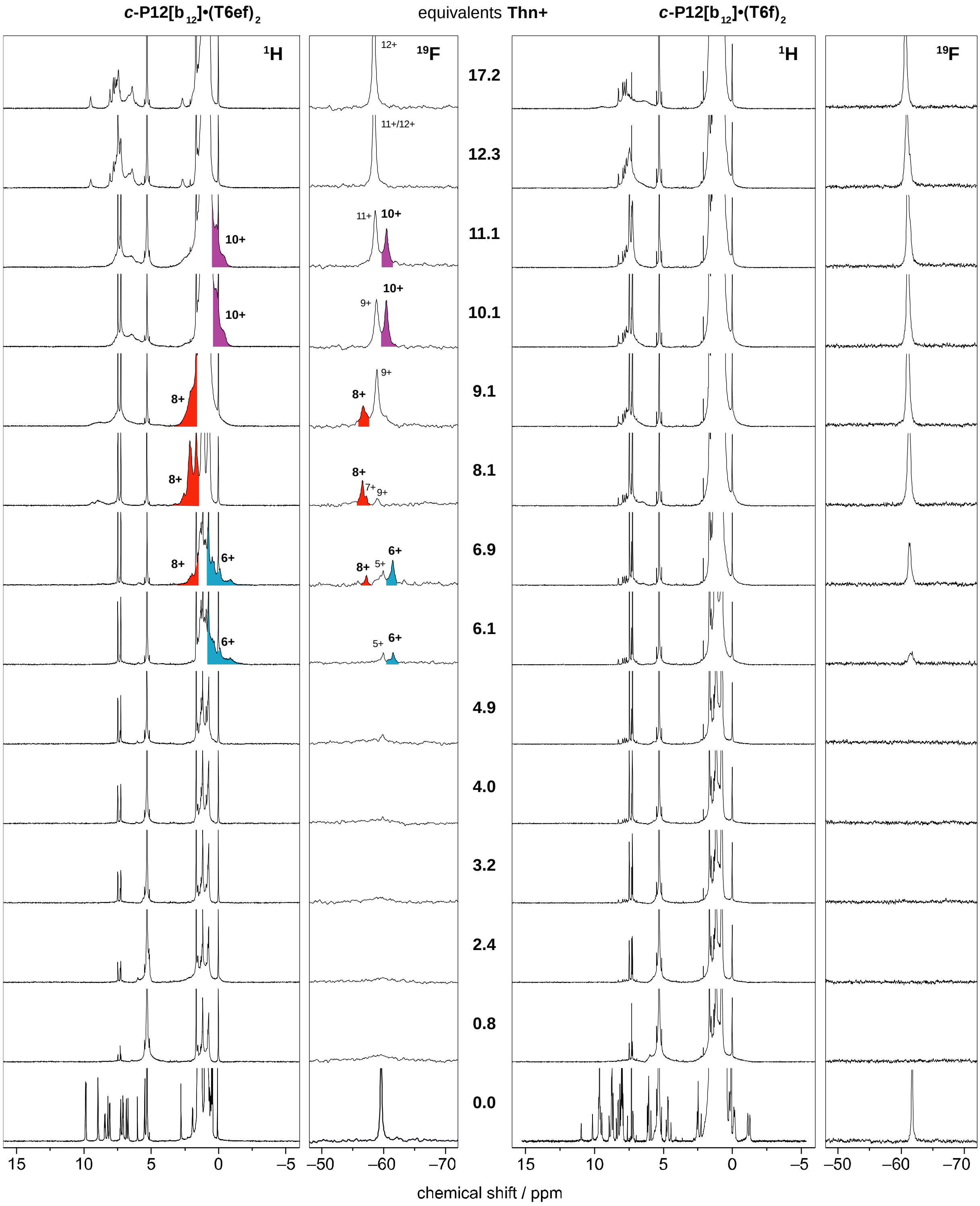

Figure 139: ^{1}H NMR (500 MHz) and ^{19}F NMR (471 MHz) of ***c*-P12[b$_{12}$]·(T6ef)$_2$** (left) and ***c*-P12[b$_{12}$]·(T6f)$_2$** (right) at oxidation states 0 to 12+.

These findings and detailed analysis are summarised in **Tables 14–16**:

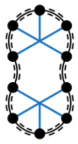

***c*-P10[b$_{10}$]·(T5)$_2$**	**0+** / 298 K		**2+**	**4+**	**6+** / 223 K		**8+** / 223 K		**10+** / 223 K	
	^{1}H	**^{13}C**			**^{1}H**	**^{13}C**	**^{1}H**	**^{13}C**	**^{1}H**	**^{13}C**
T5	—	—	—	—	—	—	13.5-10.24	—	—	—
α	2.67 2.43 2.36	143.8 143.3 143.1	—	—	—	—	—	—	9.15 8.71	—
β	5.43 5.20 5.01	119.7 119.9 120.1	—	—	—	—	—	—	7.86 7.65	—
γ	6.09 5.67 5.50	125.5 124.8	—	—	—	—	—	—	—	—
δ	6.17 5.75 5.62	130.0 131.6	—	—	—	—	—	—	—	—
ε	6.61	130.6	—	—	—	—	—	—	—	—
a	9.70 9.62 9.58 9.54	130.9	—	—	—	—	—	—	—	—
b	8.87-8.71	133.5	—	—	—	—	—	—	—	—
p	8.04 8.00	139.9	—	—	—	—	—	—	—	—
o_{in}	8.43 8.34 8.15	140.8 141.0 141.1	—	—	—	—	—	—	—	—
o_{out}	8.29 8.09 8.06	141.3 141.7	—	—	—	—	—	—	—	—
THS$_{in}$-CH$_2$	0.94	13.1	—	—	—	—	—	—	0.69 0.63	11.9 11.9
THS$_{out}$-CH$_2$	0.94	13.1	—	—	0.94 0.85 0.76	12.2 12.2 12.2	0.71 0.63	11.3 11.3	0.69 0.63	11.9 11.9
THS$_{in}$-CH$_3$	0.91 0.82 0.73	14.5 14.5 14.4	—	—	–0.94 –0.82 –1.62	12.9 12.5 12.2	2.35 1.75	15.6 14.8	0.77 0.66	14.5 14.5
THS$_{out}$-CH$_3$	0.91 0.82 0.73	14.5 14.5 14.4	—	—	1.00 0.80	14.5 14.5	0.76	14.0	0.77 0.66	14.5 14.5

Table 14: NMR data obtained for the observed oxidation states of ***c*-P10[b$_{10}$]·(T5)$_2$**.

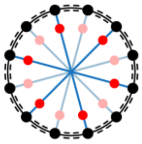

***c*-P12[b$_{12}$]·(T6ef)$_2$**	**0+** / 298 K		**2+**	**4+**	**6+** / 223 K		**8+** / 223 K		**10+** / 223 K		**12+** / 223 K	
	^{1}H	**^{13}C**			**^{1}H**	**^{13}C**	**^{1}H**	**^{13}C**	**^{1}H**	**^{13}C**	**^{1}H**	**^{13}C**
α	2.79	143.5	—	—	—	—	—	—	—	—	9.51	—
β	5.50	123.7	—	—	—	—	—	—	—	—	8.08	—
γ	6.03	132.3	—	—	—	—	—	—	—	—	7.67	—
δ	6.85	128.0	—	—	—	—	—	—	—	—	—	—
ε	6.74	129.4	—	—	—	—	—	—	—	—	—	—
ζ	7.28	132.3	—	—	—	—	—	—	—	—	—	—
η	7.11	132.2	—	—	—	—	—	—	—	—	—	—
θ	7.11	132.2	—	—	—	—	—	—	—	—	—	—
σ1	1.94	32.7	—	—	—	—	—	—	—	—	—	—
σ2	0.53	29.2	—	—	—	—	—	—	—	—	—	—
σ3–7	0.80 0.73 0.67 0.57	22.9 30.8 32.0 29.3	—	—	—	—	—	—	—	—	—	—
σ8	0.46	14.3	—	—	—	—	—	—	—	—	—	—
a	9.89	131.2	—	—	—	—	—	—	—	—	—	—
b	8.96	134.1	—	—	—	—	—	—	—	—	—	—
o$_{in}$	8.49	141.5	—	—	—	—	—	—	—	—	—	—
o$_{out}$	8.23	142.1	—	—	—	—	—	—	—	—	—	—
p	8.11	140.4	—	—	—	—	—	—	—	—	—	—
THS$_{in}$-CH$_2$	0.99	13.3	—	—	—	—	—	—	—	—	0.71	11.5
THS$_{out}$-CH$_2$	0.99	13.3	—	—	0.94 0.87	11.9 11.9	0.82 0.74 0.67	12.3 12.3 12.3	0.81	12.2	0.71	11.5
THS$_{in}$-CH$_3$	0.96 0.89 0.79	14.8 14.7 14.7	—	—	0.04 −0.11	13.4 13.0	1.74 1.65 1.57	15.4 15.4 15.4	0.39 0.18	14.2 14.2	0.80 0.73	14.2 14.2
THS$_{out}$-CH$_3$	0.96 0.89 0.79	14.8 14.7 14.7	—	—	0.96 0.82 0.70	14.2 13.8 13.8	0.75	14.7	0.86 0.74	14.6 14.6	0.80 0.73	14.2 14.2
	^{19}F				**^{19}F**		**^{19}F**		**^{19}F**		**^{19}F**	
CF$_3$^{a}	59.57		—	—	61.52		56.64		58.99		58.40	

[a] referenced with hexafluorobenzene (−164.8 ppm)

Table 15: NMR data obtained for observed oxidation states of ***c*-P12[b$_{12}$]·(T6ef)$_2$**.

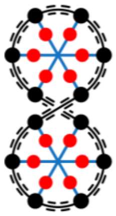

***c*-P12[b$_{12}$]·(T6f)$_2$**	**0+** / 223 K		**2+**	**4+**	**6+** / 223 K		**8+** / 223 K		**10+** / 223 K		**12+** / 223 K	
	^{1}H	**^{13}C**			**^{1}H**	**^{13}C**	**^{1}H**	**^{13}C**	**^{1}H**	**^{13}C**	**^{1}H**	**^{13}C**
T6f	—	—	—	—	—	—	—	—	—	—	—	—
α	2.56 2.49 2.27	143.11	—	—	—	—	—	—	—	—	9.44	—
β	4.80 4.68 4.48	124.1 123.2 122.5	—	—	—	—	—	—	—	—	8.09	—
δ	6.17 6.12 6.09 5.91	— — 131.5 –	—	—	—	—	—	—	—	—	—	—
a	10.96 10.14 9.70- 9.59 9.47	— — 130.1 — —	—	—	—	—	—	—	—	—	—	—
b	8.94 8.75 8.67 8.41	— 133.8 133.4 133.5	—	—	—	—	—	—	—	—	—	—
o$_{in}$/o$_{out}$/ p	8.14 8.28 8.06 8.00 7.61 7.21	141.1 141.0 141.7 140.3 — —	—	—	—	—	—	—	—	—	—	—
THS$_{in}$-CH$_2$	1.03 0.92 0.47 −1.08 −1.23	12.7 12.7 12.3 10.8 10.6	—	—	—	—	—	—	—	—	0.71 0.65	11.1 11.2
THS$_{out}$-CH$_2$	1.03 0.92 0.47 −1.08 −1.23	12.7 12.7 12.3 10.8 10.6	—	—	—	—	—	—	—	—	0.71 0.65	11.1 11.2
THS$_{in}$-CH$_3$	0.93 0.73 0.60 0.43	14.4 14.1. 14.0 13.9	—	—	0.81	13.3	0.82 0.71	14.0 14.0	0.81 0.72	14.4 14.0	0.78 0.69	14.1 14.1
THS$_{out}$-CH$_3$	0.93 0.73 0.60 0.43	14.4 14.1. 14.0 13.9	—	—	0.81	13.3	0.82 0.71	14.0 14.0	0.81 0.72	14.4 14.0	0.78 0.69	14.1 14.1
	^{19}F				**^{19}F**		**^{19}F**		**^{19}F**		**^{19}F**	
CF$_3$[a]	−61.63 −61.69 −61.73		–	–	−61.22 −61.37		−61.17 −61.36		−61.39 −60.95		−60.74 −60.54	

[a] referenced with hexafluorobenzene (−164.8 ppm)

Table 16: NMR data obtained for observed oxidation states of ***c*-P12[b$_{12}$]·(T6f)$_2$**.

3.7. Summary

The Hückel Rule was originally formulated to explain the unusual properties of benzene, and other molecules with 6 π-electrons. It is remarkable that this simple rule qualitatively correctly predicts the magnetic response of large oxidised nanorings with circuits of up to 162 π electrons. This work shows that charge and π electrons can be coherently delocalised around molecular rings with circumferences of up to 16 nm.

To summarise the experimentally observed ring currents for selected nanoring cations a plot of the difference between the chemical shifts of the **THS$_{\mathbf{in}}$** and **THS$_{\mathbf{out}}$** resonances ($\Delta\delta_{THS}$) as a function of the number of π electrons in the system is shown in **Figure 140**.

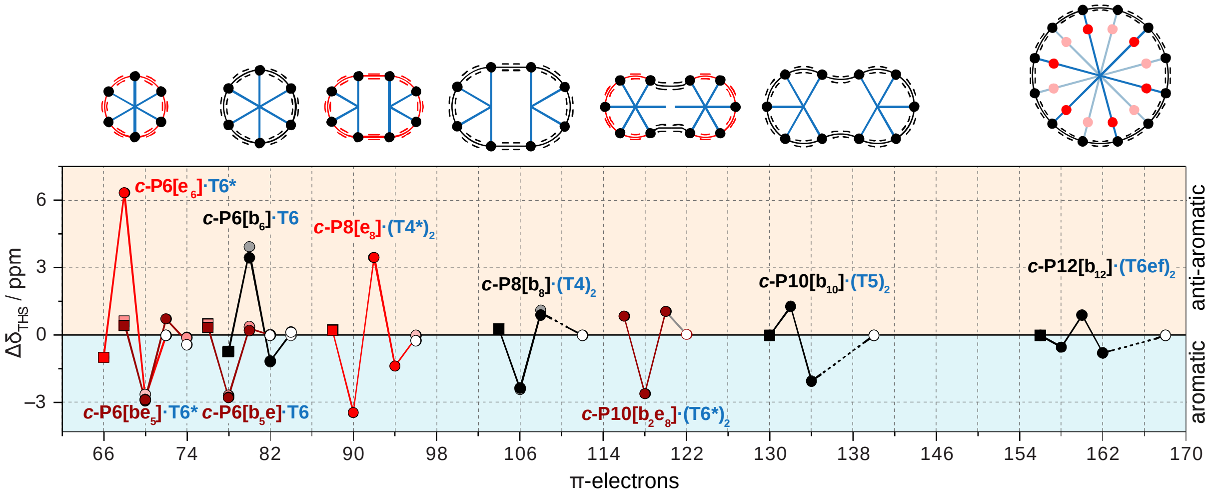

Figure 140: (top) Schematic representation of a family of related porphyrin rings with increasing number of porphyrins. Red indicates ethyne, black indicates butadiyne linkers. Black dots indicate zinc-porphyrins. Templates are represented in blue. (bottom) Plot of the observed ^{1}H NMR chemical shift difference ΔδTHS = δ**THS$_{\mathbf{in}}$** − δ**THS$_{\mathbf{out}}$** between inner and outer THS probe for each oxidation state of the nanoring. A positive or negative shift indicates a global anti-aromatic or aromatic current, respectively. Empty circles indicate the corresponding neutral species. Squares indicate oxidation states with $\overline{P_{\mathrm{OX}}} = 1$. Vertical dashed lines denote oxidation states with [4*n*+2] π-electrons. Lines connecting dots are for visual guidance only. ΔδTHS values are shown for both the –C*H*$_3$ signals (dark points) and SiC*H*$_2$ signals (faded points) of the THS chains.

Whenever a ring current in a porphyrin nanoring cations was observed, its direction (aromatic or anti-aromatic) matches the prediction of Hückel's rule. The magnitude of the ring current varies with the average oxidation state of the porphyrin units ($\overline{P_{\mathrm{OX}}} = Q/N$). The largest ring currents are observed in mixed-valence systems, where $\overline{P_{\mathrm{OX}}} \approx +0.5$ to +0.7. Global ring currents are not observed in the neutral rings ($\overline{P_{\mathrm{OX}}} = 0$), where the local porphyrin ring current dominates; in the larger rings, the ring current also vanishes when $\overline{P_{\mathrm{OX}}} = 1$ (see square points for ***c*-P8[b$_8$]·(T4)$_2$$^{8+}$**, ***c*-P10[b$_{10}$]·(T5)$_2$$^{10+}$** and ***c*-P12[b$_{12}$]·(T6ef)$_2$$^{12+}$** in **Figure 140**). The formation of a mixed valence state appears to be essential for efficient nanoscale charge delocalisation, just as the presence of a partially filled band is essential for conductance in an extended lattice.[110]

The ***c*-P12[b$_{12}$]** systems represent the largest globally (anti)aromatic species ever reported. Furthermore, it was demonstrated that changing the shape of this large supramolecular ring can switch off the induced ring current, as a result of an effective cross-section area cancelation (**Figure 141**).

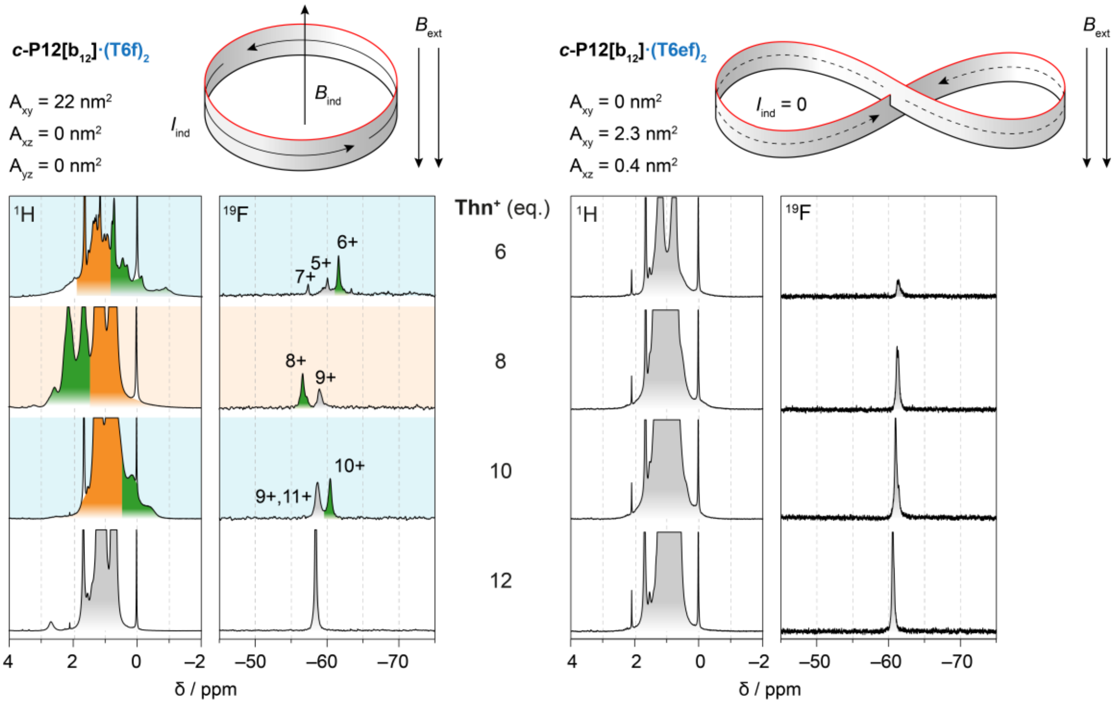

Figure 141: ^{1}H and ^{19}F NMR (500 MHz, CD_2Cl_2, −50°C) spectra of circular (left) and lemniscular (right) ***c*-P12[b$_{12}$]** cations.

The presented oxidation experiments document that the limit for aromaticity, in term of the magnetic behaviour is greater than 162 π electrons. On the other hand, the series of observed anti-aromatic states and their observed conformational stability in template-free rings suggests that the energetic difference and thus anticipated stabilisation of aromatic and destabilisation of anti-aromatic species is only subtle.

3.8. Experimental details

3.8.1. Calculations

NICS/susceptibility calculations were conducted using the GIAO methods, as implemented in Gaussian16/A.03, using the LC-ωhPBE/6-31G* (ω = 0.1) functional/basis set. The xyz coordinates of most of the optimised molecules are deposited on ChemRxiv preprint service.[111]

3.8.2. Synthetic details

Synthesis of ***c*-P6[b$_6$]·T6** was conducted by the author following a published procedure.[102] ***c*-P6[e$_6$]·T6***, ***c*-P6[be$_5$]·T6*** and ***c*-P8[e$_8$]·(T4)$_2$** were synthesised by Dr. Lara Tejerina and Dr. Michel Rickhaus according to published procedures.[106,107] ***c*-P6[b$_5$e]·T6** was synthesised by Dr. Renee Haver and Dr. Hua-Wei Jiang according to published procedure.[106] Synthesis of templates **T6ef** and **T6f** was conducted by the Dr. Michel Rickhaus and Dr. Henrik Gotfredsen and published in preprint.[111]

The corresponding template complexes were formed by titration of a template-solution (in $CDCl_3$) into a solution of the corresponding ring (in $CDCl_3$) and the excess template removed by size exclusion chromatography (BioBeads SX-1, eluent: $CHCl_3$) or a short plug (SiO_2, eluent: petrol ether, 5% CH_2Cl_2).

3.8.2.1. Synthesis of *c*-P5·T5

This synthesis was conducted and reported by Dr. Lara Tejerina adapting procedure from literature.[112]

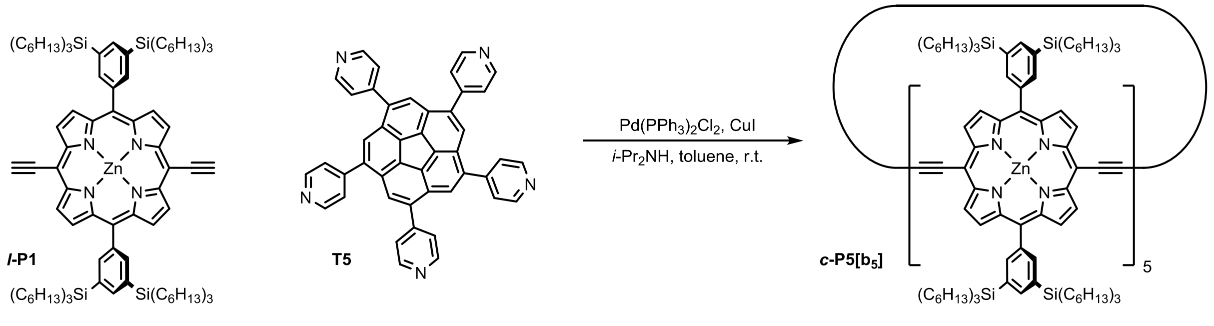

Figure 142: Scheme of ***c*-P5[b$_5$]** synthesis.

Bis(ethynyl)porphyrin monomer ***l*-P1** (130 mg, 0.076 mmol, 1 equiv.), **T5** (4.8 mg, 7.6 μmol, 0.1 equiv.) and molecular sieves were mixed and dissolved in toluene (100 mL) and *i*-Pr_2NH (1.7 mL), and the mixture was stirred for 3 h at ambient temperature. Then, 1,4-benzoquinone (33 mg, 0.31 mmol, 4 equiv.) and a well-mixed solution of $Pd(PPh_3)_2Cl_2$ (11 mg, 15.7 μmol, 0.2 equiv.) and CuI (22 mg, 0.116 mmol, 1.5 equiv.) in toluene (100 mL) and *i*-Pr_2NH (1.7 mL) was added to the reaction mixture. The mixture was stirred under Ar for 16 h. Mixture was passed through short alumina plug eluted with CH_2Cl_2. The mixture was purified on a short SEC column and by recycling GPC using toluene/1% pyridine yielding ring with the template ***c*-P5[b$_5$]·T5** as a brown solid (2.4 mg, 1.7%). Template **T5** was quantitatively removed on short SEC using excess of pyridine.

***c*-P5[b$_5$]: ^{1}H NMR** (500 MHz, CD_2Cl_2, 25 °C): δ_H = 9.54 (d, 20H, J = 4.6 Hz, H_β), 8.71 (d, 20H, J = 4.8 Hz, H_β), 8.09 (s, 20H, H_{Ar}), 7.97 (s, 10H, H_{Ar}), 1.46 – 0.58 (m, 780H, H_{THS}). ***m/z* (MALDI-ToF)** 8512 ($C_{540}H_{850}N_{20}Si_{20}Zn_5$, M^+ requires 8511 for ***c*-P5[b$_5$]**).

3.8.2.2. Synthesis of *c*-P7·T7

This synthesis was conducted and reported by Dr. Lara Tejerina adapting procedure from literature.[87]

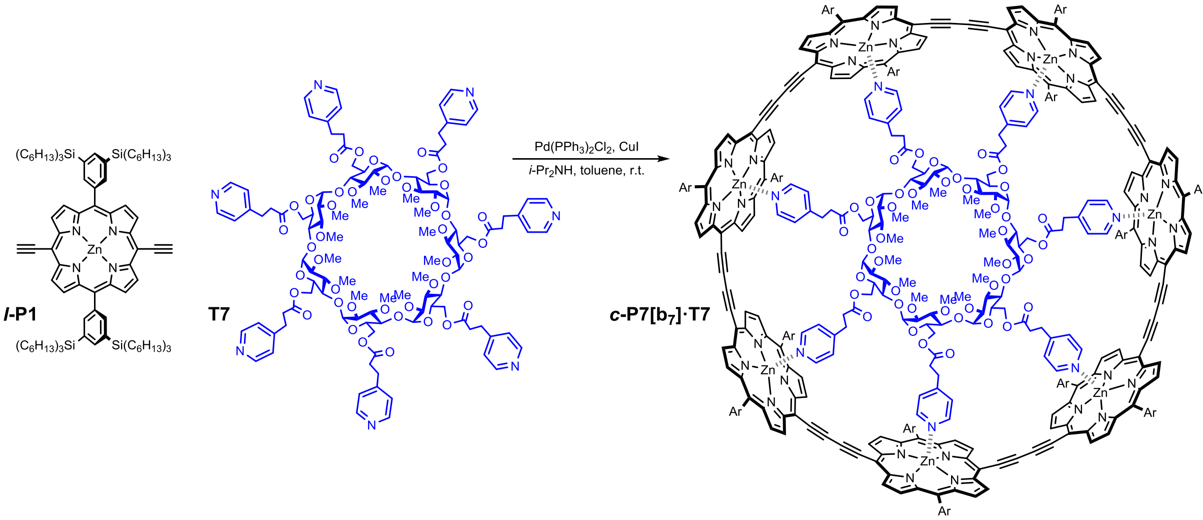

Figure 143: Scheme of ***c*-P7[b$_7$]·T7** synthesis.

β-Cyclodextrin (*β*-CD) based heptadentate template **T7** (56 mg, 24.7 µmol, 0.1 equiv.) was dissolved together with bis(ethynyl)porphyrin monomer ***l*-P1** (420 mg, 0.246 mmol, 1 equiv.) in $CHCl_3$ (150 mL) and *i*-Pr_2NH (2.5 mL), and the mixture was stirred with molecular sieves for 1h. Then, 1,4-benzoquinone (108 mg, 1 mmol, 4 equiv.) and a well-mixed solution of $Pd(PPh_3)_2Cl_2$ (28 mg, 40.0 µmol, 0.16 equiv.) and CuI (71 mg, 0.37 mmol, 1.5 equiv.) was added. The mixture was stirred under Ar for 16 h. The mixture was passed through a short alumina plug eluted with CH_2Cl_2. The mixture was purified on a short SEC and by recycling GPC using toluene/1% pyridine yielding rings ***c*-P8** (12.3 mg, 2.9%), ***c*-P9** (6.3 mg, 1.5%), ***c*-P10** (7.4 mg, 1.8%), ***c*-P11** (6.7 mg, 1.6%), ***c*-P12** (5.9 mg, 1.4%) as brown solids. The targeted ring ***c*-P7[b$_7$]·T7** was isolated by recycling GPC (toluene/1%pyr) (25 mg, 5%).

The NMR spectra were more complex compared to other nanorings as the **T7** template possess many ^{1}H NMR resonances: **^{1}H NMR** (400 MHz, $CDCl_3$, 25°C): $\delta = 9.66$ (d, 14H, $J = 4.4$ Hz, H_β), 9.60 (d, 7H, $J = 4.8$ Hz, H_β), 9.59 (d, 7H, $J = 4.8$ Hz, H_β), 8.77 – 8.75 (m, 28H, H_β), 8.46 (s, 7H, H_{Ar}), 8.41 (s, 7H, H_{Ar}), 8.00 (s, 7H, H_{Ar}), 7.95 (s, 7H, H_{Ar}), 7.91 (s, 7H, H_{Ar}), 7.87 (s, 7H, H_{Ar}), 4.99 (d, 14H, $J = 6.0$ Hz, $H_{T7(py)}$), 4.03 (br, 7H, H_{T7}), 3.31 – 3.19 (m, 35H, H_{T7}), 3.04 (s, 21H, H_{T7}), 2.94 – 2.92 (m, 7H, H_{T7}), 2.73 – 2.71 (m, 14H, H_{T7}), 2.51 – 2.49 (m, 14H, H_{T7}), 2.41 – 2.36 (m, 7H, H_{T7}), 1.47 – 1.25 (m, 730H, $H_{THS,T7}$), 1.07 – 0.77 (m, 390H, $H_{THS,T7}$). ***m/z*** (**MALDI-ToF**) 11906 ($C_{756}H_{1190}N_{28}Si_{28}Zn_7$, M^+ requires 11915 for ***c*-P7[b$_7$]**).

3.8.2.3. The concurrent synthesis of *c*-P6[b$_6$], *c*-P8[b$_8$], *c*-P10[b$_{10}$], and *c*-P12[b$_{12}$]

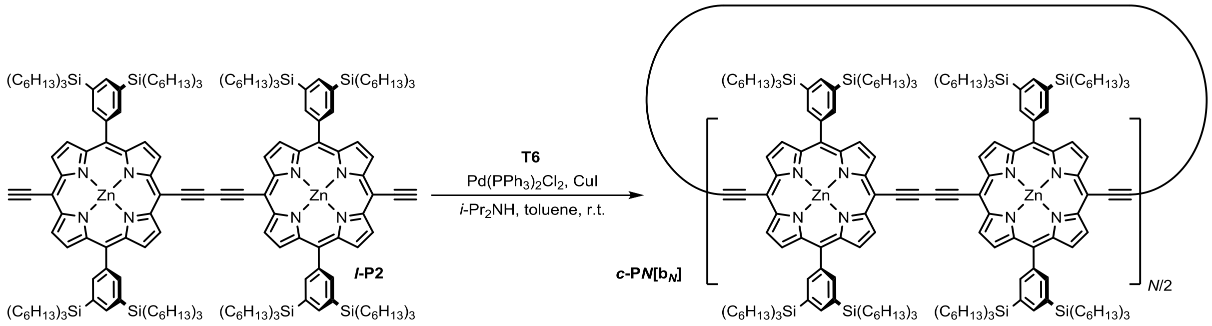

Figure 144: Scheme of concurrent synthesis of ***c*-P6[b$_6$]**, ***c*-P8[b$_8$]**, ***c*-P10[b$_{10}$]**, and ***c*-P12[b$_{12}$]**.

The concurrent synthesis of ***c*-P6[b$_6$]**, ***c*-P8[b$_8$]**, ***c*-P10[b$_{10}$]**, and ***c*-P12[b$_{12}$]** involved 200 mg of bis-ethynyl-porphyrin dimer ***l*-P2** and follows closely those of reported derivatives.[85,101,113] A typical setup includes dimer (200 mg, 58.7 μmol), template **T6** (87.8 mg, 88.1 μmol), 1,4-benzoquinone (63.5 mg, 587 μmol), CuI (112 mg, 587 μmol) and $Pd(PPh_3)_2Cl_2$ (412 mg, 587 μmol) in $CHCl_3$/*i*-Pr_2NH (10 mL/1 mL) which was stirred at room temperature for 2 h. The residual mixture was concentrated and passed over a plug of silica (eluent $CHCl_3$). It was then possible to isolate all four systems from the reaction mixture by recycling GPC. Subsequent template insertion in $CHCl_3$ yielded ***c*-P6[b$_6$]·T6f, *c*-P8[b$_8$]·(T4)$_2$**, ***c*-P10[b$_{10}$]·(T5)$_2$**, ***c*-P12[b$_{12}$]·(T6ef)$_2$**, ***c*-P12[b$_{12}$]·(T6f)$_2$** and allowed for full characterisation by NMR and MALDI–TOF mass spectrometry.

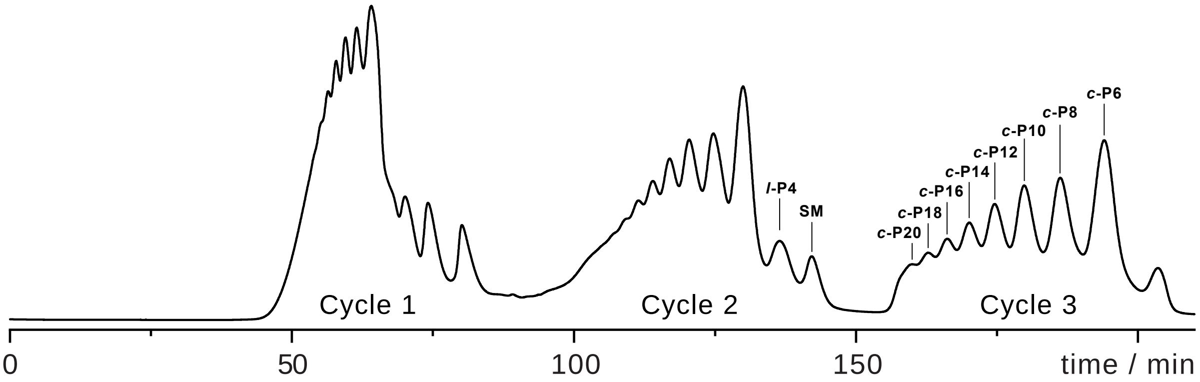

Figure 145: Recycling GPC trace (toluene/pyridine 99:1, 25°C) for the synthesis of even-numbered porphyrin rings from dimer.

c-P6[b$_6$]·T6f: **^{1}H NMR** (500 MHz, CD$_2$Cl$_2$, 25°C): δ_H = 9.67 (d, J = 4.5 Hz, 24H, H$_a$), 8.76 (d, J = 4.5 Hz, 24H, H$_b$), 8.17 (s, 12H, H$_o$), 8.08 (s, 12H, H$_{o'}$), 7.99 (s, 12H, H$_p$), 6.11 (s, 12H, H$_\delta$), 4.73 (d, J = 6.0 Hz, 12H, H$_\beta$), 2.55 (d, J = 6.0 Hz, 12H, H$_\alpha$), 1.60 – 0.64 (m, 936H, H$_{THS}$) ppm. **^{19}F NMR** (471 MHz, CD$_2$Cl$_2$, 25°C) δ_F = −61.66 ppm.

c-P8[b$_8$]·(T4)$_2$: **^{1}H NMR** (500 MHz, CD$_2$Cl$_2$, 25°C): δ_H = 9.71 (d, J = 4.3 Hz, 8H, H$_a$), 9.66 – 9.57 (m, 24H, H$_a$), 8.83 (d, J = 4.2 Hz, 8H, H$_b$), 8.79 (d, J = 4.2 Hz, 24H, H$_b$), 8.39 (s, 8H, H$_o$), 8.30 (s, 8H, H$_o$), 8.19 (s, 8H, H$_{o'}$), 8.09 (s, 8H, H$_{o'}$), 8.04 (s, 8H, H$_p$), 8.03 (s, 8H, H$_p$), 5.94 – 5.82 (m, 24H, H$_{\delta-\theta}$), 5.76 (d, J = 8.6 Hz, 8H, H$_\delta$), 5.72 (d, J = 9.0 Hz, 8H, H$_\gamma$), 5.57 (d, J = 8.5 Hz, 8H, H$_\gamma$), 5.23 (s, 8H, H$_\beta$), 5.10 (d, J = 6.2 Hz, 8H, H$_\beta$), 2.52 – 2.47 (m, 8H, H$_\alpha$), 2.43 – 2.35 (m, 8H, H$_\alpha$), 1.72 – 0.66 (m, 1248H, H$_{THS}$) ppm. ***m/z*** (**MALDI-ToF**) 13617 (C$_{864}$H$_{1360}$N$_{32}$Si$_{32}$Zn$_8$, M+ requires 13618 for **c-P8[b$_8$]**)

c-P10[b$_{10}$]·(T5)$_2$: **^{1}H NMR** (500 MHz, CD$_2$Cl$_2$, 25°C): δ_H = 9.70 (d, J = 4.2 Hz, 8H, H$_a$), 9.62 (t, J = 3.7 Hz, 16H, H$_a$), 9.58 (d, J = 4.5 Hz, 8H, H$_a$), 9.54 (d, J = 4.2 Hz, 8H, H$_a$), 8.87 – 8.71 (m, 40H, H$_b$), 8.43 (s, 8H, H$_o$), 8.34 (s, 4H, H$_o$), 8.29 (s, 8H, H$_{o'}$), 8.15 (s, 8H, H$_o$), 8.09 (s, 4H, H$_{o'}$), 8.06 (s, 8H, H$_{o'}$), 8.04 (s, 12H, H$_p$), 8.00 (s, 8H, H$_p$), 6.61 (s, 2H, H$_\varepsilon$), 6.17 (d, J = 9.1 Hz, 8H, H$_\delta$), 6.09 (d, J = 8.9 Hz, 8H, H$_\gamma$), 5.75 (d, J = 9.1 Hz, 8H, H$_\delta$), 5.67 (d, J = 8.8 Hz, 8H, H$_\gamma$), 5.62 (d, J = 8.3 Hz, 4H, H$_\delta$), 5.50 (d, J = 7.9 Hz, 4H, H$_\gamma$), 5.43 (d, J = 6.6 Hz, 8H, H$_\beta$), 5.20 (d, J = 6.7 Hz, 8H, H$_\beta$), 5.01 (d, J = 6.0 Hz, 4H, H$_\beta$), 2.67 (d, J = 6.7 Hz, 8H, H$_\alpha$), 2.43 (d, J = 6.7 Hz, 8H, H$_\alpha$), 2.36 (d, J = 6.0 Hz, 4H, H$_\alpha$), 1.80 – 0.53 (m, 1560H, H$_{THS}$) ppm. ***m/z*** (**MALDI-ToF**) 17020 (C$_{1080}$H$_{1700}$N$_{40}$Si$_{40}$Zn$_{10}$, M+ requires 17023 for **c-P10[b$_{10}$]**).

c-P12[b$_{12}$]·(T6ef)$_2$: **^{1}H NMR** (500 MHz, CD$_2$Cl$_2$, 25°C): δ_H = 9.87 (d, J = 14.9 Hz, 48H, H$_a$), 8.95 (d, J = 12.5 Hz, 48H. H$_b$), 8.44 (d, J = 23.5 Hz, 24H, H$_o$), 8.23 (s, 12H, H$_{o'}$), 8.08 (d, J = 16.1 Hz, 24H, H$_p$), 7.42 – 6.93 (m, 72H, H$_{\zeta,\eta,\theta}$), 6.85 (s, 12H, H$_\delta$), 6.73 (d, J = 8.6 Hz, 24H, H$_\varepsilon$), 6.03 (s, 12H, H$_\gamma$), 5.49 (d, J = 6.0 Hz, 24H, H$_\beta$), 2.79 (d, J = 6.2 Hz, 24H, H$_\alpha$), 1.93 (s, 24H, $H_{\sigma1}$), 1.65 – 0.71 (m, 1872H, H_{THS}), 0.74 – 0.56 (m, 12H, $H_{\sigma3–7}$), 0.52 (s, 24H, $H_{\sigma2}$), 0.46 (t, *J* = 7.3 Hz, 12H, $H_{\sigma8}$). **^{19}F NMR** (471 MHz, CD_2Cl_2, 25°C) δ_F = −58.7 ppm. ***m/z*** (**MALDI-ToF**) 20424 ($C_{1296}H_{2040}N_{48}Si_{48}Zn_{12}$, M+ requires 20427 for ***c*-P12[b$_{12}$]**).

c*-P12[b$_{12}$]·(T6f)$_2$: ^{1}H NMR** (500 MHz, CD_2Cl_2, 25°C): δ_H = 10.97 (d, *J* = 4.9 Hz, 4H, H_a), 10.15 (d, *J* = 4.2 Hz, 4H, H_a), 9.82 – 9.54 (m, 36H, H_a), 9.47 (d, *J* = 4.0 Hz, 4H, H_a), 8.94 (d, *J* = 4.3 Hz, 4H, H_b), 8.88 – 8.69 (m, 36H, H_b), 8.66 (d, *J* = 4.6 Hz, 4H, H_b), 8.41 (d, *J* = 4.4 Hz, 4H, H_b), 8.34 – 7.88 (m, 60H, H_{aryl}), 7.61 (s, 4H, H_{aryl}), 7.22 (s, 4H, H_{aryl}), 7.20 (s, 4H, H_{aryl}), 6.25 – 6.03 (m, 20H, H_δ), 5.91 (s, 4H, H_δ), 4.79 (d, *J* = 6.4 Hz, 4H, H_β), 4.74 – 4.62 (m, 16H, H_β), 4.46 (d, *J* = 6.6 Hz, 4H, H_β), 2.57 (d, *J* = 6.6 Hz, 4H, H_α), 2.54 – 2.43 (m, 16H, H_α), 2.28 (d, *J* = 5.5 Hz, 4H, H_α), 1.89 – 0.36 (m, 1800H, H_{THS}), 0.27 – 0.08 (m, 24H, H_{THS}), −0.05 – −0.30 (m, 24H, H_{THS}), −1.02 – −1.19 (m, 12H, H_{THS}), −1.20 – −1.37 (m, 12H, H_{THS}) ppm. **^{19}F NMR** (471 MHz, CD_2Cl_2, 25°C) δ_F = −61.63, −61.69, −61.73 ppm. ***m/z (**MALDI-ToF**) 20424 ($C_{1296}H_{2040}N_{48}Si_{48}Zn_{12}$, M+ requires 20427 for ***c*-P12[b$_{12}$]**).

3.8.3. Oxidations

Oxidation experiments were conducted using a well-stirred suspension of the hexafluoroantimonate salt of thianthrenium (**Thn$^+$**, E_{red} = 0.86 V versus Fc/Fc+) in CD_2Cl_2 (ca. 20–30 mM). The activity of the oxidant suspension was evaluated on the day of the corresponding experiment by moisture-free UV-vis titration of **Thn$^+$** to a porphyrin monomer of known concentration and optical profile in the neutral and 1+ state. Subsequently, all oxidation experiments were conducted in J. Young valve NMR tubes using CD_2Cl_2 stored over molecular sieves, using standard Schlenk line techniques to exclude moisture. Rubber septa (Subaseal) were meticulously avoided: we found that the introduction of small quantities of rubber (even by non-coring needles) has an immediate quenching effect on the cations. For titrations, oxidant was added in increments to a solution of porphyrin compound (ca. 1–4 mg per mL) in the NMR tube at −78°C under a counterflow of argon (**Figure 146**). Tubes were then closed and, while maintaining the temperature at −78°C, transferred to an NMR spectrometer pre-cooled to the appropriate temperature (typically −45 °C). Reaching temperatures above –10 °C for more than a few minutes generally resulted in decomposition of the samples. The NMR measurements were performed on a Bruker AVII 500 (5 mm BBFO probe). Chemical shifts are reported in parts per million (ppm). ^{1}H spectra were calibrated to residual proton signals of the solvent ($CHCl_3$ 7.26 ppm; $CHDCl_2$ 5.32 ppm). ^{13}C NMR spectra were referenced to the solvent peak ($CDCl_3$ 77.23 ppm; CD_2Cl_2 54.00 ppm). ^{19}F NMR spectra were referenced to hexafluorobenzene (−164.8 ppm). Reversibility of the oxidations was confirmed by reduction with ferrocene or decamethyl-ferrocene and reassessment of the ^{1}H NMR spectra. Titration endpoints (at which each porphyrin unit is oxidised to the 1+ state) were indicated by the disappearance of the neutral oxidant (thianthrene) resonances, and unchanging spectra when over-titrating (>2*N* equivalents). Voltammetry measurements were made using an Autolab PGSTAT 12 with a 3 mm glassy carbon working electrode, platinum wire counter electrode and $Ag/AgNO_3$ (0.01 M in acetonitrile) reference electrode. Voltammograms were referenced to the Fc/Fc+ couple (0.0 V) as an internal reference. Square wave voltammograms were acquired with a 5 mV step potential, 50 mV modulation amplitude and 2 Hz frequency. The supporting electrolyte, (tetra-*n*-butylammonium hexafluorophosphate, Bu_4NPF_6, TBAP) was dried by melting under vacuum. Inhibitor-free CH_2Cl_2 (stored over 3 Å molecular sieves) was added to the dry electrolyte to achieve an electrolyte concentration of 0.1 M. Analyte solutions were prepared by addition of this electrolyte solution to porphyrin nanoring (ca. 0.5–2 mg), and measurements were performed over 3 Å molecular sieves at −45°C (acetonitrile/dry ice bath).

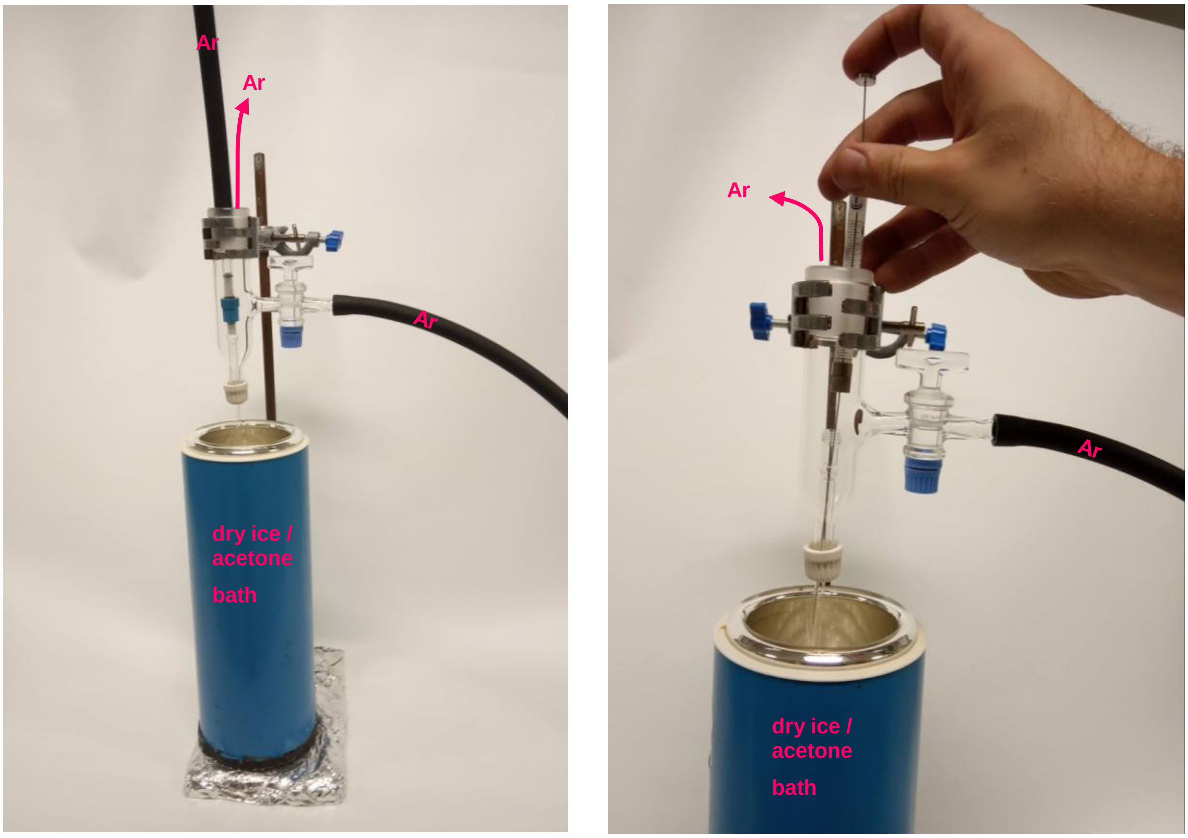

Figure 146: Photo of a setup for the addition of the oxidant to a special J. Young valve fitting NMR tube at low temperature under a strong counterflow of argon preventing moisture condensation.

3.9. References

[1] A. W. Von Hofmann, *Proc. R. Soc. London* **1857**, *8*, 1–3.

[2] M. K. Cyrański, T. M. Krygowski, *Tetrahedron* **1999**, *55*, 6205–6210.

[3] T. M. Krygowski, M. Cyrański, *Tetrahedron* **1996**, *52*, 1713–1722.

[4] J. D. Roberts, M. C. Caserio, *Basic Principles of Organic Chemistry*, Menlo Park, California 94025, **1977**.

[5] M. B. Smith, J. March, *March's Advanced Organic Chemistry: Reactions, Mechanisms, and Structure*, Wiley, **2007**.

[6] E. Hückel, *Zeitschrift für Phys.* **1931**, *72*, 310–337.

[7] E. Hückel, *Zeitschrift für Phys.* **1932**, *76*, 628–648.

[8] E. Hückel, *Zeitschrift für Phys.* **1931**, *70*, 204–286.

[9] E. Heilbronner, H. Bock, *The HMO Model and Its Application*, Wiley, London, **1976**.

[10] K. Yates, *Huckel Molecular Orbital Theory*, Academic Press New York, **1978**.

[11] J. E. Lennard-Jones, *Trans. Faraday Soc.* **1929**, *25*, 668–686.

[12] B. H. Bransden, C. J. Joachain, *Quantum Mechanics*, Prentice Hall, Harlow, **2000**.

[13] C. Cohen-Tannoudji, B. Diu, F. Laloë, S. R. Hemley, N. Ostrowsky, D. B. Ostrowsky, *Quantum Mechanics*, Wiley, New York , **2005**.

[14] R. S. Varga, *Pacific J. Math.* **1954**, *4*, 151–160.

[15] R. Aldrovandi, *Special Matrices of Mathematical Physics: Stochastic, Circulant, and Bell Matrices*, World Scientific, Singapore, **2001**.

[16] E. Heilbronner, *Tetrahedron Lett.* **1964**, *5*, 1923–1928.

[17] R. Breslow, J. Brown, J. J. Gajewski, *J. Am. Chem. Soc.* **1967**, *89*, 4383–4390.

[18] G. B. Kistiakowsky, J. R. Ruhoff, H. A. Smith, W. E. Vaughan, *J. Am. Chem. Soc.* **1936**, *58*, 146–153.

[19] D. W. Rogers, N. Matsunaga, A. A. Zavitsas, F. J. McLafferty, J. F. Liebman, *Org. Lett.* **2003**, *5*, 2373–2375.

[20] S. W. Slayden, J. F. Liebman, *Chem. Rev.* **2001**, *101*, 1541–1566.

[21] A. A. Deniz, *Science* **1999**, *286*, 1119–1122.

[22] O. Castaño, R. Notario, R. Gomperts, J.-L. M. Abboud, R. Palmeiro, J. L. Andrés, *J. Phys. Chem. A* **1998**, *102*, 4949–4951.

[23] R. Gleiter, G. Haberhauer, *Aromaticity and Other Conjugation Effects*, Wiley-WCH, Weinheim, Germany, **2012**.

[24] J. A. Pople, L. Radom, W. J. Hehre, *J. Am. Chem. Soc.* **1971**, *93*, 289–300.

[25] D. A. Ponomarev, V. V Takhistov, *J. Chem. Educ.* **1997**, *74*, 201.

[26] P. Muller, *Pure Appl. Chem.* **1994**, *66*, 1077.

[27] J. E. Bartmess, S. S. Griffith, *J. Am. Chem. Soc.* **1990**, *112*, 2931–2936.

[28] E. P. Woo, F. Sondheimer, *Tetrahedron* **1970**, *26*, 3933–3939.

[29] A. Julg, P. François, *Theor. Chim. Acta* **1967**, *8*, 249–259.

[30] J. Kruszewski, T. M. Krygowski, *Tetrahedron Lett.* **1972**, *13*, 3839–3842.

[31] T. M. Krygowski, M. K. Cyrański, *Chem. Rev.* **2001**, *101*, 1385–1420.

[32] C. P. Brock, J. D. Dunitz, *Acta Crystallogr. Sect. B* **1982**, *38*, 2218–2228.

[33] R. Mason, *Acta Crystallogr.* **1964**, *17*, 547–555.

[34] G. Ferraris, D. Jones, J. Yerkess, *Zeitschrift für Krist.* **1973**, *138*, 113–128.

[35] L. Pauling, *J. Chem. Phys.* **1936**, *4*, 673–677.

[36] K. Y. Lonsdale, *Proc. R. Soc. London. Ser. A - Math. Phys. Sci.* **1937**, *159*, 149–161.

[37] D. Sundholm, H. Fliegl, R. J. F. Berger, *Wiley Interdiscip. Rev. Comput. Mol. Sci.* **2016**, *6*, 639–678.

[38] E. I. Tellgren, A. M. Teale, J. W. Furness, K. K. Lange, U. Ekström, T. Helgaker, *J. Chem. Phys.* **2014**, *140*, 34101.

[39] K. K. Lange, E. I. Tellgren, M. R. Hoffmann, T. Helgaker, *Science* **2012**, *337*, 327–331.

[40] E. I. Tellgren, H. Fliegl, *J. Chem. Phys.* **2013**, *139*, 164118.

[41] E. Steiner, P. W. Fowler, *Phys. Chem. Chem. Phys.* **2004**, *6*, 261–272.

[42] P. W. Fowler, C. M. Gibson, D. E. Bean, *Proc. R. Soc. A Math. Phys. Eng. Sci.* **2014**, *470*, 20130617.

[43] E. Steiner, P. W. Fowler, *Chem. Commun.* **2001**, 2220–2221.

[44] P. W. Fowler, E. Steiner, *J. Phys. Chem. A* **1997**, *101*, 1409–1413.

[45] D. Geuenich, K. Hess, F. Köhler, R. Herges, *Chem. Rev.* **2005**, *105*, 3758–3772.

[46] R. Herges, D. Geuenich, *J. Phys. Chem. A* **2001**, *105*, 3214–3220.

[47] P. von R. Schleyer, C. Maerker, A. Dransfeld, H. Jiao, N. J. R. van Eikema Hommes, *J. Am. Chem. Soc.* **1996**, *118*, 6317–6318.

[48] A. Stanger, *J. Org. Chem.* **2006**, *71*, 883–893.

[49] A. Stanger, *J. Phys. Chem. A* **2019**, *123*, 3922–3927.

[50] S. Klod, E. Kleinpeter, *J. Chem. Soc., Perkin Trans. 2* **2001**, 1893–1898.

[51] C. S. Wannere, P. von R. Schleyer, *Org. Lett.* **2003**, *5*, 865–868.

[52] J. F. M. Oth, *Pure Appl. Chem.* **1971**, *25*, 573–622.

[53] D. Lungerich, A. V Nizovtsev, F. W. Heinemann, F. Hampel, K. Meyer, G. Majetich, P. v. R. Schleyer, N. Jux, *Chem. Commun.* **2016**, *52*, 4710–4713.

[54] R. M. McQuilkin, B. W. Metcalf, F. Sondheimer, *J. Chem. Soc. D* **1971**, 338–339.

[55] E. V. Anslyn, D. A. Dougherty, *Modern Physical Organic Chemistry, 6th Ed.*, Sausalito, CA: University Science, **2005**.

[56] A. Soncini, P. W. Fowler, L. W. Jenneskens, *Phys. Chem. Chem. Phys.* **2004**, *6*, 277–284.

[57] F. Diederich, H. A. Staab, *Angew. Chem. Int. Ed.* **1978**, *17*, 372–374.

[58] H. A. Staab, F. Diederich, *Chem. Ber.* **1983**, *116*, 3487–3503.

[59] I. Pozo, Z. Majzik, N. Pavliček, M. Melle-Franco, E. Guitián, D. Peña, L. Gross, D. Pérez, *J. Am. Chem. Soc.* **2019**, *141*, 15488–15493.

[60] D. Setiawan, E. Kraka, D. Cremer, *J. Org. Chem.* **2016**, *81*, 9669–9686.

[61] H. Jiao, P. von R. Schleyer, *Angew. Chem. Int. Ed.* **1996**, *35*, 2383–2386.

[62] Z. Zhou, *J. Phys. Org. Chem.* **1995**, *8*, 103–107.

[63] E. Steiner, P. W. Fowler, L. W. Jenneskens, A. Acocella, *Chem. Commun.* **2001**, 659–660.

[64] R. Herges, *Chem. Rev.* **2006**, *106*, 4820–4842.

[65] A. Jabar, R. Masrour, *Phys. B Condens. Matter* **2018**, *539*, 21–28.

[66] A. Jabar, R. Masrour, *Phys. A Stat. Mech. its Appl.* **2019**, *514*, 974–981.

[67] B. Kumar, R. L. Viboh, M. C. Bonifacio, W. B. Thompson, J. C. Buttrick, B. C. Westlake, M.-S. Kim, R. W. Zoellner, S. A. Varganov, P. Mörschel, J. Teteruk, M. U. Schmidt, B. T. King, *Angew. Chem. Int. Ed.* **2012**, *51*, 12795–12800.

[68] M. A. Majewski, Y. Hong, T. Lis, J. Gregoliński, P. J. Chmielewski, J. Cybińska, D. Kim, M. Stępień, *Angew. Chem. Int. Ed.* **2016**, *55*, 14072–14076.

[69] N. Toriumi, A. Muranaka, E. Kayahara, S. Yamago, M. Uchiyama, *J. Am. Chem. Soc.* **2015**, *137*, 82–85.

[70] E. Kayahara, T. Kouyama, T. Kato, S. Yamago, *J. Am. Chem. Soc.* **2016**, *138*, 338–344.

[71] A. Muñoz-Castro, *Phys. Chem. Chem. Phys.* **2018**, *20*, 3433–3437.

[72] J. F. M. Oth, E. P. Woo, F. Sondheimer, *J. Am. Chem. Soc.* **1973**, *95*, 7337–7345.

[73] J.-Y. Shin, K. S. Kim, M.-C. Yoon, J. M. Lim, Z. S. Yoon, A. Osuka, D. Kim, *Chem. Soc. Rev.* **2010**, *39*, 2751–2767.

[74] M.-C. Yoon, S. Cho, M. Suzuki, A. Osuka, D. Kim, *J. Am. Chem. Soc.* **2009**, *131*, 7360–7367.

[75] S. Shimizu, R. Taniguchi, A. Osuka, *Angew. Chem. Int. Ed.* **2005**, *44*, 2225–2229.

[76] J. M. Lim, J.-Y. Shin, Y. Tanaka, S. Saito, A. Osuka, D. Kim, *J. Am. Chem. Soc.* **2010**, *132*, 3105–3114.

[77] T. Soya, W. Kim, D. Kim, A. Osuka, *Chem. Eur. J.* **2015**, *21*, 8341–8346.

[78] T. Soya, H. Mori, A. Osuka, *Angew. Chem. Int. Ed.* **2018**, *57*, 15882–15886.

[79] Y. Tanaka, J.-Y. Shin, A. Osuka, *Eur.J. Org. Chem.* **2008**, *2008*, 1341–1349.

[80] T. Yoneda, T. Soya, S. Neya, A. Osuka, *Chem. Eur. J.* **2016**, *22*, 14518–14522.

[81] M. Hoffmann, C. J. Wilson, B. Odell, H. L. Anderson, *Angew. Chem. Int. Ed.* **2007**, *46*, 3122–3125.

[82] M. Hoffmann, J. Kärnbratt, M.-H. Chang, L. M. Herz, B. Albinsson, H. L. Anderson, *Angew. Chem. Int. Ed.* **2008**, *47*, 4993–4996.

[83] L. Favereau, A. Cnossen, J. B. Kelber, J. Q. Gong, R. M. Oetterli, J. Cremers, L. M. Herz, H. L. Anderson, *J. Am. Chem. Soc.* **2015**, *137*, 14256–14259.

[84] D. V. Kondratuk, S. Liu, J. Cremers, T. D. W. Claridge, S. A. L. Rousseaux, M. C. O’Sullivan, G. Gil-Ramírez, H. L. Anderson, *Angew. Chem. Int. Ed.* **2015**, *54*, 5355–5359.

[85] D. V Kondratuk, J. K. Sprafke, M. C. O’Sullivan, L. M. A. Perdigao, A. Saywell, M. Malfois, J. N. O’Shea, P. H. Beton, A. L. Thompson, H. L. Anderson, *Chem. Eur. J.* **2014**, *20*, 12826–12834.

[86] C.-K. Yong, P. Parkinson, D. V Kondratuk, W.-H. Chen, A. Stannard, A. Summerfield, J. K. Sprafke, M. C. O’Sullivan, P. H. Beton, H. L. Anderson, L. M. Herz, *Chem. Sci.* **2015**, *6*, 181–189.

[87] P. Liu, P. Neuhaus, D. V. Kondratuk, T. S. Balaban, H. L. Anderson, *Angew. Chem. Int. Ed.* **2014**, *53*, 7770–7773.

[88] J. K. Sprafke, D. V. Kondratuk, M. Wykes, A. L. Thompson, M. Hoffmann, R. Drevinskas, W. H. Chen, C. K. Yong, J. Kärnbratt, J. E. Bullock, M. Malfois, M. R. Wasielewski, B. Albinsson, L. M. Herz, D. Zigmantas, D. Beljonne, H. L. Anderson, *J. Am. Chem. Soc.* **2011**, *133*, 17262–17273.

[89] J. K. Sprafke, B. Odell, T. D. W. Claridge, H. L. Anderson, *Angew. Chem. Int. Ed.* **2011**, *50*, 5572–5575.

[90] M. C. O’Sullivan, J. K. Sprafke, D. V Kondratuk, C. Rinfray, T. D. W. Claridge, A. Saywell, M. O. Blunt, J. N. O’Shea, P. H. Beton, M. Malfois, H. L. Anderson, *Nature* **2011**, *469*, 72–75.

[91] M. D. Peeks, M. Jirasek, T. D. W. Claridge, H. L. Anderson, *Angew. Chem. Int. Ed.*

2019, *58*, 15717–15720.

[92] M. J. Frisch, G. W. Trucks, H. B. Schlegel, G. E. Scuseria, M. A. Robb, J. R. Cheeseman, G. Scalmani, V. Barone, G. A. Petersson, B. Mennucci, G. A. Petersson, H. Nakatsuji, X. Li, M. Caricato, A. V Marenich, J. Bloino, B. G. Janesko, R. Gomperts, B. Mennucci, H. P. Hratchian, J. V. Ortiz, A. F. Izmaylov, J. L. Sonnenberg, D. Williams-Young, F. Ding, F. Lipparini, F. Egidi, J. Goings, B. Peng, A. Petrone, T. Henderson, D. Ranasinghe, V. G. Zakrzewski, J. Gao, N. Rega, G. Zheng, W. Liang, M. Hada, M. Ehara, K. Toyota, R. Fukuda, J. Hasegawa, M. Ishida, T. Nakajima, Y. Honda, O. Kitao, H. Nakai, T. Vreven, K. Throssell, J. A. J. Montgomery, J. E. Peralta, F. Ogliaro, M. J. Bearpark, J. J. Heyd, E. N. Brothers, K. N. Kudin, V. N. Staroverov, T. A. Keith, R. Kobayashi, J. Normand, K. Raghavachari, A. P. Rendell, S. S. Burant, J. C. Iyengar, J. Tomasi, M. Cossi, J. M. Millam, M. Klene, C. Adamo, R. Cammi, J. W. Ochterski, R. L. Martin, K. Morokuma, O. Farkas, J. B. Foresman, D. J. Fox, **2016**, Gaussian 16, Revision A.03, Gaussian, Inc., Wallin.

[93] Z. Chen, C. S. Wannere, C. Corminboeuf, R. Puchta, P. von R. Schleyer, R. Puchta, C. S. Wannere, Z. Chen, *Chem. Rev.* **2005**, *105*, 3842–3888.

[94] S. Lipstman, I. Goldberg, *Cryst. Growth Des.* **2010**, *10*, 4596–4606.

[95] H. M. McConnell, *J. Chem. Phys.* **1957**, *27*, 226–229.

[96] M. Baranac-Stojanović, *RSC Adv.* **2014**, *4*, 308–321.

[97] R. G. Viglione, R. Zanasi, P. Lazzeretti, *Org. Lett.* **2004**, *6*, 2265–2267.

[98] M. Quiroz-Guzman, S. N. Brown, *Acta Crystallogr. Sect. C* **2010**, *66*, m171–m173.

[99] N. G. Connelly, W. E. Geiger, *Chem. Rev.* **1996**, *96*, 877–910.

[100] O. Hammerich, V. D. Parker, *Electrochim. Acta* **1973**, *18*, 537–541.

[101] M. D. Peeks, T. D. W. Claridge, H. L. Anderson, *Nature* **2017**, *541*, 200–203.

[102] M. D. Peeks, C. E. Tait, P. Neuhaus, G. M. Fischer, M. Hoffmann, R. Haver, A. Cnossen, J. R. Harmer, C. R. Timmel, H. L. Anderson, *J. Am. Chem. Soc.* **2017**, *139*, 10461–10471.

[103] N. Elgrishi, K. J. Rountree, B. D. McCarthy, E. S. Rountree, T. T. Eisenhart, J. L. Dempsey, *J. Chem. Educ.* **2018**, *95*, 197–206.

[104] M. Parvez, T. S. Sorensen, F. Sun, *Can. J. Chem.* **2002**, *80*, 245–249.

[105] S. O. Morgan, H. H. Lowry, *J. Phys. Chem.* **1930**, *34*, 2385–2432.

[106] R. Haver, L. Tejerina, H.-W. Jiang, M. Rickhaus, M. Jirasek, I. Grübner, H. J. Eggimann, L. M. Herz, H. L. Anderson, *J. Am. Chem. Soc.* **2019**, *141*, 7965–7971.

[107] M. Rickhaus, A. Vargas Jentzsch, L. Tejerina, I. Grübner, M. Jirasek, T. D. W.

Claridge, H. L. Anderson, *J. Am. Chem. Soc.* **2017**, *139*, 16502–16505.

[108] A. Soncini, P. W. Fowler, *Chem. Eur. J.* **2013**, *19*, 1740–1746.

[109] M. C. O'Sullivan, J. K. Sprafke, D. V. Kondratuk, C. Rinfray, T. D. W. Claridge, A. Saywell, M. O. Blunt, J. N. O'Shea, P. H. Beton, M. Malfois, H. L. Anderson, *Nature* **2011**, *469*, 72–75.

[110] P. P. Edwards, M. T. J. Lodge, F. Hensel, R. Redmer, *Philos. Trans. R. Soc. A Math. Phys. Eng. Sci.* **2010**, *368*, 941–965.

[111] M. Rickhaus, M. Jirasek, L. Tejerina, H. Gotfredsen, M. D. Peeks, R. Haver, H.-W. Jiang, T. D. W. Claridge, H. L. Anderson, **2019**, DOI 10.26434/chemrxiv.8953565.v2.

[112] P. Liu, Y. Hisamune, M. D. Peeks, B. Odell, J. Q. Gong, L. M. Herz, H. L. Anderson, *Angew. Chem. Int. Ed.* **2016**, *55*, 8358–8362.

[113] C. E. Tait, P. Neuhaus, M. D. Peeks, H. L. Anderson, C. R. Timmel, *J. Am. Chem. Soc.* **2015**, *137*, 8284–8293.

4

Synthesis and properties of Möbius-strip-shaped porphyrin nanorings

4.1. Abstract

This chapter discusses design and synthesis of a of large Möbius-strip-shaped porphyrin nanoring.

Firstly, a brief overview of the topological concept of the linking number, twist and writhe in cyclic conjugated molecules is presented, with emphasis put on Möbius molecules. Furthermore, a concept of Möbius aromaticity is reviewed, based on the original HMO method as well as using modern computational methods. Then, reported syntheses of Möbius molecules are summarized and various conceptual approaches toward the topology are pointed out.

This section is followed by the authors design of the Möbius-shaped porphyrin nanorings and its synthesis. Synthesis of two novel nanorings is presented, one of which is suspected of adopting Möbius-strip shape. Both nanorings are examined for their photophysical properties and challenges associated with the compounds synthesis and handling are discussed.

4.2. Introduction

A Möbius strip is a fascinating ribbon structure with one-side, or more technically with a non-orientable surface. The Mobius strip is created, when during the ribbon closure, one end is rotated to induce a half-twist (180°) (**Figure 1**). The object is named after mathematician and astronomer August Möbius who discussed its mathematical properties, although the Möbius strip was known for millennia.[1]

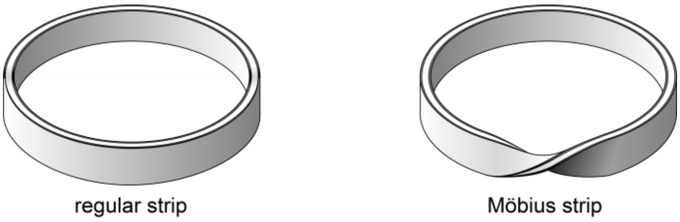

Figure 1: Strips with none (left) and one (right) half twists. Graphics created by author adapting style from literature.[2]

Besides its aesthetic value, π-conjugated systems of Möbius strip topology are expected to have reversed [4*n*]/[4*n*+2] criteria of aromaticity, relative to classical, Hückel-type systems (*vide infra*).

4.2.1. Topological considerations and theoretical studies

From a topological point of view, the cyclic, π-conjugated system can be represented with a ribbon and its topological properties can be described with Călugăreanu theorem (**Eq. 1**).[3] This, originally purely mathematical construct, was further developed by White and Fuller and brought to the context of organic chemistry by Rzepa.[4–6]

$$Lk = Tw + Wr \tag{1}$$

In **Eq. 1**, the *Lk* is linking number, *Tw* local twist number and *Wr* so-called writhe. The linking number *Lk* is an integer representing the number of half twists along the ribbon and can be also interpreted as the minimum possible number of ribbon edges crossings. A value of *Lk* = 0 represents a non-twisted ribbon (Hückel system), *Lk* = ± 1 Möbius-strip shape, *Lk* = ± 2 is double twisted ribbon (obeying Hückel aromaticity) etc. (**Figure 2**).

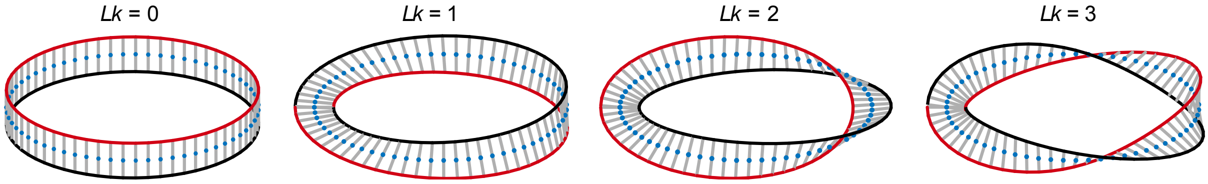

Figure 2: Ribbons with *Wr* = 0 (as central points (blue) are on the plane) and various linking number *Lk*.

The twist *Tw* and writhe *Wr* can reach any real number and without destroying (like cutting) the ribbon, only *Wr* and *Tw* can be changed by 3D distortions. Since both values are coupled, both have direct effects to conjugation and effective net-area cross-sections, but none to the linking number and Hückel/Möbius aromaticity problems.

Writhe *Wr* represents the 3D arrangement of the ribbon, specifically its chiral deformation from planarity (**Figure 3**).

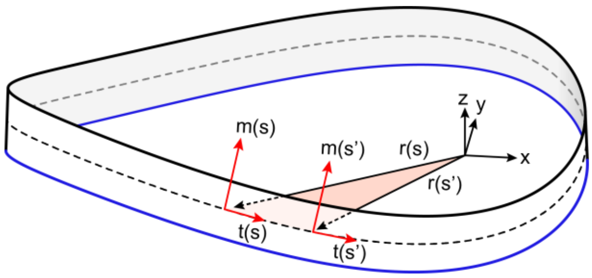

$$Wr = \frac{1}{2\pi}\oiint \frac{\boldsymbol{t}(s') \times \boldsymbol{t}(s) \cdot \left(\boldsymbol{r}(s') - \boldsymbol{r}(s)\right)}{|\boldsymbol{r}(s') + \boldsymbol{r}(s)|^3} ds ds'$$

$$Tw = \frac{1}{\pi}\oint \boldsymbol{t}(s) \cdot \left(\boldsymbol{m}(s) \times \left(\frac{d\boldsymbol{m}(s)}{ds}\right)\right) ds$$

$$\boldsymbol{t}(s) = \frac{d\boldsymbol{r}(s)}{ds} \qquad (2)$$

Figure 3: (left) Ribbon (*Lk* = 0, *Tw* = −0.2, *Wr* = 0.2) defined with its central line (dashed) and two edges (blue and black). Vectors ***m***(*s*) define the orientation of the ribbon, ***r***(*s*) position of the central line and ***t***(*s*) is tangent pointing to direction of the central line, orthogonal to ***m***(*s*). s and s' are two different arc angles (0, 2π). (right) Mathematical definitions of writhe (*Wr*) and twist (*Tw*).

Note, that *Wr* depends only on vectors *t*(s) and *r*(s) (**Figure 3**, **Eq. 2**), and is thus dependent only on the shape of the central line. The key term *t*(s')×*t*(s) describes how much the curve deviates from a straight line and its scalar product with the other term *r*(s') − *r*(s) then defines the chiral deviation from the plane. Normalizations and integration along the whole ribbon yields *Wr*.

Contrary to *Wr*, twist *Tw* depends on the *t*(s) and the orthogonal *m*(s), describing the shape and relative orientation of the ribbon edges (**Figure 3**, **Eq. 2**). The term ***m***(*s*)×(d***m***(*s*)/ds) describes how are the two ribbon edges changing its angle relative to the origin and the integration along the ribbon (defined with ***t***(s)) yields *Tw*. For discreet objects such as molecules one can simplify the term to sum of all local twists along the ribbon (**Eq. 3**)

$$Tw = \frac{1}{\pi}\sum \gamma_i \qquad (3)$$

Where γ_i is the dihedral angle in between every molecular 'joint' along the circumference. In the context of the π-conjugated systems it defines how good is the orbital overlap between neighbouring atomic orbitals (AOs). The value *Tw* = 0 means full co-planarity, maximal electronic communication.

To conclude, in the case of Möbius molecule of *Lk* = 1, with *Wr* = 0, the half-twist is distributed in local twists *Tw*, decreasing the electronic communication and increasing the MOs energy. If the half-twist of *Lk* = 1 is fully transcribed to the writhe *Wr* = 1, the system allows maximum conjugation (*Tw* = 0) (**Figure 4**).

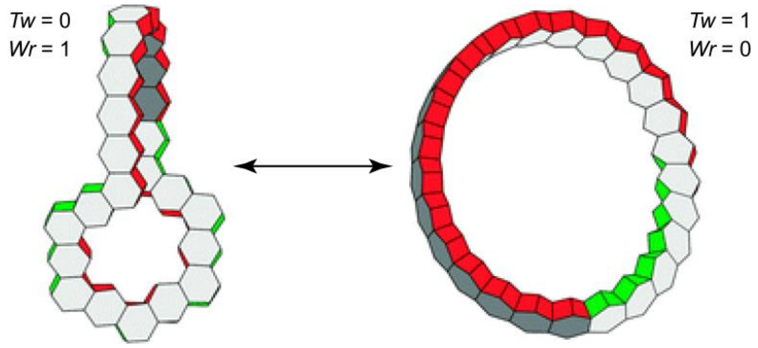

Figure 4: Möbius-strip shaped system of linking number $Lk = 1$; with either $Tw = 0$ (left) or $Tw = 1$ (right). Edited figure adapted with permission from *Chem. Comm.* **2013**, (49), 1254–1260. Copyright 2013 The Royal Society of Chemistry.[7]

In the case of a maximally conjugated system with $Wr = 1$, the 3D twist partly decreases the effective net-cross-section area. This can lead in (anti)aromatic species to attenuation of the induced ring current (**Figure 5**).[8]

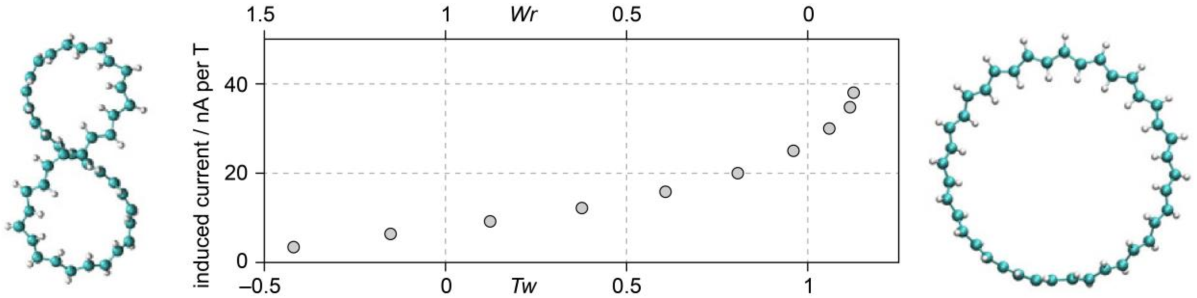

Figure 5: Induced ring current in Möbius ($Lk = 1$) aromatic [40]annulene with various writhe with depicted extreme geometries of $Wr = 1$ (left) and $Wr = 0$ (right). Although better conjugation is expected for $Tw = 0$ than for $Tw = 1$, significantly lower induced ring current is predicted as the effective area perturbed with external magnetic field is significantly smaller as a result of the 3D distortion ($Wr = 1$). Figure edited and redrawn by author, originally adapted with permission from *J. Phys. Chem. Lett.*, **2018**, (9), *7*, 1627–1632.[8]

Heilbronner first pointed out that the aromatic character of a [4*n*+2]/[4*n*] species is reversed for half-twisted (Möbius) shaped system as a result of wavefunction phase shift. He has hypothesized the different distribution of the MOs energy levels (and thus aromaticity) based on the model in which the π-conjugated path possess none (Hückel) or one half-twist (Möbius), the latter created by the continuous twist of individual *p* atomic orbitals (**Figure 6**).[9]

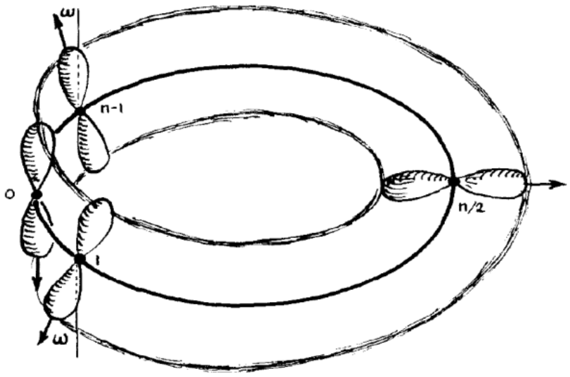

Figure 6: Original drawing of the π-conjugated system topology by Heilbronner. Reprinted with permission from *Tetrahedron Lett*. 1964, *29*, 1923–1928. Copyright 1964 Elsevier.

The twist in Möbius systems causes a phase change in between the first and n^{th} atomic orbital, changing the HMO determinant and subsequently causing different distribution of MO energy levels (**Figure 7**).

	Hückel	Möbius
molecule	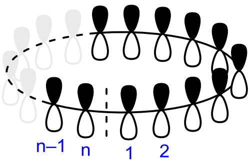	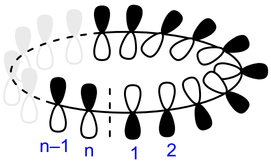
HMO determinant	$\begin{vmatrix} x & 1 & 0 & \cdots & 1 \\ 1 & x & 1 & \cdots & 0 \\ 0 & 1 & x & \cdots & 0 \\ \vdots & \vdots & \vdots & \ddots & \vdots \\ 1 & 0 & \cdots & 1 & x \end{vmatrix} = 0$	$\begin{vmatrix} x & 1 & 0 & \cdots & -1 \\ 1 & x & 1 & \cdots & 0 \\ 0 & 1 & x & \cdots & 0 \\ \vdots & \vdots & \vdots & \ddots & \vdots \\ -1 & 0 & \cdots & 1 & x \end{vmatrix} = 0$
solution for MO energies	$E_j = \alpha + 2\beta \cos\left(\frac{2\pi j}{n}\right)$	$E_j = \alpha + 2\beta' \cos\left(\frac{(2j+1)\pi}{n}\right)$
	for $j = 0, \pm 1, \pm 2, \cdots, \pm\left(\frac{n}{2} - 1\right), \frac{n}{2}$	for $j = \pm 0, \pm 1, \pm 2, \cdots, \pm\left(\frac{n}{2} - 1\right)$

Figure 7: Array of mixed atomic orbitals, associated determinant and solutions for energy estimation using the Hückel method of molecular orbitals for non-twisted (Hückel) and half-twisted (Möbius) shaped π-conjugated system.

It is important to point out that the interaction energy term β' in the Möbius system, (assuming $Lk = \pm 1$, $Wr = 0$ and $Tw = \pm 1$) is different from the β of the 'flat' Hückel topology system (with $Lk = 0$, $Wr = 0$ and $Tw = 0$). The local twist in Möbius systems causes worse overlap, attenuating the interaction energy term (**Eq. 4**).

$$\beta' = \beta \cos\left(\frac{\pi}{n}\right) \tag{4}$$

This results in a smaller spread of the highest and lowest MO energies and therefore increases the total energy of the system. Based on these simple rules, an energy diagram for the hypothetical C_8H_8 system with 8 π electrons can be plotted for both Hückel and Möbius topology in the form of so called Frost-Musulin, or in the case of Möbius system – Zimmerman's, mnemonic diagrams (**Figure 8**).

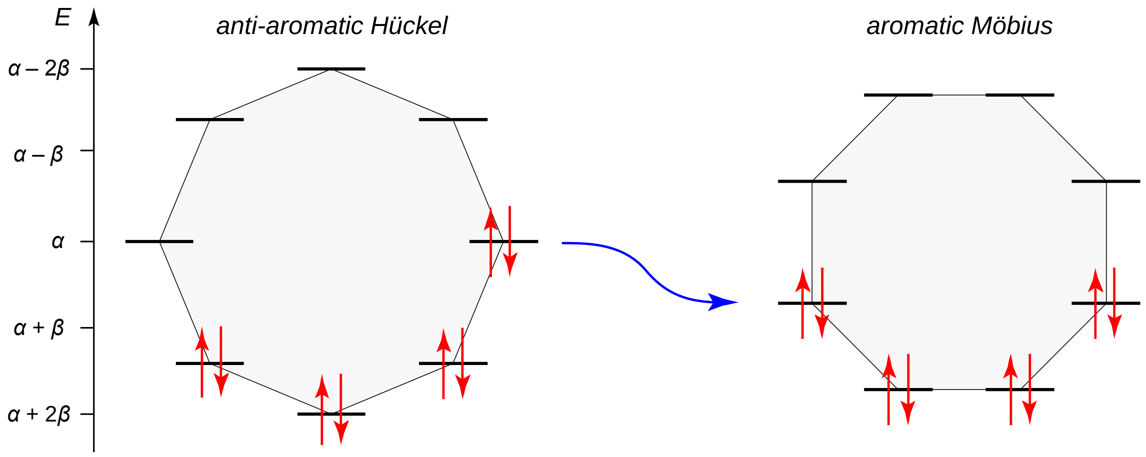

Figure 8: Frost-Musulin-Zimmermann mnemonic cycles showing the stabilization of the [4*n*] π system by changing the topology from Hückel (no twist) to Möbius (one half twist) in hypothetical, fully conjugated annulene C_8H_8 with 8 π electrons. In the case of half-occupied degenerate HOMO, inherently is assumed some degree of the Jahn-Teller distortion causing the energic lowering of one HOMO yielding a singlet multiplicity.

Using this simple HMO model and ignoring all other chemical considerations (regioisomers, longer range interactions, σ- and π- bond interactions etc.) one can calculate the total energies of the *n* π electron containing system (e.g. [*n*]annulene) in Hückel or Möbius topology. In **Figure 9**, the energy of the Hückel annulene, an idealized Möbius system ignoring the local twist ($\beta' = \beta$, dashed pale red) and 'real' Möbius and case ($\beta' = \beta \cdot \cos(\pi/n)$, red) is plotted as a function of number of π electrons *n*.

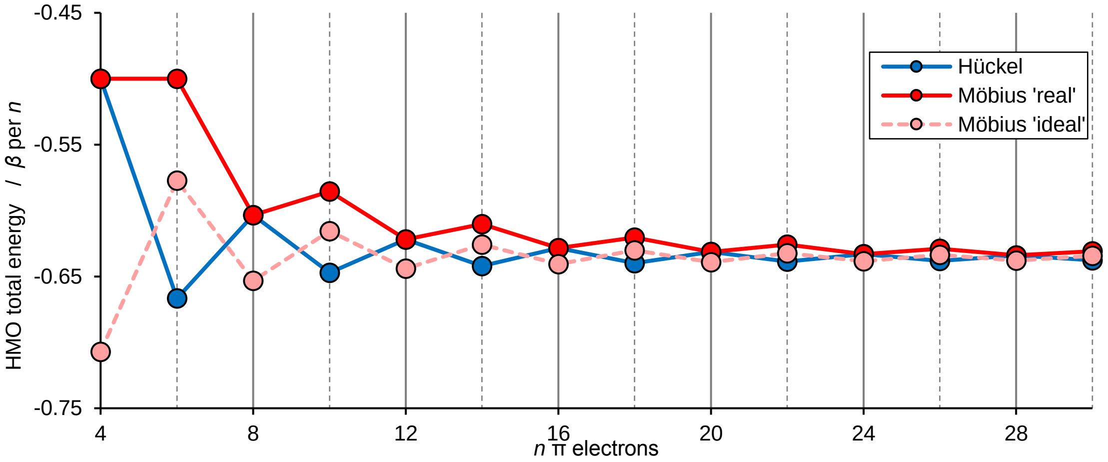

Figure 9: Total energy calculated using HMO theory for non-twisted (Hückel) and half-twisted (Möbius) shaped [*n*]annulenes, based on the sum of energy of all occupied MOs using HMO solutions summarized in **Figure 7**.

These basic arguments can allow the hypothesis that some of the annulenes, particularly middle/large [4*n*]annulenes with smaller local twists *Tw*, could adopt a Möbius conformation, driven by anti-aromatic → aromatic energy gain. However, the strain induced by the Möbius conformation is far too large to benefit from aromaticity. Many annulenes were theoretically investigated and all high-level calculations suggest that Möbius conformation is never a global energetic minimum for any annulene.[7] Although the Möbius conformers are not the lowest in energy, they can represent local minima and their magnetic behaviour, as predicted by NICS calculations, often suggests Möbius aromatic character (**Figure 10**).[10]

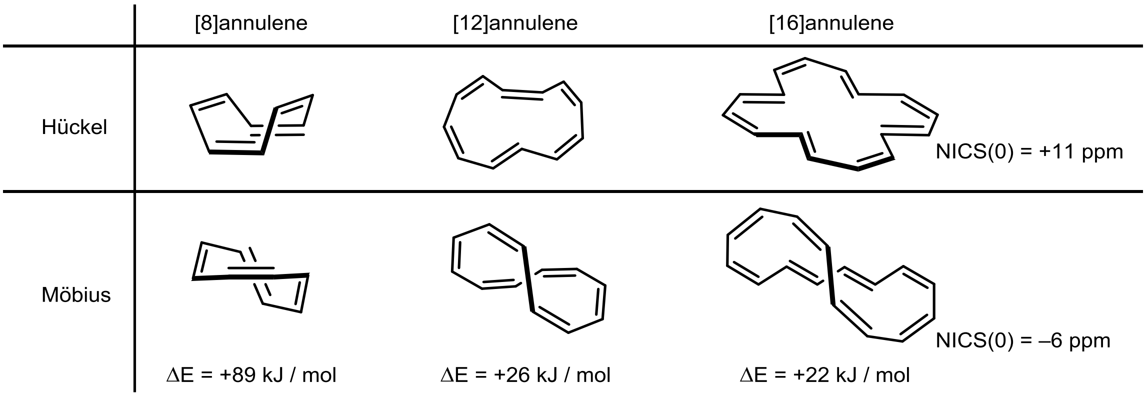

Figure 10: DFT (B3LYP/6-31G*) calculated difference between energy of Hückel and Möbius conformer in selected [4*n*]annulenes. NICS calculated in the centre of both Hückel and Möbius conformer of the [16]annulene showed expected aromaticity and anti-aromaticity, respectively.[10,11]

However, certain annulene-type-systems are suspected to spontaneously adopt Möbius confirmations. One example is the $C_9H_9^+$ cation. It was proposed that the Möbius conformation of the $C_9H_9^+$ cation is the lowest energy among all other isomers and supported with extensive theoretical investigations. The physical existence of the cation of the formula $C_9H_9^+$ was based on a deuterium labelling experiment of chloro-hydrocarbon C_9H_9Cl hydrolysis, showing an even distribution of the deuterium and suggesting existence of some fully delocalized cation intermediate (**Figure 11**).[12,13]

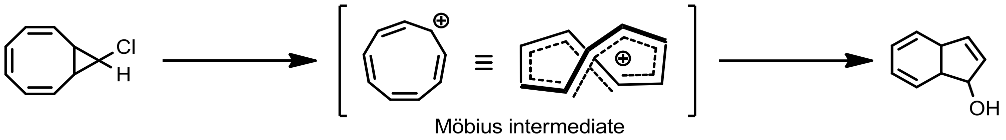

Figure 11: Cation $C_9H_9^+$ was one of the first proposed Möbius-shaped reaction intermediate.[12–14]

However, the existence of the Möbius annulene $C_9H_9^+$ is based only on indirect evidence, heavily depending on the precision of the calculations. It is anticipated that more cations and anions of annulenes could adopt the Möbius conformation as summarized in **Figure 12**.

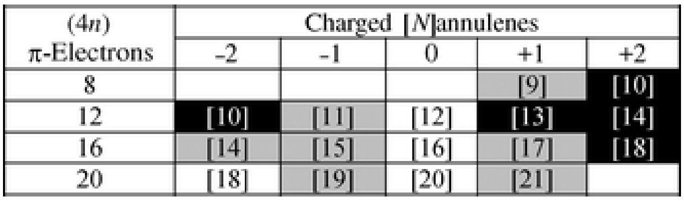

(4*n*) π-Electrons	Charged [*N*]annulenes				
	-2	-1	0	+1	+2
8				[9]	[10]
12	[10]	[11]	[12]	[13]	[14]
16	[14]	[15]	[16]	[17]	[18]
20	[18]	[19]	[20]	[21]	

Figure 12: Summary of the preferred conformation of various annulenes in various oxidation states possessing [4*n*] π electrons. No shading corresponds to the Hückel topology, greyed to the ambiguous case with both topologies close in energy and the black filling correspond, to the situation when Möbius confirmation is stabilized by more than 12.5 kJ/mol. Edited figure reprinted with permission from *Chem. Comm.* **2013**, (49), 1254–1260. Copyright 2013 The Royal Society of Chemistry.[7] Data from literature.[10,14–20]

The conclusion is, that the Möbius conformation must be enforced, rather than expected to form spontaneously, because Möbius systems tend to be more strained than Hückel ones, and the strain energy outweigh the aromatic stabilisation. If a certain property related with Möbius aromaticity is sought, the system needs to be engineered and ‘persuaded’ to adopt such a conformation.

4.2.2. Experimentally studied Möbius molecules

In the past 16 years, several successful syntheses of Möbius-strip shaped π-conjugated molecules were presented as a result of clever molecular designs (**Figure 13**).

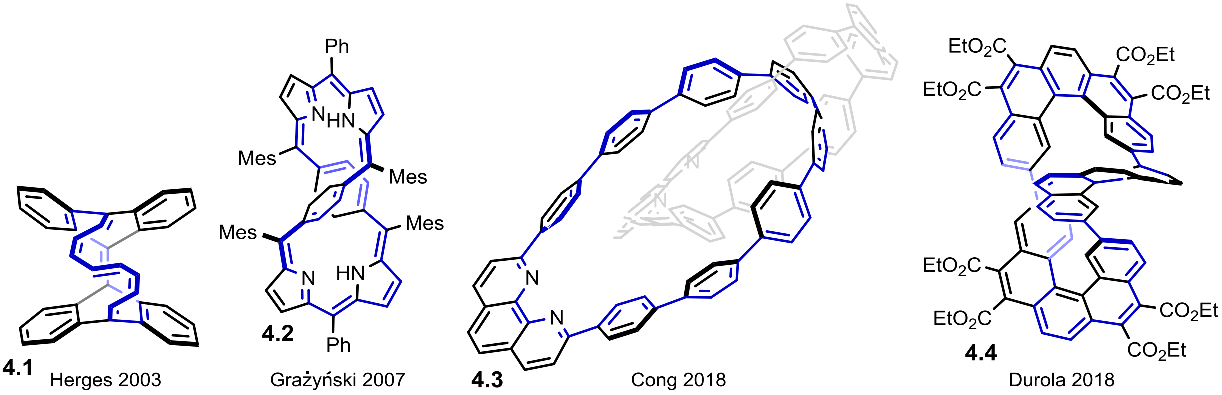

Figure 13: Different approaches toward Möbius-shaped π-conjugated paths. Formal π-conjugated path in the Möbius-strip shape is highlighted with blue.[21–24]

The very first example of a molecule with a Möbius shaped π-electron-conjugated path was designed and synthesised by Herges et al.[21] The synthesis employs [2+2] photocycloaddition of tetradehydrodianthracene with *syn*-tricyclooctadiene. The strained adduct then thermally and photochemically rearranges into two isomers and one of the products possesses the Möbius topology of the formally conjugated path of 16 π electrons (highlighted in blue) (**Figure 14**).

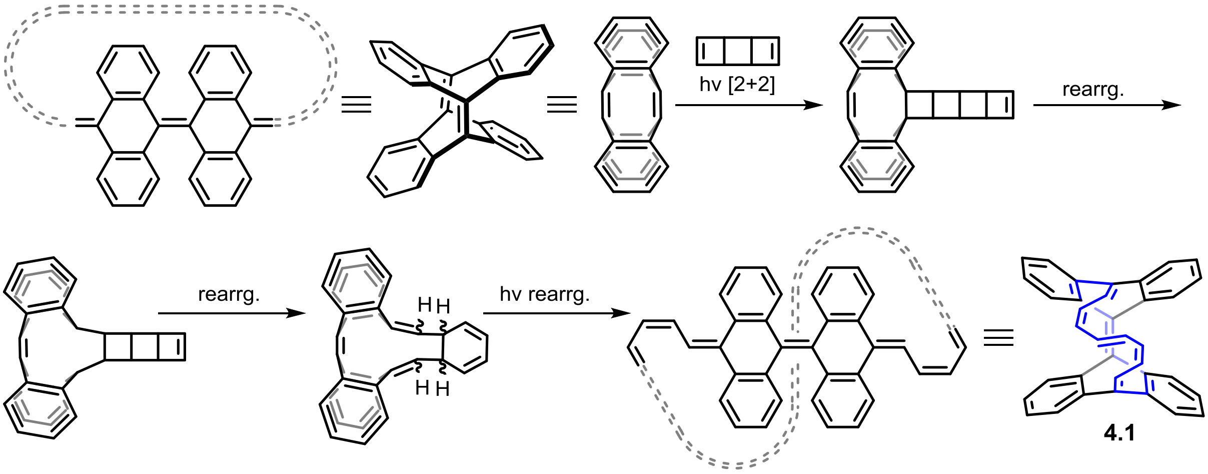

Figure 14: Simplified synthetic scheme toward first Möbius molecule.[21]

The rationale behind the synthesis is the combination of the *in-plane* and *out-of-plane* π-conjugated molecules. Formal metathesis of those two components yields to the system with *Lk* = ±1 (**Figure 15**).

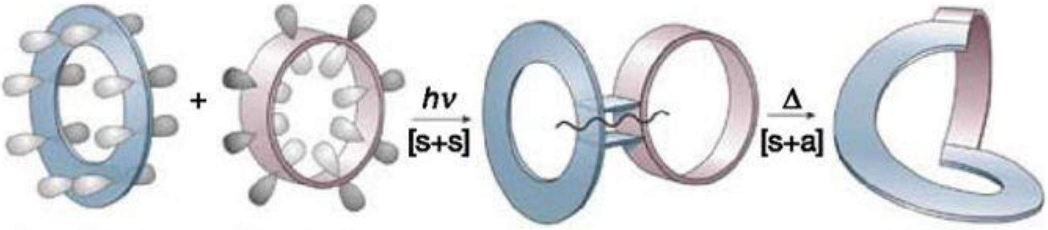

Figure 15: Concept of synthesis of the first molecule with Möbius topology of the π conjugated hydrocarbon path.[21] Synthesis employs combination of the in-plane and out-of-plane conjugation yielding the twist in the system. Reprinted by permission from *Nature*, 2003, (426), 819–821. Copyright © 2003, Springer Nature

Even though this is a very clever approach, it yields a system with very high *Tw* (*Tw* ~ 0.5).[7] Such severe local distortions, together with the need of breaking aromaticity on the two benzene rings, yield a negligible π-electron mobility along the Möbius path and thus no detectable Möbius aromaticity. The authors wishfully support the idea of the Möbius aromaticity by observing decreased bond-length alternation along the conjugated path. However, extensive critical assessment delivered by Schleyer et al. concluded that any aromatic character observed in NMR and NICS calculations should be solely attributed to the benzene rings and the whole molecule should be understood as non-aromatic in term of Möbius aromaticity.[15]

In response to the Schleyer's analysis, Herges et al. carried out extensive theoretical and comparative investigation considering 153 different annulene isomers. The authors concluded the molecule to be partly Möbius aromatic and stabilized through the Möbius aromaticity, contrary to Schleyer's finding.[25]

The second example of a Möbius-strip shaped molecule was delivered by Grażyński et al. (**Figure 16**).[22]

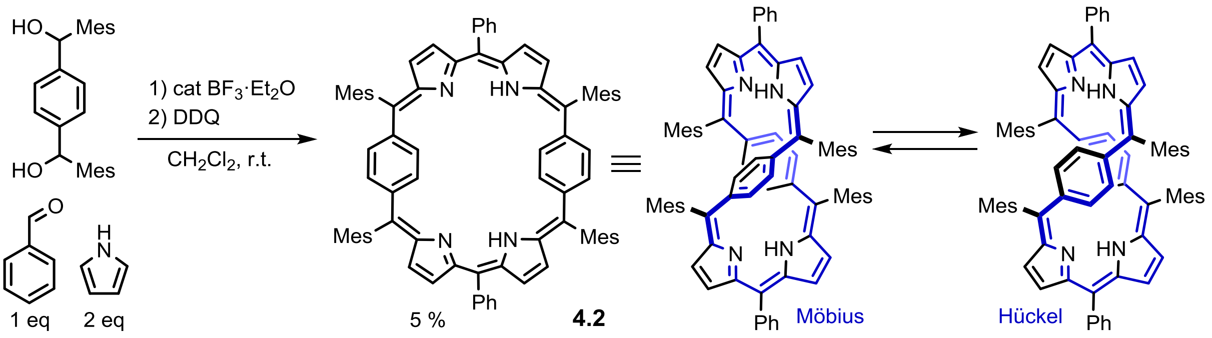

Figure 16: Synthesis of *para*-phenylene expanded porphyrin **4.2** and its two conformers with Möbius and Hückel topology.[22]

Grażyński et al. synthesised, from simple building blocks, *para*-phenylene expanded porphyrin **4.2**. Solid-state analysis (XRD) proved the desired Möbius conformation ($Lk = 1$, $Wr = 0.3$ and $Tw = 0.7$), however, solution-based ^{1}H-NMR and UV-vis absorption studies showed very high flexibility allowing dynamic interconversion between the Möbius and Hückel shapes. The authors documented the solvent and temperature dependency of the Möbius/Hückel conformer ratio. For example, the population of the Möbius conformer was higher at lower temperatures and conversely increased content of the Hückel conformer was observed at elevated temperatures. The authors also later expanded the study to radical-cations based on the same molecular scaffold.[26]

[28]Hexaphyrins in general appear to be a good scaffold allowing the Möbius conformation. Kim, Osuka et al. showed that, by varying the substitution pattern in *meso* positions and crystallisation conditions, either Hückel or Möbius conformers can be obtained in the solid state, indicating the energetic closeness of these two conformations (**Figure 17**).[27]

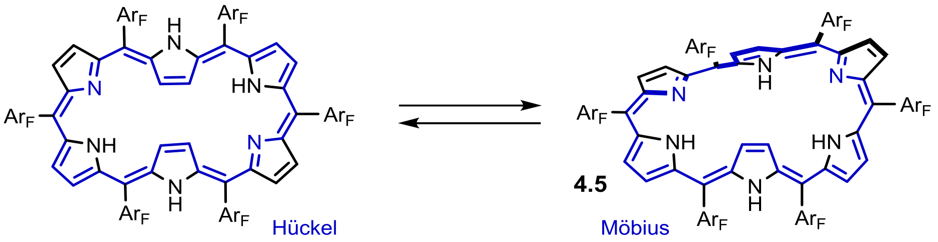

Figure 17: [28]Hexaphyrin was observed in solid state both in Hückel (left) and Möbius (right) conformation. Ar$_F$ = 2,6-difluorophenyl.[27]

Solution-based ^{1}H NMR experiments on compound **4.5** showed high flexibility and dynamic interchanging between Hückel and Möbius conformation. Upon cooling of the solution to −100°C, slower dynamics with a higher preference toward the Möbius conformation was observed, analogously to the studies of Grażyński et al. Theoretical investigations showed the expected Hückel anti-aromaticity and Möbius aromaticity of the [28] electron system, as the NICS$_{iso}$ values calculated in the centre of the Hückel and Möbius structures were 34.5 and −15.2 ppm, respectively.[27]

Kim et al. also presented the smaller, fused [24]pentaphyrin **4.6**. The high flexibility of porphyrin structures was overcome in that case by complexation of a rhodium cation. The fused expanded porphyrin **4.6** exhibits a diatropic current detectable by NMR, assignable to the [4*n*] Möbius aromaticity. XRD analysis confirmed the Möbius conformation with reduced bond length alternation, although severely distorted from good conjugation (**Figure 18**).[28]

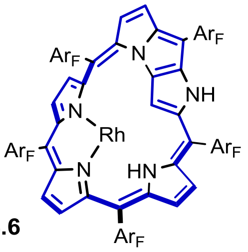

4.6

Figure 18: Partly fused [24]pentaphyrin with complexed rhodium cation. Ar_F = 1,2,3,4,5-pentafluorophenyl.[28]

Several more penta- and hexaphyrins were synthesized and have been suspected of spontaneously adopting the Möbius conformation. This could be the consequence of a 'good' ring size, and pyrrole connectivity pattern, distorting the whole cycle in 3D, in the case of hexaphyrins typically to $Wr \sim 1.2$.[4,29,30] Such distortions (as $Wr \rightarrow 1$) potentially favour the Möbius topology.[27,31]

Octaphyrins in general spontaneously adopt a lemniscular, figure-of-eight shape.[32–35] Such topology is of Hückel type, double twisted with $Lk = 2$. Due to steric repulsion, in such small molecules it is not possible to accommodate a very tight figure-of-eight shape ($Wr = 2$), leading to best electron conjugation ($Tw = 0$). Structures therefore possess rather open shapes of $Wr = 0.5$–1.5.

Octaphyrin scaffolds were employed for example by Osuka et al.[36] These authors used a pentafluorophenyl-decorated [36]octaphyrin. Insertion of one or two of various metals provided the ability to stabilise both Hückel and Möbius conformers. For example, insertion of two Pd^{2+} cations to [36]octaphyrins, depending on the connectivity, yielded either Hückel anti-aromatic or Möbius aromatic structure **4.7** (**Figure 19**).

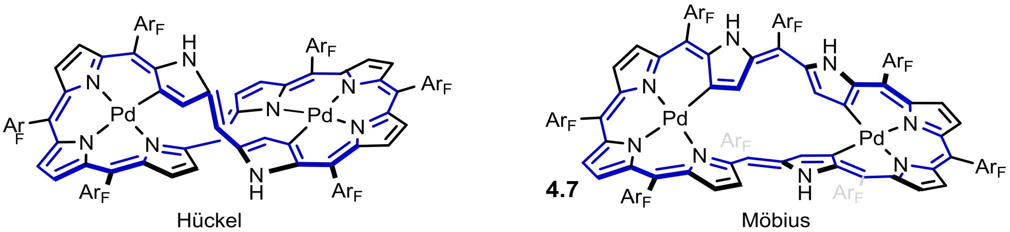

Figure 19: Hückel and Möbius shaped bis-palladium-[36]octaphyrins presented by Osuka et al.[36]
Ar_F = 2,3,4,5,6-pentafluorophenyl.

A simple change in the Pd—N or Pd—C binding mode led to subtle changes in the writhe, resulting in the preference for either Hückel or Möbius topology (**Figure 20**).

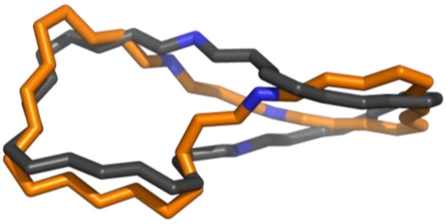

Figure 20: Periphery of the Möbius (orange) and Hückel (grey) bis-palladium- [36]octaphyrins synthesized by Osuka et al.[36] Hydrogens and inner nuclei were removed for clarity.

The authors presented conclusive NMR characterisation of the anti-antiaromaticity of the Hückel conformer, as it possessed deshielded inner *beta* nuclei resonance at 17.14 ppm and shielded outer nuclei at 8.60 ppm. In the Möbius conformer, the authors documented a diatropic ring current, as resonances of atoms pointing inside the rings were shielded to 0.24 – −2.93 ppm and outer deshielded to 8.19–7.42 ppm. This interpretation was corroborated with NICS calculated at centres of the aromatic Möbius and anti-aromatic Hückel isomers predicting values of −14.6 ppm and 38.4 ppm, respectively.

A conceptually different Möbius conformation was discovered in the solid-state by Cong et al.[23] The authors synthesised phenanthroline-containing cyclo-*para*-phenylene (CPP) catenane **4.3**. The synthesis involved first coordinating phenanthroline-containing building blocks to the copper centre, subsequent closing of the lobes with Suzuki coupling and re-aromatisation of the bent, dimethoxy-cyclohexadiene, units (**Figure 21**).

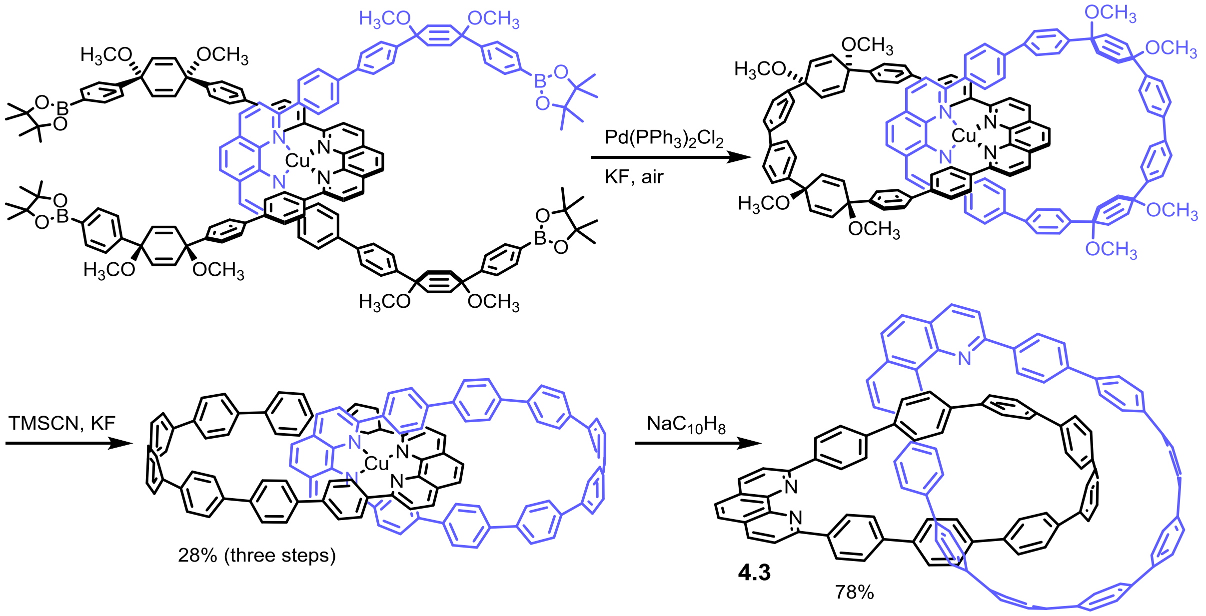

Figure 21: Synthesis of interlocked cyclo-para-phenylene catenane, folding into Möbius conformation in solid state.[23]

The authors analysed the bond length alternation and with comparison to the known CPP claimed small Möbius aromaticity character. However, significant electronic communication along the macrocycle is not expected as this would lead to de-aromatisation of many phenylene bridges. Furthermore, in the solution phase, ^{1}H-NMR of **4.3** shows fast rotation of the phenylene bridges, indication no or negligible aromatic stabilisation and even cooling to −100 °C did not lead to NMR-observable slow dynamics and preference for either conformer. The Möbius conformation is thus seen only in the solid state as a result of tight molecular packing, folding the C_2 symmetric molecule into the Möbius shape.

A recent example of a Möbius molecule was presented by Durola et al.[24] The authors synthesised, using conventional chemistry, cyclic stilbene oligomer **4.8**. Its photo-cycloaddition and further re-aromatisation transformed each stilbene part to a [5]helicene unit, creating a trimer of covalently connected [5]helicenes **4.4** (**Figure 22**).

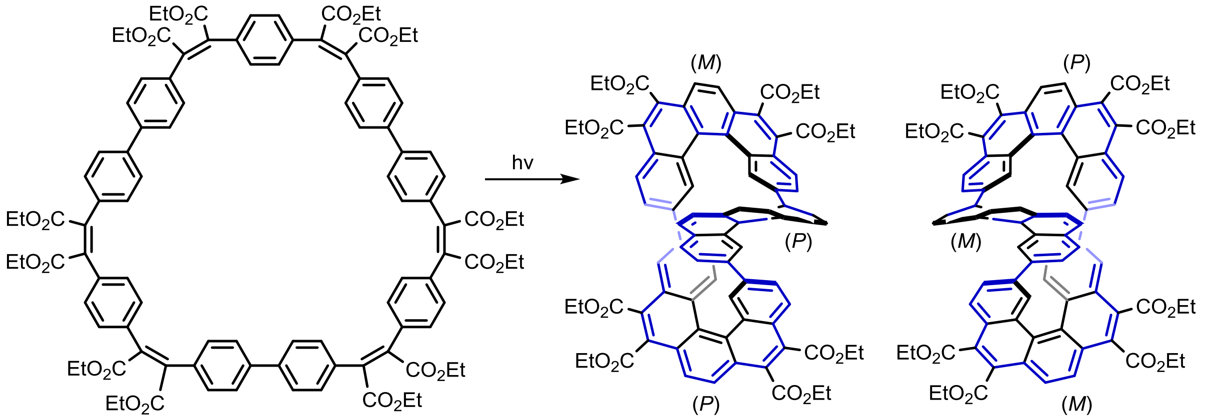

4.8 **4.4**

Figure 22: Photo-cyclisation of the stilbene parts in **4.8** yields catenated helicenes, creating Möbius-shaped π-conjugated molecule **4.4**.[24]

Among other stereoisomers, an oligomer with three connected [5]helicene units, **4.4** with (*M*,*M*,*P*) or (*P*,*P*,*M*) stereochemistry was obtained and the expected Möbius conformation confirmed with the XRD analysis. The inner part of the helicene trimer possesses linking number $Lk = \pm 1$, projected mainly to the local twists, as the topological analysis unveiled $Wr \pm 0.29$ and $Tw \pm 0.71$. The authors also isolated (*M*,*M*,*M*) and (*P*,*P*,*P*) stereoisomers, with the linking number of the inner part $Lk = \pm 3$, and with $Wr = 1.15$ and $Tw = \pm 1.85$, being thus an example of a triply-twisted Möbius conformer. Due to such severe local distortions and the aromaticity localisation character of the individual benzene cores constituting the helicene units, no experimental evidence for a Möbius global induced ring current was observed.

A conceptually analogous Möbius macrocycle was designed and presented by Herges et al. in 2014. Their approach was based on coupling of axially chiral bi-naphthyl blocks, *via* Cadiot-Chodkiewicz coupling and Sonogashira-type homocoupling reactions yielding butadiyne-linked cyclic binaphthyl trimer **4.9** (**Figure 23**).[37]

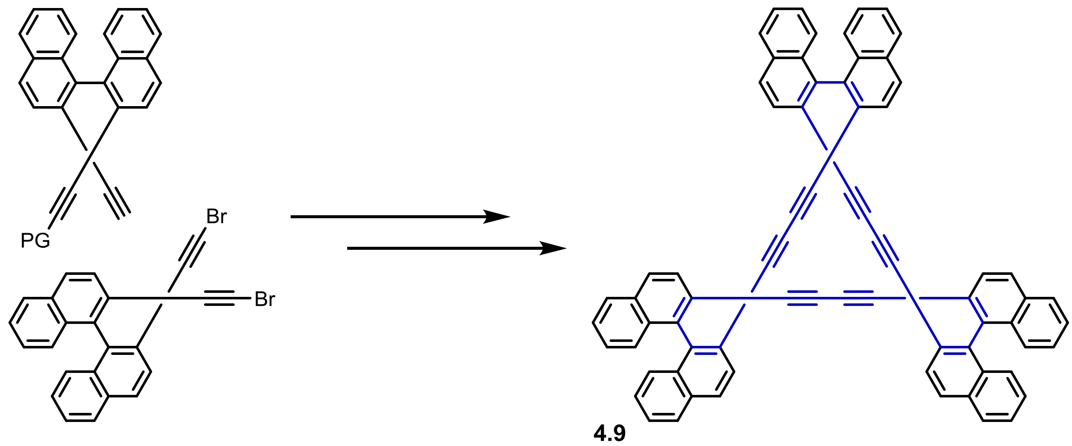

4.9

Figure 23: Cadiot-Chodkiewicz coupling followed by deprotection and homo-coupling yielded triple-twisted Möbius molecule **4.9**.

The authors correctly identified the Möbius structure as triple-twisted (unlike the misleading drawing in **Figure 23**), thus formally with *Lk* = ± 3. In the case of *Lk* = 3, values obtained from the XRD analysis shown *Tw* = 1.42 and *Wr* =1.58. Such severe local distortion inevitably causes virtually no electronic communication along the conjugated path, as in previous cases, and thus the molecule again exhibits the Möbius shape without many properties arising from the topology.

4.3. Design of porphyrin Möbius nanoring

Porphyrin nanorings represent a suitable scaffold for examining the size limit of Möbius aromaticity. Various linking numbers can be achieved by changing the conformation of individual porphyrins. 6-Porphyrin nanoring ***c*-P6[b6]** possesses, in neutral and oxidized states, a relatively low energy barrier of porphyrin-unit rotation ($\Delta G^{\ddagger}$ = 30–55 kJ/mol), suggesting a rather large conformational flexibility. The geometry minimum is a barrel shaped, 'co-planar' conformer, with Hückel topology (**Figure 24**, left), with 0° dihedral angles between neighbouring porphyrins. Another possible conformer, where every porphyrin unit has a 30° dihedral angle with the neighbouring unit would have a π-conjugated system with Möbius topology (**Figure 24**, right). The question is, however, whether such a conformer represents some special place on the energy potential surface, particularly whether it is a local minimum.

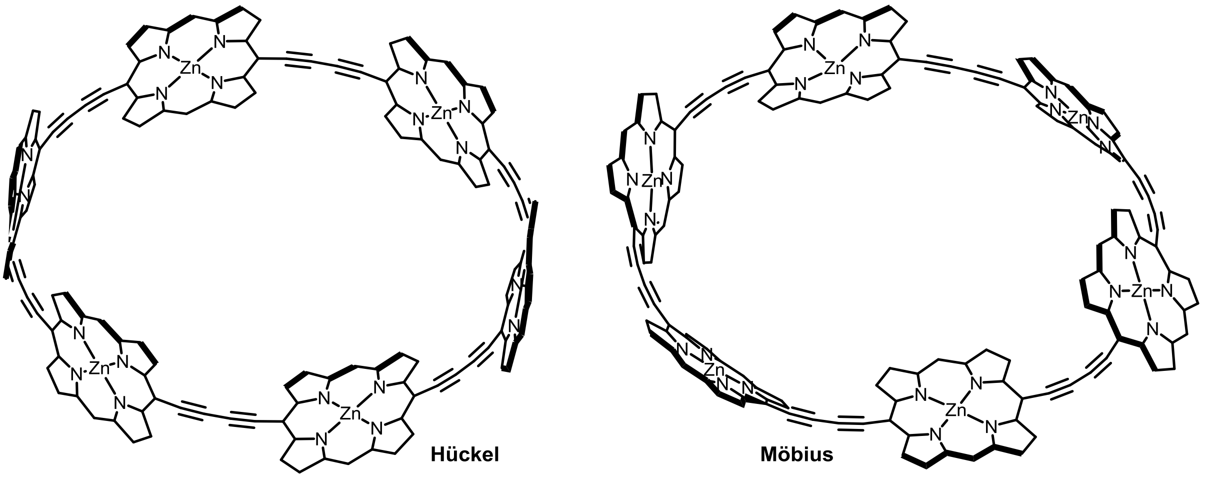

Figure 24. Hückel (left) and Möbius (right) conformation of the ***c*-P6[b6]**. Double bonds on the porphyrins omitted for clarity.

When the Möbius nanoring's geometry was assessed computationally, it was found that such a conformation is not a minimum in the neutral state, and not even for the oxidized species formally fulfilling criteria for Möbius aromaticity and Hückel anti-aromaticity (4+ oxidation state). Even if constrained (e.g. by restricting some dihedrals to ~30°), the energy gradients lead the structural geometry away from the Möbius shape toward the co-planar, Hückel, conformer, regardless the Hückel/Möbius (anti)aromaticity.

This finding, that the aromatic Möbius conformation is not spontaneously lower in energy than the Hückel anti-aromatic conformer (but is also probably not minimum at all) is supported experimentally as an absence of observation of any ring current reversal in template-free ring in Hückel anti-aromatic states. This leads to the conclusion that if such a conformation is desired, it needs to be stabilized, enforced in some way, to overcome the tendency of the system to adopt 'co-planar' structure of $Tw = 0$.

One way to induce the Möbius conformation 'spontaneously', is to imprint C_2, rather than D/C_6 symmetry. If the connectivity of some porphyrins in the macrocycle is changed from 5,15- to 5,10-, a lower π electron count is expected, although same in term of the [4*n*+2] / [4*n*] multiply. However, such a nanoring regioisomer (**4.10**) could have a very different shape (**Figure 25**).

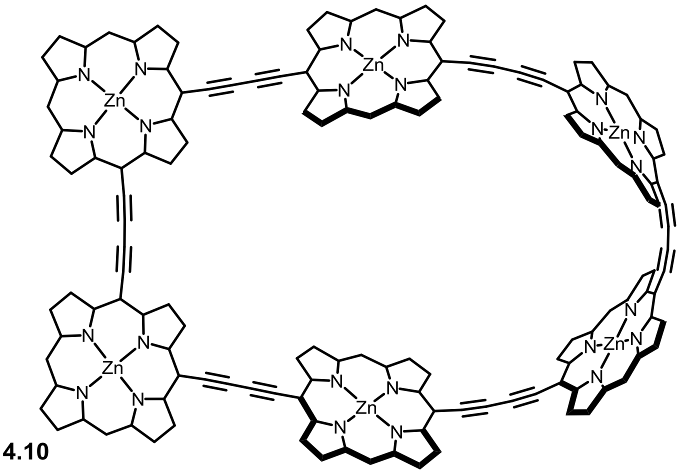

4.10

Figure 25. Regioisomer of ***c*-P6[b$_6$]** with changed connectivity at two porphyrins. Double bonds on the porphyrins omitted for clarity.

If this connectivity is changed in two adjacent porphyrin units in ***c*-P6[b$_6$]**, these two units would possess *out-of-plane* conjugation, whereas the rest of the nanoring π electrons would be *in-plane*. This requires some twist to enable communication and the 5,10- connected platform would define the C_2 symmetry. In small (6 or 7 porphyrin units) nanorings, such dihedral between two 5,10-connected porphyrins would be smaller than 90°, imprinting a half twist and therefore a Möbius conformation. This was supported by the DFT (B3LYP/6-31G*) based model, (using Gaussian 16)[38] showing the Möbius topology as a viable structure **Figure 26**.

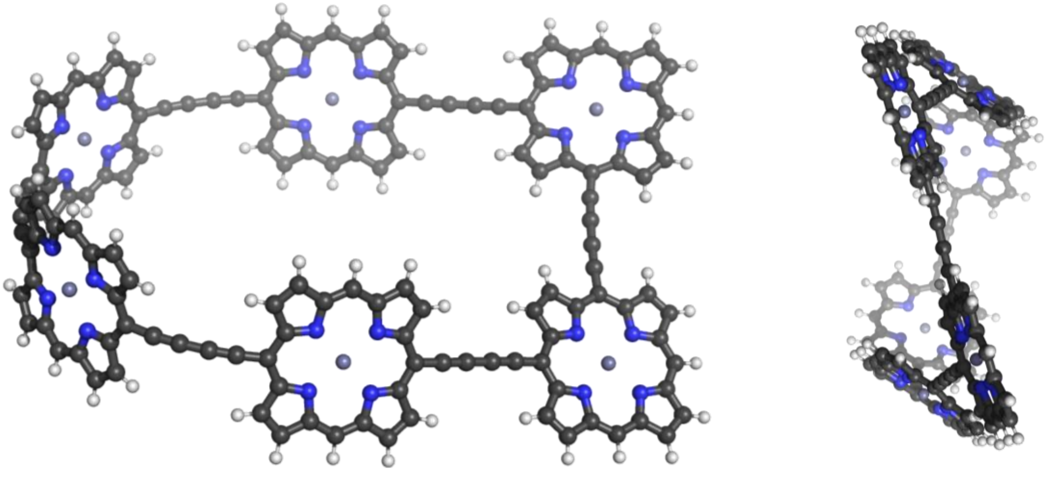

Figure 26. Molecular model of **4.10,** regioisomer of ***c*-P6[b$_6$]** with changed connectivity at two porphyrins. Geometry optimized using B3LYP/6-31G* at 4+ oxidation state.

The calculated NICS(0)$_{iso}$ (B3LYP/6-31G*) predicts Möbius aromaticity at 4+; and anti-aromaticity at 6+ oxidation states, reversed behaviour relative to the circular ***c*-P6[b$_6$]** (**Figure 27**).

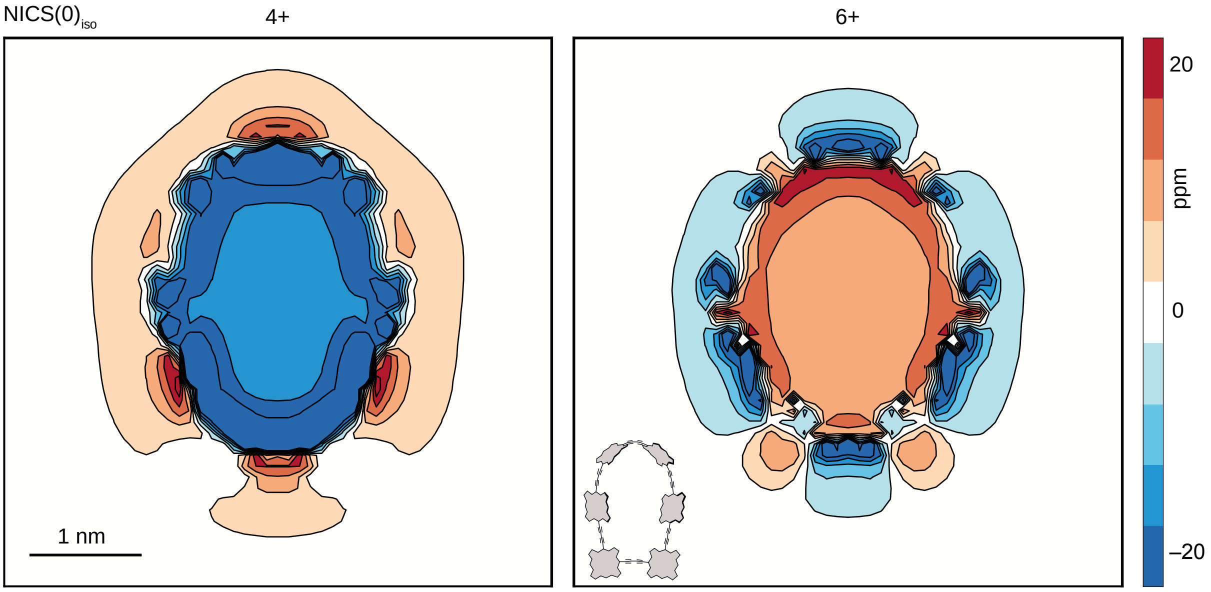

Figure 27. NICS(0)$_{iso}$ (B3LYP/6-31G*) of Möbius nanoring **4.10**, at 4+ and 6+ oxidation state. NICS were calculated on 50×50 Å grid with 1 Å spacing.

Although, conceptually, this approach could work for preparing the Möbius-shaped porphyrin nanoring, Hückel conformer could be present as well. Moreover, the synthesis and particularly the ring-closing step could be very challenging. For these reasons, the experimental study was not pursued, and the compound **4.10** was left only as a concept.

Another way to remove the strong bias toward Hückel topology in the porphyrin nanorings with 5,15-porphyrin connectivity is to enforce complete deconjugation in the nanoring. In the oxidized state, a high driving force for charge delocalisation is expected. Therefore, some small local twists, bypassing the otherwise artificially broken conjugation, might be expected to occur. Such subtle distortion would lead to non-90° dihedral angles. If the dihedral is > 90° on one side and either > 90° or < 90° on the other side, the overall shape can be of Hückel or Möbius topology, respectively. Such local twists could occur without obvious strong preference for one topology over the other (analogously to the **4.10**).

A practical way to deconjugate the nanoring is to adjust two porphyrin units into a perpendicular arrangement. This could be done by installation of a straight pyridine-containing arm (abbreviated with the index '$^{\mathbf{(1arm)}}$'), which would intramolecularly coordinate to the porphyrin across the nanoring (**Figure 28**).

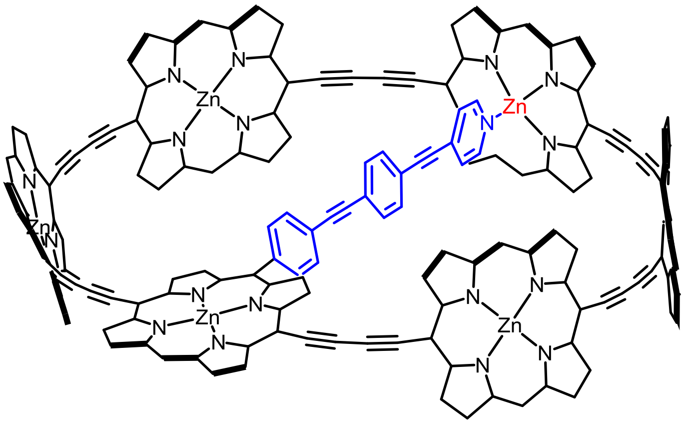

Figure 28. Simplified structure of ***c*-P6$^{(1arm)}$**, which is derived from ***c*-P6[b$_6$]** by decorating one porphyrin unit with straight, pyridine-containing arm. Double bonds on the porphyrins omitted for clarity.

Retrosynthetic analysis leads to plausible intermediates and the ***c*-P6$^{(1arm)}$** is, therefore, a synthetically feasible target (**Figure 29**).

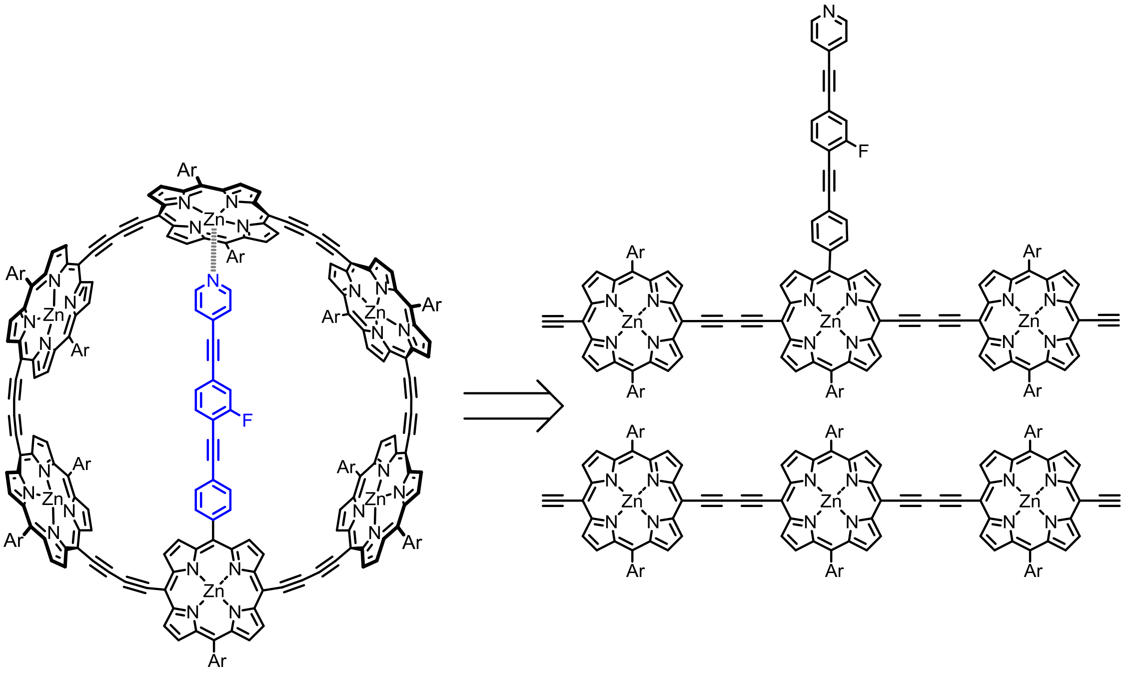

Figure 29. Basic retrosynthetic analysis of the ***c*-P6$^{(1arm)}$**. Ar = 3,5-bis(trihexylsilyl)phenyl

In the real structure of ***c*-P6$^{(1arm)}$**, a fluorine atom was included as a ^{19}F NMR probe, to report on the hypothetical global (anti)aromatic state. All free porphyrin *meso* positions were decorated in the design with 3,5-bis(trihexylsilyl)phenyl groups to improve solubility and suppress aggregation.

This concept of the intramolecular self-coordination can be extended even further by adding two further pyridine-containing arms (abbreviated with the index '$^{\mathbf{(3arm)}}$'), locking the structure in a predefined conformation, since one arm constrains two porphyrin units. If these two additional arms are bent with the 120° angle, and possess well-designed lengths, a regular pattern of 30° dihedral angles between adjacent porphyrins can be induced (**Figure 30**).

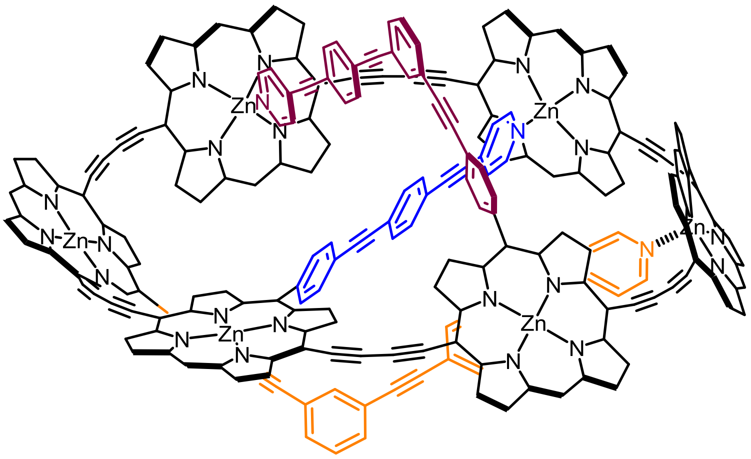

Figure 30. Simplified structure of ***c*-P6$^{(3arm)}$**, which is derived from ***c*-P6[b$_6$]** by decorating three porphyrin unit with straight, and bent pyridine-containing arms. In the self-coordinated state, π-conjugated path of the nanoring should adopt Möbius topology. Double bonds localized on the porphyrins are omitted for clarity.

The DFT (B3LYP/6-31G*) based model confirms the hypothesis of constraining the Möbius topology in the self-bound state with an evenly distributed twist (**Figure 31**, left). Practically, such a structure was designed to be decorated with solubilizing groups at the free *meso* porphyrin positions and edges of the bent arms. Furthermore, the fluorine atom as a ^{19}F NMR reporter was engineered in the approximate centre of the structure (**Figure 31**, right).

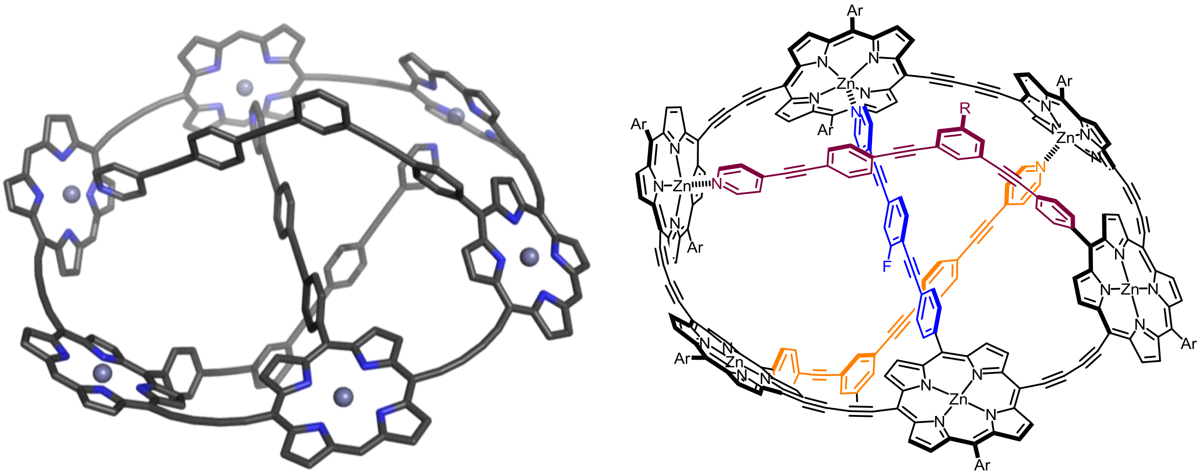

Figure 31. (left) DFT (B3LYP/6-31G*) optimized model of ***c*-P6$^{(3arm)}$**. Solubilizing groups and a fluorine atom were replaced with –H for the model. (right) Chemical structure of ***c*-P6$^{(3arm)}$**. Ar = 3,5-bis(trihexylsilyl)phenyl; R = trihexylsilyl.

The calculated NICS(0)$_{iso}$ on the porphyrin skeleton originating from the optimized structure of ***c*-P6$^{(3arm)}$** confirms the expected Möbius type (anti)aromaticity, reversed to the co-planar, Hückel conformer ***c*-P6[b$_6$]** at 4+ and 6+ oxidation state (**Figure 32**). The ***c*-P6$^{(3arm)}$** possesses high total twist number (basically $Tw = 1$) as the ring is rather planar (based on the Zn atom positions) and the linking number cannot be projected to the writhe. Nevertheless, distortions of ~30° in between porphyrin units is not expected to jeopardise the ring current in the oxidized state, as supported by the calculations, and the nanoring ***c*-P6$^{(3arm)}$** represents an attractive target.

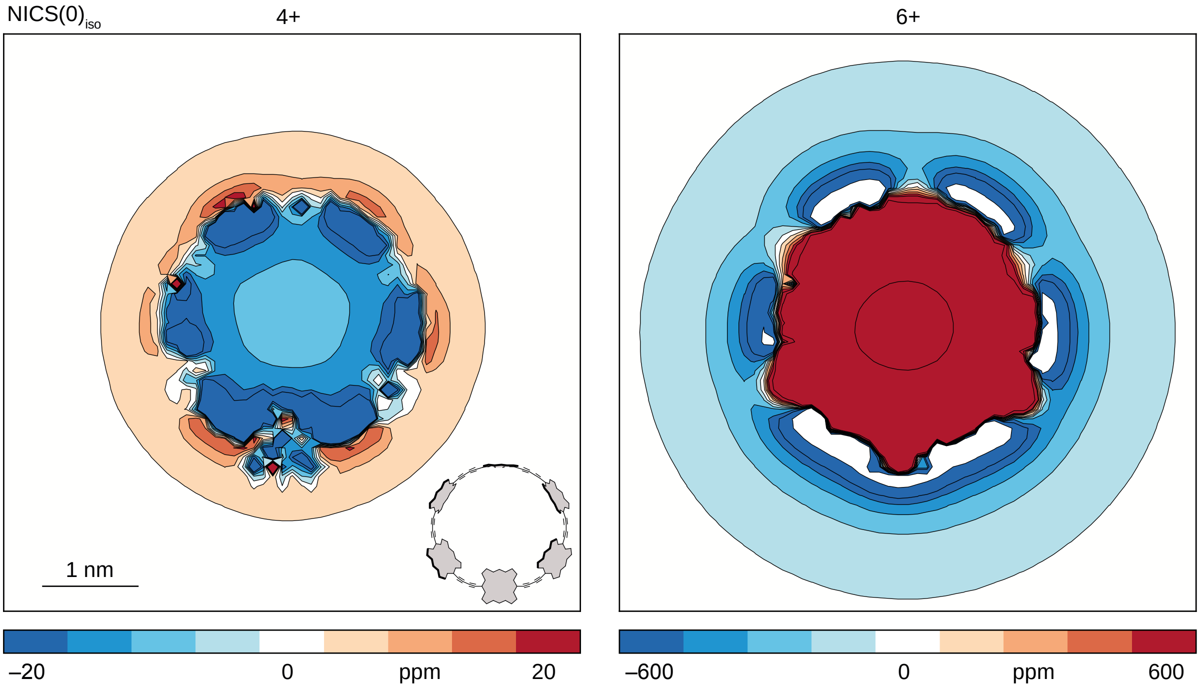

Figure 32. NICS(0)$_{iso}$ (B3LYP/6-31G*) of 4+ and 6+ oxidation state of ***c*-P6$^{(3arm)}$**. NICS were calculated on 60×60 Å grid with 1 Å spacing.

Retrosynthetic analysis of the ***c*-P6$^{(3arm)}$** leads to the route analogous to ***c*-P6$^{(1arm)}$** (**Figure 33**).

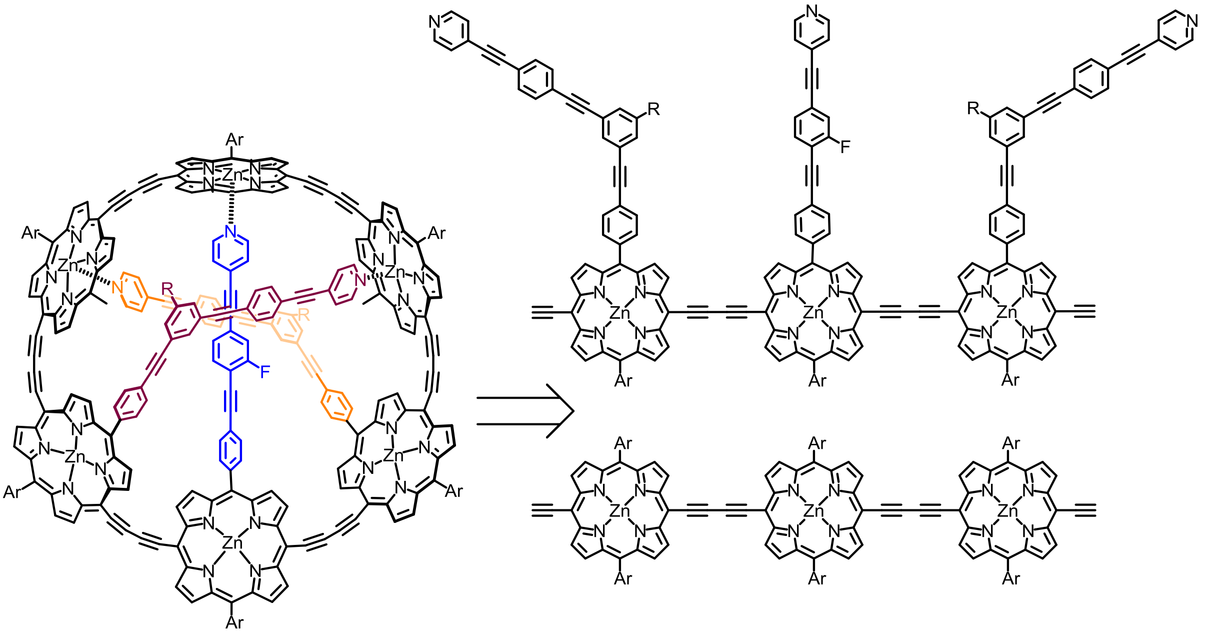

Figure 33. Most obvious retrosynthetic analysis of the ***c*-P6$^{(3arm)}$** ring closing step.

4.4. Synthesis and properties of single-crosslinked nanoring *c*-P6$^{(1arm)}$

4.4.1. Synthesis of *c*-P6$^{(1arm)}$

Synthesis of the single-pyridine-arm-decorated nanoring ***c*-P6$^{(1arm)}$** required development of a novel pyridine-arm-decorated porphyrin building block **4.11** which was assembled from two building blocks. Firstly, non-symmetric porphyrin **4.12**, with a 4-bromophenyl function on one side and bis(trihexylsilyl)phenyl solubilizing group on the other side. And secondly, the 'arm' component **4.13**, constructed by a series of Sonogashira couplings. This terminal-ethyne-containing arm block **4.13** was reacted with bromophenyl-functionalized porphyrin **4.12**, *via* copper-free Sonogashira coupling[39] yielding **4.11** (**Figure 34**).

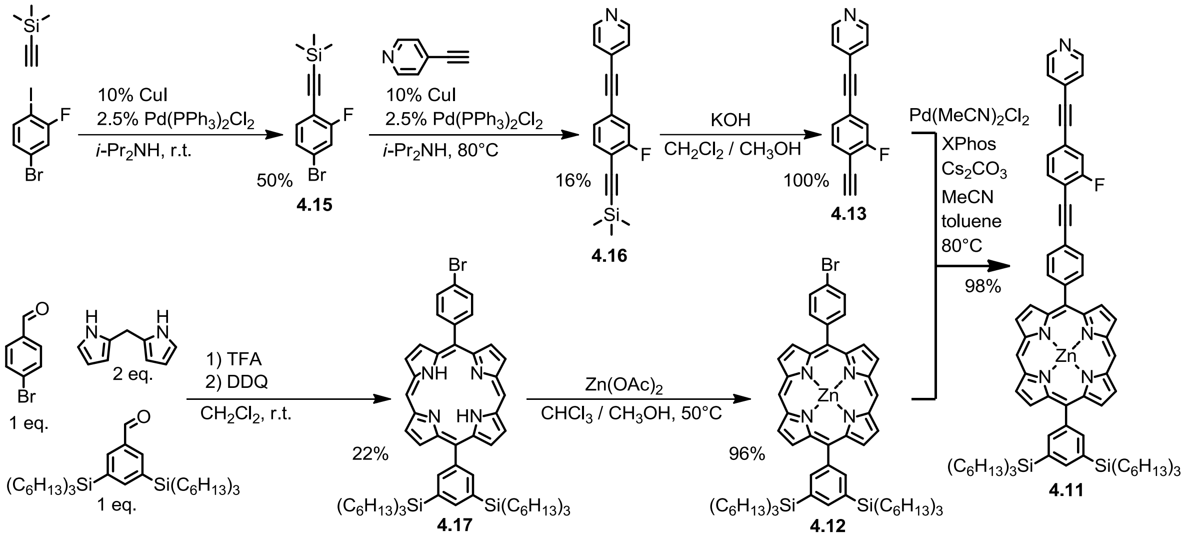

Figure 34. Synthesis of key porphyrin building block **4.11** functionalized with pyridine-containing straight arm.

The porphyrin unit **4.11** was further functionalized by bromination of the remaining *meso* porphyrin positions, using known methodology, yielding **4.14**, (**Figure 36**).

The presence of the pyridine-arm on the porphyrin units **4.11** or **4.14**, is evidenced by clear NMR signals, analogous to the resonances in a simple arm block **4.13**. ^{1}H resonances on the benzene core bearing the fluorine atom are coupled with the ^{19}F nucleus, causing a rather complex pattern of signals. These patterns together with the magnitude of the ^{1}H-^{19}F and ^{13}C-^{19}F couplings can be used for the NMR assignment, together with standard 2D-NMR techniques (^{1}H-^{1}H NOESY, ^{1}H-^{1}H COSY, ^{1}H-^{13}C HSQC, ^{1}H-^{13}C HMBC).

One might expect that the NMR signals corresponding to the arm in the decorated porphyrin **4.14** to be deshielded relative to **4.13**, as an effect of the porphyrin aromatic ring current. This effect is observable when a significant amount of pyridine is present in the NMR sample to supress the intermolecular coordination, however, it is very subtle as the nuclei **α–ε** are quite far from the porphyrin (**Figure 35**).

In the absence of pyridine, the pyridine-containing-arm coordinates intermolecularly to other units and the resonances (particularly α and β) are strongly shielded by other porphyrin units. When the pyridine content is increased, the resonances ‘travel’ toward the unaffected chemical shift suggesting fast dynamics of the system.

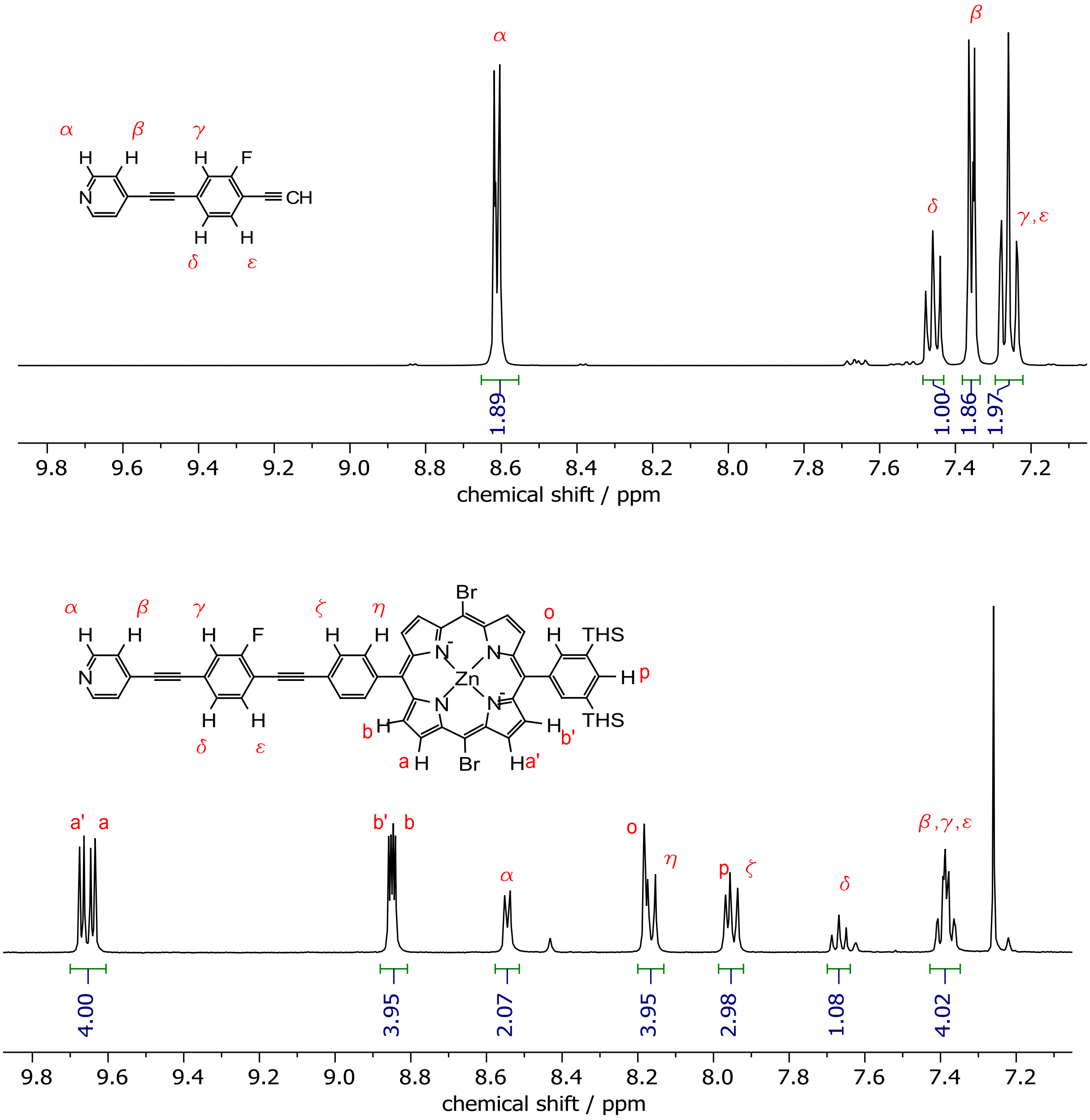

Figure 35. Comparison of ^{1}H NMR (400 MHz, $CDCl_3$) spectra of **4.13** (top) and **4.14** (bottom) with 10% of pyridine-d_5 added in the latter case.

The building block **4.14** was further transformed to the bis((trihexylsilyl)ethynyl) decorated unit **4.18** *via* Sonogashira coupling. Subsequently, **4.18** was transformed to the bare, bis(ethynyl)-substituted porphyrin **4.19**. This building block was reacted further with bis(bis(trihexylsilyl)phenyl)-solubilizing-group decorated porphyrin **4.20**, with one protected and one free terminal ethyne unit *via* Sonogashira-type homocoupling. Such homocoupling proceeds statistically, reacting two random ethyne units toward butadiyne. Among other species, desired linear porphyrin trimer **4.21** was separated from the mixture of oligomers using recycling GPC. Removal of the protecting cyanopropyl(di-isopropyl)silyl (CPDIPS) groups provided building block **4.22** (**Figure 36**).

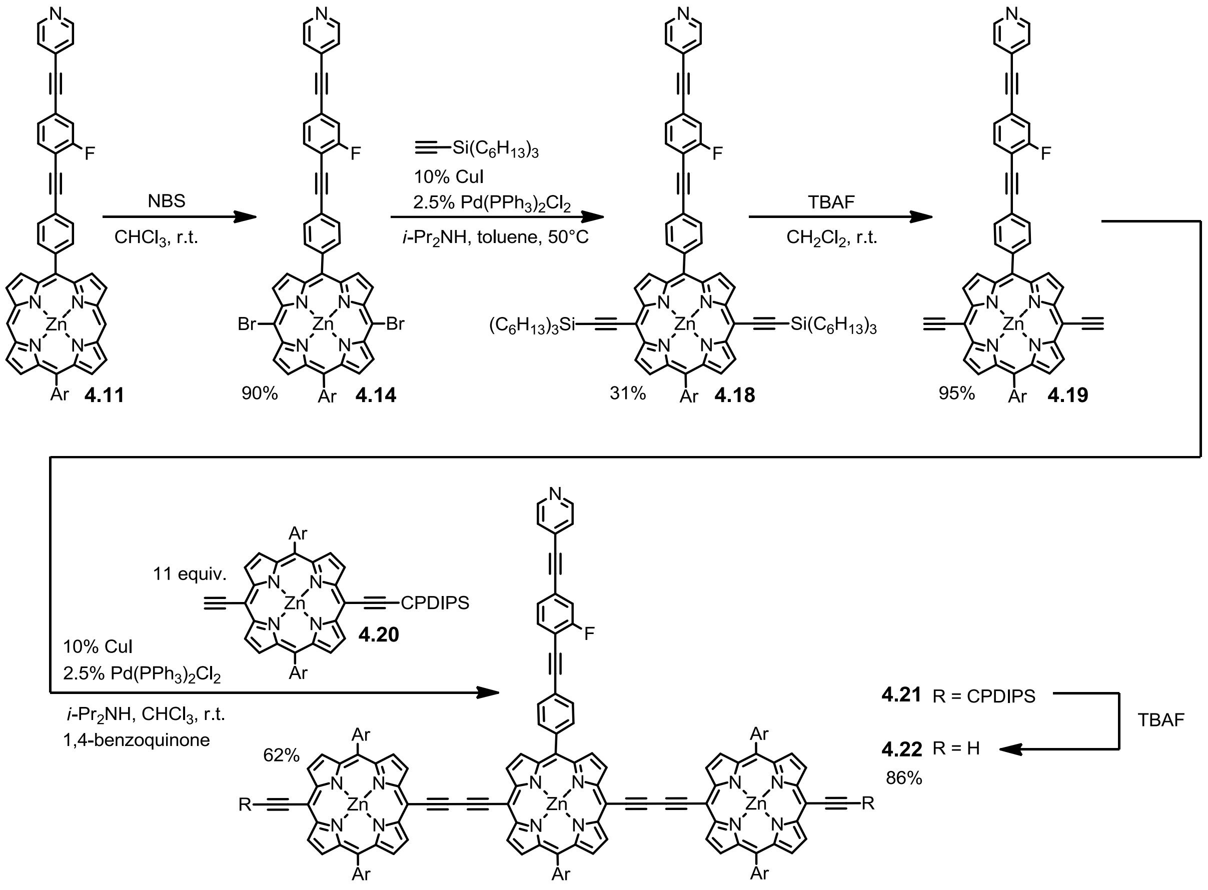

Figure 36. Synthesis of key porphyrin trimer **4.22**.

This synthetic route follows known type of chemistry and proceeded with expected yields. Symmetric linear trimer ***l*-P3** was prepared by porphyrin monomer oligomerizations as described in literature.[40] These two porphyrin trimer components were than reacted together in presence of **T6**, under the conditions of Sonogashira-type homocoupling. It was found that the pyridine-containing arm does not interfere significantly with the cyclization and the majority of the reaction mixture were species of ***c*-P6[b$_6$]·T6** size (based on the GPC retention times). The ***c*-P6[b$_6$]·T6** size fraction was separated by recycling GPC and consisted of three nanorings, as a result of statistical reaction between two trimers (A + B → A·A + A·B + B·B) (**Figure 37**).

These nanorings were not separable by their size using GPC. But since the pyridine-containing arm cannot be intramolecularly coordinated to the porphyrin across the ring, due to the presence of the strongly bound **T6** template, its presence and number significantly affects polarity of the nanorings, allowing their separation by silica chromatography.

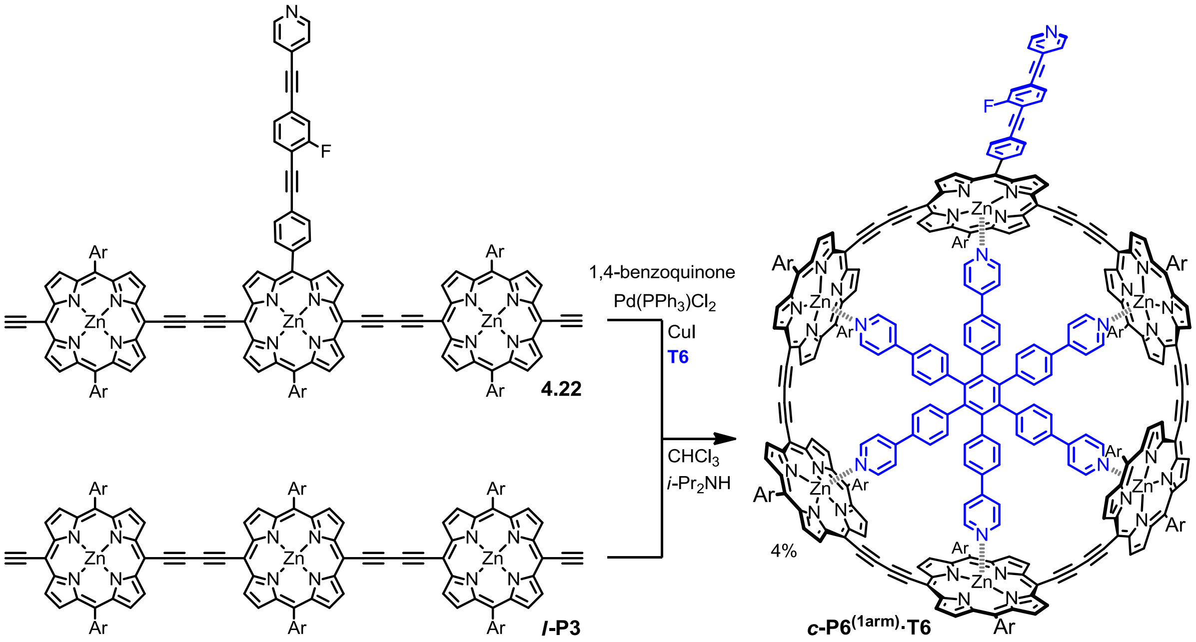

Figure 37. Synthetic scheme of mixed porphyrin trimer ***l*-P3** and **4.22** homocoupling cyclisation in presence of **T6** yielding ***c*-P6**$^{(1arm)}$**·T6**.

The NMR spectrum of the isolated ***c*-P6**$^{(1arm)}$**·T6** shows signals very analogous to the symmetric ***c*-P6[b$_6$]·T6** with extra resonances corresponding to the arm. Although, the intensity of these, arm-related, resonances is relatively weak in the spectrum (since they represent only a small fraction to the porphyrin signals), direct comparison of the ***c*-P6**$^{(1arm)}$**·T6** and ***c*-P6[b$_6$]·T6** helps the signals to visually stand out (**Figure 38**).

Symmetry point group of ***c*-P6[b$_6$]·T6** as observed by NMR is D_{6h}. The expected symmetry point group of ***c*-P6**$^{(1arm)}$**·T6** is the significantly less-symmetric C_s. However, only a subtle de-symmetrisation is observed in ***c*-P6**$^{(1arm)}$**·T6** NMR spectra, probably due to the relative remoteness of the arm to the porphyrin core, and thus such desymmetrisation has only negligible effects on the chemical shifts of the majority of NMR resonances. Effectively, most of the resonances are collapsed close together at nearly unchanged chemical shifts.

Besides the logic of the synthesis, the ***c*-P6**$^{(1arm)}$**·T6** was characterized by NMR, high resolution mass spectrometry and UV-vis-NIR absorption, which showed features significantly similar to well characterized ***c*-P6[b$_6$]·T6** (**Figure 39**).

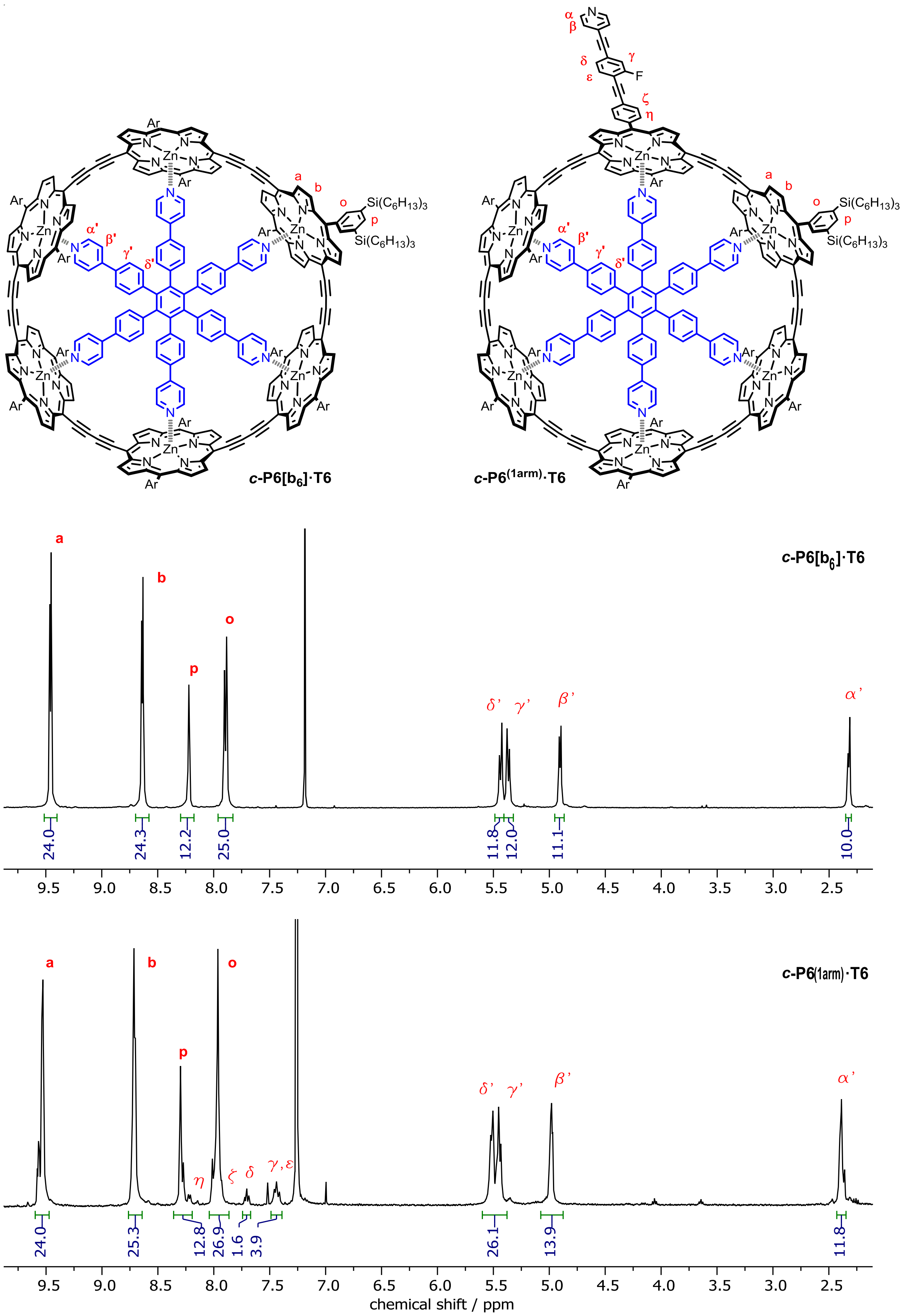

Figure 38. (top) Assignment legend for the NMR spectra. (bottom) Assigned ^{1}H NMR (400 MHz, $CDCl_3$) spectra of ***c*-P6[b$_6$]·T6** (top) and ***c*-P6$^{(1arm)}$** (bottom). Ar = 3,5-bis(trihexylsilyl)phenyl.

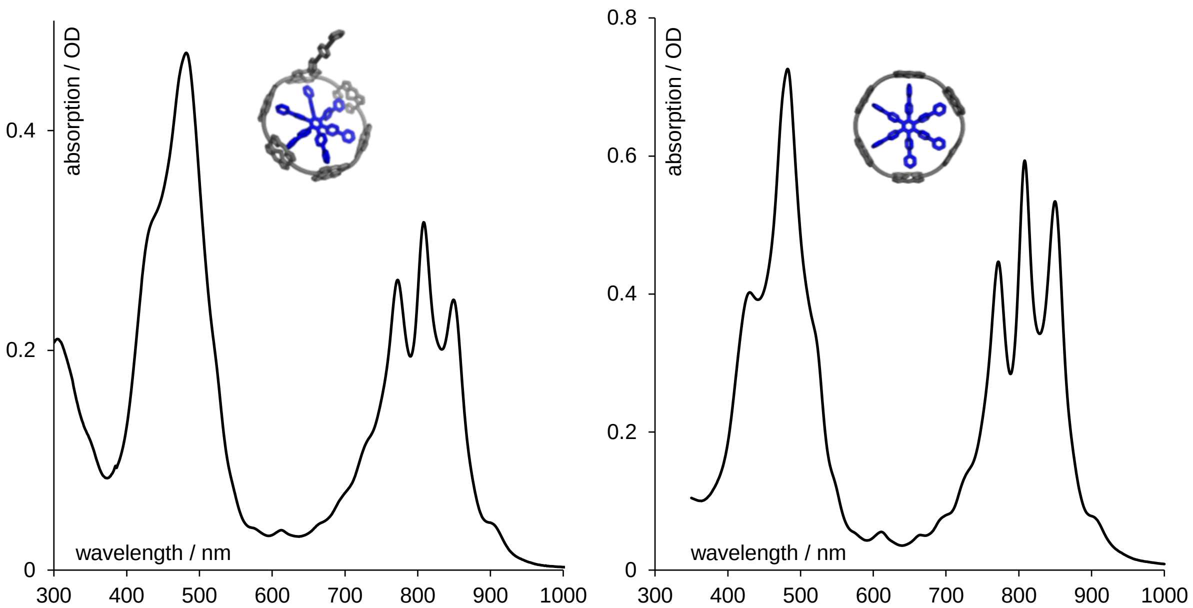

Figure 39. UV-vis-NIR absorption spectra (toluene) of ***c*-P6$^{(1arm)}$·T6** (left) and ***c*-P6[b$_6$]·T6** (right), showing spectral similarity, particularly iconic vibronic splitting in the Q band.

The ***c*-P6$^{(1arm)}$·T6** was then transformed to the template-free ***c*-P6$^{(1arm)}$** by **T6** removal, induced by presence of large excess of the strong competing ligand 1,4-diazobicyclo[2.2.2]octane (DABCO). Under these conditions, the **T6** could be removed by SEC (**Figure 40**).

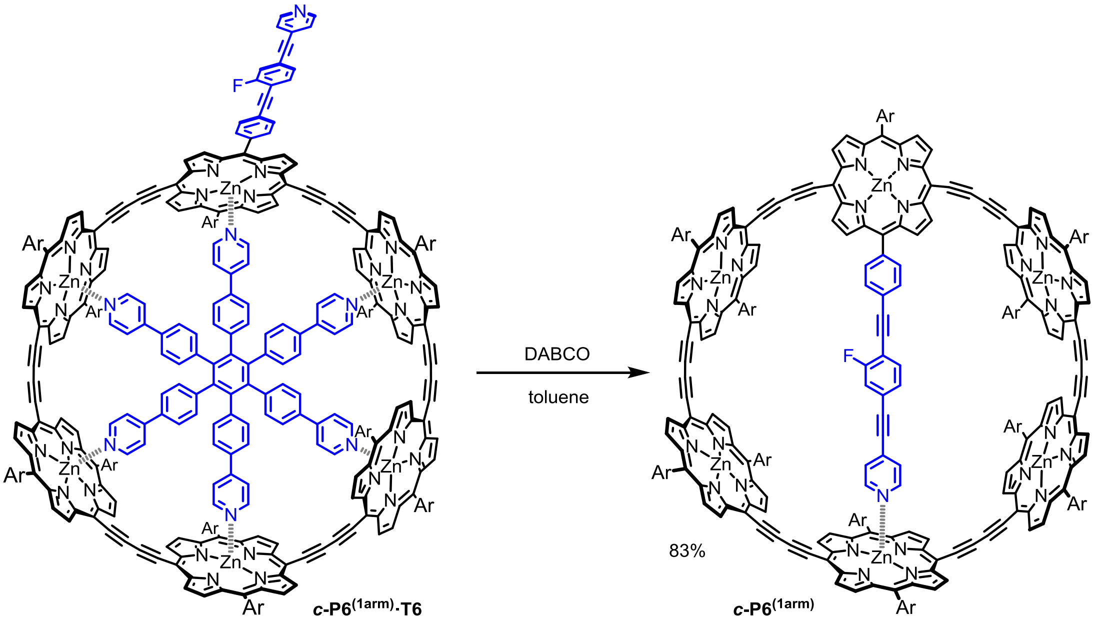

Figure 40. Synthesis of the template-free ***c*-P6$^{(1arm)}$** by decoordination of the **T6** template with strong ligand 1,4-diazobicyclo[2.2.2]octane (DABCO) and its subsequent removal by SEC.

4.4.2. Study of the template-free *c*-P6$^{(1arm)}$

The ^{1}H NMR spectrum of ***c*-P6$^{(1arm)}$** suggests that, in the absence of pyridine in CDCl$_3$, the pyridine-containing arm is fully coordinated across the nanoring. This is supported by observation of strongly deshielded resonances **α** and **β** at chemical shifts typical for pyridine coordinated to a porphyrin. Furthermore, all arm-related resonances are shielded by the porphyrin across the nanoring. The observed shielding is strongest for the resonances spatially closest to the porphyrin, following order: **α**, **β**, **γ**, **δ**, **ε**, **ζ** and **η**, fully in line with the special arrangement in self-coordinated conformer (**Figure 41**).

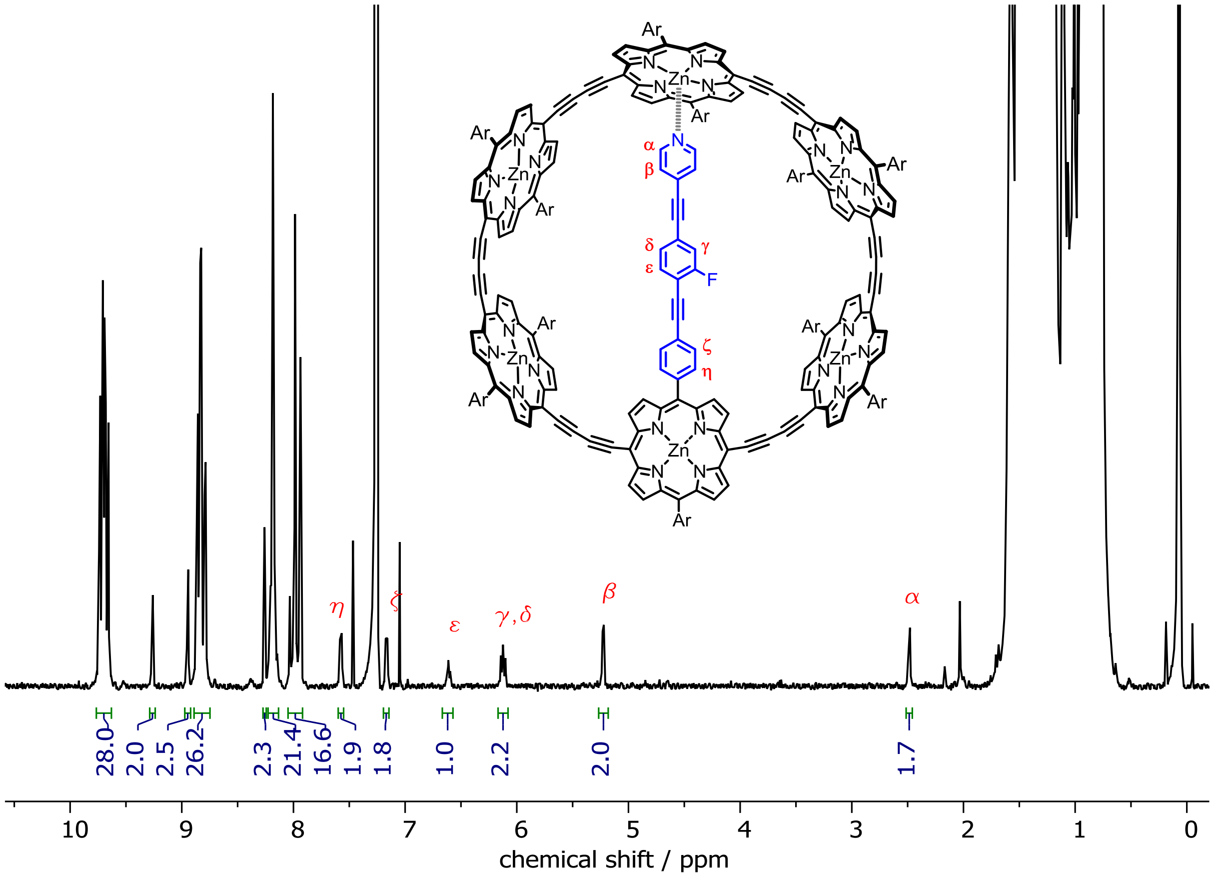

Figure 41. ^{1}H NMR (500 MHz, CDCl$_3$) spectrum of ***c*-P6$^{(1arm)}$**.

The assignment was supported by multiple ^{1}H-^{1}H and ^{1}H-^{13}C 2D NMR correlations. Although it might not be easy to assign signals of classical aromatic ^{1}H/^{13}C chemical shifts (7–9 ppm and 125–135 ppm, respectively), certain arm-related ^{1}H/^{13}C resonances are unambiguously assignable with the ^{1}H-^{13}C HSQC. For example, for **α** and **β**, the ^{1}H-^{13}C HSQC correlation unveil unique ^{13}C chemical shift of the corresponding carbon resonances at ~145 and 125 ppm, respectively. Another standing-out resonance is **γ**, which possesses unique ^{13}C chemical shift at ~118 ppm helping in further assignment (**Figure 42**).

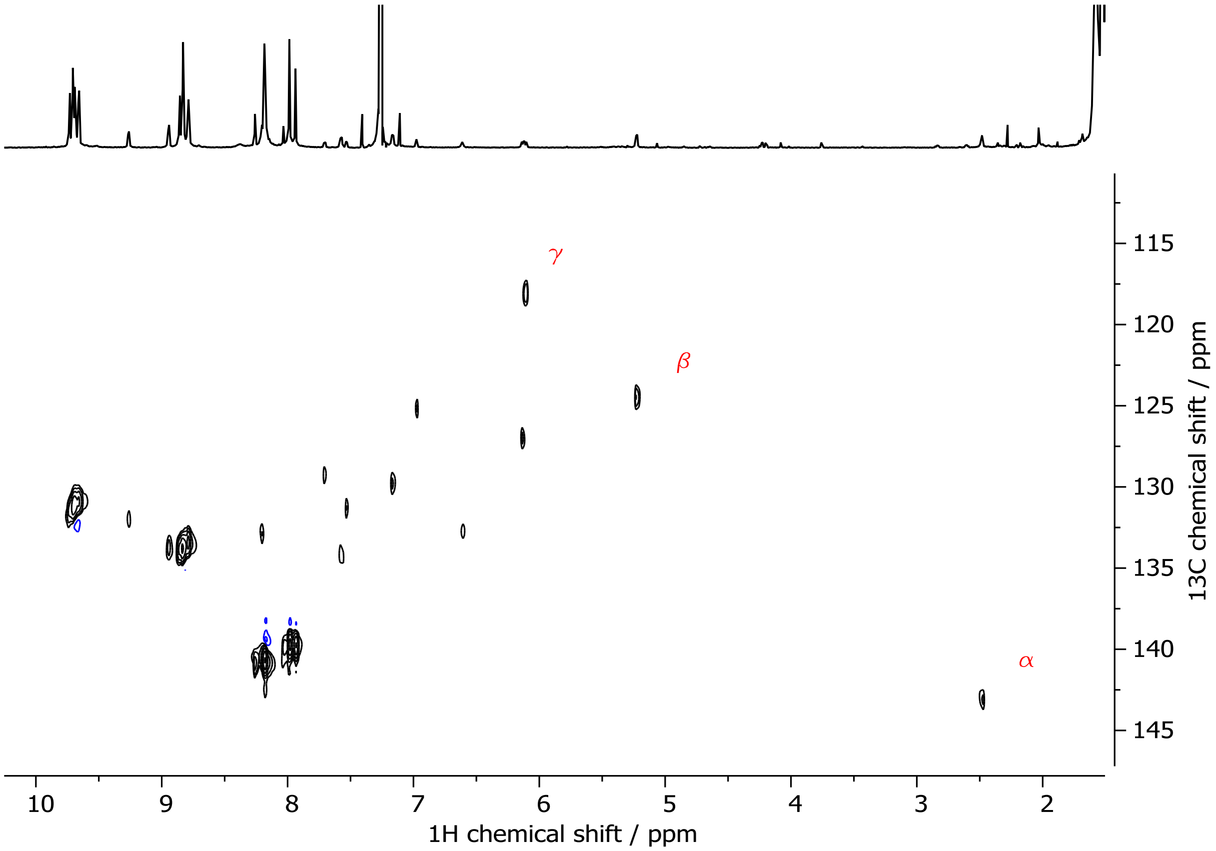

Figure 42. Selection of ^{1}H-^{13}C HSQC (700 MHz, $CDCl_3$) spectrum of ***c*-P6$^{(1arm)}$** showing cross peaks for all aromatic signals.

In the self-bound state, in the absence of pyridine, blocks of *beta* porphyrin resonances **a** and **b** are more spread out. This enables identification of some resonances and in general recognition of the number of symmetrically inequivalent nuclei of certain type.

The ***c*-P6$^{(1arm)}$** structure possesses four distinct porphyrin cores environments. The porphyrin unit to which the pyridine-containing arm is coordinated is symmetric and possess one unique set of **a** and **b** resonances (**a_6** and **b_6**). The porphyrin that covalently bears the pyridine-containing arm is fixed in *in-plane* conformation and possesses two pairs of **a** and **b** resonances, the inner and outer (**$a_1^{in/out}$** and **$b_1^{in/out}$**). The remaining two porphyrins resonances are symmetric in term of inside/outside orientation, but non-symmetric in term of order along the circumference (e.g. closer/farther to the pyridine-containing-arm-bearing porphyrin).

Therefore, in the self-bound state, 7 different **a** and **b** resonances are expected as the result of the molecular symmetry (**Figure 43**).

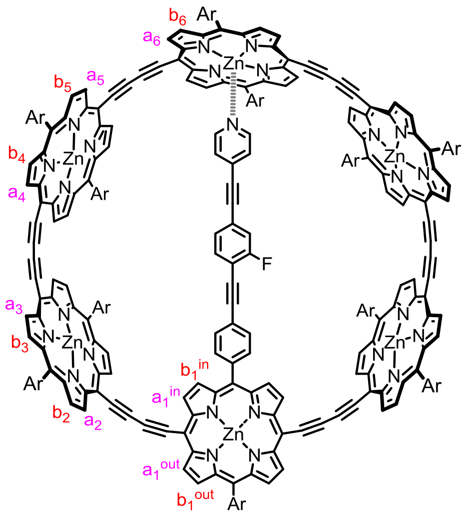

Figure 43. Label code for 7 symmetrically non-equivalent resonances of **a** and **b** type in ***c*-P6**$^{\mathbf{(1arm)}}$.

Such dissymmetry is observed in the ^{1}H NMR spectrum, where 7 **a** and **b** resonances are indeed observed. The resonances from the pyridine-arm-bearing porphyrin stand out most clearly, as the resonances are significantly shielded by the neighbouring porphyrins. The most affected are the $\mathbf{a_1}^{\mathbf{in}}$ and $\mathbf{b_1}^{\mathbf{in}}$, which are found upfield from the rest of the **a** and **b** resonances groups by 0.4 and 0.7 ppm, respectively (**Figure 44**).

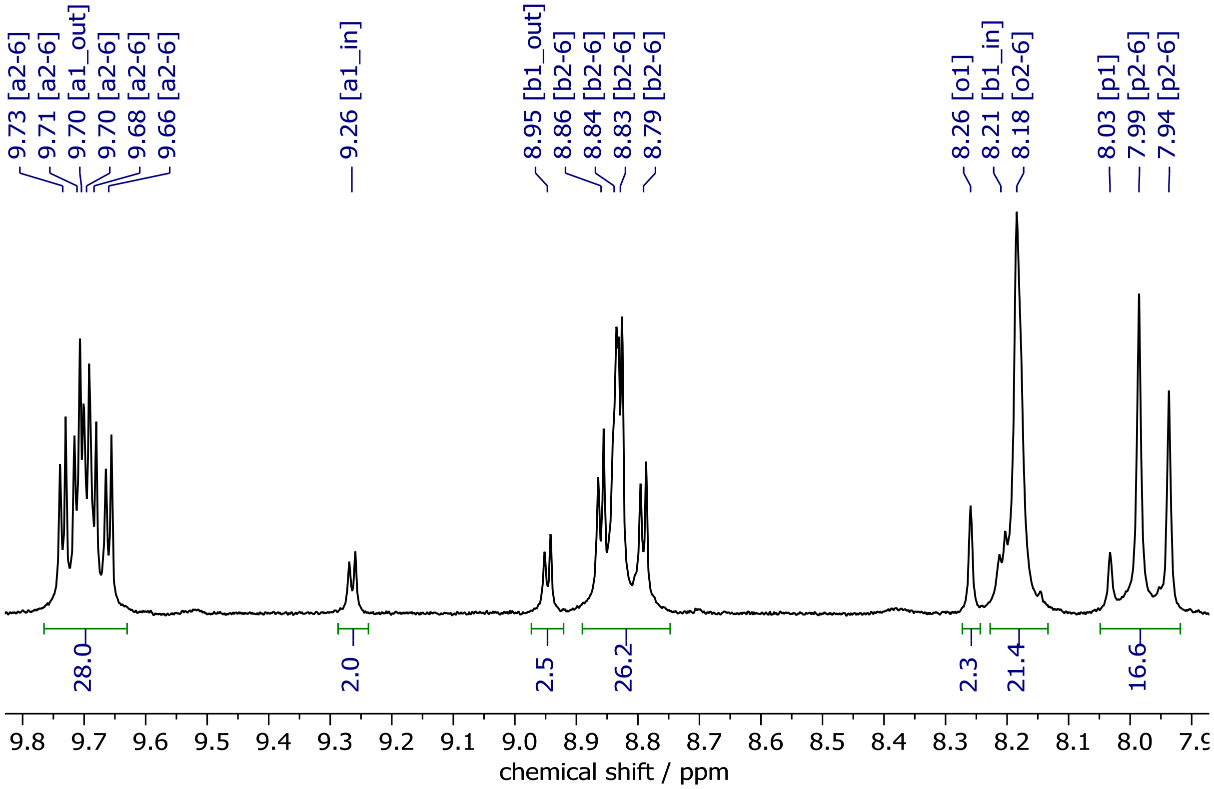

Figure 44. Section of ^{1}H NMR (500 MHz, CDCl$_3$) of ***c*-P6**$^{\mathbf{(1arm)}}$, with labelled **a** and **b** resonances.

Although the pyridine-arm is coordinated relatively strongly, excess of pyridine in the solution can cause its decoordination. This is observed by NMR as the collapsing of all non-symmetric signals of certain types into approximately one chemical shift, analogously to the ***c*-P6$^{(1arm)}$·T6** (**Figure 45**).

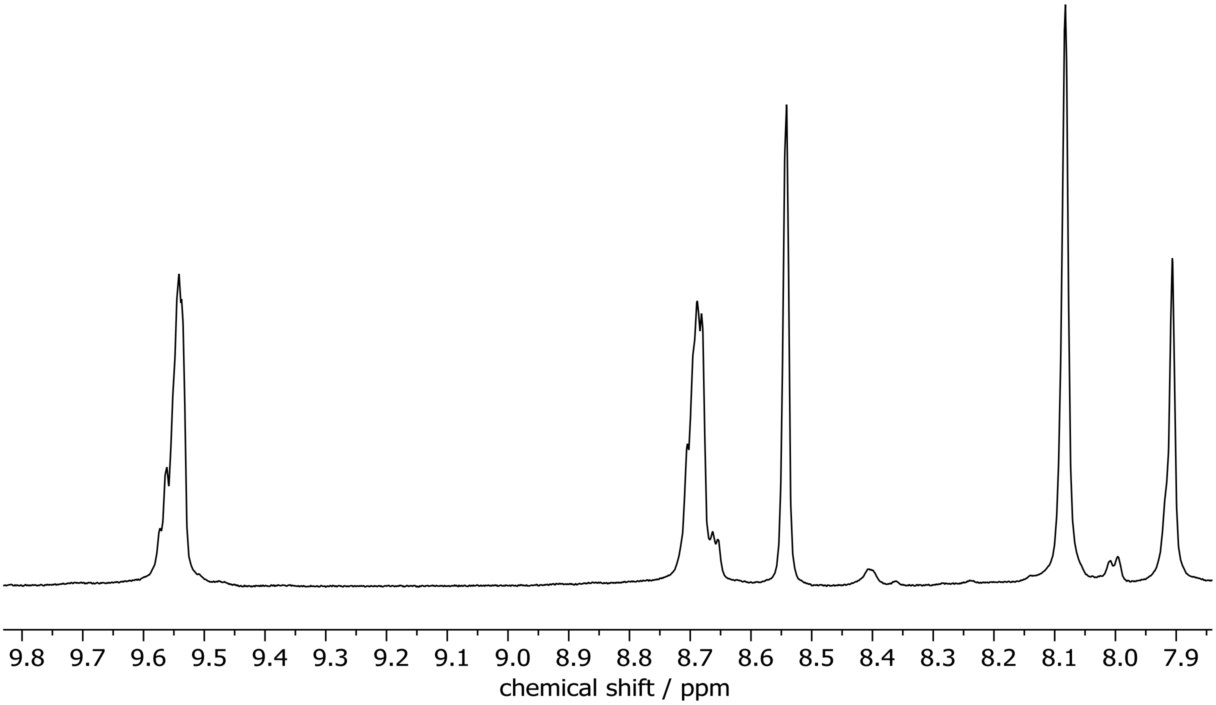

Figure 45. Section of ^{1}H NMR (500 MHz, CDCl$_3$, 10% pyridine-*d*$_5$) of ***c*-P6$^{(1arm)}$** showing collapse of originally very non-symmetric resonances **a$_{1–6}$** and **b$_{1–6}$** resonances into the **a** and **b** groups. .

Interpretation of the pyridine-arm decoordination upon addition of excess of pyridine is supported by the loss of upfielded **α** and **β** resonances of the arm. Furthermore, the UV-vis-NIR absorption spectrum changes dramatically with increasing pyridine equivalents. In toluene, in the absence of any pyridine, the spectrum possesses rather a unique shape of four peaks (**Figure 46**, left (blue)). Upon addition of a large excess of pyridine, the normal broad, three-peak pattern is observed (**Figure 46**, left (red)). This spectral feature is similar to the UV-vis-NIR spectrum of regular ***c*-P6[b$_6$]** nanoring (**Figure 46**, right).

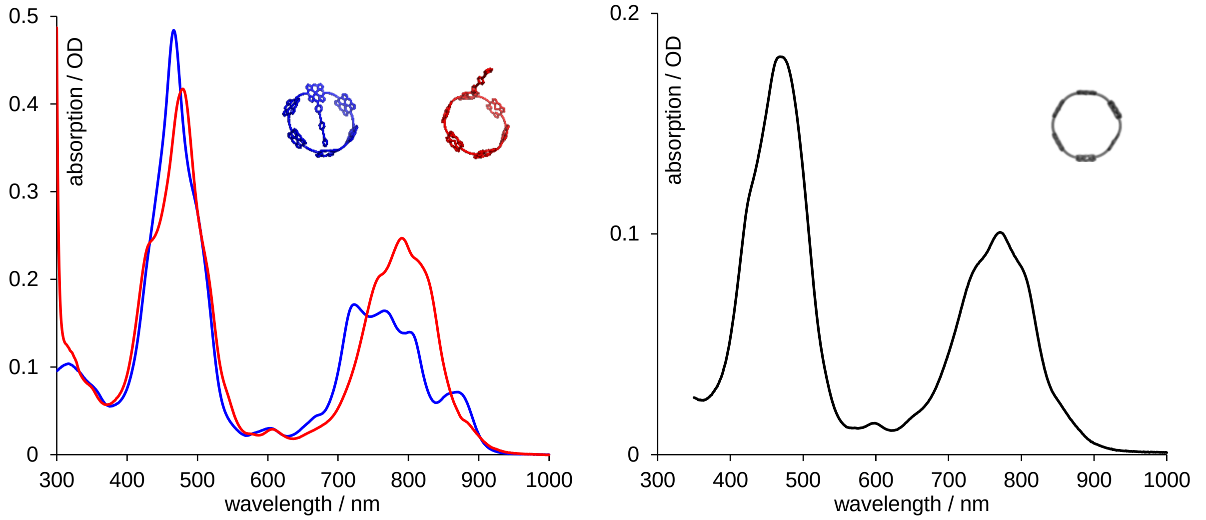

Figure 46. (left) UV-vis-NIR spectra of ***c*-P6$^{(1arm)}$** in toluene without pyridine (blue) and with pyridine (concentration *c* = 7M, red trace). Spectral similarity to ***c*-P6[b$_6$]** is observed for the state with a large excess of pyridine, serving as an argument for interpretation of the process of pyridine-arm decoordination, leading to barrel shaped conformer.

Further insight can be obtained from a UV-vis-NIR titration, during which the pyridine concentration is gradually increased (**Figure 47**).

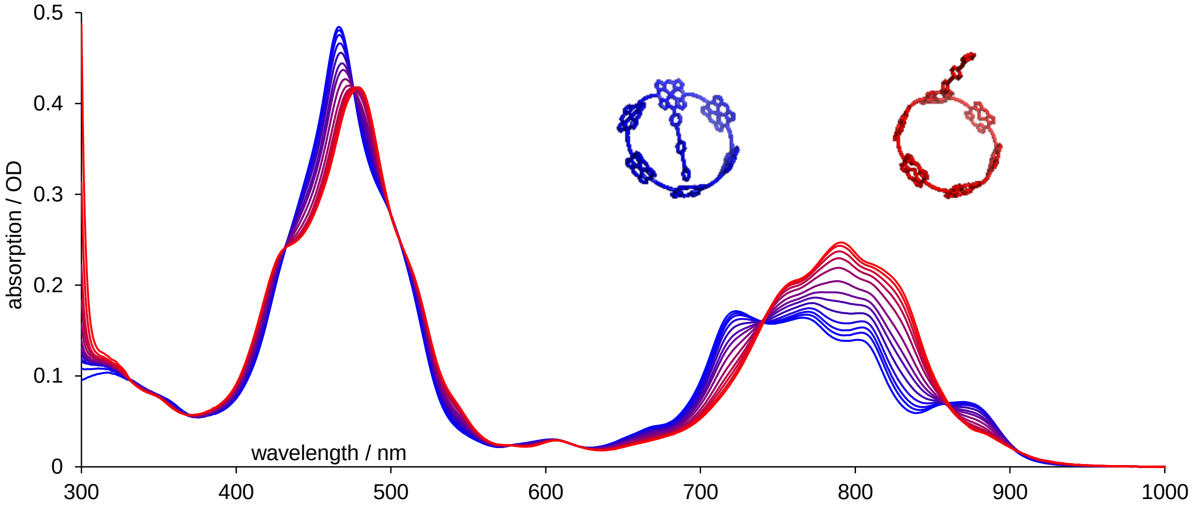

Figure 47. UV-vis-NIR absorption spectra of the ***c*-P6$^{(1arm)}$** in toluene with various concentration of pyridine (0→7 M).

The spectra possess several isosbestic points, indicating a simple A → B transformation. This transformation can be thus analysed as a 1:1 binding of pyridine to the ***c*-P6$^{(1arm)}$** with all 5 residual porphyrin sites preoccupied with pyridines. The observed ΔA as a function of pyridine concentration follow the expected behaviour and the fit can provide the binding constant K_{meas}. (**Figure 48**, data summarized in **Table 1**).

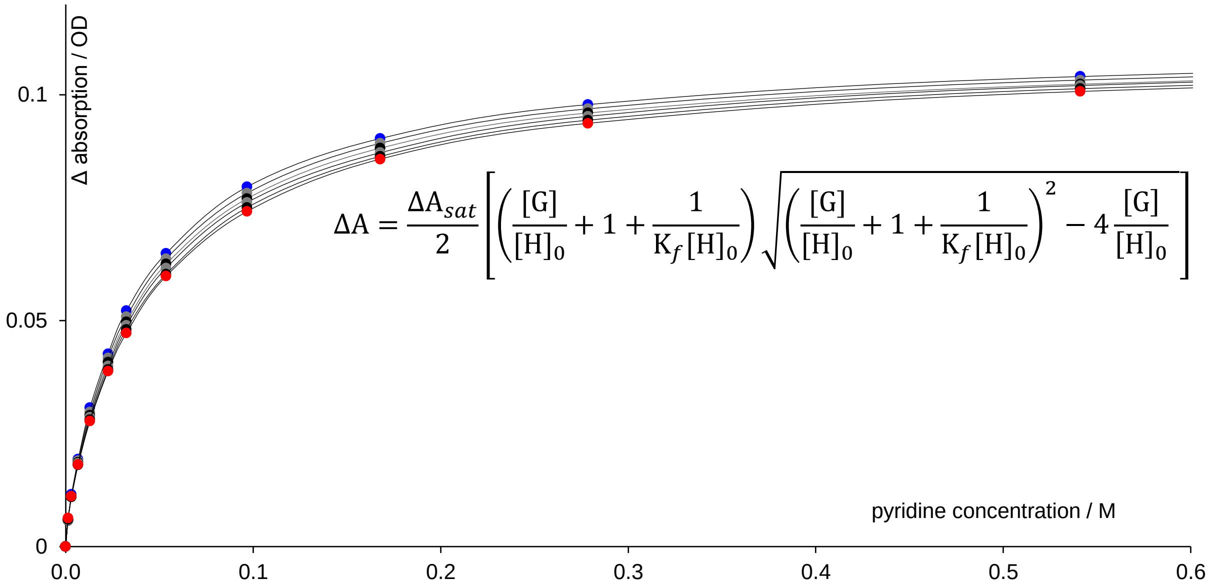

Figure 48. ΔA of ***c*-P6$^{(1arm)}$** at 800 nm as a function of pyridine concentration in toluene at various temperatures (indicated from blue to red: 25 °C → 35 °C).

temperature / K	298.15	300.15	302.15	304.15	306.15	308.15
reciprocal temp. / K^{-1}	0.003354	0.003332	0.00331	0.003288	0.003266	0.003245
fitted binding constant K_f / M^{-1}	28.6573	27.62976	26.70184	25.96868	25.18993	24.75121
logarithm ln(K)	3.355408	3.318893	3.284732	3.256891	3.226444	3.208874

Table 1. Fitted values from the pyridine denaturation of the ***c*-P6$^{(1arm)}$** at various temperatures.

Data recorded at various temperatures allows construction of a van't Hoff plot indicating negative value of Δ*S* and Δ*H* (**Figure 49**). The negative Δ*H* is interpretable as a stronger binding affinity of pyridine toward the porphyrin comparing to the arm. The negative Δ*S* is expected as the binding process consist of the two species merging into one complex.

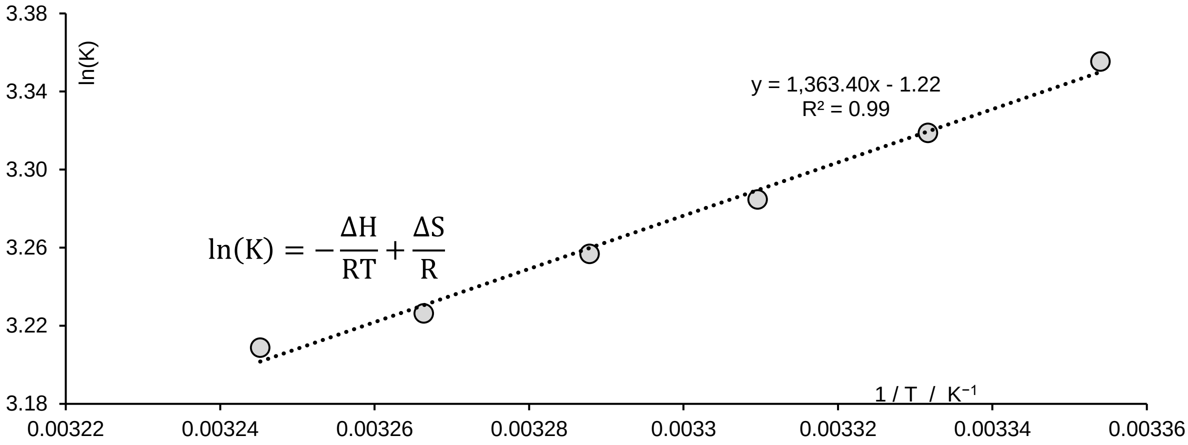

Figure 49. The van't Hoff plot of the thermochemical data of ***c*-P6$^{(1arm)}$** titration with pyridine at various temperatures.

The observed binding constant at 25 °C was 28 M^{-1}. This value corresponds to the pyridine binding affinity toward porphyrin 'occupied' with the pyridine-containing-arm. Assuming strictly only 5-valence zinc cation in porphyrin, the data could be interpreted in terms of effective molarity[41] following the scheme depicted in **Figure 50**.

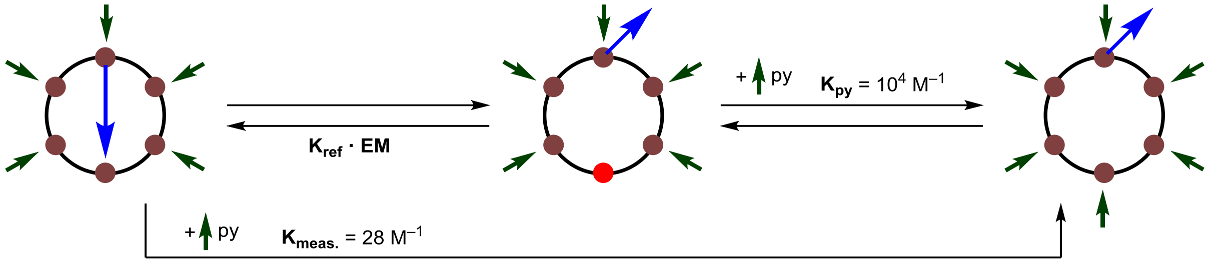

Figure 50. Cycle for analysing effective molarity of pyridine-containing-arm based on the available data.

Reference binding affinity titrations of pyridine and the free pyridine-arm toward porphyrin monomer were performed in order to obtain a more accurate relative strength of the ligands, avoiding otherwise very crude approximation of $K_{\mathrm{ref}} = K_{\mathrm{py}}$ (**Figure 51**).

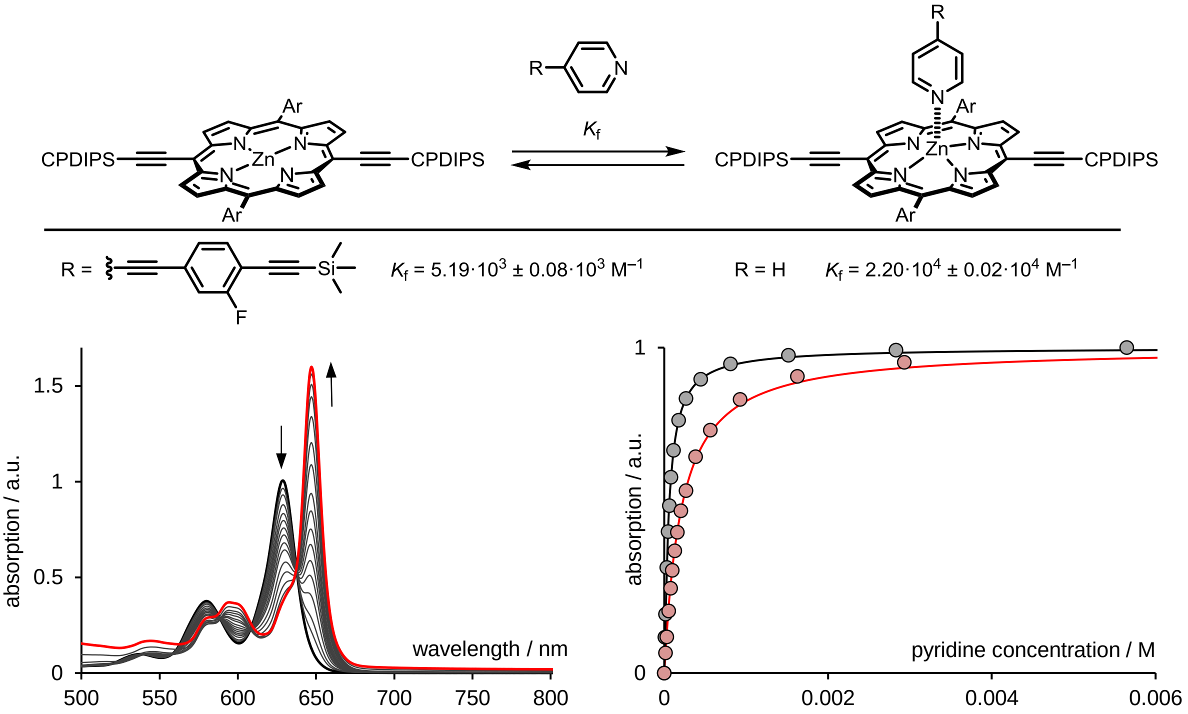

Figure 51. (top) Coordination of the pyridine or pyridine-containing arm part to the porphyrin monomer. (bottom left) Example of the vis-NIR part of absorption spectra from the titration (black line = free porphyrin, red line = saturated with pyridine ligand). (bottom right) The fit of the data assuming 1:1 binding to the data based on titration with arm (red) and pyridine (black).

Fit of the experimental data yielded $K_{\mathrm{ref}} = 5.19\times10^{3} \pm 0.08\times10^{3}\ \mathrm{M}^{-1}$ and $K_{\mathrm{py}} = 22.0\times10^{3} \pm 0.2\times10^{3}\ \mathrm{M}^{-1}$. The effective molarity (EM) based on the performed cycle (**Figure 50**) can be thus expressed as:

$$EM = \frac{K_{py}}{K_{ref} \cdot K_{meas.}} \tag{5}$$

Providing the value of the effective molarity of the pyridine-arm as $EM = 0.15$ M, which is a rather ordinary value within the range of common *EM*s.[41]

Another interesting spectroscopic behaviour observed with the ***c*-P6$^{\mathbf{(1arm)}}$** was the change in the fluorescence quantum yield.

Nanorings generally exhibit very low fluorescence quantum yields (QYs) as a result of their high symmetry, formally forbidding emission *via* $S_1 \rightarrow S_0$ transitions.[42] The exact values of the QYs are thus subjected to a relatively large error. The QYs should be, therefore, compared within one experimental campaign, as the results should be referenced to the same standards and recorded on the same instrument. On the 3,5-bis(*tert*-butyl)phenyl-decorated porphyrin series, the values of QYs were recorded for nanorings as: QY(***c*-P6[b$_6$]**) – 0.43%, QY(***c*-P6[b$_6$]·T6**) – 0.12% and for linear oligomers as: QY(***l*-P6·T6**) – 0.79%, QY(***l*-P6**) – 8.0%.[43] For the 3,5-bis(trihexyl)phenyl-decorated porphyrin nanorings, the QYs recorded were QY(***c*-P6[b$_6$]**) – 1.8%, QY(***c*-P6[b$_6$]·T6**) – 0.38%.[44] In another study on the THS systems, the QYs reported were: QY(***c*-P6[b$_6$]·T6**) – 0.7% and QY(***l*-P6·T6**) – 2.3%.[45]

For the ***c*-P6$^{(1arm)}$** in pure toluene, the measured fluorescence quantum yield was 3.6%, which is relatively high value for the porphyrin nanorings. Interestingly, upon addition of a small amount of very strong ligand *N*-methylimidazole, fully decoordinating the pyridine-containing arm, the fluorescence quantum yield drops to 1.0% (**Figure 52**).

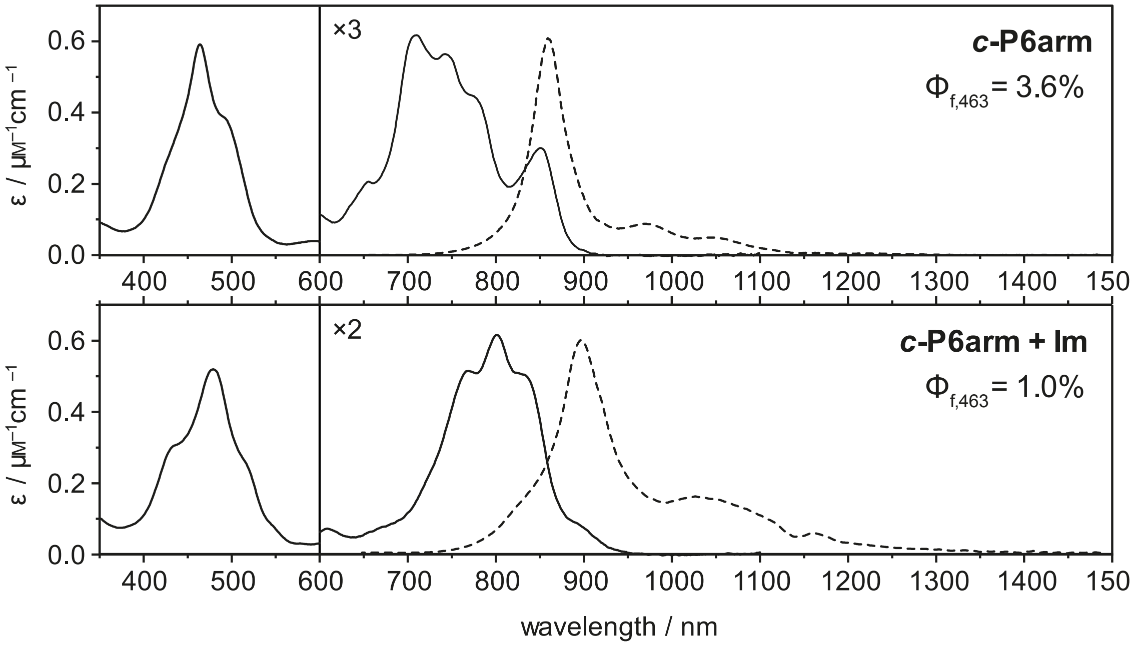

Figure 52. Absorption (solid) and fluorescence (dashed, normalized) spectra of ***c*-P6$^{(1arm)}$** in pure toluene (2 mL) (top) and toluene (2 mL) with 2 µL of *N*-methylimidazole. Optical density in the Soret band was 0.1.

Such high quantum yield of the self-bound state of ***c*-P6$^{(1arm)}$** indicates the structure is locked in the low-symmetry conformation partly allowing the radiative $S_1 \rightarrow S_0$ transition.

An NMR oxidation experiment with the ***c*-P6$^{(1arm)}$** was performed. Oxidation titration with **Thn$^+$**, under the conditions developed and discussed in **Chapter 3**, showed two observable states, 4+ and 6+. Unfortunately, the fluorine atom probe could not be followed by ^{19}F NMR as the intensity of the ^{19}F nucleus was too low and was probably partly broadened and the signal was undetectable and lost in the noise (**Figure 53**).

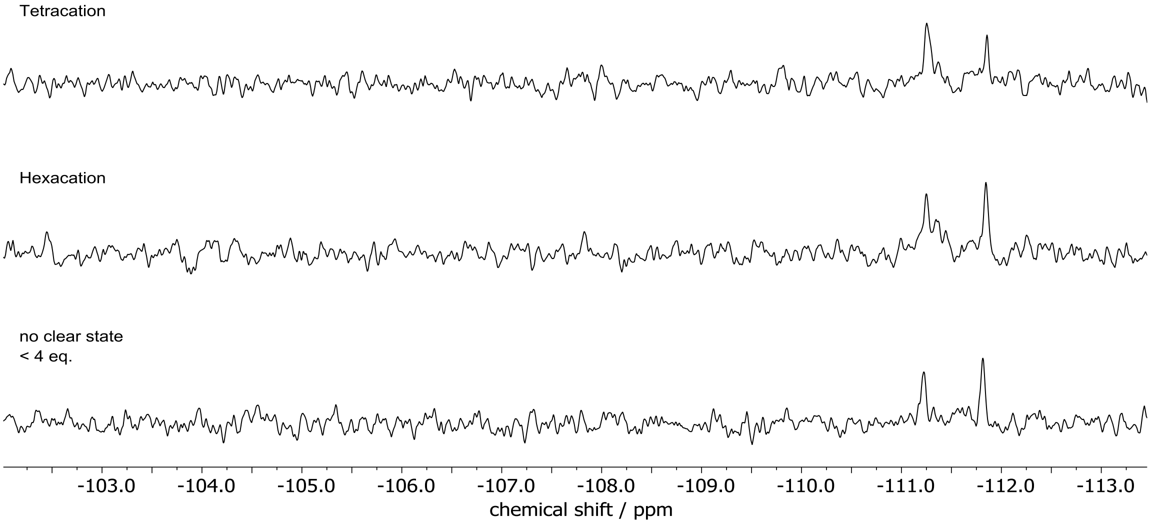

Figure 53. ^{19}F NMR (471 MHz, −50 °C, CD_2Cl_2) spectra of ***c*-P6$^{(1arm)}$** at 4+ and 6+ oxidation state and at approximately ~3+ oxidation state, where no clear signal is resolved in ^{1}H NMR channel. All visible spikes are impurities from C_6F_6, which was added as a reference. The signal would be expected around −109 ppm.

On the other hand, the ^{1}H probe showed identifiable, although broadened, signals of THS, indicating anti-aromatic and aromatic 4+ and 6+ oxidation states, respectively (**Figure 54**).

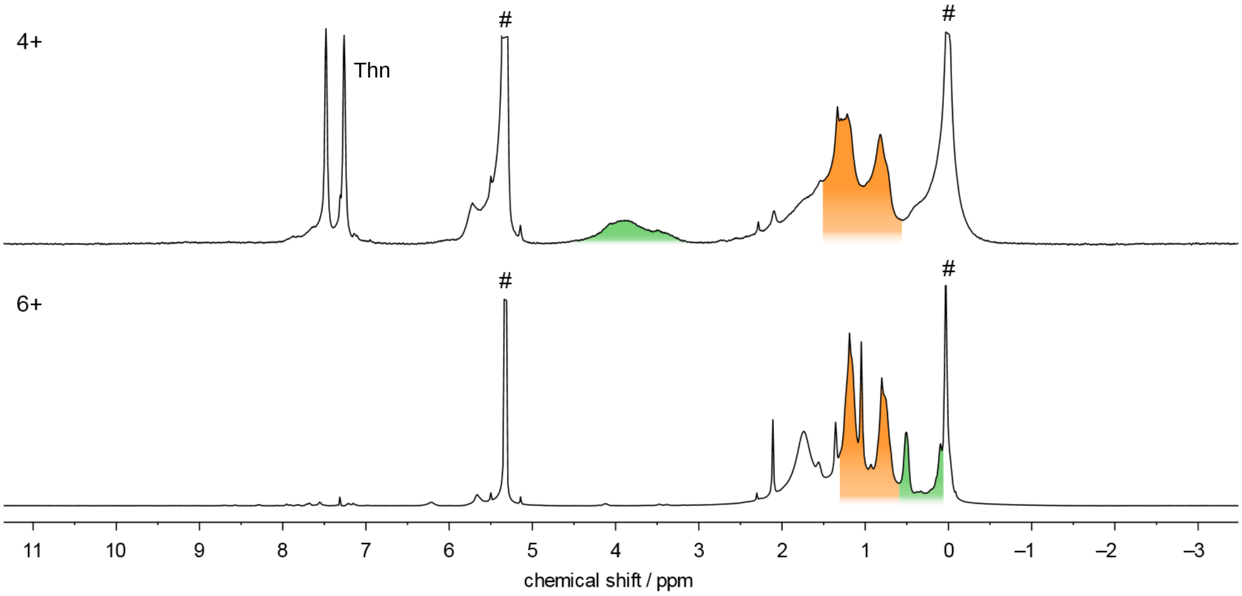

Figure 54. ^{1}H NMR (500 MHz, −50 °C, CD_2Cl_2) spectra of ***c*-P6$^{(1arm)}$** 4+ and 6+ oxidation state. # indicate residual solvent signal $CDHCl_2$ and a silicon grease impurity.

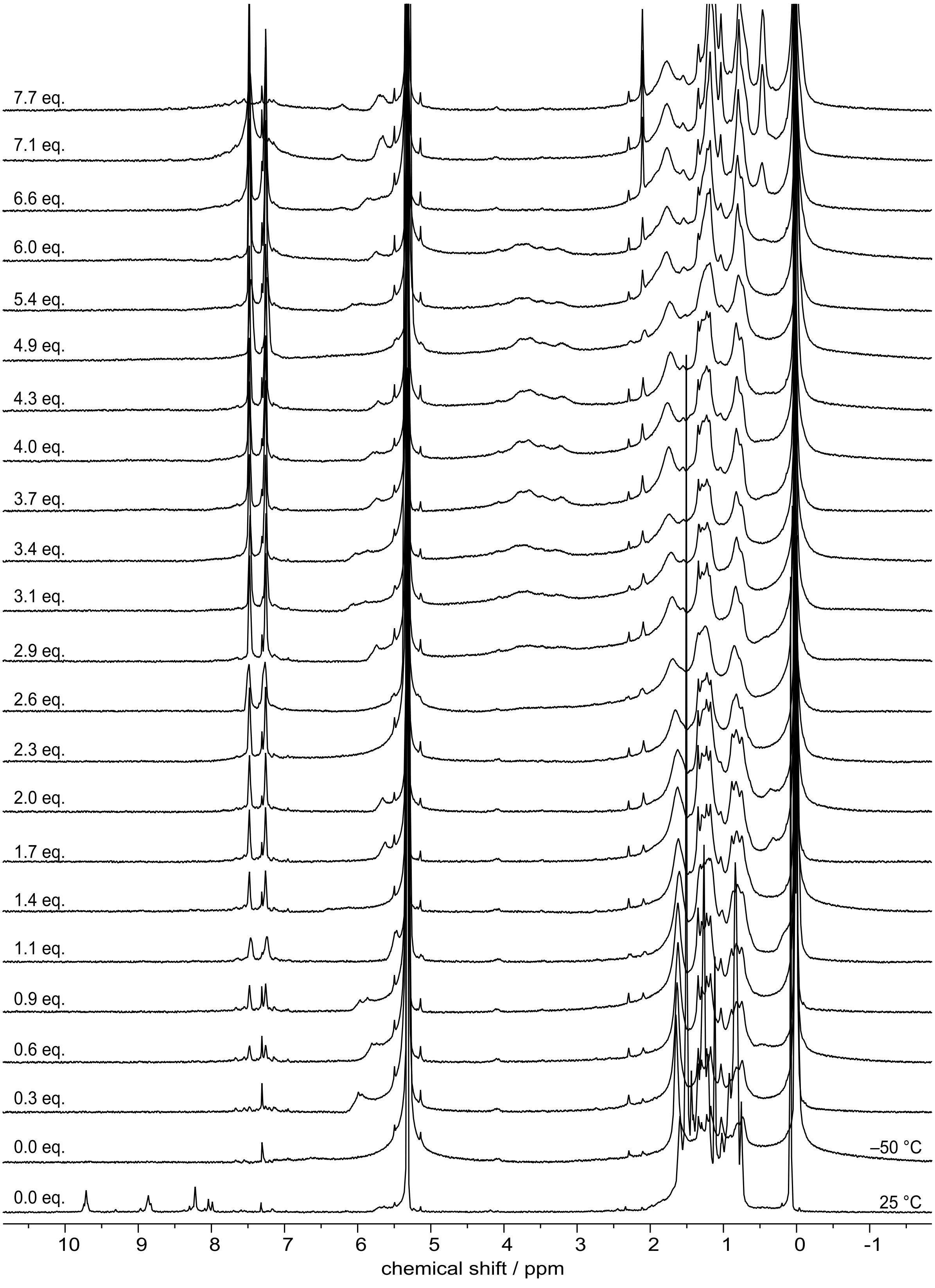

Figure 55. ^{1}H NMR (500 MHz, CD_2Cl_2) oxidation titration of ***c*-P6$^{(1arm)}$** with **Thn$^+$**.

These spectra are very similar to those observed for the ***c*-P6[b$_6$]** (**Figure 56**) leading to the interpretation that the structure completely opens-up upon oxidation to enable the communication and charge delocalization, behaving virtually as regular ***c*-P6[b$_6$]**.

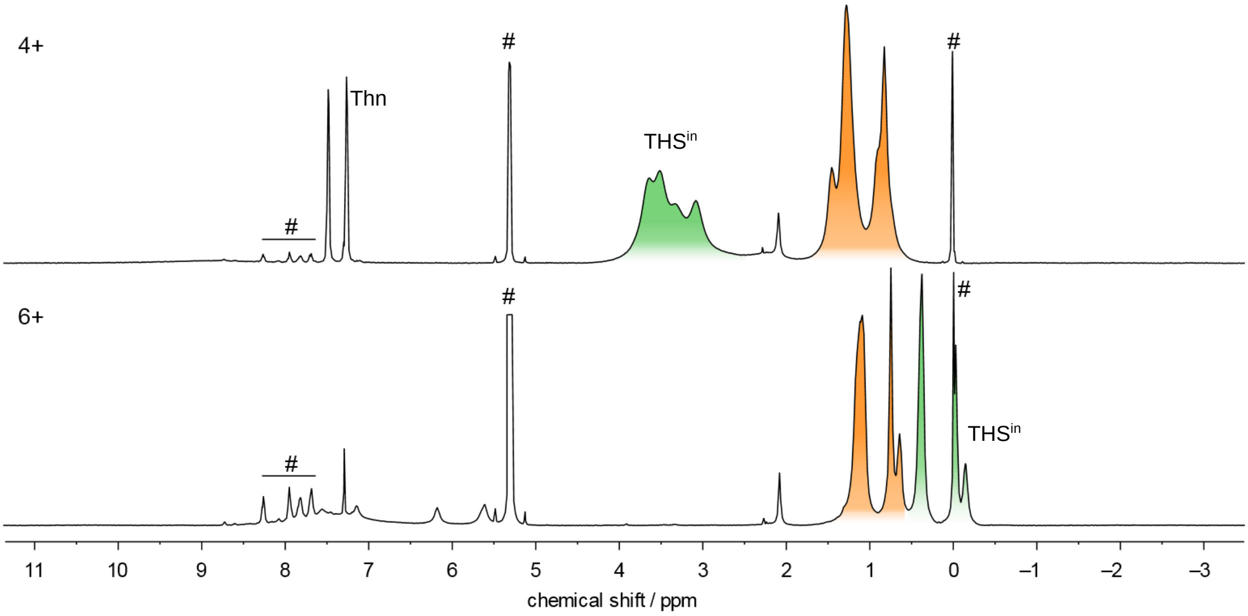

Figure 56. ^{1}H NMR (500 MHz, −50 °C, CD_2Cl_2) spectra of ***c*-P6[b$_6$]** 4+ and 6+ oxidation state as a comparison. # symbols indicate impurity originating from partly degraded **Thn**$^+$ (8.5–7.5 ppm), residual $CDHCl_2$ peak (5.32 ppm) and silicon grease impurity (0 ppm).

4.5. Synthesis and properties of triply linked Möbius nanoring *c*-P6$^{(3arm)}$

Synthesis of the ***c*-P6$^{(3arm)}$** nanoring followed closely the strategy of the synthesis of ***c*-P6$^{(1arm)}$**. The pyridine-containing-bent-arm building block **4.23** was synthesized in a series of Sonogashira coupling reactions using 1,3,5- and 1,4- substituted benzene building blocks **4.24**–**4.29**. The compound **4.23** was then reacted with the porphyrin core **4.12**, developed during ***c*-P6$^{(1arm)}$** synthesis, yielding porphyrin building block **4.31**. The **4.31** was then brominated with NBS yielding dibromoporphyrin **4.32** which was further coupled with protected ethyne (**Figure 57**).

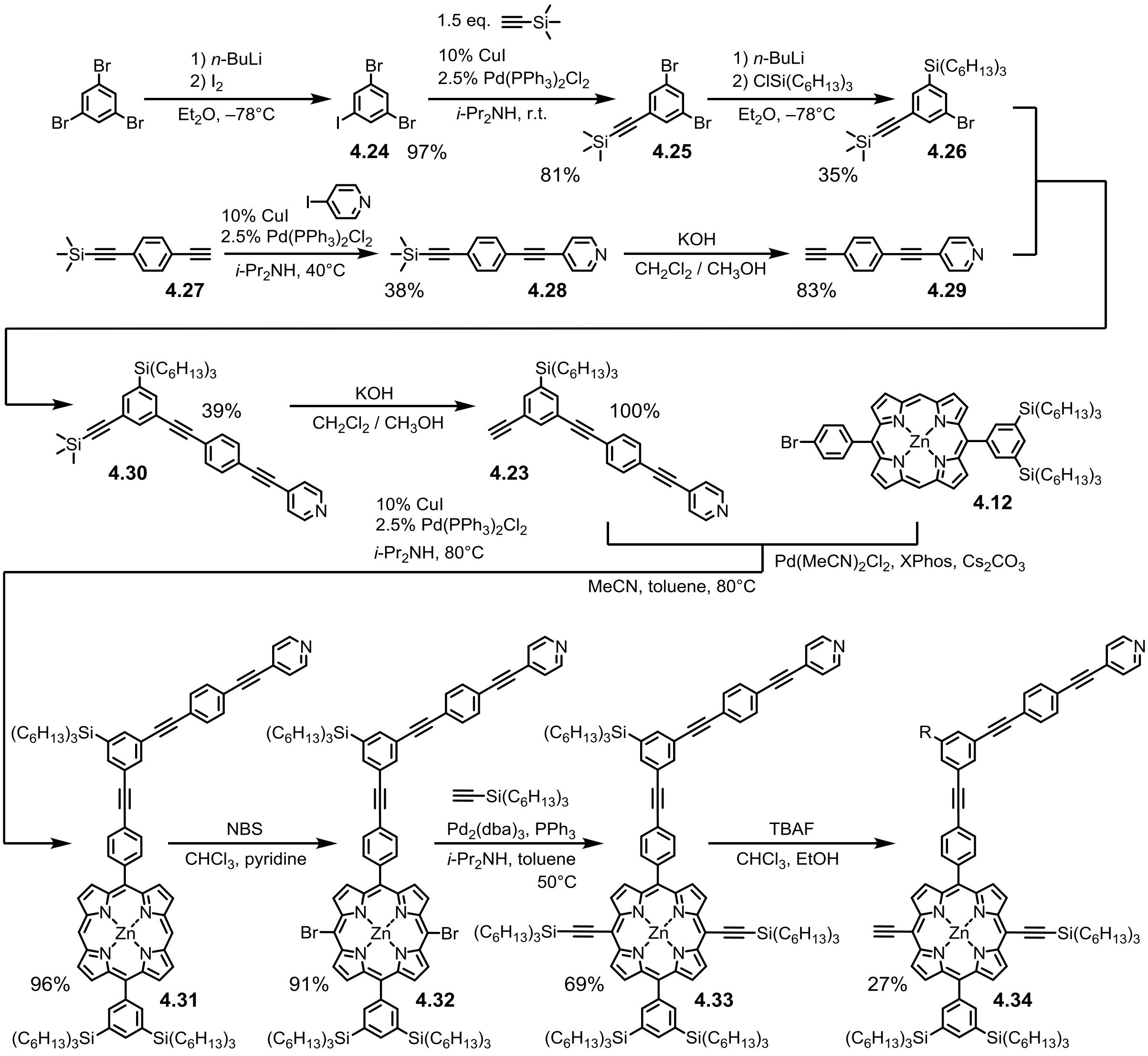

Figure 57. Synthesis of key porphyrin building block **4.34** functionalized with pyridine-containing bent arm.

The major difference from the previous route is that only partial deprotection of one of the bis(trialkyl)silyl group was desired. For such cases, CPDIPS group is often used as the polar cyano-group helps to increase differences in polarity of otherwise often very non-polar THS-decorated porphyrins. However, in this case, the pyridine-containing arm is very polar on its own, and strongly interacts with the silica. Originally tested coupling with the CPDIPS acetylene and subsequent partial deprotecting proved that the difference in the polarity is negligible making the mixture inseparable, jeopardizing the further synthesis (as the contamination with non-protected bis(ethynyl)porphyrin would lead to many unwanted reactions).

It was found that use of very non-polar trihexylsilyl protecting group, changes the polarity of the porphyrin building block more significantly, as it complements the polar pyridine part. Thus **4.32** was reacted with trihexylsilyl acetylene yielding **4.33** and careful deprotection stopped half-way through enabled the isolation of **4.34**.

This mono-protected building-block **4.34** was reacted with **4.19** providing porphyrin trimer **4.35** followed by the terminal ethyne group deprotection yielding **4.36** (**Figure 58**).

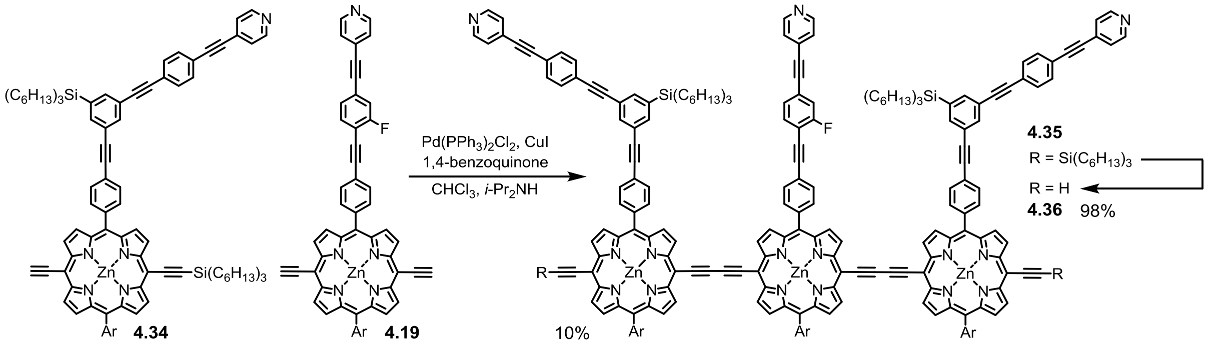

Figure 58. Synthesis of key porphyrin trimer **4.36**.

Although, this porphyrin trimer synthesis step is analogous to the synthesis of **4.21**, a significant difference is in the relative preciousness of both reacting components.

In the case of synthesis of **4.21**, the more precious material was the central block with the pyridine arm **4.19**. In such case, relatively high excess of the mono-protected **4.20** to non-protected **4.19** porphyrin was advantageous, increasing the yield of desired trimer **4.21** relatively to the **4.19**.

Contrary to that, in the synthesis of **4.35**, the mono-protected porphyrin **4.34** is far more precious and elaborate, than the symmetric building block **4.19**. This is due to the longer synthesis of the bent-arm unit and, more importantly, due to the partial deprotection step, which significantly decreases the yield, making this building block the liming compound.

It might not be obvious what ratio of the mono-protected/non-protected porphyrin monomers should be chosen to optimize yield of the porphyrin trimer relative to the precious mono-protected porphyrin **4.34**. As it is very difficult to describe such oligomerisation explicitly with kinetic equations, a random-based modelling was used. A pot, consisting of 50,000 molecules with a define ratio of mono-protected to non-protected bis(ethynyl)porphyrins was used as a starting mixture. From the pot, two molecules were randomly chosen, and their potential reaction was considered. The number of the reactive groups increases probability of the coupling, and this was set as the number of the reacting groups in the considered pair divided by four. Thus, if the pair possessed 4 reacting groups, probability of reaction was 100%. If the reacting couple possessed 3 bare ethynyl groups, the probability of the reaction was 75% etc. The ratio of mono- to non-protected porphyrins initially present in the pot was changed and the product distribution recorded (**Figure 59**).

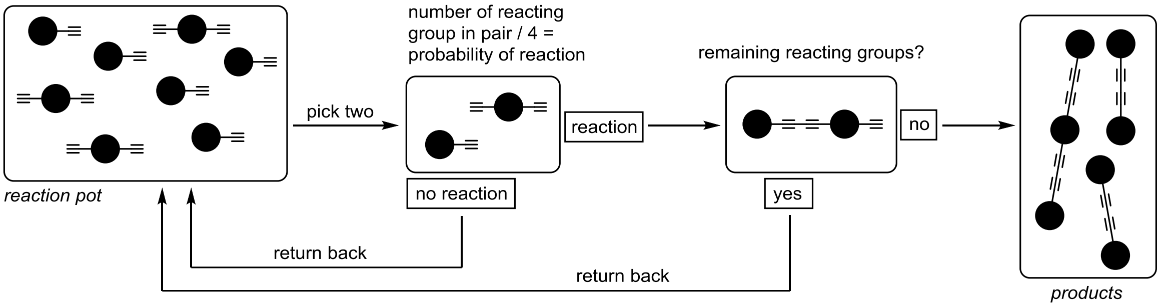

Figure 59. Algorithm used for predicting product distribution at the chosen reactant ratio.

When the theoretical yield is plotted relative to the mono-protected porphyrin as a function of the ratio, it is clear that the ratio 2:1 of mono-protected/non-protected is optimal (**Figure 60**).

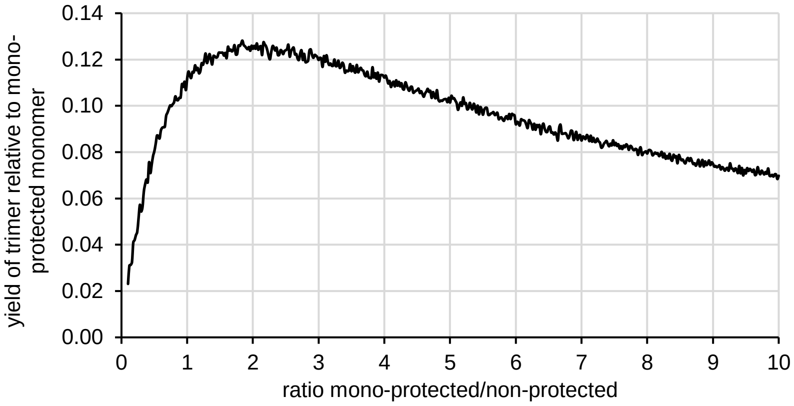

Figure 60. Theoretical maximal yield of the trimer synthesis as a function of mono-protected/non-protected bis(ethynyl)porphyrins ratios. The simulation was conducted using authors script in MATLAB on the sample of 50000 components for each ratio (testing ration from 0.1 to 10, with 0.05 step).

Synthesised trimers **4.35** and **4.36** exhibited significantly lower solubility than **4.21**, as a result of an insufficient amount of the solubilizing groups engineered to the structure. For good solubility in organic solvents, traces of pyridine presence is required, suggesting aggregation occurs. Furthermore, some degree of intermolecular cross-coordination is observed, documented nicely by the UV-vis-NIR titration of **4.35** with increasing pyridine concentration.

The increase in pyridine concentration changes the absorption features from a unique spectrum shape to the expected butadiyne-porphyrin-linked trimer spectrum (**Figure 61**).

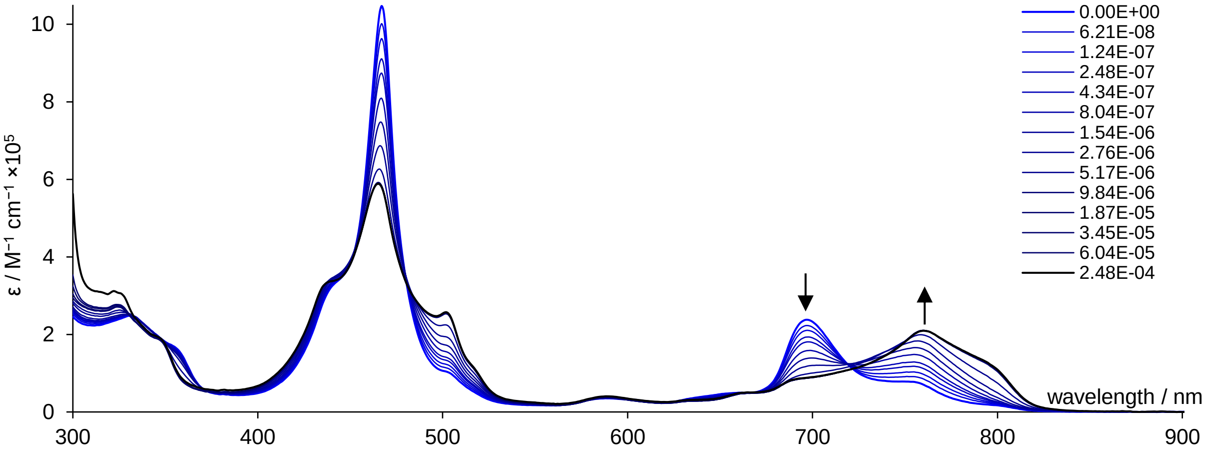

Figure 61. UV-vis-NIR absorption of the **4.35** in toluene as a function of the pyridine concentration (increasing blue → black). Spectra with high amounts of pyridine are similar to the expected spectrum of the butadiyne linked porphyrin trimer. Concentration of pyridine in legend.

The trimer was characterized using standard techniques. To understand its NMR spectrum, it is useful to compare it with the spectra of the individual ((trihexyl)silyl)ethynyl meso-position-decorated porphyrin monomers **4.18** and **4.34**, indicating certain spectral features working as a fingerprint, allowing quick visual comparison (**Figure 62**).

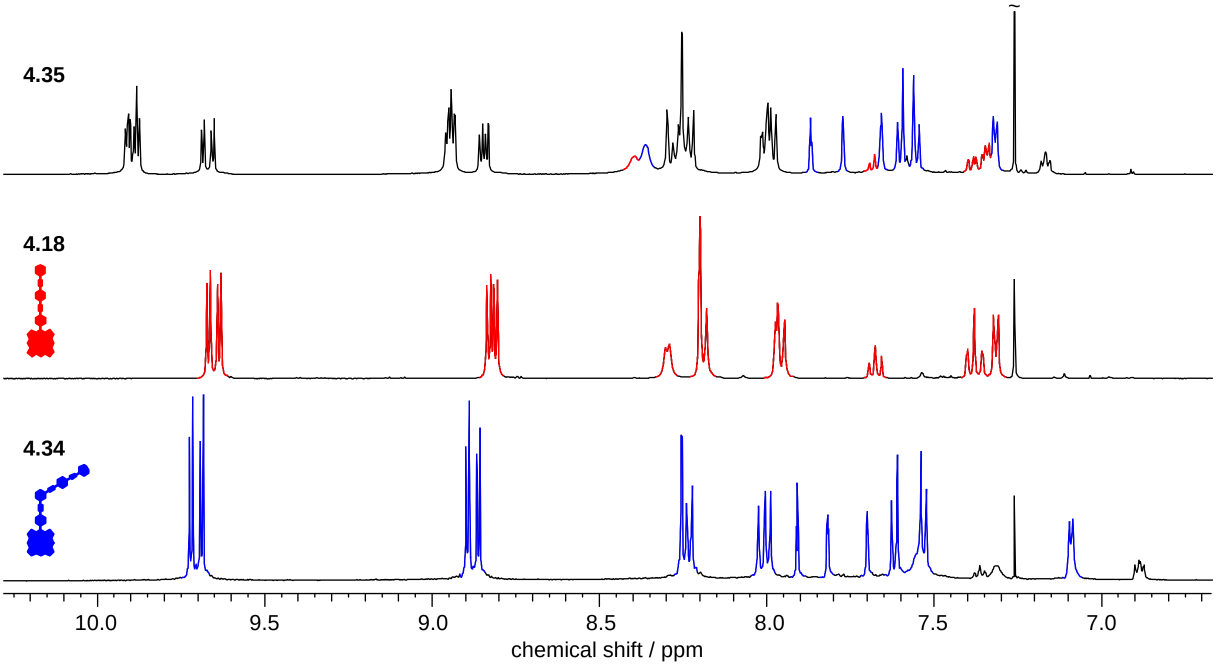

Figure 62. ^{1}H NMR (500 MHz, CDCl$_3$, 10% pyridine-*d*$_5$) of **4.35** (top), **4.18** (middle) and **4.34** (bottom). Similarities between monomer and trimer are seen for example in **4.35** and **4.34** as the three broad triplets assignable to a bent part of the 1,3,5-substituted benzene (blue, 7.9–7.6 ppm); or in **4.35** and **4.18** as the split ^{1}H signals by ^{1}H–^{19}F coupling (red, 7.3–7.6 ppm).

The cyclization of **4.36** and symmetric porphyrin trimer ***l*-P3** was carried out in the same way as in the case of ***c*-P6$^{(1arm)}$·T6** synthesis (**Figure 63**).

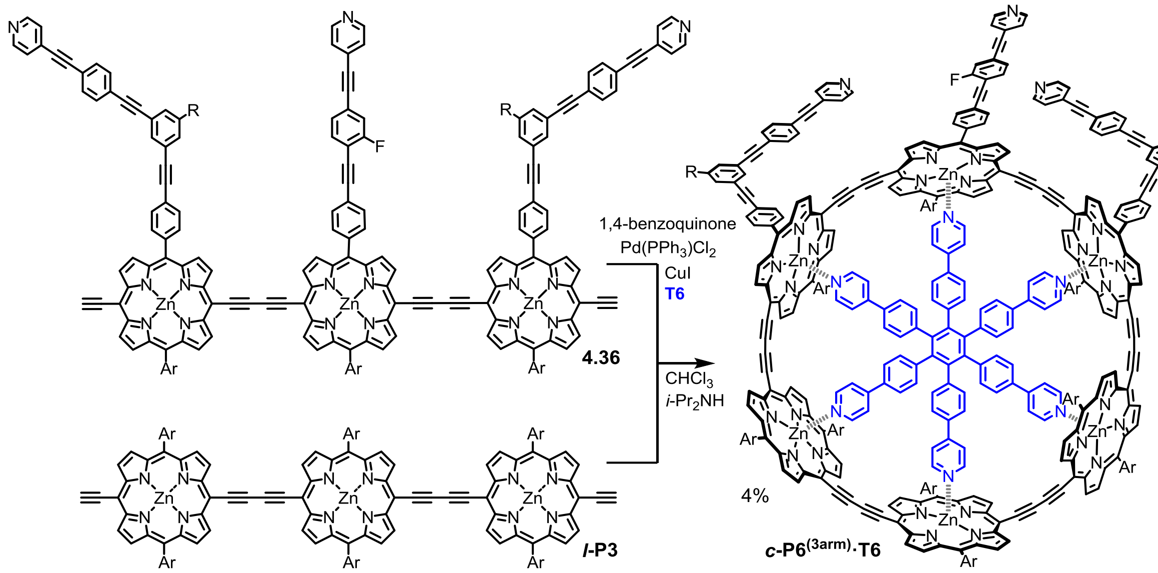

Figure 63. Synthetic scheme of cyclisation toward ***c*-P6$^{(3arm)}$·T6**. Ar = 3,5-bis(trihexylsilyl)phenyl, R = bis(trihexylsilyl).

The major product, according to GPC was the fraction of size of ***c*-P6[b$_6$]·T6**. Upon isolation, three major components were observed by TLC and separated on silica. Separation was rather challenging and probably partial degradation occurs during the separation. The ring with the template possesses rather complicated NMR spectra as multiple regioisomers are expected. Upon template removal by a large excess of the strong ligand DABCO and **T6** removal on the SEC, ***c*-P6$^{(3arm)}$** was isolated. The compound's identity was confirmed for example by high resolution mass spectrometry, documenting also the degree of chemical purity (**Figure 64**).

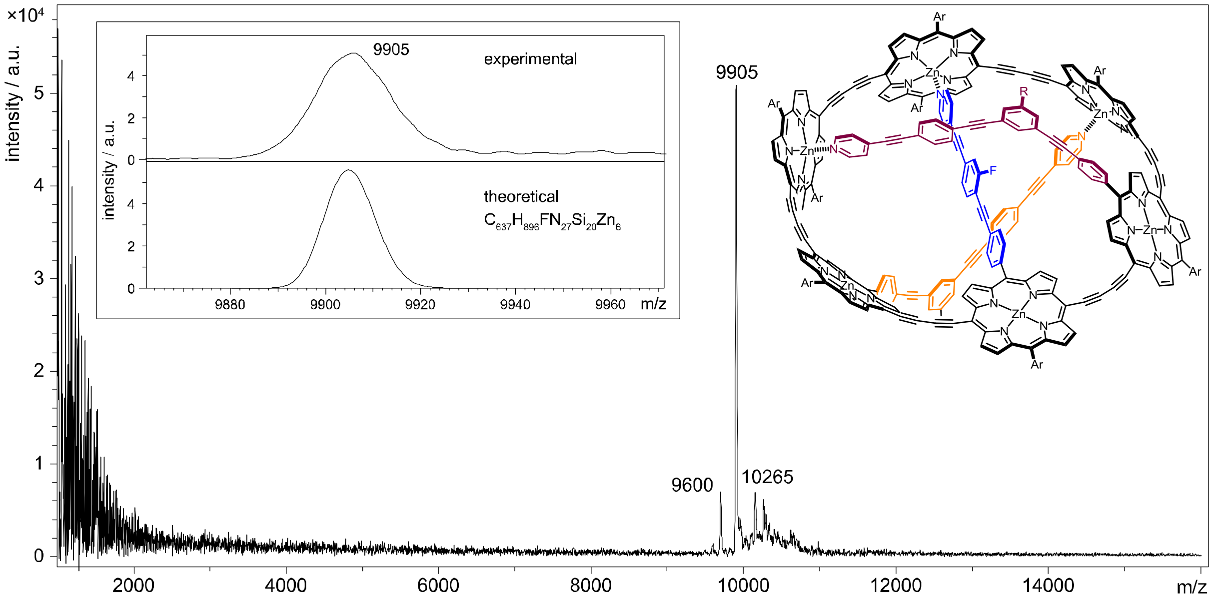

Figure 64. MALDI-ToF mass spectrum of the ***c*-P6$^{(3arm)}$** and its chemical structure. Ar = 3,5-bis(trihexylsilyl)phenyl, R = bis(trihexylsilyl).

Unfortunately, the ***c*-P6$^{(3arm)}$** exhibited extremely low solubility in the absence of pyridine. In pure CD_2Cl_2, the compound was absolutely insoluble and only very sparingly in $CDCl_3$. The best solubility in absence of pyridine was achieved with benzene-*d*$_6$, in which the compound is partly soluble, probably as a result of π-π stack induced disaggregation. In order to confirm that the spectrum corresponded to one species and determine it approximate molecular weight, a DOSY experiment was performed.

DOSY carried out on the benzene-*d*$_6$ solution of ***c*-P6$^{(3arm)}$** provided evidence that all observed peaks correspond to one species with diffusion coefficient $D = 1.731\cdot10^{-10}$ m$^2\cdot$s^{-1}. Under the same conditions (temperature, solvent), the DOSY was measured for ***c*-P6[b$_6$]·T6** and ***c*-P7[b$_7$]·T7** yielding diffusion coefficient $1.68\cdot10^{-10}$ and $1.51\cdot10^{-10}$ m^2 $\cdot$s^{-1}, respectively. This confirms that the ***c*-P6$^{(3arm)}$** in benzene is slightly smaller than ***c*-P6[b$_6$]·T6** as, according to the Einstein relation, the diffusion coefficient is inversely proportional to the diameter of the species (**Eq. 5**)

$$D = \frac{k_B T}{6\pi\mu r} \qquad (5)$$

Where k_B is Boltzmann constant, T temperature, μ solvent viscosity and r is a diameter of a sphere, as an idealized model of the molecule.

DOSY NMR also helped to obtain a cleaner spectrum, since due to limited solubility, conventional ^{1}H NMR of ***c*-P6$^{(3arm)}$** was dominated in the aromatic region by the residual solvent peak. The solvent peak corresponds to a molecule with a substantially different diffusion coefficient, therefore, the right choice of DOSY parameters allowed the acquisition of a diffusion-edited ^{1}H NMR spectrum, 'cleaned up' from the residual solvent signal (**Figure 65**).

From the diffusion-edited ^{1}H NMR spectrum, the very low symmetry of the species is evident. Two significantly shielded signals, probably corresponding to **α** (two overlapping) and two **β** signals are observed.

Small additions of pyridine led to almost instant loss of **α** and **β** signals and at the same time solubility was significantly improved. The increase of the pyridine concentration is accompanied by many chemical shift changes. Unfortunately, the right balance of pyridine or THF content to achieve good solubility without denaturation of the complex was not found (**Figure 66**).

The fact that in pyridine-free benzene solution peaks associated with the coordinated **α** and **β** signals are observed suggest that all three arms (two symmetrically inequivalent) are coordinated to some porphyrin. As DOSY has proved the size of the species to be smaller than

***c*-P6[b$_6$]**, no intermolecular coordination e.g. dimerization is expected. And, since there is only one way the pyridine arms can all reasonably intramolecularly coordinate, it can be assumed that the molecule adopts Möbius conformation.

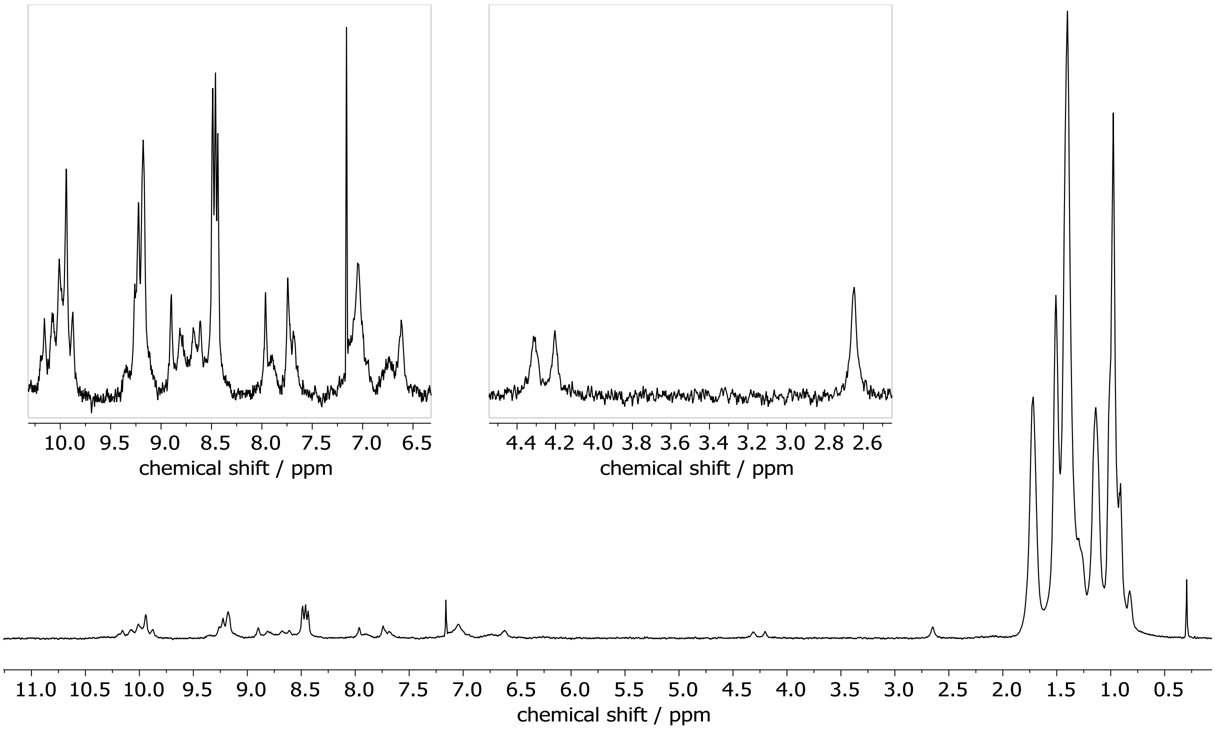

Figure 65. Diffusion edited ^{1}H NMR (600 MHz) in C_6D_6 of the ***c*-P6$^{(3arm)}$**.

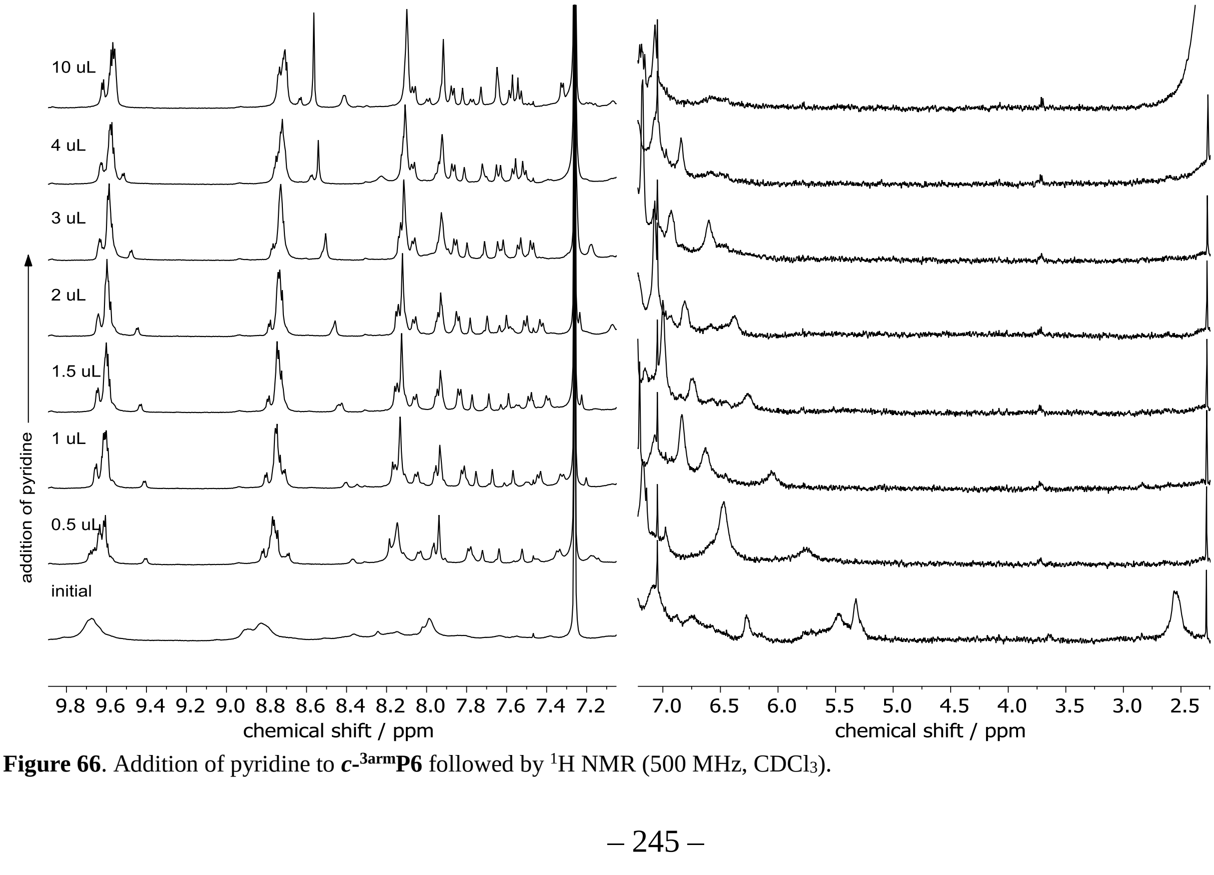

Figure 66. Addition of pyridine to ***c*-^{3arm}P6** followed by ^{1}H NMR (500 MHz, $CDCl_3$).

The pyridine-arm de-coordination and thus general conformation denaturation was also followed by UV-vis-NIR absorption. Although the spectral changes are rather subtle, clear increase and decrease of the absorption at some point of the spectrum show rather complex denaturation mechanism involving 3–4 steps (**Figure 67**).

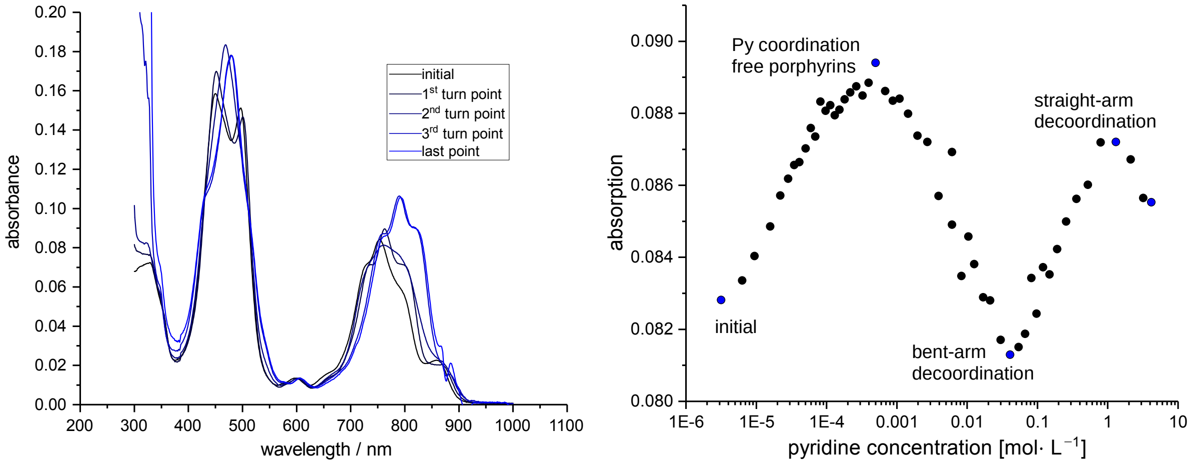

Figure 67. (left) Selected UV-vis-NIR spectra of the denaturation of the ***c*-P6$^{(3arm)}$** by pyridine in toluene. (right) Absorption at 840 nm as a function of pyridine concertation on logarithmic scale (blue coloured dots correspond to the spectra on the left).

The spectra can be plotted as a 2D contours plot as a function of pyridine concentration and a wavelength (**Figure 68**).

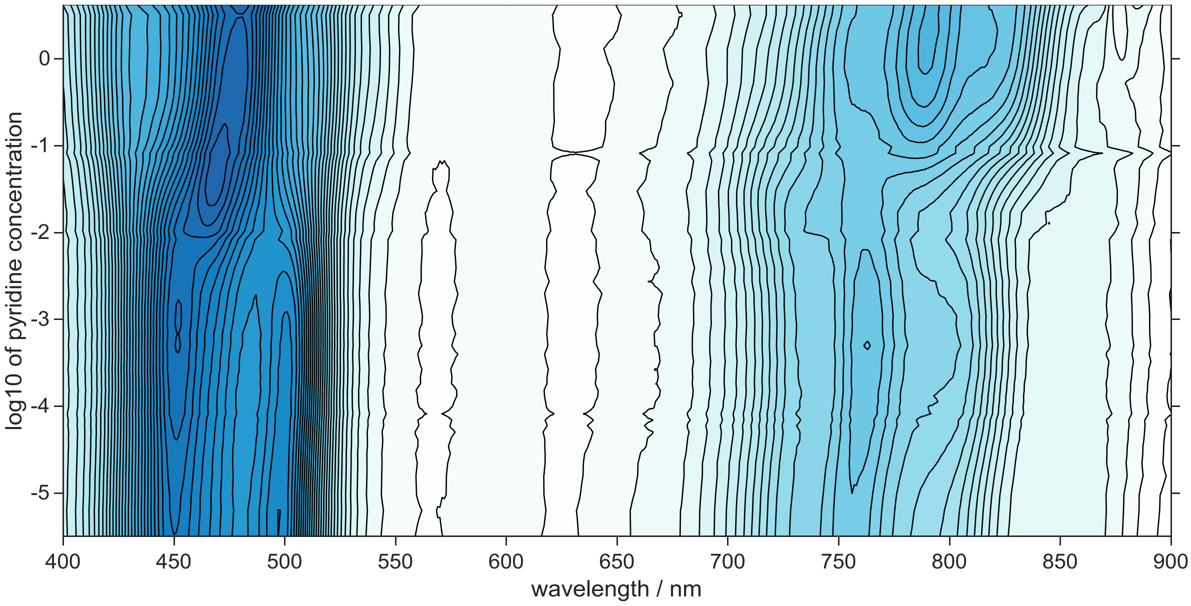

Figure 68. 2D plot of vis-NIR spectra of the denaturation of the ***c*-P6$^{(3arm)}$** against the pyridine concentration, showing three spectral changes, most apparent in range 450–500 nm.

The three processes associated with the spectral changes are interpretable as first coordinating the pyridine to unoccupied sites (pyridine concertation range of 10^{-5}–10^{-3} M), and then probably stepwise decoordination of the arms.

The straight-arm, based on the data from ***c*-P6$^{(1arm)}$** study, is expected to get decoordinated at pyridine concentrations of ~0.05–0.1 M. The ‘middle process’ occurs in the range of 10^{-3}–

10^{-2} M pyridine concentration and thus probably corresponds to the bent-arm decoordination suggesting looser binding.

As mentioned above, the pyridine-free compound was essentially insoluble in CD_2Cl_2. Unfortunately, an addition of $\mathbf{Thn}^+$ oxidant did not help to dissolve the compound as was hypothesized that charging the molecule might lead to disaggregation and increase solubility. Added $\mathbf{Thn}^+$ stayed in the solution unreacted.

Since benzene-d_6 has proven to be a better solvent for ***c*-P6**$^{\mathbf{(3arm)}}$, another NMR oxidation was tested in toluene-d_8, as a low-melting-point surrogate of benzene. Upon addition of $\mathbf{Thn}^+$, solubility of the ***c*-P6**$^{\mathbf{(3arm)}}$ partly increased and all signals of the ***c*-P6**$^{\mathbf{(3arm)}}$ disappeared, as would be expected for early (possible open shell) oxidation state. Unfortunately, no NMR signals were observed during the titration and even upon addition of excess of $\mathbf{Thn}^+$, no clear 6+ state was observed, leaving the spectrum completely silent.

Upon attempted cations reduction back to the neutral state, only a very small fraction (~20%, probably the part not in solution) of the compound could be recovered, with many insoluble stains remaining, suggesting decomposition during the oxidation.

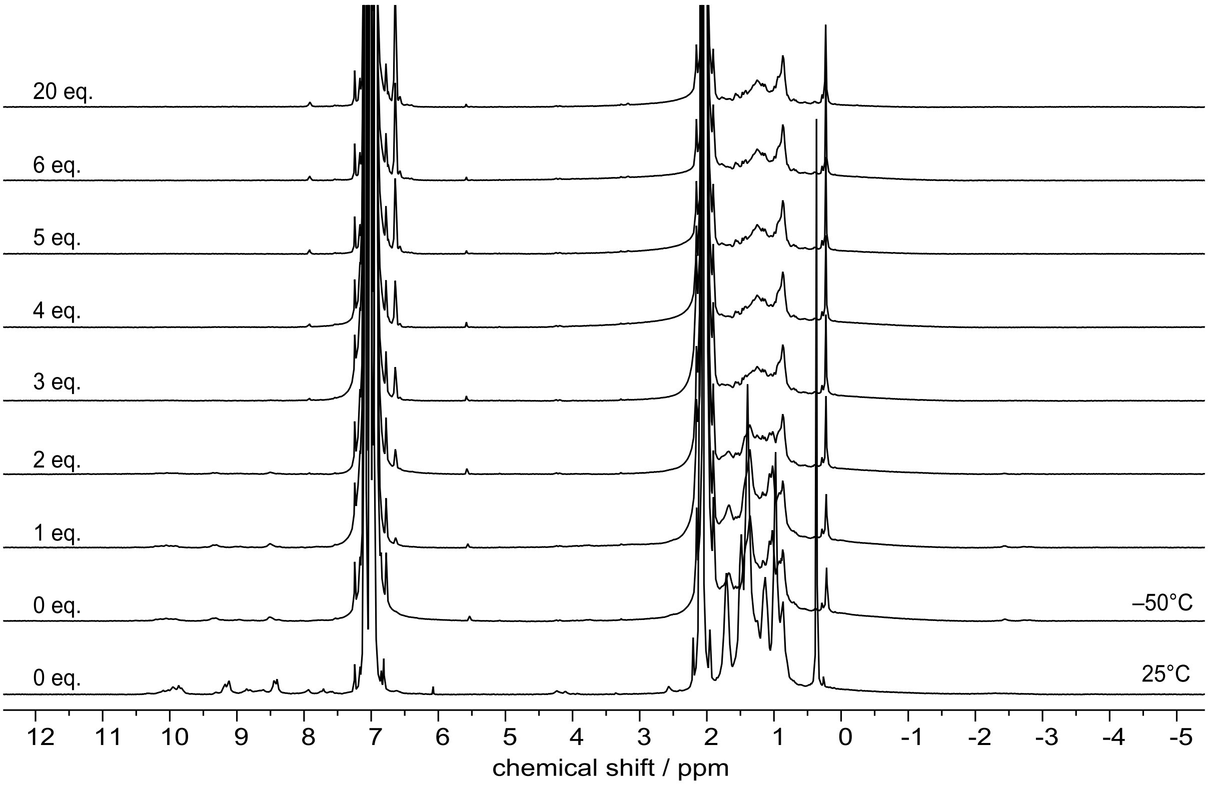

Figure 69. ^{1}H NMR (500 MHz, toluene-d_8) oxidation titration of ***c*-P6**$^{\mathbf{(3arm)}}$ with $\mathbf{Thn}^+$.

4.6. Summary

Nanoring ***c*-P6**$^{\mathbf{(1arm)}}$, with one pyridine-containing arm capable of intramolecular porphyrin coordination, was synthesized and characterized. It was found that the effective molarity of the arm is approximately 0.15 M, indicating good fit of the arm.

NMR spectroscopy proved that in absence of competing ligand, the arm is coordinated and thus effectively deconjugates the porphyrin nanoring scaffold. Such deconjugation is observed by UV-vis-NIR absorption, where, for nanoring, an unusual four-peak structure is observed. A similar vis-NIR pattern was observed for the linear hexamer ***l*-P6** wrapped around the template **T6** (***l*-P6·T6**).[42] Upon addition of competing ligand (pyridine, *N*-methylimidazole, THF), the arm is decoordinated, as documented by NMR, and the vis-NIR absorption characteristics changes to the three-peak pattern, typical for template-free nanoring ***c*-P6[b$_6$]** (**Figure 70**).

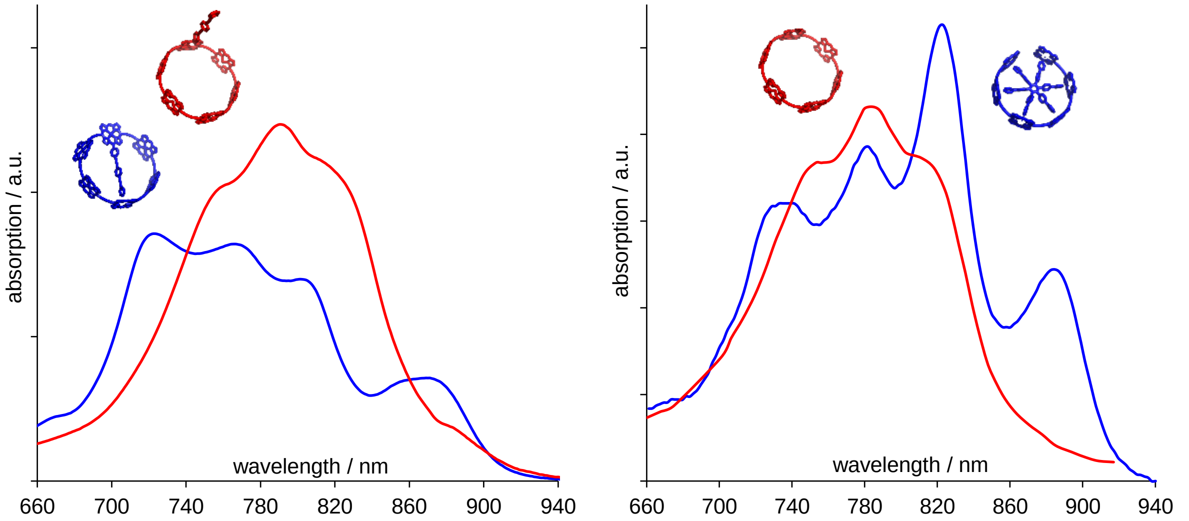

Figure 70. (left) Vis-NIR absorption of the ***c*-P6**$^{\mathbf{(1arm)}}$ in toluene in absence (blue) or presence (red) of the strong competing ligand. (right) Vis-NIR absorption spectra of ***c*-P6[b$_6$]** (red) and ***l*-P6·T6** (blue) in toluene/1% pyridine and toluene, respectively, adapted from literature.[42]

Interestingly, the deconjugated and desymmetrized state, with the arm intramolecularly bound, exhibited a relatively high fluorescence quantum yield of 3.6%. In the presence of a strong competing ligand, the quantum yield drops to 1.0%. This is in agreement with previously observed trends as the reported quantum yields of ***l*-P6·T6** are also higher than that of ***c*-P6[b$_6$]**.[42]

Unfortunately, NMR oxidation of ***c*-P6**$^{\mathbf{(1arm)}}$ yielded NMR spectra very similar to the previously tested ***c*-P6[b$_6$]**. This indicates that the structure is not maintaining its shape upon oxidation and opens up. Probably, the energy of the arm's intramolecular binding is not high enough to overcome the energy penalty resulting from not delocalizing the charge in the oxidized state.

The triply inter-linked nanoring ***c*-P6$^{(3arm)}$** was synthesized following an analogous route. Unfortunately, the compound suffered from very low solubility due to significant aggregation. This can be explained by bad molecular design, as it lacks several solubilizing groups, probably letting the short platform of three porphyrins became exposed from one side, sufficiently to enable aggregation with other molecules.

An NMR study showed that ***c*-P6$^{(3arm)}$** possesses two collapsed resonances at ~2.5 ppm, and two at 4–5 ppm, disappearing upon addition of a competing ligand (pyridine, THF). Therefore, it is reasonable to assume that in benzene-d_6 the arms are in the bound state. DOSY measurement proved that the peaks correspond to one species of size slightly smaller than regular ***c*-P6[b$_6$]** and therefore that no higher intermolecularly-coordinated oligomers are observed. Subsequently, the arms have to be bound somewhere, and the only reasonable arrangement is the Möbius shape.

NMR oxidations could not be performed due to solubility issues under standard conditions in CD_2Cl_2, and were therefore attempted in toluene-d_8, however unsuccessfully. Upon oxidation, the NMR spectrum become silent, all aromatic signals vanished and no change in the THS was observed.

Moreover, the majority of the oxidized species was decomposed, as revealed during attempted sample recovery. This could be probably due to exposure of some porphyrins and its reaction with not-strongly-bound nucleophilic bent-pyridine-containing arms in the oxidized state.

Although originally engineered in, the ^{19}F probe could not be used, due to the low concentration of the atoms in the molecule (19 / 9905) and consequently in the NMR sample. The signal was hardly detectable even when using an NMR machine with optimal sensitivity to the nucleus and acquiring multiple scans.

This leads to the possible suggestion for improvements in the next iteration: It would be advantageous to engineer in the porphyrins bearing the arms more solubilizing groups to increase solubility and prevent aggregation of the target molecule. Furthermore, if the ^{19}F reporter is desired, a symmetric 2,6-bis(trifluoromethyl)-phenylene moiety would be recommended, increasing 6× fluorine concentration while keeping simple the ^{19}F NMR signal (**Figure 71**). Also, the binding strength of the bent molecules are clearly very weak and therefore new design of the bent-arms might be beneficial, perhaps employing *N*-alkylimidazole or quinuclidine moieties.

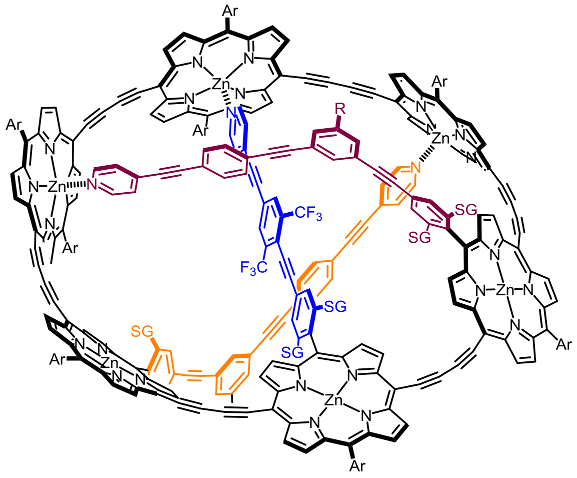

Figure 71. One of the proposed improved designs of the 2nd generation of ***c*-P6$^{(3arm)}$**. SG stand for solubilizing groups, possibly trihexylsilyl or tert-butyl groups.

It can be concluded that the author's design of a Möbius porphyrin nanoring represents a unique supramolecular strategy toward large Möbius molecules. The synthesis of a Möbius porphyrin nanoring was successful. However, the most appealing objective to observe and demonstrate the ring current, corresponding to Möbius aromaticity, was not achieved.

4.7. Synthetic and characterisation details

All assignments are based on the ^{1}H-^{1}H NOESY, ^{1}H-^{1}H COSY, ^{1}H-^{13}C HSQC and ^{1}H-^{13}C HMBC 2D NMR experiments. Compounds **4.15**,[46] ***l*-P1, 4.20** and **T6** were synthesised according to the published procedures.[42,47]

4.7.1. Straight-arm component

4-((3-fluoro-4-((trimethylsilyl)ethynyl)phenyl)-ethynyl)pyridine (4.16)

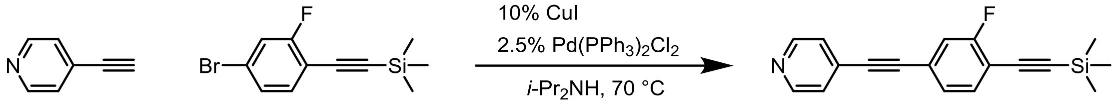

4.15 **4.16**

((4-Bromo-2-fluorophenyl)ethynyl)trimethylsilane (4.6 g, 17 mmol, 1 equiv.), 4-ethynylpyridine (2.27 g, 22.0 mmol, 1.3 equiv.), $Pd(PPh_3)_2Cl_2$ (298 mg, 0.4 mmol, 2.5%) and CuI (323 mg, 1.7 mmol, 10%) were placed in a three-neck flask. The atmosphere in the flask was replaced with nitrogen. Flask was filled with degassed *i*-Pr_2NH (40 mL) and the whole mixture was degassed by performing three freeze-pump-thaw cycles. The mixture was then stirred under nitrogen at 70 °C overnight. The formed suspension was filtrated through celite, the solids were washed with EtOAc and the filtered liquid was passed through a short silica plug. The crude product was purified on silica using CH_2Cl_2 / pyridine mixture as an eluent. Compound **4.16** was isolated as a yellowish powder (820 mg, 16%). The low yield was caused by insufficient wash of the product from the silica plug.

^{1}H NMR (400 MHz, $CDCl_3$) δ_H/ppm: 8.63 (bd, *J* = 3.5 Hz, 2H, H14), 7.45 (dd, *J* = 8.2, 7.2 Hz, 1H, H8), 7.38 (d, *J* = 6.1 Hz, 2H, H13), 7.31–7.21 (m, 2H, H6 and H9), 0.28 (s, 9H, H1). **^{13}C NMR {^{1}H}** (101 MHz, $CDCl_3$) δ_C/ppm: 162.6 (d, *J* = 252.9 Hz, C5), 150.0 (C14), 134.0 (d, *J* = 1.8 Hz, C8), 130.8 (C12), 127.6 (d, *J* = 3.6 Hz, C9), 125.6 (C13), 123.9 (d, *J* = 9.5 Hz, C7), 118.8 (d, *J* = 23.0 Hz, C6), 113.1 (d, *J* = 16.0 Hz, C4), 102.94 (d, *J* = 3.4 Hz, C2), 97.4 (C10), 92.2 (d, *J* = 3.1 Hz, C3), 89.1 (C11), −0.1 (C1). **^{19}F NMR {^{1}H}** (376 MHz, $CDCl_3$) δ_F/ppm: −109.20. **UV/vis** (CH_3CN): λ_{max} (ε) = 321 (44.4), 310 (35.4), 300 nm (44.4 ×10^3 M^{-1} cm^{-1}). **MS(HRMS-ESI)** m/z 294.11078 (MH^+, $C_{18}H_{17}FNSi$ requires 294.11088).

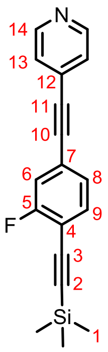

4-((4-ethynyl-3-fluorophenyl)ethynyl)pyridine (4.13)

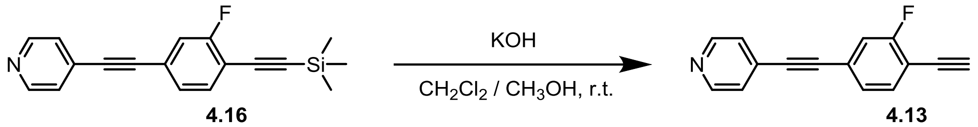

4-((3-Fluoro-4-((trimethylsilyl)ethynyl)phenyl)ethynyl)pyridine (90 mg, 0.3 mmol) was dissolved in CH_2Cl_2 (5 mL). To the KOH solution (110 mg, 2.0 mmol) in MeOH (20 mL) was slowly added and the CH_2Cl_2 solution and the resulting mixture was stirred for 2 h at ambient temperature. The mixture was extracted between water (400 mL) and CH_2Cl_2 (3×25 mL). The organic phases were joined, dried by $MgSO_4$, filtrated and filtrate was concentrated on rotatory evaporator and dried on vacuum. Product (4-((4-ethynyl-3-fluorophenyl)ethynyl)pyridine) (**4.13**) was obtained as a white solid (68 mg, 0.3 mmol, 100%).

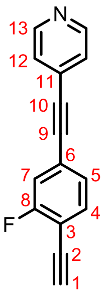

^{1}H NMR (400 MHz, $CDCl_3$) δ_H/ppm: 8.61 (d, J = 6.1 Hz, 1H, H13), 7.46 (dd, J = 8.3, 7.1 Hz, 1H, H5), 7.36 (d, J = 6.1 Hz, 1H, H12), 7.31–7.20 (m, 2H, H4 and H7), 3.42 (s, 1H, H1). **^{13}C NMR {^{1}H}** (101 MHz, $CDCl_3$) δ_C/ppm: 162.9 (d, J = 253.7 Hz, C8), 150.0 (C13), 134.1 (d, J = 2.1 Hz, C5), 130.7 (C11), 127.7 (d, J = 3.6 Hz, C4), 125.6 (C12), 124.4 (d, J = 9.3 Hz, C6), 118.8 (d, J = 22.8 Hz, C7), 112.0 (d, J = 16.0 Hz, C3), 91.9 (d, J = 3.2 Hz, C9), 89.2 (C10), 84.7 (d, J = 3.3 Hz, C1), 76.6 (C2). **UV/vis** (CH_3CN): λ_{max} (ε) = 314 (33), 305 (26.5), 292 nm (33.8 $\times 10^3$ M^{-1} cm^{-1}). **MS(HRMS-ESI)** m/z 222.07132 (MH^+, $C_{15}H_9FN$ requires 222.07135).

4.7.2. Bent-arm component

1,3-dibromo-5-idodobenzene (4.24)[48,49]

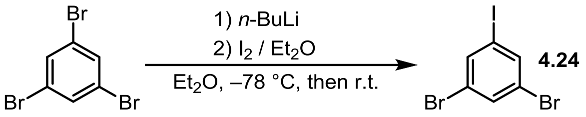

1,3,5-Tribromobenzene (8.70 g, 27.6 mmol) was dissolved in Et_2O (250 mL) under nitrogen. The solution was cooled to −78 °C and *n*-BuLi (1.6 M in hexane, 17.3 mL, 27.6 mmol) was dropwise added. The mixture was stirred at −78 °C for 3 h under nitrogen. Then iodine (9.12 g, 34.6 mmol) dissolved in Et_2O (100 mL) was dropwise added to the phenyllithium solution. The mixture was allowed to reach room temperature and stirred overnight. An excess of the iodine was quenched by saturated aqueous solution of $Na_2S_2O_3$ (100 mL) and the mixture was extracted between water (500 mL) and Et_2O (3×200 mL). Organic phases were joined and dried with $MgSO_4$, filtrated and the liquid was concentrated on rotatory evaporator. Obtained solid was dried on high vacuum to give product as a white solid (9.70 g, 26.9 mmol, 97%).

^{1}H NMR (400 MHz, CDCl$_3$) δ$_H$/ppm: 7.80 (d, J = 1.7 Hz, 2H, H4 and H6), 7.64 (t, J = 1.7 Hz, 1H, H2). **^{13}C NMR {^{1}H}** (101 MHz, CDCl$_3$) δ$_C$/ppm: 138.6 (C4 and C6), 133.8 (C2), 123.5 (C1 and C3), 94.6 (C5). In agreement with literature.[48,49]

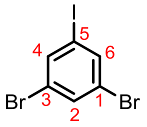

((3,5-dibromophenyl)ethynyl)trihexylsilane (4.25)

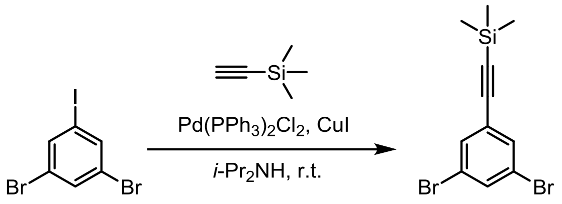

4.24 **4.25**

1,3-Dibromo-5-iodobenzene (**4.24**) (9.70 g, 26.9 mmol, 1 equiv.), Pd(PPh$_3$)$_2$Cl$_2$ (300 mg, 0.43 mmol, 1.6%) and CuI (1.0 g, 5.3 mmol, 20%) were dissolved in i-Pr$_2$NH (150 mL) and the mixture was bubbled by argon for 20 min. Trimethylsilylethyne (4.7 mL, 34 mmol, 1.3 equiv.), prior degassed by argon bubbling, was added to the reaction mixture and the solution was stirred at room temperature under nitrogen overnight. Resulting suspension was filtered through celite, washed with EtOAc and the filtered liquid was concentrated and passed through short silica plug using EtOAc as an eluent. The solution was concentrated on rotatory evaporator and dried on vacuum. Obtained oil was filtrated through cotton yielding **4.25** as brownish oil (7.46 g, 22.5 mmol, 81%).

^{1}H NMR (400 MHz, CDCl$_3$) δ$_H$/ppm: 7.61 (t, J = 1.8 Hz, 1H), 7.53 (d, J = 1.8 Hz, 2H), 0.24 (s, 9H). In agreement with literature.[48,49]

(3-bromo-5-((trimethylsilyl)ethynyl)phenyl)trihexylsilane (4.26)

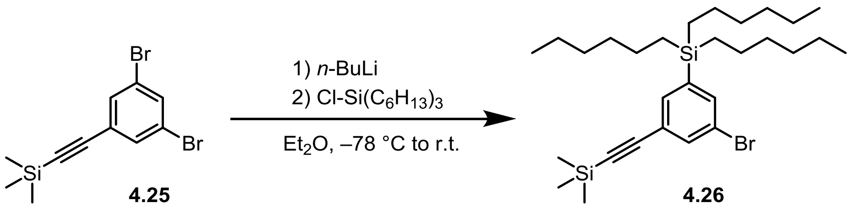

4.25 **4.26**

((3,5-Dibromophenyl)ethynyl)trimethylsilane (**4.25**) (6.0 g, 18.1 mmol, 1 equiv.) was dissolved in Et$_2$O (400 mL) and the solution was cooled to −78 °C. n-BuLi (1M solution in hexane, 18.1 mL, 18.1 mmol, 1 equiv.) was dropwise added to the solution and the whole mixture was stirred at −78 °C for 3 h under the argon. Neat chlorotrihexylsilane (6.90 g, 21.6 mmol, 1.2 equiv.) was dropwise added and the mixture was allowed to warm up to room temperature. The mixture was stirred for another 2 h and then quenched with ammonium chloride solution (100 mL) and extracted with Et_2O (3×250 mL). The organic phases were joined, dried with $MgSO_4$ and concentrated on rotatory evaporator. The product was purified by column chromatography using pentane as an eluent on large SiO_2 column (200× of SiO_2 per mass of the mixture) and obtained as a colourless oil (3.4 g, 6.3 mmol, 35%).

^{1}H NMR (400 MHz, $CDCl_3$) δ_H/ppm: 7.60 (t, J = 1.7 Hz, 1H, H6), 7.51 (dd, J = 2.0, 0.9 Hz, 1H, H2), 7.46 (t, J = 1.0 Hz, 1H, H4), 1.37–1.19 (m, 24H, H11–14), 0.95–0.86 (m, 9H, H15), 0.82–0.74 (m, 6H, H10), 0.28 (s, 9H, H9). **^{13}C NMR {^{1}H}** (101 MHz, $CDCl_3$) δ_C/ppm: 141.7 (C3), 136.7 (C2), 135.8 (C4), 134.9 (C6), 124.7 (C5), 122.4 (C1), 104.0 (C7), 95.6 (C8), 33.5 (C12), 31.6 (C13), 23.7 (C11), 22.8 (C14), 14.3 (C15), 12.3 (C10), 0.1 (C9). **UV/vis** (CH_3CN): λ_{max} (ε) = 299 (535), 291 (550), 282 (418), 262 (10540) 251 nm (9910 M^{-1} cm^{-1}). **MS(HRMS-EI)** m/z 534.2727 (M^+, $C_{29}H_{51}BrSi_2$ requires 534.2713).

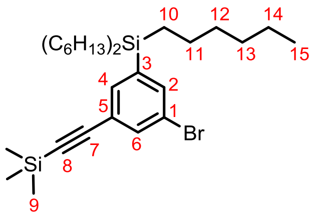

4-((4-((trimethylsilyl)ethynyl)phenyl)ethynyl)-pyridine (4.28)

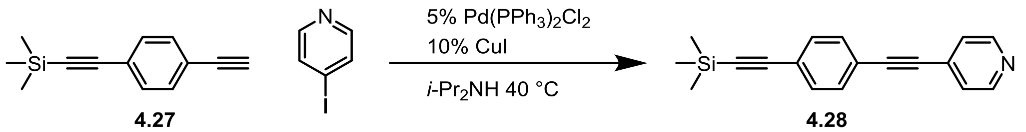

4.27 **4.28**

((4-Ethynylphenyl)ethynyl)trimethylsilane (4.45 g, 22.4 mmol, 1 equiv.) and 4-iodopyridine (4.40 g, 21.5 mmol, 1 equiv.) were dissolved in *i*-Pr_2NH (200 mL). The mixture was degassed by performing three freeze-pump-thaw cycles and during the 3rd cycle, $Pd(PPh_3)_2Cl_2$ (1.3 g, 1.1 mmol, 5% equiv.) and CuI (430 mg, 2.26 mmol, 10% equiv.) were added as solids on the top of the frozen solution. The mixture was degassed one more time and stirred overnight at 40 °C under argon. Resulting suspension was then filtered through celite (washed with EtOAc) and purified on silica (petrol ether / EtOAc 10/1) to give desired product **4.28** as pale yellow solid (2.36 g, 8.55 mmol, 38%).

^{1}H NMR (400 MHz, $CDCl_3$) δ_H/ppm: 8.61 (d, J = 3.9 Hz, 2H, H1), 7.48 (d, J = 9.0 Hz, 2H, H7 or H8), 7.46 (d, J = 8.6 Hz, 2H, H8 or H7), 7.37 (d, J = 6.0 Hz, 2H, H2), 0.26 (s, 9H, H12). **^{13}C NMR {^{1}H}** (101 MHz, $CDCl_3$) δ_C/ppm: 150.0 (C1), 132.1 (C7 or C8), 131.8 (C8 or C7), 131.3 (C3), 125.7 (C2), 124.1 (C6 or C9), 122.2 (C9 or C6), 104.4 (C10), 97.1 (C11), 93.6 (C5), 88.5 (C4), 0.0 (C12). **UV/vis** (CH_3CN): λ_{max} (ε) = 319 (47.4), 300 nm (46.4 ×10^3 M^{-1} cm^{-1}). **MS(HRMS-ESI)** m/z 276.12045 (MH^+, $C_{18}H_{18}NSi$ requires 276.12030).

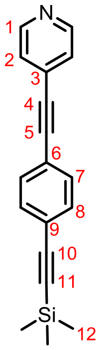

4-((4-ethynylphenyl)ethynyl)pyridine (4.29)

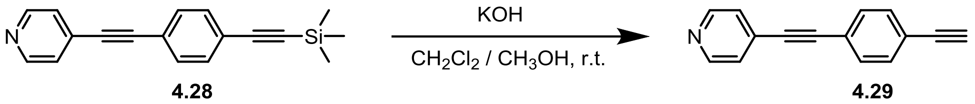

4-((4-((Trimethylsilyl)ethynyl)phenyl)ethynyl)pyridine (**4.28**) (1.8 g, 6.5 mmol) was dissolved in CH_2Cl_2/CH_3OH 1:1 mixture (80 mL). Then, KOH (0.73 g, 13 mmol) dissolved in CH_3OH (20 mL) was slowly added to the solution and resulting mixture was stirred for 30 min at ambient temperature. Mixture was extracted between water (400 mL) and CH_2Cl_2 (5×50 mL). Organic phases were joined, dried by $MgSO_4$, filtrated and filtrate was concentrated on rotatory evaporator. Purification on silica provided 4-((4-ethynylphenyl)ethynyl)pyridine (**4.29**) as yellow solid (1.1 g, 0.5 mmol, 83%).

^{1}H NMR (400 MHz, $CDCl_3$) δ_H/ppm: 8.60 (d, J = 6.0 Hz, 2H, H1), 7.48 (s, 4H, H7 and H8), 7.36 (d, J = 6.1 Hz, 2H, H2), 3.20 (s, 1H, H11). **^{13}C NMR {^{1}H}** (101 MHz, $CDCl_3$) δ_C/ppm: 149.9 (C1), 132.3 (C8 or C7), 131.9 (C7 or C8), 131.2 (C3), 125.6 (C2), 123.1 (C6 or C9), 122.6 (C9 or C6), 93.3 (C5), 88.6 (C4), 83.1 (C10), 79.6 (C11). **UV/vis** (CH_3CN): λ_{max} (ε) = 312 (24.0), 302 (19.1), 294 nm (23.3×10^3 M^{-1} cm^{-1}). **MS(HRMS-ESI)** m/z 204.08080 (MH^+, $C_{15}H_{10}N$ requires 204.08078).

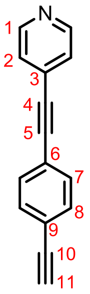

4-((4-((3-(trihexylsilyl)-5-((trimethylsilyl)ethynyl)phenyl)-ethynyl)phenyl)ethynyl)pyridine (4.30)

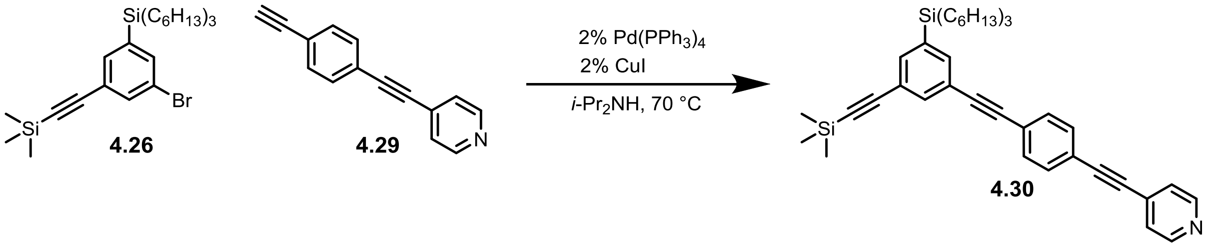

4-((4-Ethynylphenyl)ethynyl)pyridine (**4.29**) (239 mg, 1.18 mmol, 2 equiv.) and (3-bromo-5-((trimethylsilyl)ethynyl)phenyl)trihexylsilane (**4.26**) (315 mg, 0.59 mmol) were dissolved in i-Pr_2NH (80 mL). Mixture was degassed by freeze-pump-thaw and during the 3rd cycle, $Pd(PPh_3)_4$ (69 mg, 0.06 mmol, 5% equiv.) and CuI (23 mg, 0.12 mmol, 10% equiv.) were placed as solids on the top of frozen solution. One more degassing cycle was performed and the mixture was stirred overnight at 70 °C. The mixture was then filtered through celite (washed with EtOAc) and purified on silica ($CHCl_3$ / CH_3OH / pyridine – 100 / 2 / 0.5) to give moderately pure product (330 mg). Crude product was re-purified to give 4.30 as pale yellow solid (150 mg, 0.2 mmol, 39%).

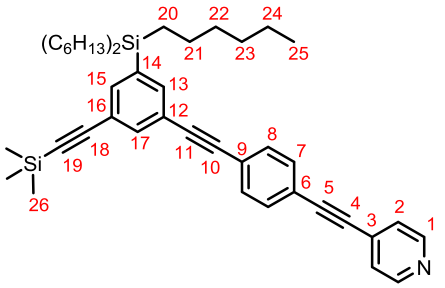

^{1}H NMR (400 MHz, CDCl$_3$) δ_H/ppm: 8.64 (s, 2H, H1), 7.64 (t, *J* = 1.6 Hz, 1H, H17), 7.56 (t, *J* = 1.3 Hz, 1H, H13), 7.52 (s, 5H, H7 and H8 and H15), 7.39 (s, 2H, H2), 1.29 (tdd, *J* = 12.5, 9.5, 4.5 Hz, 24H, H21–24), 0.88 (t, *J* = 6.6 Hz, 9H, H25), 0.78 (dd, *J* = 10.3, 5.4 Hz, 6H, H20), 0.27 (s, 9H, H26). **^{13}C NMR {^{1}H}** (400 MHz, CDCl$_3$) δ_C/ppm: 149.8 (C1), 139.4 (C14), 137.3 (C15), 136.9 (C13), 135.3 (C17), 131.9 (C7 or C8), 131.7 (C8 or C7), 131.2, 125.7 (C2), 124.1, 122.9, 122.4, 122.0, 104.7 (C18), 94.9 (C19), 93.6, 91.6 (C11), 89.3, 88.5, 77.2, 33.5 (C22), 31.5 (C23), 23.7 (C21), 22.7 (C24), 14.2 (C25), 12.2 (C20), 0.0 (C26). **UV/vis** (CH$_3$CN): λ_{max} (ε) = 341 (31.7), 322 (44.6), 267 (21.5), 253 nm (21.7 $\times 10^3$ M^{-1} cm^{-1}). **MS(HRMS-ESI)** m/z 658.42538 (MH$^+$, $C_{44}H_{60}NSi_2$ requires 658.42588).

4-((4-((3-ethynyl-5-(trihexylsilyl)phenyl)ethynyl)phenyl)-ethynyl)pyridine (4.23)

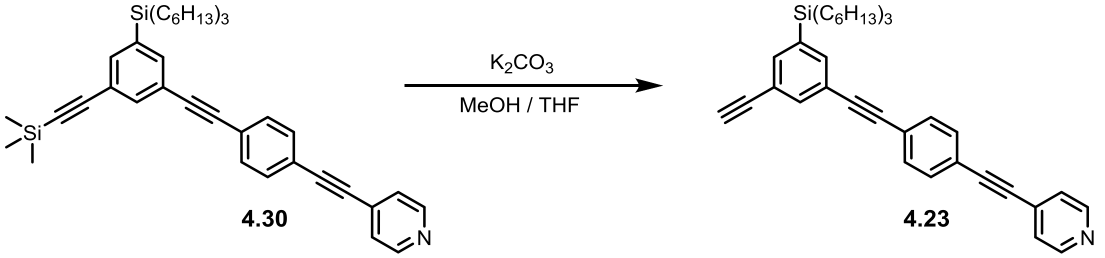

4.30

4.23

4-((4-((3-(Trihexylsilyl)-5-((trimethylsilyl)ethynyl)phenyl)ethynyl)phenyl)ethynyl)-pyridine (**4.30**) (150 mg, 0.228 mmol, 1 equiv.) and K$_2$CO$_3$ (252 mg, 1.82 mmol, 8 equiv.) were placed in a 25 mL flask followed by THF (6 mL) and MeOH (4 mL). The mixture was stirred for 2h. The mixture was concentrated on rotatory evaporator, passed through short silica plug (washed with CH$_2$Cl$_2$ / 10% pyridine). The solution was concentrated a dried to give 4-((4-((3-ethynyl-5-(trihexylsilyl)phenyl)ethynyl)phenyl)ethynyl)pyridine (**4.23**) (134 mg, 0.228 mmol, 100%).

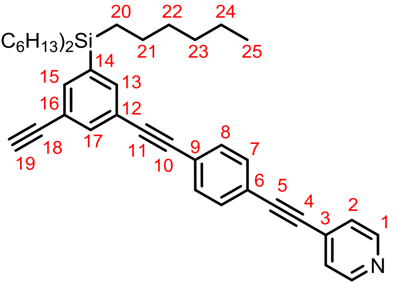

^{1}H NMR (400 MHz, CDCl$_3$) δ_H/ppm: 8.37 (s, 2H, H1), 7.37 (t, *J* = 1.6 Hz, 1H, H17), 7.35–7.29 (m, 1H, H15), 7.29 (d, *J* = 1.4 Hz, 1H, H13), 7.29–7.23 (m, 4H, H7 and H8 and H13), 7.11 (d, *J* = 4.6 Hz, 2H, H2), 2.84 (s, 1H, H19), 1.08–0.94 (m, 24H, H21–24), 0.61 (t, *J* = 6.9 Hz, 9H, H25), 0.55–0.47 (m, 6H, H20). **^{13}C NMR {^{1}H}** (400 MHz, CDCl$_3$) δ_C/ppm: 149.8 (C1), 139.6 (C14), 137.6 (C13), 137.3 (C15), 135.3 (C17), 131.9 (C7 or C8), 131.8 (C8 or C7), 131.2 (C3), 125.7 (C2), 124.1 (C6 or C9), 122.6 (C9 or C6), 122.1 (C12), 121.9 (C16), 93.6 (C5), 91.4 (C11), 89.4 (C10), 88.6 (C4), 83.3 (C18), 77.9 (C19), 33.5 (C22), 31.5 (C23), 23.7 (C21), 22.7 (C24), 14.2 (C25), 12.2 (C20). **MS(HRMS-ESI)** m/z 586.38623 (MH^+, $C_{41}H_{52}NSi$ requires 586.38635).

4.7.3. Porphyrin monomers building blocks

5-(3,5-bis(trihexylsilyl)phenyl)-15-(4-bromophenyl)porphyrin (4.17)

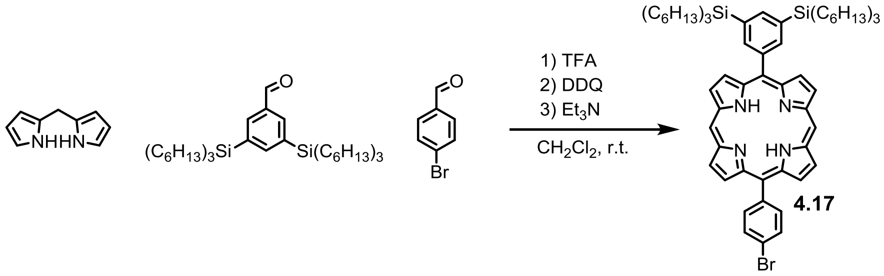

3,5-Bis(trihexylsilyl)benzaldehyde (6.8 g, 10 mmol, 1 equiv.), 4-bromo-benzaldehyde (7.5 g, 41 mmol, 4 equiv.) and dipyrromethane (7.4 g, 51 mmol, 5 equiv.) were dissolved in CH_2Cl_2 (7.5 L). The solution was saturated with nitrogen, then TFA (8 mL, 122 mmol, 12 equiv.) was added and the mixture was stirring for 3h in the dark. DDQ (17.25 g, 75.99 mmol, 7.5 equiv.) was added and the mixture was stirred for a further 40 min. Finally, triethylamine (50 mL) was added to quench the acid and DDQ and the mixture was stirred for 30 min. The solution was concentrated and passed through two big silica plugs (~200 g) eluting with a mixture of 40–60 °C petroleum ether and CH_2Cl_2 (80/20). The solvent was removed to give mixture of free base porphyrins. The mixture was purified on silica (400 g) first with 40–60°C petroleum ether and CH_2Cl_2 (10/1) to separate out bis-THS condensed product. Desired product was released from the column with 40–60 °C petroleum ether and CH_2Cl_2 (5/1). Bis-bromo porphyrin was left on the silica column. Product was concentrated and dried yielding **4.17** as a purple solid (2.5 g, 2.3 mmol, 22% relative to 3,5-bis(trihexylsilyl)benzaldehyde).

^{1}H NMR (400 MHz, $CDCl_3$): δ_H/ppm: 10.35 (s, 2H, H10), 9.43 (d, *J* = 4.6 Hz, 4H, H8 and H12), 9.13 (d, *J* = 4.6 Hz, 2H, H13), 9.07 (d, *J* = 4.6 Hz, 2H, H7), 8.39 (d, *J* = 1.2 Hz, 2H, H17), 8.16 (d, *J* = 8.3 Hz, 2H, H3), 8.07 (s, 1H, H19), 7.96 (d, *J* = 8.2 Hz, 2H, H2), 1.60–1.50 (m, 12H, H21), 1.42 (td, *J* = 7.5, 4.1 Hz, 12H, H22), 1.38–1.28 (m, 24H, H23 and H24), 1.02–0.96 (m, 12H, H20), 0.95–0.88 (m, 18H, H25), −3.05 (s, 2H, NH). **^{13}C NMR {^{1}H}** (101 MHz, $CDCl_3$) δ_C/ppm: 147.7 (C14), 146.9 (C6), 145.4 (C9), 145.3 (C11), 141.2 (C17), 140.6 (C4), 139.6 (C16), 139.5 (C19), 136.3 (C3), 135.6 (C18), 132.0 (C8), 131.7 (C12), 131.5 (C13), 130.7 (C7), 130.3 (C2), 122.6 (C1), 121.0 (C15),

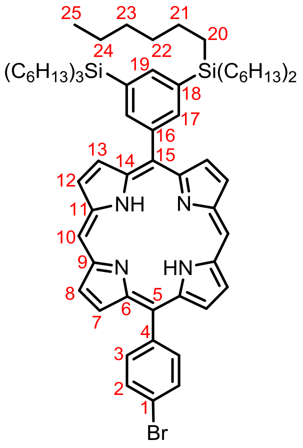

117.3 (C5), 105.5 (C10), 33.7 (C22), 31.8 (C23), 24.2 (C21), 22.8 (C24), 14.33 (C25), 12.9 (C20). **UV/vis** (toluene): λ_{max} (ε) = 631 (2.9), 576 (8.0), 539 (9.4), 504 (24.6), 409 nm (570.9 ×10^3 M^{-1} cm^{-1}). **MS (MALDI-ToF)** m/z 1107.591 (MH^+, $C_{68}H_{98}BrN_4Si_2$ requires 1107.651).

5-(3,5-bis(trihexylsilyl)phenyl)-15-(4-bromo-phenyl)zinc-porphyrin (4.12)

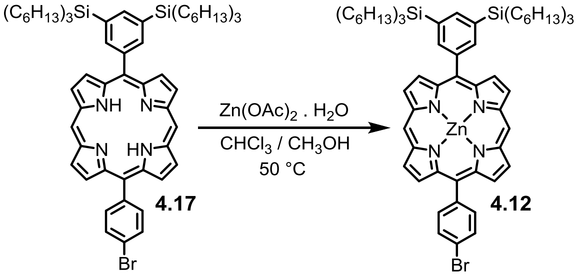

A solution of $Zn(OAc)_2{\cdot}2H_2O$ (2.14 g, 9.75 mmol) in MeOH (10 mL) was added to a solution of 5-(4-bromophenyl)-15-[3,5(trihexylsilyl)phenyl]porphyrin (**4.17**) (2.161 g, 1.953 mmol) in $CHCl_3$ (80 mL). The resulting mixture was stirred at 50 °C and monitored by TLC. Insertion of the zinc was completed after 30 min. The mixture was concentrated on rotatory evaporator and passed through a short silica plug, eluting with a mixture of 40–60°C petroleum ether / CH_2Cl_2 / pyridine (30/10/1). The solvent was removed to give the zinc porphyrin **4.12** (2.2 g, 96%) as a pink solid.

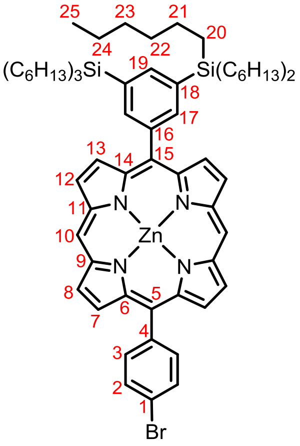

^{1}H NMR (400 MHz, $CDCl_3$): δ_H/ppm: 10.24 (s, 2H, H10), 9.40 (d, *J* = 4.5 Hz, 2H, H8), 9.38 (d, *J* = 4.4 Hz, 2H, H12), 9.10 (d, *J* = 4.4 Hz, 2H, H13), 9.06 (d, *J* = 4.4 Hz, 2H, H7), 8.33 (d, *J* = 1.0 Hz, 2H, H17), 8.15 (d, *J* = 8.3 Hz, 2H, H3), 8.01 (s, 1H, H19), 7.92 (d, *J* = 8.3 Hz, 2H, H2), 6.46 (tt, *J* = 7.6, 1.8 Hz, 1H, H28), 5.69 (dd, *J* = 7.6, 5.6 Hz, 2H, H27), 3.31 (bs, 2H, H26), 1.58–1.47 (m, 12H, H21), 1.39 (h, *J* = 6.5 Hz, 12H, H22), 1.32 (dq, *J* = 8.2, 4.2 Hz, 24H, H23 and H24), 1.00–0.92 (m, 12H, H20), 0.92–0.84 (m, 18H, H25). **^{13}C NMR {^{1}H}** (101 MHz, $CDCl_3$) δ_C/ppm: 150.5 (C14), 149.7 (C6), 149.6 (C9), 149.5 (C11), 144.2 (C26), 142.6 (C4), 141.4 (C16), 141.1 (C19), 138.9 (C17), 136.3 (C2), 135.7 (C28), 134.7 (C18), 132.7 (C13), 131.8 (C7), 131.8 (C8), 131.5 (C12), 129.7 (C3), 122.3 (C27), 121.9 (C1), 121.3 (C15), 117.6 (C5), 105.9 (C10), 33.7 (C22), 31.8 (C23), 24.2 (C21), 22.8 (C24), 14.3 (C25), 12.9 (C20). **UV/vis** (toluene): λ_{max} (ε) = 614 (0.56), 570 (3.58), 537 (24.9), 410 (611), 345 (13.2), 299 nm (20.4 ×10^3 M^{-1} cm^{-1}). **MS(MALDI-ToF)** m/z 1168.546 (M^+, $C_{68}H_{95}BrN_4Si_2Zn$ requires 1168.5563).

Straight-arm-containing porphyrin 4.11

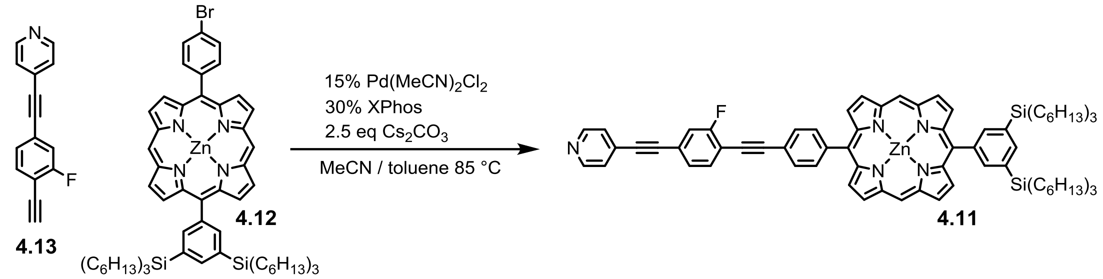

5-(4-Bromophenyl)-15-[3,5(trihexylsilyl)phenyl]zinc-porphyrin (**4.12**) (155 mg, 0.132 mmol, 1 equiv.), 4-((4-ethynyl-3-fluorophenyl)ethynyl)pyridine (60 mg, 0.27 mmol, 2 equiv.), $Pd(CH_3CN)_2Cl_2$ (1.7 mg, 7 µmol, 5% equiv.), Xphos (6.3 mg, 13 µmol, 10% equiv.) and Cs_2CO_3 (86 mg, 0.26 mmol, 2 equiv.) were placed into a Schlenk flask followed by CH_3CN (5 mL) and toluene (2 mL). Mixture was degassed by performing three freeze-pump-thaw cycles and then stirred under nitrogen at 80 °C for 3h. Mixture was concentrated on rotatory evaporator, passed through short silica plug eluted with CH_2Cl_2 / pyridine (10/1). Crude product was purified on SEC and porphyrin fraction was collected. Solution was concentrated a dried to give **4.11** as a red oil (171 mg, 0.131 mmol, 98% yield).

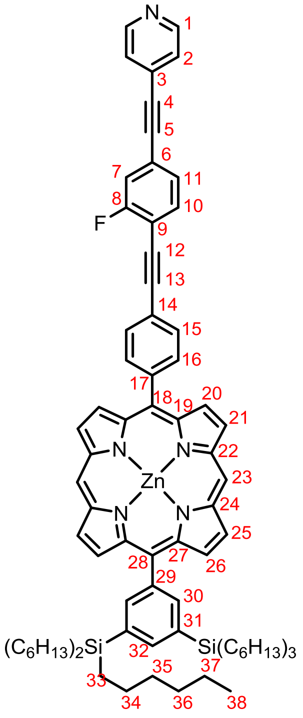

^{1}H NMR (400 MHz, $CDCl_3$ / 5% pyridine-d_5) δ_H/ppm: 10.35 (s, 2H, H23), 9.52 (d, J = 4.5 Hz, 2H, H25), 9.49 (d, J = 4.5 Hz, 2H, H21), 9.27 (dd, J = 4.3, 2.4 Hz, 2H, H26), 9.19 (d, J = 4.4 Hz, 2H, H20), 8.52 (s, 2H, H30), 8.40 (d, J = 7.7 Hz, 2H, H16), 8.19 (s, 1H, H32), 8.08 (d, J = 7.8 Hz, 2H, H15), 7.63 (t, J = 7.6 Hz, 1H, H11), 7.27 – 7.16 (m, 2H, H7 and H10), 6.64 (bs, 2H, H2), 6.13 (bd, J = 21.6 Hz, 2H, H1), 1.69 (p, J = 8.2, 7.6 Hz, 12H, H34), 1.55 (t, J = 6.8 Hz, 12H, H35), 1.52–1.42 (m, 24H, H36 and H37), 1.12 (t, J = 8.3 Hz, 12H, H33), 1.03 (t, J = 5.8 Hz, 18H, H38). **^{13}C NMR{^{1}H}** (101 MHz, $CDCl_3$ / 5% pyridine-d_5) δ_C/ppm: 162.2 (d, J = 252.9 Hz, C8), 150.5 (C19 or C22 or C24 or C27), 149.7(C19 or C22 or C24 or C27), 149.6(C19 or C22 or C24 or C27), 149.5(C19 or C22 or C24 or C27), 147.1 (C1), 144.5 (C17), 141.4 (C29), 141.2 (C30), 139.0 (C32), 135.1 (C16), 134.7 (C31), 133.5 (d, J = 2.1 Hz, C11), 132.7 (C26), 131.8 (C20 or C21 or C25), 131.6 (C20 or C21 or C25), 130.7 (C3), 130.0 (C15), 127.7 (d, J = 3.4 Hz, C10), 124.9 (C2), 123.2 (d, J = 9.2 Hz, C9), 121.37 (C18 and C28), 118.7 (d, J = 22.8 Hz, C7), 118.2 (C14), 113.6 (d, J = 16.0 Hz, C6), 106.0 (C23), 97.4 (d, J = 3.2 Hz, C13), 92.7 (d, J = 1.5 Hz, C12), 88.3 (C4), 83.2 (C5), 33.7 (C35), 31.8 (C36), 24.3 (C34), 22.8 (C37), 14.3 (C38), 12.9 (C33). **UV/vis** (toluene): λ_{max} (ε) = 618 (0.46), 576 (3.54), 541 (17.2), 413 (382), 325 nm (44.2 ×10^3 M^{-1} cm^{-1}). **MS(MALDI-ToF)** m/z 1309.797 (M$^+$, $C_{83}H_{102}FN_5Si_2Zn$ requires 1309.696).

Straight-arm-containing porphyrin 4.14

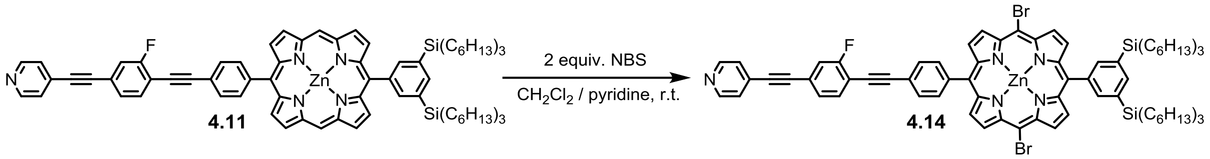

Porphyrin **4.11** (340 mg, 0.26 mmol, 1 equiv.) was dissolved in $CHCl_3$ (250 mL) and pyridine (10 mL). *N*-bromosuccinimide (92 mg, 0.52 mmol, 2 equiv.) in $CHCl_3$ (250 mL) was dropwise added to porphyrin solution. After 1h, acetone (5 mL) was added and the mixture was concentrated on rotatory evaporator. Obtained oil was re-dissolved in $CHCl_3$ (5 mL) and precipitated by MeOH (400 mL). Suspension was cooled to −20 °C, filtrated and solid was dried on vacuum yielding **4.14** as a green solid (340 mg, 0.23 mmol, 90% yield).

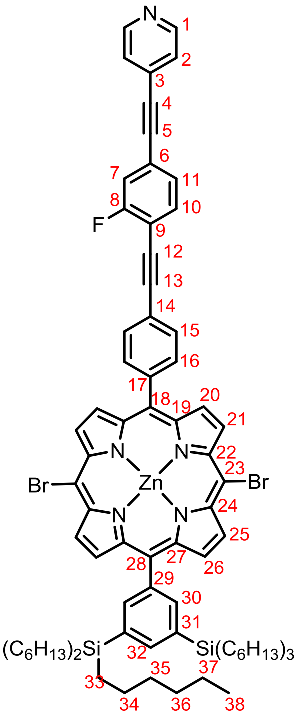

^{1}H NMR (400 MHz, $CDCl_3$ with 10% pyridine-d$_5$) δ_H/ppm: 9.67 (d, *J* = 4.7 Hz, 2H, H25), 9.64 (d, *J* = 4.7 Hz, 2H, H21), 8.85 (d, *J* = 4.7 Hz, 2H, H26), 8.85 (d, *J* = 4.7 Hz, 2H, H20), 8.54 (d, *J* = 5.9 Hz, 2H, H1), 8.18 (d, *J* = 1.1 Hz, 2H, H30), 8.16 (d, *J* = 8.1 Hz, 2H, H16), 7.97 (s, 1H, H32), 7.95 (d, *J* = 8.3 Hz, 2H, H15), 7.67 (t, *J* = 7.6 Hz, 1H, H11), 7.43–7.34 (m, 4H, H2 and H7 and H10), 1.54–1.42 (m, 12H, H34), 1.42–1.30 (m, 12H, H35), 1.33–1.20 (m, 24H, H36 and H37), 0.96–0.89 (m, 12H, H33), 0.89–0.75 (m, 18H, H38). **^{13}C NMR{^{1}H}** (101 MHz, $CDCl_3$ with 10% pyridine-d$_5$) δ_C/ppm: 162.2 (d, *J* = 252.8 Hz, C8), 151.1 (C19 or C22 or C24 or C27), 150.3 (C19 or C22 or C24 or C27), 150.2 (C19 or C22 or C24 or C27), 150.0 (C19 or C22 or C24 or C27), 149.8 (C1), 143.6 (C17), 140.71 (C30), 140.70 (C29, 139.1 (C32), 134.7 (C29), 134.7 (C16), 133.53 (C20), 133.48 (d, *J* = 1.9 Hz, C11), 133.1 (C26), 132.8 (C21 and C25), 130.7 (C3), 129.8 (C15), 127.7 (d, *J* = 3.5 Hz, C10), 125.5 (C2), 123.63 (d, *J* = 9.5 Hz, C9), 123.61 (C28), 121.7 (C14), 120.4 (C18), 118.8 (d, *J* = 22.9 Hz, C7), 113.3 (d, *J* = 16.0 Hz, C6), 104.9 (C23), 96.8 (d, *J* = 3.1 Hz, C13), 92.2 (d, *J* = 3.2 Hz, C12), 89.0 (C4), 83.3 (C5), 33.5 (C35), 31.6 (C36), 24.0 (C34), 22.6 (C37), 14.2 (C38), 12.7 (C33). **UV/vis**

(toluene): λ_{max} (ε) = 613 (6.52), 596 (8.28), 556 (21.5), 430 nm (380 ×10^3 M^{-1} cm^{-1}). **MS(MALDI-ToF)** m/z 1468.4 (M^+, $C_{83}H_{100}Br_2FN_5Si_2Zn$ requires 1467.5).

Straight-arm-containing porphyrin 4.18

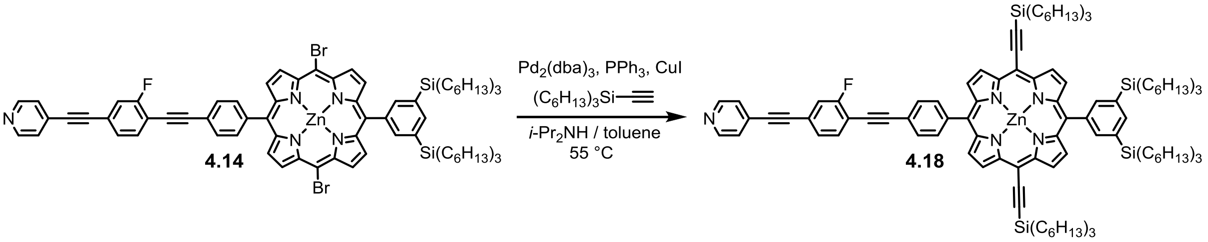

Dibromoporphyrin **4.14** (305 mg, 0.208 mmol, 1 equiv.), CuI (8 mg, 0.04 mmol, 0.2 equiv.), $Pd_2(dba)_3$ (19 mg, 0.02 mmol, 0.1 equiv.), PPh_3 (11 mg, 0.04 mmol, 0.2 equiv.), toluene (15 mL) and *i*-Pr_2NH (15 mL) were placed into a Schlenk tube (50 mL) and the mixture was degassed by performing three freeze-pump-thaw cycles. Trihexylsilylacetylene (200 mg, 0.648 mmol, 3.1 equiv.) was added and mixture was stirred overnight at 55 °C under nitrogen. The mixture was then concentrated on rotatory evaporator and passed through plug of SiO_2 eluted with CH_2Cl_2 / pyridine (10:1). The crude product was purified by column chromatography (hexane / EtOAc / pyridine, 25:1:1) yielding the pure product as green oily solid (122 mg, 0.06 mmol, 31% yield).

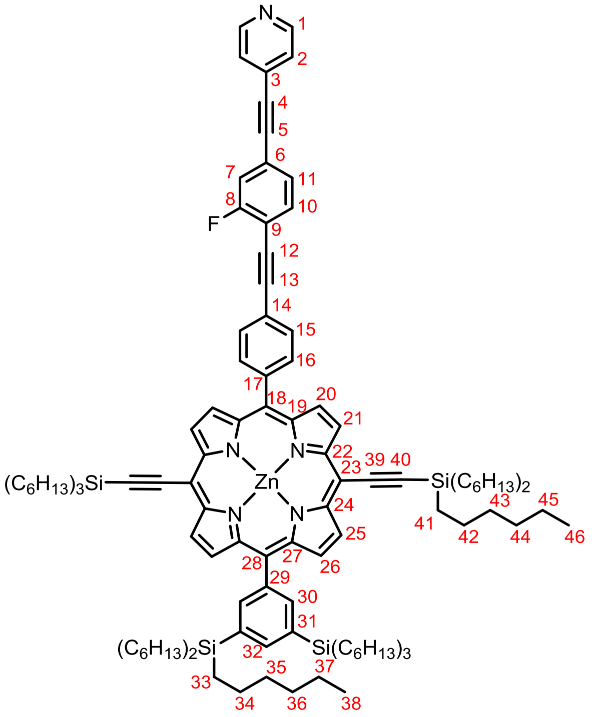

^{1}H NMR (400 MHz, $CDCl_3$, 10% pyridine-*d*$_5$) δ_H/ppm: 9.67 (d, *J* = 4.6 Hz, 2H, H25), 9.64 (d, *J* = 4.5 Hz, 2H, H21), 8.83 (d, *J* = 4.6 Hz, 2H, H26), 8.81 (d, *J* = 4.6 Hz, 2H, H20), 8.30 (d, *J* = 5.0 Hz, 2H, H1), 8.20 (s, 2H, H30), 8.19 (d, *J* = 8.2 Hz, 2H, H16), 7.97 (s, 1H, H32), 7.96 (d, *J* = 8.1 Hz, 2H, H15), 7.68 (t, *J* = 7.6 Hz, 1H, H11), 7.41–7.34 (m, 2H, H7 and H10), 7.32 (d *J* = 6.0 Hz, 2H, H2), 1.83–1.66 (m, 12H, H42), 1.58–1.43 (m, 24H, H34–35), 1.44–1.22 (m, 60H, H36–37 and H43–45), 1.05–0.97 (m, 12H, H41), 0.94–0.92 (m, 12H, H33), 0.92–0.81 (m, 36H, H38 and H46). **^{13}C NMR {^{1}H}** (101 MHz, $CDCl_3$, 10% pyridine-*d*$_5$) δ_C/ppm: 162.3 (d, *J* = 253.0 Hz, C8), 152.4 (C19 or C22 or C24 or C27), 152.3 (C19 or C22 or C24 or C27), 150.6 (C19 or C22 or C24 or C27), 149.7 (C19 or C22 or C24 or C27), 149.6 (C1), 143.9 (C17), 140.9, 140.5

(C30), 140.1 (C29), 139.1 (C32), 134.8 (C31), 134.7 (C16), 133.6 (d, *J* = 1.9 Hz, C11), 132.8 (C26), 132.0 (C20), 131.3 (C25), 131.0 (C21), 130.9 (C3), 130.0 (C15), 127.9 (d, *J* = 3.5 Hz, C10), 125.6 (C2), 124.1 (C28), 123.7 (d, *J* = 9.3 Hz, C6), 121.7 (C14 or C18), 121.0 (C18 or C14), 119.0 (d, *J* = 23.0 Hz, C7), 113.5 (d, *J* = 16.1 Hz, C9), 109.5 (C23), 101.2 (C39), 99.6 (C40), 97.1 (C13), 92.5 (d, *J* = 3.1 Hz, C12), 89.1 (C4), 83.3 (C5), 33.6 (C43), 33.5 (C35), 31.8 (C36 or C44), 31.7 (C44 or C36), 24.5 (C42), 24.1 (C34), 22.8 (C45 or C37), 22.8 (C37 or C45), 14.29 (C38 or C46), 14.27 (C46 or C38), 14.0 (C41), 12.8 (C33). **MS(MALDI-ToF)** m/z 1923.7906 (M^+, $C_{123}H_{178}FN_5Si_4Zn$ requires 1923.2462).

Straight-arm-containing porphyrin 4.19

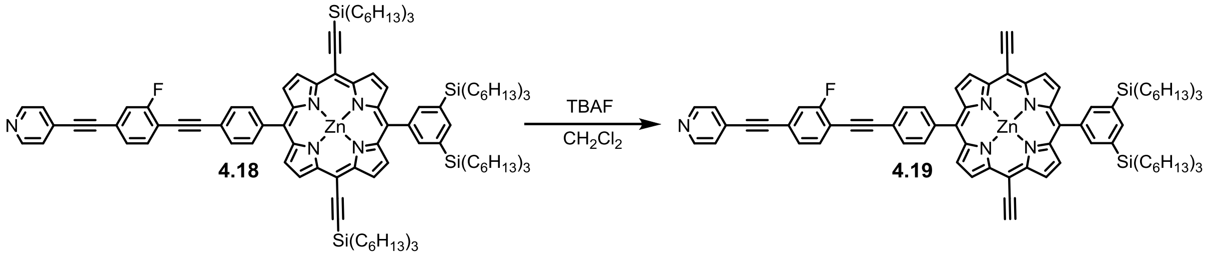

Porphyrin **4.18** (125 mg, 0.065 mmol) was dissolved in CH_2Cl_2 (50 mL). TBAF (0.7 mL, 1M in THF) was added and mixture was stirred for 4 h. The reaction was quenched with CH_3COOH (0.1 mL) and the solution was passed through short SiO_2 plug (CH_2Cl_2 / pyridine 5/1) and concentrated on rotatory evaporator. Excess of the NBu_4^+ was removed on short SEC column and the porphyrin fraction was dried yielding **4.19** as green solid (84 mg, 95% yield).

^{1}H NMR (400 MHz, $CDCl_3$ / 10% pyridine-*d*$_5$) δ_H/ppm: 9.62 (d, *J* = 4.6 Hz, 2H), 9.60 (d, *J* = 4.6 Hz, 2H), 8.81 (d, *J* = 4.4 Hz, 2H), 8.80 (d, *J* = 4.3 Hz, 2H), 8.25–8.20 (m, 2H), 8.14, 8.11 (d, *J* = 8.0 Hz, 2H), 7.92 (s, 1H), 7.89 (d, *J* = 8.0 Hz, 2H), 7.59 (t, *J* = 7.5 Hz, 1H), 7.33–7.22 (m, 5H), 4.12 (s, 1H), 1.58–1.46 (m, 12H), 1.37–1.27 (m, 12H), 1.27–1.15 (m, 24H), 0.91–0.85 (m, 12H), 0.84–0.77 (m, 18H). **^{13}C NMR {^{1}H}** (101 MHz, $CDCl_3$ / 10% pyridine-*d*$_5$) δ_C/ppm: 159.6 (d, *J* = 254.8 Hz), 152.21, 152.11, 150.6, 149.8, 149.3, 134.8, 134.6, 133.5, 130.0, 132.2, 131.1, 130.89, 130.88, 130.8, 129.9, 127.74, 127.71, 127.68, 125.5, 124.0 (d, *J* = 2.3 Hz), 118.7 (d, *J* = 28.1 Hz), 116.3 (d, *J* = 18.8 Hz), 99.4, 96.7, 92.4 (d, *J* = 7.5 Hz), 88.9, 86.5, 83.5, 83.3, 33.5, 31.6, 24.0, 22.9, 13.9, 12.6.

Bent-arm-containing porphyrin 4.31

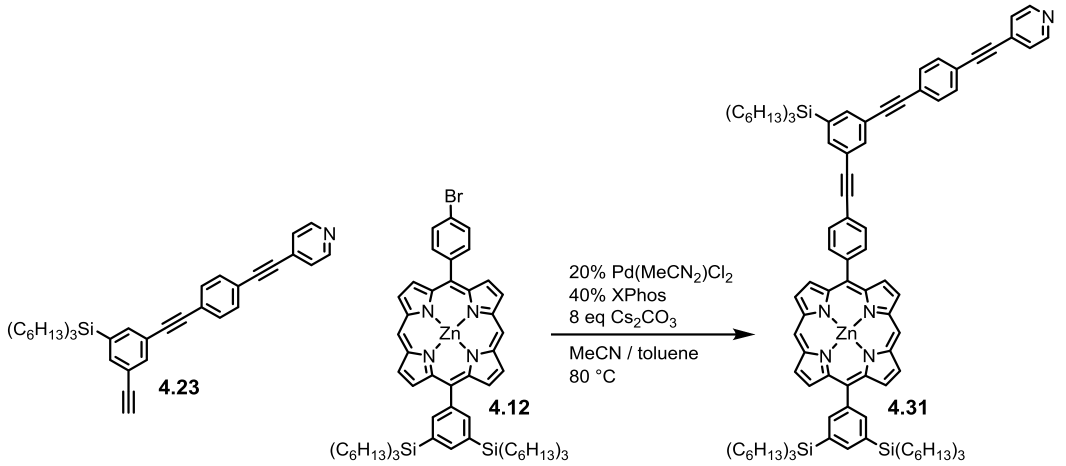

5-(4-Bromophenyl)-15-[3,5(trihexylsilyl)phenyl]porphyrin (**4.12**) (152 mg, 0.130 mmol, 1 equiv.), 4-((4-((3-ethynyl-5-(trihexylsilyl)phenyl)ethynyl)phenyl)ethynyl)pyridine (**4.23**) (152 mg, 0.259 mmol, 2 equiv.), Pd(CH$_3$CN)$_2$Cl$_2$ (6.8 mg, 28 µmol, 20% equiv.), Xphos (24.8 mg, 56 µmol, 40% equiv.) and Cs$_2$CO$_3$ (169 mg, 0.519 mmol, 4 equiv.) were placed into a Schlenk flask followed by CH$_3$CN (5 mL) and toluene (10 mL). The mixture was degassed by performing three freeze-thaw-pump cycles, and then stirred under nitrogen at 80°C for 1 h. The mixture was concentrated on rotatory evaporator, passed through short silica plug eluted with CH$_2$Cl$_2$ / pyridine (10/1). Crude product was purified on SEC column to give product as a red oil (209 mg, 0.12 mmol, 96% yield).

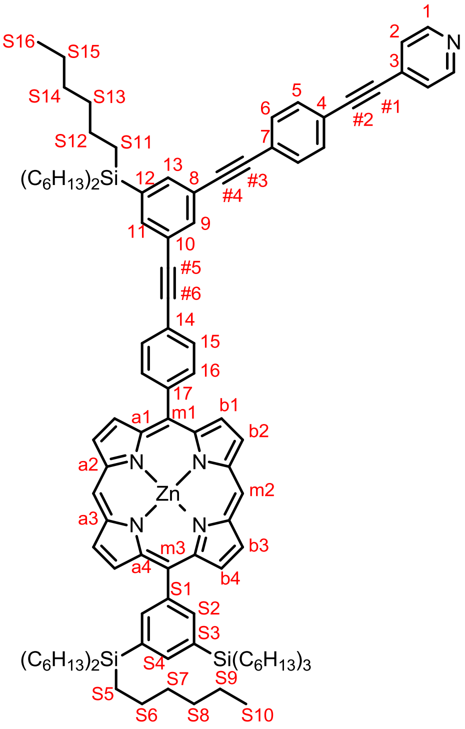

^{1}H NMR (400 MHz, CDCl$_3$, 10% pyridine-*d*$_5$) δ_H/ppm: 10.08 (s, 2H, Hm2), 9.24 (d, *J* = 4.5 Hz, 2H, Hb2), 9.23 (d, *J* = 4.4 Hz, 2H, Hb3), 8.99 (d, *J* = 4.4 Hz, 2H, Hb4), 8.93 (d, *J* = 4.4 Hz, 2H, Hb1), 8.28 (d, *J* = 5.1 Hz, 2H, H1), 8.23 (d, *J* = 6.0 Hz, 2H, HS2), 8.08 (d, *J* = 7.8 Hz, 2H, H16), 7.92 (s, 1H, HS4), 7.82 (d, *J* = 7.8 Hz, 2H, H15), 7.77 (s, 1H, H9), 7.71 (s, 1H, H11), 7.59 (s, 1H, H13), 7.42 (d, *J* = 8.2 Hz, 2H, H6), 7.36 (d, *J* = 8.1 Hz, 2H, H5), 7.11 (t, *J* = 6.1 Hz, 2H, H2), 1.45–1.05 (m, 60H, THS), 0.88–0.63 (m, 42H, THS). **^{13}C NMR {^{1}H}** (101 MHz, CDCl$_3$, 10% pyridine-*d*$_5$) δ_C/ppm: 150.0 (Ca1 and Ca4, 149.34 (C1), 149.30 (Ca2 and Ca3), 143.5 (C17), 141.1 (CS1), 140.7 (CS2), 139.3 (C12), 138.5 (CS4), 136.9 (C11), 136.5 (C13), 134.6 (C9 and C16), 134.3 (CS3), 132.1 (Cb4), 131.5 (C5), 131.4 (Cb1 and C6), 131.1 (Cb2 and Cb3), 130.7 (C3), 129.5

(C15), 125.1 (C2), 123.8 (C7), 121.6 (C4), 121.5 (C14), 120.8 (Cm3), 117.9 (Cm1), 105.6 (Cm2), 93.2 (C#2), 91.3 (C#4), 90.2 (C#6), 89.5 (C#5), 89.2 (C#3), 88.1 (C#1), 33.2 (CS7), 33.1 (CS13), 31.3 (CS14), 31.1 (CS8), 23.8 (CS6), 23.4 (CS12), 22.3 (CS9 and CS15), 13.9 (CS10 and CS16), 12.4 (CS5), 11.9 (CS11).

Bent-arm-containing porphyrin of 4.32

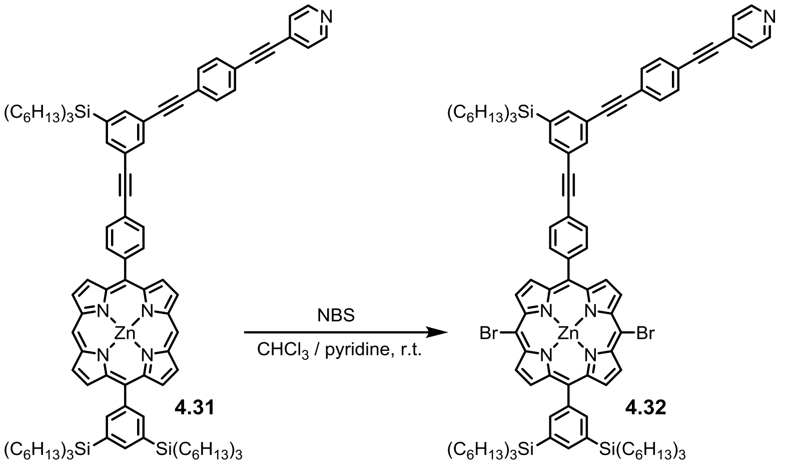

Porphyrin **4.31** (340 mg, 0.203 mmol, 1 equiv.) was dissolved in $CHCl_3$ (250 mL) and pyridine (10 mL). *N*-bromosuccinimide (92 mg, 0.52 mmol, 2 equiv.) in $CHCl_3$ (250 mL) was dropwise added to the porphyrin solution. After 10 min, acetone (5 mL) was added and the mixture was concentrated on rotatory evaporator and passed through short SiO_2 plug. Crude product was purified on SEC column and porphyrin fraction was dried yielding **4.32** as a green solid (340 mg, 0.186 mmol, 91% yield).

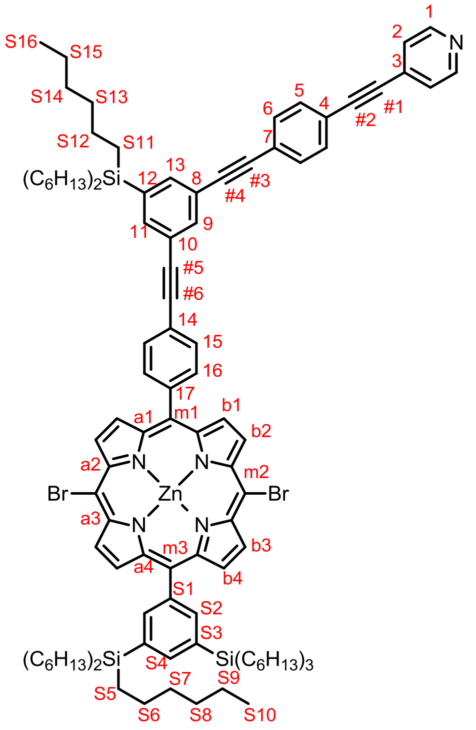

^{1}H NMR (500 MHz, $CDCl_3$, 10% pyridine-d_5) δ_H/ppm: 9.76 (d, J = 4.6 Hz, 2H, Hb3), 9.73 (d, J = 4.6 Hz, 2H, Hb2), 8.99 (d, J = 4.7 Hz, 2H, Hb4), 8.94 (d, J = 4.7 Hz, 2H, Hb1), 8.34 (s, 2H, HS2), 8.24 (d, J = 7.7 Hz, 2H, H16), 8.12 (s, 1H, HS4), 8.04 (d, J = 7.6 Hz, 1H, H15), 7.97 (s, 1H, H9), 7.90 (s, 1H, H11), 7.77 (s, 1H, H13), 7.53 (d, J = 8.1 Hz, 2H, H6), 7.33 (d, J = 8.0 Hz, 2H, H5), 6.76 (bs, 2H, H2), 1.68–1.55 (m, 12H, THS), 1.55–1.45 (m, 24H, THS), 1.46–1.32 (m, 36H, THS), 1.14–1.02 (m, 12H, THS), 1.02–0.85 (m, 33H, THS). **^{13}C NMR {^{1}H}** (126 MHz, $CDCl_3$, 10% pyridine-d_5) δ_C/ppm: 151.2 (Ca4), 150.5 (Ca), 150.3 (Ca), 150.1 (Ca), 147.1 (C1), 143.2 (C17), 140.9 (CS2), 139.7 (CS1), 139.2 (CS4), 137.3 (C11), 137.0 (C13), 135.0 (C12), 134.83 (C16), 134.78 (S3), 133.6 (Cb4), 133.2 (Cb1), 132.9 (Cb2 and Cb3), 131.7 (C5), 131.6 (C6), 131.2 (C3), 129.9 (C15), 125.3 (C2), 124.2 (C7), 123.7 (Cm3), 123.2 (C8), 122.7 (C10), 122.4 (Cm1), 121.5 (C4), 120.6 (C14), 105.0 (Cm2), 94.1 (C#2), 91.8 (C#4), 90.23 (C#6), 90.20 (C#5), 89.4 (C#3), 87.8 (C#1), 33.7 (CS7), 33.6 (CS13), 31.8 (CS18), 31.6 (CS14), 24.2 (CS6), 23.8 (CS12), 22.8 (CS9 and CS15), 14.3 (CS10 CS16), 12.8 (CS5), 12.3 (CS11). **UV/vis** (toluene): λ_{max} (ε) = 610 (8.57), 568 (13.0), 434 nm (271 $\times 10^3$ M^{-1} cm^{-1}). **MS(MALDI-ToF)** m/z 1833.42 (M^+, $C_{149}H_{221}N_5Si_2Zn$ requires 1832.83).

Bent-arm-containing porphyrin 4.33

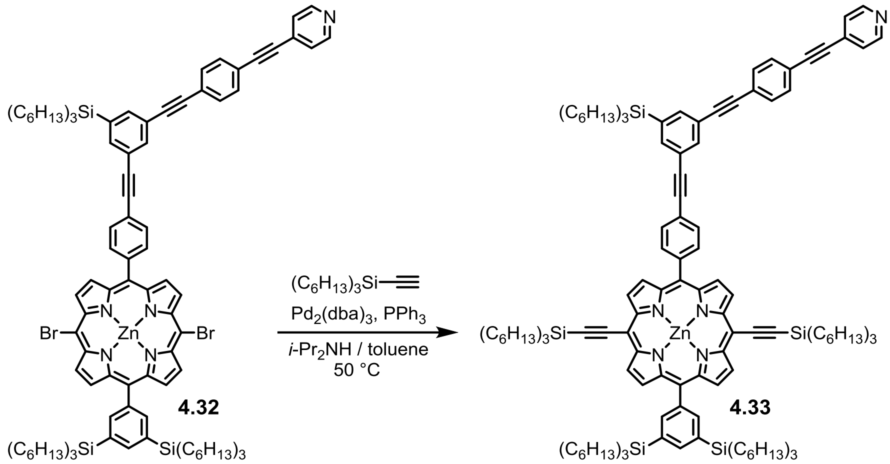

Dibromoporphyrin **4.32** (3.0 g, 1.6 mmol, 1 equiv.), $Pd_2(dba)_3$ (150 mg, 0.16 mmol, 10% equiv.), PPh_3 (86 mg, 0.33 mmol, 20% equiv.), CuI (53 mg, 0.33 mmol, 20% mmol), i-Pr_2NH (20 mL) and toluene (150 mL) were placed to a flask and degassed by performing three freeze-pump-thaw cycles. Ethynyltrihexylsilane (2.5 mL) was added and mixture was warmed up to 60 °C. Reaction progress was monitored by TLC (Petrol ether / EtOAc / pyridine, 10:1:1). After 2h, full conversion was observed, and the solution was concentrated and passed through short SiO_2 plug eluting with CH_2Cl_2/pyridine (10/1). The mixture was concentrated on rotatory evaporator and purified on SEC column and dried yielding **4.33** as green oil (2.6 g, 1.1 mmol, 69% yield).

^{1}H NMR (500 MHz, $CDCl_3$, 10% pyridine-d_5) δ_H/ppm: 9.72 (d, J = 4.5 Hz, 2H, Hb2 or Hb3), 9.69 (d, J = 4.4 Hz, 2H, Hb3 or Hb2), 8.89 (d, J = 4.5 Hz, 2H, Hb1), 8.86 (d, J = 4.6 Hz, 2H, Hb4), 8.25 (s, 2H, HS2), 8.23 (d, J = 8.1 Hz, 2H, H16), 8.02 (s, 1H, HS4), 8.00 (d, J = 8.1 Hz, 2H, H15), 7.91 (t, J = 1.7 Hz, 1H, H9), 7.82 (t, J = 1.6 Hz, 1H, H11), 7.70 (t, J = 1.7, 0.8 Hz, 1H, H13), 7.63–7.60 (m, 2H, H6), 7.56 (s, 2H, H1), 7.53 (d, J = 8.5 Hz, 2H, H5), 7.09 (d, J = 5.3 Hz, 1H, H2), 1.81 (tt, J = 8.0, 6.2 Hz, 12H, S18), 1.62–1.49 (m, 12H, S19), 1.48–

1.29 (m, 57H, THS), 1.09–1.03 (m, 12H, HS17), 1.01–0.87 (m, 63H, THS). **^{13}C NMR {^{1}H}** (126 MHz, CDCl$_3$, 10% pyridine-d_5) δ_C/ppm: 152.40 (Ca), 152.36 (Ca), 150.6 (Ca), 149.8 (Ca), 148.7 (C1), 143.4 (C17), 141.0 (CS1), 140.5 (CS2), 139.7 (C12), 139.1 (CS4), 137.3 (C11), 137.0 (C13), 135.0 (C9), 134.8 (C16), 134.7 (CS3), 132.8 (Cb4), 132.1 (Cb1), 132.0 (C5), 131.8 (C6), 131.33 (C3), 131.27 (Cb2 or b3), 131.0 (Cb3 or Cb2), 129.9 (C15), 125.4 (C2), 124.3 (C7), 124.0 (C8 or C10 or Cm1 or Cm3), 123.3 (C8 or C10 or Cm1 or Cm3), 122.7 (C8 or C10 or Cm1 or Cm3) , 121.9 (C4), 121.2 (C8 or C10 or Cm1 or Cm3), 109.5 (Cm2), 101.2 (C#7), 99.6 (C#8), 93.9 (C#2), 91.8 (C#4), 90.3 (C#6), 90.0 (C#5), 89.5 (C#3), 88.2 (C#1), 33.64 (CS7), 33.58 (CS13), 33.50 (CS19), 31.8 (CS20), 31.7 (CS8), 31.6 (CS14), 24.5 (CS18), 24.2 (CS6), 23.8 (CS12), 22.83 (CS21), 22.81 (CS15), 22.78 (CS9), 14.3 (CS10 and CS16 and CS22), 14.0 (CS17), 12.8 (CS5), 12.4 (CS11). **UV/vis** (toluene): λ_{max} (ε) = 638 (37.8), 589 (13.8), 453 (249), 440 nm (339 ×10^3 M^{-1} cm^{-1}). **MS(MALDI-ToF)** m/z 2287.56 (M$^+$, $C_{149}H_{221}N_5Si_2Zn$ requires 2287.09).

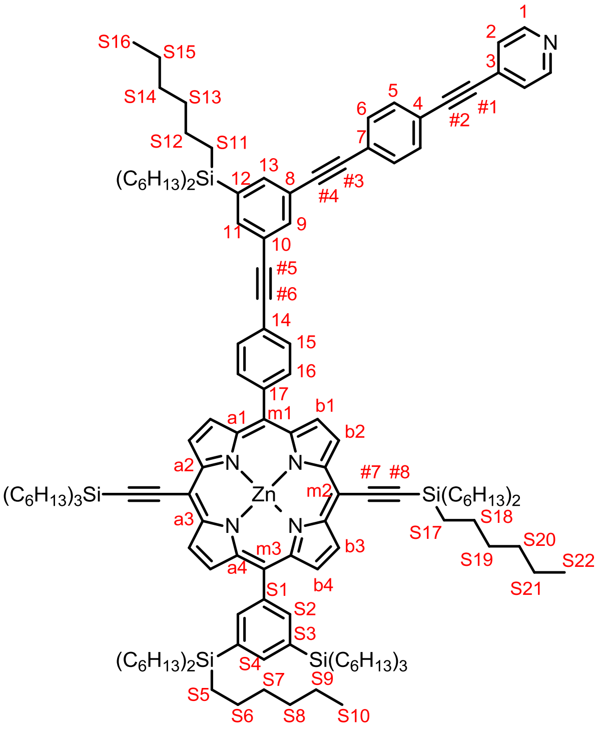

Bent-arm-containing porphyrin 4.34

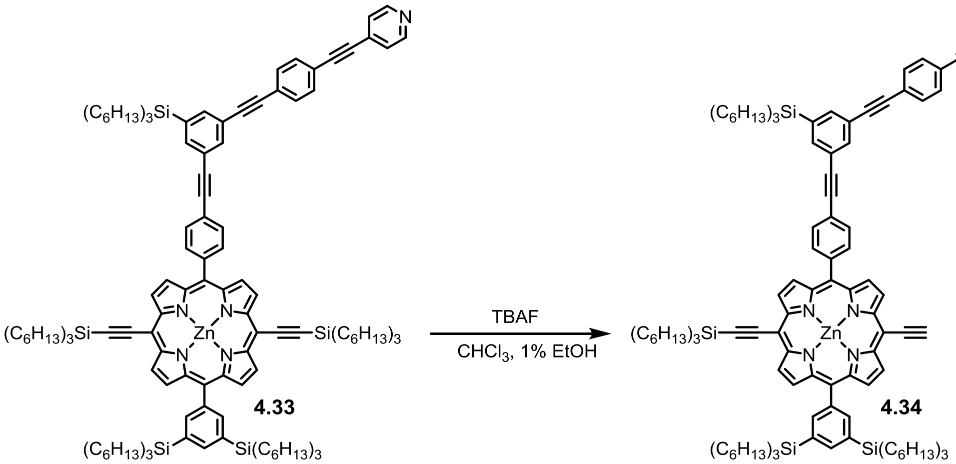

Porphyrin **4.33** (1150 mg, 0.503 mmol) was dissolved in CHCl$_3$ (300 mL) and EtOH (3 mL). TBAF (1M solution in THF, 4 mL, 4 mmol) was added and the mixture was stirred at room temperature and monitored by TLC (Petrol / EtOAc / pyridine, 10:1:1). After 4h, the desired ratio ~1:1 of mono- and bis-protected porphyrins **4.33**/**4.34** was found and the reaction was reaction was quenched with AcOH (0.3 mL) and immediately passed through SiO$_2$ plug. The mixture was purified on SiO$_2$ using gradient increate of eluent polarity (Petrol ether / EtOAc / pyridine, 40:1:1 → 10:1:1) yielding **4.34** as a green oil (270 mg, 0.13 mmol, 27%).

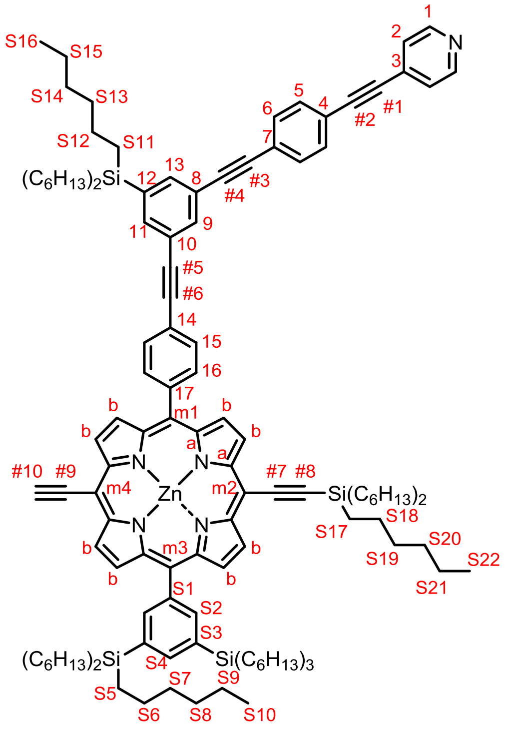

^{1}H NMR (500 MHz, CDCl$_3$, 10% pyridine-d_5) δ$_H$/ppm: 9.81–9.68 (m, 4H, Hb), 8.96–8.84 (m, 4H, Hb), 8.28 (s, 2H, HS2), 8.24 (d, J = 7.8 Hz, 2H, H16), 8.05 (s, 1H, HS4), 8.01 (d, J = 7.8 Hz, 2H, H15), 7.92 (s, 1H, H9), 7.84 (s, 1H, H11), 7.72 (s, 1H, H13), 7.61 (d, J = 8.2 Hz, 2H, H6), 7.51 (d, J = 8.2 Hz, 2H, H5), 7.45–7.35 (m, 2H, H1), 7.04 (d, J = 5.3 Hz, 2H, H2), 4.19 (s, 1H, H#10), 1.87–1.77 (m, 12H, THS), 1.62–0.76 (m, 144H, THS). **^{13}C NMR {^{1}H}** (126 MHz, CDCl$_3$, 10% pyridine-d_5) δ$_C$/ppm: 152.43 (Ca), 152.38 (Ca), 152.35 (Ca), 152.34 (Ca), 150.70 (Ca), 150.69 (Ca), 149.92 (Ca), 149.91 (Ca), 148.5(C1), 143.3 (C17), 140.9 (CS1), 140.1 (CS2), 139.7 (C12), 139.1 (CS4), 137.3 (C11), 137.0 (C13), 135.0, 134.80 (CS3), 134.75 (C16), 133.1 (Cb), 132.8 (Cb), 132.3 (Cb), 132.1 (Cb), 131.9 (C5), 131.8 (C6), 131.4 (Cb), 131.3 (C3), 131.14 (Cb), 131.14 (Cb), 130.9 (Cb), 129.9 (C15), 125.3 (C2), 124.3 (C7), 124.1 (Cm3), 123.3 (C8), 122.7 (C10), 121.9 (C4), 121.2 (Cm1 and C14), 109.5 (Cm2), 101.5 (C#7), 99.8 (C#8), 99.3 (Cm4), 93.9 (C#2), 91.8 (C#4), 90.3 (C#6), 90.1 (C#5), 89.5 (C#3), 88.2 (C#1), 86.9 (C#9), 83.4 (C#10), 33.7 (CS7), 33.6 (CS13), 33.5 (CS19), 31.79 (CS20), 31.75 (CS8), 31.6 (CS14), 24.5 (CS18), 24.2 (CS6), 23.8 (CS12), 22.82 (CS9 and CS15 and CS21), 22.79 (CS9 and CS15 and CS21), 14.31 (CS9 and CS15 and CS21), 14.30 (CS9 and CS15 and CS21), 14.0 (CS17), 12.8 (CS5), 12.4 (CS11). **MS(MALDI-ToF)** m/z 2010 (M$^+$, $C_{131}H_{183}N_5Si_4Zn$ requires 2003).

4.7.4. Porphyrin oligomers

Precursor for *c*-P6$^{(1arm)}$ 4.21

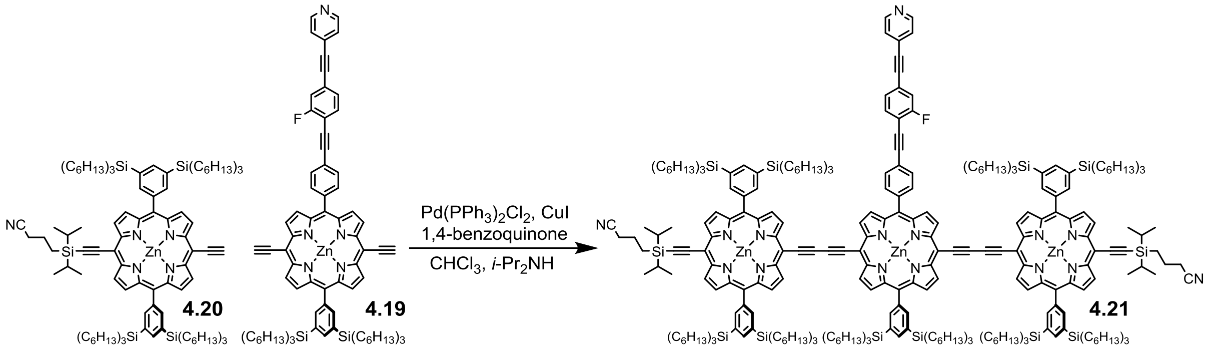

Porphyrin **4.19** (140 mg, 0.103 mmol, 1 equiv.), porphyrin **4.20** (1.37 g, 0.727 mmol, 7 equiv.) and 1,4-benzoquinone (220 mg, 2.04 mmol, 20 equiv.) were dissolved in $CHCl_3$ (250 mL) and *i*-Pr_2NH (10 mL). $Pd(PPh_3)_2Cl_2$ (70 mg, 0.1 mmol, 1 equiv.) and CuI (100 mg, 0.526 mmol, 5 equiv.) dispersed in $CHCl_3$ (4 mL) and *i*-Pr_2NH (4 mL) was added and the mixture was stirred at ambient temperature overnight. The mixture was concentrated on rotatory evaporator, filtrated through cotton (toluene / 1% pyridine) and pre-purified by short size-exclusion chromatography on Biobeads SX-1 (toluene / 1% pyridine). Crude product was purified by recycling GPC yielding **4.21** as green-brown solid (320 mg, 0.06 mmol, 62% yield).

^{1}H NMR (400 MHz, $CDCl_3$, 10% pyridine-d_5) δ_H/ppm: 9.94–9.75 (m, 8H, HAb1 and HAb1' and HBb1), 9.64 (d, *J* = 4.5 Hz, 4H, HBb1'), 9.00–8.89 (m, 8H, HAb2 and HAb2' and HBb2), 8.86 (d, *J* = 4.5 Hz, 4H, HBb2'), 8.29 (d, *J* = 5.8 Hz, 2H, H12), 8.26 (s, 10H, HS2), 8.01 (d, *J* = 8.0 Hz, 4H, H1 and H11), 8.00 (s, 5H, HS4), 7.69 (t, *J* = 7.6 Hz, 1H, H9), 7.38 (t, *J* = 9.3 Hz, 2H, H5 and H8), 7.31 (d, *J* = 5.3 Hz, 2H, H11), 2.56 (t, *J* = 6.8 Hz, 4H, H18), 2.27–2.16 (m, 4H, H17), 2.14–1–0.85 (m, 266H, THS). **^{13}C NMR {^{1}H}** (101 MHz, $CDCl_3$, 10% pyridine-d_5) δ_C/ppm: 162.4 (d, *J* = 252.9 Hz, C6), 153.18 (CAa), 153.15 (CAa), 153.08 (CBa), 152.2 (CBa), 150.79 (CBa), 150.71 (CAa), 150.4 (CBa), 149.8 (CAa), 149.4 (C1), 140.9 (CS1), 140.6 (CS2), 139.2 (CS4), 135.0 (C12), 134.9 (CS3), 133.6 (d, *J* = 2.0 Hz, C9), 133.4 (Cb2), 133.3 (Cb2), 132.9 (Cb2), 132.6 (Cb2), 131.2 (Cb1), 130.9 (Cb1), 130.8 (Cb1), 130.7 (Cβ1), 130.2 (C11), 127.9 (d, *J* = 3.5 Hz, C8), 125.5 (C2), 124.4 (Cm1), 122.0 (d, *J* = 24.4 Hz), 118.9 (d, *J* = 22.8 Hz, C19), 113.5 (d, *J* = 16.1 Hz, C4), 111.2, 101.0 (Cm2), 100.6 (Cm2), 99.6 (Cm2), 97.1 (d, *J* = 2.8 Hz, C#4), 96.3 (C#10), 92.5 (d, *J* = 2.5 Hz, C#3), 89.0 (C#1), 88.8 (C#), 88.2 (C#), 83.4 (C#2), 82.9 (C#), 82.4 (C#), 33.7 (CS7), 31.8 (CS8), 24.2 (CS6), 22.8 (CS9), 21.8 (CS17), 21.2 (CS18), 18.8 (C15), 18.5 (C15), 14.3 (CS10), 12.8 (CS5), 12.5 (C14), 10.3 (C16). **UV/vis** (toluene): λ_{max} (ε) = 728 (133), 580 (332), 492 (217), 462 nm

(510 ×10^3 M^{-1} cm^{-1}). **MS(MALDI-ToF)** m/z 5131.8 (M^+, $C_{83}H_{100}Br_2FN_5Si_2Zn$ requires 5125.3).

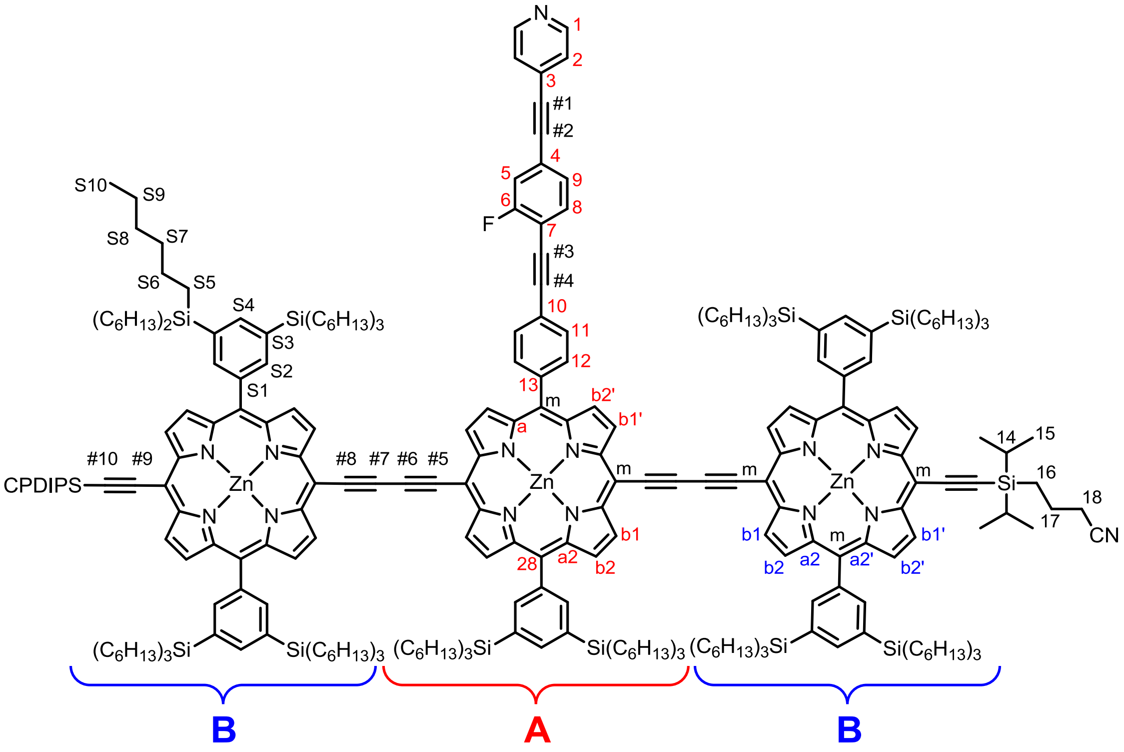

Precursor for *c*-P6$^{(1arm)}$ 4.22

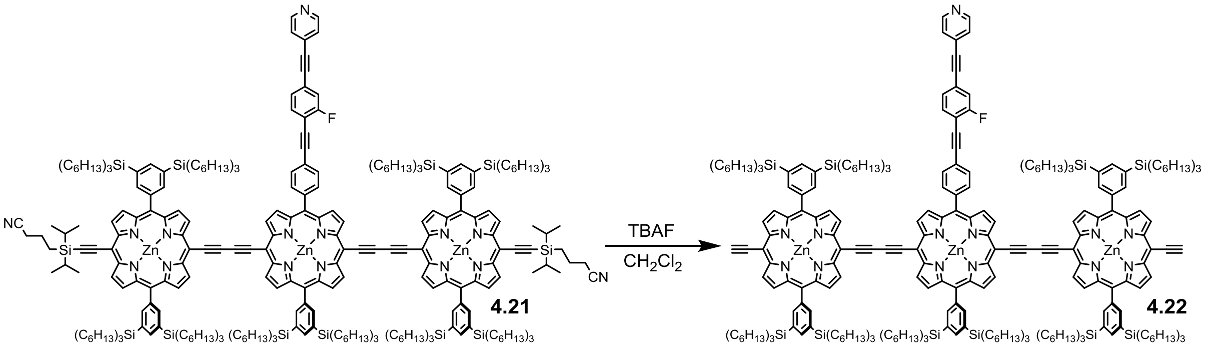

Porphyrin trimer **4.21** (50 mg, 0.01 mmol) was dissolved in CH_2Cl_2 (40 mL), TBAF (1.0 M solution in THF, 1 mL, 1 mmol) was added to a solution and the reaction mixture was stirred at ambient temperature for 4 h. Then CH_3COOH (100 µL, 1.7 mmol) was added. The reaction mixture was passed through a short silica gel plug (CH_2Cl_2 / pyridine 20%) and short SEC using $CHCl_3$ as an eluent. The solution was concentrated and dried on vacuum to yield product **4.22** as green-brown solid (40 mg, 86%).

^{1}H NMR (400 MHz, $CDCl_3$, 10% pyridine-d_5) δ_H/ppm: 9.94–9.87 (m, 8H, HAb1’ and HAb1 and HBb1), 9.68 (d, *J* = 4.6 Hz, 4H, HBb1’), 9.00–8.91 (m, 8H, HAb2 and HAb2’ and HBb2), 8.88 (d, *J* = 4.5 Hz, 4H, HBb2’), 8.30 (d, *J* = 8.0 Hz, 2H, H12), 8.28 (s, 10H, HS2), 8.16–8.11 (m, 2H, H1), 8.02 (d, *J* = 7.3 Hz, 2H, H11), 8.01 (s, 5H, HS4), 7.68 (t, *J* = 7.6 Hz, 1H, H9), 7.38 (t, *J* = 8.6 Hz, 2H, H5 and H8), 7.28 (d, *J* = 5.2 Hz, 2H, H2), 4.18 (s, 2H, H10), 1.56–1.24 (m, 240H, THS), 1.01–0.83 (m, 150H, THS). **^{13}C NMR {^{1}H}** (101 MHz, $CDCl_3$, 10% pyridine-d_5) δ_C/ppm: 161.2 (d, *J* = 252.7 Hz, C6), 152.02 (CAa), 151.99 (CAa), 151.86 (CBa), 151.1 (CBa), 149.7 (CBa), 149.6 (CAa), 149.3 (CBa), 148.7, 148.3 (C1), 139.73 (CS2), 139.67 (CS1), 138.0 (CS4), 133.8 (CS3), 133.6 (C12), 132.5 (d, *J* = 1.7 Hz, C9), 132.2 (Cb2), 132.1 (Cb2), 131.8 (Cb2), 130.0 (Cb1), 129.8 (Cb1), 129.6 (Cb1), 129.0 (C11), 126.7 (d, *J* = 3.5 Hz, C8), 124.4 (C2), 124.1 (CAm3), 123.1 (CAm1 and CBm2), 120.9 (d, *J* = 23.8 Hz, C7), 117.8 (d, *J* = 22.9 Hz, C5), 112.4 (d, *J* = 16.0 Hz, C4), 99.4 (CAm2 or CBm1), 98.8 (CBm3), 98.4 (CAm2 or CBm1), 95.9 (C#4), 91.4 (d, *J* = 2.8 Hz, C3), 87.8 (C#), 87.6 (C#), 87.0 (C#), 85.7 (C#), 82.4 (C#), 82.3 (C#), 81.7 (C#), 81.2 (C#), 32.5 (CS7), 30.6 (CS8), 23.0 (CS6), 21.7 (CS9), 13.2 (CS10), 11.7 (CS5). **MS(MALDI-ToF)** m/z 4776.0 (M^+, $C_{303}H_{442}FN_{13}Si_{10}Zn_3$ requires 4762.1).

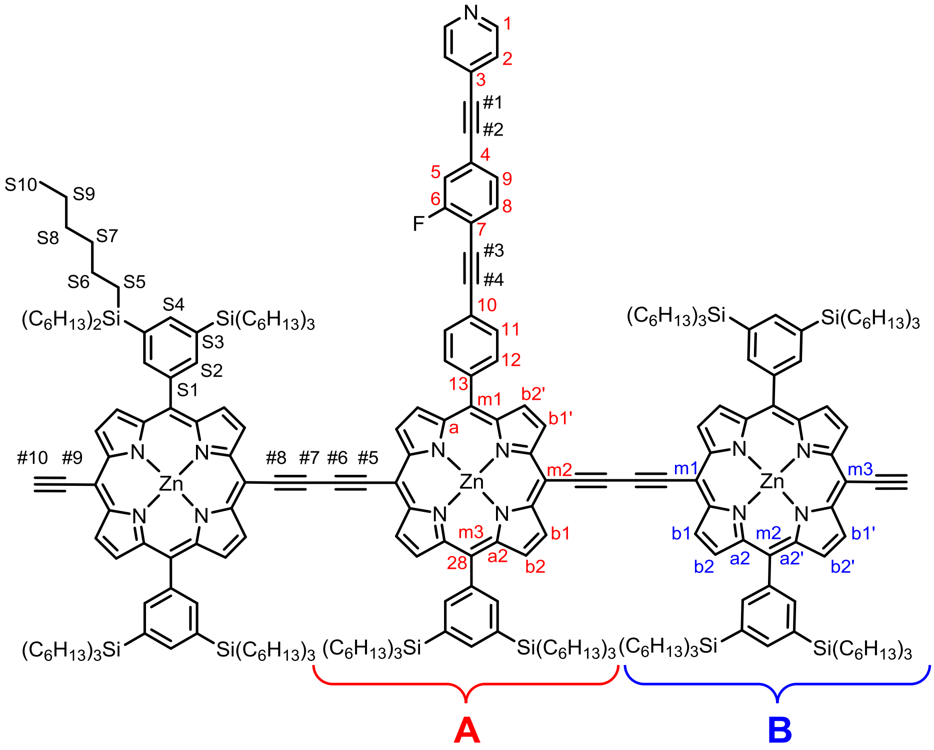

Precursor for *c*-P6$^{(3arm)}$ 4.35

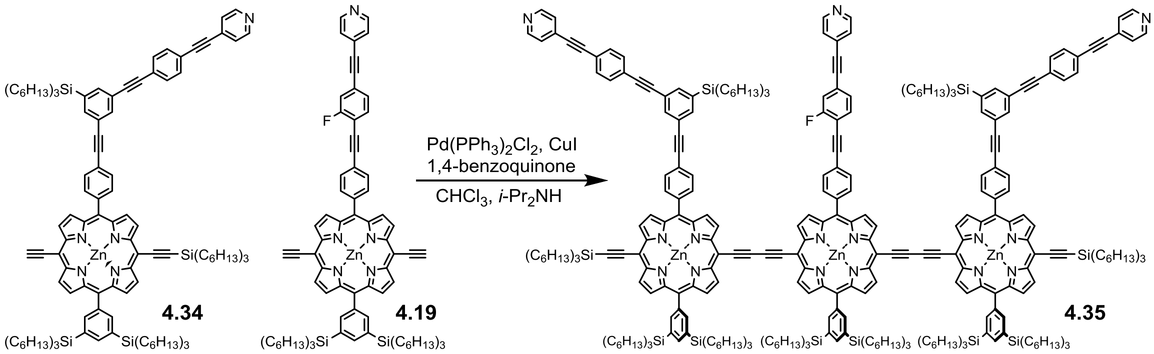

Monodeprotected porphyrin **4.34** (270 mg, 0.13 mmol), deprotected porphyrin **4.19** (80 mg, 0.06 mmol) and 1,4-benzoquinone (1 g) were dissolved in CHCl$_3$ (60 mL) and *i*-Pr$_2$NH (10 mL). Solution of Pd(PPh$_3$)$_2$Cl$_2$ (50 mg, 0.07 mmol) and CuI (50 mg, 0.26 mmol) in CHCl$_3$/*i*-Pr$_2$NH (1:1, 10 mL) was added to the porphyrins solution and the mixture was stirred at room temperature for 16 h. The mixture was then filtered through cotton and passed through SEC (~30 g) column using toluene as an eluent to remove excess of 1,4-benzoquinone and filter out poorly soluble polymers. The mixture was purified on recycling GPC yielding the desired porphyrin trimer **4.35** as a green solid (70 mg, 0.013 mmol, 21% yield relative to central part).

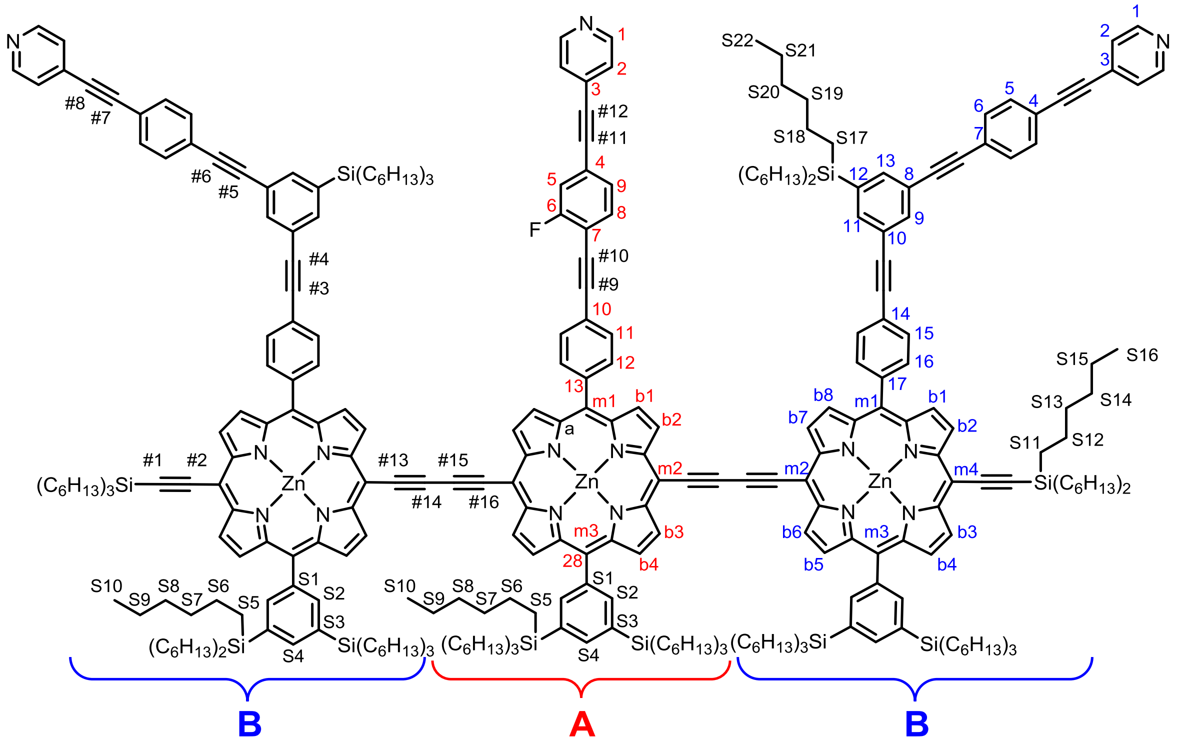

^{1}H NMR (500 MHz, CDCl$_3$, 10% pyridine-d_5) δ$_H$/ppm: 9.91 (d, *J* = 2.6 Hz, 2H, HBb7), 9.90 (d, *J* = 2.6 Hz, 2H, HAb2), 9.89 (d, *J* = 4.3 Hz, 2H, HAb3), 9.88 (d, *J* = 4.1 Hz, 2H, HBb6), 9.68 (d, *J* = 4.5 Hz, 2H, HBb2), 9.66 (d, *J* = 4.5 Hz, 2H, HBb3), 8.96 (d, *J* = 3.1 Hz, 2H, HAb1–4 or HBb5–8), 8.95 (d, *J* = 3.2 Hz, 2H, HAb1–4 or HBb5–8), 8.94 (d, *J* = 4.7 Hz, 2H, HAb1–4 or HBb5–8), 8.94 (d, *J* = 5.0 Hz, 2H, HAb1–4 or HBb5–8), 8.85 (d, *J* = 4.5 Hz, 2H, HBb1), 8.84 (d, *J* = 4.5 Hz, 2H, HBb4), 8.39 (bd, *J* = 3.3 Hz, 2H, HA1), 8.36 (bd, *J* = 3.1 Hz, 4H, HA2), 8.30 (s, 3H, HAS2), 8.27 (d, *J* = 8.2 Hz, 3H, HA12), 8.25 (s, 6H, HBS2), 8.23 (d, *J* = 8.1 Hz, 4H, HB16), 8.01 (d, *J* = 8.9 Hz, 4H, HS4), 7.98 (d, *J* = 8.1 Hz, 6H, HA11 and HB15), 7.87 (t, *J* = 1.6 Hz, 2H, HB9), 7.77 (bt, *J* = 1.1 Hz, 2H, HB11), 7.68 (t, *J* = 6.9 Hz, 1H, HA9), 7.66 (bt, *J* = 1.2 Hz, 2H, HB13), 7.60 (d, *J* = 8.5 Hz, 4H, HB6), 7.55 (d, *J* = 8.5 Hz, 4H, HB5), 7.39 (dd, *J* = 7.9, 1.3 Hz, 1H, HA8), 7.37 (dd, *J* = 9.5, 1.3 Hz, 1H, HA5), 7.34 (d, *J* = 5.8 Hz, 2H, HA2), 7.32 (d, *J* = 5.9 Hz, 4H, HB2), 1.77 (ddd, *J* = 11.7, 10.1, 6.3 Hz, 12H, HS12), 1.58–1.51 (m, 12H, HS13), 1.51–1.46 (m, 36H, HS6), 1.43–1.33 (m, 72H, HS9 and HS15 and HS18 and HS21), 1.36–1.26 (m, 108H, HS8–9 and HS14–15 and HS20–21), 1.07–1.00 (m, 12H, HS11), 0.99–0.84 (m, 138H, HS6 and HS10 and HS16–17 and HS22). **^{13}C NMR {^{1}H}** (126 MHz, $CDCl_3$, 10% pyridine-d_5) δ_C/ppm: 162.35 (d, *J* = 252.8 Hz, CA6), 153.18 (Ca), 153.17 (Ca), 153.13 (Ca), 153.11 (Ca), 152.41 (Ca), 152.37 (Ca), 150.9 (Ca), 150.7 (Ca), 150.4 (Ca), 150.10 (Ca), 149.8 (Ca), 149.7 (CA1), 149.64 (CB1), 149.5 (Ca), 143.6 (CA13), 143.2 (CB17), 140.9 (CAS2), 140.8 (CS1), 140.7 (CBS2), 139.7 (CB12), 139.3 (CS4), 139.2 (CS4), 137.3 (CB11), 137.0 (CB13), 135.01 (CS3), 134.97 (CB9), 134.87 (CS3), 134.76 (BA12), 134.74 (CB16), 133.7 (CA9), 133.42 (CBb5, CBb8, CAb1, CAb4), 133.35 (CBb5, CBb8, CAb1, CAb4), 132.8 (CBb5, CBb8, CAb1, CAb4), 132.7 (CBb5, CBb8, CAb1, CAb4), 132.6 (CBb4), 132.2 (CBb1), 132.0 (CB5), 131.9 (CB6), 131.4 (Cb2–3, Cb6–7, C3), 131.3 (Cb2–3, Cb6–7, C3), 131.2 (Cb2–3, Cb6–7, C3), 131.0 (Cb2–3, Cb6–7, C3), 130.9 (Cb2–3, Cb6–7, C3), 130.8 (Cb2–3, Cb6–7, C3), 130.7 (Cb2–3, Cb6–7, C3), 130.1 (CA11), 130.0 (CB15), 127.85 (d, *J* = 3.3 Hz, CA8), 125.70 (CA2 or CB2) , 125.67 (CA2 or CB2), 124.2 (CA7), 123.46 (CA4, CA10, CB8, CB10, CB14), 123.30 (CA4, CA10, CB8, CB10, CB14), 123.11 (CA4, CA10, CB8, CB10, CB14), 123.01 (CA4, CA10, CB8, CB10, CB14), 122.0 (CA4), 118.9 (d, *J* = 22.9 Hz, CA4), 113.5 (d, *J* = 16.2 Hz, CA7), 109.39 (Cm2, Cm4), 109.35 (Cm2, Cm4), 102.1 (C#2 or C#13 or C#16), 100.5 (C#2 or C#13 or C#16), 100.1 (C#1), 99.5 (C#2 or C#13 or C#16), 97.0 (d, *J* = 4.8 Hz, C#9), 93.7 (C#7), 92.5 (C#10), 91.7 (C#5), 90.2 (C#3), 90.1 (C#4), 89.4 (C#6), 88.8 (C#12), 88.5 (C#8), 83.4 (C#11), 82.8 (C#14 or C#15), 82.4 (C#14 or C#15), 33.67 (CAS7), 33.65 (CBS7), 33.56 (CS19), 33.48 (CS13), 31.77 (CAS8, CS14), 31.74 (CBS8), 31.61 (CS20), 24.5 (CS12), 24.18 (CAS6), 24.17 (CBS6), 23.8 (CS18), 22.80 (CS9, CS15, CS21), 22.78 (CS9, CS15, CS21), 14.3 (CS10, CS16, CS22), 14.0 (CS11), 12.8 (CS6), 12.3 (CS17). **^{19}F NMR {^{1}H}** (471 MHz, $CDCl_3$, 10% pyridine-d_5) δ_F/ppm: −109.15. **MS(MALDI-ToF)**, high-resolution measurement at EPSRC UK NMSF, Swansea, m/z 5365.3 (M^+, $C_{349}H_{464}FN_{15}Si_{10}Zn_3$ requires 5365.2).

Precursor for *c*-P6$^{(3arm)}$ 4.36

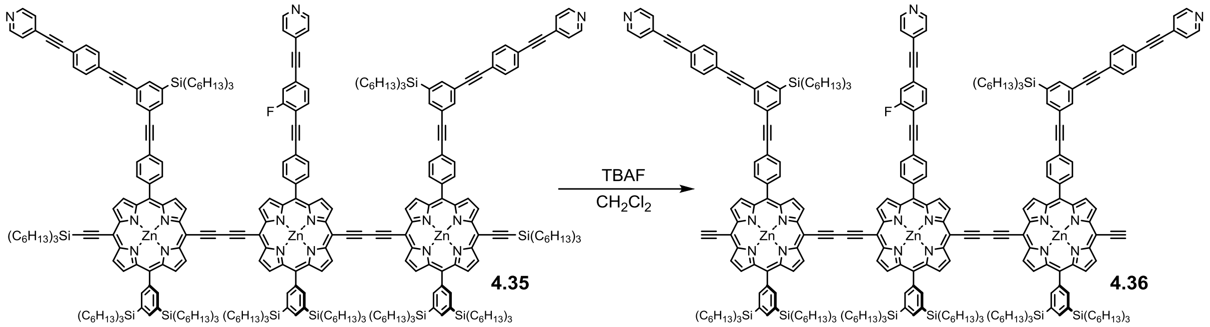

Porphyrin trimer **4.35** (40 mg, 0.007 mmol) was dissolved in CH_2Cl_2 (15 mL). TBAF (1.0 M solution in THF, 70 µL, 0.07 mmol) was added to a solution and the reaction mixture was stirred at ambient temperature for 1h. The reaction was quenched by addition of CH_3COOH (50 µL, 8.5 mmol). The solution was concentrated on rotatory evaporator and passed through a short silica gel plug (CH_2Cl_2 / pyridine (5:1)) and SEC column. Dried **4.36** was obtained as a green-brown solid (35 mg, 98%) and was used immediately for the next reaction.

^{1}H NMR (500 MHz, $CDCl_3$, 10% pyridine-d_5) δ_H/ppm: 9.92 (d, J = 4.5 Hz, 2H), 9.91 (d, J = 4.7 Hz, 2H), 9.90 (d, J = 4.6 Hz, 2H), 9.89 (d, J = 4.6 Hz, 2H), 9.69 (d, J = 4.6 Hz, 2H), 9.67 (d, J = 4.5 Hz, 2H), 8.97 (d, J = 2.4 Hz, 2H), 8.96 (d, J = 1.9 Hz, 2H), 8.95 (d, J = 1.9 Hz, 2H), 8.94 (d, J = 4.6 Hz, 2H), 8.88 (d, J = 3.8 Hz, 2H), 8.87 (d, J = 3.5 Hz, 2H), 8.45 (d, J = 5.2 Hz, 2H), 8.42 (d, J = 5.2 Hz, 4H), 8.29 (s, 3H), 8.30–8.25 (m, 2H), 8.26 (s, 6H), 8.25–8.20 (m, 4H), 8.03–7.98 (m, 2H), 7.98 (d, J = 8.1 Hz, 4H), 7.86 (t, J = 1.7 Hz, 2H), 7.77 (bt, J = 1.3 Hz, 2H), 7.71–7.64 (m, 1H), 7.65 (bt, J = 1.4 Hz, 2H), 7.60 (d, J = 8.2 Hz, 4H), 7.55 (d, J = 8.3 Hz, 4H), 7.41–7.36 (m, 2H), 7.38–7.33 (m, 2H), 7.34–7.31 (m, 4H), 4.18 (s, 2H), 1.54–0.80 (m, 312H). **MS(MALDI-ToF)** m/z 4796.7 (M^+, $C_{313}H_{388}FN_{15}Si_8Zn_3$ requires 4796.2).

Linear protected oligomer *l*-P3

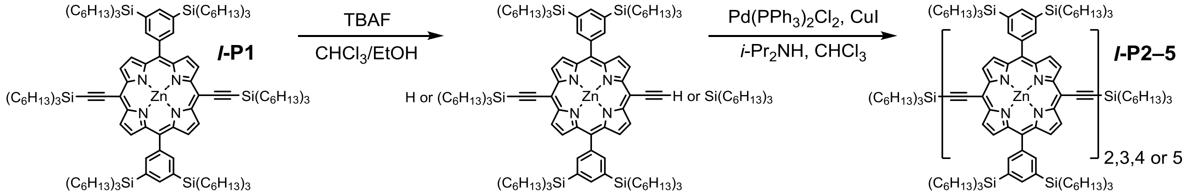

Porphyrin monomer ***l*-P1** (720 mg, 0.32 mmol) was dissolved in $CHCl_3$ (200 mL) with EtOH (2 mL). Tetra-*n*-butylammonium fluoride (1.0 M solution in THF, 1 mL, 1 mmol) was added to the solution and the reaction mixture was stirred at room temperature for 90 min until the TLC spot of mono-deprotected product become as intense and fully protected porphyrin spot. The reaction was quenched by addition of CH_3COOH (86 µL, 1.5 mmol). The reaction mixture was passed immediately through a short silica plug (CH_2Cl_2).The filtered liquid was concentrated on rotatory evaporator, dried and used for further step without purification.

To a solution of mixture of bis-, mono- and non-protected porphyrins ***l*-P1** in $CHCl_3$ (100 mL), $Pd(PPh_3)_2Cl_2$ (90 mg, 0.13 mmol), CuI (130 mg, 0.68 mmol) and 1,4-benzoquinone (200 mg, 1.9 mmol) dispersed in $CHCl_3$ (100 mL) and dry *i*-Pr_2NH (20 mL). The mixture was stirred at room temperature for 6h opened to air. Upon completion, the solution was concentrated and passed through a short silica plug, eluting with $CHCl_3$. Further purification was achieved on short SEC column, eluting with toluene / 1% pyridine and recycling GPC. ***l*-P1** and ***l*-P2** were recovered (yield n.d.), ***l*-P3** – 73 mg (12%), ***l*-P4** – 40 mg (7%), ***l*-P5** – 19 mg (3%). NMR spectra in agreement with published data.[50]

***l*-P3**$_{\mathbf{THS,THS}}$ **^{1}H NMR** (400 MHz, $CDCl_3$ / 1% pyridine-*d*$_5$) δ_H/ppm: 9.90 (d, J = 4.5 Hz, 8H), 9.69 (d, J = 4.5 Hz, 4H), 8.97 (t, J = 4.3 Hz, 8H), 8.87 (d, J = 4.6 Hz, 4H), 8.32 (s, 4H), 8.28 (s, 8H), 8.02 (s, 8H), 8.01 (s, 1H), 1.87–0.77 (m, 546H). **MS(MALDI-ToF)** m/z 5672.1 (M^+, $C_{360}H_{588}N_{12}Si_{14}Zn_3$ requires 5670.1).

Linear deprotected oligomer *l*-P3

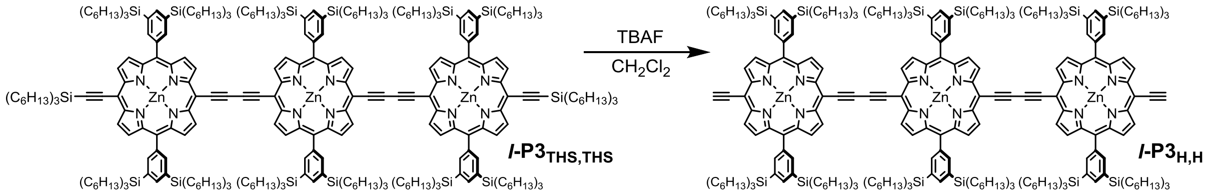

To a solution of ***l*-P3**$_{\mathbf{THS,THS}}$ (75 mg, 0.013 mmol) in $CHCl_3$ (50 mL) was added tetra-*n*-butylammonium fluoride (1.0 M solution in THF, 4 mL, 4 mmol) and a reaction mixture was stirred at room temperature for 2h. The reaction was quenched with CH_3COOH (0.3 mL) and the reaction mixture was passed through a short silica plug (CH_2Cl_2). The filtered liquid was concentrated on rotatory evaporator, dried and excess of TBAF was removed on short SEC column, eluting with toluene / 1% yielding ***l*-P3**$_{\mathbf{H,H}}$ (64 mg, 95%). NMR spectra in agreement with published data.[50]

***l*-P3**$_{\mathbf{H,H}}$. **^{1}H NMR** (400 MHz, $CDCl_3$, 1% pyridine-*d*$_5$) δ_H/ppm: 9.87 (d, J = 4.7 Hz, 4H), 9.85 (d, J = 4.7 Hz, 4H), 9.64 (d, J = 4.6 Hz, 4H), 8.93 (d, J = 4.6 Hz, 4H), 8.91 (d, J = 4.6 Hz, 4H), 8.84 (d, J = 4.5 Hz, 4H), 8.28 (s, 4H), 8.25 (s, 8H), 8.05–7.95 (m, 6H), 4.15 (s, 2H), 1.68–0.78 (m, 468H). **MS(MALDI-ToF)** m/z 5103.1 (M^+, $C_{324}H_{512}N_{12}Si_{12}Zn_3$ requires 5104.6).

4.7.5. Nanorings

Single linked nanoring *c*-P6$^{(1arm)}$·T6

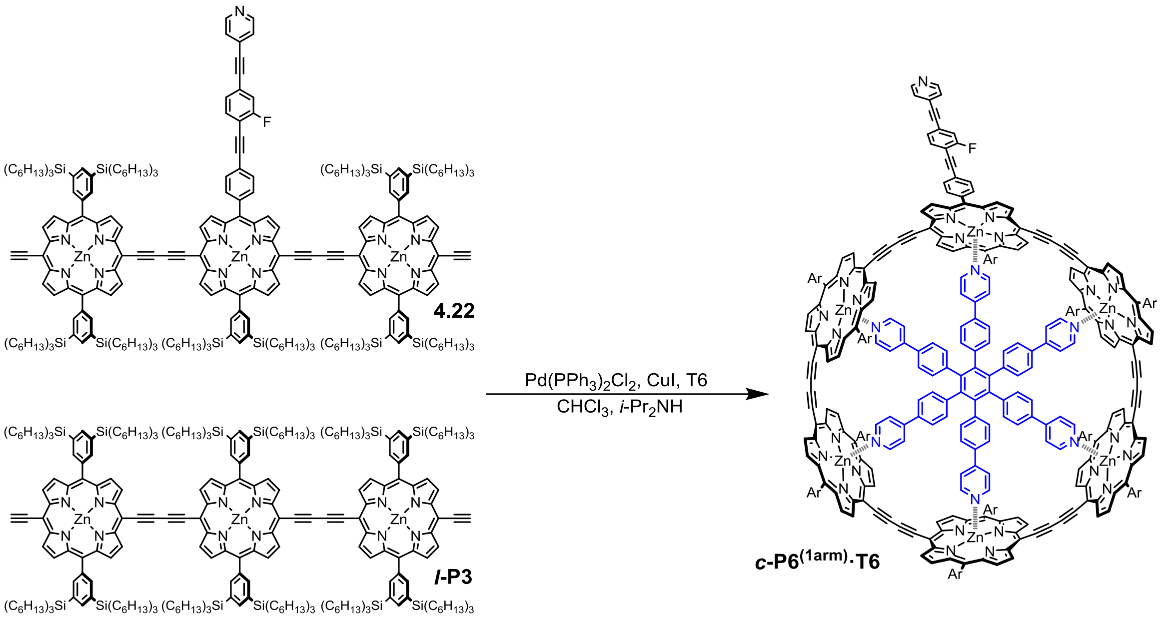

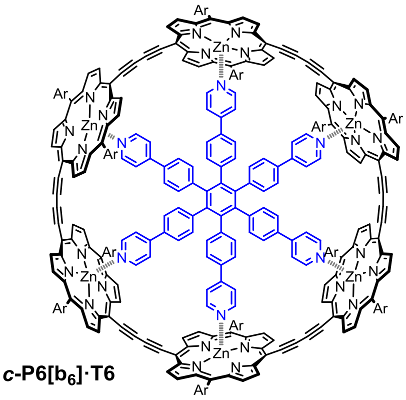
c-P6[b$_6$]·T6

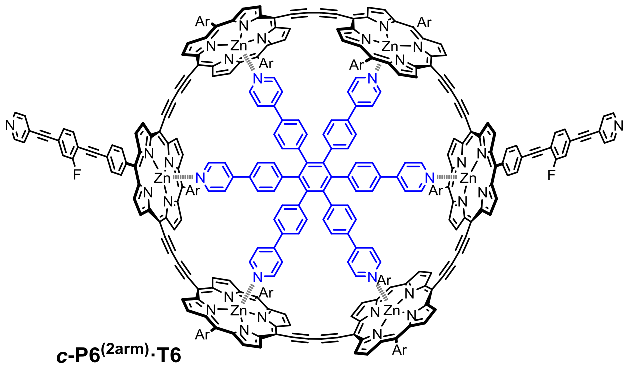
c-P6$^{(2arm)}$·T6

***l*-P3** (64 mg, 13 µmol), **4.22** (36 mg, 8 µmol), **T6** (5 mg, 5 µmol) and 1,4-benzoquinone (40 mg, 0.36 mmol) were dissolved in $CHCl_3$ (20 mL) and *i*-Pr_2NH (1 mL). Mixture was stirred at ambient temperature for 30 min. Solution of $Pd(PPh_3)_2Cl_2$ (1.5 mg, 2 µmol) and CuI (0.4 mg, 2 µmol) in $CHCl_3$ (2 mL) and *i*-Pr_2NH (1 mL) was added to the mixture. The mixture was stirred overnight and another portion of $Pd(PPh_3)_2Cl_2$ (1.5 mg, 2 µmol) and CuI (0.4 mg, 2 µmol) was added. After another 8 hours, the reaction mixture was filtrated through cotton, passed through SEC column and purified by recycling GPC. Fraction containing ***c*-P6** ring size molecules were isolated as a brown solid (16 mg).

The ***c*-P6** fraction contained three products, separable on the SiO_2 (15 g) using hexane / $CHCl_3$ / CH_3OH / pyridine mixture with the gradient increase of polarity (50 / 0 / 0 / 1) → (0/ 50 / 0 / 1) → (0 / 50 / 5 / 1).

***c*-P6[b$_6$]·T6**, R_f = 1 ($CHCl_3$ / 2% pyridine). **^{1}H NMR** (500 MHz, $CDCl_3$) δ_H/ppm: 9.46 (d, *J* = 4.4 Hz, 24H), 8.64 (d, *J* = 4.5 Hz, 24H), 8.52 (d, *J* = 3.8 Hz, 12H), 8.23 (s, 12H), 8.30 (bs, 12H), 7.98–7.92 (m, 24H), 5.44 (d, *J* = 8.5 Hz, 12H), 5.37 (d, *J* = 8.5 Hz, 12H), 4.90 (d, *J* = 6.2 Hz, 12H), 2.37–2.30 (m, 12H), 1.54–1.00 (m, 576H), 1.00–0.49 (m, 360H). **MS(MALDI-ToF)** m/z 11216.4 (M^+, $C_{720}H_{1068}N_{30}Si_{24}Zn_6$ requires 11210.5).

***c*-P6$^{(1arm)}$·T6**, R_f = 0.8 ($CHCl_3$ / 2% pyridine). Isolated 4 mg (6%). **^{1}H NMR** (500 MHz, $CDCl_3$) δ_H/ppm: 9.60–9.51 (m, 24H), 8.80–8.63 (m, 12H), 8.34–8.26 (m, 11H), 8.25–8.20 (m, 2H), 8.08–7.90 (m, 24H), 7.72–7.68 (m, 2H), 7.50–7.37 (m, 4H), 7.20–7.14 (m, 1H), 5.56–5.49 (m, 12H), 5.49–5.42 (m, 12H), 5.02–4.97 (m, 12H), 2.45–2.34 (m, 12H), 1.61–1.16 (m, 528H), 1.03–0.70 (m, 330H). **^{19}F NMR** (371 MHz, $CDCl_3$) δ_F −109.23. **MS(MALDI-ToF)** m/z 10869.5 (M^+, $C_{699}H_{998}FN_{31}Si_{22}Zn_6$ requires 10864.0).

***c*-P6$^{(2arm)}$·T6**, R_f = 0.4 ($CHCl_3$ / 2% pyridine). **^{1}H NMR** (500 MHz, $CDCl_3$) δ_H/ppm: 9.64–9.45 (bm, 24H), 8.81–8.62 (bm, 24H), 8.37–8.26 (bm, 10H), 8.05–7.90 (bm, 30H), 7.73–7.69 (bm, 4H), 7.49–7.39 (bm, 6H), 7.23–7.15 (bm, 2H), 5.56–5.51 (m, 12H), 5.50–5.35 (m, 12H), 5.04–4.91 (m, 12H), 2.46–2.36 (m, 12H), 1.66–1.16 (m, 480H), 1.01–0.69 (m, 300H). **MS(MALDI-ToF)** m/z 11522.7 (M^+, $C_{678}H_{928}F_2N_{32}Si_{20}Zn_6$ requires 10518.5).

Single linked nanoring *c*-P6$^{(1arm)}$

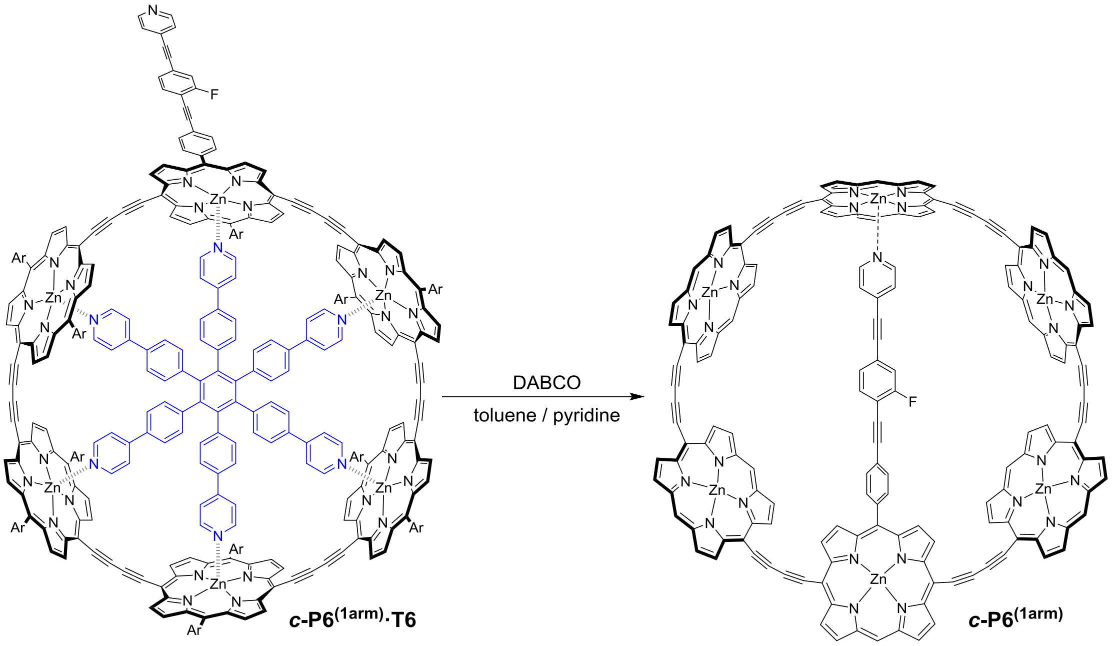

Saturated solution of DABCO (10 mL) in toluene was layered on the top of the SEC column (~100 mL) and the solution was led to replace solvent in the top part of the column. Concentrated solution of ***c*-P6$^{(1arm)}$·T6** (4 mg, 0.4 µmol) in toluene (0.5 mL) was added on the top of the column and was passed through it, eluting with toluene / 1% pyridine. Porphyrin band collected contained pure ***c*-P6$^{(1arm)}$**, which was concentrated and dried yielding brown solid (3 mg).

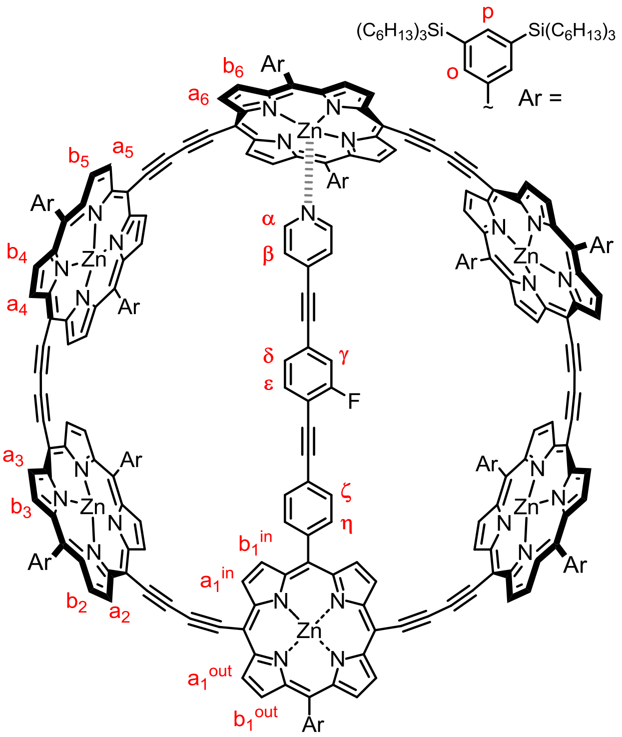

^{1}H NMR (700 MHz, $CDCl_3$) δ_H/ppm: 9.73 (d, $J = 4.4$ Hz, 4H, Ha2–6), 9.71 (d, $J = 4.5$ Hz, 4H, Ha2–6), 9.70 (d, $J = 5.2$ Hz, 2H, Ha1^{out}), 9.70 (d, $J = 4.7$ Hz, 4H, Ha2–6), 9.68 (d, $J = 4.4$ Hz, 4H, Ha2–6), 9.66 (d, $J = 4.5$ Hz, 4H, Ha2–6), 9.26 (d, $J = 5.0$ Hz, 2H, Ha1^{in}), 8.95 (d, $J = 4.9$ Hz, 2H, Hb1^{out}), 8.86 (d, $J = 4.3$ Hz, 4H, Hb2–6), 8.84 – 8.82 (m, 12H, 3×Hb2–6), 8.79 (d, $J = 4.6$ Hz, 4H, Hb2–6), 8.26 (s, 2H, Ho1), 8.21 (d, $J = 4.7$ Hz, 2H, Hb1^{in}) 8.18 (s, 20H, 6×Ho2–6), 8.03 (s, 1H, Hp1), 7.99 (s, 6H, 3×Hp2–6), 7.94 (s, 4H, 2×Hp2–6), 7.57 (d, $J = 7.8$ Hz, 2H, Hη), 7.16 (d, $J = 7.8$ Hz, 2H, Hζ), 6.61 (t, $J = 7.5$ Hz, 1H, Hε), 6.13 (d, $J = 8.4$ Hz, 1H, Hγ/δ), 6.11 (d, $J = 9.4$ Hz, 2H, Hγ/δ), 5.23 (d, $J = 6.0$ Hz, 2H, Hβ), 2.49 (d, $J = 5.3$ Hz, 2H, Hα), 1.63–0.72 (m, 858H, THS). **^{19}F NMR** (371 MHz, $CDCl_3$) δ_F/ppm: −109.93. **MS(MALDI-ToF)**, m/z 9876 (M$^+$, $C_{627}H_{950}FN_{25}Si_{22}Zn_6$ requires 9868).

For the assignment, NOE between **β** and **γ/δ** resonances was sought to prove that they are part of one arm. Furthermore, NOE between **α** and THS region was also looked for. Unfortunately, neither using 2D NOESY nor with selective NOE routines with extended mixing time, the **β** ⇄ **γ** or **α** ⇄ **THS** NOE could be detected, as probably the resonances are too far apart. The only support left for the pyridine-arm coordination is thus its ^{1}H chemical shift affected by the porphyrin coordination.

Triply linked nanoring *c*-P6$^{(3arm)}$·T6

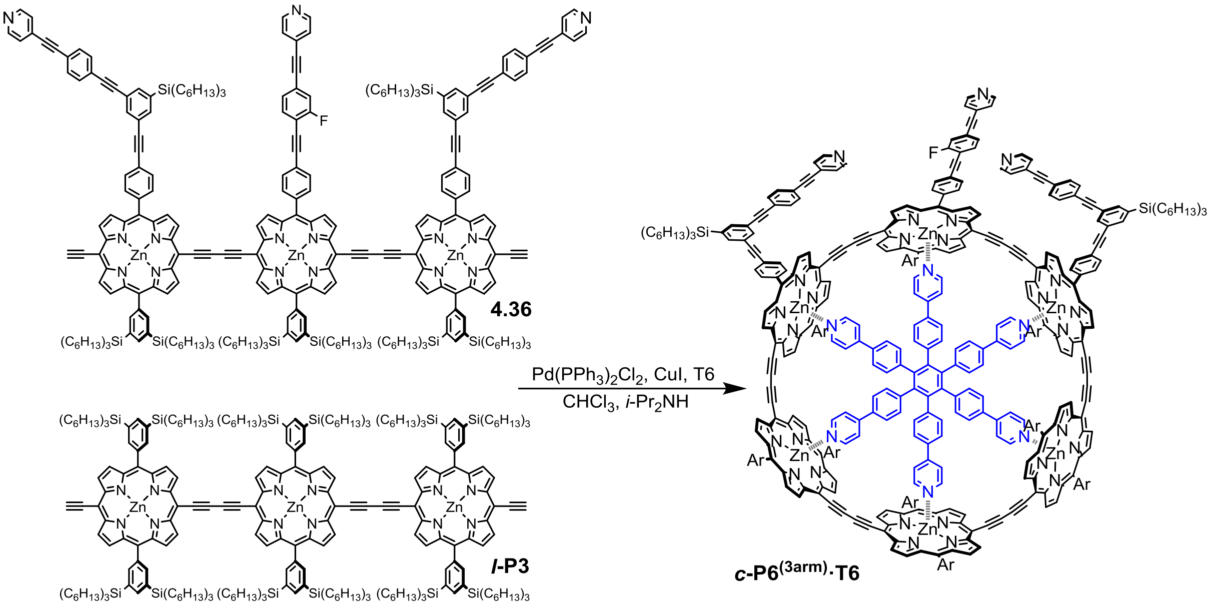

***l*-P3** (35 mg, 6.9 µmol), **4.36** (32 mg, 6.6 µmol), **T6** (6.1 mg, 6.1 µmol) and 1,4-benzoquinone (100 mg, 1 mmol) were dissolved in $CHCl_3$ (25 mL) and *i*-Pr_2NH (0.5 mL). The mixture was stirred at ambient temperature for 30 min. Then, $Pd(PPh_3)_2Cl_2$ (8.6 mg, 12 µmol) and CuI (4.6 mg, 24 µmol) were well dispersed in $CHCl_3$ (2 mL) and *i*-Pr_2NH (0.5 mL) and added to the mixture. Mixture was stirred for 8 hours at ambient temperature. Then, the reaction mixture was filtrated through cotton, passed through a SEC column to remove excess of benzoquinone. The porphyrin fraction was purified using recycling GPC, separating the ***c*-P6** fraction (13.6 mg). This fraction was purified on Et_3N passivated SiO_2 (20 g) using eluent mixture of hexane/$CHCl_3$/CH_3OH/pyridine with the gradient increasing of the polarity 10/0/0/1 → 0/100/0/1 →0/100/7/1 yielding desired fraction ***c*-P6$^{(3arm)}$·T6** (2.6 mg, 4.3%).

^{1}H NMR (500 MHz, $CDCl_3$) δ_H/ppm: 9.69–9.48 (m, 24H), 8.81–8.58 (m, 24H), 8.33–7.89 (m, 34H), 7.87 (s, 2H), 7.78 (s, 2H), 7.72–7.40 (m, 22H), 6.96 (d, $J = 9.3$ Hz, 4H), 6.89 (d, $J = 8.5$ Hz, 4H), 5.58–5.37 (m, 24H), 5.08–4.94 (m, 12H), 2.37 (d, $J = 8.7$ Hz, 12H), 1.53–0.69 (m, 780H). NMR significantly broadened as statistical mixtures of three products is expected (↑↑↑, ↓↑↑ and ↓↑↓). **MS(MALDI-ToF)** m/z 10905 (M^+, $C_{709}H_{944}FN_{33}Si_{20}Zn_6$ requires 10902).

Triply linked nanoring *c*-P6$^{(3arm)}$

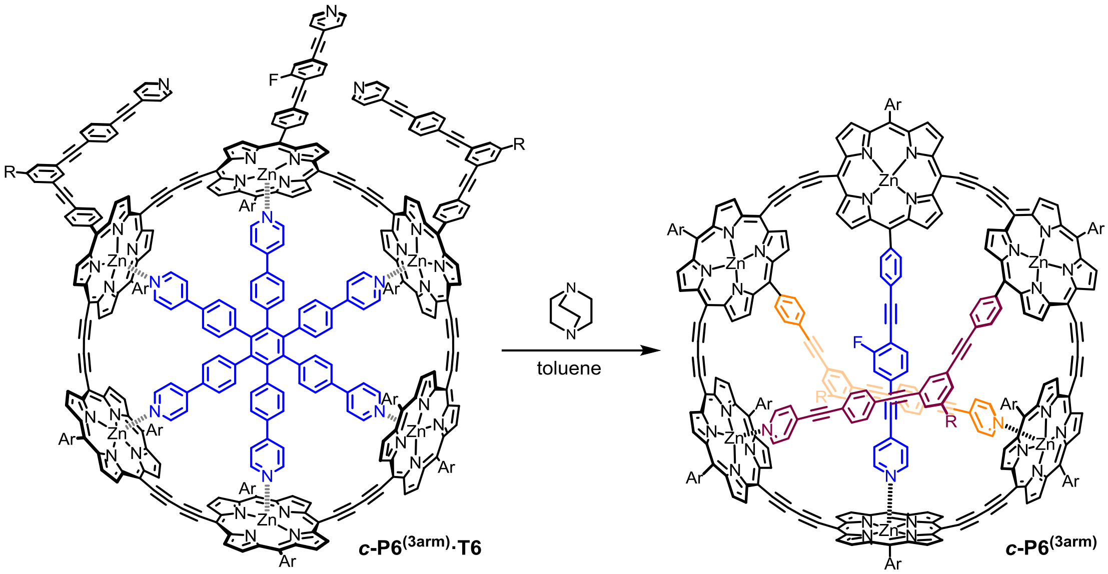

Saturated solution of DABCO (5 mL) in toluene was layered on the top of the SEC column (~50 mL) and was led to replace the top part of the solvent. Concentrated solution of ***c*-P6$^{(3arm)}$·T6** (2.6 mg, 0.2 µmol) in toluene (0.3 mL) was added on the top of the column and was washed through with toluene / 1% pyridine solution. The porphyrin band collected contained pure ***c*-P6$^{(3arm)}$**, which was concerted and dried yielding a brown solid (2 mg, 85%).

^{1}H NMR (600 MHz, C_6D_6) δ_H/ppm: 10.23–9.80 (m, 24H), 9.40–9.06 (m, 22H), 8.98–8.30 (m, 34H), 8.02–7.61 (m, 14H), 7.12–6.50 (m, 22H), 4.37–4.14 (m, 6H), 2.71–2.50 (m, 6H), 1.90–0.53 (m, 780H). **^{19}F NMR** (371 MHz, C_6D_6) δ_F/ppm: −109.32. **MS(MALDI-ToF)**, high-resolution measurement at EPSRC UK NMSF, Swansea, m/z 9905 (M^+, $C_{637}H_{896}FN_{27}Si_{20}Zn_6$ requires 9905).

Spectrum not edited with DOSY routine is presented to document the poor solubility (**Figure 72**).

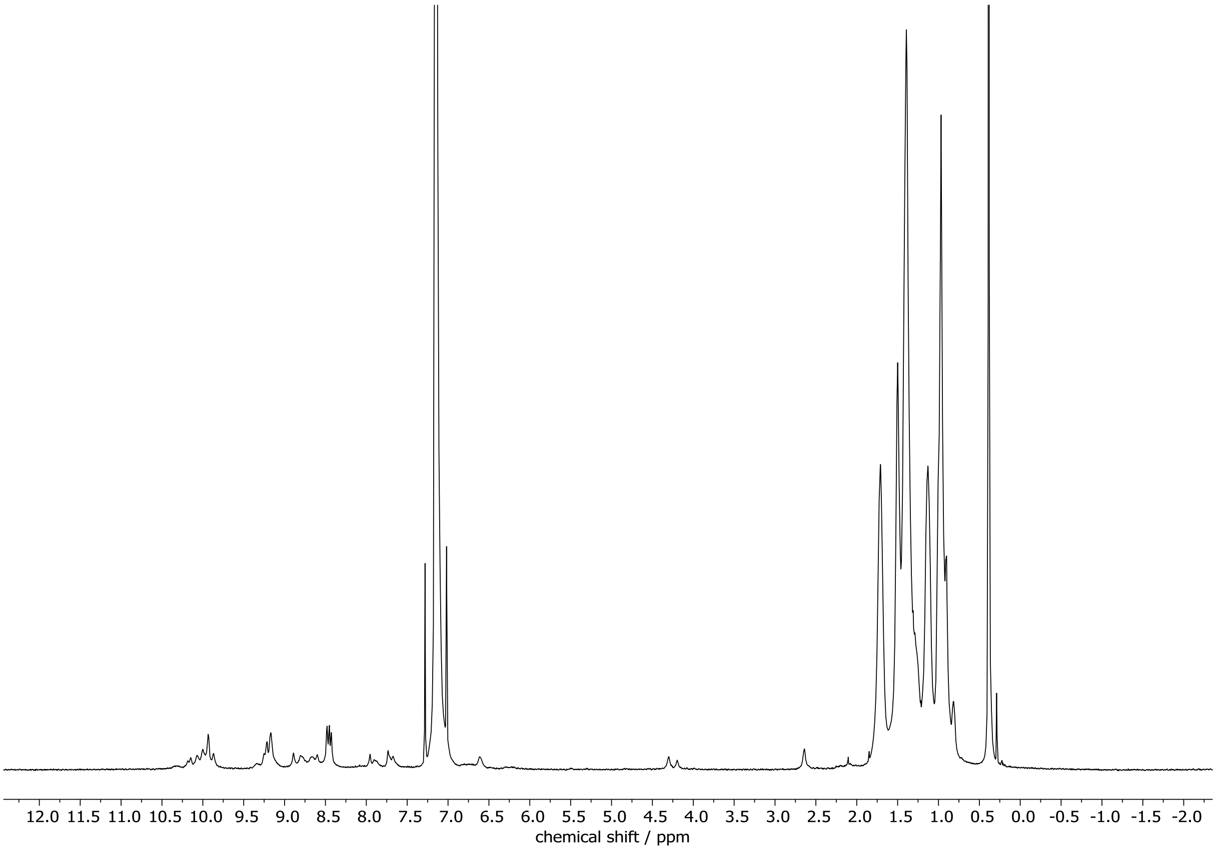

Figure 72. ^{1}H NMR (700 MHz, C_6D_6) of ***c*-P6**$^{(3arm)}$.

The best solubility was found in aromatic solvents benzene-d_6 and toluene-d_8. To increase the solubility in toluene-d_8, small amount of weakly coordinating ligand, was added. The balance between de-aggregation and pyridine-containing arm decoordination was sought by very slow increasing content of THF-d_8. Unfortunately, as soon as the intensity start rising as the compound is getting to the solution, the decoordination of arm is concurrently observed. The best balance was achieved of content of THF 0.4–0.75% in toluene. At such solvent mixture, the **α** resonances get slightly split unveiling the expected dissymmetry (**Figure 73**).

Addition of the pyridine significantly increased solubility, however was accompanied with immediate pyridine arms decoordination. This is seen as travel of **α** and **β** signals from very shielded chemical shifts of 2–3 ppm and 4–5 ppm toward expected aromatic regions of ~9 ppm and 7 ppm, respectively.

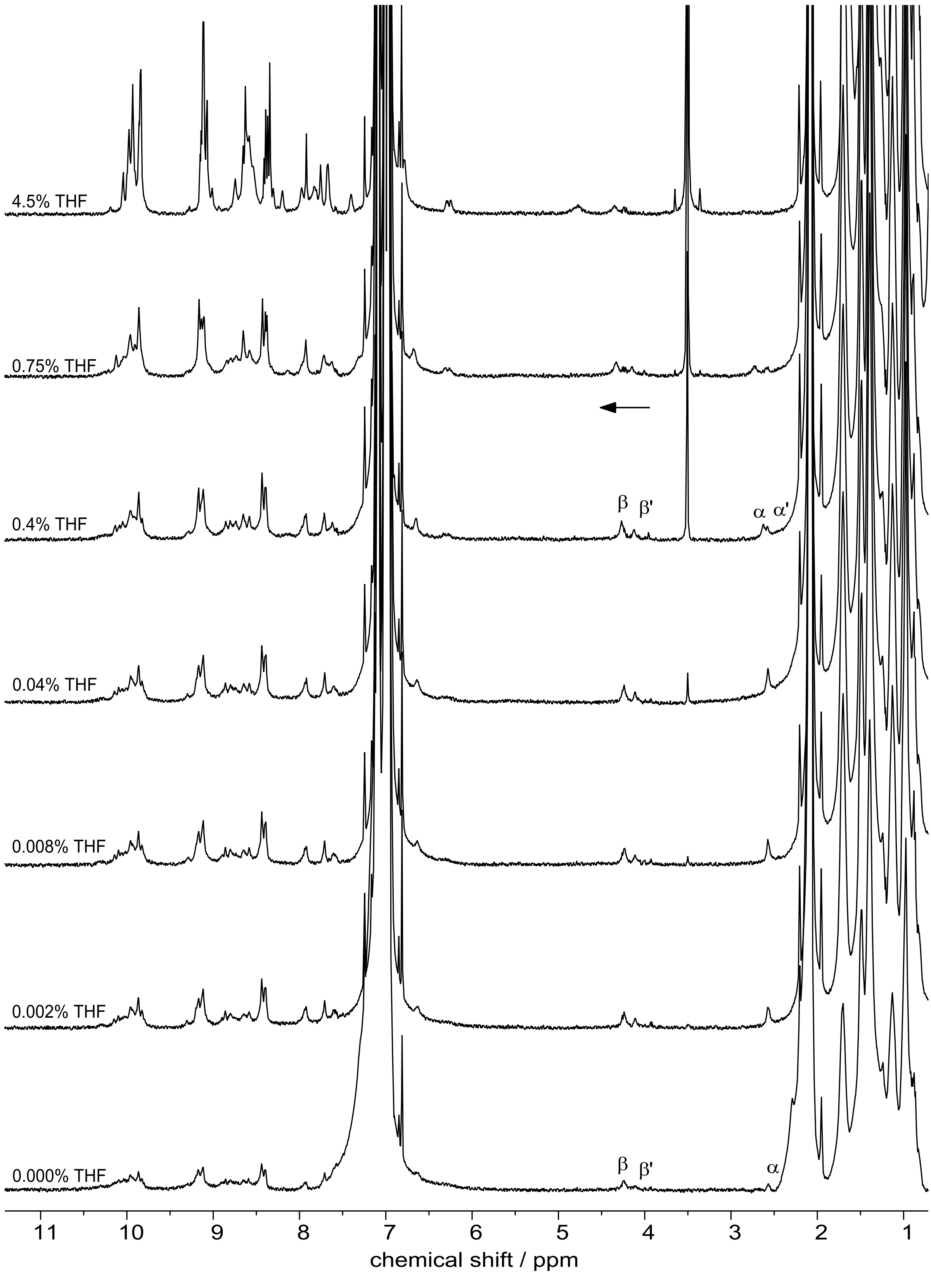

Figure 73. ^{1}H NMR (500 MHz, toluene-d_8) of ***c*-P6**$^{\mathbf{(3arm)}}$ with various amount of THF-d_8.

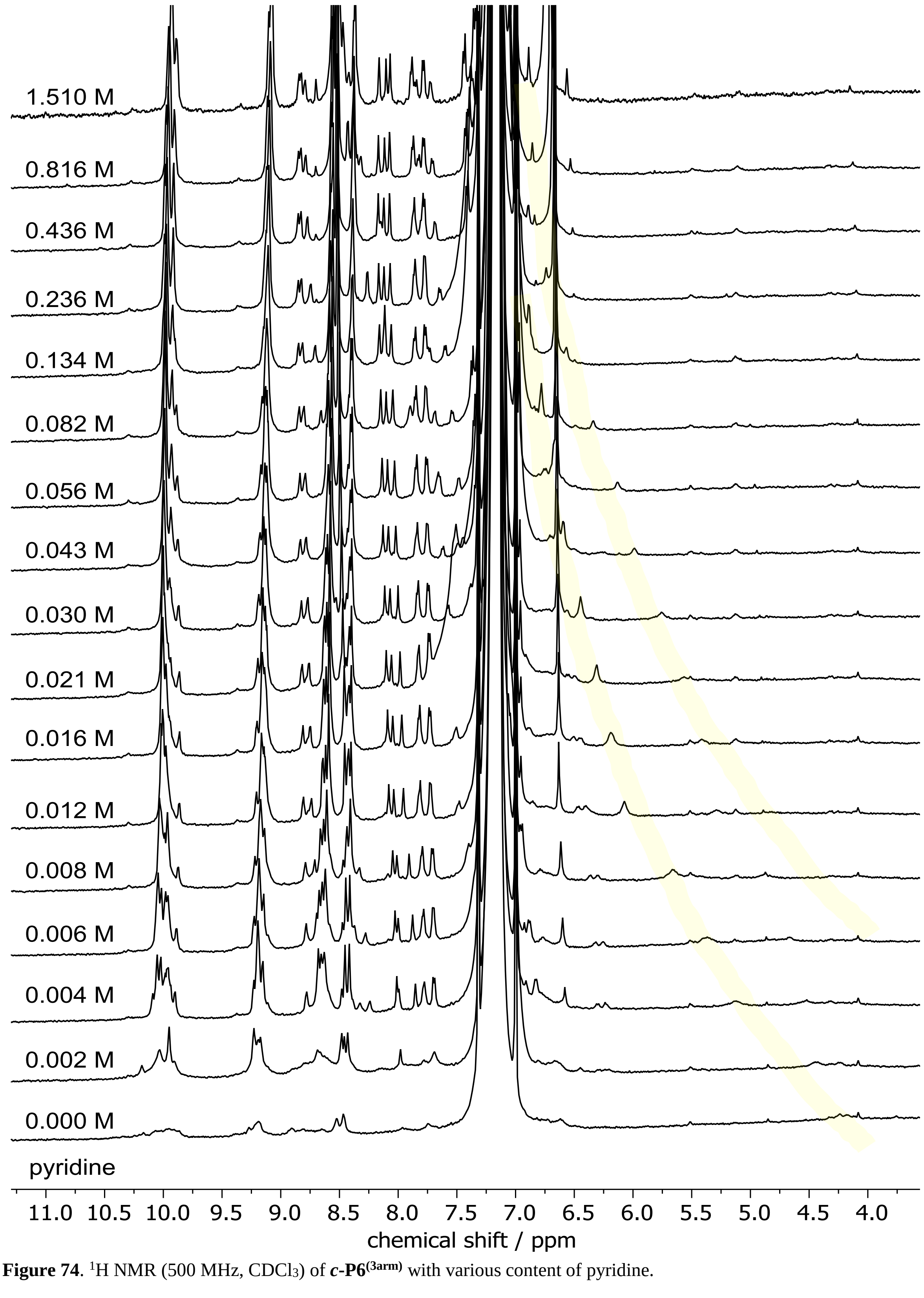

Figure 74. ^1H NMR (500 MHz, $CDCl_3$) of ***c*-P6**$^{\mathbf{(3arm)}}$ with various content of pyridine.

4.8. References

[1] J. H. E. Cartwright, D. L. González, *Math. Intell.* **2016**, *38*, 69–76.

[2] I. Karonen, "Mobius Resistor," can be found under https://commons.wikimedia.org/wiki/File:Möbius_resistor.svg, **2006**.

[3] G. Călugăreanu, *Czechoslov. Math. J.* **1961**, *11*, 588–625.

[4] S. M. Rappaport, H. S. Rzepa, *J. Am. Chem. Soc.* **2008**, *130*, 7613–7619.

[5] F. B. Fuller, *Proc. Natl. Acad. Sci. U. S. A.* **1971**, *68*, 815–819.

[6] J. H. White, *Am. J. Math.* **1969**, *91*, 693–728.

[7] G. R. Schaller, R. Herges, *Chem. Commun.* **2013**, *49*, 1254–1260.

[8] L. N. Wirz, M. Dimitrova, H. Fliegl, D. Sundholm, *J. Phys. Chem. Lett.* **2018**, *9*, 1627–1632.

[9] E. Heilbronner, *Tetrahedron Lett.* **1964**, *5*, 1923–1928.

[10] C. Castro, C. M. Isborn, W. L. Karney, M. Mauksch, P. von R. Schleyer, *Org. Lett.* **2002**, *4*, 3431–3434.

[11] R. Herges, *Chem. Rev.* **2006**, *106*, 4820–4842.

[12] P. v. R. Schleyer, J. C. Barborak, T. M. Su, G. Boche, G. Schneider, *J. Am. Chem. Soc.* **1971**, *93*, 279–281.

[13] A. G. Anastassiou, E. Yakali, *J. Chem. Soc. Chem. Commun.* **1972**, 92.

[14] M. Mauksch, V. Gogonea, H. Jiao, P. von R. Schleyer, *Angew. Chemie* **1998**, *110*, 2515–2517.

[15] C. Castro, Z. Chen, C. S. Wannere, H. Jiao, W. L. Karney, M. Mauksch, R. Puchta, N. J. R. van E. Hommes, P. von R. Schleyer, *J. Am. Chem. Soc.* **2005**, *127*, 2425–2432.

[16] M. Mauksch, S. B. Tsogoeva, *Eur.J. Org. Chem.* **2008**, *2008*, 5755–5763.

[17] M. N. Braten, C. Castro, R. Herges, F. Köhler, W. L. Karney, *J. Org. Chem.* **2008**, *73*, 1532–1535.

[18] E.-K. Mucke, B. Schönborn, F. Köhler, R. Herges, *J. Org. Chem.* **2011**, *76*, 35–41.

[19] G. Bucher, S. Grimme, R. Huenerbein, A. A. Auer, E. Mucke, F. Köhler, J. Siegwarth, R. Herges, *Angew. Chemie* **2009**, *121*, 10156–10159.

[20] E.-K. Mucke, F. Köhler, R. Herges, *Org. Lett.* **2010**, *12*, 1708–1711.

[21] D. Ajami, O. Oeckler, A. Simon, R. Herges, *Nature* **2003**, *426*, 819–821.

[22] M. Stępień, L. Latos-Grażyński, N. Sprutta, P. Chwalisz, L. Szterenberg, *Angew. Chem. Int. Ed.* **2007**, *46*, 7869–7873.

[23] Y. Y. Fan, D. Chen, Z. A. Huang, J. Zhu, C. H. Tung, L. Z. Wu, H. Cong, *Nat. Commun.* **2018**, *9*, 2–6.

[24] G. Naulet, L. Sturm, A. Robert, P. Dechambenoit, F. Röhricht, R. Herges, H. Bock, F. Durola, *Chem. Sci.* **2018**, *9*, 8930–8936.

[25] D. Ajami, K. Hess, F. Köhler, C. Näther, O. Oeckler, A. Simon, C. Yamamoto, Y. Okamoto, R. Herges, *Chem. – A Eur. J.* **2006**, *12*, 5434–5445.

[26] K. Möbius, M. Plato, G. Klihm, C. Laurich, A. Savitsky, W. Lubitz, B. Szyszko, M. Stępień, L. Latos-Grażyński, *Phys. Chem. Chem. Phys.* **2015**, *17*, 6644–6652.

[27] J. Sankar, S. Mori, S. Saito, H. Rath, M. Suzuki, Y. Inokuma, H. Shinokubo, K. Suk Kim, Z. S. Yoon, J.-Y. Shin, J. M. Lim, Y. Matsuzaki, O. Matsushita, A. Muranaka, N. Kobayashi, D. Kim, A. Osuka, *J. Am. Chem. Soc.* **2008**, *130*, 13568–13579.

[28] J. K. Park, Z. S. Yoon, M.-C. Yoon, K. S. Kim, S. Mori, J.-Y. Shin, A. Osuka, D. Kim, *J. Am. Chem. Soc.* **2008**, *130*, 1824–1825.

[29] H. S. Rzepa, *Org. Lett.* **2008**, *10*, 949–952.

[30] H. S. Rzepa, *Org. Lett.* **2009**, *11*, 3088–3091.

[31] T. Higashino, M. Inoue, A. Osuka, *J. Org. Chem.* **2010**, *75*, 7958–7961.

[32] J. L. Sessler, S. J. Weghorn, V. Lynch, M. R. Johnson, *Angew. Chem. Int. Ed.* **1994**, *33*, 1509–1512.

[33] M. Bröring, J. Jendrny, L. Zander, H. Schmickler, J. Lex, Y.-D. Wu, M. Nendel, J. Chen, D. A. Plattner, K. N. Houk, E. Vogel, *Angew. Chem. Int. Ed.* **1995**, *34*, 2515–2517.

[34] E. Vogel, M. Bröring, J. Fink, D. Rosen, H. Schmickler, J. Lex, K. W. K. Chan, Y.-D. Wu, D. A. Plattner, M. Nendel, K. N. Houk, *Angew. Chem. Int. Ed.* **1995**, *34*, 2511–2514.

[35] T. Woller, J. Contreras-García, P. Geerlings, F. De Proft, M. Alonso, *Phys. Chem. Chem. Phys.* **2016**, *18*, 11885–11900.

[36] Y. Tanaka, S. Saito, S. Mori, N. Aratani, H. Shinokubo, N. Shibata, Y. Higuchi, Z. S. Yoon, K. S. Kim, S. B. Noh, J. K. Park, D. Kim, A. Osuka, *Angew. Chem. Int. Ed.* **2008**, *47*, 681–684.

[37] G. R. Schaller, F. Topić, K. Rissanen, Y. Okamoto, J. Shen, R. Herges, *Nat. Chem.* **2014**, *6*, 608–613.

[38] M. J. Frisch, G. W. Trucks, H. B. Schlegel, G. E. Scuseria, M. A. Robb, J. R. Cheeseman, G. Scalmani, V. Barone, G. A. Petersson, B. Mennucci, G. A. Petersson, H. Nakatsuji, X. Li, M. Caricato, A. V Marenich, J. Bloino, B. G. Janesko, R.

Gomperts, B. Mennucci, H. P. Hratchian, J. V. Ortiz, A. F. Izmaylov, J. L. Sonnenberg, D. Williams-Young, F. Ding, F. Lipparini, F. Egidi, J. Goings, B. Peng, A. Petrone, T. Henderson, D. Ranasinghe, V. G. Zakrzewski, J. Gao, N. Rega, G. Zheng, W. Liang, M. Hada, M. Ehara, K. Toyota, R. Fukuda, J. Hasegawa, M. Ishida, T. Nakajima, Y. Honda, O. Kitao, H. Nakai, T. Vreven, K. Throssell, J. A. J. Montgomery, J. E. Peralta, F. Ogliaro, M. J. Bearpark, J. J. Heyd, E. N. Brothers, K. N. Kudin, V. N. Staroverov, T. A. Keith, R. Kobayashi, J. Normand, K. Raghavachari, A. P. Rendell, S. S. Burant, J. C. Iyengar, J. Tomasi, M. Cossi, J. M. Millam, M. Klene, C. Adamo, R. Cammi, J. W. Ochterski, R. L. Martin, K. Morokuma, O. Farkas, J. B. Foresman, D. J. Fox, **2016**, Gaussian 16, Revision A.03, Gaussian, Inc., Wallin.

[39] D. Gelman, S. L. Buchwald, *Angew. Chem. Int. Ed.* **2003**, *42*, 5993–5996.

[40] M. D. Peeks, C. E. Tait, P. Neuhaus, G. M. Fischer, M. Hoffmann, R. Haver, A. Cnossen, J. R. Harmer, C. R. Timmel, H. L. Anderson, *J. Am. Chem. Soc.* **2017**, *139*, 10461–10471.

[41] C. A. Hunter, H. L. Anderson, *Angew. Chem. Int. Ed.* **2009**, *48*, 7488–7499.

[42] M. Hoffmann, J. Kärnbratt, M.-H. Chang, L. M. Herz, B. Albinsson, H. L. Anderson, *Angew. Chem. Int. Ed.* **2008**, *47*, 4993–4996.

[43] J. K. Sprafke, D. V. Kondratuk, M. Wykes, A. L. Thompson, M. Hoffmann, R. Drevinskas, W. H. Chen, C. K. Yong, J. Kärnbratt, J. E. Bullock, M. Malfois, M. R. Wasielewski, B. Albinsson, L. M. Herz, D. Zigmantas, D. Beljonne, H. L. Anderson, *J. Am. Chem. Soc.* **2011**, *133*, 17262–17273.

[44] R. Haver, L. Tejerina, H.-W. Jiang, M. Rickhaus, M. Jirasek, I. Grübner, H. J. Eggimann, L. M. Herz, H. L. Anderson, *J. Am. Chem. Soc.* **2019**, *141*, 7965–7971.

[45] J. Q. Gong, L. Favereau, H. L. Anderson, L. M. Herz, *J. Phys. Chem. Lett.* **2016**, *7*, 332–338.

[46] C. Gonzalez, Y. Simón-Manso, J. Batteas, M. Marquez, M. Ratner, V. Mujica, *J. Phys. Chem. B* **2004**, *108*, 18414–18420.

[47] R. Rathore, C. L. Burns, I. A. Guzei, *J. Org. Chem.* **2004**, *69*, 1524–1530.

[48] R. Packheiser, P. Ecorchard, T. Rüffer, H. Lang, *Chem. – A Eur. J.* **2008**, *14*, 4948–4960.

[49] J. A. Swain, G. Iadevaia, C. A. Hunter, *J. Am. Chem. Soc.* **2018**, *140*, 11526–11536.

[50] C. E. Tait, P. Neuhaus, M. D. Peeks, H. L. Anderson, C. R. Timmel, *J. Am. Chem. Soc.* **2015**, *137*, 8284–8293.